Characterisation of Multiple Concentric Vortices in Hybrid Rocket Combustion Chambers

Neil Wall

Department of Mechanical Engineering

The University of Sheffield

A thesis submitted for the degree of

Doctor of Philosophy

April 2013

To my grandparents who unfortunately never got to see me complete my studies.

Acknowledgements

First of all I would like to express my sincere thanks to my supervisor Dr. Robert Howell, who has guided me through each step of my PhD and helped me in every way possible to ensure that I accomplish this research. Without his influence it would not of been possible to conduct this study and he has valiantly tried to keep me on track even in the face of numerous issues, keeping me focused on the work at hand and not let me get too distracted with finding a solution to every single problem I came across. Also the visits to Fagan's for a pub lunch were much appreciated and desperately needed at times, especially when faced with what seemed like insurmountable problems caused by the ever fickle behaviour of Fluent.

Other important people that have helped me along the way include several of my work colleagues within the CFD and experimental aerodynamics research groups, who have provided me with invaluable advice with regards to the various aspects of CFD including mesh generation, solver setup, post-processing and most importantly obtaining a converged solution. Dr. Greg Carnie and Dr. Naveed Durrani were especially helpful in highlighting the various methods and tricks of the trade to ensure that I was able to produce worthwhile results, despite the differences in our engineering backgrounds. Learning how to use CFD effectively and conduct a thorough analysis is an unrelenting and arduous task, but with their guidance I was able to increase my own knowledge on the subject and this gave me the ability to then pass on that knowledge to other colleagues.

The work involved in obtaining a PhD is neither a simple or a short lived task, and for all those moments of overwhelming joy and satisfaction that are associated with making some form of progress there are also very long periods of frustration and sheer contempt. During these periods I was thankful to be surrounded by people in a similar position who I could talk to and vent my frustrations, as we exchanged our grievances with CFD and talk about things other than work. I'd like to thank Dr. Jonathan Edwards who was particularly astute in discerning exactly when a cup of tea and a chat was needed to break the monotony of work, as was Dr. Andrew Dennison who frequently suggested trips away from the engineering department, and I appreciate my time with them. Also I'd like to thank Dr. Demian De Feo and Dr. Mohammed El Fadil who provided input on a variety of matters relating to CFD or otherwise and made the office a more friendly place to work. Additionally I'd like to thank all of my family and friends such as Dr. Nick Cooper who have supported me along the way and have taken interest in my work, even if they didn't know exactly what I was talking about most of the time. Finally I would like to thank the EPSRC, who funded my PhD and without whom this research would not have been possible.

Abstract

Recent developments in hybrid rocket technology involve producing a coaxial bidirectional vortex flow field through use of tangential oxidiser injection at the base of the combustion chamber. This is found to significantly increase engine performance by providing enhanced thermal transfer at the fuel surface, resulting in increased fuel regression rates in addition to more efficient combustion. The double helical path of the flow results in reduced reactant loss at the chamber outlet whilst confining combustion to a high temperature core region defined by the inner vortex. This also results in enhanced thermal shielding as a large radial thermal gradient is established, which affords lightweight materials to used in the construction of the combustion chamber making it suitable for weight sensitive applications such as satellite propulsion.

Analytical treatment of the coaxial bidirectional vortex has repeatedly found that it is theoretically possible to induce a vortex flow field consisting of multiple concentric vortices, which would further increase the benefits associated with the coaxial bidirectional vortex. Each additional vortex would further increase the length of the helical trajectory of the flow and allow for more compact combustion chambers to be designed which are both lightweight and highly efficient. However, the existence of multiple concentric vortices has yet to be confirmed and the parameters involved in producing such phenomenon are unknown, as are the parameters required to manipulate their behaviour. Therefore, the focus of this study is to investigate whether it is possible to induce multiple concentric vortices and affect their behaviour through parametric variation of geometrical constraints which are found to significantly influence vortex characteristics in similar cyclonic devices.

A twofold approach is employed to investigate a range of cyclone chamber configurations both experimentally and numerically, in order to ascertain the effectiveness of each method with regards to resolving complex vortical flows and to observe and similarities in the results obtained. Due to experimental constraints a hydrocyclone was used in place of a gas cyclone which is commonly used to characterise the behaviour of the coaxial bidirectional vortex. The numerical analysis was performed using CFD, where 3D simulations were necessary to adequately resolve the spatio-temporal behaviour of the flow, with specific consideration given to solver settings applicable to the resolution of intense swirling flow. While the experimental analysis was conducted using a 2D time resolved PIV method, this was applied to the meridional and azimuthal planes of the cyclone chamber to enable comparison of the number of concentric vortices and the general characteristics of the vortex.

Despite the limitations of the techniques applied it was found that it is possible to produce a confined vortex consisting of multiple concentric vortices, although the resultant flow structures are considerably more complex than initially thought. However, it was also found that the geometry of the cyclone chamber has a significant influence upon the structure of the vortex, with small chamber aspect ratios and large contraction ratios producing intense vortices which are associated with multiple concentric vortices. The position of the tangential inlets is also found to have a significant impact upon the structure of the flow, and several configurations of multiple concentric vortices were observed that are not accounted for by the analytical solutions. Another important result that was consistently observed is that the locus of zero axial velocity which defines the number of concentric vortices takes the form of modal structures, which appear to evolve in response to threshold geometrical parameters. It is thought that the underlying fluid mechanics of multiple concentric vortices are inherently linked to the harmonic characteristics of the cyclone chamber geometry, as several mechanisms have been identified which may allow for direct control over the structure of the vortex.

Contents

List of Figures

x

List of Tables

Nomenclature

Alphabetical

A Arrhenius pre exponential factor, area

a acceleration, regression rate coefficient, wave amplitude

B blowing number, tangential angular momentum

C circulation constant

c wave velocity

C_{ent} entrainment coefficient

C_F force coefficient

C_f skin friction coefficient without blowing

C_p pressure coefficient, specific heat at constant pressure

D diameter, duty cycle, mass diffusivity, velocity gradient tensor

d effective interrogation window displacement

d_{ij} component of velocity gradient tensor

E energy

e mass flux exponent

F force

f frequency

f_0 fundamental resonant frequency

G Gaussian function, instantaneous mass flux, axial flux of momentum

g gravitational acceleration

H dome height

h convective heat transfer coefficient

h_g effective heat of gasification

I impulse, base image pixel intensity field, intensity

I' cross image pixel intensity field

J_0 Bessel function of the first kind (zeroth order)

J_1	Bessel function of the first kind (1st order)
k	axial wave number, azimuth wave mode, inflow parameter
K'	entrainment parameter coefficient
k_g	gas phase conductivity
L	chamber length
l	characteristic length scale
l_R	length of resonance chamber
M	momentum
m	azimuth wave number, flow reversal mode, mass, radial wave mode
N	number of injectors, number of vortices in vortex array
n	arbitary integer, axial wave mode, carbon number, radial order of mantle
p	static pressure
p_0	total pressure
Q	flow rate, second invariant of velocity gradient tensor, mesh quality
q	thermal energy, normalised particle diameter
R	chamber radius
r	radius
$R_{II'}$	convolution function
R_u	universal gas constant
s	surface absoptivity
T	temperature, period
t	time
t_0	initial time
u	velocity
u'	root mean square of turbulent velocity fluctuations
v	volume
v_f	volume fraction
W	strain rate tensor
x	Cartesian dimension
y	Cartesian dimension
y^+	non dimensional wall distance
z	axial dimension

Symbols

$\dot{}$	rate of change with respect to time
$*$	characteristic value
α	Beltramian solution constant, order of Bessel function, thermal diffusivity
β	normalised mantle position, Bessel function parameter
χ	thickness exponent
Δ	delta
δ	boundary layer thickness
η	combustion efficiency
Γ	circulation
γ	specific ratio of heats
$\Im$	imaginary value
κ	turbulent kinetic energy
λ	eigenvalue, wavelength
$\mathbf{u}$	velocity vector
μ	dynamic viscosity
ν	kinematic viscosity
Ω	angular velocity, swirl intensity, vorticity tensor
ω	angular frequency, angular velocity, oscillation frequency, vorticity
∂	partial derivative
ϕ	azimuth angle
ψ	streamfunction
$\Re$	real value
σ	surface tension, modified swirl number
τ	eigenperiod, shear stress
θ	half apex angle relative to chamber axis, angle of convergence
υ	eigenvector
ε	turbulent dissipation rate
φ	root of Bessel function of the first kind J_1
ς	nozzle area ratio
ϑ	injector tilt angle
ξ	kinetic energy density

Subscripts

$\Im i$	imaginary part of complex variable
∞	freestream or limiting value
ϕ	tangential
$\Re$	real
$\Re i$	real part of complex variable
a	ambient
act	activation
avg	mean value
b	burn
bo	boiling
c	core
ch	chamber
chm	chemical
$core$	air core
crt	critical value
d	disc
e	exit
eas	equiangle skew
ent	entrainment
eq	equiangular element
evs	equivolume skew
f	fuel
fl	fluid
flm	flame
h	head
in	inlet
k	tangential wave mode
l	melt layer
m	radial wave mode
max	maximum
min	minimum
mlt	melting

n	axial wave mode
ox	oxygen
p	particle
pls	pulse
prt	combustion port
r	radial
ref	reference
rot	rotational
s	surface
sp	specific
sw	swirl
t	throat
th	theoretical
tot	total
tur	turbulent
v	vortex
vap	vaporisation
w	wall
x	Cartesian direction
y	Cartesian direction
z	axial

Dimensionless Numbers

Ek	Ekman number
Le	Lewis number
Ma	Mach number
Pr	Prandtl number
Re	Reynolds number
Ro	Rossby number
S	swirl number
S_k	Stokes number
Sc	Schmidt number
Sh	Strouhal number

St Stanton number

V vortex Reynolds number

Acronyms

$ACRM$ abrupt convergence resonance model

AMG algebraic multi grid

BEM blade element method

BL Beltramian

CCD charge coupled device

$CCRM$ conical convergence resonance model

CCW counter clockwise

CFD computational fluid dynamics

CL complex lamellar

$CMOS$ complementary metal oxide semiconductor

CPU central processing unit

CR chamber contraction ratio

CRZ central recirculation zone

$CTPB$ carbon-terminated polybutadiene

CVL copper vapour laser

CW clockwise

DES detached eddy simulation

DNS direct numerical simulation

DOF depth of field

$DPSS$ diode pumped solid state

EXP experimental

FEM finite element method

FFT fast Fourier transform

$FLOX$ fluorinated oxygen

FOV field of view

FSI fluid structure interaction

$HDPE$ high density polyethylene

HPC high performance computing

$HRIC$ high resolution interface capturing

HTP high test peroxide

$HTPB$ hydroxyl-terminated polybutadiene

ID inner diameter

$ISVE$ impinging stream vortex engine

LDA laser Doppler anemometry

LES large eddy simulation

LOX liquid oxygen

$MUSCL$ monotone upstream-centered schemes for conservation laws

$NASA$ national aeronautics and space administration

$Nd{:}YAG$ neodymium-doped yttrium aluminum garnet

NP nitronium perchlorate

O/F oxidiser to fuel ratio

$PBAA$ polybutadiene acrylic acid

$PBAN$ polybutadiene acrylonitrile

$PISO$ pressure implicit with splitting of operators

PIV particle image velocimetry

$PMMA$ polymethyl methyacrylate

POD proper orthogonal decomposition

$PRESTO$ pressure staggering option

PSD power spectral density

$PSPG$ pressure stabilised Petrov Galerkin

PT pump throttle

PVC precessing vortex core

QE quantum efficiency

$QUICK$ quadratic upstream interpolation for convective kinematics

$RANS$ Reynolds averaged Navier-Stokes

$RBCC$ rocket based combined cycle

$RFNA$ red fuming nitric acid

RNG renormalisation group

RSM Reynolds stress model

SBR solid body rotation

SED statistical experimental design

SEM spectral element method

$SIMPLE$ semi-implicit method for pressure-linked equations

$SIMPLEC$ semi-implicit method for pressure-linked equations corrected

SNR signal to noise ratio

SSG Speziale Sarkar Gatski

$SUPG$ streamline upwind Petrov Galerkin

TEM_{00} transverse electromagnetic (beam mode 00)

URF under relaxtion factor

$VEBH$ vortex end burning hybrid

VFP vortex flow pancake

$VIHRE$ vortex injection hybrid rocket engine

VOF volume of fluid

Chapter 1

Hybrid rocket engines

1.1 Introduction

Hybrid rocket propulsion as the name suggests is a method of chemical propulsion which combines the technologies of both solid and liquid rocket propulsion. A typical hybrid rocket consists of a solid fuel grain over which a liquid or gaseous oxidiser is introduced resulting in pyrolysis of the solid fuel once ignited. The fundamental difference between hybrid rockets and their parent technologies is how the fuel and oxidiser are mixed to sustain combustion. In Solid rockets both the fuel and oxidiser are uniformly distributed throughout the fuel grain in close proximity allowing for rapid combustion when the ignition temperature is achieved. In liquid rockets, impinging jets of fuel and oxidiser create highly turbulent regions near the oxidiser/fuel manifold which promote intense mixing also allowing for rapid combustion. The intimate mixing of oxidiser and fuel in solid and liquid rockets results in a premixed flame enabling rapid combustion to occur. In hybrid rockets combustion occurs due to a diffusion flame which is located within the boundary layer and adjacent to the fuel surface. This means that an increased turbulent time scale is required to allow for sufficient mixing to result in an oxidiser to fuel ratio O/F at which chemical reactions will take place.
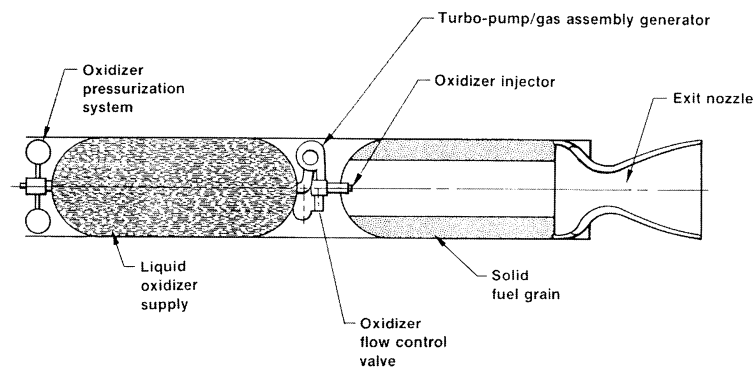
Figure 1.1: Classic hybrid rocket configuration. [1]

1.2 Advantages of hybrid rockets

Although issues still exist concerning hybrid rockets as a viable alternative method of propulsion, the inherent advantages they possess over other systems makes them an attractive prospect for military, commercial and academic research. Advantages include:

- **Safety** – Typical hybrid rocket fuels are non volatile and non toxic posing no hazard compared to solid rocket fuels, avoiding the need for stringent safety regulations imposed during grain manufacture, handling and operation. Care must be taken when handling high pressure oxidiser storage tanks with hand protection necessary for cryogenic oxidisers but the hazard level is minimal in comparison to handling solid rocket fuel.

- **Throttleability** – Like liquid systems, hybrid rockets can be throttled by controlling the oxidiser flow rate which also provides the option of thrust termination. Regression rate of the solid fuel is directly determined by oxidiser mass flux allowing for simple thrust modulation, unlike liquid rockets which require simultaneous oxidiser and fuel flow regulation.

- **Versatility** – Having less propellant design constraints allows for a lot of scope in selection of oxidisers and fuels. Additives can be incorporated into the fuel grain to enhance various aspects of hybrid rocket performance, but also be combined with a variety of oxidisers. Additives can also be incorporated into the fuel grain to increase volumetric loading or to provide an energy source to raise combustion temperature. Hybrid rockets also enable various innovative design concepts to be employed to increase regression rates related to combustion chamber, fuel grain and injector configuration.

1.3 Disadvantages of hybrid rockets

Hybrid rockets benefit from many advantages, of which a brief overview has been provided. Despite this they do suffer from some disadvantages which are detrimental to the performance characteristics of the rocket, these being:

- **Regression Rate** – The most significant factor related to poor performance of hybrid systems are low regression rates of the solid fuel. Usually this is due to the selection of fuels which require high sublimation temperatures where large activation energies are required to allow for pyrolysis. This can lead to reduced fuel regression rates where the mass flux from the fuel surface is also reduced, meaning that larger surface areas are required to achieve desirable fuel mass flow rates. An increase in wetted fuel surface area results in the need for large chambers to accommodate the fuel grains reduced volumetric efficiency (low bulk density). As a result hybrids suffer from reduced density impulse in comparison to solid rockets, although their density impulse is higher than that of liquid rockets. To combat this fuel grains with multiple ports can be employed to provide greater wetted surface area, but to the detriment of manufacturing costs as complex grain configurations are difficult to fabricate.

- **Combustion Efficiency** – Where as solid and liquid rockets benefit from rapid combustion due to a premixed flame the diffusion flame of hybrid combustion does not. This results in a further 1-2% loss of specific impulse compared to solid and liquid rockets as a consequence of the less intense mixing of oxidiser and fuel. Despite this the operating ranges of hybrid rocket specific impulses are relatively high as seen in fig 1.2 with certain fuel compositions providing the highest specific impulse of any chemical rocket.

- O/F **Shift** – During motor operation there is a positive shift in the O/F ratio displacing the theoretical performance parameters from optimum conditions. This is due fuel regression increasing the cross-sectional port area and reducing local fuel mass flux throughout operation. O/F shift can not be avoided and is more prominent in smaller combustion chambers or for rapidly regressing fuels. Currently inhibition of O/F shift is not possible but its effects can be limited with careful consideration during preliminary design stages.
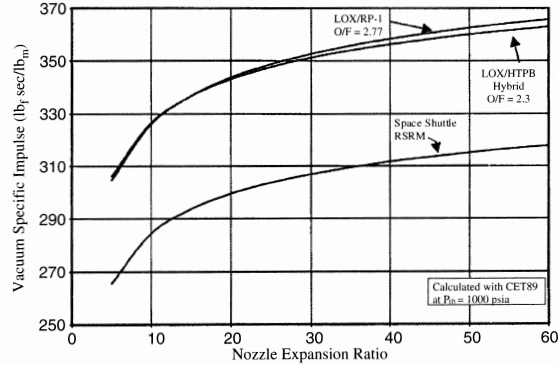
Figure 1.2: Ideal performance of various rocket technologies. [2]

1.4 Characterising performance

There are many parameters which characterise the various processes that occur during hybrid rocket engine operation, but defining performance remains the most important factor. The overall performance of an engine is inherently linked to all other processes that occur and quantification of performance is necessary to realise the effectiveness of an engine design. As with both solid and liquid rockets this is done by comparison of theoretical and actual performance metrics. Important ballistic parameters being the characteristic velocity u^* and specific impulse I_{sp}, for which theoretical values are obtained from industry standard thermochemistry codes. The theoretical or ideal engine performance relates to complete combustion of oxidiser and fuel, in which the propellants release the maximum amount of chemical energy available and effectively convert it into mechanical work, producing optimum thrust. Characteristic velocity is a function of propellant characteristics and combustion chamber design that can be calculated from the specific ratio of heats of the propellant mixture γ and the combustion chamber temperature T_{ch} using eqn 1.1. The first form of characteristic velocity in eqn 1.1 is used for empirical determination of characteristic velocity so that it can be compared to the theoretical value. The ratio between these values is the characteristic velocity efficiency of the engine, which is indicates the engines effectiveness in converting the chemical energy of the propellants into mechanical work. This is closely linked to combustion efficiency η which is another important performance parameter as this physically limits the characteristic velocity and specific impulse of an engine.

$$u^* = \frac{u_e}{C_F} = \frac{p_{ch} A_t}{\dot{m}} = \frac{I_{sp} g}{C_F} = \frac{F}{\dot{m} C_F} = \frac{\sqrt{\gamma R T_{ch}}}{\gamma \sqrt{[2/(\gamma+1)]^{(\gamma+1)/(\gamma-1)}}} \tag{1.1}$$

Combustion efficiency is a complex function of various operating conditions such as: oxidizer/fuel mixing, propellant residence time, flow regime, fuel grain design, chamber pressure and temperature. It can be defined as the ratio between the change in enthalpy per unit propellant mixture to the calculated change in enthalpy necessary to transform the propellants from initial conditions to reaction products at the operating chamber temperature and pressure. It is an important parameter as it is difficult to determine empirically, which means that the characteristic velocity efficiency is commonly used as an analog to represent variation in combustion efficiencies between engine configurations. Highly efficient combustion is desirable as it produces large characteristic velocities, but it is imperative that the pressure energy produced by combustion is effectively transformed into mechanical work. This means employing a nozzle which enables perfect expansion of the combustion gases so that the optimum thrust is achieved. Perfect expansion occurs when the pressure at the exit plane of the nozzle is equal to the ambient pressure, otherwise if the exit pressure is lower or higher than ambient conditions then the flow is overexpanded or underexpanded respectively as seen in 1.3. For overexpanded flow the $p_{e < p_a}$ condition causes flow separation in the nozzle due to the

3
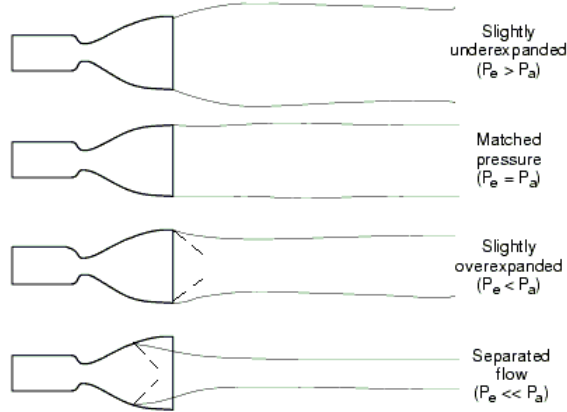
Figure 1.3: Expansion of nozzle flow. [2]

adverse pressure gradient where the effective nozzle exit area is reduced leading to a reduction in thrust comparative to perfectly expanded flow. Underexpanded flow also results in reduced thrust as the exhaust flow continues to expand past the nozzle exit, with the atmosphere providing the reactionary force to contain the plume boundary. This means that only a portion of the exhaust flow experiences a reactionary force from the nozzle reducing the effective transferal of pressure energy to mechanical work, being signified by forward motion. The nozzles effectiveness at expanding the combustion gases is defined as the thrust coefficient, which also accounts for other effects such as viscous losses and reduction in effective nozzle area due to boundary layer growth. The thrust coefficient C_F can be defined as the ratio between the actual effective exhaust velocity u_e and the characteristic velocity as in eqn 1.2, although it is actually a function of the pressure ratio across the nozzle p_{ch}/p_e, specific heat ratio of the exhaust gases γ and the nozzle area ratio $\varsigma = A_e/A_t$.

$$C_F = \frac{u_e}{u^*} = \frac{F}{p_{ch}A_t} = \sqrt{\frac{2\gamma^2}{\gamma-1}\left(\frac{2}{\gamma+1}\right)^{\frac{(\gamma+1)}{(\gamma-1)}}\left[1-\frac{p_e}{p_{ch}}\right]^{\frac{(\gamma-1)}{\gamma}}} \qquad (1.2)$$

A simple form of the thrust coefficient is eqn 1.2 which allows for the nozzle effectiveness to be found with relative ease from empirical data. The nozzle effectiveness is found from comparison of the thrust coefficient for ideal perfectly expanded flow conditions compared to the actual value which can be obtained empirically from a thrust load cell and combustion chamber pressure transducer data. Obtaining the thrust coefficient allows for determination of the engines specific impulse which is the total impulse I_{tot} relative to the weight of the propellant expressed by eqn 1.3 . Total impulse is proportional to the energy released by the propellant mixture and is defined as the product of thrust and burn time $I_{tot} = F/\Delta t_b$. Specific impulse is an important performance parameter as it indicates the relative burn time of a set propellant mass for a set target thrust or vice versa, which is vital for meeting mission specifications where designs require a constant thrust for a certain period of time. By increasing the specific impulse of an engine there is greater flexibility within the design constraints as increased thrust or longer burn times can be achieved for set operating conditions. Different oxidiser/fuel combinations produce various specific impulses which are also dependent on O/F ratio and combustion efficiency, so it is important to employ the correct oxidiser/fuel combination and operating conditions to meet design specifications. It can be seen from eqns 1.2-1.3 that all the performance parameters are closely related to each other and are defined by the same design variables in multiple expressions. Using the results of thermochemistry numerical simulations under ideal operating conditions allows for a design thrust to be calculated by imposing the corresponding nozzle throat and exit areas, which in turn allows the maximum burn time to be determined.

$$I_{sp} = \frac{u_e}{g} = \frac{u^* C_F}{g} = \frac{F}{\dot{m}g} = \frac{I_{tot}}{m_f g} \tag{1.3}$$

1.5 Engine classifications and propellant configurations

The diverse range of oxidisers and fuels available for hybrid rockets means there is great flexibility in propellant choice, with many oxidiser/fuel combinations possible. Available oxidiser/fuel combinations for hybrid rockets surpass that of both solid and liquid rockets combined when solid and liquid phases are considered. Several oxidisers and fuels can be stored in either a solid or liquid phase which means the the scope for propellant selection is further increased. The standard combination of a solid fuel and liquid oxidiser is commonly referred to as the classic configuration, with the majority of research conducted to date related to this arrangement. Typical fuels are organic hydrocarbons such as rubbers or waxes which exist naturally or can be synthesised. The majority of polymeric synthetic rubber fuels when pyrolysed will emit gaseous C_4H_6 (1,3 butadiene) whose polymer is the basis of many propellants. These require the addition of curing agents to enable long chain polymerisation so that the solid fuel possesses thermal and mechanical properties adequate for use in a combustion chamber. Apart from the classic configuration of a solid fuel and liquid oxidiser there are three main other engine classifications being cryogenic, inverse and gas generator hybrids. Cryogenic hybrids consists of an oxidiser and fuel which both exist in a liquid/gas state at room temperature, where the fuel is stored at reduced temperatures to maintain its solid composition. Cryogenic fuels are typically low carbon number saturated hydrocarbons (alkanes) which require relatively small amounts of energy for sublimation to occur (physical phase change directly from solid to gas). In comparison to classic solid fuels the energy required to produce fuel vapour is significantly less as pyrolysis does not occur unlike polymeric fuels where increased energy is required to cause: chain scission, crosslinking and cyclisation.
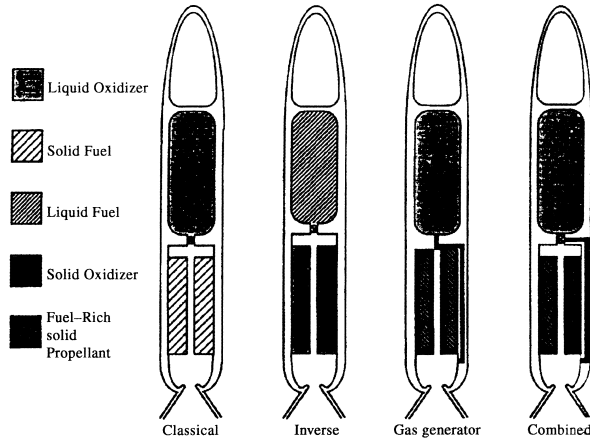
Figure 1.4: Hybrid rocket propellant configurations. [1]

Inverse hybrids are the opposite of classic hybrids and use a solid oxidiser with a liquid fuel, but are restricted to a smaller variety of propellants in comparison to classic hybrids due to limitations of solid oxidisers available. Current solid oxidisers have to be stored cryogenically or in a gelatinous state that increase the complexity of the system, placing further restrictions on grain size, with larger grains more susceptible to cracking because of relatively poor mechanical properties. Gas generator hybrids consist of a liquid oxidiser and a fuel rich solid fuel containing a low volume fraction of embedded solid oxidiser particles. They essentially operate as solid rockets with an afterburner, as the solid oxidiser sustains pyrolysis of the fuel grain producing a fuel rich exhaust. The liquid oxidiser is then injected into a post-combustion chamber where it mixes with the fuel rich exhaust sustaining further combustion at a higher O/F ratio closer to stoichiometric conditions.

Combined gas generators are more similar to classic hybrids with the addition of oxidiser injection into the combustion chamber and the post-combustion chamber. Gas generator hybrids can also utilise cryogenic and inverse oxidiser/fuel configurations, although little attention has been given to these engine types because of their increased complexity and relatively lower performance. Ducted (air ram augmented) rockets are a type of gas generator hybrid which use a RBCC (rocket based combined cycle), where the fuel rich exhaust of the combustion chamber is mixed in a secondary combustion chamber, with an incoming air stream producing roughly stoichiometric combustion. Despite there being various engine classifications classic hybrids have received the most attention to date due to their relative simplicity and increased understanding of their fundamental characteristics. Considering this the classic combination of a solid fuel and liquid oxidiser will be treated in this text as the reference configuration to which the information presented is especially relevant. The majority of studies to date focus on using polymeric synthetic fuels, predominantly being HTPB (hydroxyl-terminated polybutadiene) in the form of a solid cylindrical fuel grain and this shall be the reference material to explain hybrid motor operations.

1.6   Summary

Although the level of research into hybrid rockets is relatively immature in comparison to liquid and solid rocket technology there is already a considerable amount of work that has been conducted that covers many aspects of an engines operation. This stems from the lack of any significant innovation in hybrid rocket engine design for several decades, where research was focused primarily on characterising engine performance through assessing the effects various long chain hydrocarbons and oxidisers in classic configuration engine designs. As a result of this, suitable oxidiser and fuel configurations have been well documented and current propellant research regarding long chain hydrocarbons is primarily concerned with the addition of micronised powders to modify the bulk properties of the fuel grain or energetic additives. There is evidence to suggest that the addition of micronised powders increases fuel regression rates and there are still several candidate materials such as beryllium that may prove to be more beneficial to combustion efficiency than aluminium powders, but currently it is not possible to produce micronised powders using these materials. The polymer HTPB is commonly employed as the matrix material in these studies as it is found to produce the greatest I_{sp} out of the range of preferred polymer fuels, but it may be possible that there are other available polymers that could further increase performance and as of yet have not been implemented in hybrid rocket combustion studies. With regards to oxidisers it is found that gaseous oxygen is the preferred material as it yields the greatest I_{sp} for an acceptable O/F shift in combination with common polymeric fuels, although increased performance can be achieved through the use of $FLOX$ although it is a highly reactive an very hazardous material. For this reason O_2 or alternatively N_2O are the preferred oxidisers for use in hybrid rocket research as material availability and safety are key factors which make hybrid rocket propulsion an attractive alternative to liquid and solid rockets. Overall with respect to propellant configurations that are inert and inherently safe during both storage and operation there is little that can be investigated that can significantly affect engine performance. However since the development of liquefying fuel theory advances have been made in producing suitable fuels that are situated between long chain hydrocarbons such as HTPB and cryogenic short chain hydrocarbon fuels such as pentane. This is currently the most promising area of propellant research as dramatic increases in regression rate can be achieved, although paraffin wax has already been identified as the most suitable hydrocarbon that is not cryogenic and can benefit from atomised fuel entrainment in the embedded diffusion flame of the boundary layer. Problems have been encountered when using paraffin wax during engine operation though as the short chain hydrocarbon composition means that structural integrity is an issue and the unexposed sub layers of the fuel grain tend to melt and prevent sublimation of the fuel surface upon contact with the diffusion flame. The mechanical and thermal properties of this material therefore need to be addressed in order to prevent in depth penetration of thermal radiation and to increase the elastic modulus of the material.

Possibly the most important factor affecting combustion efficiency and engine performance is the oxidiser mass flux at the fuel surface, which is the fundamental parametric value incorporated into almost every regression rate theory and correlation. This value is related to the local oxidiser flow rate which determines the ideal conditions that result in optimum fuel regression rates. If the oxidiser mass flux is insufficient it results in 'cooking' of the fuel grain, or if excessive it will result in 'flooding' of the combusting boundary layer and therefore can greatly affect engine operations. The oxidiser mass flux can be deduced from experimental data and is dependent on various parameters such as propellant selection and chamber geometry, but within the turbulent heat transfer regime of fuel regression increased oxidiser mass flux produces increased regression rates. This can be attributed to the increased momentum of the oxidiser flow which promotes increased turbulence in the boundary layer, in addition to an associated decrease in the height of the combusting boundary layer. As a result the diffusion flame embedded within the boundary layer is in closer proximity to the fuel surface, which increases heat transfer that aids sublimation. The increased local turbulence increases the mixing of the propellant and enhances thermal energy release and combustion efficiency. Therefore it is imperative that any techniques that can positively influence the fundamental transport processes in the boundary layer be implemented, as the effectiveness of the boundary layer combustion is what effectively determines the efficiency of the engine.

Chapter 2

Vortex combustion chambers

2.1 Introduction

Numerous investigations have been conducted in modifying the flow field within hybrid rocket combustion chambers with focus mainly on controlling how the oxidiser streams are injected into the chamber. Several techniques have been developed in an attempt to increase the performance of hybrid rockets with varying success, as benefits associated with increased fuel regression rates are accompanied by undesirable factors such as instabilities, increased complexity, non-uniform ablation, oxidiser jet dissipation and vortex choking. Certain injection methods are applied in conjunction with unique chamber geometries and fuel grain configurations so that certain flow structures can be induced. There are several hybrid designs which utilise these unique flow structures to enhance engine performance and meet specific mission requirements, but only a few have been sufficiently investigated. Currently the application of vortex flow fields through use of tangential oxidiser injection has proven to yield the highest regression rates compared to other techniques. For this reason combustion chamber configurations which employ this method are starting to attract more attention from both the academic and industrial research communities.

2.2 Cyclone combustors

Although the use of a coaxial bidirectional vortex in a combustion chamber is not a new concept, it was Knuth et al [57] who first introduced this unique flow field to hybrid rocket applications. Other examples of the combusting flow structure can be found in type 2 variable modulation cyclone combustors operating in mode II as seen in fig 2.1, as well as gaseous fission rockets seen in fig 2.2, which possibly provided the inspiration for the VIHRE configuration.

Earlier work conducted by Krepec et al [4] investigated vortex flow structures in vortex chambers using tangential injectors located at the head and base of the chamber. This allowed for characterisation of the flow for different injector configurations where head, base and combined injection was investigated. Numerical methods were able to determine 2D axisymmetric solutions of the streamlines and provide an insight into the behaviour of the flow as seen in fig 2.3. It is clear that all the injection methods produce complex flow structures, but it is the aft tangential configuration seen in 2.3a which produces the least complex flow whilst providing the highest mean path length through the chamber. Flow entrained into the recirculation regions due to head or combined injection may result in increased path length and higher residence times. Despite increased residence time being beneficial to combustion efficiency by allowing more time for reactions to occur, extended recirculation times may be detrimental to performance of the engine. As the combusted flow may not exit through the nozzle, whilst uncombusted flow can exit if entrained in the jets that progress along the chamber walls or chamber axis. This is especially true for the combined head and base injection configuration, which forms a permanently recirculating vortex ring at an axial location dependent on the relative momentum of each stream. The added complexity of predicting the effects of re-

8

circulation regions during initial development of a hybrid rocket design in addition to their effects upon boundary layer combustion is undesirable. It is for these reasons that aft tangential injection is the most suitable method for applications in VIHRE configurations, where a relatively predictable flow field that increases flow residence time is desirable to increase combustion efficiencies. Krepec et al [4] provided a detailed study of the coaxial bidirectional vortex for chambers with a $\frac{L}{D} = 1.5$ aspect ratio, while Knuth et al [57] used this parameter to effectively develop the VIHRE concept for propulsion applications.

(a) Cyclone combustor cross section.

(b) Operating modes of cyclone combustors.
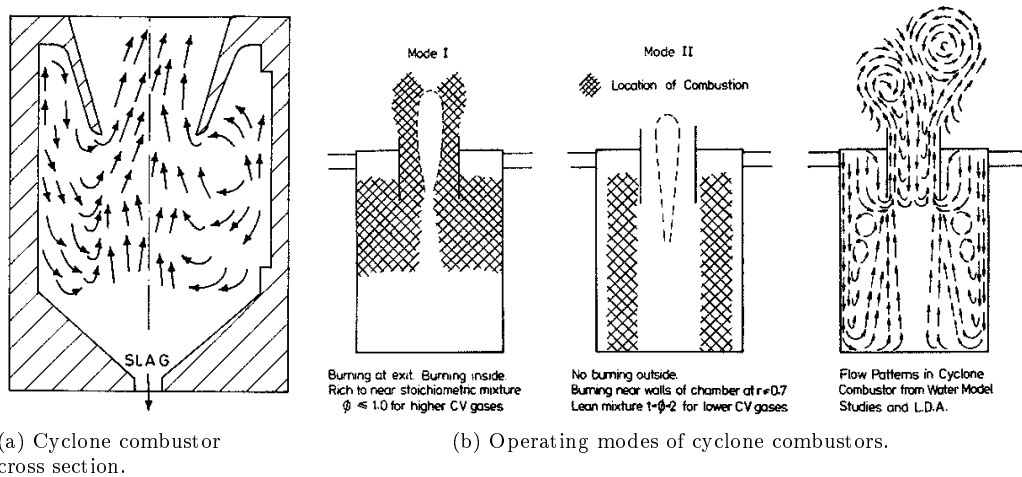
Figure 2.1: Internal flow in cyclone combustors. [3]

(a) Toroidal flow field.

(b) Combustion chamber cross section.
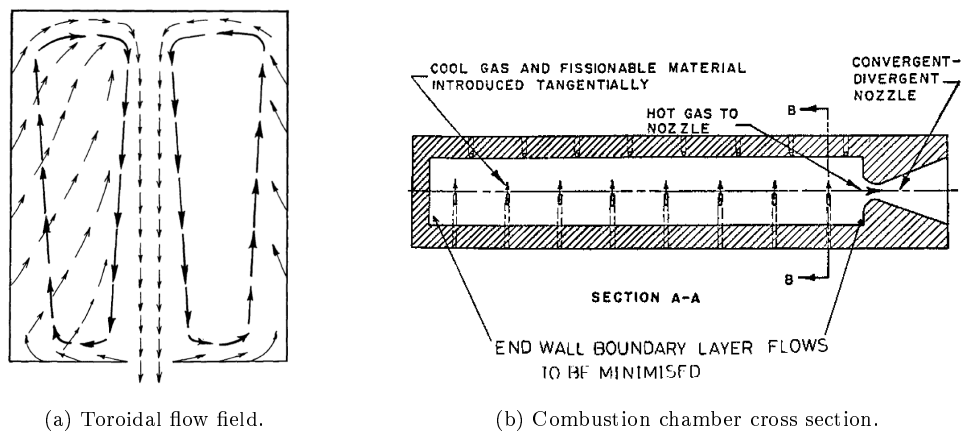
Figure 2.2: Nuclear gaseous fission rocket engine. [3]

(a) Base injection.   (b) Head injection.   (c) Combined
                                                     injection.
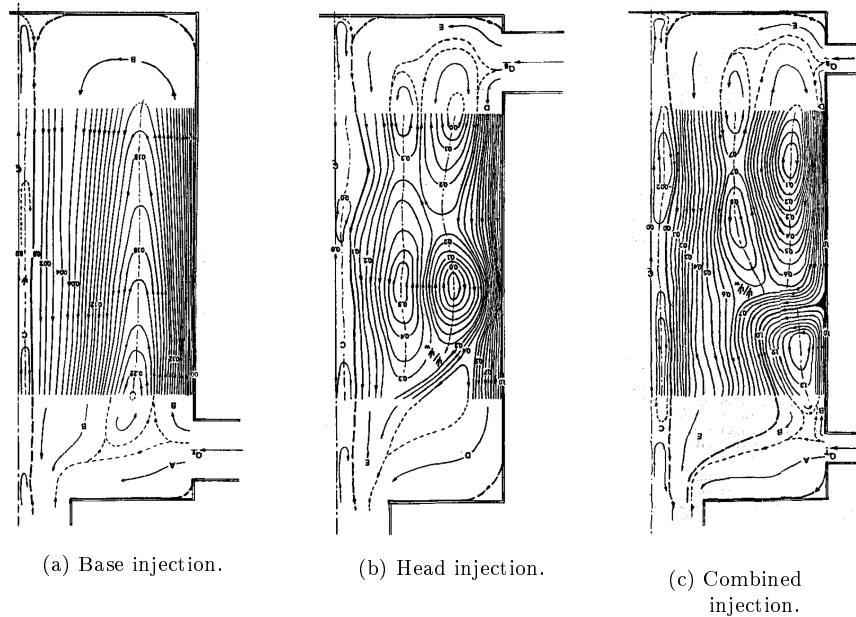
Figure 2.3: Possible injector configurations in vortex chambers. [4]

2.3   Vortex flow pancake hybrid rocket engine

Haag et al [6] employed tangential injectors located at the periphery of the combustion chamber to induce vortex flow fields and because of the low $\frac{L}{D}$ ratio it was dubbed it the vortex flow pancake (VFP). This engine configuration is shown in fig 2.4 and was developed specifically to be the main propulsion unit for small satellites and able to provide orbit insertion capabilities. A two fuel disc configuration was employed to increase the available wetted surface area, with a beveled circular port in the lower fuel grain to allow flow to exit through the nozzle as displayed in fig 2.5.

Although Haag et al [5] did not measure oxidiser mass fluxes or regression rate, it was found that by increasing the injection velocity of the oxidiser that the net mass flow rate through the nozzle increased. This is indicative of increased regression rates, which are likely due to the high injection velocities reducing the height of the boundary layer on the fuel discs. As a result there would be increased heat transfer to the fuel surface from the increased proximity to the flame sheet, causing the fuel mass flux to increase with the associated increase in regression rate. As the range of injection velocities did not relate to high oxidiser mass fluxes for similar injector dimensions and velocities tested in classic hybrid rockets the VFP did not display any variation in total mass flow rate over the chamber pressures tested, meaning that combustion was controlled by diffusion kinetics. It is therefore presumed that the VFP was not operating at oxidiser mass fluxes high enough to exhibit pressure sensitive fuel regression where the rates of chemical kinetics are a controlling factor. Despite operating at relatively low oxidiser mass fluxes the lack of pressure sensitivity indicates that convective heat transfer was comparably higher than the radiative heat transfer, which becomes increasingly important in classic hybrid combustion at low oxidiser fluxes where it can be the dominant heat transfer mechanism. This effect can be attributed to the increased heat transfer caused by the vortex flow field which can at relatively low injection velocities produce intense shear flow increasing turbulence levels in the combusting boundary layers. The effects of the combusting vortex flow can be seen in the upper and lower spent fuel grains shown in fig 2.6 where distinct patterning can be seen on the fuel surface. It is also interesting to note that there are areas of relatively high regression at the edge of the nozzle port and at the centre of the lower and upper fuel grains respectively, indicating intense regions of recirculation.

(a) Combustion chamber cross section.

(b) Tangential injector configuration.
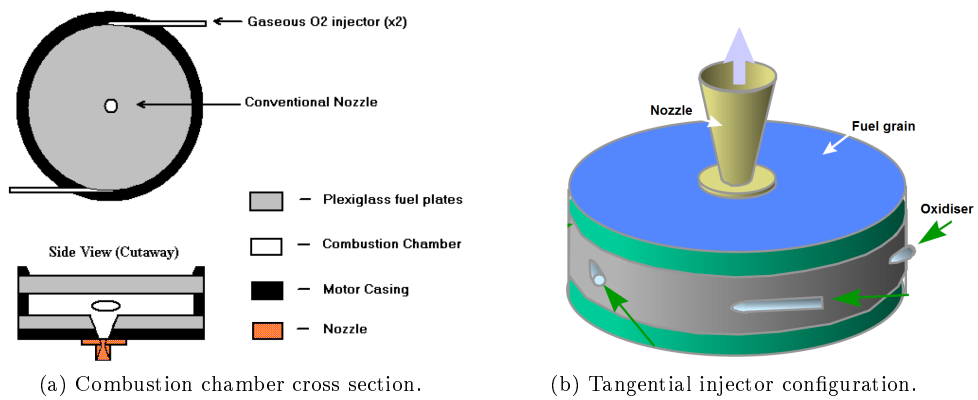
Figure 2.4: Vortex flow pancake rocket engine. [5]
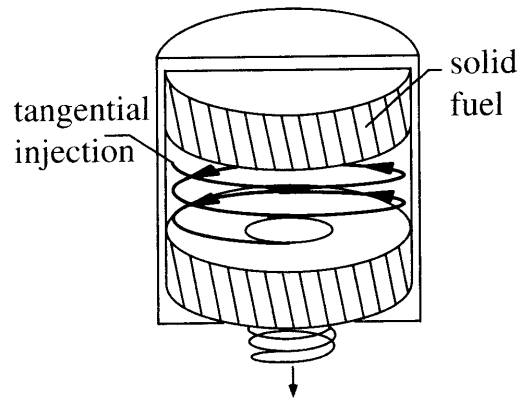
Figure 2.5: Fuel grain configuration and flow field in the VFP. [1]

(a) Head fuel grain.

(b) Base fuel grain.
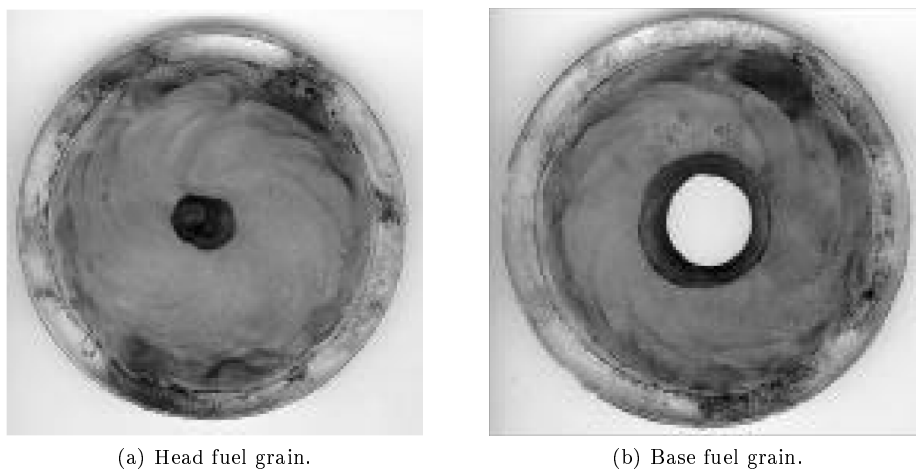
Figure 2.6: Post-fired fuel grains from VFP engine. [6]

The rotational effects of the flow were also investigated to determine whether the magnitude of angular momentum produced by VFP would be detrimental to specific applications such as small satellite propulsion where the satellite trajectory could be affected. Negligible spin effects were observed which was consolidated through comparison of the actual and theoretical characteristic velocities, where it was found that the difference between the actual and theoretical values were small indicating that the chamber was relatively unaffected by the motion of the vortex flow structure. This can be explained by the significant acceleration of the flow produced when passing through the nozzle where the axial flux of axial momentum increases tremendously. This is due to the expansion of hot exhaust gases in the divergent section of the nozzle which effectively aligns the flow direction parallel to the axis of the chamber. While the flow still has axial flux of angular momentum, it is small in comparison to the axial flux of angular momentum which negates the sum rotational effects of the vortical flow. This is an important finding as it means that spin induced effects from swirling flows in other hybrid rocket engine configurations will likely be negligible and can be effectively dismissed. Rice et al [58] also investigated tangential 'vortex' injection end burning hybrid (VEBH) rockets, but used only a single fuel disc which was located at the head of the chamber as seen in fig 2.7. Similar effects to those observed by Haag et al [6] occurred, where regression rate was found to be unaffected by chamber radius meaning that scaling of the VFP engine may be possible though further characterisation of the engine is required. It was also noted that chamber pressure did not influence regression rate behaviour but again this may not be the case for increased oxidiser mass fluxes. Despite these similarities Rice et al [58] found that the initial separation between the fuel disc and the injector did have an effect on fuel regression with sensitivity to this separation distance being twice that velocity effects. Although no specific explanation was given for this it is postulated that there is a variation in the flow field structure because of the single fuel disc configuration which may affect recirculation regions in the chamber.

(a) Internal recirculation zones. (b) Flow patterns in fuel grain.
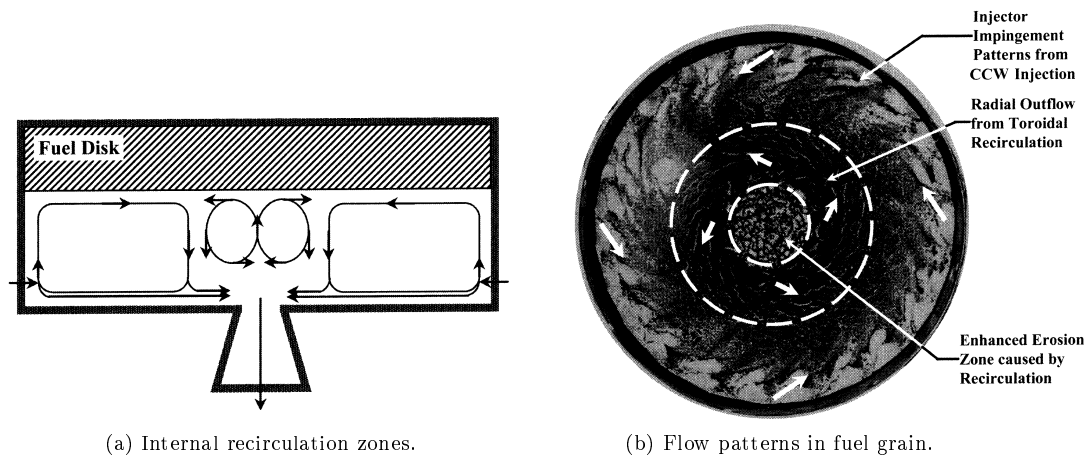
Figure 2.7: Toroidal flow field in the VEBH rocket engine. [1]

2.4   Vortex injection hybrid rocket engine

2.4.1   VIHRE characteristics

Although the injection techniques employed by Knuth et al [7] are similar to those of Haag et al [5], variations in chamber geometry, fuel grain geometry and injector locations produce very different flow fields, which in turn alter the regression rate characteristics of the fuel. Unlike VFP engines, VIHRE configurations have relatively larger chamber aspect ratios with values in the range of $\frac{L}{D} = 1.5 - 2.57$ tested in contrast to the VFP aspect ratio of $\frac{L}{D} = 0.416$. Though the majority of studies conducted have focused on an $\frac{L}{D} = 1.5$ ratio which have been empirically proven to produce the highest regression rates. The most salient feature of the VIHRE is the vortex flow field induced by the tangential injection of oxidiser at the base of the chamber with injectors located at an axial position close to the convergent entrance of the nozzle. The VIHRE configuration is being developed by Orbitec while the U.S army is developing a similar impinging stream vortex engine (ISVE) [59] for high performance hybrid and liquid rocket applications indicating large interest in vortex flow fields.

The aft tangential injector ring seen in fig 2.8 establishes a coaxial bidirectional vortex flow structure where a helical vortex is formed at the walls of the chamber which progresses axially towards the head of the chamber. The flow then ingresses radially and forms a concentric vortex of decreased radius which propagates towards the nozzle and exits the chamber. The exact location where flow turning occurs and the polarity of the axial velocity changes is known as the 'mantle' which indicates the transition from the outer to the inner core vortex and is a large non translating annular recirculation region. VIHRE configurations operate in the high swirl regime $S > 0.6$ and the complex flow field is a result of vortex breakdown at the chamber exit which results in the formation of a phenomenon known as the precessing vortex core (PVC). This is defined as the inner vortex and commonly exhibits a helical coherent structure. The helical flow at the chamber periphery is described as a free vortex while the PVC or inner vortex is a forced vortex. The forced vortex exhibits solid body rotation because of the application of torque from the flow where particles rotate about their own axis denoting rotational flow. Alternatively particles in the free vortex do not rotate about their own axis meaning the flow is irrotational. The forced vortex has constant angular velocity with increasing radial position while the tangential velocity increases to a maximum value signifying the edge of the vortex core. This is because of the intense frictional effects along the chamber axis where viscous effects are significant and result in the application of torque. The co-swirling flow arrangement has the benefits of higher combustion efficiencies, shorter recirculation zones, reduced flame length and a weaker sensitivity to alterations in hardware operating conditions [3]. This is important for VIHRE development as it allows for more flexibility in design and a stable coherent vortex pair can be maintained for a wide range of engine parameters. The coaxial bidirectional vortex as seen in fig 2.9 has been found to have numerous beneficial effects on motor operation and
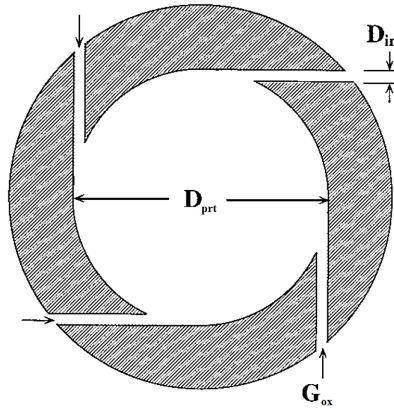
Figure 2.8: Tangential injector configuration of VIHRE. [7]

(a) Helical pathlines of vortical flow.　　　(b) Meridional plane streamlines.
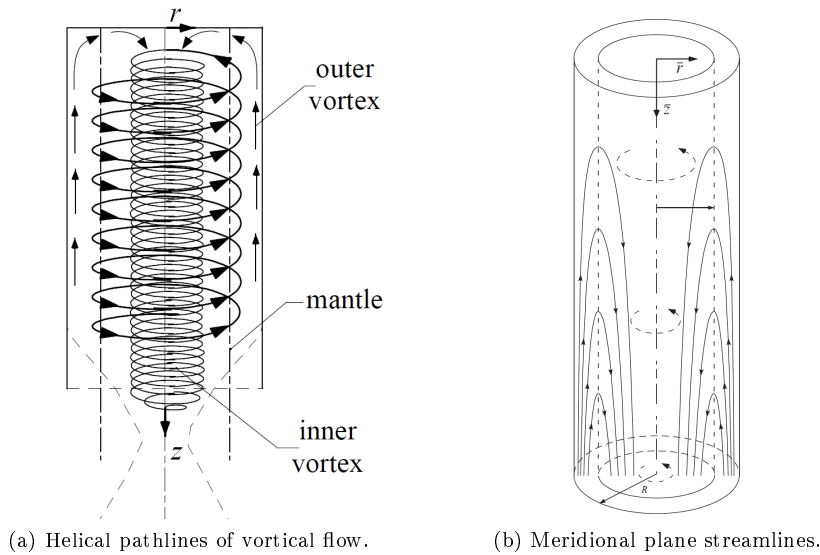
Figure 2.9: Characteristic of the bidirectional vortex. [8]

provides an effective means of increasing performance of a hybrid rocket. Such as the increased mixing that occurs in the inner vortex where reactants not burnt in the diffusion flame adjacent to the fuel surface reactants are transported from the outer to inner vortex. These then undergo combustion within the inner vortex, increasing combustion efficiency as the amount of uncombusted species exiting the chamber are minimal. This also has the benefit of separating the high temperature combustion zone of the inner vortex from the diffusion flame of the outer vortex. The region between the vortices acts as a thermal buffer with hot combustion gases located at the centre of the chamber and cooler oxidiser flow at the periphery.

During VIHRE operation the radial flow caused by the reactionary centripetal forces causes the hot lower density combustion gases to remain in the inner vortex whilst the colder and denser gases are transported to the outer vortex. It is this mechanism of recirculation which enables relatively complete combustion of fuel and oxidiser, resulting in the high combustion efficiencies observed experimentally. The effects of this radial flow are most prominent at the head end of the chamber which is indicative of the flow transferal from the outer to the inner vortex. It is this region which exhibits optimal oxidiser/fuel mixing conditions with large radial velocity gradients occurring with the flow in close proximity to the head of the chamber. This results in increased levels of turbulence as significant flow shear effects are present from the influence head end boundary layer as intense mixing occurs during the transition from the outer to the inner vortex, O/F ratios suitable to sustain combustion occur within the head region of the inner vortex. This is an important design feature of the VIHRE as it effectively splits the combustion chamber into a high temperature and relatively low temperature region. Typical temperatures in the core vortex are approximately $T_c = 3500k$ and lower fuel surface temperatures of around $T_s = 1000k$ in the outer vortex. Combined with the conductive dissipation of thermal energy at the fuel surface to the virgin fuel below results in relatively low temperature chamber walls relative to the core vortex temperature. This is an important feature which has great impact on VIHRE chamber design with respect to viable chamber casing materials and their relative thickness as it allows for increased design flexibility that can reduce the gross weight of the engine, which has specific benefits for space propulsion systems where reduced payload mass can significantly affect the cost of a launch. The doubly convoluted helical path through the chamber also means that VIHRE configurations have higher characteristic chamber lengths L^* for reduced physical lengths L. In comparison to classic axial injection configurations the VIHRE has a considerably higher L^* where the characteristic length is the mean flow path length through the chamber. The increased flow residence time associated with high L^* causes increased combustion efficiencies as it enables further energy release from subsequent product reactions.

14

2.4.2 VIHRE experimental findings

It can be seen from the pressure and thrust profiles in fig 2.10 for a VIHRE chamber configuration with $\frac{L}{D} = 1.5$ that there is little variation in either during engine operation which indicates stable combustion. This is due to the minimal variation in O/F throughout the fuel grain which results from the centrifugal force field induced by the outer vortex. The tangential injection maintains a relatively constant oxidiser mass flux over the fuel surface which results in uniform regression rates indicated by the post firing fuel grain in fig 2.11. It was also noted during testing that VIHRE combustion displays negligible pressure dependency on regression rate as the amount of radiative heat transfer is small in comparison to the convective heat transfer. The large convective heat transfer is the mechanism which produces the impressive increases in regression rates in comparison to classic axial configurations and is caused by the effect the coaxial vortex field has on reducing the thickness of the boundary layer height. Knuth et al [7,57] found that during testing the most influential engine parameters on regression rates are oxidiser mass flux G_{ox}, chamber aspect ratio $\frac{L}{D}$, contraction ratio $\frac{D_{ch}}{D_t}$, oxidiser injection velocity and local mass flux [57]. Although later analysis [9] highlights exactly how sensitive regression rate is to these individual factors by separating each parameter for comparison where normalised sensitivity values were obtained by analysing the data using statistical experimental design (SED) techniques. This processed the design variables tested and returned a sensitivity value for each variable normalised by the most significant parameter which are shown in fig 2.12, where positive values indicate regression rate is proportional to the magnitude of the variable and inversely proportional for negative values.
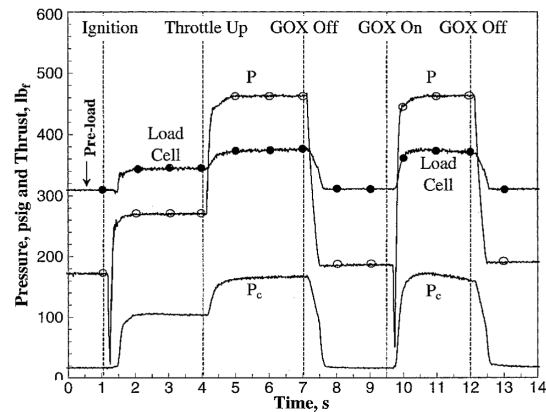
Figure 2.10: Chamber pressure and thrust profiles in response to oxidiser throttling. [9]
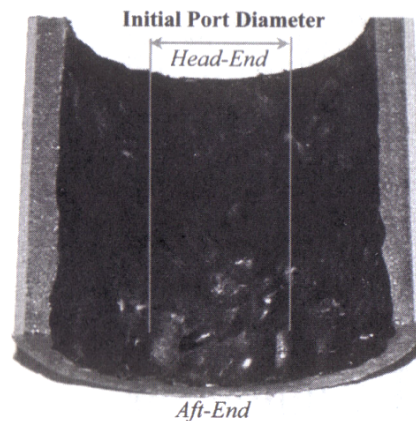
Figure 2.11: Post-fired VIHRE fuel grain. [1]

15
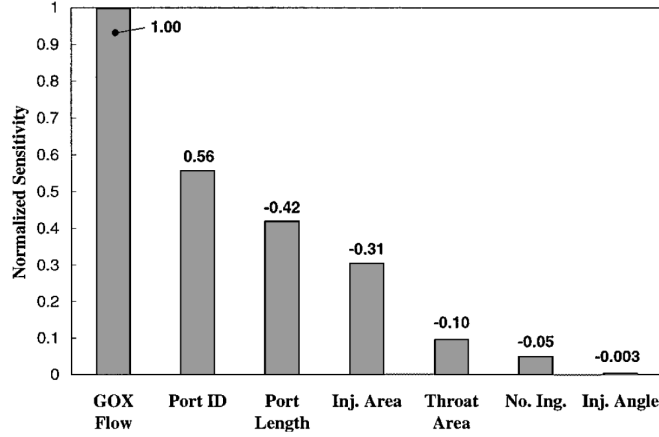
Figure 2.12: SED analysis of combustion chamber parameters. [9]

This analysis has great significance with regards to VIHRE design as it identifies the importance of each design parameter, in contrast to the initial empirical findings which made conclusions based on lumped parameters that are unable to distinguish between cause and effect. As expected oxidiser mass flux is found to have the most impact on regression rate which is obvious when considering that regression rate is generally characterised by the form $\dot{r} = aG^e$. Apart from the oxidiser flow and number of injectors all other parameters are related to the dimensions of the chamber, thus indicating the significant effect chamber geometry has on VIHRE performance influencing the coaxial vortex structure and the relative heat transfer it produces. In earlier studies Knuth et al [7] discovered that for identical $\frac{L}{D}$ ratios operating under similar conditions there were noticeable differences between the regression rates obtained. This was explained by the difference in chamber radius, where increasing the chamber radius results in increased tangential velocities and vortex angular momentum which reduces the height of the boundary layer where the decreased distance between the fuel surface and flame sheet enhances heat transfer, which subsequently increases the regression rate. This has been analytically proven by Majdalani and Vyas [60] for the specific case of a bidirectional vortex chamber where the proportional relationship $\delta_w \sim V^{-1}$ is observed. The height of the tangential boundary layer at the wall is denoted byδ_w and V in eqn 2.1 is the vortex Reynolds number. This is a dimensionless group used to characterise the coaxial bidirectional vortex and is a function of chamber aspect ratio and proportional to $V \sim \frac{D}{2L}$. This formulation implies that reducing the length of the chamber is also beneficial to engine performance by decreasing the height of the boundary layer at the chamber wall. Eqn 2.2 describes the modified swirl number σ which supplements V and is used throughout analyses by Majdalani [23, 61, 62] in place of the classic swirl number S. This solution corroborates the results of the statistical sensitivity analysis performed by Knuth et al [9] which show that shorter and wider chambers associated with low $\frac{L}{D}$ ratios are conducive to producing higher regression rates. The higher regression rates are resultant of larger chamber radii where the undesirable effects of O/F shift may be minimised as they respectively increase and decrease fuel surface mass flux for increasing radius. The effects of which can be seen in fig 2.10 which displays a relatively steady neutral thrust profile during operation even after engine restart.

$$V = Q_{in}Re_{in}\left(\frac{R}{L}\right) = \frac{A_{in}}{RL}Re_{in} = \frac{\left(N\pi r_{in}^2\right)u_{in}\rho}{\mu L} \tag{2.1}$$

$$\sigma = \frac{1}{Q_{in}} = \frac{SR}{\pi r_t} \tag{2.2}$$

$$Re_{in} = \frac{\rho u_{in}R}{\mu} \tag{2.3}$$

16
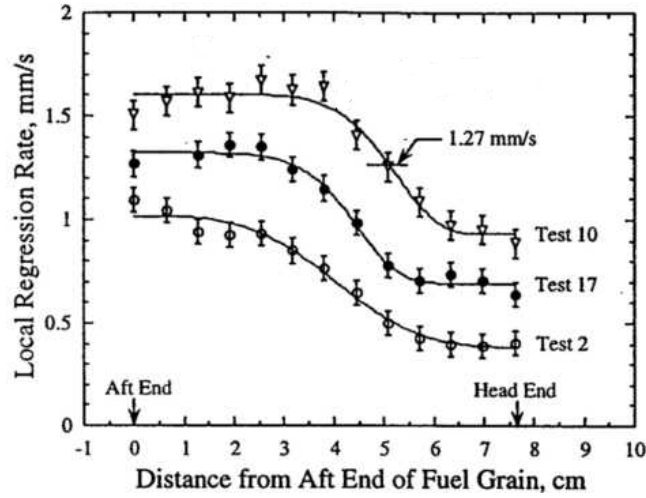
Figure 2.13: Regression rate at multiple axial positions in chamber. [7]
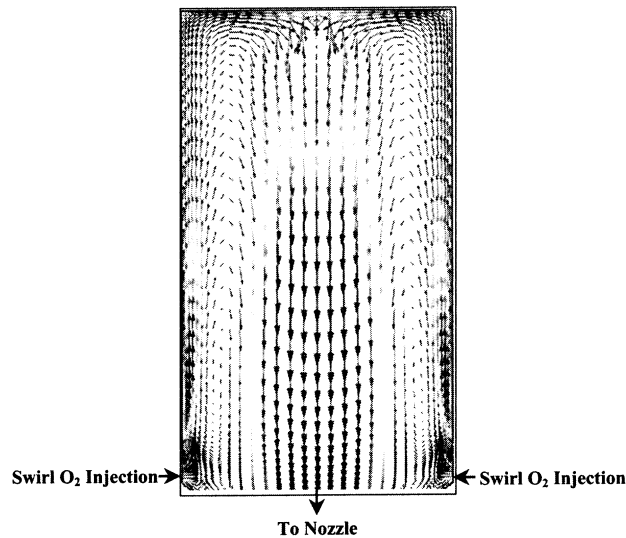
Figure 2.14: Numerical flow field of the bidirectional vortex. [1]

The total cross sectional area of the tangential injectors is another important contributing factor because for a set oxidiser mass flow rate a reduction of the total inlet area will result in higher injector mass fluxes and increased inlet tangential velocities as $G_{in} = \frac{\dot{m}}{A_{in}}$. Although the oxidiser mass flux is found to be the most influential performance parameter the oxidiser flow velocity is implicitly coupled to this and is also important. The ability to sustain stable combustion and produce uniform fuel regression is dependent on the availability of oxidiser flow which in VIHRE configurations follows a double convoluted helical path. Due to the increased length of the helical path the oxidiser jets are susceptible to viscous dissipation at lower axial distances from the injection location in comparison to classic axial configurations. High shear stresses and increased densities associated with thin boundary layers results in diffusion and dissipation of tangential momentum of the oxidiser jets. This also relates to a decrease in vortex strength along the chamber as the tangential momentum of the flow decreases with increased axial distance from the injectors. Again seen in the inverse proportionality $V \sim \frac{1}{L}$ found by Majdalani and Vyas [61] which explains why increased chamber length is detrimental to regression rate.

17

(a) Low flow.   (b) High flow.
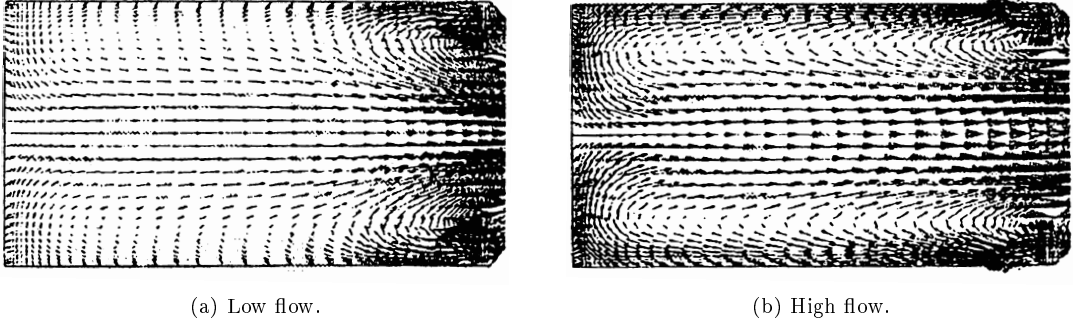
Figure 2.15: Velocity vector plots of bidirectional vortex and the effect of inlet velocity. [10]

The injector fluxes tested showed that the resultant oxidiser velocities were not adequate to produce axially uniform O/F ratios to allow uniform fuel regression which can be seen in fig 2.11. The decrease in vortex strength with increasing distance from the injectors is also in agreement with numerical simulations conducted by Knuth et al [10]. This shows that reduced oxidiser injection velocities are unable to produce strong bidirectional vortex structures that encompass the whole length of the chamber displayed by fig 2.13. Wall [63] conjectured that the introduction of a secondary set of injectors placed at $0.5L$ may prevent the reduction in regression rates at the head of the chamber. Through personal communication with Knuth [64] it was found that this method had already been unsuccessfully implemented as the tangential momentum from the secondary injectors was significantly higher than the tangential momentum from the aft injectors at the axial position $0.5L$. The momentum of the secondary injectors was found to cause the oxidiser flow from the aft injectors to migrate radially towards the axis and become entrained in the core vortex. This leads to decreased oxidiser residence times which were detrimental to the combustion efficiency and therefore means that increasing the injection velocity is likely to be the most suitable technique for producing uniform regression rates. This would also enhance the relative strength of the outermost vortices, resulting in enhanced heat transfer to the fuel surface as the increased velocity magnitudes leads to a reduction in boundary layer height. Dhir and Chang [65] investigated heat transfer of tangentially injected swirl flow in pipes and found similar results for non combusting flow where reduced heat transfer occurred in regions of low tangential momentum and was indicative of weak vortices. The employment of tangential injection is an effective method of increasing heat transfer to the surface due to the reduction of boundary layer height caused by increased tangential momentum with higher injection velocities causing increased heat transfer.

$$\frac{M_\phi}{M_{tot}} = \frac{\dot{m}_\phi}{\dot{m}_{tot}} \frac{\rho A_{prt}}{\rho A_{in}} = cos^2\left(\vartheta\right) \frac{G_{in}}{G_{ox}} \tag{2.4}$$

$$Pr \equiv \frac{\Delta p}{\Delta r} \approx \frac{p_e - p_h}{r_e - r_h} \tag{2.5}$$

The statistical sensitivity analysis shows that regression rates are relatively unaffected by the number of injectors and their respective upsweep angle, with only a minor dependence found to exist on nozzle throat area. The effect of nozzle geometry was reported in previous work by Knuth et al [57] where increasing the contraction ratio was found to be beneficial. This can be related to the containment of the vortex structure where smaller nozzle radii are able to prevent inlet oxidiser flow from exiting directly through the nozzle and not contributing to combustive exothermic reactions. The increase in chamber radius linked to contraction ratio dependency also reduces escaping oxidiser flow as higher radial pressure gradients are present in larger diameter chambers, which prevent radial ingress of flow towards the nozzle throat forcing the flow to follow the helical path to the chamber head. The numbers of injectors and their upsweep angle have an almost negligible effect on regression rate although fewer injectors with small upsweep angles appear to be preferable. Although studies conducted varied the number of injectors in the range $N = 4 - 42$ the analysis infers that one or

two injectors produce optimum results. This is not strictly the case as the coaxial vortex requires at least two or more injectors to allow for a symmetrical injection pattern to increase the coherency and stability of the vortex structure. Another reason for having more than two injectors is that it can lead to non uniform fuel regression where the oxidiser jets are unable to produce a constant O/F ratio across the fuel surface. The finding of the minimal effect of injector upsweep angle was not predicted by Knuth et al [57] as they expected a certain degree of upsweep angle to aid vortex axial procession along the fuel surface. During cold flow (non combusting) tests oil was introduced into the flow and was found to migrate at an angle of $\theta = 28°$ relative to the normal of the chamber axis. In light of this, injectors were fabricated with a $\vartheta = 28°$ tilt angle so that oxidiser flow would be parallel to the bulk flow to increase the strength of the vortex. Although upon ignition it was noticed that the combusting flow field realigned the oxidiser jets to an almost $\vartheta = 0°$ angle, implying that small injection angles are most suited to increasing the strength of the vortex. This is further indicated by eqn 2.4 which shows that increased upsweep angle leads to a reduction in tangential momentum which in turn is detrimental to the relative strength of the vortex. The Prandtl ratio in eqn 2.5 is used to link the viscous and thermal diffusion rates of the flow to empirically obtainable quantities to estimate how the vortical flow affects heat transfer at the chamber walls.

2.4.3 VIHRE regression rate correlations

As VIHRE configurations employ a coaxial bidirectional flow field to increase performance the specific heat transfer characteristics are different to those found in axial flow classic hybrid configurations. This means that the solid fuel regression model developed by Marxman and Gilbert [66] and expressed in eqn 2.6 is not able to account for the increased convective heat transfer from the effects of swirling flow. This led to Knuth et al [9] developing regression rate models that are able to predict these effects by including work by Dhir and Chang [65] and Chiaverini et al [67] and through incorporating the relative effects of chamber geometry. Initially a model based on the findings of the statistical sensitivity analysis were used to produce a regression rate correlation which involves the engine parameters that fuel regression was most sensitive to. A least squares fit was produced to express regression rate as a function of $\frac{L}{D}$ ratio, injector mass flux, local mass flux and contraction ratio CR being the most influential parameters on regression rate. This correlation resulted in eqn 2.7 where the contraction ratio is defined as the ratio between the average combustion port diameter and the throat diameter $\frac{D_{avg}}{D_t}$. A good correlation was found between the predicted and actual regression rates for various engine configurations with all data falling within the $\pm10\%$ error band. This is shown in fig 2.16 where the legend relates to different engine configurations VH-20, VH-100 and VH-200 which respectively have increased chamber dimensions and maximum thrusts. As expected the larger engines which require higher injector mass fluxes to produce stable coherent vortex pairs display higher regression rates than the smaller engines.
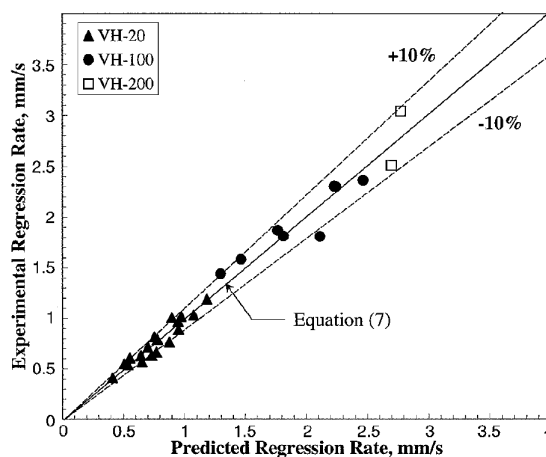
Figure 2.16: Effects of chamber scaling on fuel regression rates. [9]

$$\frac{\rho_f \dot{r}}{G} = 0.023 Re_{prt}^{-0.2} Pr^{-0.7} \left(\frac{St}{St_{ref}} \right) B \tag{2.6}$$

$$\dot{r} = 0.0085 \left(\frac{D_{avg}}{D_t} \right)^{0.45} \left(\frac{L}{D} \right)^{-0.59} G_{in}^{0.45} G^{0.37} \tag{2.7}$$

Although the regression rate model based on geometric variables provides a reasonable prediction of regression rates it is purely an empirical correlation. This resulted in Knuth et al [9] developing a semi-empirical model based on the model of Marxman and Gilbert [66] developing the relative vortex strength momentum ratio found by Dhir and Chang [65] to explain increased heat transfer in pipes because of swirling flow. The Arrhenius law developed by Chiaverini et al [67] was also incorporated to characterise solid fuel regression of a HTPB fuel as a function of temperature, as expressed by eqn 2.8. Modifications required for the relationships are proposed by Dhir and Chang [65] to account for fuel surface blowing effects and the associated reduction in convective heat transfer. Despite this a regression rate model specifically applicable to VIHRE configurations were attained which considers the complex physicochemical processes related to the pyrolytic decomposition of the fuel expressed by eqn 2.9.

$$\dot{r} = A e^{\left(\frac{-E_{act}}{R_u T_s} \right)} \tag{2.8}$$

$$\frac{\rho_f \dot{r}}{G} = 0.082 Re_{prt}^{-0.33} \left(\frac{St_{sw}}{St_{ref}} \right) \left(\frac{St_v}{St_{sw}} \right) B \tag{2.9}$$

2.5   Summary

Significant increases in oxidiser mass flux have been observed by departing from classic engine configurations with axial oxidiser injection and investigating the effects various oxidiser injection methods which produce an array of flow fields within the combustion chamber. The most effective methods thus far involve the use of tangential injectors to impart swirl to the flow which has been found to significantly increase regression rates as the swirling flow increases heat transfer to the fuel surface. Replacing axial injectors with tangential injectors in classic chamber geometries does yield increased regression rates especially in combination with spiral fluted fuel grains but increased turbulence levels within the boundary layer are found to have the greatest impact on regression rate in comparison to the increased heat transfer associated with swirling flow. However by far the most effective and innovative method for increasing fuel regression rate is to induce a bidirectional vortex by locating the tangential inlets at the base of the chamber which promotes enhanced heat transfer at the fuel surface in addition to increased turbulent mixing and greater effective chamber lengths so that complete combustion can occur. By employing a bidirectional vortex it is possible to obtain regression rates of up to ten times higher than comparable classic engine configurations which means that vortex combustion chambers are currently one of the most promising areas of hybrid rocket research. However these types of rocket engines are still a relatively new concept and have yet to receive significant attention from the research community as the increased complexity associated with their fundamental fluid mechanics prevents vortex rocket engines from being fully characterised without substantial effort. Oxidiser mass flux is still an important variable with regards to influencing the regression rate as are parameters related to chamber geometry which can also affect engine performance. Additionally there are some analytical and anecdotal findings which indicate the possible existence of complex tertiary flow patterns which are currently yet to be confirmed or associated with any design variables. Therefore there is plenty of scope to investigate the fundamental fluid mechanics that occur within these engine configurations as well as the influence of chamber geometry and the possible impact it may have upon tertiary flow structures.

Chapter 3

Confined vortex flow

3.1 Introduction

Confined vortices have widespread applications and are found in a variety of devices, which depend entirely on the physical properties of a vortex rather than mechanical processes due to their simple but reliable operation. However, despite the large amount of devices which rely on the characteristics of confined vortices there is relatively little information available concerning their fundamental fluid mechanics with regards to the operation of cyclonic devices. From a design standpoint, attention is focused on the effectiveness of the device rather than the underlying processes which allow it to operate, while research into the physical behaviour of confined vortices commonly neglects their applications. Confined vortices are produced by complex fluid motions that are affected by many variables and are associated with a large range of phenomenon which makes it difficult to characterise a vortex without in depth understanding of the physical mechanisms that dictate their behaviour. Therefore it is necessary to investigate these physical mechanisms in order to understand how confined vortices can be exploited in order to increase the effectiveness of cyclonic devices such as the vortex injection hybrid rocket engine.

3.2 The bidirectional vortex

The cold flow structure in the VIHRE is similar to that of a Ranque-Hilsch vortex tube depicted in fig 3.1 as it employs a bidirectional vortex induced by tangential inlet flow at one end of the device. The flow can be described by the Thomson-Rankine vortex, although commonly referred to as the Rankine combined vortex seen in fig 3.3 which accounts for both the forced and free vortex although this is for an inviscid fluid. Due to this assumption the effects of viscosity must also be considered and how both viscous and turbulent energy dissipation affect the velocity profile in physical flows. This vortex model regards the fluid as inviscid, but it forms the basis of more complex vortex models where to the addition of viscous core effects provide a simple model for predicting physical vortex flow. The constituent velocity profiles of the Rankine vortex can be seen in fig 3.2 and the formulations of the circulation for the free and forced vortex are expressed by eqns 3.1-3.2 respectively. The combined velocity profile for the Rankine vortex can be seen in fig 3.3 where the intersection of the dashed lines represents the peak tangential velocity magnitude, where as the solid line represents a physical vortex subject primarily to the effects of viscosity. This tangential velocity profile represents a physical vortex similar to those observed in cyclonic devices such as a cyclone separator as shown in fig 3.7 where it can be seen that the sharp peak of the Rankine combined vortex is replaced with a transition region. The reduction of tangential velocities in the transition region are indicative of increased local turbulence intensities where viscous effects result in increased viscous dissipation of tangential momentum. The non linear regions in the tangential velocity profiles caused by fluid viscosity effectively mean that the vortices are quasi-free and quasi-forced as the transition region and near wall region have varying gradients.

(a) Single tangential inlet configuration.

(b) Vortex motion and heat exchange.
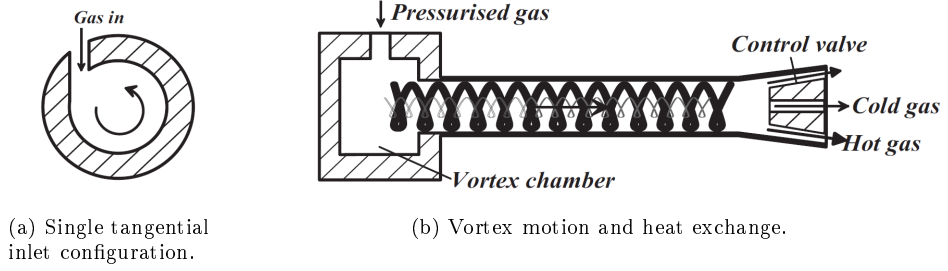
Figure 3.1: The Ranque-Hilsch vortex tube. [11]

Despite this the vortices are commonly referred to as free and forced vortices, which will be the considered treatment throughout this study. Significant dissipation of tangential momentum is undesirable as it can lead to a reduction in coherency of the vortex core affecting the stability of the vortex structure and specifically its ability to enhance performance with regards to cyclonic combustion chambers. The effects of this viscous dissipation and turbulent energy dissipation are most pronounced at the transitional radius from the forced to free vortex. The Rankine combined vortex is characterised by a linear velocity gradient within the forced vortex, where the fluid is undergoing solid body rotation and has a constant angular velocity where the magnitude of the tangential velocity is greatest at the periphery of this region of the fluid. This increase in the magnitude of the tangential velocity component with regards to radius is expressed simply as $u_\phi = \omega r$ and is applicable to the majority of the forced vortex even when viscous or turbulent effects influence the flow. As the flow is also rotational it has a non trivial axial vorticity component and can considered to be the core region of the flow as the intensity of the vortex is greater than in the irrotational region of the flow. The free vortex has zero vorticity and a constant value of circulation, while the forced vortex which is defined as the curl of the velocity vector increases inversely proportional to the radius. Therefore the vorticity increases as the fluid approaches the centre line or vortex filament of the flow, which means circulation also increases as does vorticity, which can be considered to represent the amount of circulation per unit area. Terminology related to vortical flows can be semantical and open to interpretation but for the purposes of this study the forced vortex will be considered to be a concentrated vortex and constitute the core flow of the vortex. In the same vain the PVC will also be considered to constitute the core flow of the vortex but will be used to describe the boundary of the reversed flow that occurs along the axis of the vortex which separates this tertiary flow from the bulk fluid. The actual reversed flow within the boundary of the PVC is referred to as the central recirculation zone (CRZ) in order to replicate terminology found in existing literature [68].

(a) Free vortex (irrotational).

(b) Forced vortex (rotational).
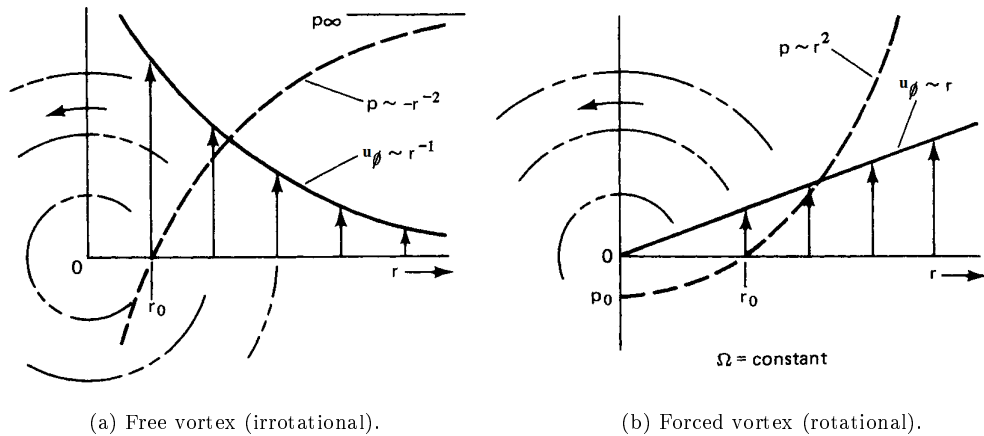
Figure 3.2: Constituent parts of the Rankine vortex. [12]

22
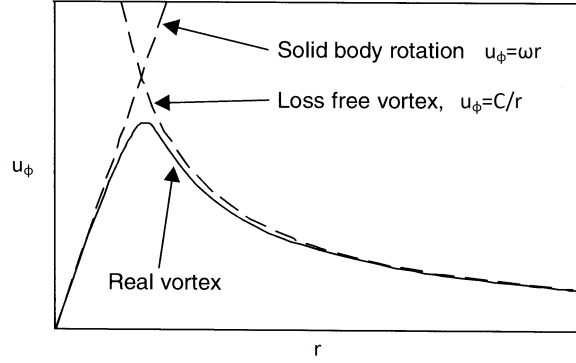
Figure 3.3: Tangential velocity profile of the physical composite vortex. [11]

After the peak tangential velocity is reached at the periphery of the solid body rotation region of fluid it transitions to the irrotational free vortex where the tangential velocity profile can be expressed by eqn 3.1. As seen in fig 3.3 the magnitude of the tangential velocity component exhibits hyperbolic decay relative to an increase in radius. The form of the tangential velocity component within the irrotational region of the fluid can be expressed by $u_\phi = \frac{C}{r}$, where C is the circulation constant and is commonly used to simplify the form of the velocity component which is expressed as $C = \frac{\Gamma}{2\pi}$. This describes not only the tangential velocity component but the absolute velocity as well, as the Rankine vortex does not account for typical physical vortical flows which also have radial and axial velocity components. As mentioned previously the Rankine vortex serves as the template for more complex vortex models which account for these velocity components and this is especially important when reversed core flow such as that produced by a PVC is present.

$$\Gamma = \int_0^{2\pi} u_\phi r . \partial\phi = 2u_\phi \pi r \tag{3.1}$$

$$\Gamma = \int_0^{2\pi} \omega r . r \partial\phi = 2\pi r^2 \omega \tag{3.2}$$

Numerous studies have investigated the coaxial bidirectional vortex and its application in such industrial devices as vortex tubes, cyclone separators and combustors. Despite this, a lot of the focus of these studies has been directed towards understanding how the flow field affects relevant performance criteria of the device such as separation or combustion efficiency. As part of the ongoing research into VIHRE configurations analytical analyses have been performed by Majdalani et al [23, 60–62, 69] which iteratively increase in complexity and provide a detailed step by step treatment of the coaxial bidirectional vortex with regards to VIHRE design. The solutions they present are applicable to the general form of the vortex structure, but it is the application to VIHRE configurations that is the main objective while problem specific effects such as wall transpiration [70] and hydrodynamic instability [8] are accounted for in associated literature. The Majdalani-Vyas vortex model [69] represents a relatively advanced analytical model to describe such flows but a fully unified model of the processes that occur within a VIHRE is yet to be realised. However its current capabilities do include treatments for non reacting viscous incompressible flow with considerations for compressible flow being currently investigated, although there is still a major omission with regards to the behaviour of the PVC and the CRZ associated with the flow. From a chamber design standpoint, important design parameters such as $\frac{L}{D}$ ratio, total inlet area, nozzle throat area, injection Reynolds number and swirl intensity are included and provide the possibility of parametric optimisation studies if a numerical code based on this model is developed. The analytical approach has been used in conjunction with experimental studies where conclusions have been drawn with regards to the effects of chamber geometry and injection velocities on relative strength and dimensions of the

23

vortex [9]. Subsidiary components of the analytical study relate to specific regions of the flow, acquiring an understanding of how design parameters affect the effectively high viscous regions of the forced vortex core flow and the tangential boundary layers present at the chamber walls [60]. The effects of enhanced thermal transfer due to swirling flow have been investigated by Dhir and Chang [65] and are included in the development of semi-empirical fuel regression laws [9]. This effect is currently not entirely considered in the analytical treatment of the tangential boundary layers due to the focus on non reacting flow. When used in conjunction with the evolving analytical model of the flow for VIHRE configurations it may prove useful in making initial predictions of VIHRE performance. Chamber configurations realised through parametric investigation of the Majdalani-Vyas vortex model could be implemented to ensure maximum convective heat transfer and effective oxidiser/fuel mixing would occur.

The coaxial bidirectional vortex is a complex flow structure and because of this the solution is broken down into several parts where the complexity of the solution progressively increases. In this way the many aspects of the flow field can be integrated sequentially into each successive solution so that eventually a full solution to the flow can be obtained. Initially an analytical steady, rotational, axisymmetric, incompressible and inviscid solution was formed in order to establish some of the salient features of the flow structure. These features include the bi-polar vortex flow, the free vortex and the non translating vortex layer or locus of zero axial velocity which will is referred to as the 'mantle'. The exact inviscid solution relates to a non combusting case where sidewall injection and radially regressing walls simulating solid fuel regression is neglected, instead only the bulk gas flow from oxidiser injection is considered. As expected the inviscid solution obtains $u_\phi = \frac{1}{r}$ for the tangential velocity profile [62], describing the free vortex that is depicted by the various vortex models in fig 3.5. The chamber axis represents a singularity at which the tangential velocity tends to infinity due to asymptotic behaviour in accordance with the Biot-Savart law. Consideration is then given to the momentum equation in the azimuth direction which leads to a boundary layer equation that describes the forced vortex near the chamber axis. This inner expansion is then matched with the outer expansion that relates to the free vortex, resulting in what is referred to as the complex lamellar solution [61]. A more complex formulation of the core flow is later realised when a shear stress distribution similar to that of Coutte flow is assumed which negates the singularity at the axis and allows the effects of laminar and turbulent flow in the core to be addressed. This also allows for the influence of Reynolds number and swirl distribution on the radius of the forced vortex to be included, although it is indicated that further experimental and numerical data must be produced prior to extending the theory to vortical flows with higher Reynolds numbers [71]. A solution to the tangential boundary layers at the periphery of the chamber are also included in a later study to account for the no slip boundary condition that occurs in physical flow due to momentum dissipation within the boundary layer [72].

3.3 Non linear Beltramian vortex model

Unlike previous investigations of columnar vortices Majdalani et al [62] incorporate the effects of axially confined flow because of the large influence chamber geometry is believed to have upon the flow. Several models now exist for describing the bidirectional vortex, but the recent non-linear Beltramian formulation [13, 18, 19] provides the most suitable current vortex model to reference as it provides a treatment for possible flows with multiple flow reversals, which is related to the objectives of this investigation. As with the complex lamellar vortex model the inviscid profile of the free vortex serves as the foundations on which further additions to account for viscous effects are applied. The Bragg-Hawthorne equation is used here as a starting point where the fluid is assumed to be steady, incompressible and axisymmetric which allows the Stokes stream function to be retrieved. The Bragg-Hawthorne equation can be seen in eqn 3.3 where eqns 3.4-3.5 represent the tangential angular momentum and total stagnation pressure head respectively. The non linear Beltramian solution has harmonic axial dependence which results in the general solution containing Bessel functions where the radial distributions of flow variables including the individual velocity components and axial vorticity have zeroes which coincide with the zeroes of Bessel functions of

24

the first kind. The Bessel equation seen in eqn 3.6 is a known solution to the Laplace equation which describes fluid potential, but can also be used to describe other important physical properties such as magnetism and thermal energy and therefore has applications in a large spectrum of fields. Bessel functions are also commonly referred to as cylinder functions, as the roots of Bessel functions represent the antinodes of standing waves in a cylindrical geometry. So the harmonic response of a system can be determined via the associated Bessel function, which allows for modal analysis so that positions of zero displacement can be ascertained as well as the frequencies required for certain modes to occur.

$$\frac{\partial^2 \psi}{\partial r^2} - \frac{1}{r}\frac{\partial \psi}{\partial r} + \frac{\partial^2 \psi}{\partial z^2} = r^2 \frac{\partial p_0}{\partial \psi} - B\frac{\partial B}{\partial \psi} \tag{3.3}$$

$$B = ru_\phi \tag{3.4}$$

$$p_0 = p + \frac{1}{2}\rho u^2 \tag{3.5}$$

$$x^2 \frac{\partial^2 y}{\partial x^2} + x\frac{\partial y}{\partial x} + \left(x^2 - \alpha^2\right)y = 0 \tag{3.6}$$

The radial profiles of various flow properties for the non-linear Beltramian model are presented in fig 3.4 and describe the tangential, radial and axial velocity components in addition to the magnitude of axial vorticity, pressure gradient and radial pressure drop in the chamber. The variables V and z refer to the vortex Reynolds number and axial coordinate normalised by chamber length respectively so that various influences such as inlet flow rate, swirl intensity and chamber geometry can be assessed. When viscous core effects are added to the model the effect upon the tangential velocity profile is clear as the asymptotic behaviour of the inviscid formulation is avoided. Apart from the inverse radial proportionality of the free vortex, it can be seen in the solid body rotation region that the gradient of the forced vortex is fairly linear and exhibits a relatively broad peak where the transition to irrotational flow occurs. This tangential velocity profile is similar to that of the Burgers-Rott vortex seen in fig 3.6a but differs in the fact that the Burgers-Rott vortex model is a single cell solution and therefore is unidirectional with regards to axial flow, as opposed the Majdalani-Vyas vortex which is specifically formulated to describe bidirectional flow. The tangential velocity profile of the Burgers-Rott vortex is similar to that of the Oseen-Lamb vortex but differs in several ways such as the addition of radial and axial velocity components. The Oseen-Lamb vortex considers temporal effects and the influence of fluid shear on the radial decay of the vortex although both refer to axisymmetric conditions. As well as being exact solutions of the incompressible Navier-Stokes equations they are also both Gaussian solutions which can be described by eqns 3.7-3.8. In addition to this the Burgers-Rott vortex also includes a term for kinematic eddy viscosity to account for dissipation effects due to turbulence, but this is a scalar variable and does not account for the anisotropic turbulence that occurs in physical vortical flows.

$$u_\phi = \Gamma G\left(\frac{r}{\delta_c}\right) \tag{3.7}$$

$$G\left(x\right) = \frac{1}{4\pi}e^{-\frac{x^2}{4}} \tag{3.8}$$

The tangential velocity profile of the Sullivan vortex can also be seen in fig 3.6b which is an exact solution of the Navier-Stokes equations, where the closed solution refers to a two cell vortex which enables bidirectional flow. This is important as it allows for the existence of a CRZ along the axis of the vortex and is suitable for describing the behaviour of the PVC, which means it is commonly used in investigations of tornadoes [15] as it can account for downdrafts. It also incorporates a term for suction strength similar to the Burgers-Rott vortex, which is also finds applications related to such meteorological phenomenon. A comparison of the Burgers-Rott and Sullivan vortex can be seen in fig 3.6 where the streamlines clearly show the difference between a single cell and double

cell vortex model. This is also reflected in the axial velocity profiles where the abscissa present for the Sullivan model indicates the separation between these cells and the transition in axial direction, which is referred to as the mantle by Majdalani [62]. It is also worth noting that the influence of the CRZ can be seen in the tangential velocity profile of the Sullivan vortex, where the gradient of the forced vortex is linear for a significantly lesser radial proportion of the profile. When the tangential velocity profiles of the Burgers-Rott and Sullivan vortex are overlaid as shown in fig 3.5 it can be seen that the Sullivan vortex produces a higher peak tangential velocity, with the transition from free to forced vortical flow being more abrupt as denoted by the increased local gradients. It is also a better approximation of the Rankine vortex in the irrotational region of the fluid as it deviates from the hyperbolic curve at a reduced radial position, which suggests that the Sullivan vortex is less affected by the effective viscosity component compared to the Burgers-Rott vortex model.

(a) Tangential velocity profile.

(b) Radial velocity profile.

(c) Axial velocity profile.

(d) Vorticity magnitude profile.

(e) Pressure gradient profile.

(f) Pressure drop profile.
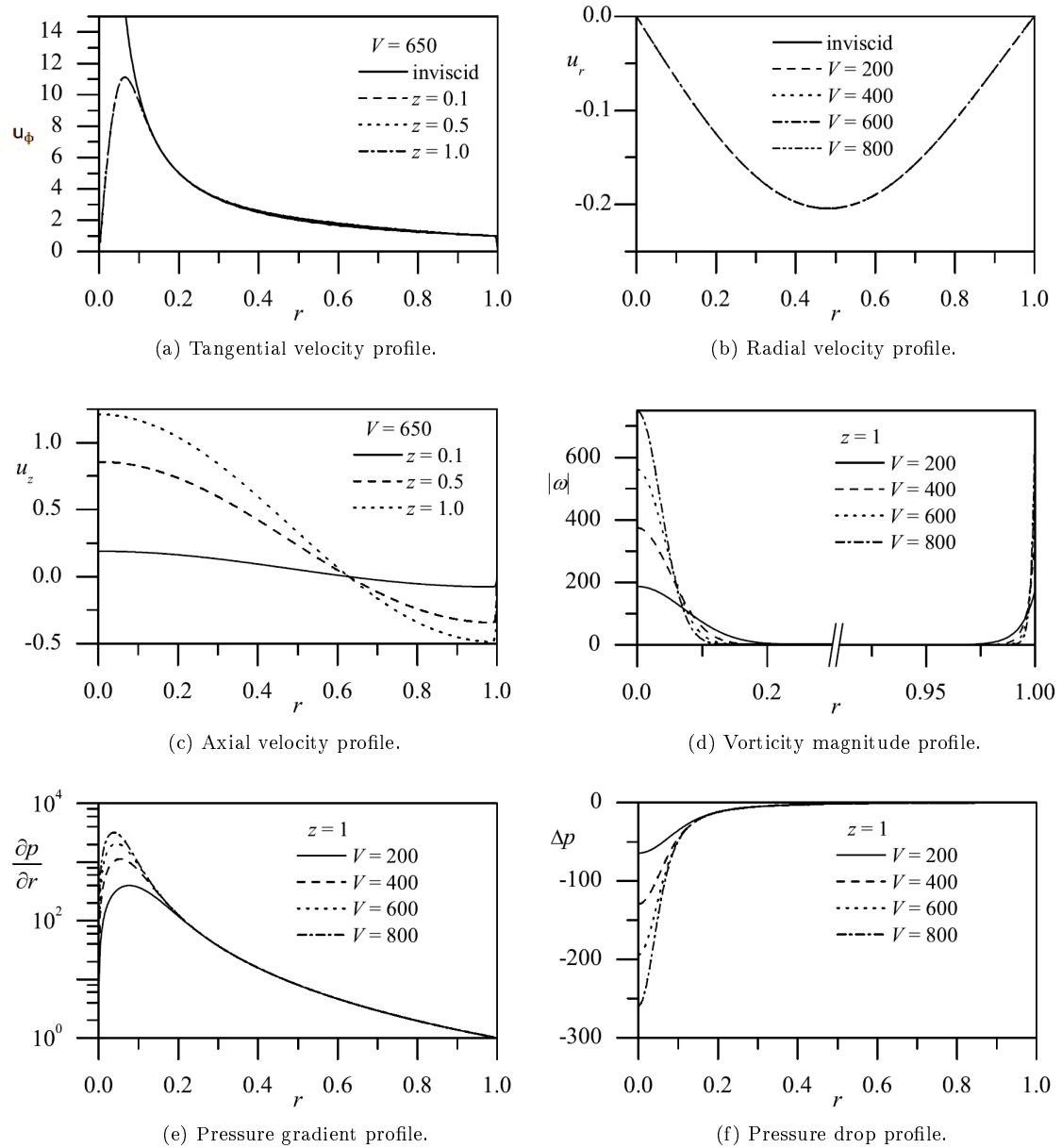
Figure 3.4: Radial profiles produced by the non linear Beltramian solution. [13]
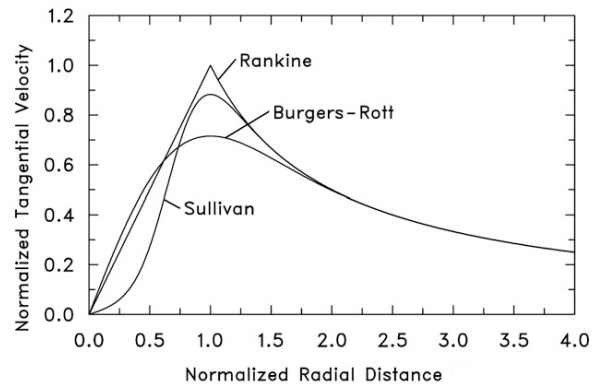
Figure 3.5: Normalised tangential velocity profiles for several vortex models. [14]
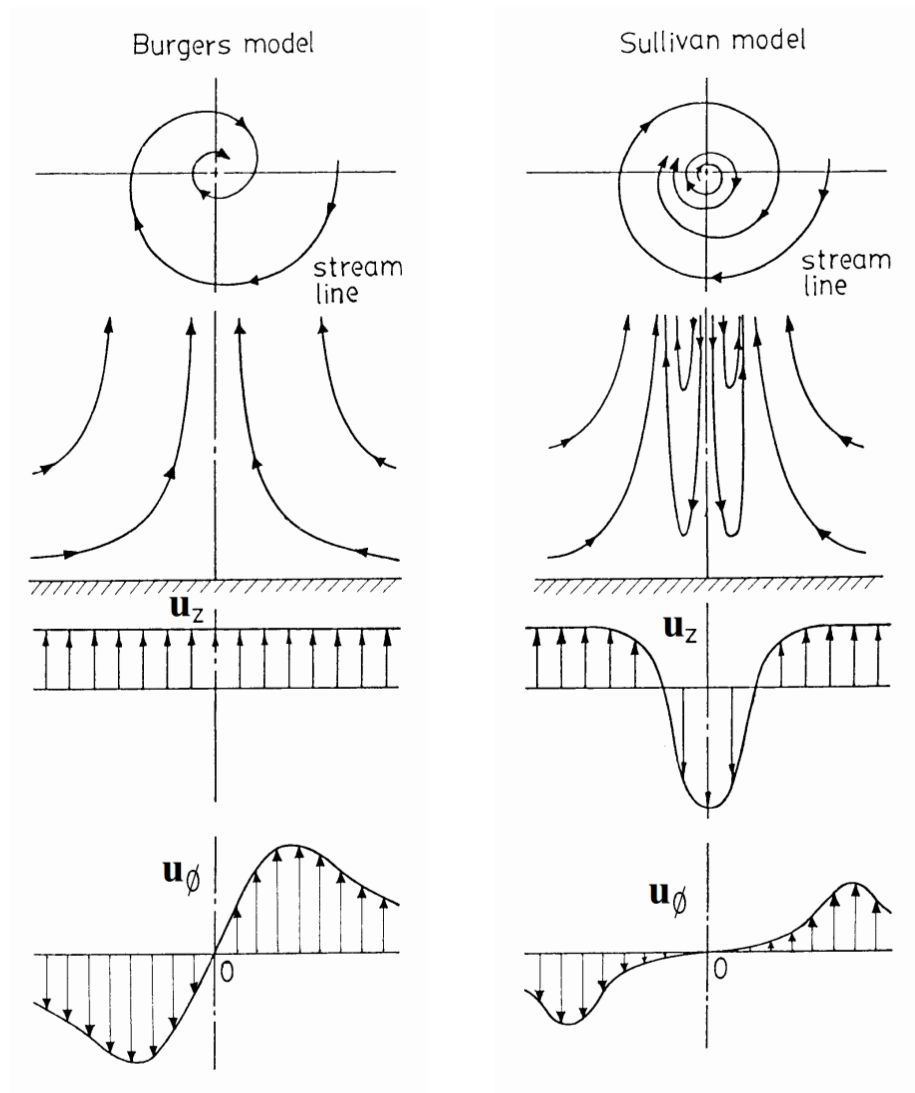
(a) Burgers vortex (single cell).

(b) Sullivan vortex (double cell).

Figure 3.6: Flow characteristics of the Burgers and Sullivan vortex models. [14]
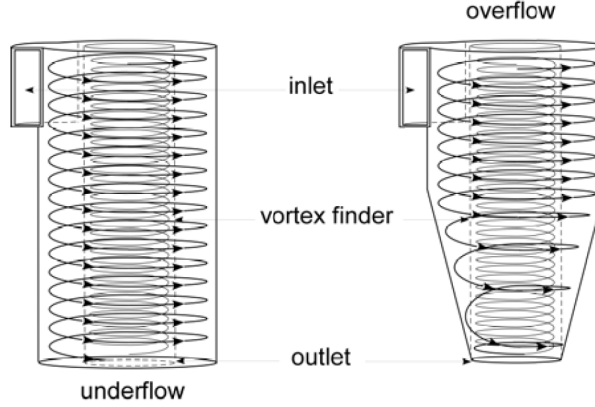
Figure 3.7: Bidirectional vortex flow in common cyclone geometries. [15]

To account for viscous effects in the vortex core and at the periphery of the chamber both regions in the fluid are considered to be representative of boundary layer flow. The dimension of the viscous core is obtained from the radial position at which the velocity component is $u = 0.99u_{max}$, where the viscous core is cylindrical due to the assumption of axisymmetric flow and the negligible axial variance of the resultant velocity profile. A similar insensitivity is found to apply to the boundary layer at the chamber walls, where the thickness of the core and outer boundary layers for the non linear Beltramian solution are described by eqns 3.9-3.10 respectively, where eqn 3.11 is the constant α. The effect of the vortex Reynolds number on the normalised radius of the viscous core at the head of the chamber can be seen in fig 3.8a where it is clear that as the intensity of the vortex increases the radius of the vortex core decreases due to the localised increase in velocity. The same applies to the thickness of the boundary layer attached to cylindrical chamber wall which displays a similar relationship to the vortex Reynolds number in that it is inversely proportional $\delta_w \approx \frac{1}{V}$. The characteristic thickness of the inner and outer boundary layers are displayed in fig 3.8b and indicate that above values of $V = 100$ the peripheral boundary layer becomes increasingly thinner relative to the radius of the vortex core. Examples of these characteristic dimensions are listed in table 3.1 for several axial stations in the chamber over a range of vortex Reynolds numbers and also serve to highlight the axial insensitivity of the boundary layer solutions.

(a) Vortex core thickness.

(b) Boundary layer thickness.
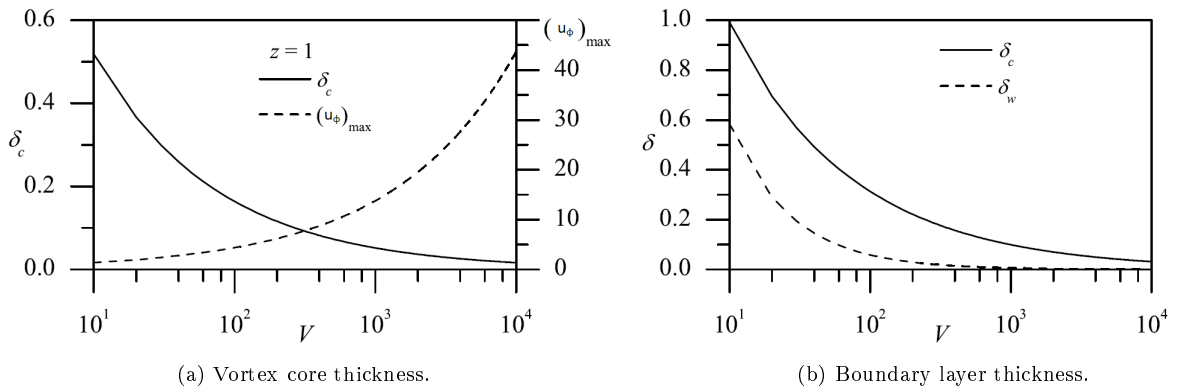
Figure 3.8: Inner and outer layer thickness in relation to vortex Reynolds number. [16]

	Inner boundary layer, δ_c					Sidewall boundary layer, δ_w				
z	$V = 200$	$V = 400$	$V = 600$	$V = 800$	$V = 1000$	$V = 200$	$V = 400$	$V = 600$	$V = 800$	$V = 1000$
0	0.2218	0.1569	0.1281	0.1109	0.0992	0.0295	0.0147	0.0098	0.0074	0.0059
0.25	0.2218	0.1569	0.1281	0.1109	0.0992	0.0295	0.0147	0.0098	0.0074	0.0059
0.5	0.2218	0.1568	0.1281	0.1109	0.0992	0.0295	0.0147	0.0098	0.0074	0.0059
0.75	0.2217	0.1568	0.1281	0.1109	0.0992	0.0294	0.0147	0.0098	0.0074	0.0059
1	0.2217	0.1568	0.1281	0.1109	0.0992	0.0294	0.0147	0.0098	0.0074	0.0059

Table 3.1: Inner and outer boundary layer thickness at various axial positions. [16]
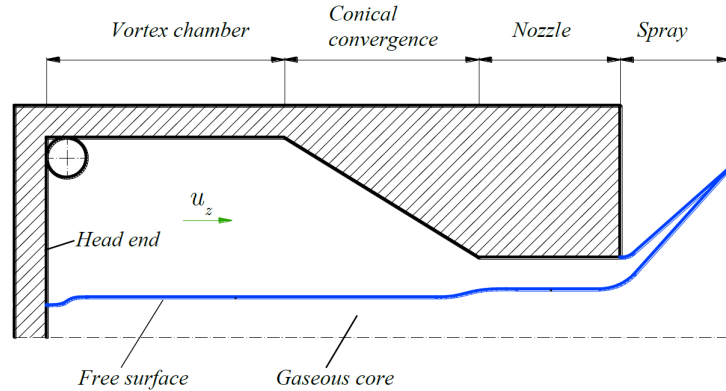
Figure 3.9: Profile of the gaseous core in a swirl injector. [17]

The axial invariance stems from the dominant tangential component of the resultant velocity profile which is found to remain constant irrespective of axial position. The axial and radial velocity components are affected by the axial coordinate to some degree but their axial sensitivity does not significantly influence the resultant velocity profile which is reasonably valid, although physical flows do exhibit a small amount of axial invariance. This is most notable at the head wall of the chamber where the presence of a solid boundary causes increased radial flow and the structure of the vortex is not representative of that seen in the bulk of the fluid. An example of this can be seen in fig 3.9 which depicts the steady-state free surface of the PVC in a swirl atomiser and the variation in radius with respect to length due to the variation in the magnitude of the absolute velocity. In this region of the chamber the magnitude of the axial velocity component is significantly lower than in the rest of the chamber while the opposite is true for the radial velocity component, although this is still small in comparison to the tangential velocity component. The dominant tangential velocity component also exhibits increased magnitude and is therefore indicative of increased angular velocity in addition to the reduced static pressure of the flow. Therefore to ensure conservation of angular momentum, the radius of the core decreases and the reduced static pressure caused by conservation of energy results in an increased radial pressure gradient to maintain equilibrium. A similar effect can be seen in the convergent section of the chamber where the fluid is been accelerated towards the exit, so is subject to a larger axial velocity component which results in a smaller tangential velocity component that causes the radius of the core to expand.

$$\delta_c \approx \sqrt{\frac{\beta_{m,0} J_1 \left(\lambda_m \beta_{m,0}\right)}{2\pi z^2 \kappa^2 \lambda_m^3} \left(-V + \sqrt{V^2 + 64\pi^2 z^2 \kappa^2 \lambda_m^2 \ln\left(10\right)}\right)} \tag{3.9}$$

$$\delta_w = 1 - r_w \approx \frac{2\pi}{V\alpha} \ln\left(100\right) \tag{3.10}$$

$$\alpha = \frac{\lambda_0}{2\beta_{m,0} J_1 \left(\lambda_0 \beta_{m,0}\right)} \left(\frac{1}{8}\lambda_0^2 - 1\right) \approx 4.91131 \tag{3.11}$$

29

(a) Radial velocity profile.   (b) Axial velocity profile.
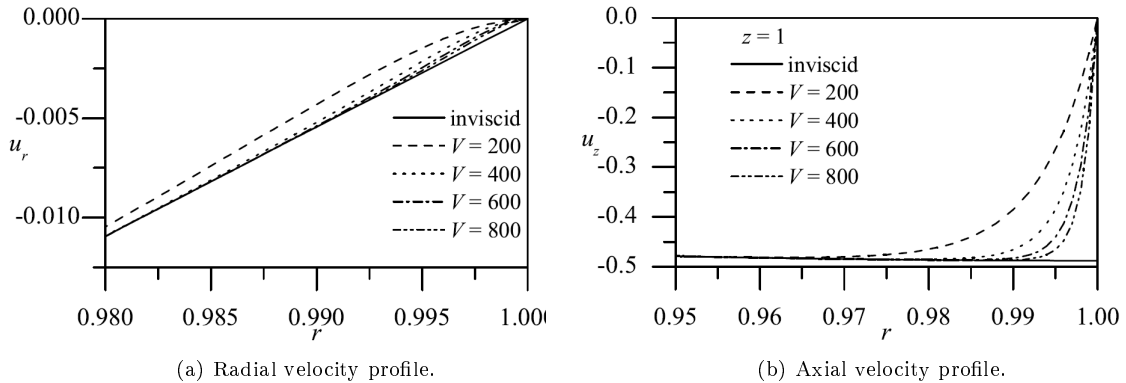
Figure 3.10: Velocity components in close proximity to chamber wall. [18]

The radial velocity profile displayed in fig 3.10a shows that the radial velocity is seemingly unaffected by the vortex Reynolds number and emulates the inviscid profile. Upon closer inspection of the radial velocity profile near the periphery of the chamber, it is found that increasing the vortex Reynolds number results in the viscous solutions tending towards the behaviour of the inviscid solution. This can be seen in fig 3.10a and is attributed to the reduced height of the boundary layer associated with larger vortex Reynolds numbers, where the reduced variation in the radial velocity in conjunction with the reduced radial distance it occurs over results in almost inviscid behaviour. As with all the radial profiles presented in fig 3.4 these represent bidirectional vortical flows as seen in cyclonic devices which exhibit flow fields described by fig 3.7, where there is a single flow reversal and therefore also a single mantle. Unlike the tangential velocity profile, the axial velocity profile obtained by the non linear Beltramian solution seen in fig 3.4c exhibits axial variance with regards to the magnitude of the velocity component. However, the point of zero axial velocity where flow reversal occurs is invariant and according to the formulation of the axial velocity component determined by the Bessel function of the first kind J_0, which relates to a mantle located at a normalised radial position of $\frac{r}{R} = 0.628$. In relation to the analytical solution, the mantle denotes the radial position at which the mass and momentum of the respective inner and outer axial flows are in equilibrium. This effect has also been observed experimentally by Vastitas et al [73] where the radial position of the mantle displays a weak sensitivity to inlet flow conditions as opposed to chamber geometry.

The analytical value corresponds well to both experimental and numerical results, with table 3.2 listing the mantle locations recorded by Smith [56] for a flat base gas cyclone. The increased radial positions obtained by Smith et al are a attributed to differences in chamber geometry as gas cyclones incorporate a vortex finder for gas overflow at the head of the chamber. The presence of the PVC is also assumed to cause radial displacement of the mantle which is a likely shortcoming of the analytical solution and will need to be addressed to better emulate physical vortex flow. In

Site	$L - z$ [in]	r [in]	Radial fraction
1	0.0	2.13	0.7083
2	1.5	2.15	0.7166
3	3.0	2.15	0.7166
4	4.5	2.15	0.7166
5	6.0	2.17	0.7233
6	7.5	2.20	0.7233
7	9.0	2.20	0.7233
Mean		2.16	0.7211

Table 3.2: Mantle positions obtained experimentally from a gas cyclone. [56]

(a) CFD. [10]

(b) Linear Beltramian. [18]
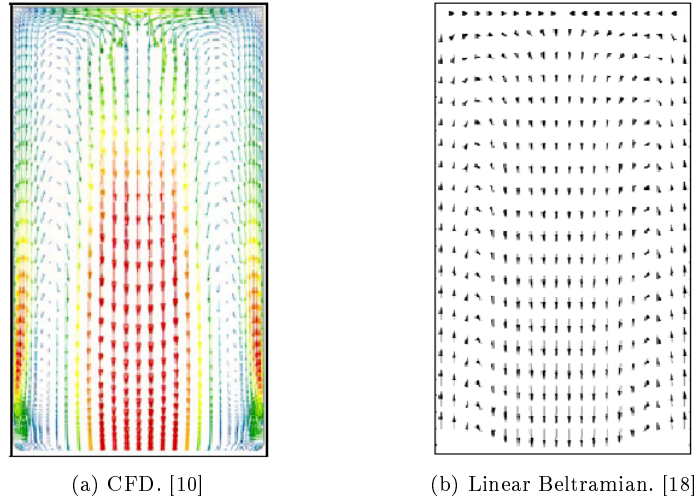
Figure 3.11: Vector fields produced by numerical and analytical methods.

addition to this, mantle positions obtained from numerical investigations conducted by Hoekstra et al [74] on gas cyclones found the mantle was to occur at $\frac{r}{R} = 0.675$, which also indicates radial displacement. Again this is thought to be a result of variations in chamber geometry where the design of the gas cyclone consisted partially of conical geometry. Another possible source of error can be attributed to the data averaging techniques and least squares data fitting methods employed, but despite this the results are still in good agreement with the analytical theory. As with the radial velocity component, the axial velocity component within the viscous boundary layer shown in fig 3.10b tends towards the inviscid solution as the vortex Reynolds number is increased and the height of the boundary layer is reduced. Numerical analysis of the bidirectional vortex was performed using an in house finite difference Navier-Stokes solver where it was assumed that the flow is steady-state and axisymmetric, allowing for a simple 2D quadrilateral mesh to be used [10]. The calculated numerical and linear Beltramian vector fields describing the flow of the bidirectional vortex are presented in fig 3.11 where it is noted that there is favourable agreement between the solutions [75]. The specific boundary conditions and physical models used to calculate the numerical solution are not included in the literature but is it is clear that from the axisymmetric assumption and the lack of reversed flow in the vortex core the computational model inadequately predicts the flow.

The radial distribution of axial vorticity magnitude can be seen in fig 3.4d, where it is clear that as the vortex Reynolds number increases so does the magnitude of the axial vorticity in the core flow. This is also accompanied by a progressive reduction of the radius of the forced vortex indicated by the respective abscissa on the horizontal axis, which denote the transition from forced to free vortical flow. As the vortex Reynolds number increases so does the relative intensity of the vortex, as the swirl component increases as a result of increased inlet velocities and further confined chamber geometry resulting in a an intense coherent vortex. This is directly related to vortex stretching in the axial direction so that conservation of angular momentum is observed, resulting in a reduced vortex core radius. An irrotational fluid has zero vorticity due to the lack of shear induced by rotational flow, upon closer inspection of the axial vorticity distribution it is found that despite initial appearances the free vortex displays a small amount of vorticity on the order of $\mathcal{O}\left(n^{-3}\right)$ with respect to the maximum value occurring at the chamber axis. This may cause issues with data extraction of numerical data as determining the locus of zero axial vorticity provides a simple method for identifying coherent structures in the flow such as the forced vortex, although this method is unable to distinguish between regions of vorticity and shear.

The radial pressure gradient seen in fig 3.4e for the non linear Beltramian theory is found to produce a similar approximation to the complex lamellar theory, where the pressure gradient can be estimated by $\frac{\partial p}{\partial r} \approx \frac{1}{r^3}$. The non linear Beltramian theory incorporates the vortex Reynolds number

rather than the inflow parameter κ which makes it dependent on chamber geometry in addition to inlet boundary conditions, but the pressure gradient profile is still fairly insensitive to these parameters. As expected fig 3.4e shows that the pressure gradient increases in relation to greater vortex Reynolds numbers and the maxima tend towards the chamber axis as the radius of the forced vortex decreases with the increasing swirl intensity. Dhir and Chang [65] produced a formulation describing the swirl intensity for a unidirectional vortex within a cylindrical geometry which was then later adapted by Majdalani [76] so that it could be applied to bidirectional vortex flow, the result of which can be seen in eqn 3.12. It is apparent that this suggests that swirl intensity is greatest at the head of the chamber where the transition from negative to positive axial flow occurs and the streamlines display maximum curvature. This is beneficial with regards to engine performance as it indicates that there is increased localised turbulence that results in enhanced mixing of the propellants, which is likely to result in increased combustion efficiency as a lesser proportion of unreacted material will escape the chamber [77]. This also suggests that placing tangential inlets at the head of the chamber would result in enhanced performance as the additional tangential momentum produced by the flow would result in increased swirl strength, signified by the increase in the swirl number and swirl intensity parameters. Apart from affecting combustion efficiency the head of the chamber may also provide a suitable location for tertiary oxidiser injection so that the O/F shift that occurs during engine operation can be directly controlled.

$$\Omega \simeq \frac{0.866244}{\kappa z} = \frac{5.44277}{z}\sigma L = 2.45011\frac{S}{(z/L)} \tag{3.12}$$

The radial static pressure distribution displayed in fig 3.4f refers to the pressure drop $\triangle p$ of the static pressure p in the chamber relative to the centre of the head wall boundary p_0 which are both normalised by the dynamic pressure at the inlet $\frac{1}{2}\rho u^2$. In accordance with the radial pressure gradient it can be seen that by increasing the vortex Reynolds number and in turn the intensity of the vortex, the increased velocity magnitude results in an increased pressure drop in the vortex core. This reduced pressure will cause a reduction in the radius of the forced vortex as the forces in the non inertial frame are no longer in equilibrium as centripetal force becomes greater than the pressure component where the resultant net force acts in the negative radial direction. The non linear Beltramian formulation of the pressure drop in the chamber accounts for both radial and axial coordinates but finds that the influence of the axial coordinate is several orders lower than the radial contribution. Therefore the analytical solution is relatively insensitive to axial position and it can be assumed that for adequately short chambers that the radial profile is representative of the pressure distribution throughout the chamber. The equation describing the pressure drop in the chamber is rather complex, but the complex lamellar solution provides a similar solution that emulates the behaviour of the non linear Beltramian solution over the majority of the chamber radius. It can be seen in fig 3.12d that these respective models begin to diverge within the core region of the flow where the complex lamellar model does not account for the increased radial pressure gradient captured by the non linear Beltramian solution. This results in a pressure profile reminiscent of the non linear Beltramian solution but at a reduced vortex Reynolds number, which is indicative of a tangential velocity component of lesser magnitude as seen in fig 3.12a. The peak tangential velocity is approximately half that of the Beltramian solutions with the transition from the forced to free vortex occurring at a greater radius, which also indicates that the swirl intensity is reduced as would be expected from a flow with a lower vortex Reynolds number. If the tangential, radial and axial velocity components in figs 3.12a-3.12c are considered it can be seen repeatedly that the complex lamellar solution appears to underestimate the magnitude of the velocity component in each case, further suggesting that the vortex predicted by the complex lamellar model is less intense than that found by the Beltramian solutions. Regarding the pressure drop in the chamber, it can be assumed that the complex lamellar solution provides a simplified alternative to the Beltramian solution that could be adapted to better emulate the profiles obtained by the Beltramian solutions if a scale factor was applied to the vortex Reynolds number. In spite of this, the radial pressure drop of the complex lamellar solution is still valid across a large radial portion of the chamber and can be estimated by a simple hyperbolic approximation $\triangle p \simeq \frac{1}{2r^2}$ and provides a convenient method for comparing the analytical solution to both experimental and numerical data. Due to the asymptotic nature of this

(a) Tangential velocity profile.

(b) Radial velocity profile.

(c) Axial velocity profile.

(d) Pressure drop profile.
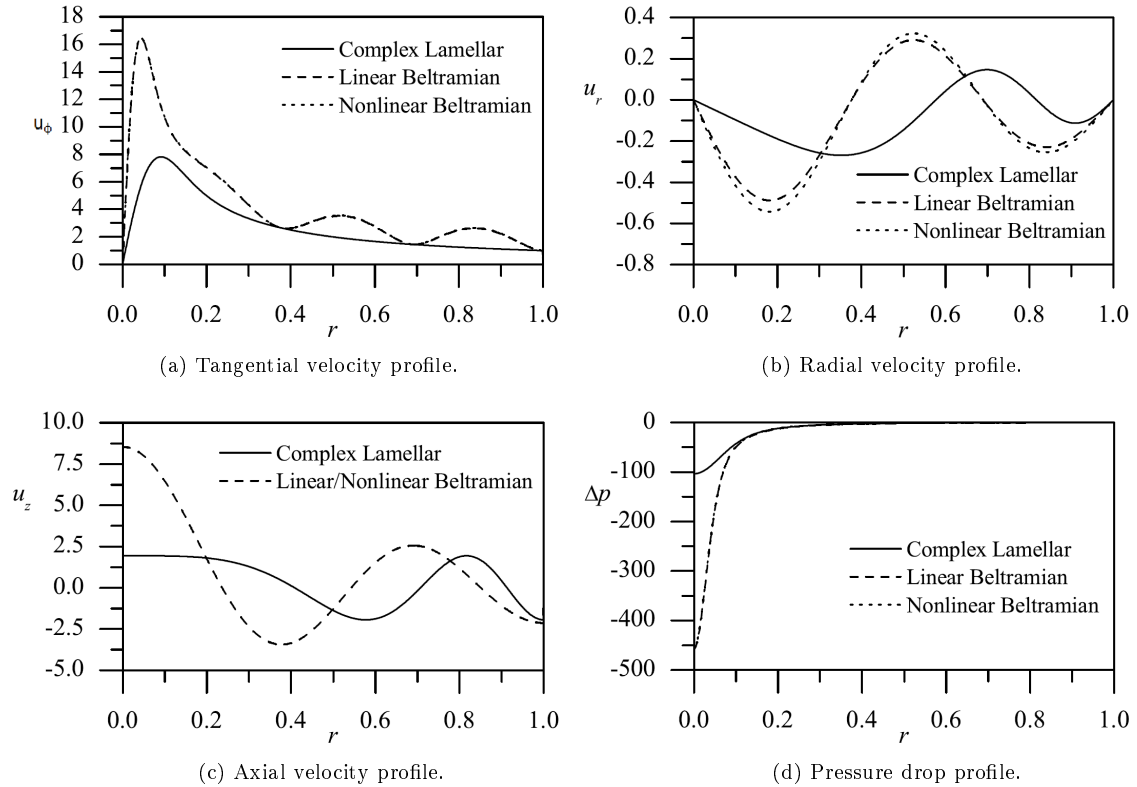
Figure 3.12: Radial profiles produced by the analytical solutions. [19]

function and the large range this value occurs over, the pressure drop appears to increase linearly with respect to radius within the irrotational region of the flow. Therefore care must be taken when analysing experimental and numerical data to ensure that appropriate post processing techniques are applied to account for the non linear form of the radial pressure drop profile.

Related studies with specific relevance to the bidirectional vortex focus on solving the problem in spherical coordinates [75] and also for conical chambers, which sets out to overcome some of the deficiencies encountered by Bloor and Ingham [78] when describing the flow in cyclonic separators using the Bragg-Hawthorne equation [76]. Through use of the Bragg-Hawthorne equation the most recent incarnation of the bidirectional vortex model has been formulated to account for compressibility effects describing linear Beltramian flow. This incidentally reveals that the mantle exhibits axial variance which has been reported both experimentally and numerically [24,26,56,74,79], indicating the models improved abilities to replicate physical flow conditions [18]. It is also found that the gradient of the axial velocity component also increases, reminiscent of those seen in spinning solid rocket motors and additionally that the mantle position is also affected by the inflow swirl parameter and becomes more sensitive at higher Reynolds numbers [13]. This suggests that the flow reversal patterns could be directly affected by flow properties, although the requirement for large Reynolds numbers and intense swirl could be compared to the energy based solutions of the bidirectional vortex. It was found that through use of Lagrangian optimisation, energy states describing the flow could be derived where flows with large amounts of kinetic energy were associated not only with increased inlet velocities but also reduced chamber aspect ratios [80]. A bi-global instability analysis was also conducted for the complex lamellar, linear Beltramian and non linear Beltramian bidirectional vortex models which set out to parametrically identify stability criteria which may be employed from a design perspective to ensure coherent vortex flow within the chamber. It is suggested that bi-global analysis is more suitable than the alternative local non parallel method, which is more suited to describe hydrodynamic instability in solid rocket motors, as VIHRE configurations possess greatly reduced chamber aspect ratios so certain assumptions such as the parallel

(a) Complex lamellar.   (b) Linear Beltramian.   (c) Nonlinear Beltramian.
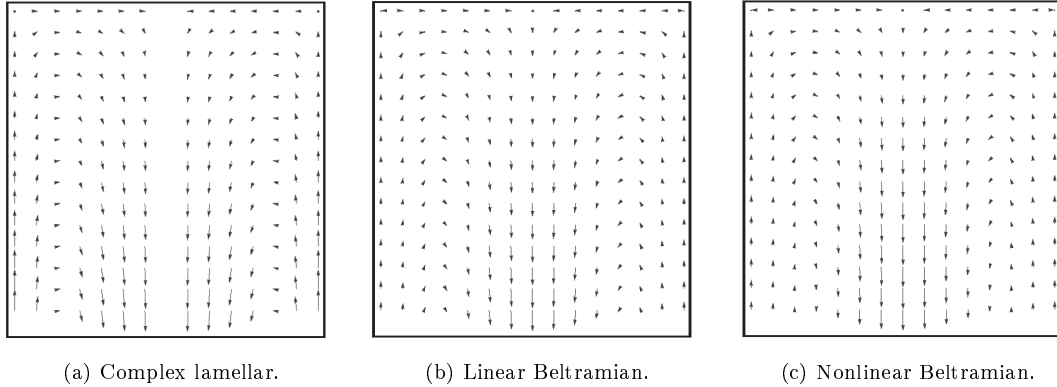
Figure 3.13: Vector fields produced by the analytical solutions. [13]

(a) Complex lamellar.   (b) Linear Beltramian.   (c) Nonlinear Beltramian.
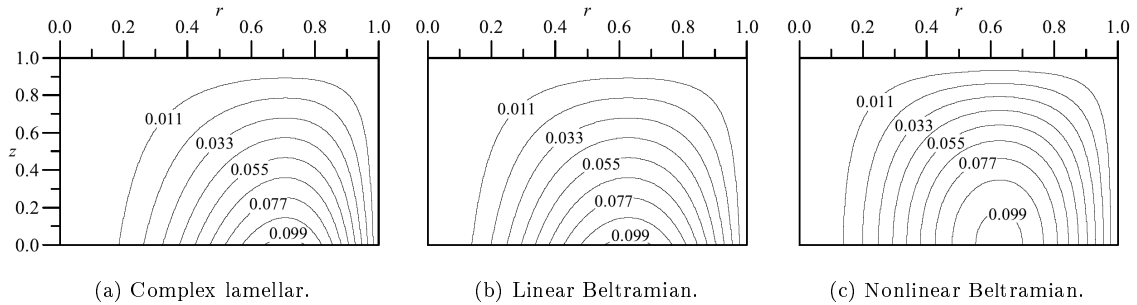
Figure 3.14: Streamlines produced by the analytical solutions. [13]

flow assumption do not hold true [81]. Distinct mean profiles relating to complex lamellar, linear Beltramian and non linear Beltramian which can be seen in fig 3.13 and fig 3.14 are used to make comparisons between the various vortex models. The spectral characteristics of the flow were calculated so that eigensolutions could be retrieved, enabling the influence of chamber geometry and swirl intensity upon hydrodynamic instability to be assessed. It was found that when the flow was asymmetric that oscillations observed in the mean flow stream lines caused by hydrodynamics waves had greater amplitudes than those for when the flow is axisymmetric and therefore was more prone to instability. This is easily demonstrated in cyclonic separators where a vortex produced by a single tangential inlet is more unstable relative to a chamber with two tangential inlets. As the vortex core commonly exhibits pronounced precession and contains a helical vortex filament, where multiple inlets are able to produce more coherent vortices and are more columnar in form as well as displaying increased resistance to axial perturbations.

Apart from this the bi-global instability analysis also found that regions susceptible to instability occur where there are large curvatures in the streamlines, such as the head wall of the chamber where it is postulated that the flow could breakdown, although this is also to be expected at the base wall of the chamber also if multiple flow reversals are present. Again this can be explained physically by using vortex breakdown as an example, where the impingement of flow at a solid boundary causes instability in the structure of the vortex, resulting in some mode of disruption to the vortex. Regarding VIHRE design, this is especially important if multiple mantles are required as dissipation of the vortex could interrupt flow reversal and effectively lead to a reduction the performance of the engine. Increased swirl intensity was found to be beneficial with regards to the stability of the flow due to the increased tangential velocity component preventing the vortex from deviating from axisymmetric flow conditions. A significant finding was that an aspect ratio of $\frac{L}{D} = 0.75$ is considered to be a near optimum chamber geometry, conducive to stable flow conditions and less susceptible to unstable modes. This is an interesting result as it provides further evidence that not only is chamber geometry an important variable with regards to vortex flow but low aspect ratio

34

chambers are more suitable for producing coherent vortices with intense swirl. Unrelated to the bidirectional vortex are recent advancements in the theoretical modelling of wall transpiration in hybrid rocket engines due to fuel pyrolysis. Uniform velocity profiles are applied that are orthogonal to the curved boundary of the chamber and represent fuel surface transpiration, while the parabolic velocity profile at the head of the chamber represents the velocity profile of oxidiser flow injection through a porous boundary. The formulation of the oxidiser velocity profile is also sinusoidal which allows for investigation of hydrodynamic instability in the chamber as the axial harmonics of the chamber can be realised. The current model relates to classic axial flow hybrid rocket engines and the flow is assumed to be axisymmetric, rotational and incompressible, so it provides a framework further additions to be made such as the inclusion of bidirectional vortex flow. This solution is presented as the first step in the development of increasingly complex models of gas dynamics in hybrid rocket engines which will include full treatment of viscous effects as well as radially regressing walls emulating fuel surface regression [82].

3.4 Multiple solutions

In finding the solution of the initial inviscid solution of the coaxial bidirectional vortex, Vyas et al [62] noted that when the equation describing the axial velocity has multiple roots, there can be several radial positions in a chamber where axial velocity is zero. This introduces the possibility of creating vortical flows containing multiple mantles and therefore multiple flow reversals. As a result, Vyas et al [23] investigated this further and developed an additional analytical solution to account for the effects multiple mantles would have upon the properties of the flow. Subsequent more complex treatments of the bidirectional vortex focus predominantly on resolving the flow fields that occur in the VIHRE and various other cyclonic devices. It was apparent that the further more complex formulations of the axial velocity component also exhibited solutions with multiple roots. Despite the current lack of numerical and experimental data regarding bidirectional vortices containing multiple mantles, they provide an important avenue of research with regards to increasing the effectiveness of VIHRE operations. As the ability to induce such flows would result in increasingly convoluted helical pathlines throughout the chamber which would increase its effective length L^* in addition to increasing the residence time of the flow in the chamber, allowing for more complete combustion of the reactants to occur. It would also promote enhanced mixing of the oxidiser and pyrolysed fuel, especially at the head of the chamber where increased species transport would result from the presence of several vortex tubes, which in turn would aid combustion. Apart from increasing the combustion efficiency of the chamber, the additional radial layers of the vortex would provide increased thermal shielding as the combusting flow is further confined to the near axis region of the flow. Typical temperatures within the vortex core of a VIHRE are approximately $T_c = 3500K$ while the temperatures at the wall of the chamber are found to be approximately $T_s = 600K$, which is already a significant drop in temperature over a relatively small radial distance. Increased thermal shielding allows for the use of thinner refractory materials to be used to construct the chamber or even other lighter materials that were not previously viable. This could have a significant impact upon the total weight of the chamber and considering the potential applications of VIHRE in providing propulsion for satellites, spacecraft and missiles the decreased weight would be of great benefit. Another factor which could reduce the total weight of the engine stems from the increased effective length of the chamber, where an engine with a low aspect ratio could have the same effective chamber length as a much larger chamber. This has already been demonstrated when comparing current VIHRE designs to classic axial flow hybrid rockets, but further reductions in size would result in compact and highly efficient engines.

As mentioned previously the non linear Beltramian solution currently provides the most recent and comprehensive treatment of the bidirectional vortex with regards to characterising the behaviour of the flow when several mantles occur. The comparison of the velocity and static pressure drop profiles for the complex lamellar, linear Beltramian and non linear Beltramian models seen in fig 3.12 relates to a flow reversal mode $m = 2$ that indicates the presence of three mantles. This condition describes the flow field seen in fig 3.15 which represents the next possible flow configuration in a
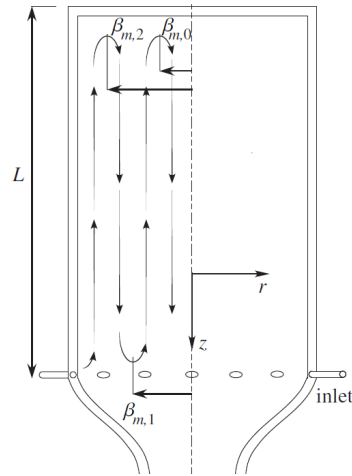
Figure 3.15: Hypothetical triple flow reversal that is indicative of quadruple vortex. [19]

(a) Single flow reversal (double vortex).

(b) Triple flow reversal (quadruple vortex).
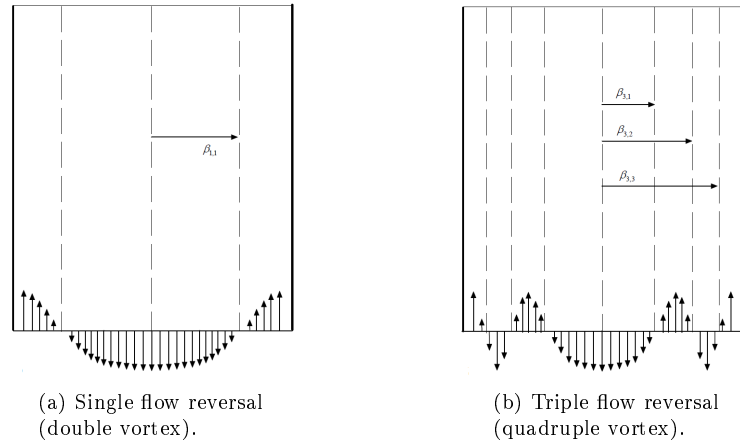
Figure 3.16: Axial velocity profiles and mantle positions associated with multiple flow reversals. [19]

VIHRE when the tangential inlets are situated at the base of the chamber. The variable β refers to the normalised radial position the mantle occurs at, while the subscripts m and n refer to the flow reversal mode and the radial ordering of the mantles. Examples of the multiple mantle configurations are displayed in fig 3.16 which relate to cases with single and triple mantles respectively where the inward radial shift of the first mantle in fig 3.16b can be seen, due to the occurrence of additional mantles. These radial locations are obtained by finding the roots of the Bessel function of the first kind J_0 then normalising these values by λ_m which is referred to as the placeholder of the roots or more specifically the eigenvalue of the axial velocity formulation. The eigenvalue is similarly determined by obtaining the roots of another Bessel function of the first kind J_1, which incidentally provides the zeroes of the radial velocity component as well as indicating the positions of minima in the tangential velocity profile. A plot of the Bessel functions of the first kind J_0, J_1 are shown in fig 3.17 for clarity and also to highlight the need to normalise the roots of J_0 by those of J_1 to ensure that the mantle position lies within the range $0 < \frac{r}{R} < 1$, as well as creating a zero at the periphery of the chamber due to the no slip condition imposed at the walls.

The flow reversal modes and their respective eigenvalues and normalised mantle positions are presented in table 3.3 where it can be seen that as the flow reversal mode increases the grouping of the outermost mantles becomes more dense. This suggests that the radial gradients of velocity and pressure in such flows will be significantly higher than in the standard single mantle case to enable the large streamline curvature required to cater for additional vortex tubes within the chamber.
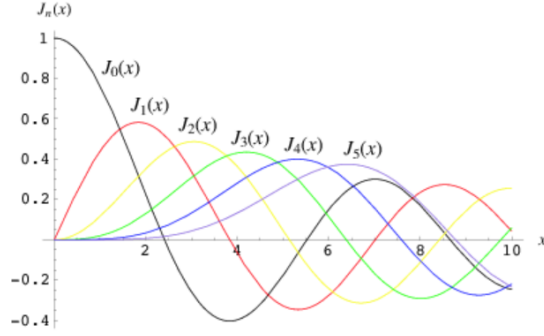
Figure 3.17: Plot of Bessel functions of the first kind. [20]

m	λ_m	$\beta_{m,0}$	$\beta_{m,1}$	$\beta_{m,2}$	$\beta_{m,3}$	$\beta_{m,4}$	$\beta_{m,5}$	$\beta_{m,6}$	$\beta_{m,7}$	$\beta_{m,8}$	$\beta_{m,9}$	$\beta_{m,10}$
0	3.832	0.628										
2	10.174	0.236	0.543	0.851								
4	16.471	0.146	0.335	0.525	0.716	0.907						
6	22.760	0.106	0.243	0.380	0.518	0.656	0.794	0.932				
8	29.047	0.083	0.190	0.298	0.406	0.514	0.622	0.730	0.838	0.947		
10	35.332	0.068	0.156	0.245	0.334	0.423	0.511	0.600	0.689	0.778	0.867	0.956

Table 3.3: Mantle positions obtained from the normalised roots of J_0. [19]

This also implies that to induce a bidirectional vortex with multiple mantles, the magnitude of the inlet flow velocity must be increased significantly so that an adequately intense vortex is established. The increased magnitude of the velocity components and the resultant reduced radius of the vortex core provides the necessary conditions for several parabolic streamlines. Currently all the analytical, numerical and experimental work pertaining to the bidirectional vortex has been based on vortex chambers of similar design with minimal variation in geometrical characteristics, such as the aspect and contraction ratio. A more significant omission though is related to the axial position of the tangential inlets as they are always situated at the base of the chamber or in a singular case located at half of the chamber length [25, 79]. There is a relatively large degree of confidence in the ability of the analytical solutions of the bidirectional vortex to predict physical flow conditions and there are repeated appearances of multiple roots in the formulation of the axial velocity component. It seems obvious that specific solutions regarding vortex chambers with tangential inlets positioned at the head of the chamber should also be produced as the current bulk of the theory is applicable to such configurations. In the knowledge that the mantles are found to be coincident with the roots of J_0 normalised by λ_m then the mantle positions of chambers with tangential inlets at the head of the chamber can easily be retrieved in light of this omission.

(a) Subsonic flow.

(b) Supersonic flow.
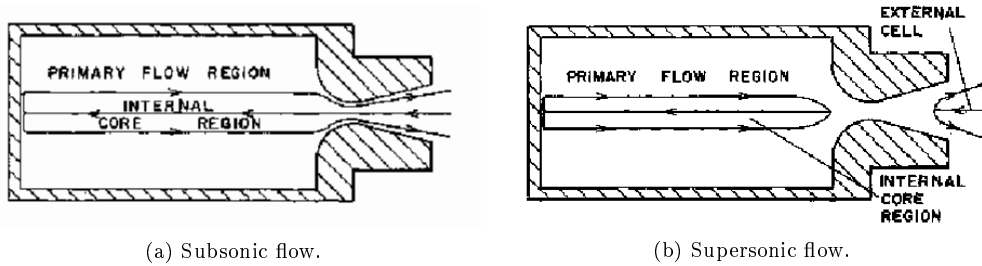
Figure 3.18: Internal cell structure of the CRZ in relation to sonic conditions at throat. [21]

37

(a) Increasing kinetic energy.   (b) Decreasing kinetic energy.
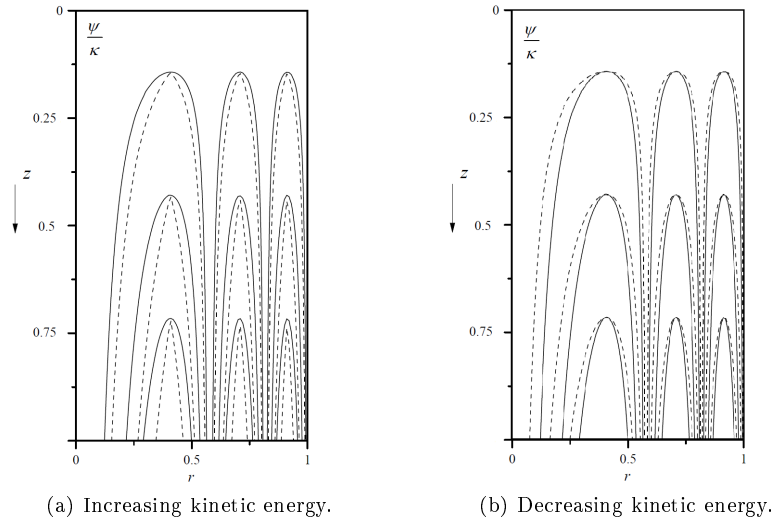
Figure 3.19: Streamlines in the meridional plane in response to the kinetic energy of flow. [22]

Figure 3.20: Post-fired fuel grain from the head of a VIHRE combustion chamber. [23]

When the energy based solution was specifically used to assess the effects of energy content of the flow upon the roots of the axial velocity formulation, it was found that theoretically the number of mantles and therefore the amount of flow reversal in the chamber increases relative to increased kinetic energy within the flow [22]. This agrees with the assumption that velocities of greater magnitude are required to produce the large radial gradients to allow for the streamline curvature associated with the presence of multiple mantles. The effects of the kinetic energy content of the flow upon the streamlines are shown in fig 3.19 for a triple mantle configuration where the the solid lines represent the streamlines of the baseline bidirectional vortex, where as the dashed lines represent the streamlines obtained when the kinetic energy is either increased and decreased respectively. Currently there is little evidence to corroborate this, although it has been indicated through analysis of regression patterns in spent fuel grains such as that seen in fig 3.20 that complex vortex flows containing more than a single mantle are possible. More importantly though, the fuel grain was recovered from a vortex hybrid rocket engine with a low aspect ratio $\frac{L}{D} \approx 0.4$, which in combination with the knowledge that increased tangential velocities are conducive to intense coherent vortices gives credence to the findings of the energy based solution of the bidirectional vortex. The energy based solution also investigated the effects of chamber length on the flow and defines critical geometrical parameters that limit the number of mantles that may occur providing a general relationship between chamber geometry and maximum possible flow reversal.
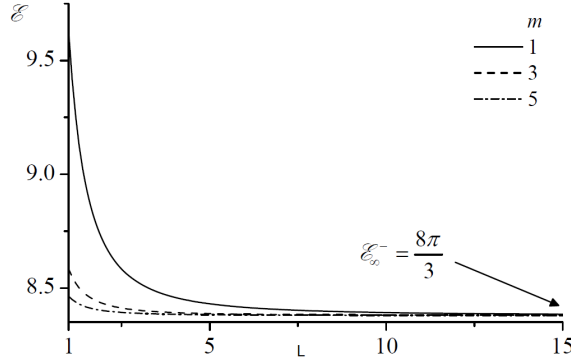
Figure 3.21: Variation in the kinetic energy of the flow with respect L. [22]

The graph seen in fig 3.21 plots the kinetic energy of the flow against the length of the chamber, which enabled a critical chamber aspect ratio to be obtained. Above this value the variation in the kinetic energy content of the flow is below 1% of the final asymptotic value. The critical aspect ratio for the single mantle case is found to be $\frac{L}{D} = 1.976$ which is effectively $\frac{L}{D} = 2$ and beyond this value it can be assumed that as $\frac{L}{D} \to \infty$ only a single mantle can exist in the chamber. Fig 3.21 also includes the energy content plots for the cases where there are 3 and 5 mantles which reveal that the critical aspect ratios are $\frac{L}{D} = 1$ and $\frac{L}{D} = 0.5$ respectively, which indicates that chambers with lower aspect ratios are better suited to inducing a bidirectional vortex with multiple mantles. Apart from the patterns observed in the spent fuel grain in fig 3.20 which infer the presence of bidirectional flow with multiple mantles, an investigation conducted by Chiaverini et al [79] currently provides the most compelling evidence to corroborating their existence. Particle image velocimetry (PIV) was employed to characterise the velocity components in the azimuthal plane of a gas cyclone in order to emulate the non reacting oxidiser flow in a VIHRE. A high pressure gas supply was used to ensure that the flow at the outlet of the chamber was choked, where the Mach disc occurring at the throat severs the internal flow of the PVC from the external flow. This means that the CRZ is unable to exist beyond the confines of the chamber and establish a cylindrical form but instead must form a closed cell along the axis of the chamber as seen in fig 3.18b. The effects of injector pressure drop and chamber aspect ratio were assessed through analysis of the tangential velocity profiles obtained from the PIV vector maps. This method is unable to resolve the out of plane axial velocity component, which meant that flow reversal had to be determined visually from rings of seeding particle residue that accumulated on the observation window at the head of the chamber. Light rings were formed in regions of negative axial flow and dark rings in regions of positive axial flow directed towards the outlet of the chamber. Therefore the radial position of the mantles could be obtained by determining the boundaries of these ring formations. It is subjective but several light rings were observed which indicated the presence multiple mantles, the positions of which are presented in table 3.4. Anderson et al [25] also produced numerical data for the chamber configurations investigated in the PIV study. This is also presented in table 3.4 and was obtained through use of the 3D Navier-Stokes solver Fluent employing the Reynolds stress turbulence model and uniform second order upwind discretisation scheme. Both the numerical and empirical data shown in table 3.4 relate to a chamber configuration and inlet flow conditions that were arguably able to produce a bidirectional vortex with multiple mantles, although it is not stated under what conditions this occurred. It can therefore only be assumed that these observations were made for a chamber with a low aspect ratio and a large pressure drop across the tangential inlets. This is based on conclusions drawn from analytical, numerical and experimental investigations, as this combination is most likely to result in an intense confined vortex, with the flow containing a large amount of kinetic energy. If so this would require a chamber with an aspect ratio of $\frac{L}{D} = 0.7$ and an a pressure drop of $\triangle p = 0.2 p_{ch}$ across the tangential inlets with regards to the range of parameters tested. The variable p_c refers to the maximum static pressure in the chamber which occurs at the

			Experimental			Computational		
n	$\beta_{2,n}^{(CL)}$	$\beta_{2,n}^{(BT)}$	$\beta_{2,n}^{(EXP)}$	$\left\vert\beta_{2,n}^{(CL)}-\beta_{2,n}^{(EXP)}\right\vert$	$\left\vert\beta_{2,n}^{(BT)}-\beta_{2,n}^{(EXP)}\right\vert$	$\beta_{2,n}^{(CFD)}$	$\left\vert\beta_{2,n}^{(CL)}-\beta_{2,n}^{(CFD)}\right\vert$	$\left\vert\beta_{2,n}^{(BT)}-\beta_{2,n}^{(CFD)}\right\vert$
0	0.408	0.236	0.296	0.112	0.060	0.305	0.103	0.069
1	0.707	0.543	0.594	0.113	0.051	0.385	0.322	0.158
2	0.913	0.851	0.803	0.110	0.048	0.787	0.126	0.064

Table 3.4: Non dimensional radial error in the mantle positions. [19]

intersection of the chamber wall and the injector where the flow enters the chamber. It was claimed that the radial positions of four mantles were obtained, where the outermost mantle occurred at $\frac{r}{R} = 0.955$ and $\frac{r}{R} = 1.0$ in the experimental and numerical results respectively. Despite being treated as a mantle and also being used in a comparison with the results of the initial solution of the bidirectional vortex with multiple roots [23], it was later realised that this did not represent an actual mantle. The fact that the supposed outer mantle obtained by the CFD occurred at the wall of the chamber meant that this was indicative of the no slip condition imposed at the solid boundaries of the chamber. The supposed outermost radial position obtained from experimental observations is based on the variation in pixel intensity, which denotes the transition between positive and negative axial flow. It is likely that the pixel intensity observed at the periphery of the chamber is lower than that created by the flow at a small radial distance from the chamber wall due to the effects of the viscous boundary layer dissipating the momentum of the flow and preventing particle accumulation on the viewing window at the head of the chamber. However, this was corrected for in the Beltramian solutions concerning multiple mantles [19], which treats the findings of Rom et al [79] to represent a flow configuration containing three mantles. This also satisfies the geometrical criteria which states that chambers with tangential inlets located at the base of the chamber are only capable of producing a vortex with an odd amount of mantles. The experimental and numerical data obtained by Rom et al [79] is compared in table 3.4 to the mantle positions retrieved from both the complex lamellar and Beltramian solutions. The error in the normalised radial coordinate of the mantles predicted by the Beltramian solutions are approximately half that of the complex lamellar solution, highlighting the suitability of the non linear Beltramian model in describing complex vortical flows.

3.5 Influence of boundary conditions

Although little is known about what affects the structure of the mantle, the complex lamellar [69], Beltramian [13,18] and energy based [22,80] solutions of the bidirectional vortex provide some insight into what parameters may influence the behaviour of the flow. Despite the obvious differences seen in the radial profiles produced by the complex lamellar and Beltramian solutions as depicted previously by fig 3.12, they are both in agreement that the number of mantles the flow can sustain is related to the intensity of the vortex. This is demonstrated in fig 3.22 which describes the effect of increasing the flow reversal mode upon various flow properties obtained by the non linear Beltramian solution. It can be seen that each velocity component exhibits a greater magnitude relative to higher flow reversal modes, as does the magnitude of the axial vorticity which signifies an escalation in vortex stretching. This is indicative of a concentrated vortex core, which is also visible in the reduced radial position of the peak tangential velocity in fig 3.22a and the peak of the radial static pressure gradient tending towards the chamber axis. When it is considered that inlet flow conditions have been found to have a significant impact upon the intensity of the core within the bidirectional vortex [79] it is wise to assume that if the structure of the bidirectional vortex is affected by the magnitude of the inlet flow velocity then the embedded mantle structure will also likely be affected.

(a) Tangential velocity profile.

(b) Axial velocity profile.

(c) Radial velocity profile.

(d) Vorticity magnitude profile.

(e) Pressure gradient profile.

(f) Pressure drop profile.
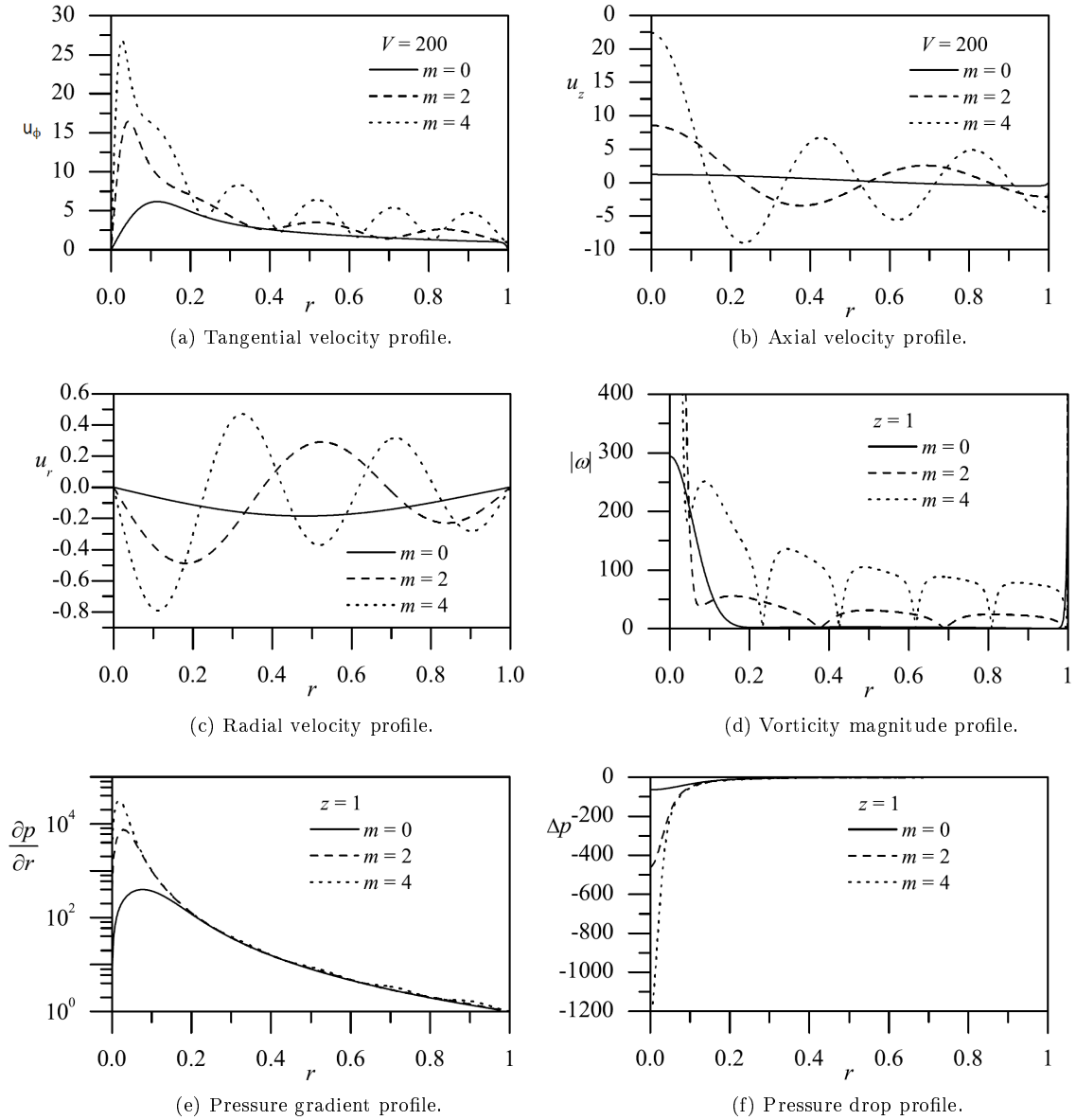
Figure 3.22: Radial profiles of the non linear Beltramian solution for multiple mantles. [19]

Although the energy based solution focuses on the kinetic energy content of the vortex rather than the individual components of the flow, it does find that larger amounts of kinetic energy are required to ensure the formation of multiple mantles. This corroborates the findings of the Beltramian solutions where the resultant velocity magnitude needs to be sufficiently large and impart substantial kinetic energy into the flow to enable the formation of further mantles. It was found that for a discrete amount of mantles the kinetic energy content of the flow decreased as the length of the chamber was increased and that there is a critical chamber length beyond which it is no longer possible to sustain multiple mantles. Through analysing the kinetic energy content distribution curves for various mantle configurations as displayed previously in fig 3.21 it was possible to determine several critical chamber aspect ratios. This provides geometrical criteria that can be applied to vortex chamber designs in order to ensure a predetermined range of mantle configurations are possible, given that the kinetic energy content of the flow is sufficiently large enough. This effectively demonstrates that in order to produce a bidirectional vortex with multiple mantles a chamber with a low aspect ratio is required, such as the VEBH [58] which has an aspect ratio of $\frac{L}{D} \approx 0.4$. This engine configuration was

responsible for creating the spent fuel grain displayed previously in fig 3.20 that provides possible evidence of multiple flow reversals. The PIV investigation conducted by Anderson et al [25] also indicates that low aspect ratio chambers are more conducive to producing intense concentrated vortices associated with increased kinetic energy content in the flow.

The energy based solution also states that as the kinetic energy content of the flow is increased the gradient of the streamlines in the axial plane of the chamber increases, reducing the radial dimension of the individual vortex tubes as seen earlier in fig 3.19a, where the innermost vortex tube exhibits the greatest deformation. It was noted that as the flow reversal mode increases, the grouping of the outermost mantles becomes increasingly dense, but this is only representative of a vortex with a discrete amount of kinetic energy. No consideration is given to the interstitial flow structures which represent an intermediate state between the vortices predicted by the Beltramian solutions that have a discrete number of mantles. It can be postulated that as the kinetic energy content of the flow is increased the flow field deviates from the discrete Beltramian solutions, where the reduced thickness of the vortex tubes and circumferential boundary layer results in an outward radial shift. This radial shift would also therefore be applicable to the position of the mantles and as the radial coordinate of each mantle increases it would tend towards the prescribed radial positions of the next possible flow reversal mode $\beta_{m,n} \rightarrow \beta_{(m+2),(n+2)}$.

This would provide a sufficiently large toroidal volume within the chamber to enable the production of a further two mantles to satisfy the requirements of a higher order flow reversal mode. If the mantles are produced within the inner region of the vortex before undergoing radial expansion like the rings of a tree, then the maximum flow reversal mode will be determined by the dimensions of the innermost mantle. More importantly though, the maximum number of mantles possible will be determined by the outlet dimensions of the chamber. As a mantle will not be able to exist within the radial boundary defined by the outlet, as the flow will be able to escape the chamber and preventing further flow reversal. Therefore consideration must be given to the dimensions of the outlet to ensure that the radius of the innermost mantle for a prescribed mantle configuration is equal to or greater than the radius of the outlet. During live firings of VIHRE configurations it was found that the greatest reduction in efficiency stems from oxidiser flow circumventing the bidirectional vortex and propagating directly to the chamber exit. So by reducing the radius of the nozzle throat excessive oxidiser loss can be prevented, but this is at the cost of the effective cross sectional area of the throat. As the intense vortical flow results in a phenomenon known as 'vortex choking', where the flow rate through the chamber is related to the intensity of the vortex, which is exploited by devices such as vortex amplifiers to throttle the outlet flow [83]. However, this means a compromise must be made between the desired amount of mantles that occur in the chamber and the maximum mass flow rate through the chamber, which in terms of VIHRE performance is a trade off between effective chamber length, combustion efficiency and maximum achievable thrust.

If it is only possible for a vortex chamber with tangential inlets at the base of the chamber to sustain an odd number of mantles then this would mean that in order for a transition to a higher order flow reversal mode, that the inception of the new inner mantles would need to occur simultaneously once there was sufficient volume available for the new vortex tubes to occupy. If the vortex tubes are all considered to share a coincident vortex filament they must also traverse the full length of the chamber to ensure that the vortex filament does not end within the fluid. When the kinetic energy content of the flow is increased the inner vortex tubes will initially have insufficient kinetic energy to produce the large curvature in the streamlines necessary for the streamlines to exist over the length of the chamber. If so the vortex tube may increase in length as the kinetic energy content of the flow is increased, but would still not be able to fully traverse the length of the chamber until a sufficient amount of kinetic energy is imparted to the flow. Therefore in order to fulfill the requirement that a vortex filament only terminates at a boundary of the fluid domain, it could be possible for both the inner vortex tubes and mantle structures to form a loop connected to either the head or base wall of the chamber. These vortex tubes would protrude into the bulk flow and continue to increase in length until the opposite axial boundary is reached, allowing for bifurcation as two individual mantles are established. If additional mantles are created in this manner then it could be argued that shorter chambers are more suited to enabling higher order flow reversal modes, as suggested by the energy based solution [22]. In order to maintain a large helical trajectory through the chamber to ensures

increased fluid residence time, it would require multiple vortex tubes and large axial dimensions so that the production of additional vortex tubes is counteracted by the reduced chamber length. If however the mantles are produced in the core flow, this would necessitate reduced chamber length as opposed to the outer mantles that can exist at greater chamber lengths. It may be possible to create a vortex chamber with variable axial geometry that enables higher order flow reversal modes but minimises the reduction of the pathlines through the chamber.

Chapter 4

Experimental and numerical methods

4.1 Introduction

An extensive body of knowledge detailing the analytical solution of the bidirectional vortex has been formulated in order to gain a thorough understanding of the fundamental fluid mechanics occurring in vortex chambers [13, 16, 18, 19, 72, 81, 84]. Information regarding the radial location of the mantle has been extracted and validated to some extent using both numerical and empirical methods, providing suitable techniques for further investigations. The non linear Beltramian solution of the bidirectional vortex reveals that there are multiple roots to the formulation of the axial velocity component indicating that it may be possible for multiple mantles to exist [13]. This implies that the flow could form several concentric vortex tubes which change axial direction at both the head and base of the chamber, forming a complex intertwined vortex structure. This is a feature which would further increase the benefits associated with the bidirectional vortex that occurs in VIHRE configurations and similar cyclonic devices, allowing for highly efficient and compact combustion chambers. Currently there is little experimental evidence pertaining to confined vortices exhibiting multiple flow reversals and direct measurements of the axial velocity component have yet to be made in order to confirm this phenomenon. Therefore there is an obvious need to further investigate the possible existence of vortices containing multiple mantles, in addition to characterising what flow conditions may lead to their formation. As a result of this, the main objective of this study will be concerned with the identification of vortical flows containing multiple mantles and attempting to isolate the parameters which affect these toroidal recirculation zones.

4.2 Parametric investigation

Based on the analysis of the Beltramian and energy based solution of the bidirectional vortex concerning multiple mantles, several criteria have been identified that may possibly affect the structure of the mantle. By reviewing the arguments posed in the previous chapter, it was decided to focus on investigating parameters that are most likely to yield flows containing multiple mantles based on the evidence that infers their existence. In summary of the findings of the analytical solutions it can be inferred that variables which can be controlled directly to manipulate the mantle structure are the inlet flow velocity, chamber aspect ratio and chamber contraction ratio. In addition to suggesting that a vortex chamber with variable axial geometry may also provide an environment conducive to production of multiple mantles. It is for this reason that this study will concentrate predominantly on assessing the effects of parameters that apply to cylindrical vortex chambers as described throughout the treatment of the bidirectional vortex, so that direct comparisons can be made with data acquired in this study. However, the analytical solutions only consider chamber geometries where the tangential inlets are located at the base of the chamber, but in order to fully characterise geometrical influences on the mantle it is deemed that this investigation should also evaluate chamber designs with tangential inlets positioned at the head of the chamber as well. This
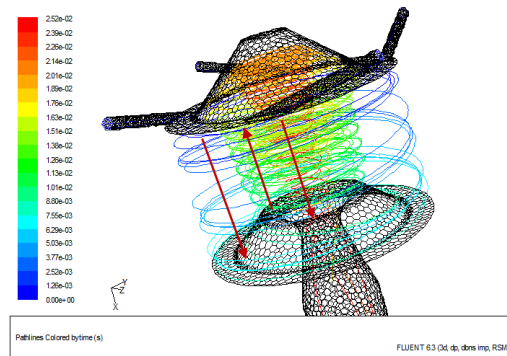
Figure 4.1: Preliminary CFD indicating triple vortex flow.

decision is corroborated by the preliminary CFD results seen in fig 4.1 which show triple vortex flow is possible when head injection is employed. Due to the unknown mechanisms that form the mantle structure a parametric study of each variable was conducted to isolate its effects upon the flow, so that a relationship between individual parameter and the resultant mantle structure can be established. It is intended to catalog the individual effects of these parameters on the mantle structure to provide a framework for further studies, enabling specification of design criteria to allow vortex chambers to be designed that ensure multiple flow reversals.

Both numerical and experimental methods shall be employed to assess a range of vortex chamber configurations to provide a sufficient amount of data so that incisive conclusions can be drawn about the influence of the test parameters. To do this CFD will be used to produce the numerical evidence as it has been proven repeatedly to be a useful tool for calculating flow fields within vortex chambers where bidirectional vortices occur [10, 24, 63, 74, 84]. PIV will be used to visualise the physical vortex as it provides the most appropriate non intrusive flow measurement technique for obtaining the mantle structure by determining the axial velocity distribution in a cross section of the chamber. Although gas cyclones have been employed previously as an analog of the non combusting flow conditions in a VIHRE this increases the complexity of the PIV experimental approach as additional equipment and facilities are required. This approach would require a continuous high pressure gas supply to allow multiple experiments to be conducted, in addition to an experimental rig that it capable of operating under high pressure, whilst providing adequate optical access to the chamber. The difficulty of preparing the flow for PIV measurements also increases as an atomising seed generator is required and a compromise between particle size needs to be established to ensure both penetration of the vortex core and sufficient light scatter. As a result of this it was decided to use a hydrocyclone instead as an analog as the range of geometrical parameters to be investigated remain unaffected and a range of inlet flow velocities can easily be produced from a readily available continuous water supply. The use of an incompressible fluid also results in choked flow at the outlet of the chamber and allows for the effects of vortex choking upon the flow to be assessed. Additionally because of the significantly higher viscosity of water similar inlet Reynolds numbers to those in gas cyclones result in reduced flow velocities, which is beneficial with regards to the field of view (FOV) of the high speed PIV camera. As the lower velocities mean that the vortex can be adequately captured at a much lower frame rate, which means that a higher resolution image can be obtained and the optics can be arranged to increase the cross sectional area of the chamber under examination. However, the use of water as a working fluid in combination with intense vortical flow also introduces the problem of the air core, which denotes the CRZ formed within the PVC due to vortex breakdown and because of the negative pressure gradient that arises. Standard PIV practice is to employ a side scattering arrangement where the laser sheet is orthogonal to the sensor plane of the camera so that the seeding particles scatter a sufficient magnitude of light and the laser sheet is not incident with the camera in order to avoid damaging the sensor. This allows for a relatively simple linear mapping of the FOV, so that perspective image effects and dewarping operations can be avoided when calculating the vectors. But in a hydrocyclone the surface of the air core which

Pump Throttle	0%	25%	50%	75%	100%	Aspect Ratio	0.4	0.6	0.8	1.0	1.2	1.4	Contraction Ratio	5	10	20	40	60	80	100	Dome Height (mm)	5	10	15	20	25	30	35
Pump Throttle																												
0%	X									●						●												
25%		X								●						●												
50%			X				●	●	●	●	●	●		●	●	●	●	●	●	●		●	●	●	●	●	●	●
75%				X						●						●												
100%					X					●						●												
Aspect Ratio																												
0.4			●				X									●												
0.6			●					X								●												
0.8			●						X							●												
1.0	●	●	●	●	●					X				●	●	●	●	●	●	●		●	●	●	●	●	●	●
1.2			●								X					●												
1.4			●									X				●												
Contraction Ratio																												
5			●							●			X															
10			●							●				X														
20	●	●	●	●	●		●	●	●	●	●	●			X							●	●	●	●	●	●	●
40			●							●						X												
60			●							●							X											
80			●							●								X										
100			●							●									X									
Dome Height (mm)																												
5			●							●						●						X						
10			●							●						●							X					
15			●							●						●								X				
20			●							●						●									X			
25			●							●						●										X		
30			●							●						●											X	
35			●							●						●												X

Table 4.1: Chamber configuration test matrix.

constitutes the boundary of the PVC scatters a large amount of light which is not only detrimental to the detection of particles in close proximity to the vortex core but also prevents a large amount of the laser light from penetrating the full cross section of the air core. This leads to a reduced effective FOV as there is either increased localised light pollution or insufficient light scatter from particles which results in an insufficient contrast and signal to ratio (SNR) to produce an accurate PIV vector map.

To ensure the data obtained from this study is applicable to a wide range of cyclonic devices all geometrical and inlet flow parameters will be non dimensional in form so that they are scalable and independent of fluid properties. This means that the main parameters to be investigated are the inlet Reynolds number, chamber aspect ratio and chamber contraction ratio for vortex chambers with tangential inlets located at either the base or head of the chamber. Although these variables are chosen primarily for their likely influence on the mantle structure they are also chosen because they represent the range of parameters which have been found to most significantly affect the performance of VIHRE configurations during live firings [9]. The statistical experimental design analysis displayed previously in fig 2.12 shows that performance is significantly affected by oxidiser mass flux, with greater flow rates yielding improved results. After that the engine is most sensitive to variations in the diameter and length of the chamber, with large radius and short engine configurations indicating low aspect ratios being preferable. Although a reduction in the cross sectional area of the throat is found to be beneficial it displays little normalised sensitivity, which is likely due to the relatively small range of outlet radii tested. Also the chamber configurations tested exhibited large aspect ratios relative to the range considered in this study and are unable to theoretically sustain multiple flow reversals and benefit from their presence. It is therefore assumed that the influence of the chamber contraction ratio will be more significant in low aspect ratio chambers where it is possible to produce multiple mantles, although this will need to be verified empirically. It is worth noting that both the analytical solutions and statistical experimental design analysis agree that while the

46

inlet flow velocity is an important parameter all the other influential parameters are related to the chamber geometry, which is something that is widely reflected in literature on cyclonic devices. If the mantle structure is found to be heavily reliant upon chamber geometry, then this would provide a simple and effective means of manipulating the flow structure and once control parameters are defined could be easily be applied to the design of various cyclonic devices.

No specific range of Reynolds number were chosen for investigation but rather chosen arbitrarily as the relative inlet flow velocity is produced by variation of the throttle of the pump that is used to supply water to the experimental rig. Although this means that it is not possible to obtain a specific inlet Reynolds numbers due to the lack of precision in adjustment of the pump throttle that would required to achieve this. However, this was a minor concern as the range of Reynolds numbers produced by the pump were sufficiently large enough to induce a fully developed air core along the chamber axis. This allows for the assumption that once the air core has been established the flow can be considered to be fully developed and in a quasi steady state condition and represent the mean behaviour of the flow. Five different Reynolds numbers were investigated for both base and head injector configurations which relate to a percentage that lies between the supply pump throttles PT maximum and minimum range where the pump throttle values used were $PT = 0\%, 25\%, 50\%, 75\%,$ and 100%. Despite the initial value of $PT = 0\%$ inferring that the flow velocity should be zero, this only indicates the lowest inlet velocity produced by the pump at minimum throttle conditions. Although the Reynolds number is the main inlet parameter of interest, the vortex Reynolds number is also included as an important parameter for comparison as it is also incorporates other parameters related to chamber geometry. The vortex Reynolds number is shown below in eqn 4.1 in a simplified state and although it may not be apparent this number incorporates the geometric swirl number as denoted by eqn 4.2.

$$V = \frac{A_{in}\rho u_{in}}{\mu L} \tag{4.1}$$

$$S = \frac{\pi R r_t}{A_{in}} \tag{4.2}$$

As stated previously, current vortex engine chamber configurations are predominantly designed with aspect ratios of either $\frac{L}{D} \approx 0.4$ or $\frac{L}{D} \approx 1.5$ and have been postulated to produce different numbers of mantles. Also there is little evidence regarding gas cyclones and hydrocyclones with compact geometries as they are generally long slender devices with much larger aspect ratios than seen in typical VIHRE designs. It is for this reason that the range of chamber aspect ratios investigated will lie within the limits of the currently available vortex engine configurations, as it is hypothesised that within these limits transition to higher order flow reversal modes will occur. As with the inlet Reynolds number study it was deemed that six test cases would be sufficient to observe changes in the flow structure and these aspect ratios are $\frac{L}{D} = 0.4, 0.6, 0.8, 1.0, 1.2$ and 1.4 respectively, which are included in the test matrix presented in table 4.1. To ensure minimal variation between the experiments apart from the test parameter, the radius of the chamber remains constant for all configurations investigated and also allows for modular apparatus. A similar approach was taken with regards to defining the various chamber contraction ratios in that the most common value used in the design of VIHRE configurations was used as a benchmark, then upper and lower limits to define the range were set accordingly. This results in a selection of seven contraction ratios that are presented in table 4.1, where the normalised radial magnitude of the outlet section shows that theoretically it should be possible to sustain bidirectional vortices containing between 1-7 mantles. It was decided to extend the upper limit of the maximum contraction ratio investigation because it is assumed that this would increase the probability that a bidirectional vortex with multiple mantles may occur.

(a) $\frac{L}{D} = 0.4$ (b) $\frac{L}{D} = 0.6$ (c) $\frac{L}{D} = 0.8$

(d) $\frac{L}{D} = 1.0$ (e) $\frac{L}{D} = 1.2$ (f) $\frac{L}{D} = 1.4$
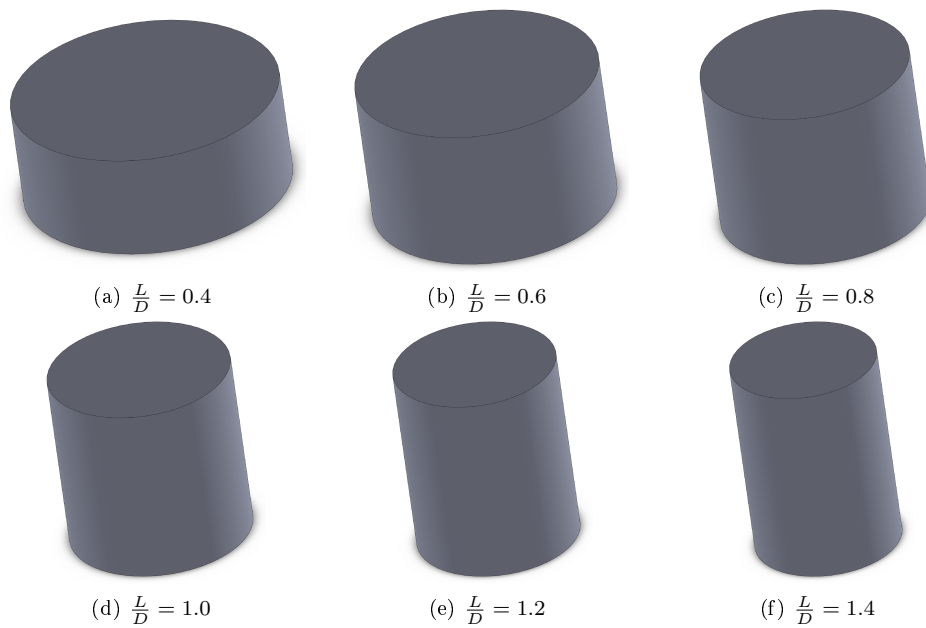
Figure 4.2: Chamber configurations for the aspect ratio study.

(a) $CR = 5$ (b) $CR = 10$ (c) $CR = 20$

(d) $CR = 40$ (e) $CR = 60$ (f) $CR = 80$

(g) $CR = 100$
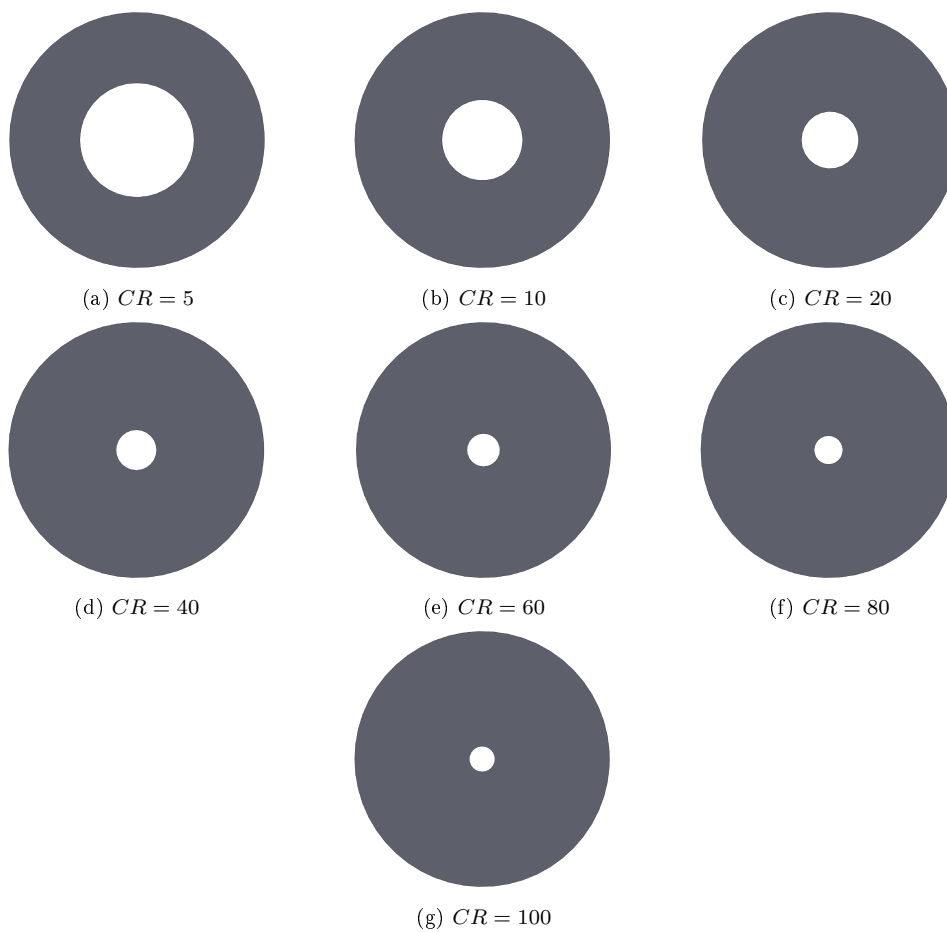
Figure 4.3: Chamber configurations for the contraction ratio study.

4.3 Vortex chamber design

In order to facilitate the large number of chamber configurations a modular experimental rig was designed so that a single piece of apparatus could be produced that enables all 46 test chambers to be realised while still allowing optical access to the axial and azimuthal planes of the chamber. A cut away diagram of the test chamber is displayed in fig 4.4 with the various modular components labelled for clarity. In order to emulate the idealised chamber geometry described in the analytical solutions the design of the chamber represents a compromise between basic cylindrical geometry, available manufacturing techniques and spatial discretisation of the fluid domain. It was deemed that 4 tangential inlets were sufficient to create a stable coherent vortex and minimise the effects of vortex core precession commonly associated with cyclonic devices with a single tangential inlet [26, 74, 85]. A single injector plate is used to provide the swirling flow to both the head and base injector chamber configurations which means that the rotational direction of the vortices are counter clockwise and clockwise respectively relative to the plan view of the chamber, although this was not replicated in the numerical domains seen in fig 4.5. It is assumed that the variation in rotational direction has negligible influence on the structure of the vortex and allows for a simplified experimental setup with fewer components required. The radius of the injectors are $r_{in} = 4mm$ as this provides an adequately large cross sectional area to produce a suitable range of inlet Reynolds numbers given the specifications of the fluid supply line, where the injectors intersect the chamber periphery tangentially and occupy a normalised radial position of approximately $0.8 < \frac{r}{R} < 1$. The length of the inlet sections are also designed to be sufficiently long enough to ensure fully developed flow before the fluid enters the chamber. Due to the modular design and specifically the influence of injector plate it is not possible to provide full optical access to the entire axial plane of the chamber. Although efforts were made to minimise the reduction in length of the FOV a compromise had to be made with respect to the design of the injector plate. This is to ensure a prescribed range of inlet Reynolds numbers are possible but allows for adequate clearances and tolerancing to be maintained so that the component could be manufactured. The Plexiglas window was designed to be flush with the head plane of the chamber but despite this the injector plate design results in a $20mm$ reduction in the axial plane FOV with respect to length.
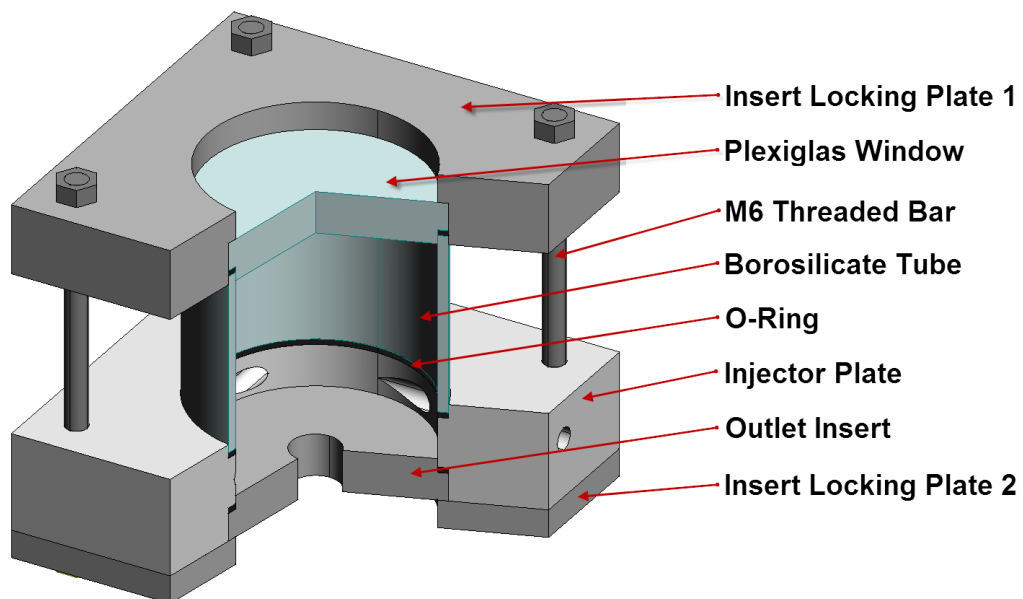
Figure 4.4: Components of the modular test chamber.

The majority of the components forming the experimental rig are fabricated from aluminium as the naturally forming protective oxide layer is adequately inert when in contact with water and air to prevent rust. Various lengths of borosilicate tube are used to produce the range of chamber aspect ratios and was chosen because of its superior optical quality in comparison to other available materials such as extruded *PMMA*, which is susceptible to striations. However the Plexiglas window to provide optical access to the azimuthal plane of the chamber is manufactured from a monolithic cast block of *PMMA* which has polished surfaces making it suitably transparent for accurate PIV measurements. The rubber O-rings seals are made from Viton as the axial deformation caused by compression forces could be calculated to ensure minimal deviation from the prescribed aspect ratios of the test chamber, with petroleum jelly also used in addition to O-rings to provide watertight seals between all the components. Threaded bars with locking nuts run through the length of the experimental rig and also through the optics bench on which the high speed camera is mounted to ensure the axial plane of the chamber is consistently parallel to the camera sensor plane.

(a) Base tangential injectors.   (b) Head tangential injectors.
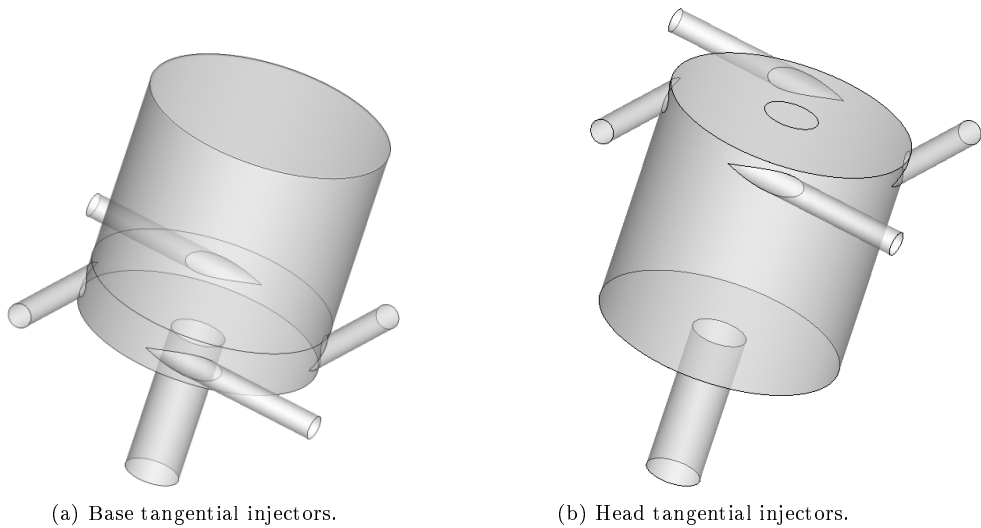
Figure 4.5: Axial position of the tangential injectors.

4.4   CFD pre-processing

Despite the axisymmetric assumptions of the analytical solutions the bidirectional vortex is fundamentally a 3D flow structure and needs to be modeled as such to obtain a realistic solution. It is for this reason that CFD studies were conducted entirely in 3D with the base CAD geometry replicating the exact chamber geometry of the experimental rig which is prescribed by the parametric design criteria. Previous initial numerical studies of the non reacting flow field in VIHRE configurations were conducted in 2.5D by assuming the resultant flow was axisymmetric and steady-state [10], although it is known that the PVC embedded in the flow is a 3D time-dependent structure that exhibits periodicity. A later numerical study conducted by Fang et al [24] employed 3D geometry to partially solve this problem although the solutions calculated were steady-state, which is a valid assumption despite the precession of the vortex core. The PVC can be assumed to be quasi steady-state due to its periodicity and the steady-state numerical solution relates to the average position of the PVC. Although the CFD study conducted by Fang et al [24] was concerned with vortex injection liquid rocket engines the CAD geometry constructed is similar to that of the VIHRE chamber configurations investigated experimentally [7, 9], employing $N = 4$ tangential base injectors for a chamber with an aspect ratio of $\frac{L}{D} = 1.5$. This study also provides suitable guidelines for performing CFD studies of similar cyclonic devices and is consulted in addition to various numerical studies of gas cyclones [74, 85–90] and hydrocyclones [91–102] for information on how to simulate flow within vortex chambers.

(a) Simplistic CAD geometry.   (b) Global tetrahedral mesh.
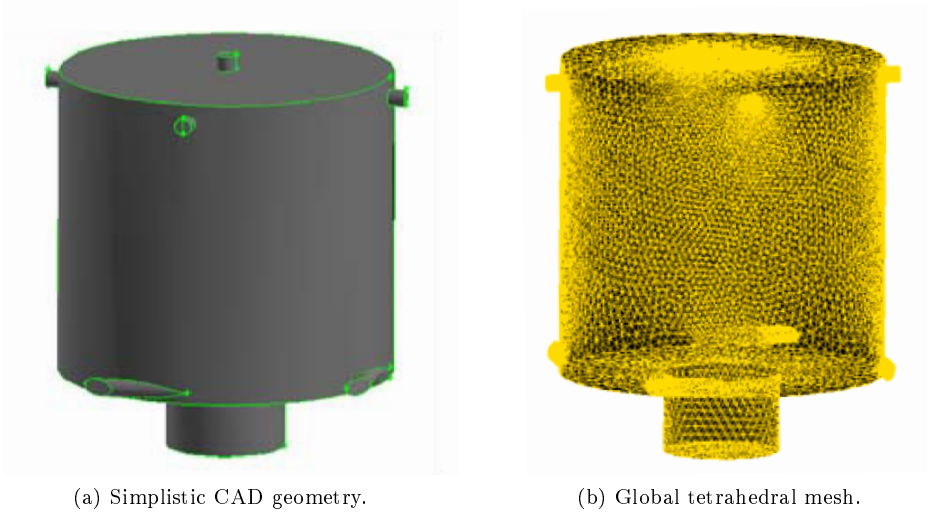
Figure 4.6: Numerical fluid domain used in previous studies. [24]

The CAD geometry required to describe the range of test chambers is relatively simple but care must be taken when designing areas where curved surfaces intersect and provide adequate clearances as consideration must be given to how the mesh can be applied effectively in these regions. In fig 4.6 the basic CAD geometry produced by Fang et al [24] is depicted along with the global wireframe mesh. It can be seen that all inlet and outlet sections incident with the chamber exhibit extended boundaries which allows for the flow to fully develop in the inlet sections. With regards to standard CFD practice the domain is extended in this manner and especially at the outlet to minimise the occurrence of reversed flow on the boundaries during calculations. As reversed flow is a common indicator that the solution is not converged and requires further iterations, or the result of incorrect boundary conditions or solver setup. However with regards to vortex chambers, reversed flow at the outlet is to be expected due to the region of negative pressure in the core which forms the CRZ.

When comparing the basic geometry in fig 4.6a to the decomposed geometry in fig 4.7b it is clear that the CAD geometry constructed by Anderson et al [25] is more complex and consists of several components. The original monolithic volume has been decomposed into multiple sub volumes which is necessary to allow for specific meshing strategies to be applied in different regions. The mesh seen in fig 4.6b is a global tetrahedral mesh and is completely unsuitable with regards to simulating cyclonic flow as the overall quality of the mesh is poor and no consideration is given to the effects of numerical diffusion. Building a mesh correctly is an important step in any CFD analysis but is even more critical when simulating intense vortical flows, as various design criteria must be adhered to in order to avoid an invalid solution. A picture of the experimental test rig used by Anderson et al [25] and the local meshing scheme applied to one of the tangential injectors can be seen in fig 4.7 which highlights the correct usage of geometry decomposition to enable region specific meshing. The tangential intersection between the periphery of the chamber and the injector necessitates the use of tetrahedral elements because it results in a mesh that is of higher quality and able to better map the geometry in comparison to a mesh containing hexahedral elements. Anderson et al [25] only used tetrahedral elements at these intersections to account for the complex geometry, while employing a body fitted hexahedral mesh in the rest of the fluid domain. This is because the quality of structured hexahedral element meshes are generally much higher than those of unstructured tetrahedral element meshes.

(a) Vortex chamber experimental rig. (b) Volume decomposition at injector interface.
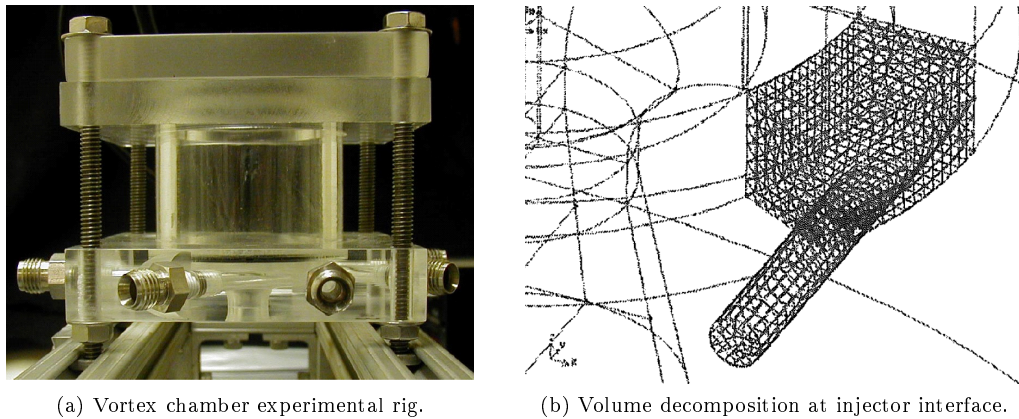
Figure 4.7: Multiple tangential injectors influencing meshing strategy. [25]

A region where the quality of the mesh is crucial is near the chamber axis where the vortex core occurs. It is well documented that the vortex core is associated with large velocity and pressure gradients, which with regards to CFD requires increased spatial resolution and high order numerical discretisation schemes to be employed so that these gradients can be accurately reconstructed. As a result of this it was deemed necessary to increase the radial mesh density in the core of the chamber by approximately twice that of the adjacent fluid regions, where the radius of the outlet was used to determine the boundary of this region. This can be seen in fig 4.8b where the dark circle denotes the transition from the outer region to the core mesh, where a transition in the structured mesh type can also be seen. Due to the geometry a mapped mesh is applied to the bulk of the fluid domain in the azimuthal plane, where a suitable compromise is made between the number of nodes at the periphery and inner boundary of the mapped region. This is to ensure that the paved mesh within the core of the chamber is sufficiently dense but allows for a reasonable distribution of elements at the periphery of the chamber that are also suitable for interfacing with the unstructured regions of the mesh. A transition from a mapped mesh to a paved mesh was chosen because a purely mapped mesh results in highly skewed elements near the axis of the chamber and results in a singularity, while a butterfly mesh would require a rectangular core geometry and could not be extruded along the length of the chamber. It is possible to create a circular quasi butterfly mesh using advanced meshing tools like Pointwise but the only available meshing tool available was Gambit 2.4.6, which was also used to both create and decompose the CAD geometry. Despite this, all the meshes created for the CFD study were of a very high quality with over 97% of the elements in each mesh exhibiting an equiangle skew of $Q_{eas} \leq 0.5$ and results in superior meshes to those seen in previous numerical studies of the bidirectional vortex.

Prior to finalising the mesh parameters, a grid sensitivity study was conducted to investigate the influence of the spatial resolution of the mesh upon the numerical results calculated for a set of consistent boundary conditions. Due to the inlet flow being incompressible it was possible to apply the velocity inlet boundary condition for the injectors, where the mass flow rate through the fluid domain can be controlled directly through adjustment of the boundary conditions. A pressure outlet boundary condition was applied at the exit of the fluid domain as it provides control over several variables at the outlet such as back pressure magnitude and distribution, as well as the ability to define the volume fraction which is demanded by the solver for multiphase calculations. All other surface boundary conditions are set as walls, where the non slip condition will be enforced by the CFD solver, while the volumes are either specified as fluid or solid depending on the specific chamber configuration due to the modular mesh design.

Six meshes were created to assess the effects of grid density which were all based on a single chamber configuration and created using similar meshing strategies. The total element count was approximately doubled for each successive mesh by initially increasing the radial density of the core mesh then applying a set of design criteria relative to this dimension to the rest of the geometry. The

(a) Injector interface.

(b) Core region.
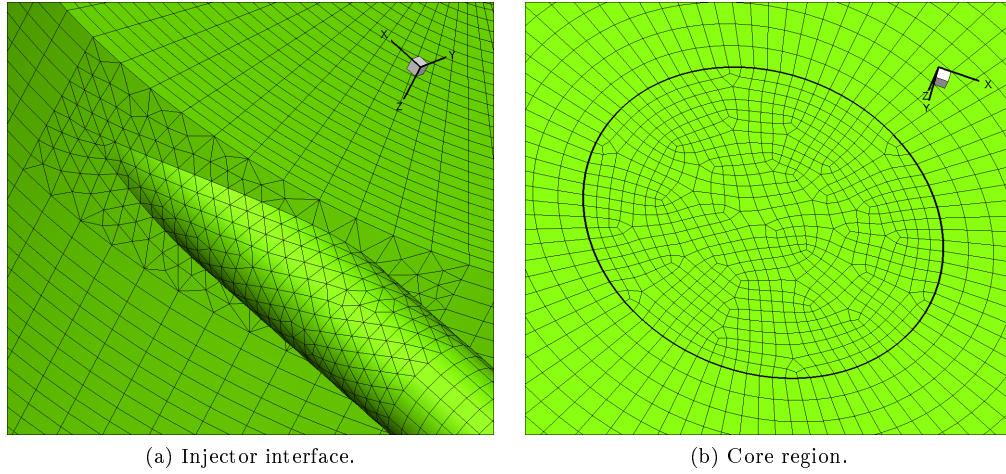
Figure 4.8: Localised increase in mesh density required for accurate solutions.

meshes used in the grid independence study can be seen in fig 4.9 where the reference geometry was a chamber configuration with head injectors with an aspect ratio of $\frac{L}{D} = 1.0$ and a contraction ratio of $CR = 20$. These hybrid meshes contain a total of approximately 19×10^3, 59×10^3, 129×10^3, 228×10^3, 448×10^3 and 727×10^3 elements respectively. The initial parameter used to determine grid independence is the mantle structure in the axial plane of the chamber, where minimal variation in the mantle structure with respect to the total number of elements will be used to indicate adequate spatial resolution. The resultant mantles are plotted in fig 4.10a but due to this visual method being subjective other criteria need to be established. Therefore the tangential velocity profiles produced by the various meshes will also be assessed, as seen in fig 4.10b which represents the tangential velocity distribution at the midpoint of the chamber $\frac{z}{L} = 0.5$. As the dominant component of the bidirectional vortex is the tangential velocity component it provides a suitable means of determining the characteristics of the vortex and can therefore be used to determine when there is minimal variation in the structure of the vortex.

It is clear from fig 4.10 that the plots of the mantle structure and the tangential velocity profile both agree that there is little variation in either variable when the total elements contained in the mesh is above 129×10^3, which suitably defines the threshold limit required for grid independence. It must be noted, that although there are some visible variations in the mantle structures in the outer regions of the chamber the locus of zero axial velocity that defines the boundary of the PVC is almost identical for the meshes above the threshold, which indicates that the core region of the mesh is sufficiently dense. This is also corroborated by the tangential velocity profile, where there is minimal variation in the gradient of either the forced vortex or free vortex. Additionally the radial position that defines the transition from the forced to free vortex varies by a maximum of 0.42% of the chamber radius. While the mesh consisting of 129×10^3 elements was found to be a suitable candidate, it was decided to follow the mesh design criteria used to create the grid containing 228×10^3 elements instead. The higher resolution mesh was used as a precaution, in case other unknown flow variables that could prove vital to characterising the bidirectional vortex and mantle structure required increased spatial resolution.
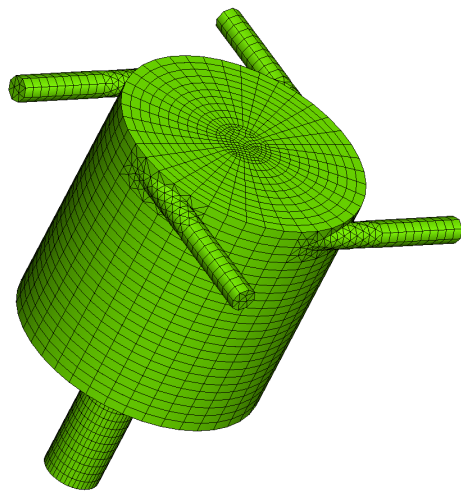
(a) Elements $=19 \times 10^3$
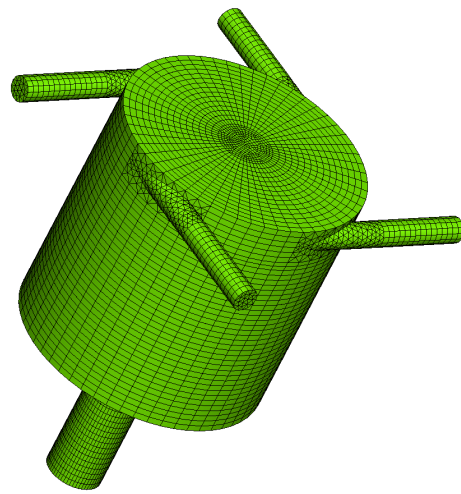
(b) Elements $=59 \times 10^3$
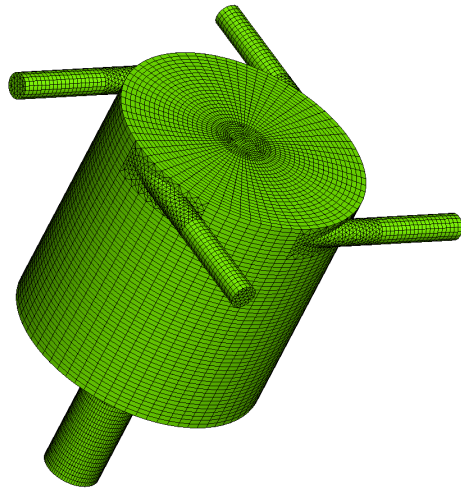
(c) Elements $=129 \times 10^3$
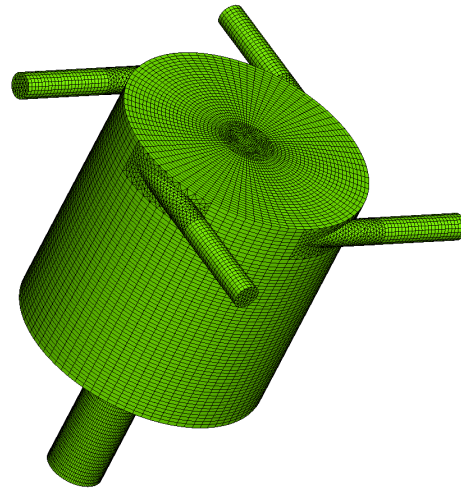
(d) Elements $=228 \times 10^3$
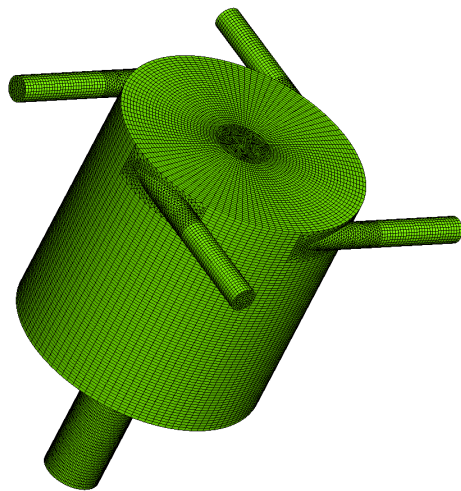
(e) Elements $=448 \times 10^3$
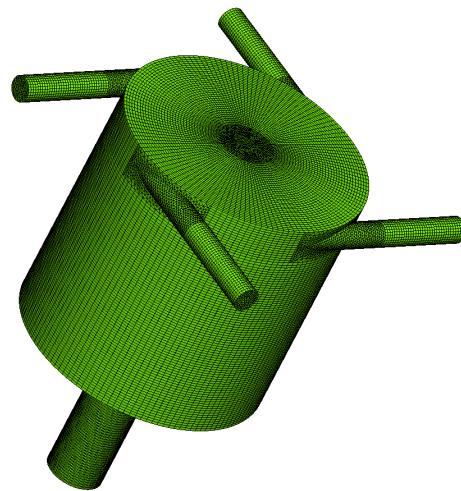
(f) Elements $=727 \times 10^3$

Figure 4.9: Numerical meshes used to determine grid independence.

(a) Mantle structure.

(b) Tangential velocity profile.
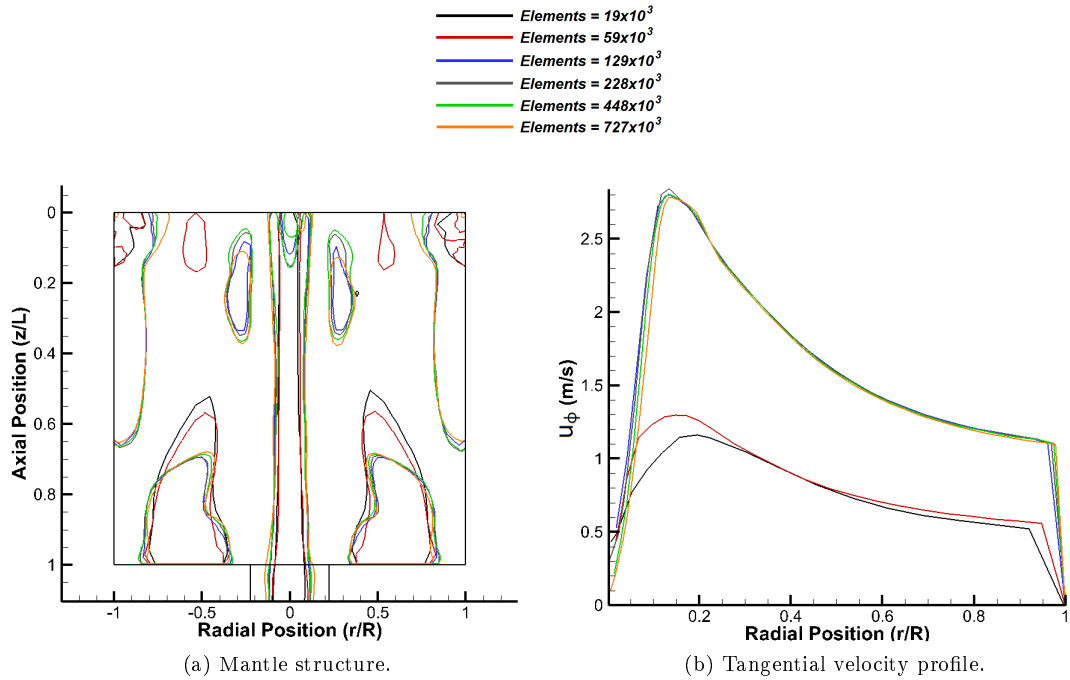
Figure 4.10: Key findings of the grid independence study.

4.5   CFD solver setup

Due to the large amount of CFD calculations that are required to cover all the parametric test conditions it was decided to use a Reynolds averaged Navier-Stokes (RANS) model to calculate turbulence rather than use an inherently transient method such as large eddy scale (LES) simulation. As stated previously, it is thought that the form of the mantle is fairly independent of time, which has been proven experimentally through laser Doppler anemometry (LDA) measurements of the flow in gas cyclones [26]. This means that the high spatio-temporal resolution afforded by LES calculations is not necessary as the mantle is effectively a steady-state phenomenon and the main objective is to observe the general form of the structure rather than obtain a dimensionally precise solution. There is of course a significant increase in computational resources associated with LES calculations, which in terms of industrial design prohibit their widespread use as the benefits provided by the enhanced accuracy of the solution are insubstantial relative to the increased complexity and resources required for the calculations. LES calculations were considered but it was found that a mesh with sufficient grid density would need to contain approximately 1.5×10^6 elements in total, which would significantly extend the time frame required to obtain 50 solutions. Therefore it was deemed an unacceptable approach, as multiphase simulations of highly swirling flows also introduce other complexities and considerations regarding solution stability and convergence issues that would also need to be addressed. In spite of this, numerical studies of gas cyclones have shown that the Reynolds stress model (RSM) which is the most complex RANS model available in Fluent is well suited to performing calculations of intense confined vortices [27]. The plots of tangential velocity and axial velocity for a pair of cyclonic separators can be seen in fig 4.11, where the experimental LDA data is presented alongside the CFD solutions calculated using both LES and the RSM turbulence model. It is clear that the RSM model adequately captures both the forced and free regions of the vortices as seen in the tangential velocity profiles and produces comparable results to the more complex LES solutions. What is more important with regards to this current study is that the RSM model is capable of calculating both the radial mantle positions resultant from flow reversal, but also the CRZ within the PVC as depicted by fig 4.11.

(a) Tangential velocity. (b) Axial velocity.
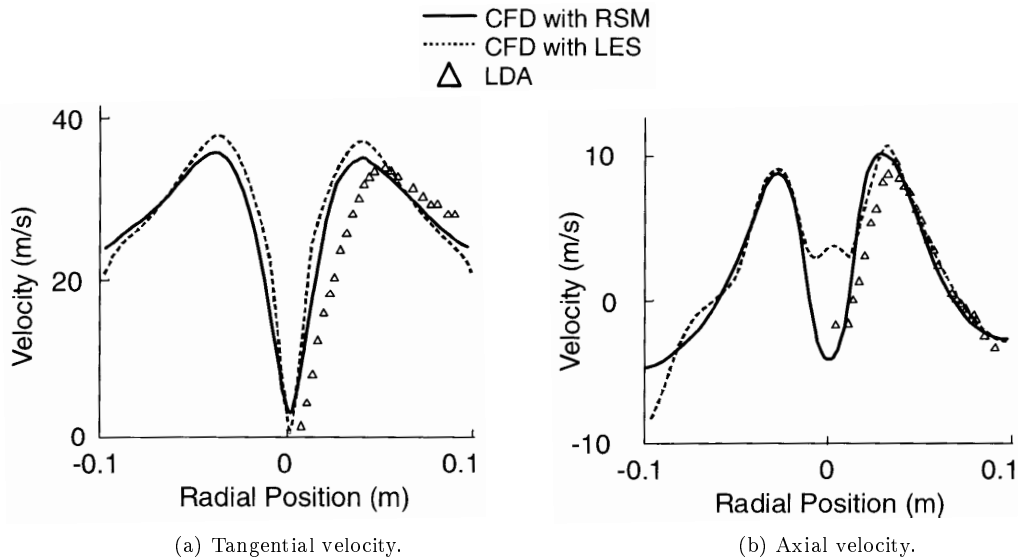
Figure 4.11: Velocity profiles produced by RSM and LES solutions. [26]

Although Fluent offers two RANS models that specifically cater for swirling flows, the less complex $\kappa - \varepsilon$ renormalisation group (RNG) is not suited to flows with extreme streamline curvature or problems where the flow can be considered to exhibit a high amount of swirl $S > 0.6$. Many studies still continue to employ the $\kappa - \varepsilon$ RNG model in calculations of cyclonic devices and are thus unable to produce accurate results that properly characterise the flow, specifically within the vortex core where the magnitude of the axial velocity component is underestimated and prevents the identification of a PVC. This is highlighted in fig 4.12 where the axial velocity distribution calculated by Fluent by various methods at the midpoint of a gas cyclone is compared to experimental LDA data. What is immediately apparent is that both the $\kappa - \varepsilon$ RNG and RSM model are incapable of resolving the PVC when first order discretisation schemes are applied due to the insufficient gradient reconstruction of the convective fluxes. As discussed previously, the velocity and pressure gradients within cyclonic devices are greatest within the core region of the vortex, which means that in order to accurately resolve these numerically requires higher order spatial discretisation schemes to minimise the error in reconstructing these physical gradients. The results produced by the $\kappa - \varepsilon$ RNG model with second order discretisation do show a reduction in the magnitude of the axial velocity along the axis of the chamber but still do not indicate reversed flow and therefore do not indicate the presence of a PVC. Apart from this, the the maximum axial velocity is overestimated by a small amount relative to the experimental data, but the minimum axial velocity is grossly overestimated and this causes the radial position of the mantle to move inwards due to the increased axial velocity gradient. When the results for the RSM model with second order discretisation are compared to the LDA results there is a clear correlation between both sets of data and the numerical model accurately predicts the axial velocity distribution within the vortex core. There is still some discrepancy between the experimental and numerical data with regards to the position of the mantle and the minimum axial velocity in the outer regions of the chamber, but the results for the RSM turbulence model with second order discretisation provide the most accurate method for calculating the flow in a gas cyclone.

The $\kappa - \varepsilon$ RNG turbulence model employs two transport equations to model the turbulent kinetic energy κ and turbulent energy dissipation ε for 3D problems, while the RSM model employs seven transport equations to resolve the individual Reynolds stresses in the flow. Six of these transport equations describe the Reynolds stresses that are used in place of the turbulent kinetic energy transport equation, while the seventh transport equation describes the turbulent dissipation rate. As the RSM model requires five additional transport equations to be solved relative to the $\kappa - \varepsilon$ RNG model there is an associated increase in the demand on computational resources, where the
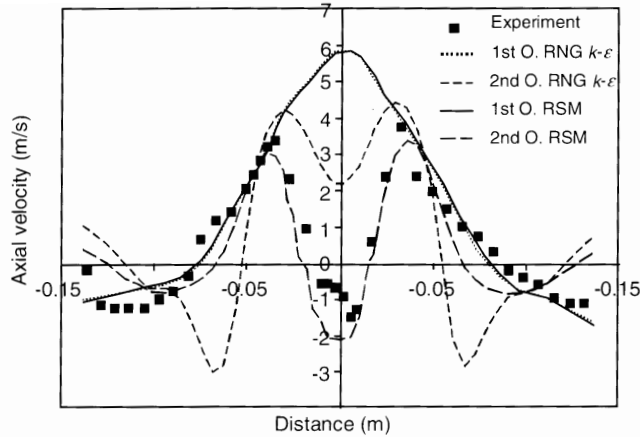
Figure 4.12: Axial velocity profiles produced by the RSM and $\kappa - \epsilon$ RNG turbulence models. [27]

CPU calculation time is increased by approximately 50-60% per iteration and the memory requirement is increased by approximately 15-20% [28]. Despite this, numerical studies of cyclonic flows have concluded that the increased accuracy afforded by the RSM model far exceeds the additional computational resources and increased wall time required to obtain the final solution. The $\kappa - \varepsilon$ RNG model resolves eddy viscosity through use of a turbulent viscosity μ_{tur} term, which is a scalar variable that results in the turbulence being considered as isotropic. However, by resolving the Reynolds stresses, the RSM model does not require a turbulent viscosity parameter and can account for the anisotropy of the turbulence which physically occurs in highly swirling flows, where there is large curvature of the streamlines. In omitting the anisotropy of the turbulence, the $\kappa - \varepsilon$ RNG model is unable to correctly resolve the vortices that occur in cyclonic devices which is why the axial velocity profiles displayed in fig 4.12 do not correlate well with the experimental data. Ansys states that the use of the RSM model is a must when the flow features are a result of the anisotropy in the Reynolds stresses, with examples including cyclone flows, highly swirling flows in combustors, rotating flow passages and the stress-induced secondary flows in ducts [28]. Therefore the RSM model was chosen to calculate the turbulent flow in all the test chamber configurations based on this recommendation and existing experimental evidence. However, the Reynolds stress transport equations are derived from taking moments of the exact form of the momentum equation which is then multiplied by a fluctuating property to emulate physical fluctuations before it is Reynolds averaged. In doing this though several terms of the exact formulation of the momentum equation remain unknown and assumptions have to be made in order to close the set of equations, in the form of model constants. Although the default model constants provided in Fluent are applicable to a wide variety of flows, they are obtained from experimental data which means that they may not be specifically applicable to the problem that is being investigated. This in addition to the high degree of coupling in the momentum equations and the turbulent stresses in the flow which cause issues with regards to solution stability. This can preclude a solution from being obtained, as solution divergence is a likely possibility if necessary precautions are not taken to counteract the conservative solver settings.

Although the SSG quadratic pressure-strain model [103] is suggested for problems with streamline curvature to provide increased accuracy, it is also detrimental to the stability of the solution when used simultaneously with multiphase formulations, as neither can be considered to be numerically robust. Despite various solver configurations being implemented, a converged solution was never obtained when the quadratic pressure-strain model was active and multiple adjustments to the solver required to temporarily stabilise the solution would be at the expense of solution accuracy if convergence were achieved. For this reason it was decided that the linear pressure-strain model of Gibson and Lauder [104] would suffice as numerical studies of hydrocyclones found that accurate results could still be obtained due to the effectively linear form of the SSG model for such flows,

57
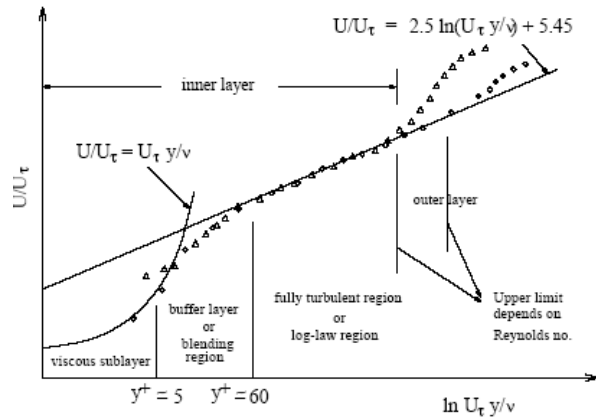
Figure 4.13: Log law region of the boundary layer. [28]
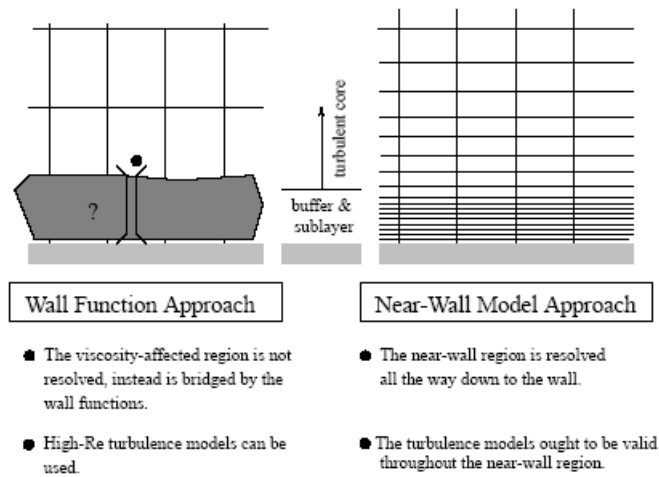
Figure 4.14: Wall function approach for resolution of the boundary layer. [28]

negating the use of a quadratic formulation [98]. However, in using the linear pressure-strain model a correctional term for wall reflection effects needs to be applied so that a satisfactory solution can be determined within the logarithmic region of the turbulent boundary layer. A standard wall function was chosen which calculates the near wall velocity of the turbulent boundary layer, which is interpolated from the plot in fig 4.13, this defines the limits of the logarithmic law profile where an adequately accurate solution can be obtained. The boundary layer is comprised of three sections, which are the viscous sublayer that is adjacent to the wall, the buffer layer which bridges the laminar and turbulent regions of the boundary layer and the outer turbulent layer, where the logarithmic law is valid. The standard wall function is generally adopted in resolving the boundary layers within cyclonic devices as the intense swirling flow is associated with large Reynolds numbers which would require a very fine mesh resolution at the walls in order to resolve the viscous sublayer. This is not particularly necessary with regards to confined cyclonic flows as the structure of the boundary layer is of little interest relative to the fidelity of the results in the core region of the flow. Therefore standard wall function provide an adequate treatment of the near wall flow while also significantly reducing the total number of mesh elements. A comparison of the wall functions available are shown in fig 4.14, which also highlights the increased grid density required to satisfy the $y^+ \approx 1$ condition for the near wall treatment. As opposed to $30 < y^+ < 200$ which is acceptable when the boundary layer is resolved using the logarithmic law region.

As a result of using the RSM model, the turbulent boundary conditions of fluid domain need to be defined in terms of the Reynolds stresses but these values are not easily obtained experimentally, so the turbulence intensity and hydraulic diameter is used in lieu of this. The cylindrical form of the injectors allows the hydraulic diameter to be defined exactly, while the turbulence intensity can be estimated by eqn 4.3 which is derived from experimental data for pipe flows and is directly applicable to the injectors used in this study. The fluid domain within the injectors is extended to allow for fully developed turbulent flow to occur before the flow enters the chamber, where an appropriate inlet turbulent intensity also ensures this will occur. As it was not possible to obtain measurements at the exit of the chamber, the back flow turbulent intensity was set to $I_{tur} = 0$ as the outflow would effectively be ejected into quiescent air. The Reynolds stresses that occur at the wall boundary conditions of the chamber are calculated by solving the κ equation ,which despite producing global values are problem specific as they are calculated from the flow rather than from the logarithmic law that occurs by default.

$$I_{tur} = \frac{u'}{u_{avg}} = 0.16 Re_{in}^{-\frac{1}{8}} \tag{4.3}$$

Hydrocyclones are examples of multiphase gas-liquid flows, where a PVC is present that can be defined as a free surface flow with the two phases being immiscible and effectively stratified due to the radial pressure gradient that is produced by the vortex. In order to reproduce these conditions numerically a multiphase model must be activated and based on the definition of hydrocyclonic flow the most appropriate method available is the volume of fluid (VOF) approach. The VOF model is commonly used when there is a definite persistent boundary between two or more non interpenetrating phases whether they be gas, liquid or solid and is suitable for when the secondary phase occupies over 10% of the fluid domain. The primary fluid phase was assigned a volume fraction v_f where the volume fraction of each mesh element will either be $v_f = 1$ or $v_f = 0$, which indicates that the fluid element contains the primary phase alone or is completely devoid of it respectively. The other condition $0 < v_f < 1$ indicates that the element contains a mixture of the phases but as they are immiscible this also denotes the location of an inter phase or free surface boundary. Although the VOF can be used to calculate steady-state problems it is more commonly used for transient tracking of the inter phase boundary, which is beneficial with regards to hydrocyclonic flow as it allows for the precessional behaviour of the PVC to be determined. The implicit time discretisation scheme available to the VOF model was chosen as it is more numerically robust than the explicit scheme, which may exacerbate the numerical instability commonly associated with the RSM turbulence model. However, in choosing the implicit scheme the range of spatial discretisation methods available to apply to the volume fraction convective fluxes are reduced, which affects the maximum possible spatial resolution of the inter phase boundary. This meant that the modified HRIC discretisation scheme was chosen for the VOF model while the PRESTO! method was chosen for the pressure-velocity coupling to account for streamline curvature, while the other flow variables employed the QUICK discretisation scheme.

Due to the large variety of test chamber configurations both the solution and wall time required for the second step of the solution vary significantly in order to satisfy adequate convergence criteria. Throughout each step of the solution adequate convergence is achieved when each of the residual errors is below 1.0×10^{-4}, but there are also other specific convergence criteria which apply to the transient parts of the solution. In the second part of the solution a CRZ region appears at the exit of the fluid domain, which then ingresses further along the axis of the outlet section as time progresses and the negative region of the pressure field is established. Eventually the CRZ will impinge on the head boundary of the chamber, indicating vortex breakdown has occurred and form a column of reversed flow signifying the formation of the PVC and denoting partial convergence of the second stage. During the second part of the solution the mantle structure evolves with respect to time and continues to change even when the PVC is formed. However, the calculation continues until the structure of the mantle is deemed to have stabilised and there is negligible change in the structure over a period of approximately 5.0×10^3 time steps. In the third stage of the solution the VOF equation is activated, with the primary phase volume fraction defined as $v_f = 1$ and $v_f = 0$ at the inlets and outlet respectively. A mesh adaption register is then created for the isovolume of negative

pressure that defines the PVC and is then numerically patched with the secondary phase air to automatically establish the air core. The solution is then run until all convergence criteria have been met, which means all components of the residual error are below 1.0×10^{-4} and are unable to be reduced any further, as seen in the appendix in fig C.5a. In addition to this, the mass flux balance error must be below 1.0×10^{-6} to ensure conservation of mass, while the mass flow rate at the inlets and outlet of the chamber are also monitored consistently and convergence will be not attained until there are no oscillations in the magnitude of the mass flow rate with respect to time. Other more subjective criteria are to monitor the structure of the PVC and mantle for variations and to confirm that the vortex is fully developed and quasi steady state.

4.6 Experimental PIV setup

Planar PIV measurements were taken in the meridional plane of the vortex chamber for all 46 test configurations while measurements in the azimuthal plane of the chamber were only conducted for 29 test configurations due optical access and time limitations. Efforts were made to obtain a stereoscopic PIV system but unfortunately this was not possible so a time resolved planar PIV technique was employed instead, where the axial and tangential velocity profiles were obtained independently of each other on separate occasions. Two different high speed cameras were used to acquire images in the meridional and azimuthal planes of the chamber, which were a Photron FASTCAM ultima APX and Photron FASTCAM APX-RS respectively, these are both more than adequate for obtaining images of hydrocyclonic flow. The Photron FASTCAM ultima APX can acquire images at a maximum resolution of 1024x1024 pixels up to 2000*fps* and consists of a separate camera head and processor, which makes it ideal for macro imaging applications where the small working distance required is not impeded by the dimensions of the unit. The Photron FASTCAM APX-RS is capable of acquiring images at a maximum resolution of 1024x1024 pixels up to 3000*fps,* but is a monolithic unit and introduces additional complexities into the experimental setup. Both cameras were fitted with a Nikon AF Micro-Nikkor 60*mm* f/2.8D macro lens which ensures that it is possible to obtain images with a high fill factor which results in increased spatial resolution of the FOV, enabling smaller interrogation zones to be used during cross correlation. Illumination was provided by an Oxford Lasers LS 20-50 20W copper vapour laser which emits a monochromatic beam with a wavelength of $\lambda = 532nm$. This is the approximate wavelength at which the cameras CCD sensor exhibits peak quantum efficiency (QE) and therefore enhances the contrast of illuminated particles. The laser emits $E_{pls} = 5mJ$ pulses with a period of $T = 25ns$ when operating at a default repetition rate of $f = 10kHz$, resulting in a $D = 0.025\%$ duty cycle that effectively emulates a constant wave laser for low speed imaging applications. The beam is transmitted via a fibre optic cable to an Oxford Lasers FiberSheet attachment that forms the light sheet, where an series of external lens can be adjusted to control the beam waist thickness and planar expansion of the sheet. The main concern with regards to the lens arrangement is to position the two plano convex or cylindrical lenses appropriately so that the beam waist occurs at the chamber axis and the light sheet is sufficiently thin with a relatively uniform thickness across the FOV. Then the final plano convex lens is positioned to adjust the vertical throw of the light sheet so that the whole of the FOV is illuminated, but also to ensure that the light sheet is not over expanded such that it would be detrimental to the luminance of the FOV. The lenses were arranged to provide a beam waist of approximately $x = 1mm$ which expanded to approximately $x = 2mm$ at the edge of the FOV and is sufficiently thin to provide adequate luminance and prevent increased localised particle densities being detected.

Flow seeding tests using various materials were conducted to establish which particles displayed acceptable light scattering properties within the vortex chamber but were also small enough that they follow the flow accurately. It was found that the most suitable and readily available material was ground white pepper, which despite being prone to agglomeration still exhibits an average aggregate particle size of $D_p = 50\mu m$ as shown in image shown in fig 4.15 which was obtained by a microscope under x100 magnification. Table 4.2 lists various materials used to seed liquid flows for PIV measurements along with the mean diameter of the particles for which the movement of the seeding material is considered to be representative of the motion of the bulk fluid. The diameters
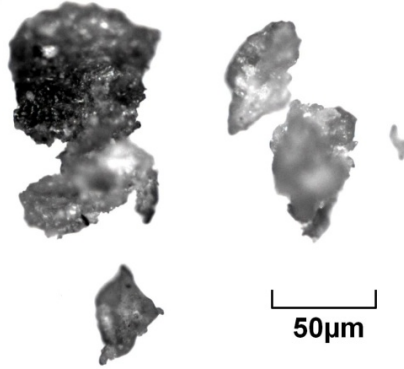
Figure 4.15: White pepper particles magnified $x100$.

of polystyrene particles and hollow glass spheres are approximately an order of magnitude larger than aluminium flakes and seeding the flow with hollow glass spheres is preferable in the majority of PIV applications involving a liquid medium, due to their good scattering efficiency and sufficiently small velocity lag in addition to their spherical shape [41]. The response time of a particle relative to the flow is important in determining whether the tracer particle is effectively representing the motion of the flow or not and can be calculated by the particle Stokes number which is described in the appendix by eqn D.1. The particle Stokes number assumes that the geometry of the particle is spherical, therefore the closer the actual particle geometry is to a sphere the more accurate the calculated response time of the seeding material will be. The Stokes particle number predicts the fluid response time and is defined as the ratio between $t_p$and t_{fl} which are the characteristic particle and fluid times respectively. The characteristic particle time t_p can be estimated by eqn 4.4 which is the relaxation time of the fluid and is derived from the Stokes drag law, although this becomes increasingly invalid at higher velocities where Stokes drag does not apply or when the fluid acceleration is not constant. When $S_k < 0.1$ the particle motion is predominantly determined by the direction of the flow and gravitational effects on the particle are negligible. Based on peak tangential velocities obtained from preliminary CFD a maximum particle Stokes number of $S_k = 0.0174$ was calculated. This confirms the seeding particles ability to accurately represent the behaviour of the flow and penetrate the vortex core, as well as the less intense outer free vortex. As the particles are relatively large they are subject to Mie scattering as the normalised diameter defined by eqn 4.5 is in excess of unity $q > 1$, where the average intensity of the light increases approximately with q^2 or decreases with increased distance from the particle according to the inverse square law $I \propto 1/r$. The average seeding particle diameter was found to be a good compromise between producing sufficient light scatter and accurately tracing the flow path, although the characteristic time of the particles were based on spherical rather than irregular flake geometry.

$$t_p = D_p^2 \frac{\rho_p}{18\mu} \tag{4.4}$$

$$q = \frac{\pi D_p}{\lambda} \tag{4.5}$$

Images in the meridional plane of the chamber were recorded at the maximum resolution of 1024x1024 pixels and at the maximum possible frame rate of $2000fps$, while images in the azimuthal plane of the chamber were recorded at a resolution of 722x722 pixels and a frame rate of $4000fps$. Due to the limitations in the setup of the optical components for PIV measurements in the azimuthal plane of the chamber, the pixel resolution of the FOV was reduced from the maximum possible resolution of 1024x1024 pixels. It was found that a frame rate of $4000fps$ was required to effectively capture the motion of the seed particles within the forced vortex, so 722x722 pixels represents the maximum resolution possible for adequate resolving the flow. Examples of images recorded in the

Type	Material	Mean diameter in μm
Solid	Polystyrene	$10 - 100$
	Aluminum flakes	$2 - 7$
	Hollow glass spheres	$10 - 100$
	Granules for synthetic coatings	$10 - 500$
Liquid	Different oils	$50 - 500$
Gaseous	Oxygen bubbles	$50 - 1000$

Table 4.2: Common PIV seeding materials and mean D_p. [41]

meridional and azimuthal planes are shown in fig 4.17 where the effects of increased light scatter caused by the PVC can be seen, this adversely affects the contrast of particles in the right hand side of the chamber. As the mantle structure is thought to remain constant irrespective of time it was deemed necessary to capture a sufficiently large amount of images so that an ensemble vector field could be obtained that effectively represents the flow over a period of time that exceeds the timescale of the salient features of the flow. As a result of this it was decided to capture 1000 images in both the meridional and azimuthal planes of the chamber which relates to periods of $T = 0.5s$ and $T = 0.25s$ respectively and is the maximum amount of images that could be required when the camera settings described above were applied. It was found that these timescales are sufficiently long in comparison to the period of the PVC and each series of images is able to capture multiple revolutions of the PVC, which describes the dominant characteristics of the flow. The main objective of the study is to obtain results that describe the time averaged properties of the bidirectional vortex by acquiring continuous high speed images. The temporal characteristics of the flow can also be resolved, which allows the behaviour of the mantle structure with regards to time to be observed. In addition to this, other properties of the flow such as the radial velocity component can be assessed to determine whether or not the positions of zero radial velocity are also independent of time. Validation of the seeding density and high speed camera settings in both planes of the test chamber was conducted according to the PIV general rules of thumb [43] which are listed below, to ensure that the images acquired have appropriate seeding densities, spatial resolution of particles and temporal displacement.

- Seed particles should be 3-5 pixels in diameter.

- There should be approximately 5-15 particles per interrogation region.

- The maximum particle displacement should not exceed 25% of the interrogation window size.

Diagrams detailing the experimental setup for the PIV measurements of the meridional and azimuthal planes are displayed in figs 4.17a and 4.17b respectively, with table 4.3 detailing the various apparatus that are used in the experiments. It can be seen in fig 4.17b that a mirror is used in combination with the high speed camera to acquire images in the azimuthal plane of the chamber as it was the only suitable solution due to the size of the camera and lack of available supports for vertical mounting of the camera. This approach results in a reversed image, but is easily rectified during post processing of the data and as mentioned previously it is assumed that the rotational direction of the flow has little or no bearing on the characteristics of the vortex. However, the increased complexity of this method does introduce the possibility of perspective distortion so great care needs to be taken to properly align the optical components with the chamber axis so that linear mapping of the FOV is valid.

Each separate PIV measurement is conducted three times so that a sufficient amount of data is collected and that the mean properties of the flow can be calculated in order to minimise the effects of erroneous results, where the following experimental procedure is replicated exactly. Initially the water reservoir is filled from the external mains supply to specific height so that the pressure head that the centrifugal pump has to overcome remains constant throughout the experiments. The
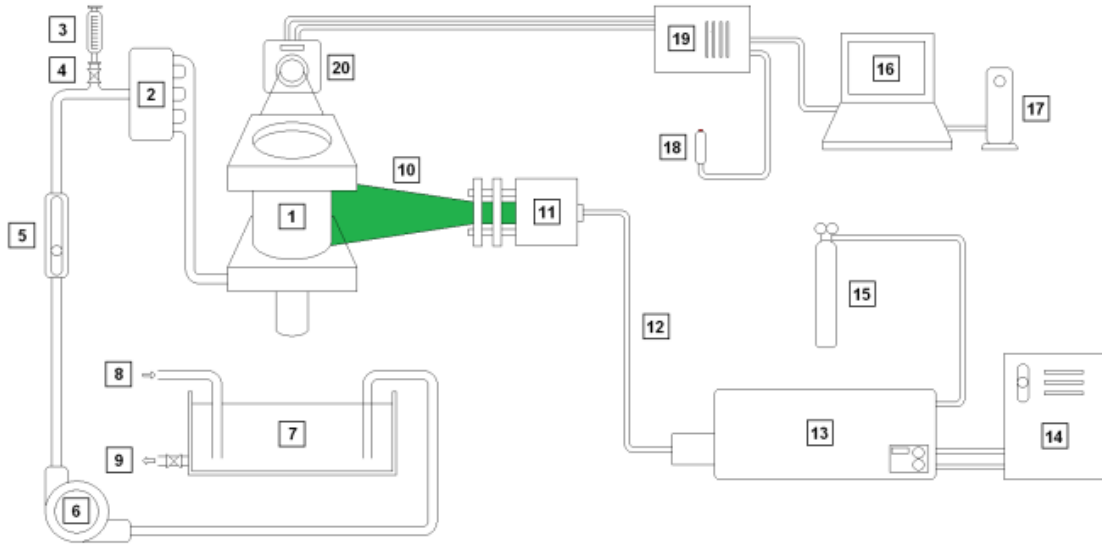
(a) Interrogation region in meridional plane of chamber.
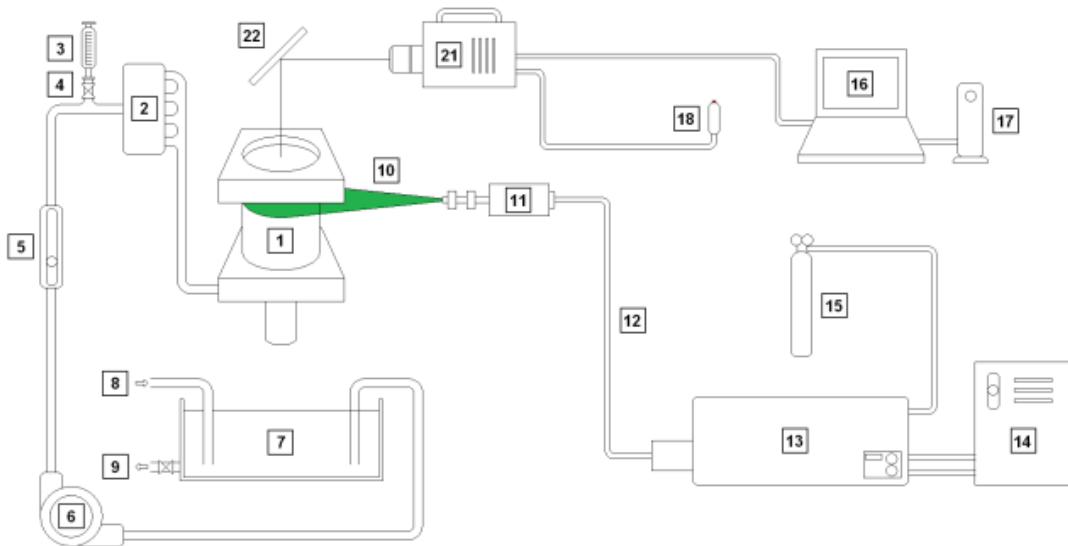
(b) Interrogation region in azimuthal plane of chamber.

Figure 4.16: Diagram of the experimental setups employed to acquire PIV images.

Item	Description
1	Vortex chamber and discharge tube
2	4-Way manifold with isolation valves
3	50ml Syringe
4	Ball valve
5	Rotameter
6	Centrifugal water pump
7	Water resevoir
8	External water supply
9	Ball valve and external drainage
10	Laser light sheet
11	Light sheet forming optics
12	Fibre optic cable
13	Copper vapour laser
14	Recirculation chiller
15	Gas cylinder (Neon 99%) and pressure regulator
16	Laptop computer
17	External hard drive
18	Manual trigger switch
19	Photron FASTCAM ultima APX processor
20	Photron FASTCAM ultima APX camera head and macro lens
21	Photron FASTCAM APX-RS camera and macro lens
22	Mirror

Table 4.3: List of apparatus used to perform PIV experiments.

water pump throttle is then set to a predetermined percentage of the maximum throttle before being activated, where the flow is directed towards the test chamber and passes through the rotameter. As the pump is situated below the PIV setup is has to overcome a negative pressure head so that the flow is level with the optics bench on which the experimental rig is situated. Prior to the flow entering the chamber a ball valve on the supply line is opened briefly to allow for a partially soluble mixture of water and seeding particles to be injected into the flow via a syringe, this mixture consists of $30ml$ of water and ground white pepper by $6.2wt\%$. As seeding mixture is partially soluble it was observed that after several measurements that the flow in the chamber became clouded and led to a reduction in the contrast of the images acquired. As a result of this the reservoir was periodically emptied when data had been acquired after every two test chamber configurations in a single plane which prevented the results from being adversely affected.

After the flow is seeded it enters a 4-way manifold, where each of the isolation valves remains completely open to minimise pressure losses before being directed along one of four $6mm$ bore copper pipes that orthogonally direct the flow into the injector plate. The bidirectional vortex is already fully developed at this point, but upon entering the chamber there is an approximate delay of $T = 3s$ before the manual trigger is activated and the camera commences recording, to allow the seeding flow to become homogeneously distributed throughout the flow. The high speed camera will then record 1000 images over a period of $T = 0.5s$ or $T = 0.25s$ for the meridional and azimuthal plane measurements respectively, over which periods the flow will remain adequately seeded to enable an accurate PIV vector map to be obtained. When the flow exits the chamber it is directed into the water reservoir positioned directly beneath the experimental rig, down the discharge tube which terminates at the base of the reservoir therefore making it necessary for it to have multiple holes drilled in it so that the ambient pressure is always equal to the atmospheric pressure. It should be noted that in the experimental setup for both the meridional and azimuthal plane PIV measurements the synchroniser unit which is commonly employed to coordinate the laser pulses with the electronic shutter of the camera is not included. This is due to the high repetition rate of the laser $f = 10kHz$, which means that each camera exposure is assured to be provided with sufficient scattered light, even without precise timing as required by standard frame straddling PIV methods. There can be a maximum of either 5 or 3 laser pulses per exposure for the images obtained from the meridional and

azimuthal planes of the chamber respectively. However, this does introduce the problem of multiple exposures, as the spatial distribution of the tracer particles do not represent a single point in time but rather several separated by the period of the laser $T = 1.0 \times 10^{-4}s$. This effect can be seen in both the images acquired from the meridional plane in fig 4.17a and the azimuthal plane in fig 4.17b. In fig 4.17a the multiple particle exposure is limited to the vortex core where increased light scatter from the PVC prevents this region from producing accurate vector information. The image obtained from the azimuthal plane of the chamber in fig 4.17b also displays evidence of multiple particle exposures within the forced vortex, but unlike the image in fig 4.17a this region of the flow is still capable of producing useful vector information. Due to the dominant tangential velocity component of the flow and the solid body rotation of the fluid in the forced vortex the particles within this region of the flow follow an almost circular path with equal angular displacement between exposures. This means that although multiple exposure are detected in each frame the vector of the fluid motion is consistent and the additional exposures effectively increase the local particle density, providing increased vector accuracy in the interrogation zone when cross correlation is performed. The images acquired in the meridional plane are separated by $T = 500\mu s$ and the images acquired from the azimuthal plane are separated by $T = 250\mu s$, while the image resolution results in a spatial resolution of $88\mu m^2$ and $115\mu m^2$ respectively that represents the size of a single pixel.

<div align="center">(a) Meridional plane.   (b) Azimuthal plane.</div>
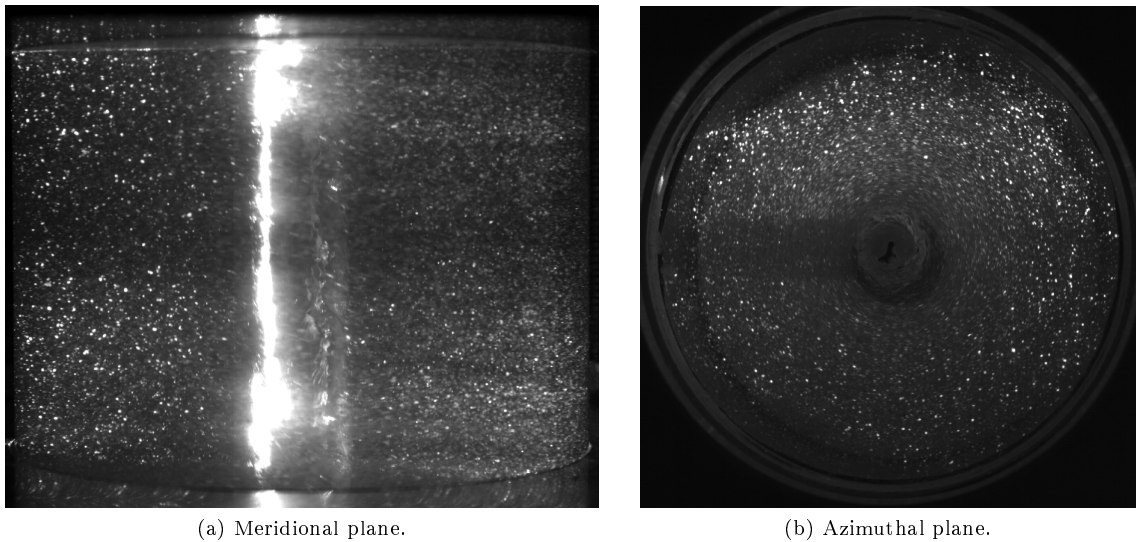
Figure 4.17: PIV images acquired from the interrogation regions of the vortex chamber.

Chapter 5

Results

5.1 Introduction

Due to the very small amount of literature referring to mantle structure in confined vortex flows there is currently no information available that provides any evidence for the influence of the test variables considered here. As a result, only a fraction of the information related to the configurations investigated is presented here and represents what are thought to be the most influential variables with regards to the vortex and mantle structure. It is hoped that some correlation can be made between the data presented here and the mantle structures observed, although identification of the fundamental fluid mechanics and mechanisms responsible for various phenomenon may be beyond the scope of this study. Despite this, the most pertinent variables are presented here and relate to the axial and tangential aspects of the flow, as well as information regarding the dimensional and spectral characteristics of the vortex core, due to this being a prominent feature in confined vortex flows.

As the precessing vortex core and the associated air core are dominant features in the flow and of a periodic nature, the Strouhal number and rotational frequency are included to give an insight into the influence of flow conditions upon the spectral characteristics of the PVC in addition to dimensional characteristics. The Strouhal number has been included for a similar reason to that of the vortex Reynolds number, as it incorporates several important variables, but like non-dimensional groups there does not appear to be a universal definition as they are applicable to a wide class of flows. It was deemed that the following description of the Strouhal number was most appropriate for the type of flow considered here and is expressed by 5.1.

$$Sh = \frac{f_{PVC}D}{u_{in}} \qquad (5.1)$$

5.2 Data extraction methods

The most important values taken from the empirical and numerical data are presented in various tables and categorised according to the respective test parameter. This data is presented alongside contour plots of the axial and tangential planes of each respective chamber configuration. All of the data was post-processed and presented using Tecplot 360 with some additional calculations performed using LabVIEW and Mathematica. In order to complement the tangential plane PIV data, the tangential plane data taken from the CFD results was extracted from a similar axial position 1mm from the head of the chamber towards the outlet of the chamber. This position was initially chosen for the PIV tangential plane experiments to minimise the amount of laser light scatter in order to maximise the image contrast captured by the cameras sensor. However, an oversight during post-processing led to the azimuth plane data for chamber configuration with head injectors to be extracted from an axial position of 1mm from the head of the chamber as opposed to 21mm, which corresponds to the axial position of the laser sheet used in the PIV experiments. It was also

later found during analysis of the CFD data that the tangential plane was likely positioned too near to the head wall boundary where the large radial gradients present were not representative of the bulk flow. This is because the flow properties of interest remain relatively linear throughout most of the chamber length apart from at the end wall boundaries as displayed in figure 5.1. These results were taken at a normalised radial position of $\frac{r}{R} = 0.5$, with the linear range being approximately located between axial positions of $\frac{z}{L} = 0.05 - 0.95$. The accompanying tangential data plane is located at a normalised axial position of $\frac{z}{L} = 0.013$, for a chamber aspect ratio of $\frac{L}{D} = 1.0$. All plots displaying either the axial or radial distribution of flow variables are uniformly colour coded with regards to specific test parameters to allow for comparison between the various chamber configurations. In cases where both CFD and PIV data is available the CFD results will be represented by lines with circular markers while the PIV results will be represented by plain lines. However when there is only CFD data available such as for the radial pressure distribution within the chamber, the results will be represented by plain lines.

Due to the relatively low flow velocities in the vortex chambers the axial pressure profiles as seen in 5.1e-5.1f they do not remain constant relative to axial coordinate but rather the pressure increases towards the bottom of the chamber. This can be attributed to the inclusion of the gravity term and the relatively high density of water which is sufficient to result in a axial pressure gradient due to the hydrostatic head. It can be seen that an axisymmetric flow condition could be assumed due to the small deviation in the azimuth plane data with respect to chamber length. This is an important factor which becomes clear during the processing of the PIV data taken from the tangential plane, as it can be used to resolve the mantle locations for the cross section of the vortex chamber despite the lack of information regarding the axial velocity component of the flow. This is done by taking the cylindrical form of the Navier-Stokes equations where gravity is assumed to be constant and counteracted by the pressure field and the fluid is also assumed to be incompressible and axisymmetric so that $\partial u_\phi = 0$, resulting in 5.2. By rearranging this equation the axial velocity gradient with respect to chamber length can be obtained in terms of the chamber radius and radial velocity. If this equation is then differentiated again it produces the second axial velocity derivative, which after simplifying terms it will result in 5.3.

$$\frac{1}{r}\frac{\partial}{\partial r}\left(r u_r\right) + \frac{\partial u_z}{\partial z} = 0 \tag{5.2}$$

$$\frac{\partial^2 u_z}{\partial z^2} = \frac{u_r}{r^2} \tag{5.3}$$

This means that when $\frac{\partial^2 u_z}{\partial z^2} = 0$ there is an inflexion point that refers to an abscissa when axial velocity is plot against chamber length, where the location of an abscissa also relates to a point where $u_z = 0$ and therefore indicates the location of a mantle. Despite being unable to calculate an approximate radial position of the mantles for the whole chamber it is still possible to make comparisons between the CFD and PIV mantle structure at the head end of the chamber, which validates the method usefulness as a tool in the identification of the mantle structure. A similar method was used successfully employed by Halasz et al [105] to obtain information pertaining to the axial velocity component from tangential plane PIV data for a vortex mixer . Despite the successful application of this method in other studies, it was abandoned due to the influence of the analytical theory, as it states that the position of zero axial velocity occurs where the roots of the J_0 Bessel function are normalised by the placeholder root of the J_1 Bessel function. The derivation presented here however indicates that the mantle will occur when the radial velocity is zero, which is found to be at a different radial location to that of the axial velocity. Through further study of the non-linear Beltramian formulation of the radial velocity as seen in 5.4 it soon becomes apparent that the locus of zero radial velocity can instead be found. This is when the roots of the J_1 Bessel function are normalised by the placeholder root of the J_1 Bessel function, which additionally means that when n mantles are observed only $n - 1$ radial zeroes will occur. Clearly this method can not be used to indicate the position of the axial zeroes and is most likely only applicable to simple vortex flow.

(a) Tangential velocity (Base Injection).

(b) Tangential velocity (Head Injection).

(c) Radial velocity (Base Injection).

(d) Radial velocity (Head Injection).

(e) Static pressure (Base Injection).

(f) Static pressure (Head Injection).
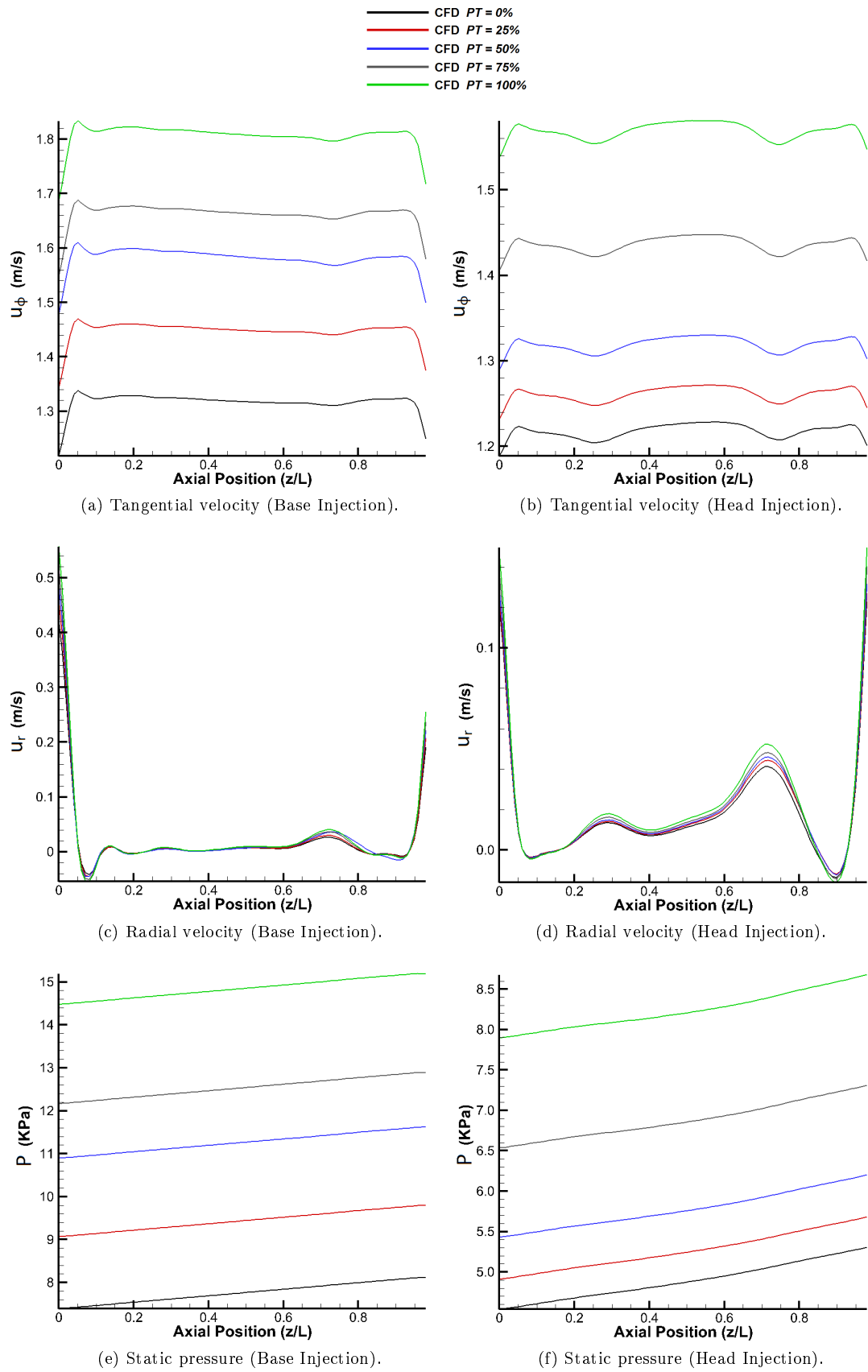
Figure 5.1: Axial distributions of flow variables in reference chamber configurations.

68

$$u_r = -\frac{\pi\kappa}{2\beta_{m,0}J_1\left(\lambda_m\beta_{m,0}\right)}cos\left(\frac{\pi z}{2\left(\frac{L}{R}\right)}\right)J_1\left(\lambda_m r\right)\left(1 - e^{-\frac{V}{2\pi}\alpha(1-r)}\right) \tag{5.4}$$

As explained previously several dimensionless groups have been included in the tabulated data to characterise the general aspects of the flow by combining several parameters for comparison. Other variables with specific relevance to the flow are also included that detail the variation in the dimensional and spectral characteristics of the vortex core. All dimensional values presented in the tables regarding the vortex core are non-dimensional, as they have been divided by the chamber radius to allow for comparison to the results for other chamber configurations. Included are radii for the air core that develops along the chamber axis, where the radius is taken to be the start of the interface between the air and fluid for simplicity. The thickness of the multiphase interface is set aside due to the difficulty in trying to extract measurements from the tangential plane PIV. The vortex cores observed in the tangential plane PIV did show signs of precession about the chamber axis but this was minimal in the majority of cases and allows the air core radius to be resolved through measurement of its circumference using images taken from the tangential plane PIV.

A virtual instrument was created using LabVIEW IMAQ software which calculated the mean radius of the air core by placing 20 markers at various positions around its circumference. This was done for several frames that were spaced 50 frames apart so that an average value for the air core could be obtained despite the variation of phase angle and any deformation the vortex core. The radius of the bulk fluid undergoing solid body rotation was then taken from the tangential plane data and obtained by extracting a radial sample along a line orthogonal to path of the laser sheet before it encounters the air core interface. After which the tangential velocity gradient with respect to the radius could be calculated, where the turning point of the tangential velocity gradient relating to the approximate peak of the tangential velocity plot, indicates the transition from the free to forced vortex. The difference between the total forced vortex and air core radius is also included so that the fluid region of the forced vortex can be compared for different configurations. In addition to the peak tangential velocities recorded, the ratio of peak tangential velocity to inlet velocity is also included to give an improved realisation of the relative vortex strength because of the variation in the inlet velocities, where effects other than the influence of inlet Reynolds number are primarily of interest.

All of the data is extracted from either the meridional plane seen in fig 5.2a or the azimuthal plane seen in 5.2b. The example plot seen in fig 5.3a is a plan view of the extraction plane and details the various features of the flow extracted from the azimuthal plane of the chamber. This plot is to be used in conjunction with fig 5.3b as a reference point so that the data extracted from the azimuth plane throughout this investigation can easily be interpreted and understood. Data presented in flow variable plots such as fig 5.3b are extracted from a single radial sampling region at an azimuth angle which remains constant for all chamber configurations. This was done as it was found there was little variation in the data due to variation in azimuth angle and therefore a single sampling region was deemed to be sufficient in describing the characteristics of the flow.

(a) Meridional Plane. (b) Azimuthal Plane.
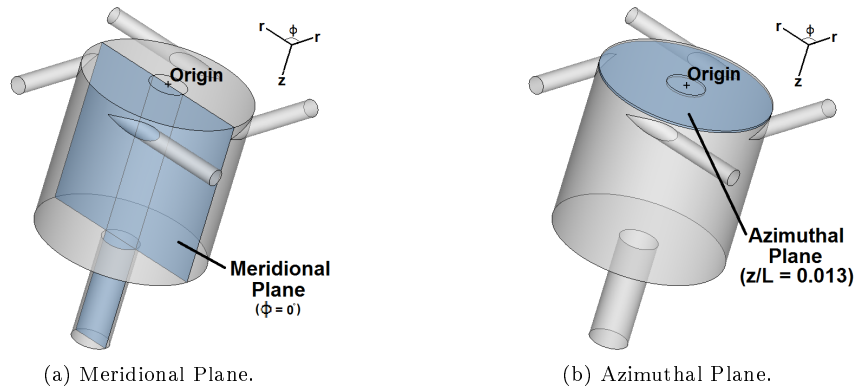
Figure 5.2: Data extraction planes.

(a) Example plot of data in the azimuthal plane. (b) Example tangential velocity profile.
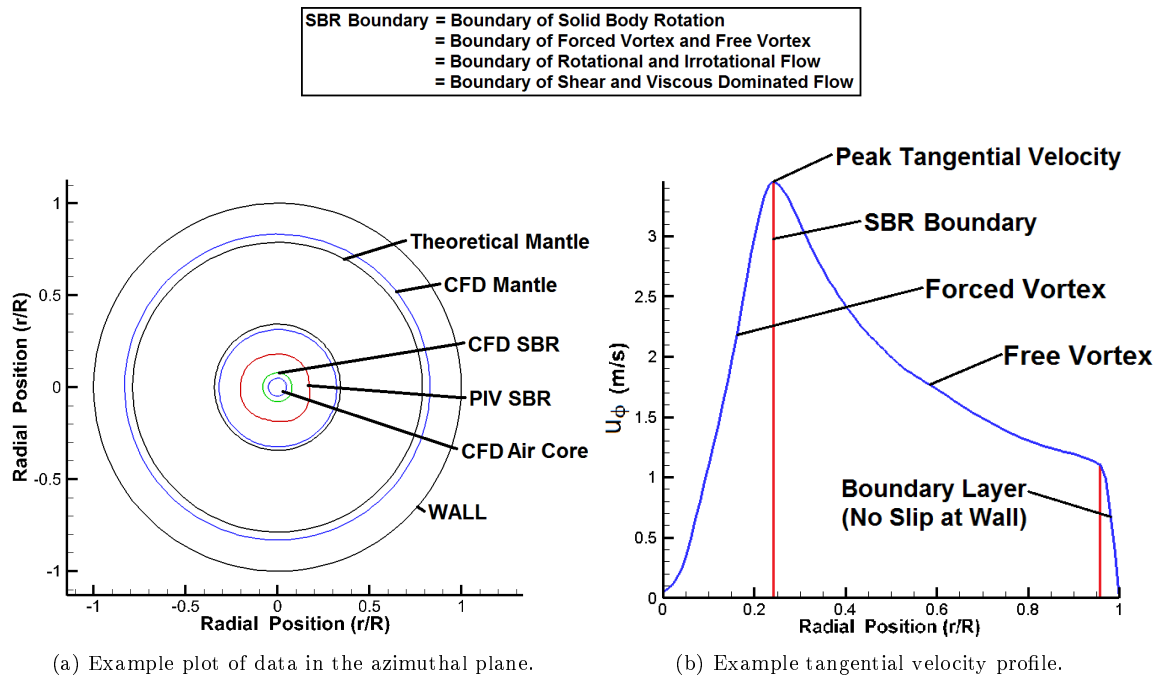
Figure 5.3: Typical plots generated from data extracted from the azimuthal plane.

The example plot of data extracted from the meridional plane of the chamber seen in fig 5.2a is also intended as a reference point and illustrates the features of the axial velocity data obtained. It can be seen that the CFD data is presented in left part of the chamber and the PIV data is in the right part, which is consistent throughout the results. The maximum and minimum axial velocities are extracted from both the CFD and PIV data sets and included in the tabulated data presented. Limitations of the post-processing software meant that the upper and lower limits of the contour maps were only set to the maximum and minimum axial velocity values applicable to both the CFD and PIV data. Due to the relatively large discrepancy between the velocity magnitude ranges obtained by the experimental and numerical methods it is difficult to distinguish via the contour plot levels how the axial velocity varies throughout the chamber for the PIV data. This is because the maximum and minimum values occur predominantly within the core region of the flow where it was not possible to accurately resolved the flow using PIV due to intense scattering by the air core interface that occurred. However, the maximum and minimum axial velocities used for each range of chamber configurations investigated remained constant to allow for some comparison of the axial flow. The values of maximum and minimum axial velocity are taken from the test chambers with the lowest pump throttle for both base and head injector configurations, which allows to an extent to observe the variation of the vortex core characteristics in relation to inflow velocity.

Both the axial and radial co-ordinates have been normalised by the respective chamber dimensions so that the mantle structure can be easily compared to other configurations and the contour maps of the locus of zero axial velocity or mantles have been highlighted by thick black lines so that variations in their structure can be clearly observed. Vectors are also included which use the radial and axial velocity components of the flow respectively to represent the x and y components of the velocity vector. Further limitations of the post-processing software meant that only a single variable could be used per velocity component and meant that the contamination of the velocity vectors for the PIV data resultant of the significant out of plane velocity component caused the radial component to be significantly higher than the axial component. This makes it difficult to identify the axial direction of the flow, but in order to resolve this another variable was substituted for the radial component which represents 10% of the recorded magnitude. In doing this the axial and radial components are of a comparable magnitude as predicted by the CFD and seen in previous

studies [92, 93, 98, 99]. This obviously has an effect on the CFD data, but it was deemed acceptable because the main focus of the study is to identify the mantle structure, which is indicated by the axial direction of the flow. So for visualisation purposes it is important to observe the axial flow path through the chamber and despite the reduction of the radial velocity in the CFD data the variation in resultant direction of the vectors is very similar to those using an unmodified radial velocity component. This means that it is an acceptable compromise, considering how it enables us to observe the variation in the axial direction of the flow for the PIV data. Due to the inherent problems associated with the PIV technique used here the aforementioned methodology was applied throughout all the axial plane data sets in this study which simultaneously display both CFD and PIV data.
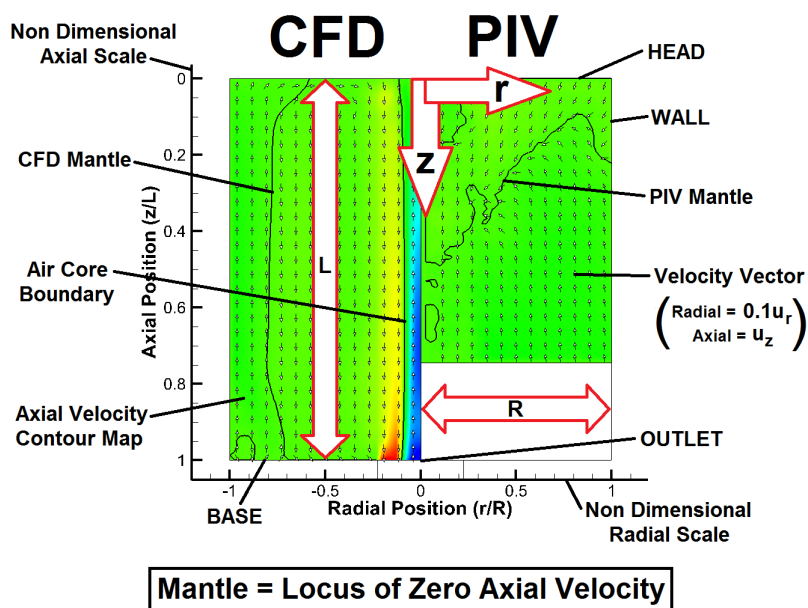
Figure 5.4: Example plot of data in the meridional plane.

5.3 Effect of inlet Reynolds number

5.3.1 Base injection

In this part of the study the chamber geometry remains constant with an aspect ratio of $\frac{L}{D} = 1.0$ and a contraction ratio of $CR = 20$ and represents the baseline experimental configuration, with the aspect ratio being chosen as it represents an intermediate value between other chamber designs [5–7, 9, 57, 58]. The contraction ratio was chosen because it refers to a common ratio used to size the nozzle throat radius in similar vortex rocket engine chamber designs [4, 9, 10, 57]. Apart from the inlet Reynolds number the only other experimental parameter that differs is the location of the tangential inlets. The effects of injector locations based at the base and head of the chamber were considered because of the possible strong influence this may have on the mantle structure embedded in the flow. Table 5.1 contains various parameters describing the flow main characteristics of the flow for base injector configurations. As expected the inlet velocity, inlet Reynolds number and vortex Reynolds number all increase relative to PT. This trend is displayed throughout the data for several values including the PVC frequency, peak tangential velocity, PVC angular velocity as well as the maximum and minimum axial velocities.

(a)

Variable	Symbol	PT=0	PT=25	PT=50	PT=75	PT=100
Precessing Vortex Core Frequency (CFD)	f_{PVC} (Hz)	90.78	100.97	110.09	117.53	128.51
Liquid Dimension of Forced Vortex (PIV)	$r_{SBR}\text{-}r_{core}$	0.143	0.145	0.172	0.182	x
Liquid Dimension of Forced Vortex (CFD)	$r_{SBR}\text{-}r_{core}$	0.065	0.064	0.064	0.063	0.063
Normalised Forced Vortex Radius (PIV)	r_{SBR}	0.225	0.227	0.255	0.265	x
Normalised Forced Vortex Radius (CFD)	r_{SBR}	0.146	0.145	0.145	0.144	0.144
Normalised Air Core Radius (PIV)	r_{core}	0.082	0.082	0.083	0.083	x
Normalised Air Core Radius (CFD)	r_{core}	0.081	0.081	0.081	0.081	0.081
Strouhal Number (PIV)	Sh	3.59	3.47	3.45	2.91	x
Strouhal Number (CFD)	Sh	7.23	7.36	7.39	7.54	7.65
Vortex Reynolds Number	V	2.51E+03	2.75E+03	2.98E+03	3.12E+03	3.36E+03
Inlet Reynolds Number	Re	3.80E+04	4.16E+04	4.51E+04	4.72E+04	5.09E+04
Inlet Pressure (CFD)	p_{in} (Kpa)	9.15	11.04	13.12	14.53	17.13
Inlet Velocity	u_{in} (m/s)	0.98	1.07	1.16	1.22	1.31
Pump Throttle	PT(%)	0	25	50	75	100

(b)

Variable	Symbol	PT=0	PT=25	PT=50	PT=75	PT=100
Maximum Axial Velocity (PIV)	u_z (m/s)	0.09	0.09	0.19	0.11	0.10
Minimum Axial Velocity (CFD)	u_z (m/s)	-2.15	-2.39	-2.72	-2.80	-3.06
Maximum Axial Velocity (CFD)	u_z (m/s)	1.64	1.79	1.94	2.04	2.21
PIV Normalised Boundary layer height at chamber wall	δ_w	0.03	0.03	0.03	0.03	0.03
CFD Normalised Boundary layer height at chamber wall	δ_w	0.02	0.02	0.02	0.02	0.02
PIV Free Vortex Inverse Gradient ($\partial r/\partial u_\phi$)	$\partial r/\partial u_\phi$	99.94	111.56	113.66	144.39	x
CFD Free Vortex Inverse Gradient ($\partial r/\partial u_\phi$)	$\partial r/\partial u_\phi$	68.13	75.03	82.86	86.41	94.05
PIV Forced Vortex Angular Velocity ($\partial u_\phi/\partial r$)	ω (rad/s)	283.43	298.95	323.12	284.99	x
CFD Forced Vortex Angular Velocity ($\partial u_\phi/\partial r$)	ω (rad/s)	570.37	634.43	691.69	738.43	807.43
Peak Tangential Velocity Ratio (PIV)	u_ϕ/u_{in}	2.54	2.47	2.76	2.43	x
Peak Tangential Velocity (PIV)	u_ϕ (m/s)	2.49	2.65	3.21	2.95	x
Peak Tangential Velocity Ratio (CFD)	u_ϕ/u_{in}	3.31	3.36	3.37	3.42	3.46
Peak Tangential Velocity (CFD)	u_ϕ (m/s)	3.25	3.59	3.92	4.16	4.54
Pump Throttle	PT(%)	0	25	50	75	100

Table 5.1: Flow variables for chambers with base injection.

Despite the increase in several variables relative to the inlet velocity it is interesting to note that dimensional variables related to the vortex appear to remain relatively constant, where the air core and forced vortex show little variation in radial position with respect to the inlet velocity. This is also true of the estimated non-dimensional boundary layer height, which remains constant for both the CFD and PIV data for all the configurations tested, but it must be noted that this variable is only accurate to 0.01 due to the methods used during post-processing. It is found that any variation present is minimal and infers that there is little variation in the boundary layer height as there is only a $0.01R$ discrepancy between the non-dimensional boundary layer height of the CFD and PIV data. This is not true for the radius of the forced vortex, where the PIV data reports a larger region of fluid undergoing solid body rotation compared to the CFD. This could possibly be a result of the CFD underestimating the effective turbulent viscosity and lead to reduced shear that allows for a smaller forced vortex, but this remains unknown as turbulent quantities are not available for the PIV data. As a direct result of the increased forced vortex radius, the PIV data also exhibits lower angular velocities and precession frequencies of the PVC which are approximately half of those obtained via CFD. Despite this both the CFD and PIV data still suggest that there is minimal variation in mantle structure apart from the $PT = 50\%$ test case. The invariability of characteristic dimensions with respect to inlet velocity suggests that the vortex structure is relatively unaffected by inlet flow conditions but rather influenced by chamber geometry and becomes apparent through analysis of the flow structure present in other configurations. The only data presented here which appears to be anomalous is the peak tangential velocity obtained via PIV for the $PT = 50\%$ configuration as it is clearly larger than the other peak tangential velocities, which is also reflected by the angular velocity and frequency of the PVC. This may be responsible for the different mantle structures observed within the PIV data for this configuration, as the spectral characteristics of the vortex flow are thought to have great impact upon large scale coherent flow structures [55, 106–109].

Fig 5.5 displays radial plots for the tangential velocity, radial velocity, axial vorticity and pressure respectively, where the radial pressure plot only is representative of the CFD data due to the lack of suitable equipment used for the experimental study. Fig 5.5a clearly shows that the tangential velocity increases with respect to PT, with the CFD displaying remarkably similar profiles with an almost linear increase in velocity magnitude. The PIV tangential velocity profiles do not exhibit the same consistency as the CFD data but still indicate that there is a definite increase in tangential velocity relative to increased inlet velocity. The gradient of the forced vortex with respect to radius is the angular velocity, and as expected increases as the inlet velocity is increased. What is not immediately apparent is the effect this has upon the gradient of the free vortex though as the reciprocal of the gradient can be also seen to increase as a result of increased inlet velocities, seen in table 5.1b. Again this is to be expected, as the peak tangential velocity increases and results in larger gradients as the tangential velocity remains zero at the chamber axis and walls for all configurations. The radial velocity plot seen in fig 5.5b is included as it can be used to compare the relative inward and outward radial flow within the chamber, as well as possible radial suction effects from the Ekman layer because of the close proximity to the chamber head boundary. The radial profile agrees with the analytical theory in that there is no radial zero when there is a single mantle that spans the length of the chamber. The polarity of the radial velocity component does vary and indicate radial zeroes are present within the air core and the phase interface regions, but the radial velocity profile transitions from the behaviour predicted by the analytical theory within this region where the liquid volume fraction reduces to zero and is a likely result of the analytical theory not accounting for reversed flow in the vortex core. Due to the limitations of the VOF model and the HRIC discretisation method, the phase interface is not an instant transition from liquid to gas but rather a gradual transition from one to another, where the midpoint of the phase interface essentially represents the transition point. This effect is also noticeable in the source PIV images acquired in the tangential plane, although this is more likely to be due to light refraction caused by the irregular surface profile of the interface and gives the appearance of a multiphase region of finite thickness, as exhibited by the CFD data. Despite this, measurements of the air core were made using the inner boundary of the multiphase interface for both the CFD and PIV so that more accurate comparisons could be made.

(a) Tangential velocity profile (CFD & PIV).

(b) Radial velocity profile (CFD & PIV).

(c) Axial vorticity profile (CFD & PIV).

(d) Static pressure profile (CFD).

(e) Normalised pressure profile (CFD).
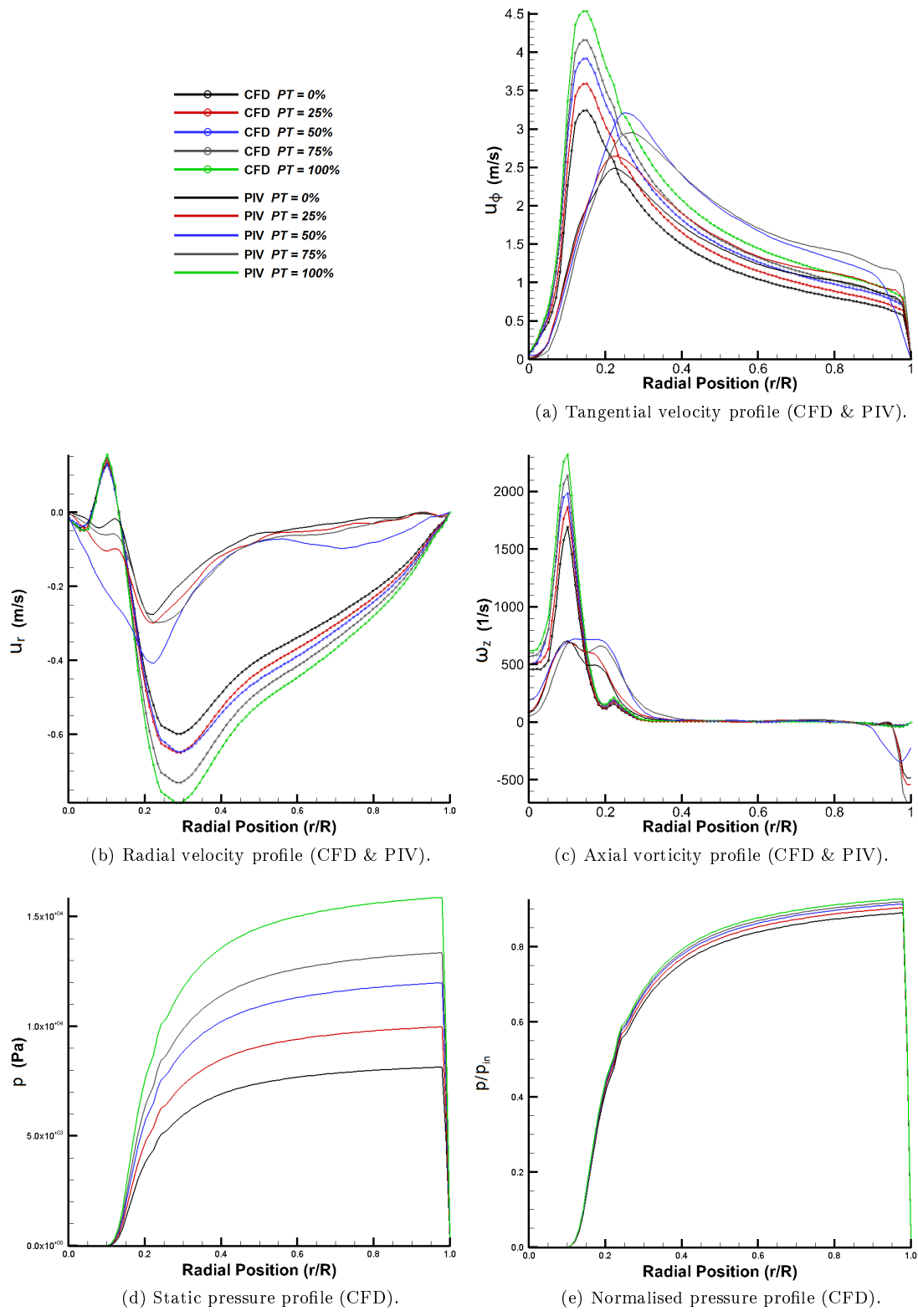
Figure 5.5: Tangential profiles for vortex chambers with base injection.

As with the tangential velocity data the radial velocities obtained from the CFD are larger than those from the PIV and the $PT = 50\%$ test case yet again appears irregular in comparison to the other configurations for both the CFD and PIV data, with regards to the magnitude of the peak value. The radial velocity is apparently being underestimated by the CFD as it is similar to the $PT = 25\%$ configuration, while the PIV data displays an increased peak radial velocity, but lacks the maxima and minima exhibited within the radial range $0 < \frac{r}{R} < 0.17$ as for the other configurations. It is worth noting that the relatively large radial velocities are a result of the close proximity to the head wall boundary where the effects of flow turning are most predominant. This is also observed at the base wall boundary of the chamber near the intersection with the outlet, where the flow is accelerated inwards towards the chamber axis because of the larger radial pressure gradient caused by the proximity to the tangential inlets. This is also reflected previously in fig 5.5b where the radial velocity near the head wall boundary is over an order of magnitude larger in comparison to the mean value throughout the chamber. Despite the obvious differences between the datasets they do compare relatively well in that they display similar characteristics when considering the shape of the plotted curves. Within the air core region $\frac{r}{R} < 0.082$ the CFD clearly shows that there is inward radial flow near to the chamber axis but an outward radial flow in close proximity to the phase interface. The PIV data is unable to provide any corroborating evidence in this region as the seeding technique used in this study was obviously unable to penetrate the air core, as the seeding material is inappropriate for investigation of air flow and means that no reliable velocity vectors are produced within the air core region of the flow.

The radial plot for axial vorticity can be seen in fig 5.5c, where increased vorticity exists near the central region of the chamber but then decays to zero for the majority of the outer chamber radius. This is to be expected as the free vortex does not have vorticity due to it being a potential flow and irrotational, whilst the forced vortex is rotational and is experiencing solid body rotation. As with the radial velocity, the axial vorticity is significantly higher near the head wall boundary, such has been displayed previously by fig 5.5b. This again is caused by the stationary boundary and the resultant increase in localised shear, leading to a larger radial velocity gradient relative to the tangential velocity gradient, as the axial vorticity is defined as the velocity gradient orthogonal to the azimuthal plane or cross sectional plane of the chamber. Again the CFD data exhibits higher peak values with large gradients whilst the PIV data displays smaller peak values and reduced gradients. The region of maximum axial vorticity is spread over a larger radial section of the chamber and may be due to a discrepancy between the physical and numerical effective eddy viscosity, where the CFD underestimates the effects of turbulent dissipation and localised shear. This means there is less resistance to vortex stretching in the axial direction, allowing for increased axial vorticity as angular momentum needs to be conserved. At the periphery of the chamber, the PIV data shows that the axial vorticity becomes negative and is likely caused by the non-slip condition at the wall and the presence of the boundary layer producing shear flow. The vector of the shear force is opposing the vector of the dominant component of the flow, which is the tangential component, causing the tangential velocity gradient to increase and in turn resulting in localised negative axial vorticity. The increased shear associated with the PIV data is also evident in fig 5.5a and fig 5.1a where it is shown that despite the radial resolution of the data, the supposed boundary layer height obtained for the PIV data is larger than that calculated by the CFD throughout the dataset. The reduced tangential velocity gradients near the peak values in fig 5.5a also show that there is increased turbulent dissipation at the interface between the forced and free vortex for the PIV data. In the case of the classic Rankine vortex the fluid is assumed to be inviscid which results in a sharp interface at the forced and free vortex, where the peak represents the theoretical maximum tangential velocity. As the effects of viscosity and more importantly turbulence affect the flow then the interface between the forced and free vortex tends towards a plateau rather than a sharp peak as seen in the results.

(a) $PT = 0\%$.

(b) $PT = 25\%$.

(c) $PT = 50\%$.

(d) $PT = 75\%$.

(e) $PT = 100\%$.
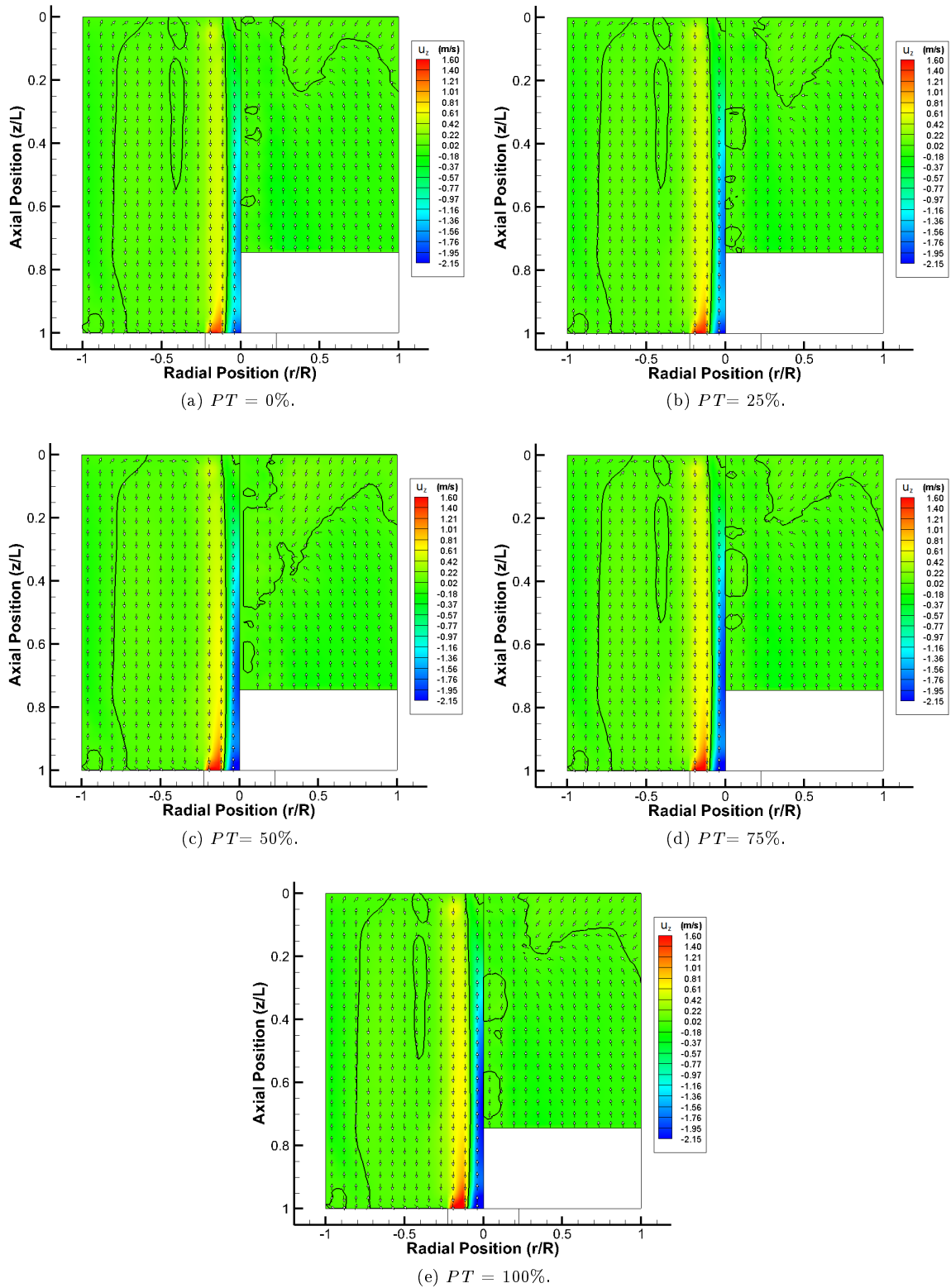
Figure 5.6: Axial velocity contour plots for vortex chambers with base injection.

As data regarding the radial pressure distribution for the physical experiments could not be obtained, only the CFD data is presented in fig 5.5d. Despite this, the CFD data adequately displays the effects of inlet Reynolds number upon pressure the distribution in the chamber. It is clear that by increasing the inlet Reynolds number the maximum chamber pressure is also increased, which reaches a maximum value near the periphery of the chamber, where the transition from boundary layer flow to bulk flow occurs. Upon further inspection of the maximum chamber pressure and the radial pressure gradient, it becomes apparent that both scale linearly with respect to increasing Reynolds number. The magnitude of the pressure gradient decays as it approaches the radial position of maximum pressure and appears to tend towards linearity, although is actually subject to a squared inverse radial proportionality. The radial pressure gradient is akin to that of the tangential velocity profile, as it exhibits a relatively linear gradient that occurs throughout the liquid portion of the forced vortex, then suddenly it changes at the boundary of solid body rotation, where it begins to transition to an inverse radial proportionality. Despite the overall smooth appearance of the radial pressure profiles presented in fig 5.5e, it is quite clear that there is a sudden variation in the pressure gradient at $\frac{r}{R} = 0.2244$. This represents the non-dimensional outlet radius for the chamber configurations investigated here and can be attributed to the structure of the mesh, where the geometry and mesh quality criteria mean that there is a transition at this radius between prism elements which populate the core region and hexahedral elements which constitute the majority of the mesh. As a result, there is evidence of numerical diffusion at this interface which produces a non physical undulation in the radial pressure profile. This can be effectively ignored as it has little or no bearing on the mantle structures observed in this part of the study, but the effects of this mesh interface can also be observed in the tangential velocity and axial vorticity profiles, which exhibit similar undulations. This radial position relates to the peak radial velocity for the PIV data and represents a sudden change in the radial velocity gradient of the CFD data as it reaches its maximum value. In this case the variation in the radial velocity profile is thought to be due to the influence of the chamber geometry rather than the properties of the mesh.

Displayed in fig 5.6 are the combined CFD and PIV data sets for the axial plane data for chambers with base injectors for variation in the inlet Reynolds number. Fig 5.7 displays the mantle structures from both the CFD and PIV data for all base inlet configurations overlaid on each other to allow further comparison of the variation of mantle structure relative to inlet flow conditions. Due to the issues described earlier, these plots are primarily included so that the mantle structure and the axial direction of the flow can be identified. It is worth noting that the axial velocity profiles obtained by the PIV do not span the whole length of the chamber and important regions of the flow could not be captured. Optical access to the axial plane of the chamber was limited to sections of the chamber constructed from borosilicate tube due to the design of the experimental rig. This also meant that the axial position of the laser sheet in the tangential plane was different depending on the axial position of the inlets. The laser sheet was setup normal to the chamber axis at distances of 21mm and 1mm from the datum at the chamber head for base and head injectors respectively, although as stated earlier the CFD results for head injector configurations were taken from the 1mm azimuth plane due to an error.

It can be seen that the mantle structures calculated by the CFD do not vary significantly over the range of inlet Reynolds numbers tested and display a single mantle which spans the length of the chamber. The reversed flow boundary present in the discharge tube is omitted here as no variation was observed and the focus of this study is concentrated on the mantle structure within the confines of the vortex chamber. Fig 5.6 does indicate bi-polar flow similar to that exhibited in the VIHRE. Despite the discrepancies in the mantle structures between the CFD and PIV results, it is clear that fig 5.6 excluding fig 5.6c display similar loci of zero axial velocity for both sets of data. It is unknown why the CFD data in fig 5.6c does not display the inner mantle structure located at approximately $\frac{r}{R} = 0.4$ that is seen in the other results, but is thought to be anomaly as the CFD plot in fig 5.6c appears to display a similar mantle structure in the outer part of the chamber. This could possibly be due a flow transition, which results in an evolving mantle structure as the flow adapts to a variation in the test parameters. It is unknown why this has occurred for the chamber configuration in fig 5.6c, but evidence of mantle structure evolution can clearly be seen when the effects of chamber aspect ratio are assessed, where chambers with an aspect ratio $\frac{L}{D} = 1.0$ appear
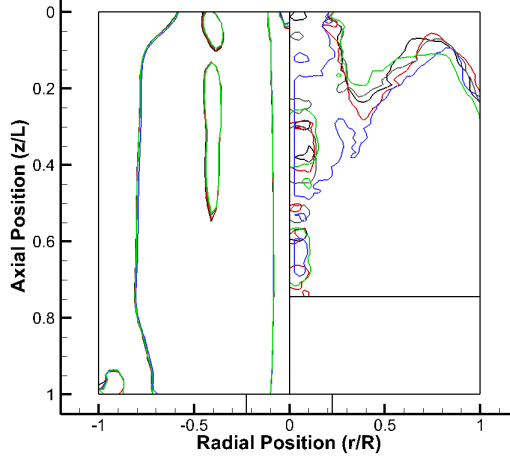
Figure 5.7: Axial plot of combined mantles for chambers with base injection.
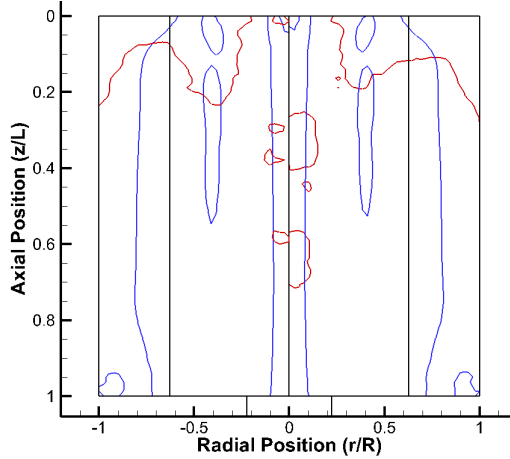
Figure 5.8: Axial plot of overlaid mantles for limiting parameters tested.

to represent a transition point between two distinct mantle structures. Despite this, it must be noted that fig 5.6c still displays a full length chamber mantle and the reversed flow boundary along the chamber axis is practically identical to those seen in fig 5.6. This is made even more apparent when looking at fig 5.7, which shows all the mantles from the experimental and numerical results simultaneously. It is very clear that despite the anomaly referred to in fig 5.6c that all the of the CFD mantle structures are effectively identical.

When the CFD and PIV mantles are overlaid on each other as shown in fig 5.7 it is interesting to note that if the mantle is considered to be a curve, then the maxima and minima of the PIV mantles appear to coincide with the mantle structure obtained by the CFD and is observed consistently throughout other parts of the study. The left hand side of the chamber represents the mantles for the $PT = 0\%$ test case, while the right side represents the mantles for the $PT = 100\%$ test case in order to highlight the minimal variation in the mantle structure over range of inlet Reynolds numbers investigated. This suggests that there does exist some correlation between the CFD and PIV data as both methods appear to infer that mantle structure is unaffected by the inlet Reynolds number. In fig 5.8 the mantle position predicted by the analytical theory is also included for a visual comparison of to those obtained by the CFD and PIV, which is indicated by the vertical line at $\frac{r}{R} = 0.628$. This position represents the non-dimensional singular root of the Bessel function of the first kind J_0, this relates to bi-polar flow where the root has been normalised by the fundamental

root 3.832 of the Bessel function of the first kind J_1. It can be seen that neither mantle structure appears to coincide with the radial position of the predicted mantle in the axial plane, but they do occur in close proximity near the head end boundary of the chamber. This again raises the question of whether or not the flow is undergoing a transition from one mantle structure to another and consideration must also be given to other factors such as the non-linear form of the mantles produced by the CFD and PIV in comparison to the linear forms predicted by the analytical theory. This questions how applicable the analytical solutions are to the mantle structures observed in this study as there is no definite correlation between the various mantle structures seen in the axial plane data.

As mentioned previously the analytical and CFD mantles do intersect near the head end of the chamber, which can be clearly seen in fig 5.9 and display the various mantle in the tangential plane of the vortex chamber. As with fig 5.8, the theoretical mantle position and chamber boundary are represented by the black lines while the CFD mantles and SBR boundary are highlighted by blue and green lines respectively. Like all the axial plane data, the results are in good agreement apart from the results for the base inlet configuration at $PT = 50\%$, but there is a remarkable correlation between not only the analytical and CFD for the $PT = 50\%$ case but also for the calculated PIV mantle in the right hand side of the chamber. The supposed mantle structures that appear at the periphery of the chamber are actually regions of localised reversed flow, which are a result of the time averaged transient conditions recorded. The inner mantle positions display little variation with respect to time, but these supposed mantles are still in a continuous state of flux and unable to form a consistent structure. This means that they will be effectively dismissed for this investigation, although there is a possibility that they may have some influence on the structure of the flow, although such transient behaviour is beyond the scope of this study.

It can be seen in fig 5.9 that the outermost CFD mantle for all configurations are almost identical and correlate equally as well with the location of the theoretical mantle, despite indicating a further mantle structure near the core. Despite the data for the $PT = 50\%$ test case appearing to omit the vortex ring, it shows a clear variation in the mantle structure in comparison to other configurations tested and further supports the idea that there may be some variable that is responsible for causing a transition from one flow reversal state to another. It is not entirely obvious in the CFD mantles presented here, but there is also evidence of periodic rather than axial symmetry which is also observed to different extents throughout the entire investigation. The boundary of solid body rotation indicated by the green lines display minimal variation in the size of the forced vortex with regards to increasing the inlet Reynolds number. However, unlike the mantle structure the shape of the SBR boundary remains circular and does not deform and result in periodic symmetry like the mantle structure. When considering the form of the tangential velocity profiles in fig 5.5a and their relative magnitude in comparison to the radial and axial velocity components, it is obvious that the tangential component of the flow is the most dominant and is possibly less susceptible to the influence of underlying flow mechanisms. It is these unknown mechanisms that are responsible for deforming the mantle structure from a circular to periodic symmetry and may be caused by the respective energy levels of the flow, where the effects of these complex underlying mechanisms may have negligible effects on the bulk flow undergoing rotation about the chamber axis. Only the large scale coherent structures embedded within the flow are affected because of the decreased energy content they possess, relative to the energy levels associated with the motion of the bulk flow. This requires further investigation of the energy spectra within the flow and can only be obtained through proper orthogonal decomposition (POD) so that the lower energy modes in the flow which are not immediately apparent can be investigated and provide some insight into the periodic symmetry observed.

(a) $PT = 0\%$.

(b) $PT = 25\%$.

(c) $PT = 50\%$.

(d) $PT = 75\%$.

(e) $PT = 100\%$.
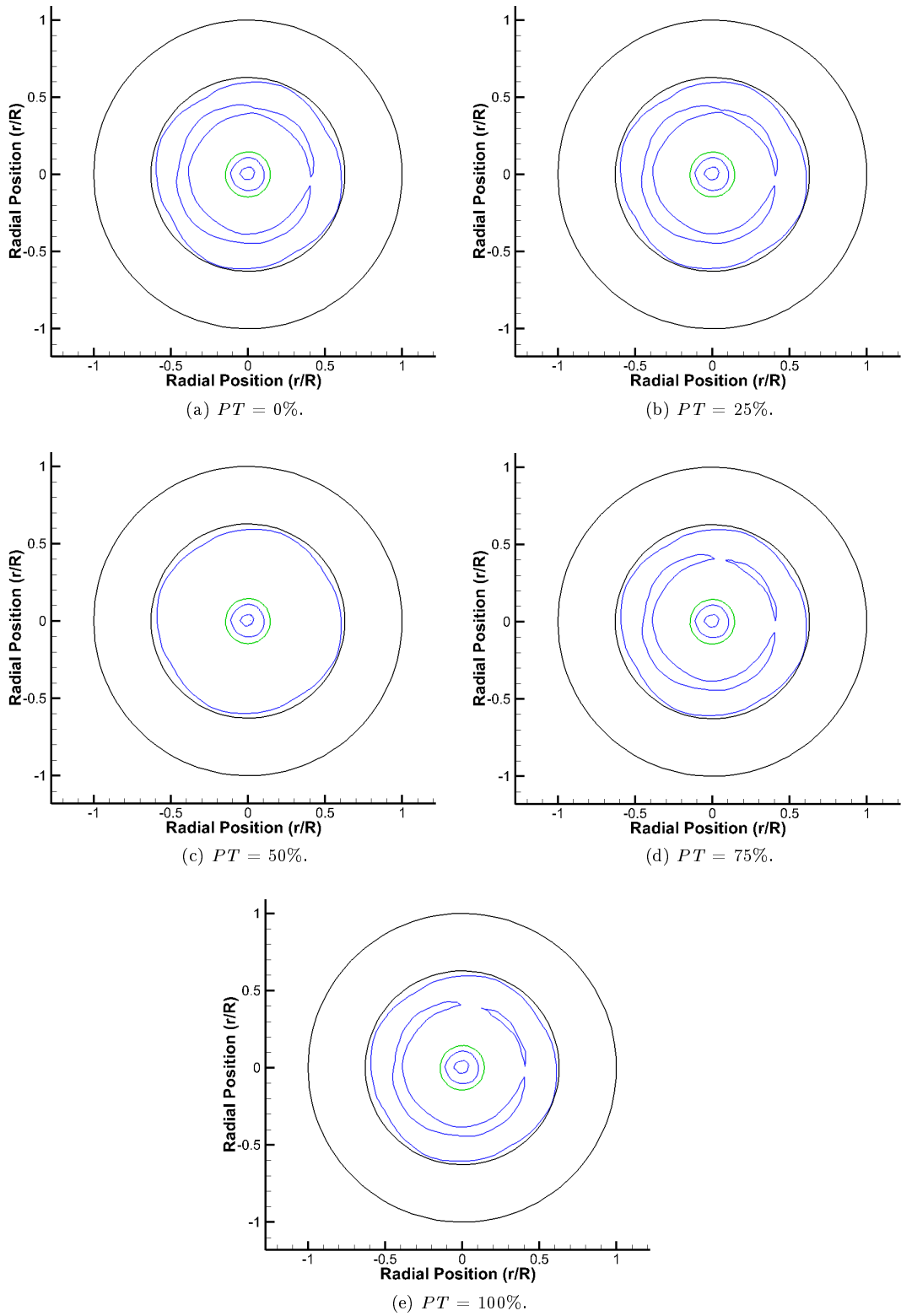
Figure 5.9: Azimuthal plot of CFD mantle and SBR structure for chambers with base injection.

5.3.2   Head injection

Table 5.2 contain various parameters describing main characteristics of the flow for head inlet chamber configurations for varying inlet Reynolds number. As with the results for the base inlet configurations, the inlet velocity and associated Reynolds numbers increase as the PT is increased although they are not directly proportional. Both the CFD and PIV data show that the non dimensional radius of the air core is lower than that of the base inlet configurations, but is to be expected considering the location of the inlets relative to the axial position the tangential plane measurements were taken from. Figs 5.1e and 5.1f shown earlier, indicate that there is a reduction in static pressure with increased axial distance from the tangential inlets. A reduction in the air core radius occurs because of the increased energy levels in the flow and increased momentum, which results in increased vortex stretching. The CFD and PIV air core radii display some discrepancy, but over all are in good agreement with the PIV data, reporting a slightly larger air core than the CFD. The radial positions of the transition from the forced to free vortex in the CFD data also show that the region of fluid undergoing solid body rotation is reduced, but unexpectedly this is not the case for the PIV data which shows that the transitional radius is similar to that of the base inlet configurations. This is also reflected by the peak tangential velocity normalised by the inlet velocity, which shows that the values for the head inlet configuration PIV data are larger than those of the base inlet configurations. The opposite is true for the CFD data, but the discrepancy is larger, with the highest peak tangential velocity ratio for the head inlet configurations being lower than that of the lowest peak tangential velocity ratio for the base inlet configurations. A higher tangential velocity relative to the PIV data is expected, as seen for the base inlet configurations where a smaller forced vortex is associated with larger angular velocities.

The CFD for the head inlet configurations finds that the angular velocity of the forced vortex is significantly lower than those reported for the base injector configurations, but upon closer inspection of the CFD data it was found that the turbulent viscosity calculated for the head inlet configurations was over 20 times higher than for the base inlet configurations. This only seems to occur near the tangential measurement plane near the head of the chamber where radial flow is increased. The effects of this are apparent when comparing fig 5.5a & fig 5.10a, where the vastly increased turbulent viscosity affects the tangential velocity profile producing a plateau rather than a peak. Despite the increased radial velocity component, the overall resultant velocity magnitude is reduced as a direct consequence of the localised increase in shear in close proximity to the head boundary. The reduced tangential velocity profile could also be a result of insufficient radial mesh resolution as this was found to have a similar effect during the grid sensitivity study. However, this does not appear to be the case here as both base and head inlet configurations have identical mesh properties within the core region where the large velocity gradients would cause this behaviour. Additionally fig 5.5a clearly shows that the mesh is suitable for producing tangential velocity profiles with large gradients. This means that the reduced peak tangential velocity must be attributed to the close proximity of the tangential inlets to the head boundary of the chamber and something which is also seen in later results for head inlet configurations, where both the CFD and PIV tangential velocity data is available for comparison.

As with the base inlet configuration data, the maximum and minimum axial velocities increase relative to an increase in the inlet Reynolds number. The CFD data again reports that the peak negative axial velocity is higher than the peak axial velocity, but this is to be expected as the flow undergoes acceleration as it approaches the chamber outlet. This is not reflected in the results for the PIV data, but as mentioned previously the maximum and minimum values for axial velocity occur in the core region of the flow which is in close proximity to the air core interface, where insufficiently accurate velocity data was obtained due to significant laser light scatter. Both the CFD and PIV data also show that the boundary layer height at the periphery of the chamber remains constant relative to an increase in the inlet Reynolds number, while also being identical to the values obtained for the base inlet configurations.

Table (a):

PT(%)	0	25	50	75	100
Pump Throttle	0	25	50	75	100
Inlet Velocity — u_{in} (m/s)	0.94	0.97	1.01	1.09	1.18
Inlet Pressure (CFD) — p_{in} (Kpa)	5.63	6.08	6.70	8.02	9.64
Inlet Reynolds Number — Re	3.65E+04	3.76E+04	3.92E+04	4.23E+04	4.58E+04
Vortex Reynolds Number — V	2.41E+03	2.49E+03	2.59E+03	2.80E+03	3.03E+03
Strouhal Number (CFD) — Sh	5.59	5.56	5.54	5.53	5.53
Strouhal Number (PIV) — Sh	4.09	4.23	4.39	3.92	x
Normalised Air Core Radius (CFD) — r_{core}	0.061	0.061	0.061	0.061	0.061
Normalised Air Core Radius (PIV) — r_{core}	0.061	0.068	0.073	0.077	x
Normalised Forced Vortex Radius (CFD) — r_{SBR}	0.133	0.134	0.136	0.137	0.138
Normalised Forced Vortex Radius (PIV) — r_{SBR}	0.239	0.252	0.256	0.288	x
Liquid Dimension of Forced Vortex (CFD) — $r_{SBR}\cdot r_{core}$	0.072	0.073	0.075	0.076	0.077
Liquid Dimension of Forced Vortex (PIV) — $r_{SBR}\cdot r_{core}$	0.178	0.184	0.183	0.211	x
Precessing Vortex Core Frequency (CFD) — f_{PVC} (Hz)	67.35	69.12	71.64	77.26	83.69

(a)

Table (b):

PT(%)	0	25	50	75	100
Pump Throttle	0	25	50	75	100
Peak Tangential Velocity (CFD) — u_{ϕ} (m/s)	2.20	2.28	2.38	2.59	2.82
Peak Tangential Velocity Ratio (CFD) — u_{ϕ}/u_{in}	2.34	2.35	2.36	2.37	2.39
Peak Tangential Velocity (PIV) — u_{ϕ} (m/s)	2.88	3.26	3.57	3.87	x
Peak Tangential Velocity Ratio (PIV) — u_{ϕ}/u_{in}	3.06	3.36	3.54	3.55	x
CFD Forced Vortex Angular Velocity ($\partial u_{\phi}/\partial r$) — ω (rad/s)	423.14	434.31	450.11	485.42	525.83
PIV Forced Vortex Angular Velocity ($\partial u_{\phi}/\partial r$) — ω (rad/s)	309.61	330.90	357.23	344.51	x
CFD Free Vortex Inverse Gradient ($\partial r/\partial u_{\phi}$)	78.22	80.35	83.26	89.12	95.76
PIV Free Vortex Inverse Gradient ($\partial r/\partial u_{\phi}$)	99.32	114.03	136.37	162.89	x
CFD Normalised Boundary layer height at chamber wall — δ_w	0.02	0.02	0.02	0.02	0.02
PIV Normalised Boundary layer height at chamber wall — δ_w	0.03	0.03	0.03	0.03	x
Maximum Axial Velocity (CFD) — u_z (m/s)	1.40	1.45	1.51	1.63	1.77
Minimum Axial Velocity (CFD) — u_z (m/s)	-2.11	-2.19	-2.28	-2.48	-2.70
Maximum Axial Velocity (PIV) — u_z (m/s)	0.18	0.18	0.18	0.19	0.27

(b)

Table 5.2: Flow variables for chambers with head injection.

The radial profiles for tangential velocity, radial velocity, axial vorticity and static pressure distribution are displayed in fig 5.10. The tangential velocity profile shows that the peak value for the PIV data scales relatively linearly with respect to increasing the inlet Reynolds number, while the CFD data exhibits a more linear increase, this is not immediately apparent unless the non dimensional peak tangential velocities in table 5.2b are referred to. This shows that there is little variation in the peak tangential velocity ratio with respect to variations in PT unlike the PIV data which displays a steadily increasing amplification of the tangential velocity with respect to an increase in PT. This is also observed for both the CFD and PIV data for the base inlet configurations, although this does not apply to the CFD data presented in fig 5.10a. This is probably due to the chamber geometry, where the close proximity of the tangential inlets to the head boundary is found to have a significant impact upon the flow properties. Despite this, the incremental positive shift of the peak tangential velocity also results in a similar incremental increase in the gradient of the forced vortex and the inverse gradient of the free vortex. The increasing gradient of the forced vortex indicates that the precession frequency of the vortex core increases proportional to the increasing inlet Reynolds number. This has been observed consistently throughout this part of the study and may have a significant impact upon the flow if the spectral characteristics of the vortex are found to have a significant impact upon the embedded mantle structure. This remains to be seen and the evidence thus far would seem to suggest otherwise, as the radial velocity profile seen in fig 5.10b is very different to that seen earlier in fig 5.5b. Giving an indication that although the tangential velocity profiles appears to be unaffected by the mantle structure this is not the case for the radial velocity profile. This is also indicated by the analytical theory and describes how an increase in the number of mantles observed directly relates to the number of radial zeroes. The peak inward velocity magnitudes are considerably smaller than that for the corresponding base inlet configurations and is a probable result of increased turbulent dissipation rate with respect to the CFD results.However, this also appears to be the case for the PIV data as well, despite the PIV tangential velocity data reporting an increase in peak values relative to the data for base inlet configurations which opposes this.

The radial velocity profiles for the PIV data appear to emulate the theoretical profiles until the radial zero at approximately $\frac{r}{R} = 0.7$, where the negative radial velocity near the periphery is a likely effect of taking measurements in close proximity to the head chamber boundary and the tangential inlets. The increased radial pressure gradient is most likely responsible for forcing the flow inwardly and counteracting any outward radial component. A plot of the relevant J_1 Bessel function is included in fig 5.12 to clarify the predicted direction of the radial flow and also draws attention to the obvious discrepancy between the observed and predicted location of the radial zero. The analytical theory states that it should appear at $\frac{r}{R} = 0.546$ rather than $\frac{r}{R} = 0.7$, which further highlights that although the analytical theory is an important tool it is still basic in that it describes the flow as relatively axially invariant. It is unable to consider various important effects that occur physically, such as the reversed flow in the core region and the large radial gradients near the boundaries of the chamber. However, the theory treats the problem as being axisymmetric, which at first appears to be a valid assumption, although this is not the case and is easily proved by the quasi periodic nature of the vortex core as it precesses about the chamber axis. Upon closer inspection though, it becomes more apparent that the flow exhibits other periodic properties irrespective of time. In regard to the radial velocity, this is made apparent by fig 5.15a which is a contour plot of the radial velocity from the tangential plane and clearly shows that the velocity distribution exhibits a $\frac{\pi}{2}$ periodicity, a feature which is also replicated in the mantle structure seen in fig 5.17.

(a) Tangential velocity profile (CFD & PIV).

(b) Radial velocity profile (CFD & PIV).

(c) Axial vorticity profile (CFD & PIV).

(d) Static pressure profile (CFD).

(e) Normalised pressure profile (CFD).
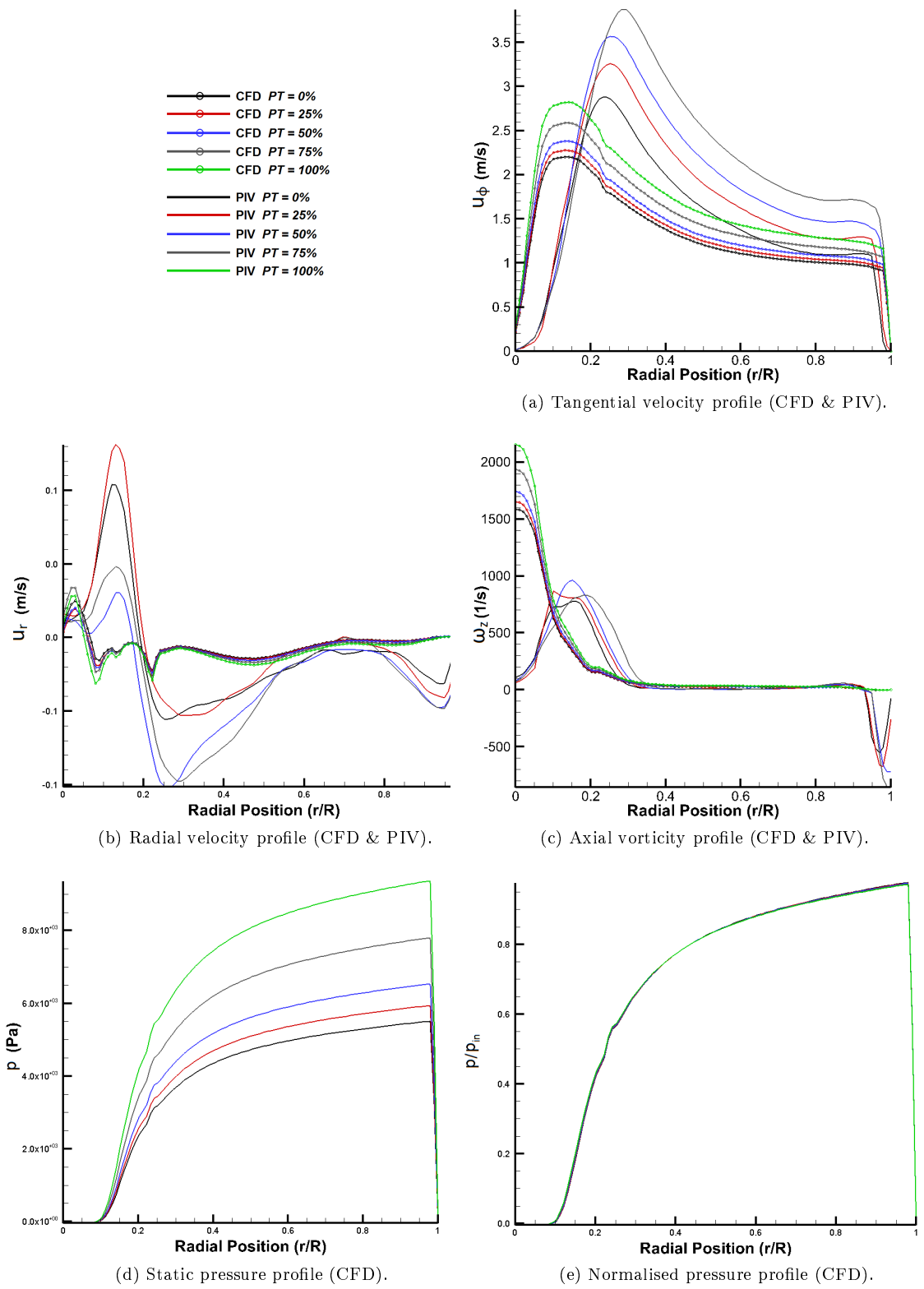
Figure 5.10: Tangential profiles for vortex chambers with head injection.

The discrepancy of the radial zero observed in fig 5.10b is caused by periodicity, which causes the position of the zero radial velocity locus to vary relative to azimuthal position in the chamber and provides a further explanation for why the analytical, numerical and experimental data are not in agreement for this case. Regarding the CFD data displayed in fig 5.10b, the radial velocity profiles do show similarities to the PIV data within the liquid region of the flow, although they do not directly coincide and are of a lower magnitude the peak inward radial velocity occurs at around the same position. Additionally it also displays the same maxima and minima with the minima occurring at approximately the same radial location to that of the PIV data. However, the radial velocity profiles do differ greatly within the core region of the flow after the midpoint transition within the phase interface. As explained previously, this is to be expected as the PIV data is erroneous and should be ignored, due to the multiphase nature of the flow and the lack of a flow seeding in this region. Within this core region there is inward then outward radial flow as the chamber axis is approached, which is opposite to that seen in the base inlet configurations. A possible explanation for this is due to the influence of the Ekman layer and the increased radial pressure gradient relative to that induced by the base inlet configurations. There is possible localised Ekman pumping, forcing the fluid away from the axis of the chamber as the shear and pressure forces are not in equilibrium. The region of positive radial velocity adjacent to the chamber axis is a likely result of the presence of a small recirculation bubble attached to the head boundary of the chamber and is a result of vortex breakdown, as the rotating air core encounters a solid boundary. This small recirculation zone can be clearly seen in the axial plane data in fig 5.11 and a similar phenomenon is observed for the liquid vortex prior to the inception of the air core, where an air bubble is observed at the same position. The rotation of the fluid results in a region of negative pressure, which eventually leads to the production of a relatively stable quasi periodic coherent flow structure, defined as the PVC. This 'bubble' type vortex breakdown is also seen in the discharge tube just after the intersection of the chamber and outlet and is covered in further detail in B.1.

Fig 5.10c depicts the radial distribution of axial vorticity for the head inlet configurations and is immediately seen to be very similar to that seen for the base inlet configurations. The axial vorticity distribution presented here shows that the peak value is positive, although this is not actually the case due to the direction of rotation of the flow, which is opposite to that present for the base inlet configurations. As explained earlier this is due to the modular design of the experimental rig and was also replicated in construction of the CAD geometry and mesh. As a result all of the head inlet configurations produced negative tangential velocities, although this was altered during post-processing to allow for easier comparison to the data from the base inlet configurations, also resulting in a positive axial vorticity distribution.

The only difference for the head injector configurations is that the maximum axial vorticity occurs along the chamber axis for the CFD data, whereas the peak axial vorticity for the base inlet configurations occurs at the midpoint of the phase interface, before dropping significantly near the chamber axis. This is possibly due to increased vortex stretching in the axial direction for the head inlet configurations and could arise from the proximity to the tangential inlets and the increased axial momentum they provide in this region of fluid relative to the base inlet configurations, as the axial vorticity distribution is also greatly affected by proximity to the head and base boundaries of the chamber. Fig 5.10d & fig 5.10e display the radial distributions of actual static pressure and values normalised by the average static pressure at the inlets respectively. The pressure profile exhibits a quadratic increase in magnitude up until approximately half of the chamber radius where the increase in pressure relative to chamber radius appears to be linear as the radial pressure gradient decreases. As with the base inlet configurations a similar trend is observed with respect to the increase in static pressure magnitude relative to increased PT, where the lowest chamber pressures are associated with the lowest inlet pressures and also scale linearly with the inlet flow rate. This is clearly seen in fig 5.10e where there is minimal variation in the radial profile of normalised chamber pressure, reflecting this linear increase in pressure magnitude with respect to inlet conditions.

(a) $PT = 0\%$.

(b) $PT = 25\%$.

(c) $PT = 50\%$.

(d) $PT = 75\%$.

(e) $PT = 100\%$.

Figure 5.11: Axial velocity contour plots for vortex chambers with head injection.

Presented in fig 5.11 are the axial velocity contour plots in the axial plane for the head inlet configurations, where it is immediately obvious that there is very little variation in the mantle structure with respect to increased inlet flow. Something which is clear i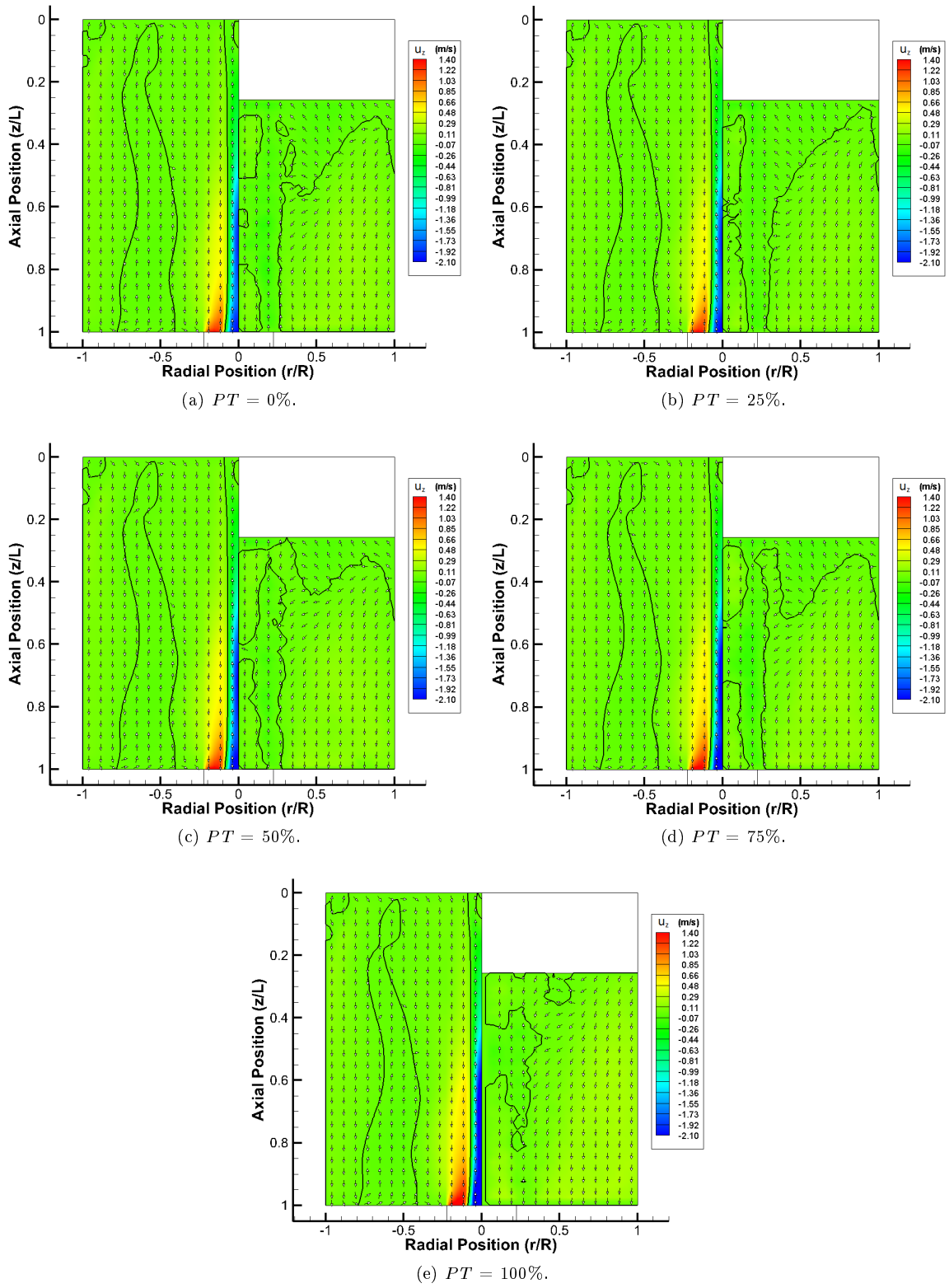n the CFD results but also seen in the PIV results is that there is relatively little variation in the mantle structure, despite the issues explained earlier with the measurement technique used. Again the numerical and experimental results differ from the analytical theory in that the mantles do not form discrete radial tubes that separate the chamber. These increasingly complex structures are likely to be the result of the vastly increased complexity of the flow physics associated with the actual physical flow rather than the simplified conditions assumed by the theory. The most prominent example of this seen for the head inlet configurations is the apparent single mantle that forms a long loop stemming from the base of the chamber. This extends to the region near to the head wall boundary and consists of a single mantle rather than two discrete structures as expected. Despite this, the velocity vectors do show that there is triple vortex flow, as the vortex propagates towards the base of the chamber before changing direction and heading towards the chamber head, before finally changing direction again as the flow is directed toward the chamber exit in the region around the vortex core. To the authors knowledge this type of flow has not been previously observed in an open vortex chamber that has inlet and outlet flow. The analytical theory also does not consider the possibility of confined vortical flows with an even number of mantles, as it ignores the possible effects of placing the tangential inlets at the head of the chamber rather than the base. This is clearly shown in the CFD data, while the PIV data suggests that the mantle structure is relatively constant with respect to increased inlet flow rates, but unfortunately there is no solid experimental evidence to support the observations of the CFD study. This means that the relationship between any test parameters and the resulting mantle structure will remain conjecture until proper experimental methods can be applied to similar chamber configurations.

Despite the apparent discovery of a new type of vortex flow that is indicated by the CFD results, the study as a whole will have to remain as a set of guidelines to describe how chamber geometry can affect embedded flow structures. The mantle structures resultant from the various inlet flow rates are seen in fig 5.11c, where the mantles are overlaid so that clearer comparisons can be made. As with the base inlet configurations, it is clear that the effect of inlet flow rate has negligible effect on the mantle structure and it does not span the length of the chamber. What is not immediately apparent is that the mantle does actually span the length of chamber but not in the axial plane of the results, as the structure exhibits axial periodicity. As mentioned previously for the base inlet configurations the mantle appears to be periodic, but this can only be observed in the radial plane of the chamber. The effect of this periodicity upon an axial slice of the mantle is seen in fig 5.13b, which represents its structure when rotated about the chamber axis by $\phi = 0°,15°$and $45°$ degrees relative to the axial plane used throughout the study. The periodic nature of the flow becomes even more apparent when the whole 3D structure of the mantle is considered, as depicted by fig 5.14, where not only is periodicity observed but also the complexity of the mantle structure, which in this case forms a single convoluted surface that spans the length of the chamber. It also indicates that the mantle structure present in the head inlet configurations is similar to those for the base inlet configurations in that it exhibits a period of $\frac{\pi}{2}$. A similar periodicity can be seen in fig 5.15a, which shows that this is also true of the radial velocity for the $PT = 50\%$ case. It is not immediately obvious in the CFD data but the PIV data finds that the $\frac{\pi}{2}$ period is also found to occur in the tangential velocity distribution for the $PT = 50\%$ case, which can be seen in fig 5.16b. The regions of maximum tangential velocity are found to occur at three distinct points in the chamber each separated by $\frac{\pi}{2}$, but position of the fourth point is not detected because of the light scatter from the air core preventing adequately lit particle images to be captured. Despite this obvious departure from the assumption of axial symmetry, the radial position of peak tangential velocity varies little and the radial profile of the forced to free vortex transition point remains circular, as seen in the majority of results presented. This means that it is only the localised velocity distribution near this transition region that appears to be affected, which also results in a variation from a sharp to smooth peak in the tangential velocity profile relative to angular position in the plane.
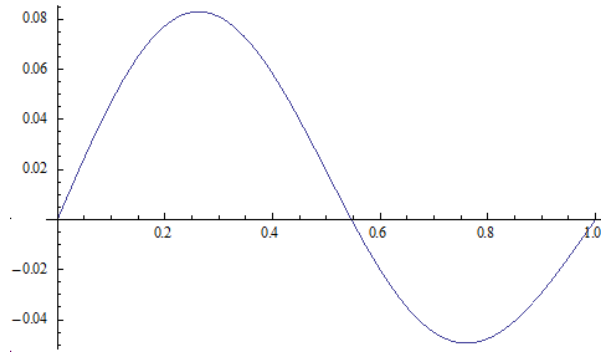
Figure 5.12: Plot of the Bessel function of the first kind J_1 normalised by the first placeholder.

(a) PT = 0-100%.

(b) Azimuth angles $\phi = 0°, 15°, 45°$.
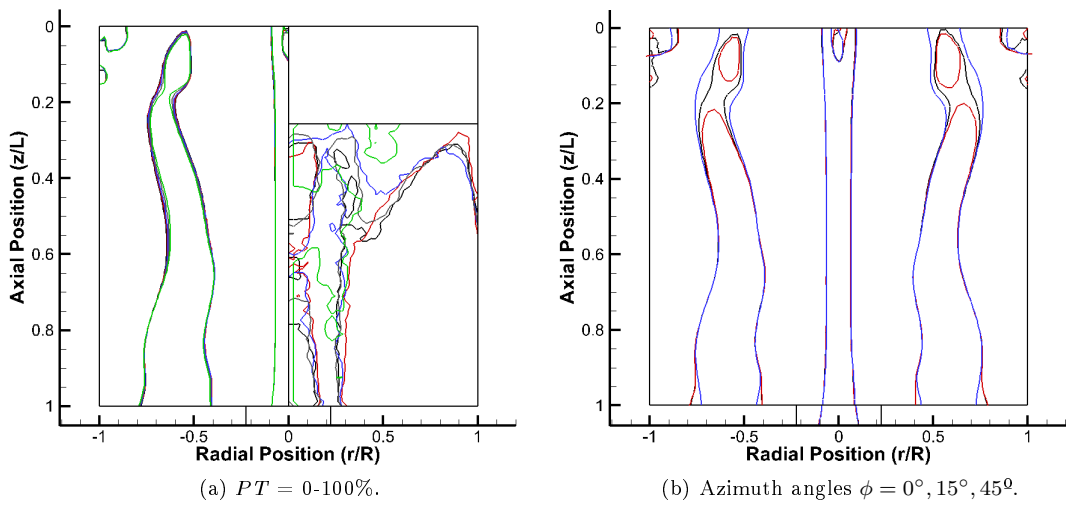
Figure 5.13: Axial plot of combined mantles for chambers with head injection.

If evidence of periodicity can be seen in all three velocity components throughout all the data in the study, then it is clear that the assumption of axial symmetry must be reconsidered as the phenomenon responsible for the mantle structure must be inherently 3D. This means that the current analytical theory is unable to completely describe what is physically occurring in a vortex chamber as it is not physically axisymmetric and any numerical work conducted must be done in 3D. The 3D computational conditions should already be automatically assumed to be the only appropriate method, as the presence of the quasi-periodic PVC demands a full 3D method to be used to capture this behaviour of this phenomenon. The most obvious explanation of this periodicity would be to link it to the number of tangential inlets, as they represent the only non axisymmetric component in the design of the vortex chamber. The number of tangential inlets remains constant throughout the combined CFD and PIV study and the $\frac{\pi}{2}$ periodicity is observed repeatedly throughout the results where 4 tangential inlets are present.

(a) Head of chamber.

(b) Base of chamber.
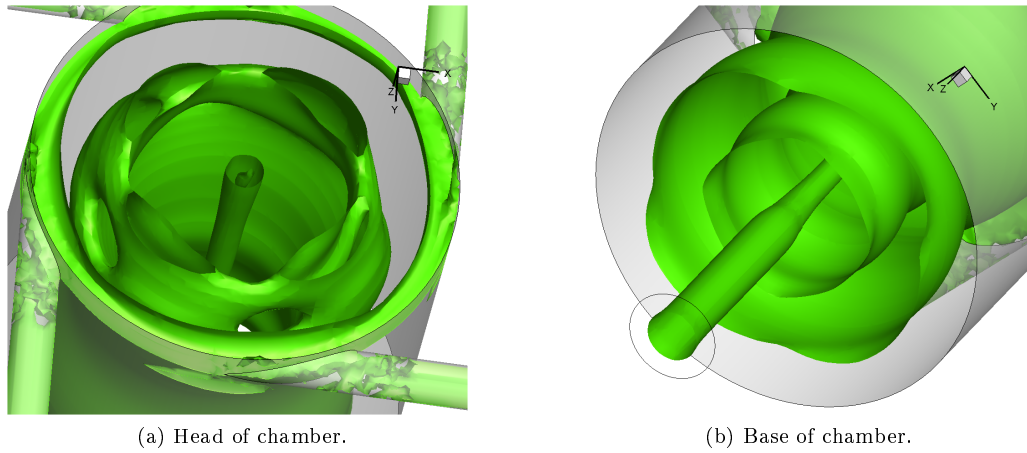
Figure 5.14: Example of 3D structure of mantle in chambers with head injection.

(a) CFD.

(b) PIV.
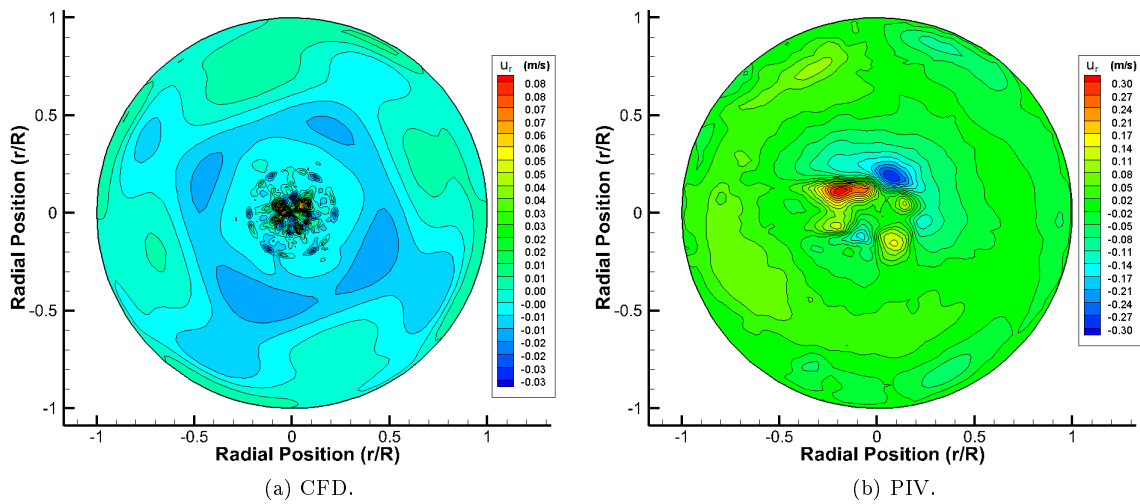
Figure 5.15: Azimuthal plane radial velocity contour plot.

(a) CFD.

(b) PIV.
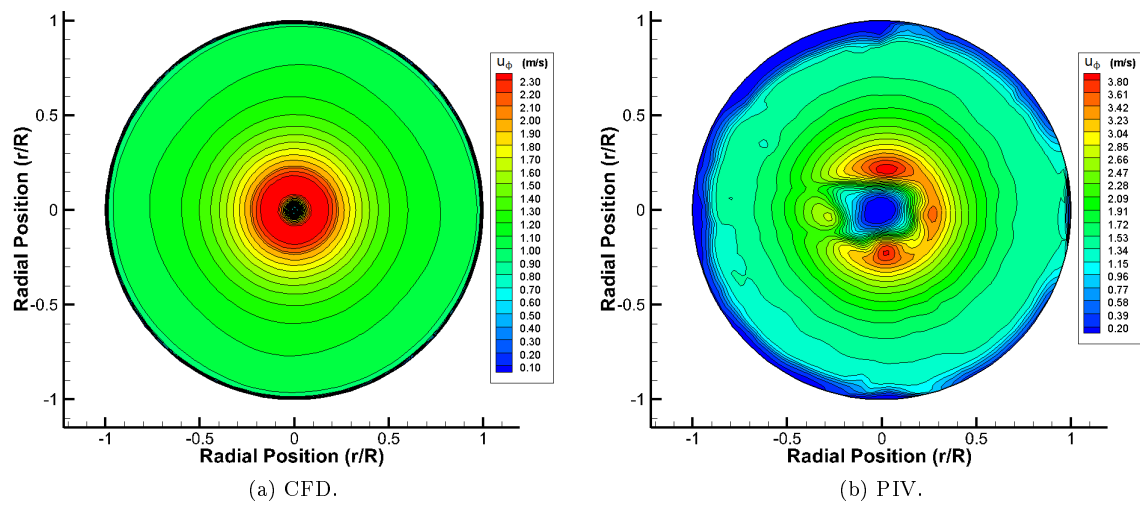
Figure 5.16: Azimuthal plane tangential velocity contour plot.

The mantle structures obtained for the effects of inlet Reynolds number for head inlet chamber configurations can be seen in fig 5.17. Due to the non linear form of the mantle as observed earlier, fig 5.17f is included to display various radial cross sections of the structure at different axial stations for the $PT = 50\%$ case. These stations were set at non dimensional axial positions of $\frac{z}{L} = 0.02, 0.5$ and 0.98, which relates to the base, midpoint and head of the chamber, where the mantles are coloured by the red, green and blue lines respectively. What is immediately noticeable is that there is minimal variation in the mantle structure and SBR transition radius throughout the data. This reflects what is seen in the axial plane plots of the mantle structure, in that for the range of inlet Reynolds numbers tested there appears to be no correlation between the locus of zero axial velocity and inlet flow velocity. This is also indicated by the identical study where chambers with tangential inlets located at the base of the chamber are used, but unlike the results for the base inlet chamber configurations, the mantle structures obtained in this study display a clear periodic symmetry. Considering the proximity to the tangential inlets this gives credence to the possibility that chamber geometry may be responsible for the form of the mantle structure, especially as the number of periodic sections observed can be directly linked to the number of tangential inlets. Further evidence regarding the influence of the tangential inlets can be seen at the periphery of the chamber, where the inlets merge with the chamber and result in localised regions of flow reversal. This region of localised flow reversal is also obvious in the apparent mantle that exists near the periphery of the chamber, which also displays periodicity. A similar feature can be observed in the region near the tangential inlets for the base inlet configurations, although for both of the chamber configurations this only occurs in close proximity to the tangential inlets and an axial boundary. This suggests that the mantle structure is the result of some complex underlying mechanism which is influenced by chamber geometry. As this locus of zero axial velocity is localised and does not greatly influence flow reversal in the bulk of the fluid and should not be referred to as a mantle an the presence of this feature is likely to be able to be removed by aligning the tangential inlets closer to the base or head boundaries. As this would prevent localised axial flow in both directions, which would also prevent the small supposed mantles observed at the intersection between the tangential inlets and the chamber.

The actual mantles that have been obtained by the CFD for the head inlet configurations do not display any correlation to the theoretical axisymmetric mantle positions shown by the inner black circles. This may be due to the increased complexity of the mantle structure relative to the mantles obtained for the base inlet configurations, for which there is an excellent correlation between the analytical and numerical results when there is a single flow reversal. As the flow becomes more complex by introducing further vortex tubes and with flow reversal not just occurring at the axial boundaries of the chamber, then deviation from theoretical conditions must be assumed as the analytical theory is unable to fully describe the processes that physically occur in the vortex chamber. An interesting feature of the flow can be seen in fig 5.17f by comparing the mantle structure obtained at the head and the midpoint axial position of the chamber. It is clear that although the mantle structure at the head of the chamber is periodic, it is axisymmetric in the middle of the chamber and the mantle structure forms concentric circles as predicted by the analytical theory when axisymmetric boundary conditions are applied. The mid chamber plane represents a point in the chamber where the flow is at the greatest distance from an axial boundary. Therefore it could be assumed that the axial boundaries have little or no influence on this region of the chamber, where it is only the circular chamber wall which will affect the mantle structure as it is located at the maximum axial distance from the tangential inlets. The mantle structure seen at the base of the chamber also exhibits periodic symmetry and suggests that the proximity to an axial boundary is also responsible for variation in the localised mantle structure and contributes to the argument that the mantle is influenced by chamber geometry.

(a) $PT = 0\%$.

(b) $PT = 25\%$.

(c) $PT = 50\%$.

(d) $PT = 75\%$.

(e) $PT = 100\%$.

(f) Mantles for head, middle base region of chamber.

Figure 5.17: Azimuthal plot of CFD mantle and SBR structure for chambers with head injection.

As with the mantles recovered from the head of the chamber, the mantle structure in the rest of the chamber does not exhibit any correlation to the mantle radii predicted by the analytical theory. Even at the midway point of the chamber where the form of the mantle is axisymmetric, there is a large discrepancy between the analytical and numerical results. This may be due to the lack of discrete mantles spanning the length of the chamber and may possibly represent a transitional structure which occurs during the onset of further concentric cylindrical tubes with zero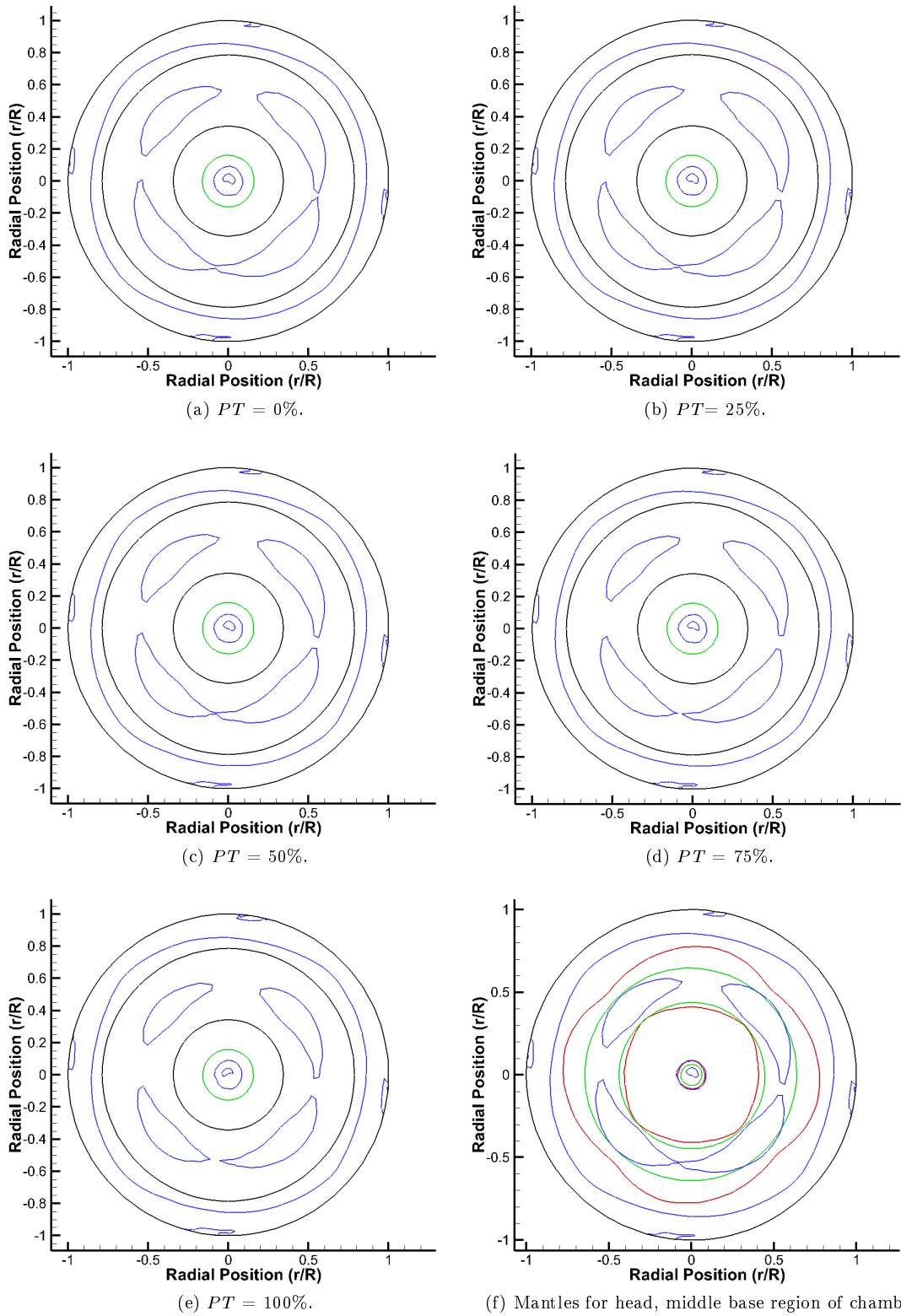 axial velocity. It is not completely clear what can be deduced from the mantle structure and the periodic nature of the flow but it is clear that all the structures observed are examples of mode shapes. These are more commonly associated with other areas of physics such as solid mechanics, optics, electromagnetism and quantum mechanics, where mode shapes are produced when a system is in resonance. Specific mode shapes or eigenmodes occur when the system is perturbed at a specific frequency, all of which are all dependent upon the container geometry. The geometry is responsible for the wave dispersion and interference patterns that occur and which result in the standing wave structures that are indicative of a system in resonance. The nodes of the standing waves represent physical points within the geometry which exhibit zero displacement and do not undergo deformation in terminology applicable to solid mechanics. As with the majority of the results which exhibit periodic symmetry, the resulting mantle structures form mode shapes and comprise of several low order modes, where the patterns that occur are due to the formation of a standing wave structure in the fluid. Each mode relates to a standing wave with specific properties that when superimposed upon each other result in complex mode shapes as seen in the results.

When the mode shapes of the axial velocity component are considered, it is the mantle or locus of zero axial velocity that represents the position of the antinodes of the waveform. The nodes are represented by the radial positions of maximum and minimum axial velocity relative to the sign of the waves amplitude. For standing waves to occur the system needs to be in resonance, where the standing wave is formed from the superposition of an initial waveform and the reflected waveform. The radial plane of the cyclonic flow investigated here is directly comparable to a circular membrane that has a zero displacement boundary condition imposed at its periphery and the resultant mode shapes display significant similarity to those indicated by the mantle positions, dependent on what modes are excited. Regarding the fluid inside the vortex chambers investigated here, the radial standing wave arrangement requires an axial perturbation so that the mode shapes can be formed. This is provided by surface of the vortex core interface, which has a helical fluted structure and is indicative of longitudinal waves traversing the length of the vortex core. It is these axial disturbances propagating along the vortex core which produce radial oscillations in the fluid as the vortex core rotates. In relation to fluid mechanics, this type of internal wave is only possible when the fluid medium is rotating and is not to be confused with gravitational surface waves. In addition to this, the radial waveform is orthogonal to the axial waveform of the vortex core and means that the wave is also transverse. Both of these characteristics mean that the radial waves responsible for the formation of the mantle structure are actually inertial waves, which are most commonly associated with atmospheric or planetary core dynamics, where inertial waves arise from the interaction of the fluids rotation and a non inertial frame restoration force defined by the Coriolis force.

Examples of a circular membrane perturbed at its centre can be seen in fig 5.18, these are representative of the mantle structures observed in fig 5.17f for various axial positions in the chamber. These images were obtained using FEM, where the wave equation was calculated for an oscillating membrane and it can be seen that the results display a remarkable resemblance to the mantle structures produced by the CFD. The specific modes that have been excited are $(0, 3)$ and $(4, 2)$, where the individual mode descriptors relate to the number of radial and azimuthal nodes respectively. These are otherwise known as wavenumbers and describe the spatial frequency of the waves, which in this case are described by angular wavenumbers. The areas coloured green and red relate to regions of maximum amplitude, being either positive or negative and the black areas represent the antinodes where there is zero displacement and is used as an analogue to the mantle structure. The mantle structure in fig 5.18b is identical to that of mode $(0, 3)$ alone, as the amplitude of mode $(4, 2)$ is negligible and is an example of an axisymmetric cylinder mode which have zero azimuthal nodes. As the amplitude of mode $(4, 2)$ increases the effect it has upon periodic symmetry becomes clear, with a larger amplitude occurring in fig 5.18a relative to fig 5.18c. When the effects of mode

92

(a) Large influence from (4, 2) mode.

(b) No influence from (4, 2) mode.

(c) Small influence from (4, 2) mode.
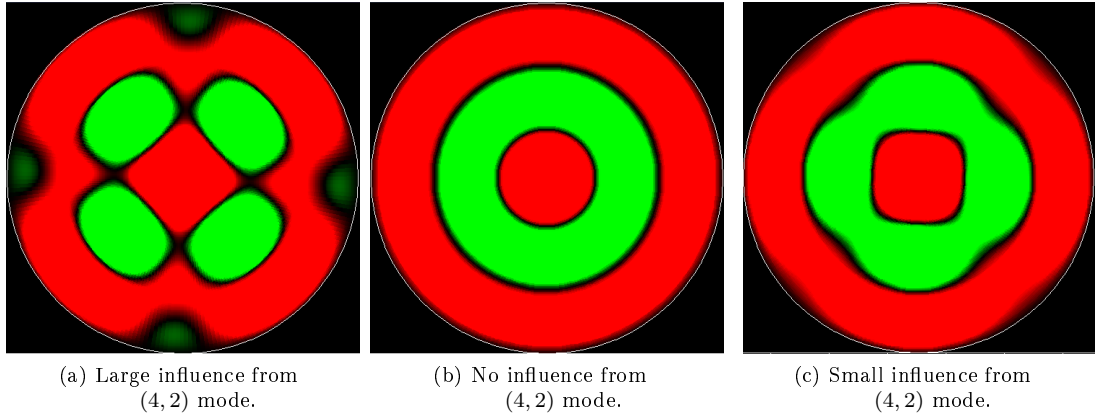
Figure 5.18: Mode shapes of an oscillating circular membrane perturbed by modes (0, 3) & (4, 2).

amplitude are considered and when these combined mode shapes are related to the head, middle, base regions of the vortex chamber for fig 5.18 respectively, then it is possible to start understanding how the chamber geometry is influencing the embedded structures within the flow. At the midway position in the chamber, it was observed that the mantle structure consists of concentric circles which indicates that the cylindrical mode (0, 3) is dominant. At the axial chamber boundaries, the (4, 2) mode has greater influence and is most significant in the head region where the tangential inlets are located. This would suggest that the number of tangential inlets does influence the mantle structure in some way although it may also be coincidental as the periodicity of the mantle structure is reliant on the composite mode shapes, which are directly related to the axial perturbation frequency. The (4, 2) mode may not be a direct result of the inlet geometry but could be caused by the large velocity gradients associated with both the head wall boundary and the tangential inlets perturbing this mode. This would also explain why the mantle structure exhibits periodicity at the base of the chamber where the geometry is axisymmetric but is also in close proximity to the base boundary.

A possible explanation to why the structure differs at the head of the chamber relative to the cylindrical mode exhibited in the middle of the chamber is that the amplitude of the (4, 2) mode is greatest in the head region, due to the increased momentum being introduced locally from the tangential jets. This may be responsible for increasing the magnitude of the local maximum and minimum axial velocity component, but if this is the case then it would mean that physically an axially invariant mantle structure would be difficult to obtain as the flow properties would have to remain relatively constant throughout the length of the chamber. Similar mode shapes can be observed in similar cylindrical geometries where there are no tangential inlets. An analogue to the mantle structure geometry is an annular pipe filled with water, an example of which can be seen in fig 5.19a, which details the mesh and geometry used in an FSI simulation of this configuration [29], while the deformation of the structure and subsequently the fluid can be seen in fig 5.19b, corresponding to the azimuth wavenumber $k = 4$. The original cylindrical structure is equivalent to the mantle structure observed at the midway position of the vortex chamber, as seen in fig 5.18b and only represents the (0, 3) mode, while the mode shape of the deformed annulus is representative of the combined (0, 3) and (4, 2) modes. The simulation does not include rotation effects but this is moot because it is the mode shape of the cylindrical geometry which is important here, as it shows that when a fluid is rotating and propagation of inertial waves occurs, then if the azimuth wavenumber $k = 4$ that the mode shapes found in the FSI study here will be similar to those exhibited by the mantle structure.

Although the modal analysis here was concerned with FSI, the same results can easily be reproduced for a solid annular prism and highlights the fact that the mantle structure is directly affected by the chamber geometry. The FSI results also specifically take the form of mode shapes which are the result of the system being perturbed by a discrete frequency value. The range of discrete frequencies that can be perturbed will be limited by the shape of the geometry, which means that

(a) Solid & fluid domain mesh.

(b) Deformed domain characterised by mode shape.
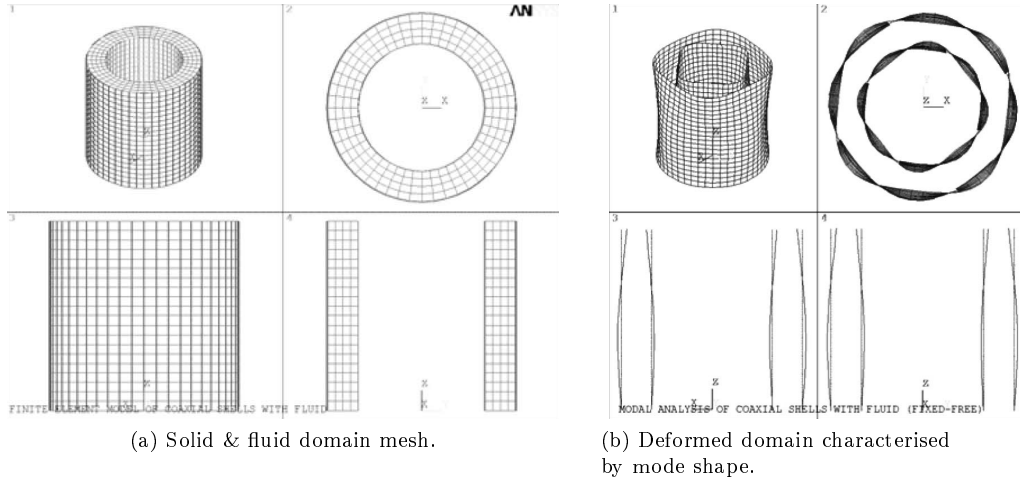
Figure 5.19: FSI modal analysis of a thin walled vessel & fluid annulus. [29]

the amount of mode shapes or inertial modes will also be limited. If it is possible to identify what inertial modes are possible in a specific geometry then it is also conceivable that the conditions required to perturb a specific mode shape can also be applied through design. In turn this would provide the means to control the amount of flow reversals within a vortex chamber by manipulating the behaviour of the flow and the mantle structure prior to actual operation through intelligent design. Considering that the PVC is the only quasi-periodic structure with regards to time present in the flow and that inertial waves stem from the axial propagation of waves along the vortex core, then the spectral characteristics of the vortex core must play a vital role in affecting the shape of the mantle structure in combination with the chamber geometry. As they respectively provide the source of disturbance and boundaries required to set up the standing wave arrangement which leads to the formation of the mantle structure. Similar mode shapes can also be created if an octupole source is located at the centre of a circular reflecting boundary where the mode shapes arise from the interference patterns of the waveforms.

5.4 Effect of aspect ratio

5.4.1 Base injection

In the part of the study investigating the effect of chamber aspect ratio upon the flow, the contraction ratio remained constant at $CR = 20$ as did the number of tangential inlets. As mentioned previously the range of aspect ratios investigated intend to bridge the gap between the chamber aspect ratios employed by VIHRE and VFP designs, as there was evidence to suggest that multiple flow reversals occurred in the VFP, whilst a single flow reversal was confirmed for the VIHRE engine. Therefore it is necessary to investigate the intermediary chamber aspect ratios to identify any transition from single to multiple flow reversals and to do this the following aspect ratios were chosen $\frac{L}{D} = 0.4, 0.6,$ 0.8, 1.0, 1.2 and 1.4. The data displayed in tables 5.3 are the most salient values taken from the aspect ratio study for chamber configurations with base injectors. Due to limitations in the experimental setup, tangential plane PIV data was not acquired for the study into the effects of chamber aspect ratio and several of the key parameters needed to assess the structure of the vortex are not available. This means that any conclusions will be mainly drawn from the available CFD data, although the inlet Reynolds number study has indicated that the CFD is reliably accurate in reproducing the trends that are observed empirically. It is immediately obvious is that the inlet pressure increases almost linearly as the aspect ratio is reduced and the inlet velocities for all chamber configurations display little variation in magnitude, and no discernible trend can be observed. Additionally figures 5.20d and 5.20e show that the chamber pressure increases as the aspect ratio is decreased.

Table (a):

Variable	Symbol						
Precessing Vortex Core Frequency (CFD)	f_{pvc} (Hz)	131.83	126.11	117.96	111.15	101.30	54.06
Liquid Dimension of Forced Vortex (CFD)	$r_{SBR}-r_{core}$	0.069	0.065	0.064	0.063	0.086	0.101
Normalised Forced Vortex Radius (CFD)	r_{SBR}	0.150	0.146	0.145	0.144	0.147	0.162
Normalised Air Core Radius (CFD)	r_{core}	0.081	0.081	0.081	0.081	0.061	0.061
Strouhal Number (CFD)	Sh	8.80	8.48	7.99	7.46	6.84	3.69
Vortex Reynolds Number	V	7.49E+03	4.96E+03	3.69E+03	2.98E+03	2.47E+03	2.09E+03
Inlet Reynolds Number	Re	4.53E+04	4.50E+04	4.47E+04	4.51E+04	4.48E+04	4.43E+04
Inlet Pressure (CFD)	P_{in} (Kpa)	18.26	16.17	14.32	13.12	11.79	7.88
Inlet Velocity	u_{in} (m/s)	1.17	1.16	1.15	1.16	1.16	1.14
Aspect Ratio	L/D	0.4	0.6	0.8	1.0	1.2	1.4

(a)

Table (b):

Variable	Symbol						
Minimum Axial Velocity (PIV)	u_z (m/s)	-0.24	-0.23	-0.20	-0.27	-0.48	-0.47
Maximum Axial Velocity (PIV)	u_z (m/s)	0.18	0.16	0.35	0.20	0.30	0.34
Minimum Axial Velocity (CFD)	u_z (m/s)	-2.37	-2.16	-2.23	-2.32	-2.23	-2.67
Maximum Axial Velocity (CFD)	u_z (m/s)	1.17	1.65	1.58	1.56	1.54	1.46
CFD Normalised Boundary layer height at chamber wall	δ_w	0.02	0.02	0.02	0.02	0.02	0.02
CFD Free Vortex Inverse Gradient ($\partial r/\partial u_\phi$)	$\partial r/\partial u_\phi$	101.64	94.10	87.08	82.86	79.22	87.64
CFD Forced Vortex Angular Velocity ($\partial u_\phi/\partial r$)	ω (rad/s)	828.30	792.39	741.15	698.41	636.50	339.68
Peak Tangential Velocity Ratio (CFD)	u_ϕ/u_{in}	4.15	3.89	3.64	3.38	3.16	1.88
Peak Tangential Velocity (CFD)	u_ϕ (m/s)	4.85	4.51	4.19	3.92	3.65	2.15
Aspect Ratio	L/D	0.4	0.6	0.8	1.0	1.2	1.4

(b)

Table 5.3: Flow variables for chambers with base injection.

Although there is little variation in the inlet velocity and therefore the inlet Reynolds number, the vortex Reynolds number becomes significant in this part of the study. As the formulation of the vortex Reynolds number is greatly dependent on chamber geometry and specifically the chamber aspect ratio. So it provides a useful initial reference value to gauge the relative strength of the vortex, as it can be calculated prior to any testing and used as a parametric design variable. Here it effectively predicts that as the chamber aspect ratio is reduced, the relative strength of the confined vortex will increase therefore meaning increased circulation. This is confirmed by comparing the magnitudes of peak tangential velocity occurring at the periphery of the SBR region. Even after being normalised by the inlet velocity the peak tangential velocity clearly increases as the chamber aspect ratio is decreased. As with the relationship between the inlet pressure and aspect ratio, the peak tangential velocity is found to scale linearly below aspect ratios of $\frac{L}{D} = 1.4$. As the angular velocity of the forced vortex region is calculated using this value and the fairly invariant forced to free vortex transition radii display the same linear increase in magnitude with decreasing aspect ratio.

95

(a) Tangential velocity profile (CFD).

(b) Radial velocity profile (CFD).

(c) Axial vorticity profile (CFD).

(d) Static pressure profile (CFD).
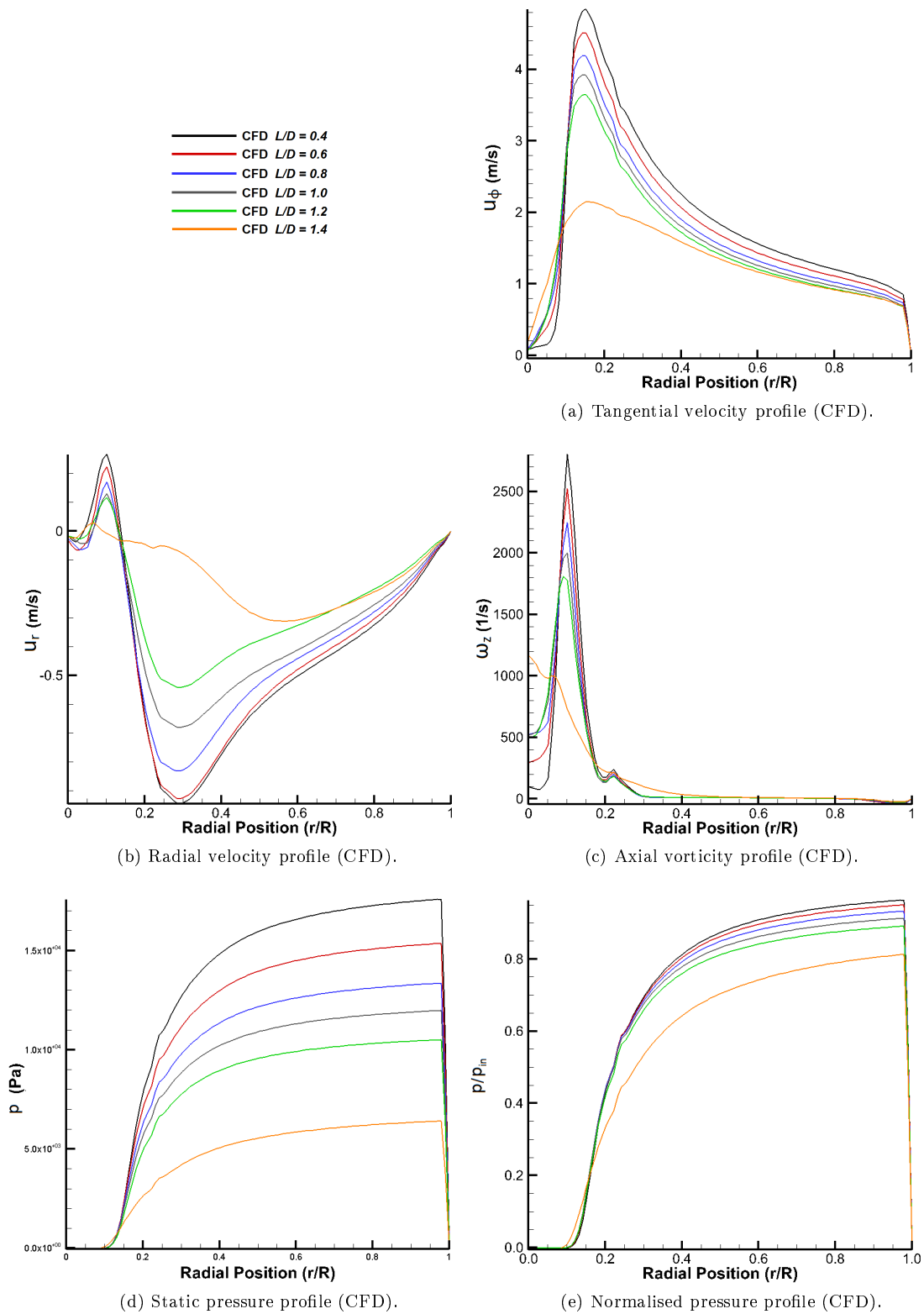
(e) Normalised pressure profile (CFD).

Figure 5.20: Tangential profiles for vortex chambers with base injection.

The tangential velocity profiles presented in fig 5.20a provide a better visual means for assessing the variation in vortex strength relative to chamber aspect ratio. As they also highlight the variation in the gradient of the free vortex and also the minimal change in the boundary layer at the periphery of the chamber, as expressed in table 5.3b where there is a significant discrepancy between the maximum and minimum axial velocities obtained via the CFD and PIV. As explained previously, this is due to the lack of resolution of the data in the core region of the flow where the maximum values for axial velocity are expected. Either way it is difficult to observe any appreciable trend in the data due to the small range of the values and it is only PIV data taken from the tangential plane that provides suitably accurate results for proper analysis. As with the CFD data obtained for the inlet Reynolds number study, the radius of the forced vortex in this part of the study displays little variation with respect to the effects of the parametric variable being investigated. So it is to be expected that the rotational frequency of the PVC scales linearly with the chamber aspect ratio as it is mainly dependent upon the magnitude of the peak tangential velocity.

An interesting feature pertaining to the geometry of the vortex core is shown by the data of the normalised radii of the air core. Unlike the central flow reversal region in the inlet Reynolds number study, the radius of the air core does not remain constant relative to chamber aspect ratio, but rather it is described by one of two discrete radii. The reduction in the normalised air core radius is $\frac{r}{R} = 0.02$ and occurs when the chamber aspect ratio drops below $\frac{L}{D} = 1.2$. At first this may seem insignificant as this reduction represents an approximate 25% decrease in the radius of the air core, and considering the radii are discrete values rather than continuous means it warrants further investigation. When considering the axial plane velocity contour plots in fig 5.22 the significance of this becomes apparent, as there is a clear transition in the mantle structure between the chamber aspect ratios $\frac{L}{D} = 1.0 - 1.2$ and provides further evidence that the vortex chamber geometry plays a critical role in the formation of the mantle structure. When considering the effects of chamber aspect ratio, it would be prudent to assume that it is likely to be the length of the chamber responsible for any significant change in the form of the mantle. As it is the axial propagation of waves along the vortex core that is responsible for inertial waves in a rotating fluid medium such as this. So like any other geometry that provides a cavity where Helmholtz resonance can occur, the length of the chamber is instrumental in affecting the possible range of harmonics in the chamber. This highlights the importance of chamber geometry as a controlling factor of what range of discrete frequencies, and therefore what inertial modes are possible.

Fig 5.20 shows the radial distributions of tangential velocity, radial velocity, axial vorticity, pressure and normalised pressure respectively, where it is immediately apparent that in each plot the chamber configuration with base tangential inlets and an aspect ratio of $\frac{L}{D} = 1.4$ represents an anomaly and should be effectively excluded from any analysis. This is also indicated by the data presented in table 5.3, where the various values pertaining to the $\frac{L}{D} = 1.4$ chamber configuration do not concur with the linear relationships relative to aspect ratio displayed by the other chamber configurations. The maximum and minimum values of radial velocity as seen in fig 5.20b exhibit an increase in magnitude relative to a decrease in the chamber aspect ratio, although not according to the more linear relationship seen for the tangential velocity profile seen in fig 5.20a. This may be due to the smaller range of radial velocities that are more susceptible to fluctuations in the flow or a possible result of the complex periodic structures embedded within the flow. The radial velocity profiles here may emulate those seen in the inlet Reynolds number study for base tangential inlets, in accordance with the theory that only a single mantle spanning the length of the chamber is present because there is no abscissa in the radial velocity plot within the bulk fluid. If the axial velocity contour plots in fig 5.22 are consulted, then it can be seen that this is true despite the presence of convoluted mantle structures in the vortex chambers with lower aspect ratios. The radial velocity contour plot for the chamber with aspect ratio $\frac{L}{D} = 0.4$, as seen in fig 5.21 is also included to again draw attention to the non-axisymmetric form of the radial velocity component. This periodicity is not as apparent when compared to the radial velocity distribution near the tangential inlets, but it does show that these periodic structures occur throughout the length of the chamber, although in this case to a lesser extent compared with larger chamber aspect ratios.
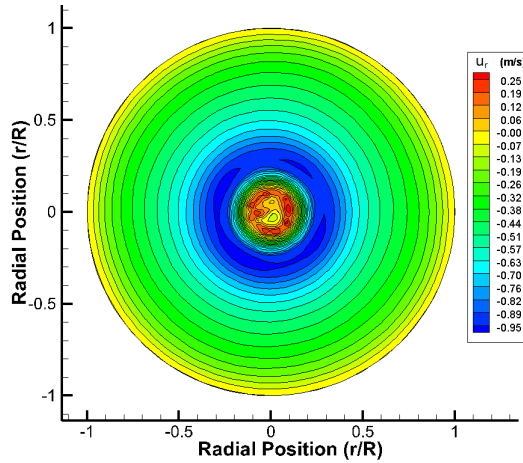
Figure 5.21: Radial velocity contour plot of chamber with aspect ratio $\frac{L}{D} = 0.4$.

Again the radial plots for axial vorticity and pressure distribution also display the same similarities as the data for the Reynolds number study into chambers with inlets located at the base of the chamber. The peak axial vorticity occurs within the region of solid body rotation, which is to be expected as the vortex is being stretched as the flow is accelerated towards the outlet. The axial vorticity is supposed to be zero at the periphery of the forced vortex to indicate the transition from rotational to irrotational flow, but it is located at the base of the axial vorticity spike and does exhibit decay towards zero as the radial position increases. The radial pressure distributions seen in figures 5.20d and 5.20e both exhibit a quadratic form until approximately half the chamber radius where the pressure displays a more linear increase relative to an increase in radial position, despite still being inversely proportional to the square of the radius. As indicated by the values in table 5.3a, the pressure within the chamber increases linearly with a decrease in the chamber aspect ratio and is clearly depicted in fig 5.20e.

Axial velocity contour plots including overlaid mantle positions can be seen in fig 5.22, where the effects of chamber aspect ratio can be identified. As pointed out earlier, when the dimensions of the air core were examined there is a sudden increase in the radius of the air core between vortex chambers with aspect ratios $\frac{L}{D} = 1.0 - 1.2$. It is not immediately apparent but this can be seen visually in the core region of the fig 5.22, despite the varying magnifications of the images. What is more apparent however, is the transition in the mantle structure between the vortex chambers with aspect ratios of $\frac{L}{D} = 1.0 - 1.2$, where it is clear that further internal mantles are being formed in addition to the single outer mantle that spans the length of the chamber. These first appearing in the $\frac{L}{D} = 1.0$ chamber as two localised regions of flow reversal which then merge as the chamber aspect ratio is reduced even further. Despite this transition not being clear in the mantles produced by the PIV data, the vector maps do display a departure from the bidirectional flow commonly associated with vortex chambers with larger aspect ratios. The PIV data for the $\frac{L}{D} = 0.4$ case indicates multiple flow reversals in the upper region of the chamber, where if it was possible to acquire results could provide evidence of multiple mantles. The PIV data is subjective, due to the errors in the method mentioned previously and it must be noted that both the CFD and PIV data sets do agree that by reducing the aspect ratio of the chamber there is a definite effect upon the resultant mantle structure. However, the complimentary inner mantles that are indicated in the CFD data do not span the length of the chamber as predicted by the analytical theory. A possible explanation for this could be due to the proximity of the tangential inlets near the base of the chamber preventing the mantles from attaching to the base chamber boundary. Whether this is due to localised flow effects from the increased momentum of the inlet jets as they enter the chamber or from the effects of chamber geometry is unknown. There is a definite case for further investigation into the effects of vortex chamber aspect ratio on mantle structure, to not only confirm these findings, but to also assess the impact of the geometry and axial position of the tangential inlets.

(a) $\frac{L}{D} = 0.4$.

(b) $\frac{L}{D} = 0.6$.

(c) $\frac{L}{D} = 0.8$.

(d) $\frac{L}{D} = 1.0$.

(e) $\frac{L}{D} = 1.2$.

(f) $\frac{L}{D} = 1.4$.
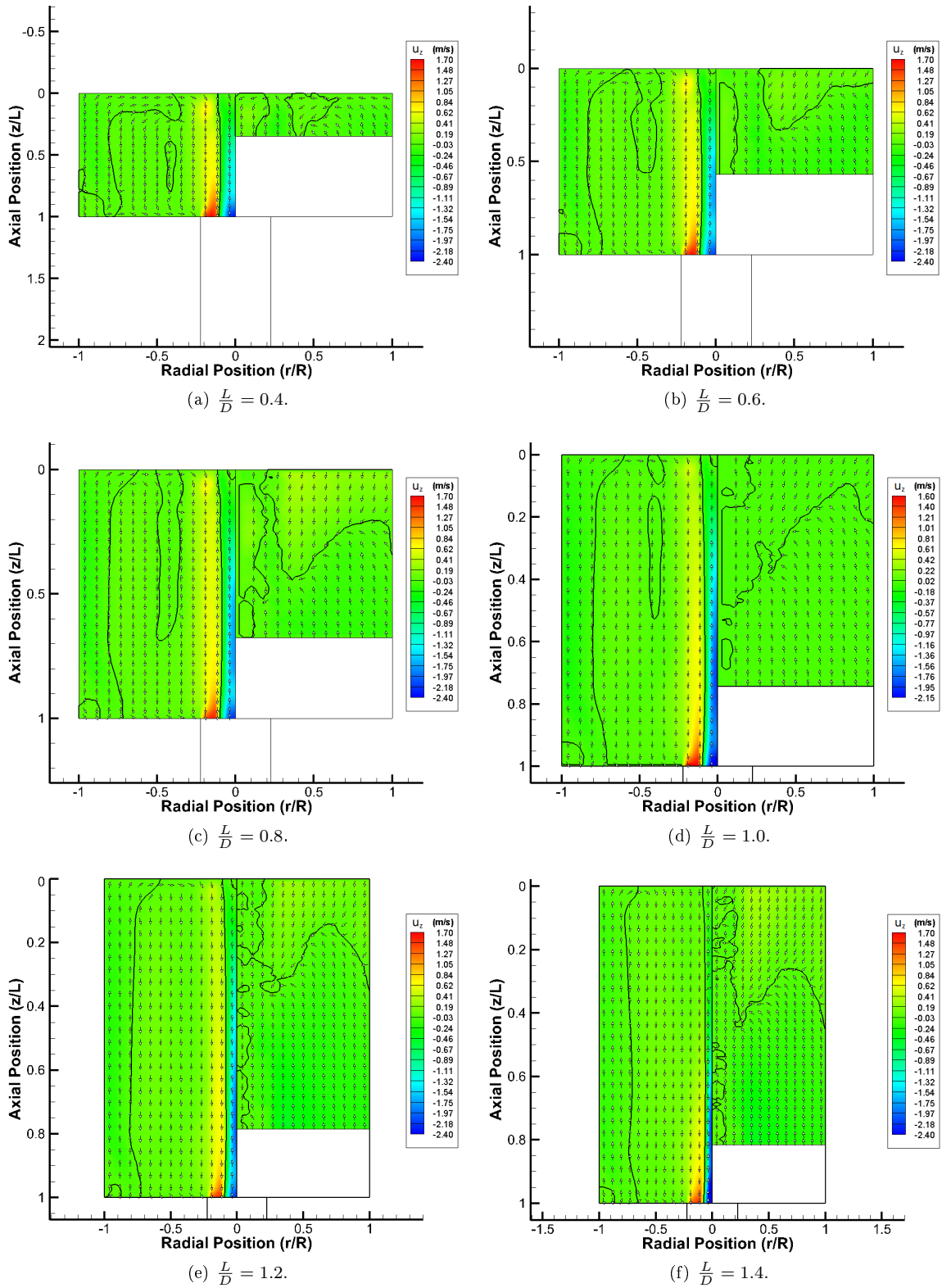
Figure 5.22: Axial velocity contour plots for vortex chambers with base injection.
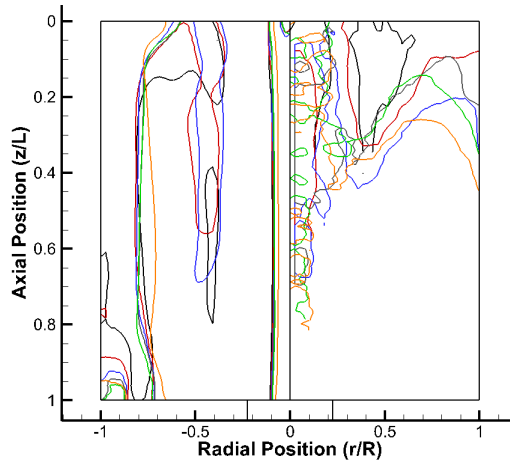
Figure 5.23: Axial plot of combined mantles for chambers with base injection.

In fig 5.23 axial dimensions of the mantle structures for all the various chamber aspect ratios have been altered so they all appear to have and aspect ratio of $\frac{L}{D} = 1.0$. This allows for direct comparison of the mantle structures to better assess the effects of chamber aspect ratio. Direct observations cannot be made for the mantles from the PIV data, as they display less consistency in their structure relative to those seen in the inlet Reynolds number study, where minimal variation in the mantle structures of the PIV data were reflected by those obtained from the CFD data. Considering this, it can be assumed that a similar relationship is true for mantle structures presented here, where the lack of any clear similarity in the mantle structures from the PIV data is a reflection of the evolving mantle structures seen in the CFD data.

A cross section of the mantle structures for the various chamber aspect ratios can be seen in fig 5.24. Again it is clear that as the aspect ratio transitions from $\frac{L}{D} = 1.0 - 1.2$ that there is also a transition in the mantle structure, as further inner loci of zero axial velocity develop, but all of the structures seen in fig 5.23 display periodic symmetry, similar to that seen for the inlet Reynolds number study. The vortex chambers with aspect ratios $\frac{L}{D} = 0.8 - 1.4$ exhibit mantle structures reminiscent of mode shapes, where the amplitude of the higher order non cylindrical mode is greater as the aspect ratio is decreased. This possibly infers that the axial dimension of the chamber is directly linked to the influence of higher order mode structures, as opposed to the lower order cylindrical modes that have been shown to be the result of the cross sectional geometry. It is also worth noting that the chamber configurations with aspect ratios $\frac{L}{D} = 1.2 - 1.4$ display a single mantle, which agrees well with the radial position predicted by the analytical theory and suggests that the analytical theory is suitable for predicting flow reversal patterns when the mantle structure is relatively simple.

(a) $\frac{L}{D} = 0.4$.

(b) $\frac{L}{D} = 0.6$.

(c) $\frac{L}{D} = 0.8$.

(d) $\frac{L}{D} = 1.0$.

(e) $\frac{L}{D} = 1.2$.

(f) $\frac{L}{D} = 1.4$.

Figure 5.24: Axial plot of combined mantles for chambers with base injection.

5.4.2 Head injection

Table 5.4 contain the most important figures relating to the vortex chamber configurations with tangential inlets at the head of the chamber for chamber aspect ratios $\frac{L}{D} = 0.4 - 1.4$. Unlike the data obtained for the chamber configurations with tangential inlets at the base of the chamber, there are less obvious trends in this dataset with regards to the CFD results. The first thing to note is that the inlet velocity and Reynolds number appear to be relatively unaffected by variation in the vortex chambers aspect ratio. Despite being unlike the data seen previously in table 5.4, the range of the values is greater and can be attributed to the $\frac{L}{D} = 0.4$ case which stands out as an anomalous value. This anomaly however, is the result of empirical findings, as it was the inlet flow rates from the PIV experiments which were used to calibrate the CFD calculations.

As expected when the vortex Reynolds number is referred to, the variation of the inlet velocity has little impact due to the relatively small range of the values and the si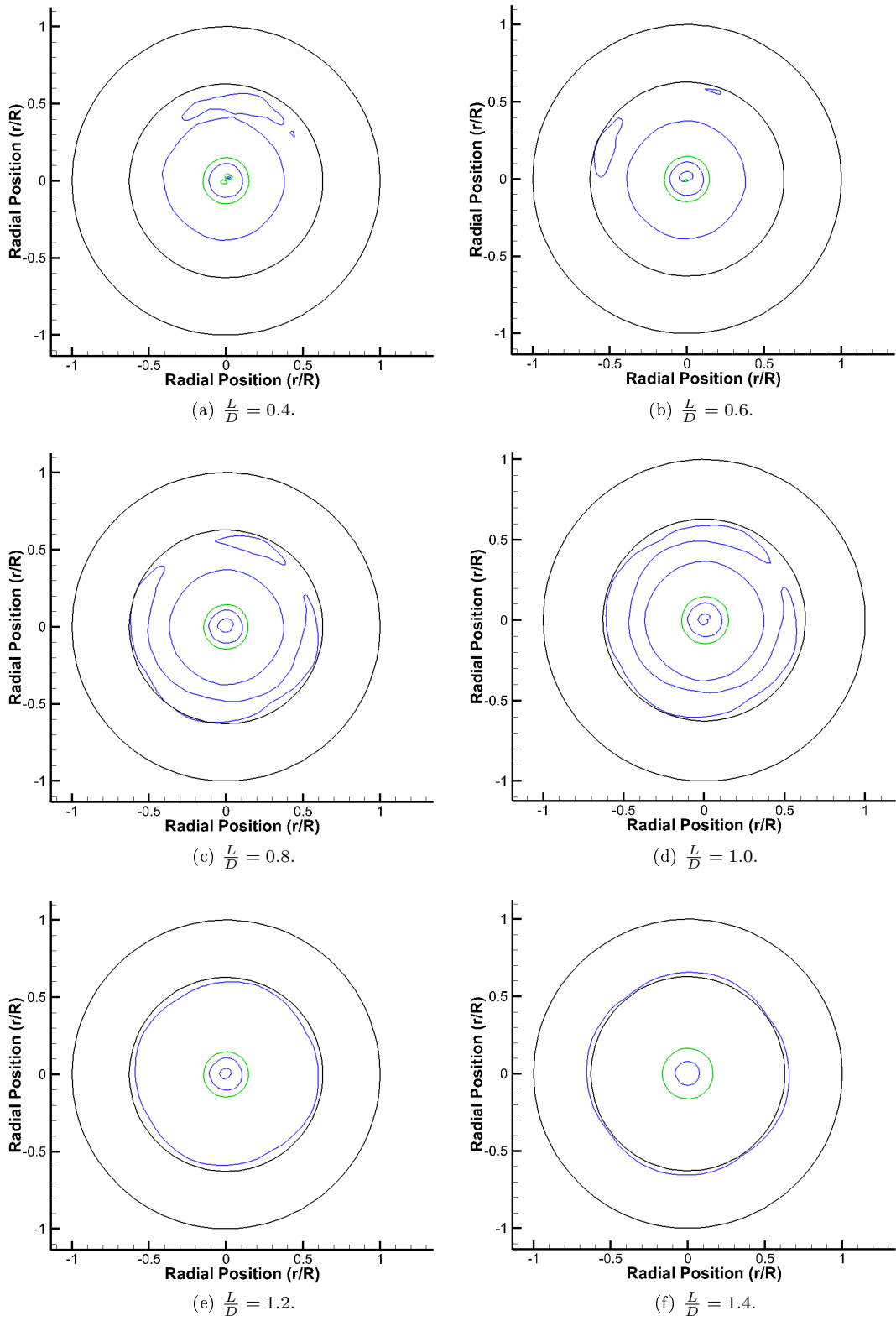gnificant effect of the chambers aspect ratio upon this non dimensional group. The vortex Reynolds number increases as the chamber aspect ratio is reduced, signifying the possible existence of a stronger vortex within vortex chambers with low aspect ratios. The magnitude of the inlet pressure however, appears to increase as the aspect ratio decreases, while the value for the $\frac{L}{D} = 0.4$ chamber configuration stands out as an anomalous value. This highlights, that although the chamber aspect ratio is an important variable with regards to determining chamber pressure the same is also true of the inlet velocity, as the reduced chamber pressure can be directly attributed to the relatively low inlet velocity of the $\frac{L}{D} = 0.4$ chamber configuration. The inlet pressure does not increase linearly as it does for the chamber configurations with base injectors, and displays a sudden twofold increase in magnitude between chambers with aspect ratios of $\frac{L}{D} = 0.8 - 1.0$. This sudden increase is also interestingly seen in the normalised radius of the air core and occurs between the same two chamber configurations. The sharp increase in the radius of the air core is seen in the previous data when a certain threshold value of the chambers aspect ratio was reached. However, this sudden increase in the radius air core is not reflected in the radial pressure distribution like it is here and is even more evident when comparing the radial pressure distributions displayed in fig 5.25d and 5.25e, to those seen earlier for the chamber configurations with base tangential inlets. The radius of the air core may exhibit a sudden increase in magnitude, but the same cannot be said of the radius of the forced vortex which displays little invariability with respect to the chamber aspect ratio, apart from the $\frac{L}{D} = 1.2$ case which appears to be an anomalous value. Again the frequency of the PVC appears to increase as the chamber aspect ratio decreases, as a result of the similar dimensions of the SBR region and the increasing tangential velocities induced.

Despite the low inlet velocity of the $\frac{L}{D} = 0.4$ case, it still produces a relatively high tangential velocity and when normalised by the inlet velocity results in the maximum peak tangential velocity ratio for the range of aspect ratios investigated. This is unlike the results for the chamber configurations with base inlets, where the normalised peak tangential velocity does not scale linearly with the aspect ratio. Rather it does not scale linearly for the entire range of chamber aspect ratios, but exhibits two regions of linearity with similar gradients. This transition occurs between $\frac{L}{D} = 0.8 - 1.0$, where there is a sudden increase in the magnitude of the peak tangential velocity as the chamber aspect ratio is reduced. The angular velocity data for the forced vortex appears sporadic due to the relatively low tangential velocity of the $\frac{L}{D} = 0.4$ case and the anomalous forced vortex radius from the $\frac{L}{D} = 1.2$ case. However, if these values are put aside, it shows that as with the peak tangential velocity, the angular velocity of the forced vortex nearly doubles in magnitude between the transition of chamber aspect ratios $\frac{L}{D} = 0.8 - 1.0$. The boundary layer at the periphery of the chamber does not appear to vary relative to the chambers aspect ratio, but there should be variation in this dimension due to the range of local velocities experienced at this location across the dataset, which is not observed due to the radial resolution of the data.

(a)

Variable		0.4	0.6	0.8	1.0	1.2	1.4
Precessing Vortex Core Frequency (CFD)	f_{Pvc} (Hz)	128.40	121.94	114.79	100.67	153.52	54.40
Liquid Dimension of Forced Vortex (CFD)	$r_{SBR}-r_{core}$	0.073	0.070	0.068	0.108	0.046	0.110
Normalised Forced Vortex Radius (CFD)	r_{SBR}	0.154	0.151	0.149	0.159	0.097	0.161
Normalised Air Core Radius (CFD)	r_{core}	0.081	0.081	0.081	0.051	0.051	0.051
Strouhal Number (CFD)	Sh	11.25	8.89	7.99	7.77	10.60	3.86
Vortex Reynolds Number	V	5.71E+03	4.57E+03	3.59E+03	2.59E+03	2.42E+03	2.02E+03
Inlet Reynolds Number	Re	3.45E+04	4.15E+04	4.35E+04	3.92E+04	4.39E+04	4.27E+04
Inlet Pressure (CFD)	p_{in} (Kpa)	10.20	13.54	13.29	6.70	6.82	6.03
Inlet Velocity	u_{in} (m/s)	0.89	1.07	1.12	1.01	1.13	1.10
Aspect Ratio	L/D	0.4	0.6	0.8	1.0	1.2	1.4

(b)

Variable		0.4	0.6	0.8	1.0	1.2	1.4
Minimum Axial Velocity (PIV)	u_z (m/s)	-0.13	-0.04	-0.15	-0.16	-0.33	-0.37
Maximum Axial Velocity (PIV)	u_z (m/s)	0.58	0.23	0.25	0.18	0.26	0.34
Minimum Axial Velocity (CFD)	u_z (m/s)	-1.50	-1.89	-2.05	-2.22	-3.09	-2.71
Maximum Axial Velocity (CFD)	u_z (m/s)	1.12	1.36	1.43	1.30	1.59	1.40
CFD Normalised Boundary layer height at chamber wall	δ_w	0.02	0.02	0.02	0.02	0.02	0.02
CFD Free Vortex Inverse Gradient ($\partial r/\partial u_\phi$)	$\partial r/\partial u_\phi$	78.58	87.89	82.96	83.26	99.39	107.31
CFD Forced Vortex Angular Velocity ($\partial u_\phi/\partial r$)	ω (rad/s)	593.31	697.84	699.00	373.62	556.37	322.94
Peak Tangential Velocity Ratio (CFD)	u_ϕ/u_{in}	4.00	3.84	3.63	2.29	1.86	1.84
Peak Tangential Velocity (CFD)	u_ϕ (m/s)	3.56	4.11	4.06	2.32	2.10	2.03
Aspect Ratio	L/D	0.4	0.6	0.8	1.0	1.2	1.4

Table 5.4: Flow variables for chambers with head injection.

Either way, this is not currently a variable that poses any significant interest with regards to manipulating the embedded mantle structure. Again there is an obvious discrepancy between the magnitude of the maximum and minimum axial velocities retrieved from the CFD and PIV data. This is due to the methods involved in obtaining these values, and there are no appreciable trends in the data or discernible conclusions that can be drawn from these figures.

Fig 5.25 displays the radial distributions of tangential velocity, radial velocity, axial vorticity and the actual and normalised radial pressure distributions for chamber configurations with tangential inlet at the head of the chamber. The sudden increase in tangential velocity between chambers with aspect ratios $\frac{L}{D} = 0.8 - 1.0$ has already been mentioned for the plot in fig 5.25a and highlights some of the other variations for this velocity component. This includes the reduced velocity gradient of the forced vortex for cases $\frac{L}{D} = 1.0 - 1.4$, which display a more linear increase towards the region of turbulent diffusion at the peak of the tangential velocity profile. This region of turbulent energy diffusion also has a lesser gradient than the chambers with aspect ratios $\frac{L}{D} = 0.4 - 0.8$, but whilst appearing broader it occupies the same radial proportion of the chamber. This is to be

(a) Tangential velocity profile (CFD).

(b) Radial velocity profile (CFD).

(c) Axial vorticity profile (CFD).

(d) Static pressure profile (CFD).
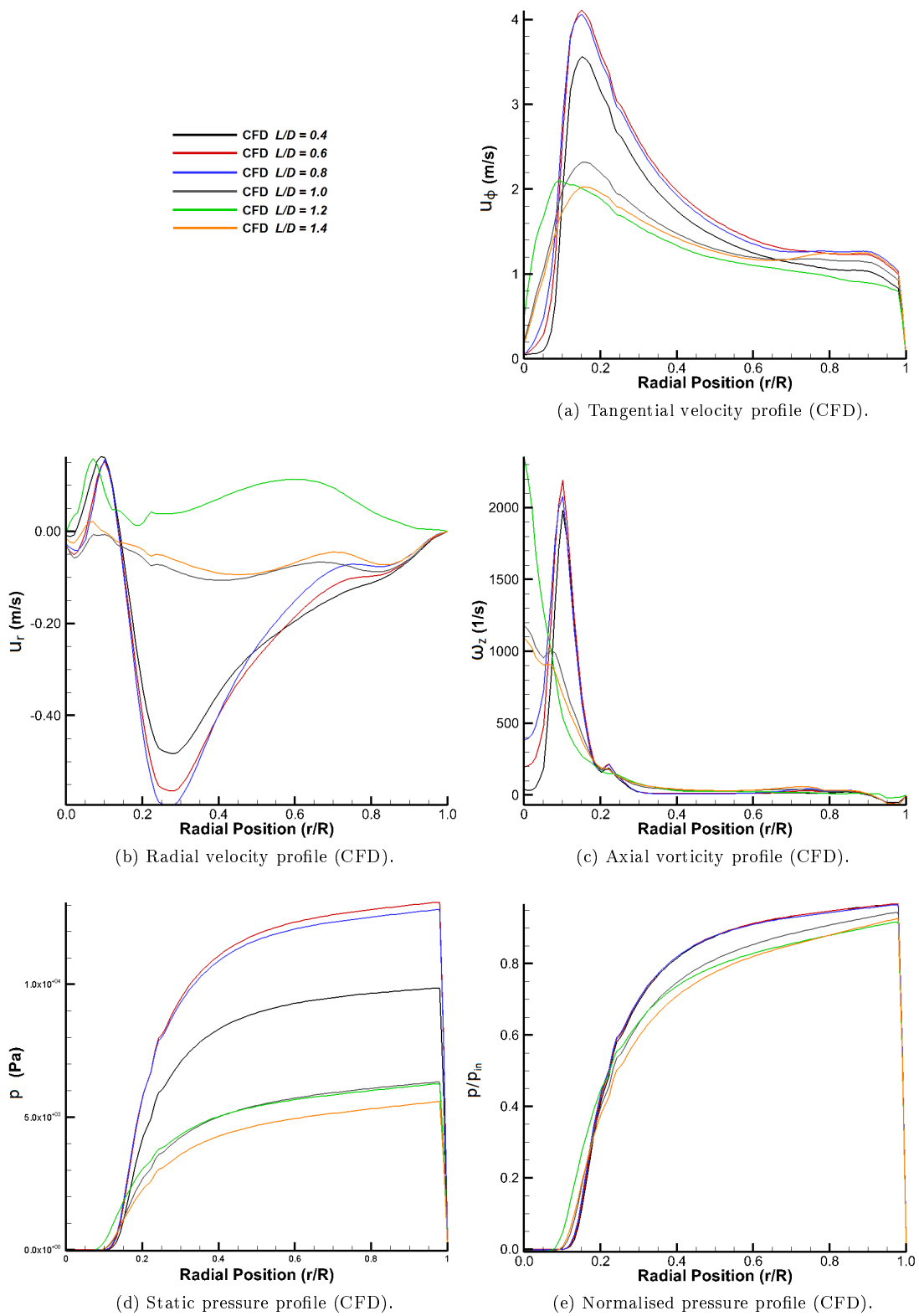
(e) Normalised pressure profile (CFD).

Figure 5.25: Tangential profiles for vortex chambers with head injection.

expected, as the gradient of the free vortex is also less due to the reduced peak tangential velocities, although the velocity profiles for the $\frac{L}{D} = 1.0 - 1.4$ cases display less conformity than those for the $\frac{L}{D} = 0.4 - 0.8$ chamber geometries. This is also reflected in the radial velocity profiles seen in fig 5.25b, where the chamber configurations with lower aspect ratios are more representative of the radial velocity profiles seen for other chamber geometries with head injectors. This proposes the question of exactly how reliable are the results, considering the bulk of the results in this part of the study are generated by CFD and adhere to stringent convergence guidelines., it is hard to gauge whether apparently anomalous data is the result of insufficiently accurate data or due to complex underlying mechanisms in the flow.

While CFD analysis of intense swirling flows is notoriously difficult, the same is also true of swirling flows in general due to their inherently complex nature. Despite this, the radial velocity profiles certainly indicate a transition in the flow properties between chamber aspect ratios of $\frac{L}{D} = 0.8 - 1.0$, and all display negative inward radial flow at the head of the chamber. All apart from the $\frac{L}{D} = 1.2$ chamber configuration, which has repeatedly provided spurious data and shall be ignored with regards to comparing the effects of chamber aspect ratio upon flow properties. The radial distribution of axial vorticity seen in fig 5.25c is another clear example of how the flow properties suddenly change when the chamber aspect ratio falls below $\frac{L}{D} = 1.0$. None of the results appear to have zero axial vorticity at the radial position of the SBR transition for the results from chamber aspect ratios of $\frac{L}{D} = 0.4 - 0.8$, despite this behaviour being seen in previous datasets. The maximum axial vorticity occurs within the phase interface region and in close proximity to the innermost radial position where the volume fraction of the liquid phase is $v_f = 1$. The same however cannot be said of the higher aspect ratio chamber configurations, where the axial vorticity increases towards the centre line of the chamber, which could also provide a possible indicator to why the air core dimensions for these chamber configurations is different. The actual radial pressure distribution seen in fig 5.25d is one of the most pertinent examples of the significant difference in flow properties that occur in a vortex chamber with an aspect ratio below $\frac{L}{D} = 1.0$. As it shows a clear increase in chamber pressure relative to both inlet velocity and chamber aspect ratio, with greater radial pressure gradients in the fluid region of the forced vortex also observed. When normalised by the inlet pressure it is still clear that there is a definite divide in the data, this being the direct result of chamber aspect ratio, where the chambers with aspect ratios $\frac{L}{D} = 1.0 - 1.4$ again display non uniformity as opposed to the other chamber configurations.

The data so far has repeatedly indicated that a transition in the properties of the flow occurs between chambers with aspect ratios $\frac{L}{D} = 0.8 - 1.0$. This is well described by the mantle structures obtained from the axial velocity contour plots displayed in fig 5.26, where it is clear that a sudden change in the mantle structure occurs between these two chamber configurations. Additionally the mantle structures either side of this transition point take similar forms, that also may be linked to be behaviour seen in the results so far where the data appears to be separated into two distinct groups. For chamber configurations with aspect ratios $\frac{L}{D} = 1.0 - 1.4$ the mantle structure is similar to that observed earlier in fig 5.14 and exhibits a complex periodic structure that spans the length of the chamber. However, the mantles that appear in fig 5.26 appear to have different structures due to the periodic form of the full 3D mantle and form of the 2D mantle form varies relative to the azimuth angles of the meridional plane. When the mantles are overlaid on top of each other as seen in fig 5.27b, it is clear that the mantle structures are similar in form despite any variation in azimuth angle relative to the other forms.

This angular shift in the mantle structure raises questions about the influence of chamber geometry upon the azimuthal angle of the mantle structure, as the mantle structures obtained from the inlet Reynolds number study were all observed at identical azimuth angles and the geometry was constant throughout. This yet again provides an argument for the fact that it is the chamber geometry which is the crucial factor in manipulating the mantle structure. Apart from this, the axial orientation of the vectors maps for the chambers with aspect ratios $\frac{L}{D} = 1.0 - 1.4$ do show that in regions where the mantles can be considered to be two independent structures that there is triple vortex flow. In these cases the flow propagates away from the tangential inlets located at the head of the chamber before turning back towards the head and then finally being directed towards the outlet, as the flow is contained within the vortex core. This triple vortex flow is also observed
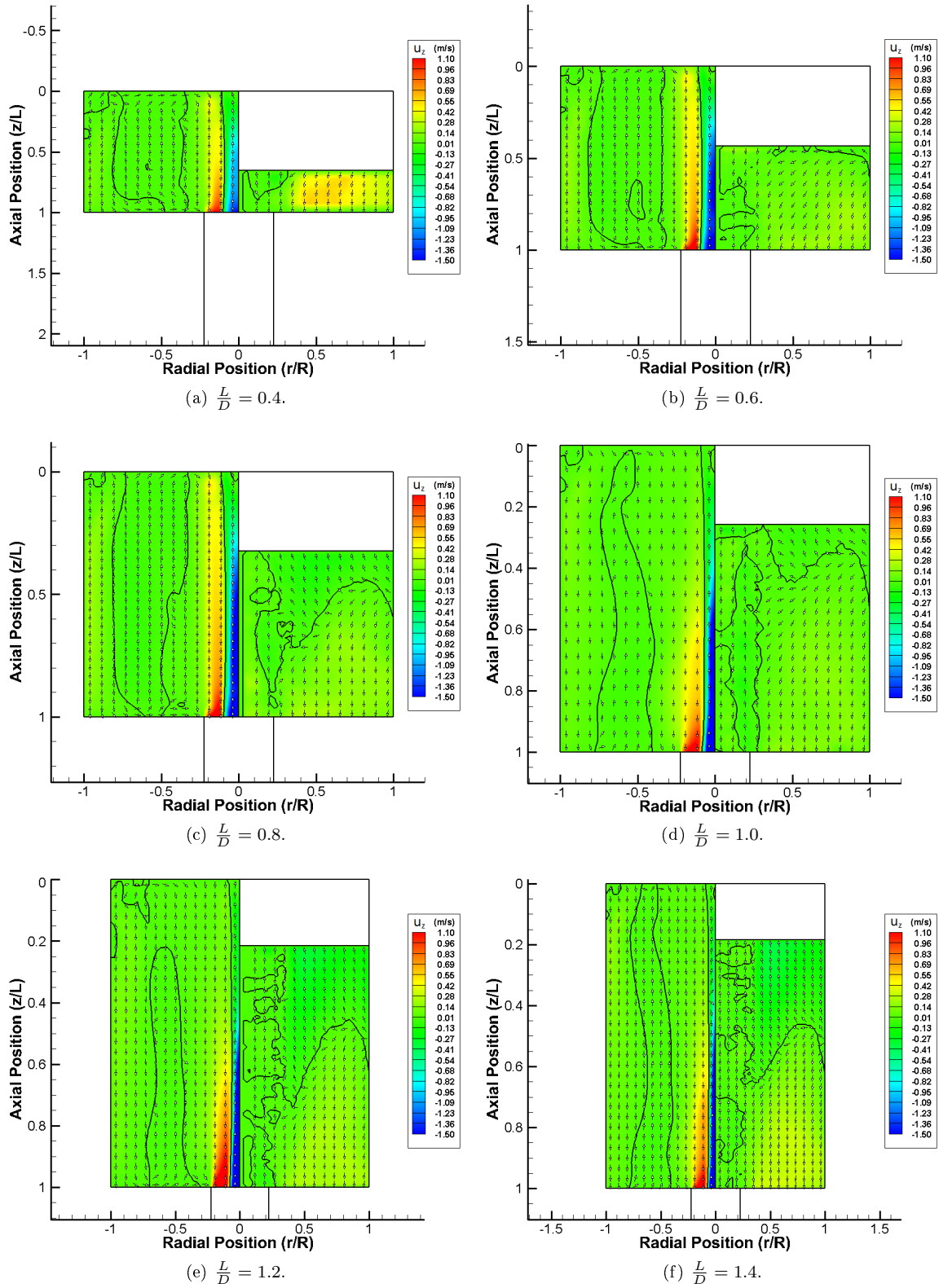
(a) $\frac{L}{D} = 0.4$.

(b) $\frac{L}{D} = 0.6$.

(c) $\frac{L}{D} = 0.8$.

(d) $\frac{L}{D} = 1.0$.

(e) $\frac{L}{D} = 1.2$.

(f) $\frac{L}{D} = 1.4$.

Figure 5.26: Axial velocity contour plots for vortex chambers with head injection.

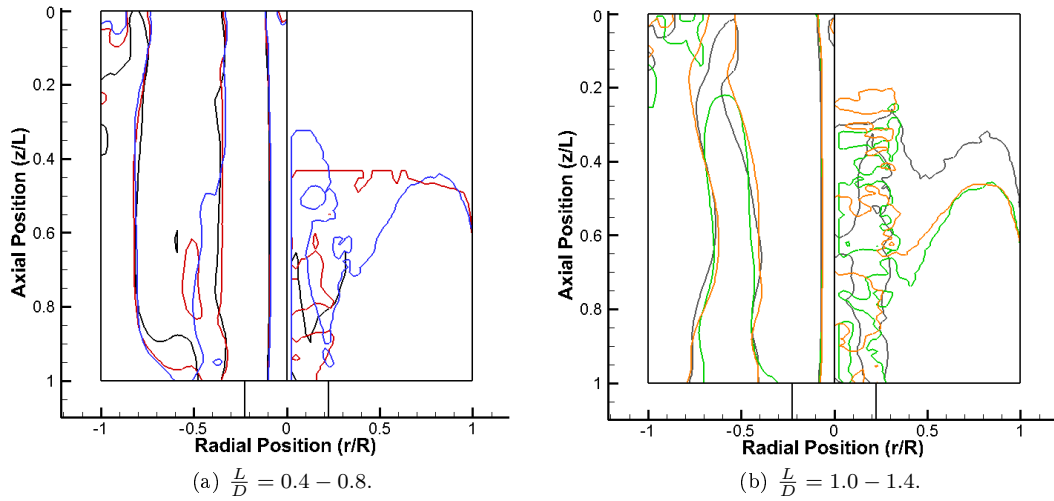(a) $\frac{L}{D} = 0.4 - 0.8$. (b) $\frac{L}{D} = 1.0 - 1.4$.

Figure 5.27: Axial plot of combined mantles for chambers with head injection.

in the chamber configuration with aspect ratios $\frac{L}{D} = 0.4 - 0.8$, despite the obvious variation in the structure of the mantle, although be it with the flow reversals occurring at different positions within the chambers. The mantle structures for these chamber configurations have been overlaid in fig 5.27a to allow for easier comparison of their respective structures, which also show that despite the variation in the length of the chamber they compare well. The mantle structures seen in the chambers with aspect ratios $\frac{L}{D} = 0.4 - 0.8$ do display similarities and the structures are effectively unchanged in the upper half of the chamber as the aspect ratio is reduced. However, the mantle structure in the bottom half of the chamber and especially in the region near to the base boundary condition exhibit the greatest variation with respect to the chambers aspect ratio. It is assumed that the increasing radial gradients associated with reducing the length of the chamber are resulting in the increasing curvature of the outermost mantle, causing it to intersect the base at a smaller radial position than expected. This prevents what could possibly result in two mantles that span the length of the chamber parallel to the axis that would replicate the ideal conditions which correspond to the predictions of the analytical theory. In order to achieve a more idealised mantle form, the effects of the increased radial gradients near the base of the chamber would need to be negated somehow. This would probably be most likely through manipulation of the flow properties via chamber geometry, although this would require a full understanding of the influence of geometrical parameters and require this to be integrated into the design of the chamber.

Both the mantle structures and the boundaries of the SBR region for the various chamber configurations are seen in fig 5.28. As mentioned previously, the transition in flow properties has been observed to occur between the chamber configurations with aspect ratios $\frac{L}{D} = 0.8 - 1.0$, but this is not so apparent for the plots seen here. As the mantle structures seen in the axial contour plots of fig 5.26 show the mantles to be primarily one of two forms, unlike what is seen here where there is less obvious distinction between the chambers with aspect ratios of $\frac{L}{D} = 0.4 - 0.8$ and $\frac{L}{D} = 1.0 - 1.4$ respectively. This can partly be attributed to the erroneous data obtained from the $\frac{L}{D} = 1.2$ case, as it is clearly of insufficient quality relative to the other results despite the fact it still exhibits periodic symmetry. If this particular example is ignored then it can be seen that as the aspect ratio is reduced from $\frac{L}{D} = 1.4$ to $\frac{L}{D} = 1.0$ there is a definite change in the mantle structure. This is reminiscent of what has been shown previously in fig 5.6 for the inlet Reynolds number study where the chamber configuration had tangential inlets located at the head of the chamber. More specifically the mantles seen here are similar to those seen in **fig 5.17f** for chamber configurations with aspect ratios $\frac{L}{D} = 1.4$ and $\frac{L}{D} = 1.0$, at axial positions at the head and midpoint of the chamber. These are examples of when the higher order non cylindrical mode displays has a greater amplitude, resulting in a more definitive periodic mantle structure. The same is true here and would suggest that as the chamber aspect ratio is reduced the influence of the higher order modes present in the chamber

(a) $\frac{L}{D} = 0.4$.

(b) $\frac{L}{D} = 0.6$.

(c) $\frac{L}{D} = 0.8$.

(d) $\frac{L}{D} = 1.0$.

(e) $\frac{L}{D} = 1.2$.
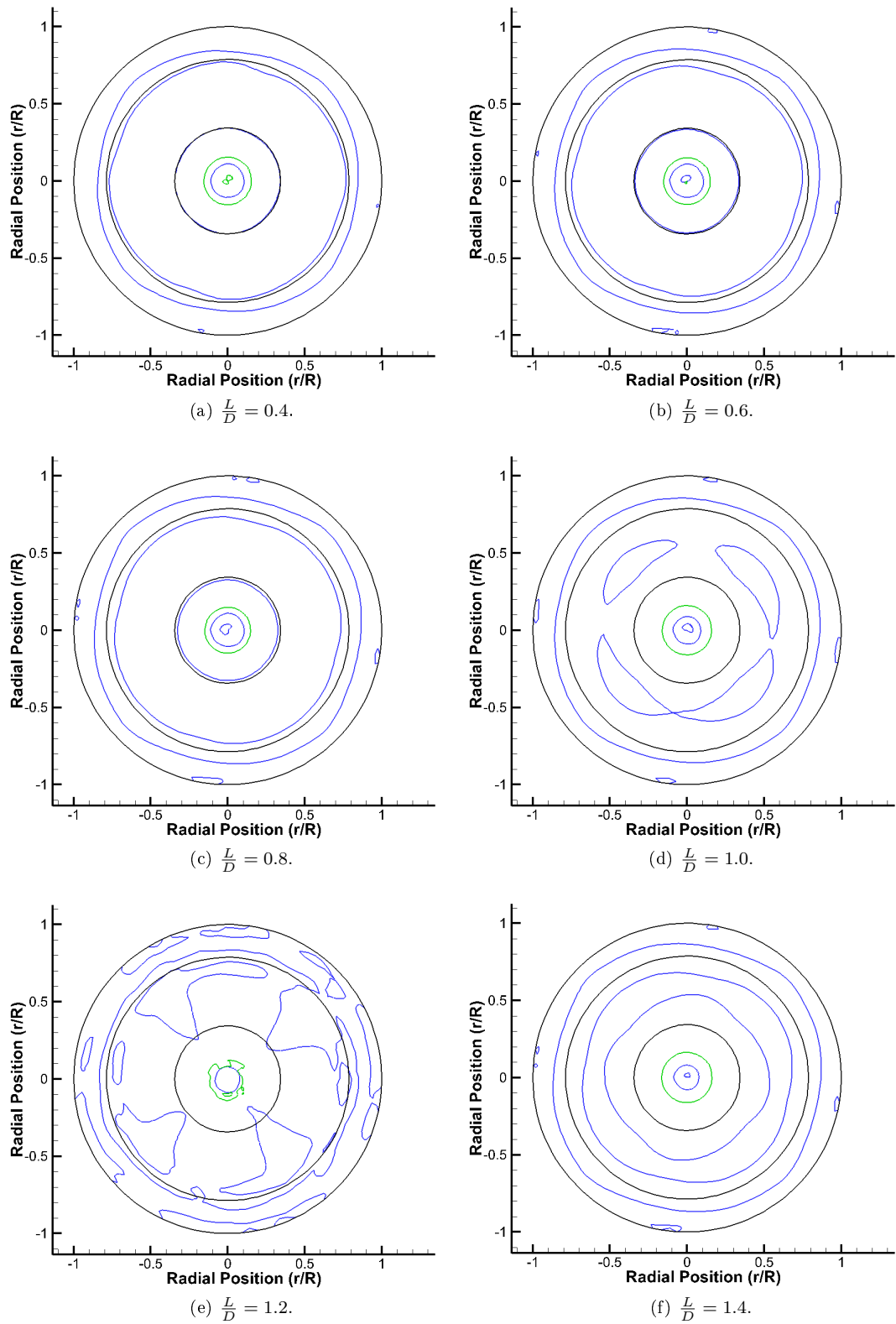
(f) $\frac{L}{D} = 1.4$.

Figure 5.28: Azimuthal plot of CFD mantle and SBR structure for chambers with head injection.

become more dominant. The mantle structure seen in fig 5.28d for the $\frac{L}{D} = 1.0$ case represents the chamber configuration which results in the greatest amount of periodicity for the $(4, 2)$ mode, but then as the chamber aspect ratio is reduced to $\frac{L}{D} = 0.8$ this effect decreases significantly. This suggests that the contribution of the $(4, 2)$ mode reaches its peak amplitude in the range $\frac{L}{D} = 0.8 - 1.0$ before mantle structure morphology changes as the influence of this mode is reduced. As the mantle structures seen in chambers with aspect ratios $\frac{L}{D} = 0.4 - 0.8$ are of a different form to that seen for $\frac{L}{D} = 1.4$ where the influence of the $(4, 2)$ mode is decreased. Then it could be assumed that because they are also periodic in form and are subject to the influence of a different non cylindrical mode, which means that the variation in aspect ratio of the vortex chamber could be responsible for causing different inertial modes to occur. The change in the axial dimension of the chamber limits the possible discrete spectra of frequencies that can occur in the chamber and therefore also the possible range of inertial modes and resultant mantle structures.

5.5 Effect of contraction ratio

5.5.1 Base injection

Table **5.5** contains an array of flow related information for the set of chamber configurations where the radius of the outlet section is varied to alter the contraction ratio of the chamber, where the tangential inlets are located at the base of the chamber. A non uniform range of contraction ratios were chosen for this investigation due to the need for a sufficient decrease in outlet radial dimension as the contraction ratio was increased. Therefore smaller increments in the contraction ratio were applied at lower values where a small variation in the contraction ratio results in a much larger variation in the outlet radius, relative to the same variation in contraction ratio at higher values. As with the study of chamber aspect ratio, it was decided that the range of contraction ratios should extend to values that are representative of contraction ratios seen in similar vortex devices such as hydrocyclones, which normally have low contraction ratios. It was also decided to also encompass other vortex driven devices of interest such as the VIHRE combustion chamber which employs a contraction ratio of $CR = 20$ [10]. Additionally it was decided to investigate what happens at more extreme chamber contraction ratios such as $CR = 100$, where it is expected that the confined vortical flow is likely to exhibit complex behaviour.

As a result of using a large range of contraction ratios, it was difficult to obtain adequately converged CFD solutions above values of $CR = 40$ due to the chamber contraction ratio been the dominant variable in controlling the radius of the PVC and the induced air core, which adversely affects convergence at reduced radii. At higher contraction ratios this results in large numerical gradients within the core region of the flow, which prevents solution convergence when the necessary combination of physical models were employed. This posed a problem with regards to the CFD, although it was still possible to obtain PIV results for the whole range of contraction ratios. The values for inlet velocity clearly show that as the contraction ratio is increased the inlet velocity steadily decreases, while the inlet pressure increases, although no measured pressure data is available for the experimental data. The inlet velocities were taken directly from the experimental rig, and the reduced flow rate that occurs at higher contraction ratios does suggest that this is a result of reduced pressure drop at the injectors, which must be due to increased chamber pressure. This stands to reason as the flow is incompressible and is subject to vortex choking at the outlet, so the reduction in effective cross sectional area of the outlet is limiting the flow rate through the chamber for the assumed total pressure provided by the pump. The inlet Reynolds number obviously increases as the contraction ratio is reduced, but this also applies to the vortex Reynolds number as well.

The vortex Reynolds number suggests that increasingly intense vortices occur in chambers with lower contraction ratios, but this is primarily caused by the magnitude of the inlet velocity and indicates a possible flaw in the formulation of the vortex Reynolds number as the opposite is observed experimentally. This stems from the formulation of the vortex Reynolds number which does include the geometrical swirl number, but is cancelled out by other terms so the effect of the outlet radius is not accounted for. The formulation of the geometric swirl number indicates that chambers with a smaller contraction ratios will result in higher swirl numbers, that are representative of intense swirling flows with greater tangential velocity contributions. From a design standpoint these non dimensional groups are useful in determining the possible behaviour of vortical flow, but are predominantly formulated from variables relating to chamber geometry and can not account for the actual properties of the flow. These non dimensional groups are also intended to be used with specific vortex chamber configurations, as they are borne out of the necessity to provide a means of comparison when other variables that need to be obtained experimentally are not available. Regarding their applicability to chambers with varying contraction ratios, a more suitable alternative would be to use the original form of the swirl number as seen in eqn 5.5. This is effectively a ratio of the tangential and axial component of the flow and is commonly measured when possible in experiments at the chamber exit. The variables used to calculate the Strouhal number used in this investigation, and as seen previously in eqn **5.1** does not incorporate variables pertaining to the outlet either. However, this Strouhal number increases when the rotational frequency of the PVC increases, in addition to an increase in the chamber radius. This is more effective in representing the original formulation of the swirl number, which is defined as the ratio of the tangential and axial components of the flow. The tangential velocity component and PVC frequency are directly linked by the angular velocity of the forced vortex, therefore a large PVC frequency is generally associated with a tangential velocity component of greater magnitude and indicative of an intense vortex.

$$S = \frac{G_\phi}{G_x r_t} \hspace{4cm} (5.5)$$

If the data in table 5.5a is referred to, then it is clear that both the CFD and PIV data display a significant increase in the angular velocity of the forced vortex as the contraction ratio is increased. This is also reflected by the increase in both the peak tangential velocity and the frequency of the PVC for both sets of data. This is also seen in the normalised peak tangential velocity data, which is seen in the bulk of the data presented thus far and indicates that the flow is almost independent of inlet flow conditions, but rather is reliant on chamber geometry. No discernible trend has yet to be been seen in any of the values for maximum and minimum axial velocity within the chamber, but the CFD data for this part of the study shows that the magnitude of the axial velocity component increases relative to an increase in the chamber contraction ratio. It is difficult to distinguish due to the relatively small range of values, but the PIV results appear to suggest that the maximum axial velocity increases similarly to the CFD results, although the opposite is true for the minimum axial velocity.

Although the Strouhal number data seen in table 5.5a does not consider the outlet dimensions of the chamber, it does clearly show that as the contraction ratio increases so does the Strouhal number. This infers that the PVC is exhibiting a greater amount of oscillatory behaviour in chambers with larger contraction ratios due to the increased rotational frequency, which also signifies the presence of an increasingly intense vortex as the angular velocity increases. Non dimensional groups are a useful tool for characterising various types of flow but care must be given to assess what are the important variables that need to be compared. Consideration must be given to deciding whether the specific formulation of a non dimensional group is applicable to the type of flow being investigated and the variables that define it. In specific reference to vortex chambers with various contraction ratios, consideration must be given to the chamber dimensions that form the parametric variable of interest, these being the radii of the vortex chamber and the outlet.

As expected from experimental observations, the normalised radius of the air core of the confined vortex is found to decrease as the contraction ratio of the chamber is increased, which is also indicated by the experimental and numerical data. The same is also true for the radius of the forced vortex, with the exception of the chamber with a contraction ratio $CR = 80$, which display a relatively

(a)

Contraction Ratio CR	Inlet Velocity u_{in} (m/s)	Inlet Pressure (CFD) p_{in} (Kpa)	Inlet Reynolds Number Re	Vortex Reynolds Number V	Strouhal Number (CFD) Sh	Strouhal Number (PIV) Sh	Normalised Air Core Radius (CFD) r_{core}	Normalised Air Core Radius (PIV) r_{core}	Normalised Forced Vortex Radius (CFD) r_{SBR}	Normalised Forced Vortex Radius (PIV) r_{SBR}	Liquid Dimension of Forced Vortex (CFD) $r_{SBR}.r_{core}$	Liquid Dimension of Forced Vortex (PIV) $r_{SBR}.r_{core}$	Precessing Vortex Core Frequency (CFD) f_{PVC} (Hz)
5	1.19	2.81	4.62E+04	3.05E+03	0.86	1.01	0.303	0.324	0.411	0.497	0.108	0.173	13.19
10	1.18	6.07	4.57E+04	3.02E+03	2.95	2.24	0.182	0.175	0.243	0.322	0.061	0.147	44.57
20	1.16	11.31	4.51E+04	2.98E+03	7.27	3.86	0.081	0.095	0.148	0.245	0.067	0.150	108.30
40	1.09	x	4.23E+04	2.80E+03	x	5.48	x	0.046	x	0.187	x	0.141	x
60	1.03	x	4.01E+04	2.65E+03	x	5.42	x	0.032	x	0.186	x	0.154	x
80	0.96	x	3.73E+04	2.46E+03	x	7.02	x	0.022	x	0.152	x	0.130	x
100	0.91	x	3.54E+04	2.34E+03	x	7.56	x	0.012	x	0.141	x	0.129	x

(b)

Contraction Ratio CR	Peak Tangential Velocity (CFD) u_ϕ (m/s)	Peak Tangential Velocity Ratio (CFD) u_ϕ/u_{in}	Peak Tangential Velocity (PIV) u_ϕ (m/s)	Peak Tangential Velocity Ratio (PIV) u_ϕ/u_{in}	CFD Forced Vortex Angular Velocity ($\partial u_\phi/\partial r$) ω (rad/s)	PIV Forced Vortex Angular Velocity ($\partial u_\phi/\partial r$) ω (rad/s)	CFD Free Vortex Inverse Gradient ($\partial r/\partial u_\phi$)	PIV Free Vortex Inverse Gradient ($\partial r/\partial u_\phi$)	CFD Normalised Boundary layer height at chamber wall δ_w	PIV Normalised Boundary layer height at chamber wall δ_w	Maximum Axial Velocity (CFD) u_z (m/s)	Minimum Axial Velocity (CFD) u_z (m/s)	Maximum Axial Velocity (PIV) u_z (m/s)
5	1.33	1.12	1.88	1.58	82.87	96.95	78.84	123.38	0.02	0.03	0.94	-1.01	0.16
10	2.65	2.25	2.67	2.27	280.07	212.38	87.89	113.38	0.02	0.03	1.07	-1.15	0.17
20	3.91	3.37	3.46	2.98	680.45	361.34	82.86	113.66	0.02	0.03	1.62	-2.28	0.19
40	x	x	3.52	3.22	x	481.43	x	99.52	x	0.04	x	x	0.24
60	x	x	3.27	3.17	x	450.34	x	88.21	x	0.04	x	x	0.24
80	x	x	3.22	3.36	x	543.12	x	79.62	x	0.04	x	x	0.26
100	x	x	3.06	3.36	x	555.38	x	73.44	x	0.04	x	x	0.20

(a)   (b)

Table 5.5: Flow variables for chambers with base injection.

111

linear increase in radius relative to the variation in outlet radius. This linear increase in both the air core and SBR radius with respect to the outlet radius is virtually identical for both the PIV and CFD datasets and highlights the importance of the dimension of the chamber outlet in affecting the geometry of the vortex. This provides a valuable insight into predicting vortex geometry based purely on chamber geometry, which could be used to induce a vortex with prespecified characteristics based on a range of known inlet flow conditions as those used in this study. This does mean though that the actual dimension of the outlet radius should be used as the primary variable that vortex characteristics are compared to rather than the contraction ratio. It is also worth noting that in other parts of the study where the chamber contraction ratio remains constant that there is little appreciable variation in the non dimensional radii of the air core and forced vortex. Some variation is attributed to significant changes in the mantle structure and the relative increases in chamber pressure and the peak tangential velocity respectively. Variation of the chamber contraction ratio through adjustment of the outlet radius has found to have the most significant influence on the vortex structure. This may possibly be controlled by relatively simple means if it is found to have a significant impact on the mantle structure and needs to be manipulated in order to affect tertiary flow behaviour.
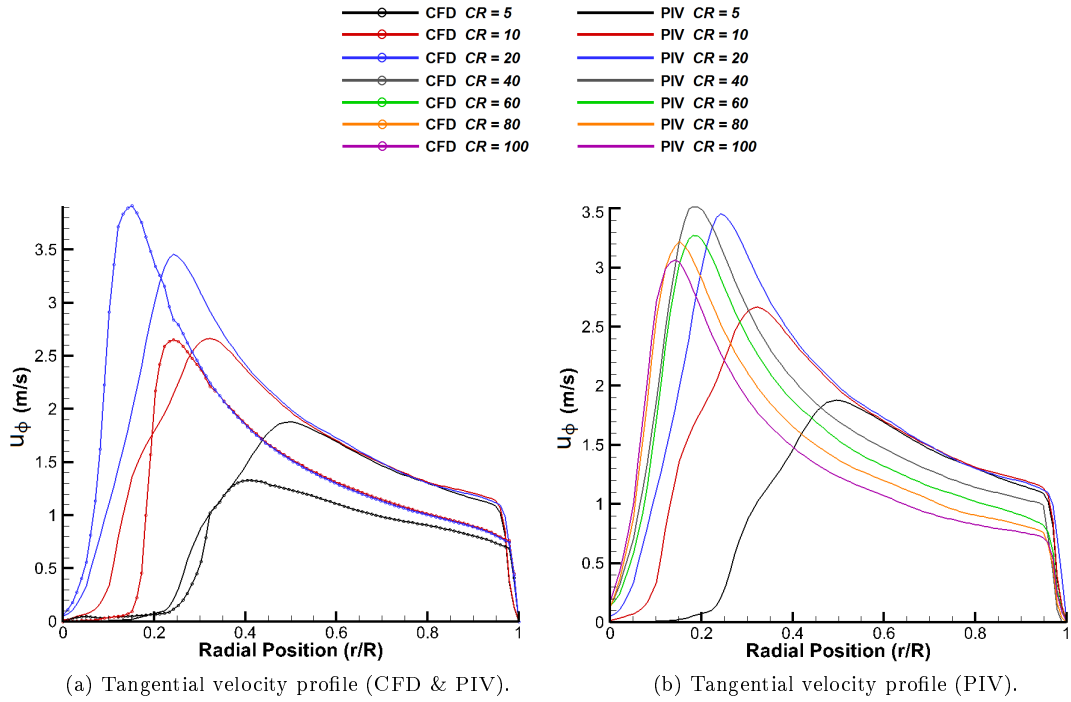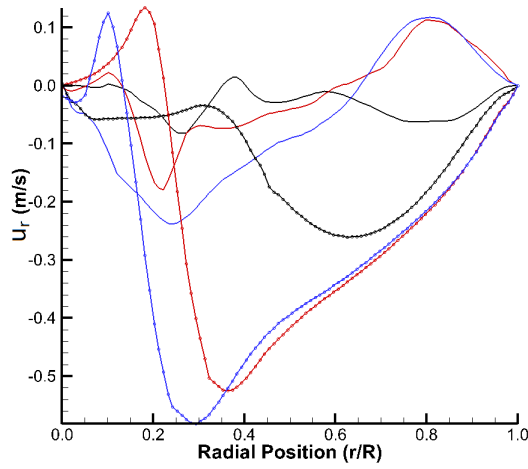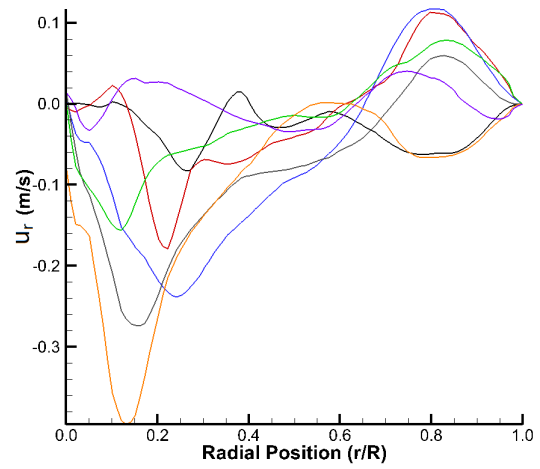
(a) Tangential velocity profile (CFD & PIV).   (b) Tangential velocity profile (PIV).

(c) Radial velocity profile (CFD & PIV).

(d) Radial velocity profile (PIV).

(e) Axial vorticity profile (CFD & PIV).

(f) Axial vorticity profile (PIV).

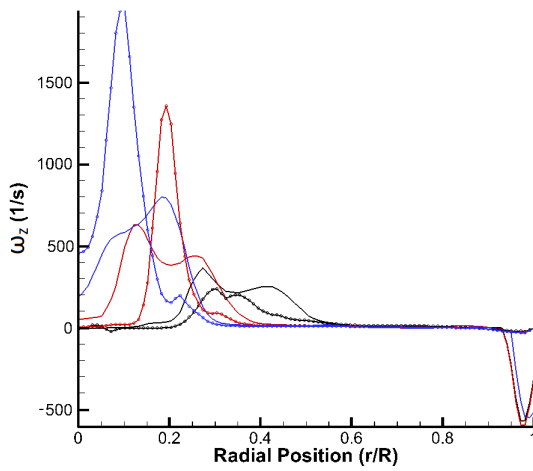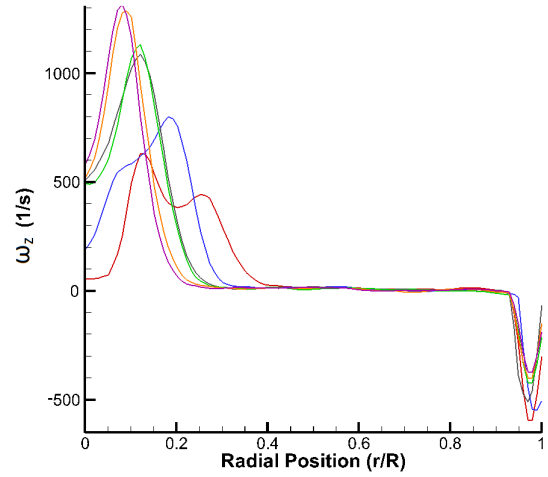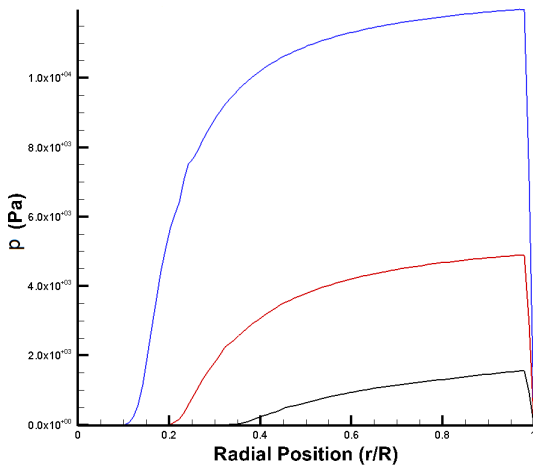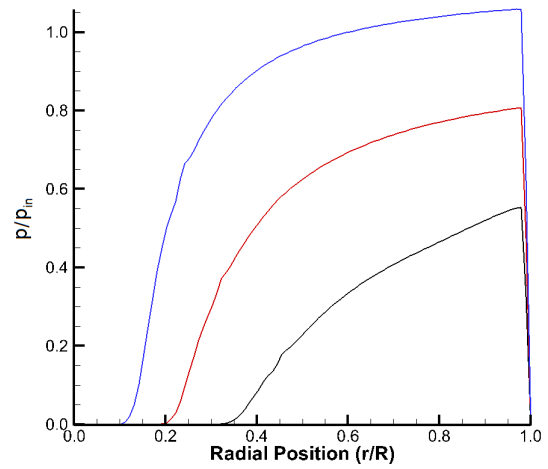(g) Static pressure profile (CFD).

(h) Normalised pressure profile (CFD).

Figure 5.29: Tangential profiles for vortex chambers with base injection.

113

For clarity the radial distribution plots for the contraction ratio study for configurations with base injectors have been split into two categories and are depicted in fig 5.29. In these plots both PIV and CFD data is available and allow comparison between the two datasets, but also it is only the PIV results which are available for the whole range of contraction ratios investigated. Fig 5.30a shows the tangential velocity profile for the PIV and CFD results for chambers with contraction ratios $CR = 5 - 20$, representing a range of chamber geometries commonly seen for various confined vortex devices. It is clear that the CFD results only display a higher peak tangential velocity magnitude when $CR = 20$, whilst at $CR = 10$ the forms are very similar, but at $CR = 5$ the velocity magnitude is lower as the form of the profile appears to deviate. The CFD data for the $CR = 5$ case does not display similarity with regards to the gradient of both the forced and free vortex regions of the chamber. It is interesting to note that despite the difference in the gradient of forced vortex between the PIV and CFD data, the gradient of the free vortices are very similar. The peak of the tangential velocity profile becomes more defined as the contraction ratio increases and the effects of turbulent energy dissipation appear to affect a smaller proportion of the radial profile. In spite of the results for the $CR = 5$ case in the CFD data where there is obviously an anomaly within the SBR region of the flow, the other CFD results exhibit similar behaviour. This is a reassuring result as this kind of behaviour is described in various viscous vortex models such as that proposed by Sullivan [14] where an increased Reynolds number causes the peak of the profile to increase and move towards the axis. As stated previously, the Sullivan vortex model also allows for reversed flow in the vortex core which is observed experimentally and numerically through the formation of the air core, which indicates the presence of air flow with a negative axial velocity component.

A relationship can be seen between the chambers with contraction ratios $CR = 5 - 20$ in the PIV data, but this does not apply to the other tangential velocity profiles for the upper range of contraction ratios seen in fig 5.30b. The profiles display a steadily increasing inverse relationship to the radial coordinate as the contraction ratio is increased, but are not coincident with the positions of the $CR = 5 - 20$ chamber configurations. Instead the peak tangential velocity of the PIV data occurs for the $CR = 40$ case before steadily decreasing in magnitude as the contraction ratio is increased further. The peak value decreases and the radial transition point from forced to free vortex moves radially inwards, as well as the gradient of the forced vortex indicating a more intense vortex. This is corroborated by the axial vorticity distribution for the PIV data seen in fig 5.29f, where the magnitude of the vorticity increases relative to a greater contraction ratio. As with the results in table 5.5a, the data suggests that the increased contraction ratio restricts the allowable radius of the SBR and air core, which through conservation of angular momentum results in higher rotational speeds and velocity components, especially the tangential contribution. The axial vorticity plots also show this is true as the axial vorticity is seen to be greater at reduced radial positions, which indicate increased vortex stretching in the axial direction as a result of the need to conserve angular momentum. The radial velocity distributions displayed in fig 5.29c relate to the CFD and PIV data for contraction ratios $CR = 5 - 20$ and show that the peak inward radial velocities calculated by the CFD are much larger than those obtained via PIV. It does not exhibit a negative radial component near the periphery of the chamber as seen in the PIV data, which indicates a sign reversal and the presence of an abscissa in the outer portion of the chamber. This is indicative of flow reversal in this region, signifying the presence of a mantle which is predicted by the Majdalani vortex model [13], but unfortunately this cannot be confirmed due to the insufficient accuracy of the PIV data in the axial plane of the chamber. The abscissas seen in the CFD radial velocity profiles that occur within the SBR portion of the flow lie within the region of the flow where the volume fraction transitions from water to air. This denotes the multiphase surface where the flow is suddenly accelerated towards the outlet where localised flow reversal is likely to occur. When this radial position is compared to the radial position of the air core, the small variation in radial coordinate infers that the radial velocity abscissas do indicate the presence of a mantle in close proximity.

The radial static pressure and normalised pressure distributions seen in figs 5.29g and 5.29h clearly show that as the contraction ratio of the chamber is increased so does the magnitude of the chamber pressure. The radial pressure gradient of the inner region of the chamber also increases, while the opposite is true as the periphery of the chamber is approached. Consideration should also be given to the whole radial pressure profile, which with regards to cyclonic flow is referred to as the

114

cyclone pressure drop. This is due to the sharp decrease in pressure associated with the large radial pressure gradients in the core region of the flow, caused by the increased rotation of the PVC. As with the radial dimension of the SBR and the air core, the radial pressure profile can be related to in terms of chamber geometry. From the standpoint of a designer, the pressure drop is a key variable in determining the separation efficiency of a vortex chamber with regards to particle laden flow. It is common practice to predict the radial pressure drop purely through means of formulating a pressure distribution, which is based solely on chamber geometry and inlet flow rate and is applicable to a certain range of operating conditions and geometrical variables.

Pressure drop models for cyclones are widely available in literature with prominent examples including those of Stairman [110] and Barth [111]. In comparison of the radial pressure distributions predicted by the complex-lamellar and Beltramian solutions, it was found that despite the many differences between the models the formulation of the pressure drop in the chamber can be effectively described by the simple inverse square relationship to the chamber radius $\triangle p \simeq p_{in}\left(1 - \frac{1}{2r^2}\right)$. The radial pressure gradient can also be similarly described by the simple relationship $\frac{\partial p}{\partial r} \approx \left(1 - \frac{1}{r^3}\right)$, which is reminiscent of the profiles produced by the models mentioned that are specifically tailored towards cyclone design. This provides a convenient method for determining whether the CFD results produce pressure distributions similar to those in cyclonic devices where empirical data is used to derive analytical representations of the flow. Additionally this confirms numerically, the validity of certain aspects of the Beltramian solutions in their application to predict the behaviour of confined vortices.

(a) $CR = 5$.

(b) $CR = 10$.

(c) $CR = 20$.

(d) $CR = 40$.

(e) $CR = 60$.

(f) $CR = 80$.
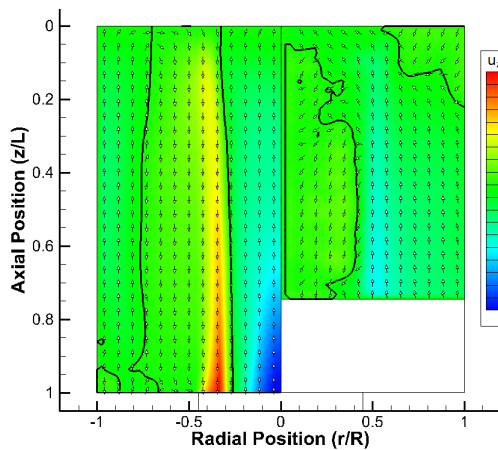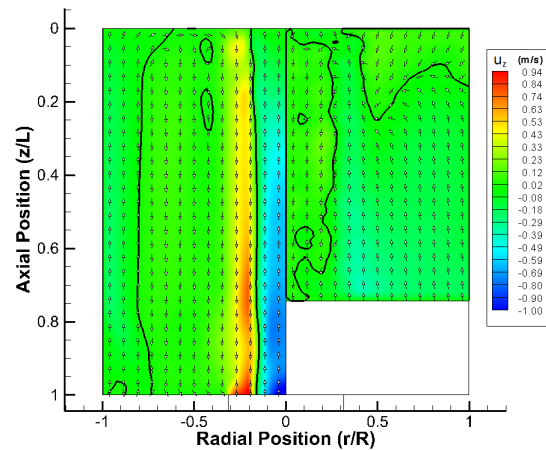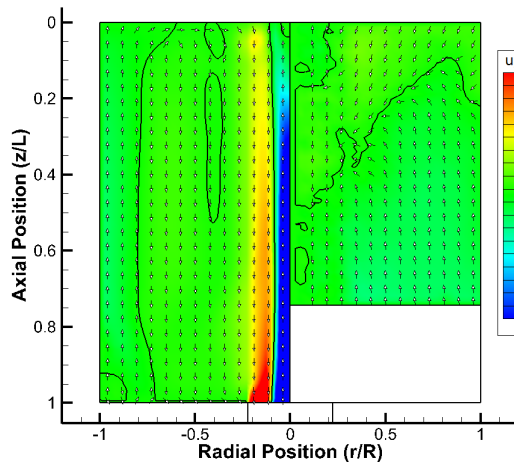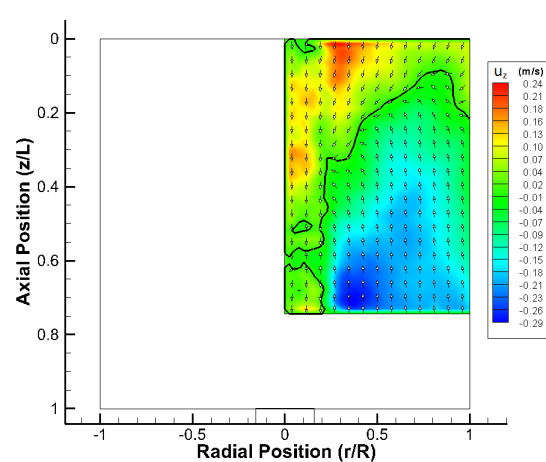
(g) $CR = 100$.
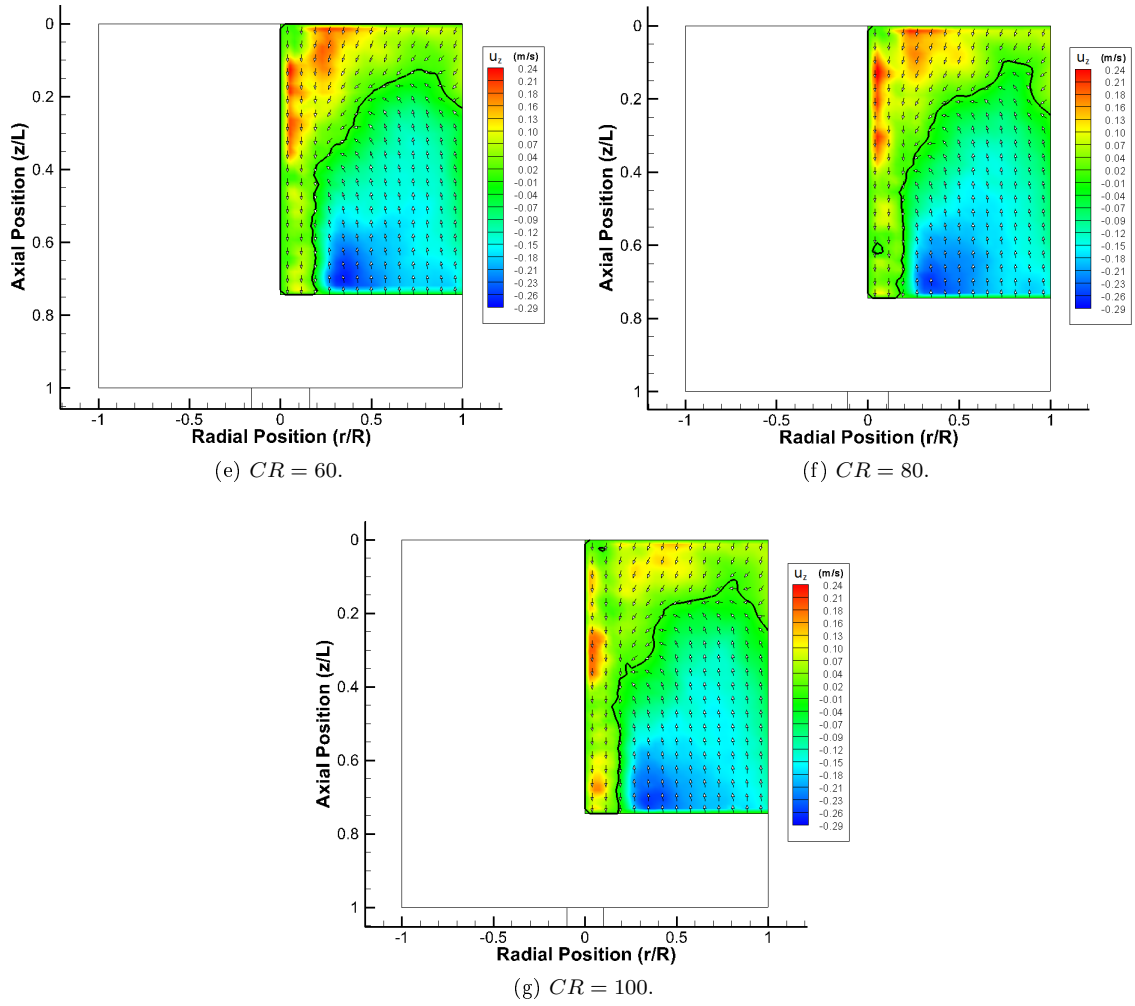
Figure 5.30: Axial velocity contour plots for vortex chambers with base injection.

(a) $CR = 5 - 20$.

(b) $CR = 40 - 100$.
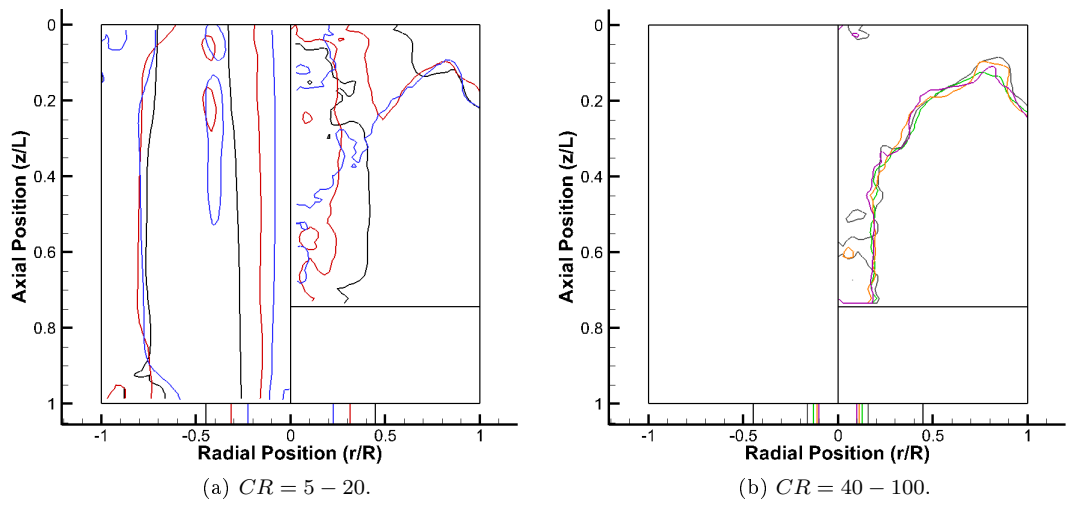
Figure 5.31: Axial plots of mantles for chambers with base injection.

116

Displayed in fig 5.30 are the axial velocity contour maps with the overlaid mantle positions for chamber configurations that have contraction ratios in the range $CR = 5 - 100$, when base injectors are employed. As mentioned previously, the CFD data is only available for the chambers with contraction ratios below $CR = 40$, which means that it is unknown whether the structure of the mantle is affected by larger contraction ratios. It can only be assumed that like the results from the chamber aspect ratio study, that there is a threshold geometrical condition beyond which the structure of the mantle will begin to evolve. Based on the tangential velocity profiles obtained by PIV in the azimuthal plane of the chamber it is thought that this threshold geometrical value is between $CR = 20 - 40$, as this is where the form of the tangential velocity profile begins to diverge from that seen for chambers with $CR = 5 - 20$. The variation in the tangential velocity profile is not as significant as that seen in the chamber aspect ratio study, when a transition in the mantle structure is found to occur. Consideration must be given to the evidence which suggests that variation in the tangential velocity is possibly indicative of change in the mantle structure and that it is likely to occur beyond a certain threshold value. Despite this, it is still unknown whether a transition does occur between chamber contraction ratios of $CR = 20 - 40$ and requires further investigation to confirm whether this is true or not.

For the chamber contraction ratios where CFD data is available, it can be seen in fig 5.31a that they all exhibit a single mantle that spans the length of the chamber and occupies approximately the same radial position in all cases. As with the mantles seen throughout this investigation none are of the idealised cylindrical form predicted by the analytical theory, which makes direct comparisons to the radial zeroes of the Bessel function of the first kind J_1 difficult. Another interesting feature is the development of the closed loop mantle rings that appear in the chamber for the $CR = 10$ case, which can then be seen to develop further as the contraction ratio is increased to $CR = 20$. This certainly suggests that the contraction ratio has some impact upon the structure of the mantle and that these mantle rings may increase in size and possibly span the length of the chamber as the contraction ratio is increased. There is some variation in the mantle structure of the PIV data in the meridional plane, but unfortunately no appreciable conclusions can be drawn from this due to the inappropriate method used to obtain the data. As one of the dominant features of the bidirectional vortex is the PVC, and the chamber contraction ratio is found to greatly influence its properties, in addition to other properties of the flow that it may affect the structure of the mantle more significantly than any other parametric variable investigated in this study. This is something which is also indicated by the Beltramian theory and therefore necessitates further investigation, as the small amount of CFD data presented here indicates that even at relatively large contraction ratios it is still possible to manipulate the shape of the mantle. To further highlight this, the mantle positions for chambers with contraction ratios in the range of $CR = 5 - 20$ and $CR = 40 - 100$ are shown in figs 5.31a and 5.31b respectively. The small variation in the radial position of the single mantle that spans the length of the chamber can be clearly seen in fig 5.31a and is seemingly unaffected by the significant variation in the radius of the PVC as the contraction ratio increases. This again also raises the question of whether or not the mantle structure is affected by the dimensions of the PVC, and if so to what extent does this occur. The mantles seen in fig 5.31a are relatively similar and they all approximately occur at $\frac{r}{R} = 0.75$ rather than $\frac{r}{R} = 0.628$ as predicted by the Beltramian theory, so they must be being radially displaced by some mechanism in the flow.

Displayed in fig 5.32 are some of the salient features of the vortices taken from the azimuthal plane of the chamber, with the blue lines indicating the outer mantle and inner PVC calculated by CFD. The green lines indicate the boundary of the SBR region of flow for the CFD and the equivalent found from PIV are depicted by the red lines. It is immediately obvious that for the chamber with the contraction ratio $CR = 5$, that the flow exhibits significant periodic symmetry similar to that observed in both the inlet Reynolds number and chamber aspect ratio study, further demonstrating the influence of cylindrical harmonics on the structure of the vortex. This effect is not as pronounced in the chambers with higher contraction ratios but there is still some evidence of the mantles in the CFD data tending towards a quadrilateral form. This may be the result of the mantle loops which appear in the chamber configuration with $CR = 10$, which could be indicative of the flow structure being forced into a different mode and therefore producing a different mantle structure as the mode shape is affected. This effect can be seen in the chamber aspect ratio study for

(a) $CR = 5$.

(b) $CR = 10$.

(c) $CR = 20$.
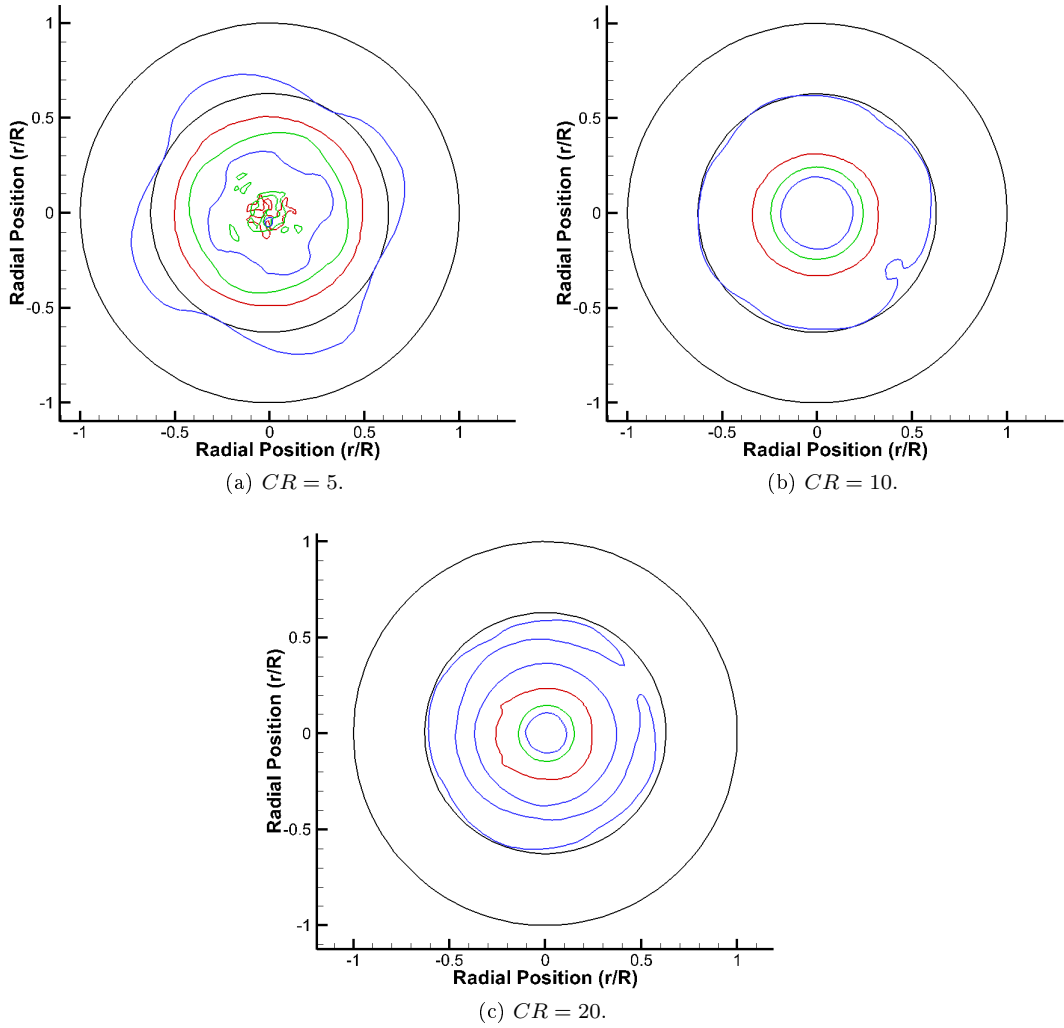
Figure 5.32: Azimuthal plots of combined mantles and SBR for chambers with base injection.

both configurations with base and head injectors, where the mantle structure undergoes a transition between $\frac{L}{D} = 0.8 - 1.0$ and the radial mode shape denoted by the mantle in the azimuthal plane of the chamber also exhibits this transition. As explained previously, this is evidence of higher order modes being perturbed, as the energy in the flow increases due to the increased intensity of the bidirectional vortex and causes the inception of these different mode shapes. They may not exhibit the same extent of periodicity as chambers containing less intense vortices though, because the higher order modes initially need more energy to be invoked and even further energy to perturb them significantly in order to produce less cylindrical forms.

Although it was noted that in the meridional plane of the chamber, the mantle positions do not appear to correlate well to those predicted by the Beltramian theory, although this is not true in the azimuthal plane of the chamber close to the head wall. As fig 5.32 shows the mantles in each contraction ratio in the range $CR = 5 - 40$ coincide with the theoretical mantle position at $\frac{r}{R} = 0.628$, which is denoted by the inner black circle, even despite the obvious effects of periodicity. Apart from this it can be seen that the SBR boundary extracted from the PIV data is consistently greater than that of the CFD data by approximately 9% of the chamber radius, despite the comparable peak tangential velocities.

(a) Azimuth plane.

(b) Meridional plane.
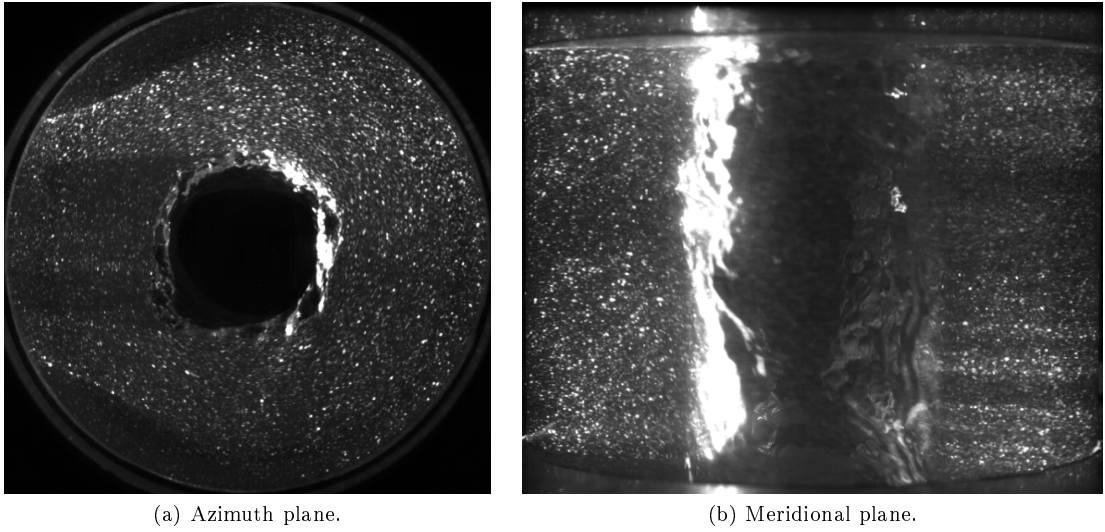
Figure 5.33: PIV images for chamber configuration $CR = 5$ with base injectors.

(a) Triangle.

(b) Square.

(c) Pentagon.
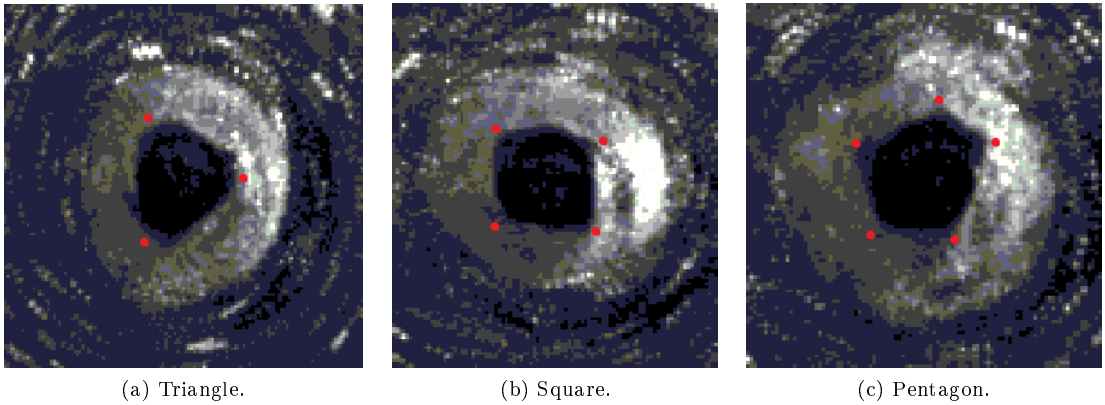
Figure 5.34: Mode shapes observed in deformed boundary of PVC.

Despite the obvious difference in shape of the air core boundary of the CFD and PIV data, it is reassuring to see that they are in good agreement with respect to the average radius of the air core. The PIV data does not indicate any periodicity in the flow, but this is not the case physically as can be seen in fig 5.33a, where the boundary between the water and the air is irregular in shape. This boundary appears to be tending towards a quadrilateral form from a circular one, whilst also displaying the same period as seen in fig 5.32a for the CFD data. The irregularity of this shape can be seen repeatedly throughout the high speed footage of the azimuthal plane of the vortex chambers, but the form of the air core boundary is not only limited to quadrilateral shapes. In fig 5.34 the air core region of the chamber with a contraction ratio of $CR = 40$ has been enlarged so that the various polygons that form the PVC boundary can be compared. It is clear that these shapes are indeed not circular, but more comparable to a triangle, square and pentagon respectively, and occur at separate points in time. The presence of polygonal structures within the core of the vortex is not an uncommon occurrence, but is more commonly associated with atmospheric dynamics. An example of this can be observed occurring at the southern pole of the planet Saturn as seen in fig 5.35, which is due to baroclinic instability. Baroclinic instability with regards to meteorology requires a free surface for the gravitational waves to propagate which is replicated in a closed container such as a vortex chamber by the free surface provided by the boundary of the PVC.
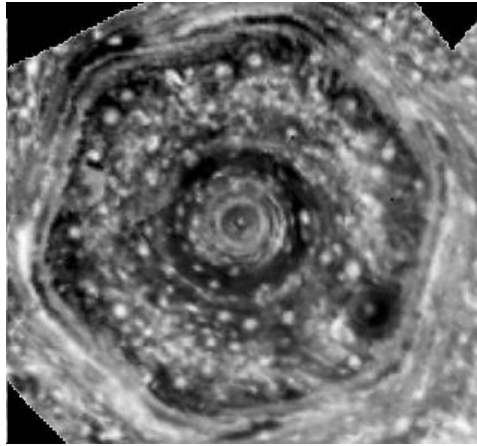
Figure 5.35: Hexagonal mode shape observed in the atmosphere above Saturn's south pole. [30]

(a) Triangular.   (b) Rectangular.   (c) Pentangular.
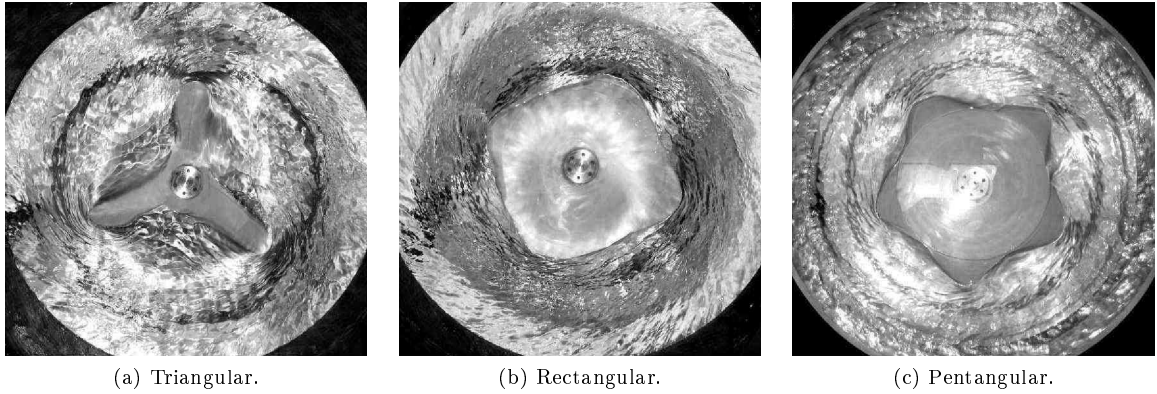
Figure 5.36: Mode shapes observed in a cylindrical container of fluid subject to SBR. [31]

These conditions can easily be replicated in a laboratory by rotating an open cylindrical vessel containing fluid [31], as those seen in fig 5.36 where similar polygonal structures are observed. It is speculated that these forms are the result of vibrations induced by the motor used to rotate the container, where variation in the angular velocity caused different shapes to be observed associated with the vibrational frequency of the motor. Therefore if the fluid is perturbed axially at specific frequencies then it is possible to observe a specific polygon that defines the boundary of the PVC. Deformation of the PVC will be reflected in the shape of the vortex core boundary and examples of similar deformation upon columnar vortices such as those which occur in vortex chambers can be seen in fig F.5. The helical lines that traverse the length of the vortex core represent lines of fixed phase and are expressed by $kz + m\phi = constant$, where m represents the respective mode number. The fact that the structure of the vortex core is described as a mode shape here and is reliant on a perturbation frequency gives further credence to the idea that the mantle structure is a mode shape induced by the characteristics of the vortex core. These mode shapes also arise from the vortex core being perturbed at a specific frequency, as the rotation of the deformed vortex core is responsible for oscillations in the fluid which are in the form of inertial waves.

It is immediately clear that when $m = 4$ the cross section of the vortex core is similar to that observed in fig 5.33a for the chamber with a contraction ratio of $CR = 5$. The bending modes described by $m = \pm 1$ show the origin of the circular form of the vortex core to deviate from the chamber axis, when this is coupled with the rotation of the vortex core it indicates precession of the vortex and therefore the presence of a PVC, which is only possible when the flow is perturbed axially. The shape of the vortex core has been observed to exhibit several modes relating to various polygons,

but it is also circular and displays some precession about the chamber axis. However, the shape of the vortex core is predominantly an irregular shape which exhibits precession and contains aspects of several modes at once, similar to the behaviour seen in the mantle structure. This would suggest that the vortex core is in a constant state of flux and being perturbed by a range of frequencies, which result in the various defined and irregular shapes forming the boundary of the PVC. The existence of multiple frequencies affecting the vortex core is also observed experimentally as the PVC boundary appears to be formed from the superposition of multiple different waves. This can be seen in fig 5.33b where it is clear that the vortex core is defined by a complex surface, which appears to allow waves to propagate axially in both directions, as they propagate from the exit plane of the chamber before being reflected by the head wall chamber boundary. If it is possible to perturb the vortex core at specific frequencies, which in the case of cylindrical harmonics are referred to as eigenfrequencies, then it would be possible to control what mode shapes would occur. More importantly if the shape of the vortex core and its angular velocity which describes the frequency of the radial oscillations can be characterised, then it is possible to produce inertial waves at specific eigenfrequencies in the fluid, which relate to specific mantle structures. Therefore the specific amount of flow reversal can be controlled through chamber geometry and application of the correct boundary conditions.

5.5.2 Head injection

Table 5.6 contains the most salient data taken from the CFD and PIV studies for the chamber contraction ratio study, where head injectors are employed to sustain the bidirectional vortex. In comparison to the data for the contraction ratio study with base injectors, the inlet velocities in this part of the study and the associated inlet Reynolds numbers are consistently lower when head injectors are employed. It can be seen for chambers with contraction ratios of $CR = 10 - 20$ that the inlet pressure for the base injector chamber configurations is approximately 50% than those recorded for the head injector configurations. However, when the normalised radial dimensions of the air core are referred to, it is clear that the head injector configurations produce vortices with smaller vortex cores and therefore result in a larger effective throat area relative to the base injector configurations. This indicates that the intensity of the vortices produced in the contraction ratio study with head injectors is higher, as the reduced PVC radius is caused by additional vortex stretching, caused by increased vorticity within the core flow. The inlet velocities are lower, although the resultant peak tangential velocities produced are approximately of the same magnitude as those for the base injector configurations, with a remarkable correlation between the peak tangential velocities obtained by the PIV for both data sets. This increased intensity is caused by the azimuth plane being in close proximity to the injectors and head wall boundary, where the inlet velocity may be reduced, but the flow in this region is still subject to increased shear and turbulence.

The angular velocities presented in table 5.6a for the CFD are considerably lower than the PIV results, this is due to the reduced radius of the SBR region used to calculate the angular velocity. This is not the case for the PIV data, where both the magnitude of the peak tangential velocity and the radius of the SBR are very similar over the full range of chamber contraction ratios and therefore means that the angular velocities are almost identical to those of the chamber configurations with base injectors. This of course influences the range of PVC frequencies in a similar manner, with the values calculated from the CFD data being progressively smaller with increased contraction ratio, while the frequencies calculated from the PIV data are similar. As mentioned for the base injector configurations, the vortex Reynolds number incorrectly predicts that the intensity of the vortex decreases with increased contraction. The Strouhal number identifies the correct behaviour primarily through inclusion of the PVC frequency, which is found to increase linearly with respect to outlet radius over the range $CR = 5 - 40$. Again, as is the case with the majority of data presented thus far, the height of the boundary layer at the periphery of the chamber varies little of the range of contraction ratios, and both the head and base injector configurations display similar trends. Additionally nothing of interest can be discerned from the axial velocity data obtained from the PIV study, while the CFD study suggests that the magnitude of the maximum and minimum axial velocities increase with greater contraction ratios, reflecting what is found for the base injector configurations.

Table (a):

Contraction Ratio CR	Inlet Velocity u_{in} (m/s)	Inlet Pressure (CFD) p_{in} (Kpa)	Inlet Reynolds Number Re	Vortex Reynolds Number V	Strouhal Number (CFD) Sh	Strouhal Number (PIV) Sh	Normalised Air Core Radius (CFD) r_{core}	Normalised Air Core Radius (PIV) r_{core}	Normalised Forced Vortex Radius (CFD) r_{SBR}	Normalised Forced Vortex Radius (PIV) r_{SBR}	Liquid Dimension of Forced Vortex (CFD) $r_{SBR}\text{-}r_{core}$	Liquid Dimension of Forced Vortex (PIV) $r_{SBR}\text{-}r_{core}$	Precessing Vortex Core Frequency (CFD) f_{PVC} (Hz)
5	1.05	2.34	4.06E+04	2.68E+03	1.31	1.15	0.267	0.288	0.383	0.497	0.116	0.209	17.55
10	1.01	4.14	3.90E+04	2.58E+03	2.97	2.62	0.152	0.170	0.215	0.322	0.063	0.152	38.36
20	1.01	6.70	3.92E+04	2.59E+03	6.31	4.30	0.061	0.073	0.120	0.250	0.059	0.177	81.68
40	0.95	20.16	3.67E+04	2.43E+03	20.13	6.32	0.051	0.053	0.079	0.187	0.028	0.134	244.11
60	0.89	×	3.47E+04	2.29E+03	×	6.25	×	0.031	×	0.186	×	0.155	×
80	0.89	×	3.44E+04	2.28E+03	×	7.60	×	0.015	×	0.152	×	0.137	×
100	0.84	×	3.25E+04	2.15E+03	×	8.23	×	0.015	×	0.138	×	0.123	×

Table (b):

| Contraction Ratio CR	Peak Tangential Velocity (CFD) u_{ϕ} (m/s)	Peak Tangential Velocity Ratio (CFD) u_{ϕ}/u_{in}	Peak Tangential Velocity (PIV) u_{ϕ} (m/s)	Peak Tangential Velocity Ratio (PIV) u_{ϕ}/u_{in}	CFD Forced Vortex Angular Velocity $(\partial u_{\phi}/\partial r)$ ω (rad/s)	PIV Forced Vortex Angular Velocity $(\partial u_{\phi}/\partial r)$ ω (rad/s)	CFD Free Vortex Inverse Gradient $(\partial r/\partial u_{\phi})$	PIV Free Vortex Inverse Gradient $(\partial r/\partial u_{\phi})$	CFD Normalised Boundary layer height at chamber wall δ_w	PIV Normalised Boundary layer height at chamber wall δ_w	Maximum Axial Velocity (CFD) u_z (m/s)	Minimum Axial Velocity (CFD) u_z (m/s)	Maximum Axial Velocity (PIV) u_z (m/s)
5	1.65	1.57	1.88	1.80	110.26	96.97	99.20	113.17	0.02	0.03	0.55	-0.41	0.09
10	2.02	2.01	2.66	2.65	241.04	212.12	73.45	117.34	0.02	0.03	0.92	-1.34	0.15
20	2.39	2.37	3.41	3.37	513.19	349.73	83.26	136.37	0.02	0.04	1.51	-2.28	0.16
40	4.73	5.00	3.52	3.72	1533.77	481.69	87.89	103.17	0.02	0.04	2.67	-3.55	0.18
60	×	×	3.27	3.66	×	450.34	×	90.07	×	0.04	×	×	0.13
80	×	×	3.22	3.63	×	543.12	×	80.44	×	0.04	×	×	0.08
100	×	×	2.98	3.56	×	555.99	×	69.89	×	0.04	×	×	0.10

(a)   (b)

Table 5.6: Flow variables for chambers with head injection.

The tangential velocity, radial velocity, axial vorticity and pressure profiles are displayed in fig 5.37. Due to the lack of CFD data above chamber contraction ratios of $CR = 40$ the data obtained from the full range of contraction ratios for the PIV study is presented separately. Unlike the contraction ratio study of chamber configurations with base injectors, it was possible to obtain CFD data over an extended range of $CR = 5 - 40$ and allows the hypothesised mantle transition between $CR = 20 - 40$ to be analysed in further detail. The tangential velocity profiles obtained from the CFD data shown in fig 5.38a exhibit a similar reduction in the radius of the SBR relative to the PIV data, as seen for the base injector configurations. In this case the magnitude of the peak tangential velocity is considerably lower for the CFD in comparison to the PIV data and the gradient around the transitional radius from the forced to free vortex is also considerably less. This has been seen repeatedly in the CFD data for the head injector configurations and is attributed to the variation in the axial location of the azimuth plane, which is located at a distance of $1mm$ and $21mm$ for the CFD and PIV data respectively.

The CFD tangential velocity profiles produced for the chamber aspect ratio study do not exhibit this behaviour to the same extent as the inlet Reynolds number study, but this is partially due to the lack of PIV data to compare it to. However the results from the aspect ratio study do indicate that some chambers exhibit a similar broad peak in the tangential velocity profile after a geometric threshold has been passed, after which there is a transition in the structure of the mantle. It is assumed from the analysis of the data for the contraction ratio study with base injectors that this transitional threshold occurs between chamber contraction ratios of $CR = 20 - 40$, and may be responsible for the sudden transition in the CFD tangential velocity profiles between these contraction ratios. It is not as pronounced, but can this be seen in fig 5.38b, where the tangential velocity profile for the PIV data for a chamber with $CR = 40$ deviates from the behaviour of the profiles seen for chambers with contraction ratios in the range $CR = 5 - 20$. This behaviour is identical to that seen for the base injector configurations, where the gradient of the free vortex differs to the common slope which forms the profile of the free vortex for the chambers with contraction ratios in the range $CR = 5 - 20$. It can also be seen in fig 5.38b that not only are the peak tangential velocities of the base and head injector configurations very similar, but the tangential profiles are almost indistinguishable from one another and exhibit identical behaviour over the full range of contraction ratios. Therefore, the chamber with a contraction ratio of $CR = 40$ produces the largest peak tangential velocity, which then gradually decreases with greater contraction ratios. The gradient of the forced vortex also increases accordingly, signifying an increase in the intensity of the vortex in addition to reductions in both the radius of the SBR and incidentally the boundary of the PVC.

The combined plot of radial velocity for the CFD and PIV data can be seen in fig 5.37c, where it is immediately clear that the average magnitude of the radial velocity is considerably lower for the CFD data and does not exhibit the same maxima and minima that occur in the PIV data. This is similar to what is seen in the radial velocity plots for the head injector chamber configurations in the inlet Reynolds number study, where it is difficult to make any distinct observations when comparing the two sets of data. When the radial velocity distributions for the PIV data seen in fig 5.37d are referred to, it can be seen that the minimum radial velocity occurs within the forced vortex, where the flow appears to be directed inwardly towards the chamber axis as the core flow propagates towards the chamber outlet. Apart from this, for the majority of chamber contraction ratios, the radial flow at the periphery of the chamber represents the maximum radial velocity that occurs. This can possibly be attributed to the azimuthal observation plane being situated above the axial position of the head injectors. When the combined CFD and PIV plots of axial vorticity in fig 5.37e are consulted, it becomes apparent that as the contraction ratio is increased the maximum axial vorticity found by the CFD, which occurs in close proximity to the chamber axis is greater than that obtained from the PIV. This is also the likely result of the increased turbulence in this region, which causes increased velocity gradients to occur in this region with regards to the CFD data and therefore result in increased axial vorticity.

Although both the CFD and PIV data corroborate what is seen in the tangential velocity plot in fig 5.38a in that the radial position of zero axial vorticity occurs at a lesser distance from the chamber axis. This indicates that the PIV data finds the transition from the forced to free vortex to occur at a greater non dimensional radius in comparison to the CFD data. It can be seen that the axial vorticity distributions for the PIV data displayed in fig 5.37f that the radial position of zero vorticity gradually tends towards the chamber axis as the contraction ratio is increased as expected, due to the increased vortex stretching that reduces the radius of the vortex core. This is also indicated by the progressive increase of the maximum axial vorticity that occurs, apart from the chamber configuration with $CR = 80$, which exhibit a larger peak axial vorticity than the chamber configuration with $CR = 100$. Despite this, it is interesting to observe how the axial vorticity profile of the chambers with contraction ratios $CR = 5 - 10$ exhibit similar profiles, which then appears to change in form for $CR = 20$, before the larger contraction ratios in the range $CR = 40 - 100$ which all display similar behaviour. Again, this may be possible evidence of a transition in the flow structure that begins to occur as the contraction ratio is increased beyond $CR = 20$, which would be in agreement with findings for both the base and head injector chamber configurations in the contraction ratio study. If this were the case, it may provide a possible although simplistic means of determining whether the mantle structure is evolving in lieu of axial velocity data in the meridional plane of the chamber.
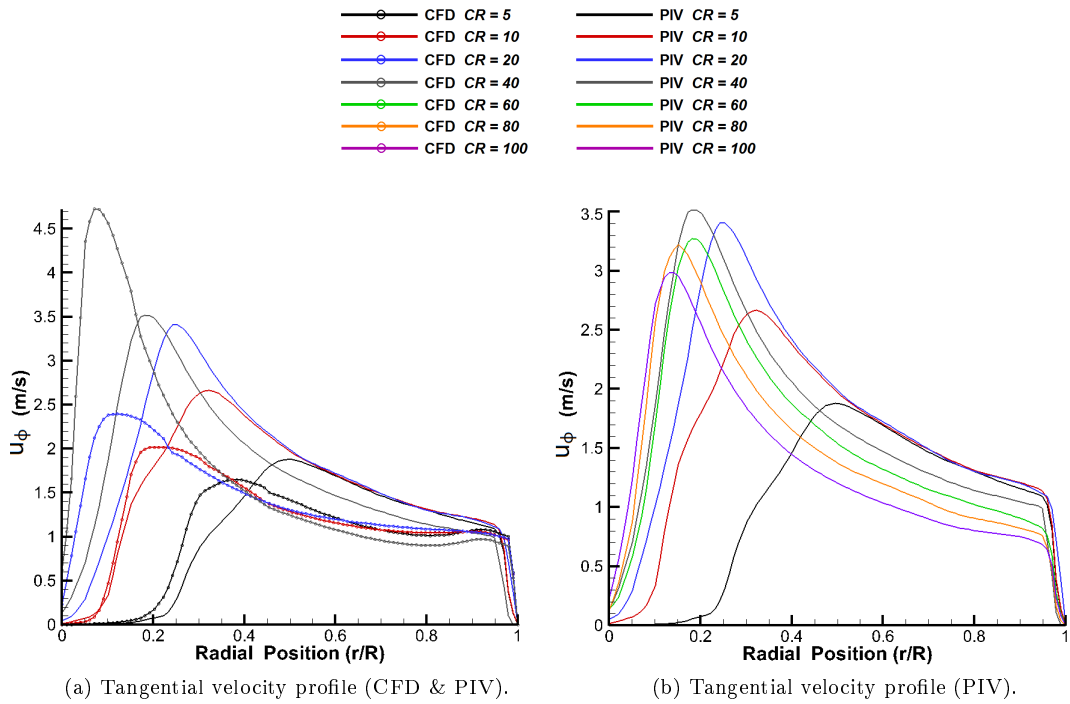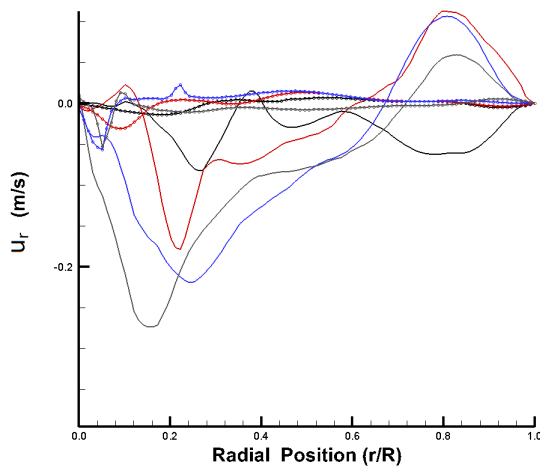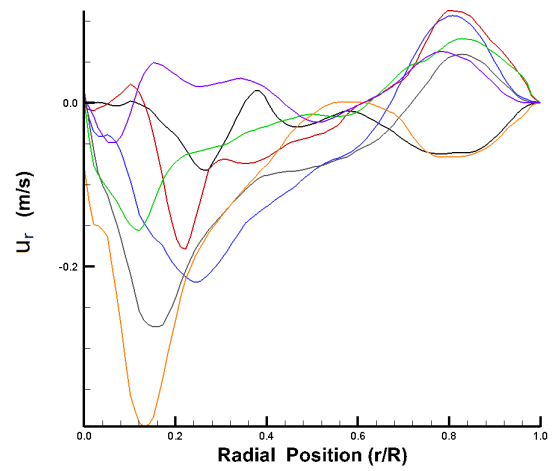
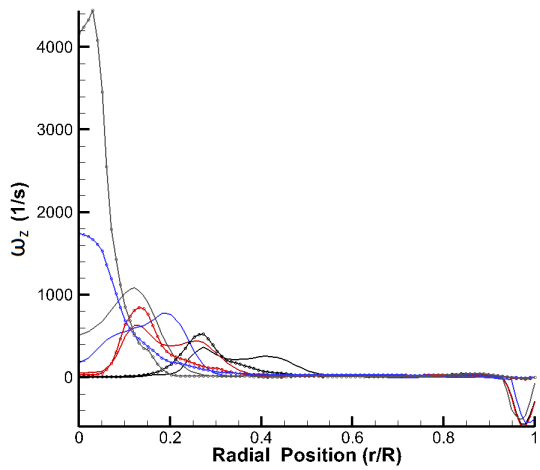(a) Tangential velocity profile (CFD & PIV).   (b) Tangential velocity profile (PIV).
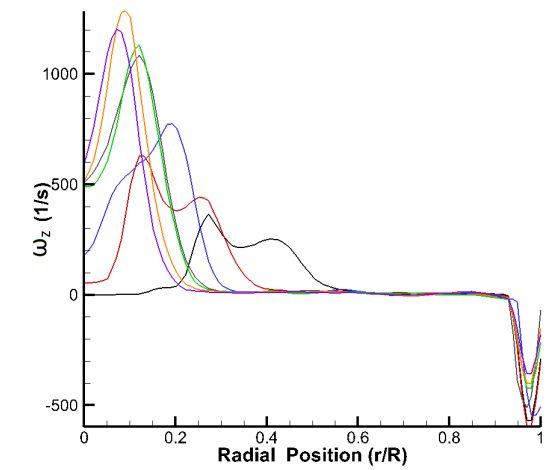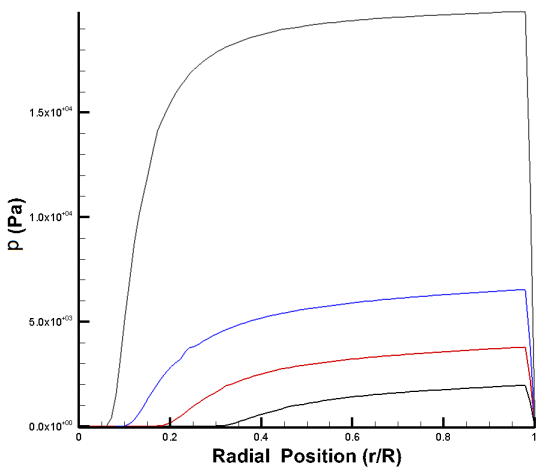
(c) Radial velocity profile (CFD & PIV).
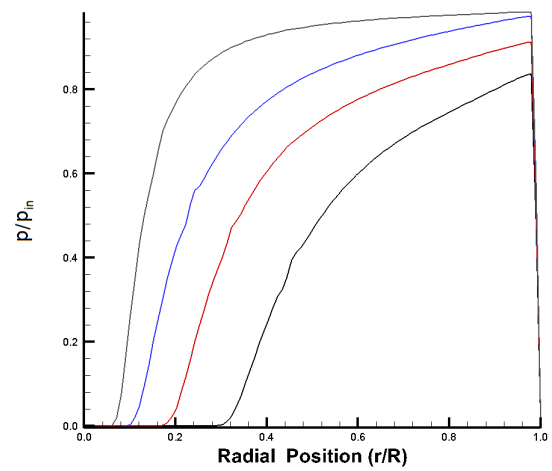
(d) Radial velocity profile (PIV).

(e) Axial vorticity profile (CFD & PIV).

(f) Axial vorticity profile (PIV).

(g) Static pressure profile (CFD).

(h) Normalised pressure profile (CFD).

Figure 5.37: Tangential profiles for vortex chambers with head injection.

When the static pressure distribution extracted from the CFD data that shown in fig 5.37g is consulted, it is obvious that there is a large increase in the maximum chamber pressure between chambers with contraction ratios of $CR = 20 - 40$, which is significantly larger than the progressive increase over the range $CR = 5 - 20$. All the chambers configurations display a similar radial dependence, where the decrease in static pressure can be approximated by a similar inverse square function relative to the chamber radius. The steep pressure gradient seen for the $CR = 40$ case is indicative of an intense vortex, which due to conservation of angular momentum and results in a small vortex core, also the negative radial pressure is greater than the opposing Coriolis force and therefore produces a reduction in the radius of the air core. When the static pressure is normalised by the pressure at the inlet as shown in fig 5.37h it allows for the comparison of the pressure distribution irrespective of inlet conditions, where the large inlet pressures seen in the $CR = 40$ case are obviously responsible for the large disparity between the chambers with contraction ratios $CR = 20 - 40$. As with the tangential velocity and axial vorticity plots the normalised pressure distribution in fig 5.37h indicates how the radius of the PVC reduces as the contraction ratio increases, denoted by the intersection on the horizontal axis.

Despite the appearance of zero pressure within the PVC, this is not the case and is due to the scale of the vertical axis which prevents a comparison from being made visually between the various chamber configurations. Upon closer inspection it is found that the magnitude of the negative static pressure relative to atmospheric pressure pressure increases relative to larger contraction ratios. This is to be expected, as vortices of greater intensity produce a larger pressure drop within the chamber and induce an increased amount of reversed flow along the chamber axis, which is a result of the increased adverse pressure gradient. Despite the appearance of zero pressure within the PVC throughout the results in this investigation, the static pressure in the air core is negative and must be below ambient pressure in order for the air core to fully develop and invoke the PVC. Therefore it can be inferred that for whatever parameter is being investigated, the maximum negative pressure within the PVC will always occur in chambers that sustain the most intense vortices, which can be determined from the dimensions of the air core and the peak magnitude of the tangential velocity component. In addition to this it is again clear that by increasing the contraction ratio, the pressure gradient within the core flow increases while the gradient at the periphery decreases, as it tends towards an asymptote due to the $\triangle p \simeq p_{in} \left(1 - \frac{1}{2r} \right)$ relationship. The normalised pressure gradient drop can be better expressed by $\triangle p \simeq p_{in} \left(1 - \frac{1}{nr} \right)$, where increasing n results in a pressure profile associated with larger contraction ratios.

(a) $CR = 5$.   (b) $CR = 10$.

(c) $CR = 20$.

(d) $CR = 40$.

(e) $CR = 60$.

(f) $CR = 80$.

(g) $CR = 100$.
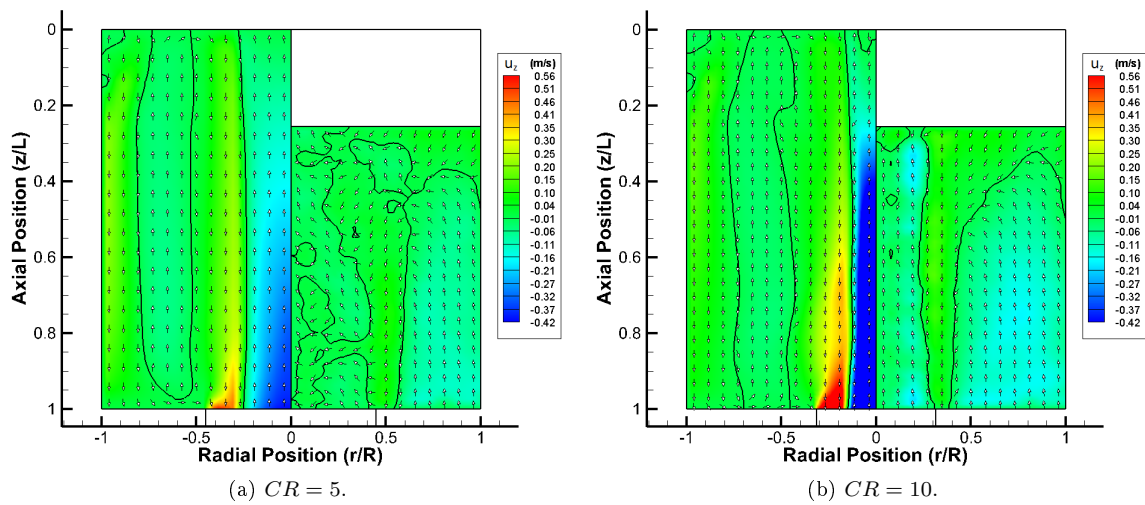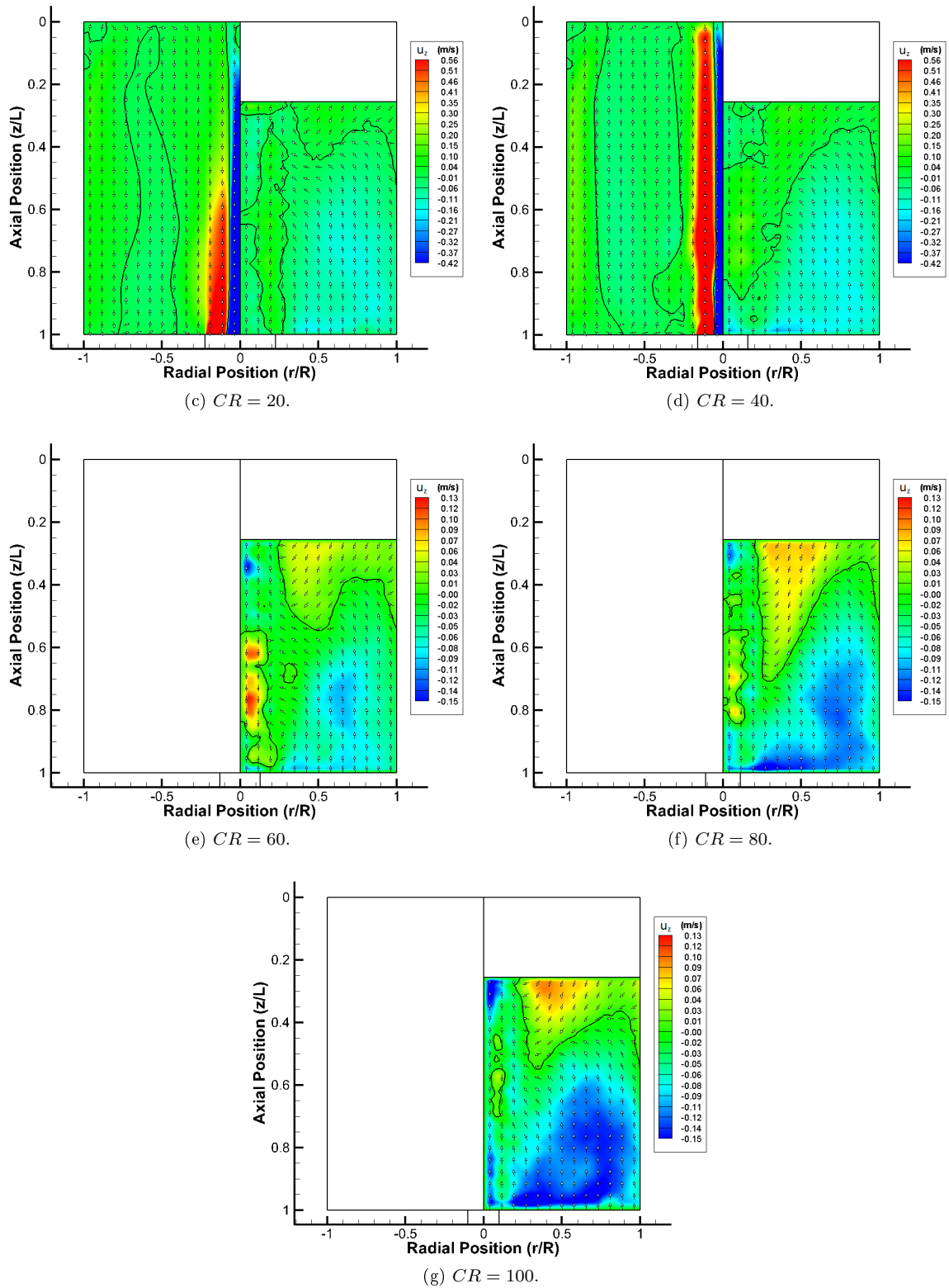
Figure 5.38: Axial velocity contour plots for vortex chambers with head injection.

The axial velocity contour maps and their respective mantle structures are shown in fig 5.38, where only chambers with contraction ratios in the range of $CR = 5 - 40$ display both the CFD and PIV data in the meridional plane of the chamber. In fig 5.39a the results for the chamber configuration with $CR = 5$ are displayed and it is immediately clear that the vectors indicate a the existence of a triple vortex, where the loop that forms the mantle extends to approximately 97% of the chamber length, emanating from the head wall boundary. The radial component of the vectors have been minimised, allowing for easier recognition of the axial flow, where it can be seen that the vectors which define the path of each vortex tube are parallel to the chamber axis. This indicates that the flow propagates along the full length of the chamber, and is important because the mantle is defined by the locus of zero axial velocity and can occur anywhere where the flow is undergoing localised flow reversal. Therefore a mantle structure may be present in the flow, but the path of the flow does not traverse the full length of the chamber, which is essential to increase the effective length of the chamber with regards to VIHRE performance. As the contraction ratio is increased to $CR = 10$, it can be seen in fig 5.39b that now the mantle separates into two distinct parts which both span the length of the chamber but still allows the vortex tubes to span the length of the chamber, as denoted by the vertical alignment of the vectors. From the analysis of the tangential velocity plots taken from the azimuthal plane of the chamber, it is suggested that the chambers with contraction ratios in the range $CR = 5 - 20$ exhibit similar behaviour and that this may be reflected in the embedded flow structures.

(a) $CR = 5 - 10$.

(b) $CR = 20 - 40$.

(c) $CR = 60 - 100$.

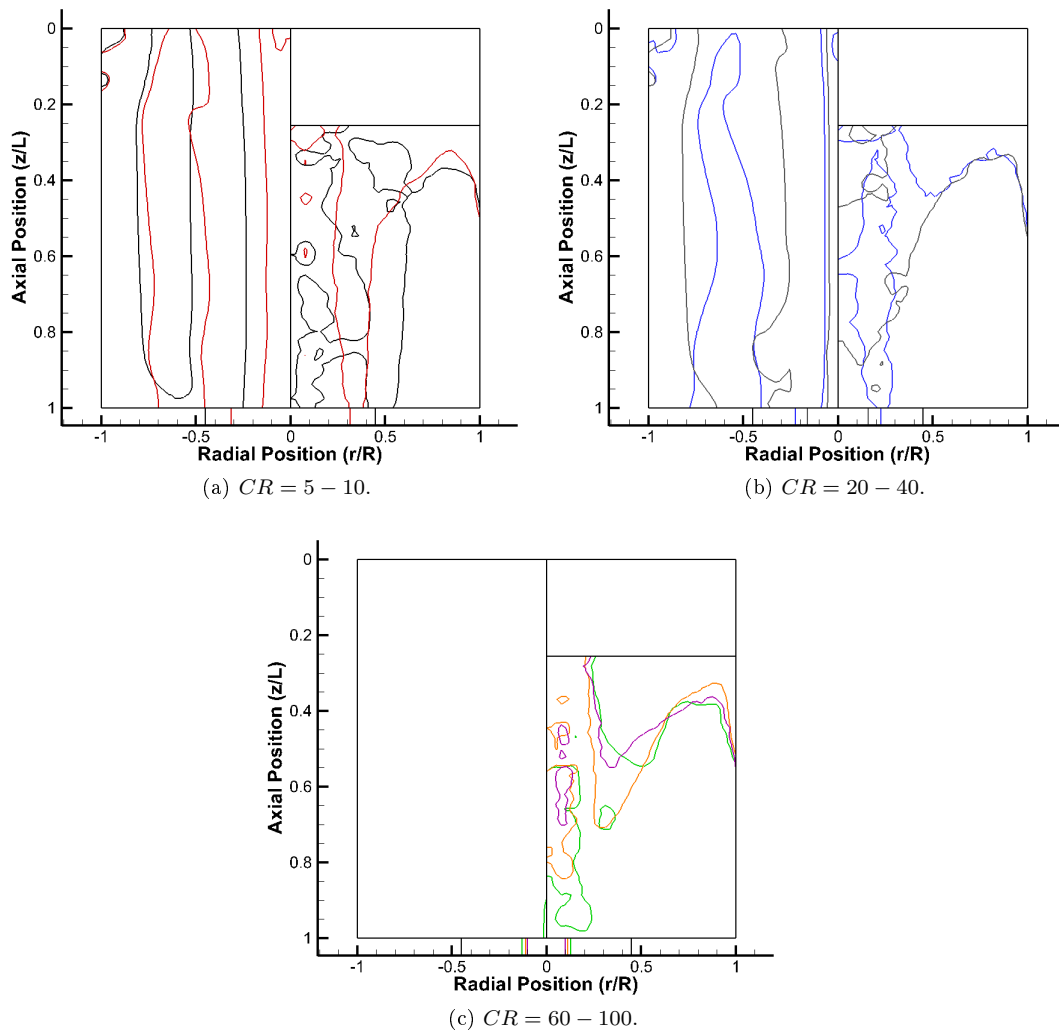Figure 5.39: Axial plot of mantles for chambers with head injection.

When comparing the mantle structures in fig 5.39a and 5.39b, it is apparent that while the structures are not identical they are similar, with the mantle seemingly propagating the full length of the chamber and evolving into a new structure. This is also evident in fig 5.38c, where the mantle structure for the chamber configuration with a contraction ratio of $CR = 20$ is also similar in form to that seen in fig 5.39b, especially near the head of the chamber where there is increasing curvature in the form of the mantle. When the contraction ratio is $CR = 20$, the mantle does not appear to span the length of the chamber anymore, but the mantle structure exhibits periodicity and therefore does span the full length of the chamber, which can be seen if the azimuth angle of the meridional plane is altered. This is reflected to an extent in the description of the axial vorticity plots in fig 5.37e, where the $CR = 20$ case represents a transition between the behaviour of the flow associated with the lower and upper range of contraction ratios of $CR = 5 - 10$ and $CR = 40 - 100$ respectively. Both the results for the base and head injection chamber configurations in the contraction ratio study indicate that there is a possible transition in the structure of the flow between $CR = 20 - 40$, which was not able to be confirmed in the base injection part of the study due to CFD convergence issues.

It is clear in fig 5.38d that the mantle structure is considerably different to that seen in fig 5.38c and it can only be assumed that the significant variation in the form of the mantle is inherently linked to the transitional behaviour observed in the results taken from the azimuthal plane of the chamber. It is also worth noting that as the structure of the mantle has evolved, the average radial position of the inner mantle has moved towards the chamber axis, while the outer mantle remains at approximately the same position. Apart from this, the increased radial separation between the individual mantles and their attachment to both end wall boundaries results in the flow vectors being again aligned with the chamber axis and indicating that the vortex tubes extend across the while length of the chamber. The overlaid mantle structures are displayed in fig 5.39, where the chambers with contraction ratios $CR = 5 - 10$ are shown in fig 5.39a, and those with contraction ratios $CR = 20 - 40$ are shown in fig 5.39b to highlight both the similar and different forms respectively. As with all the PIV mantles presented thus far, it is difficult to draw any distinct conclusions from the resultant mantle profiles and the analysis must be limited to the CFD data as it has been proven to produce reliable results.

The mantle and SBR boundaries extracted from the CFD and PIV data are shown in fig 5.40, where the mantle for the PIV data is omitted as it is not possible to extract it from the azimuthal plane data. In fig 5.40a the outer mantle for the chamber with a contraction ratio of $CR = 5$ can be seen to coincide with the theoretical mantle predicted by the Beltramian solution for a triple vortex. The inner mantle is considerably displaced from the radial position of the other theoretical mantle and occurs at a similar radius as the SBR boundary taken from the PIV results. Yet again, it is seen that no mantles are present within the boundary of the SBR, which means that flow reversal may only be possible in the outer region of the chamber where the flow is irrotational. If this is true, then it could provide an insight into producing vortices with multiple flow reversals as the geometry of the chamber could be controlled in order to invoke a vortex with predetermined characteristics, where the radius SBR is lower than the innermost radius of a specific flow reversal mode. This allows a range of flow reversal modes to occur within the chamber with a desired flow reversal mode being possible once a range of variables has been established that affect the mantle structure.

The results from the azimuthal plane of the chamber with a contraction ratio of $CR = 10$ are shown in fig 5.40b, which indicates the transitional structure of the mantle as seen in the results from the meridional plane of the chamber. The outer mantle is no longer coincident with the theoretical mantle position and has moved towards the chamber axis, while the inner mantle has moved outwardly but both exhibit periodicity and a similar form to fig 5.18b, which means that the flow is subject to the specific conditions that result in a partially perturbed $(4, 2)$ mode shape. It is interesting to see that while the mantle structure in fig 5.40b displays a periodic form, neither the SBR from the CFD or PIV data exhibits any obvious signs of periodicity. The same is true of the results in fig 5.32a as well, where it is known that the physical vortex is not axisymmetric and can be seen in fig 5.33a to exhibit significant deformation of the vortex core as it rotates about the chamber axis, and therefore is unable to result in a circular SBR boundary.

(a) $CR = 5$.

(b) $CR = 10$.

(c) $CR = 20$.

(d) $CR = 40$.
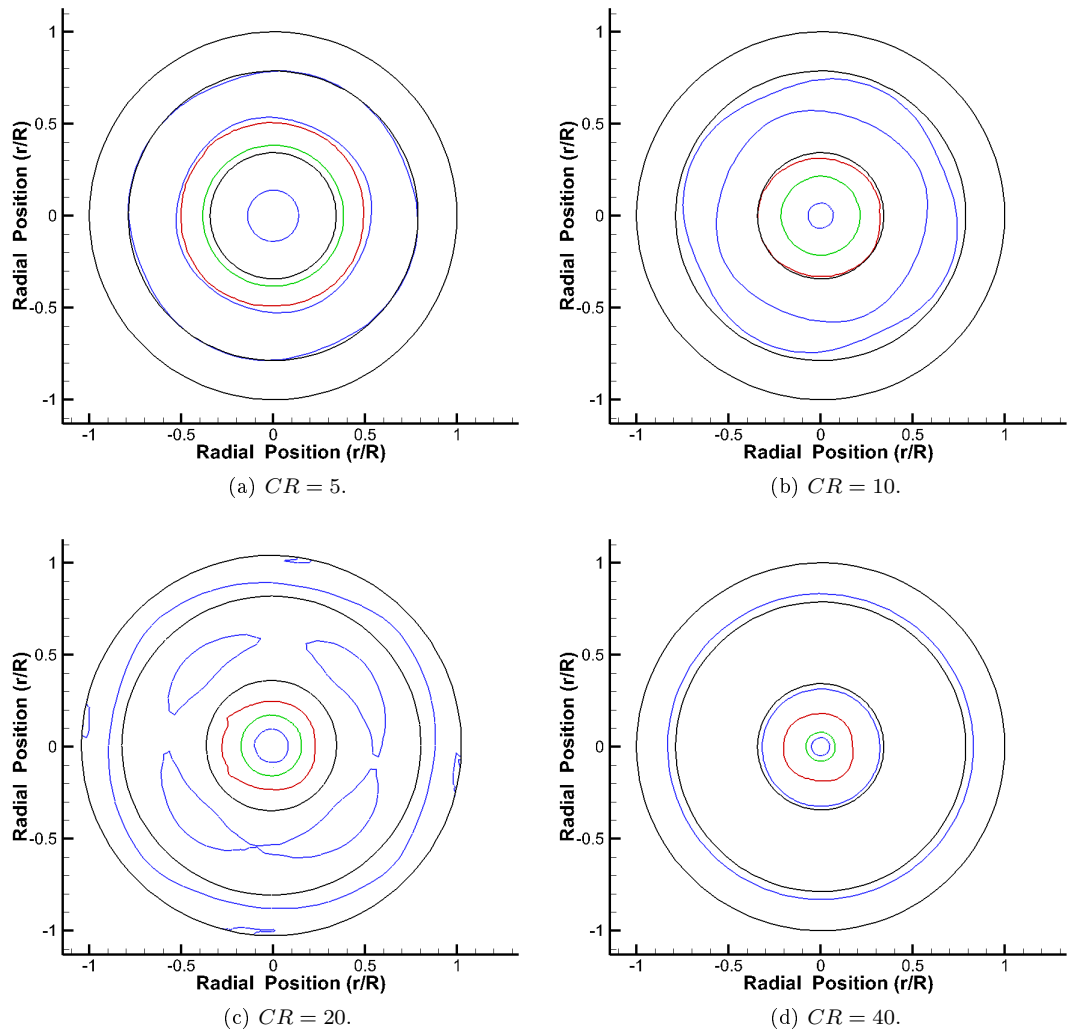
Figure 5.40: Axial plot of combined mantles and SBR for chambers with head injection.

(a) Azimuth angle ϕ.

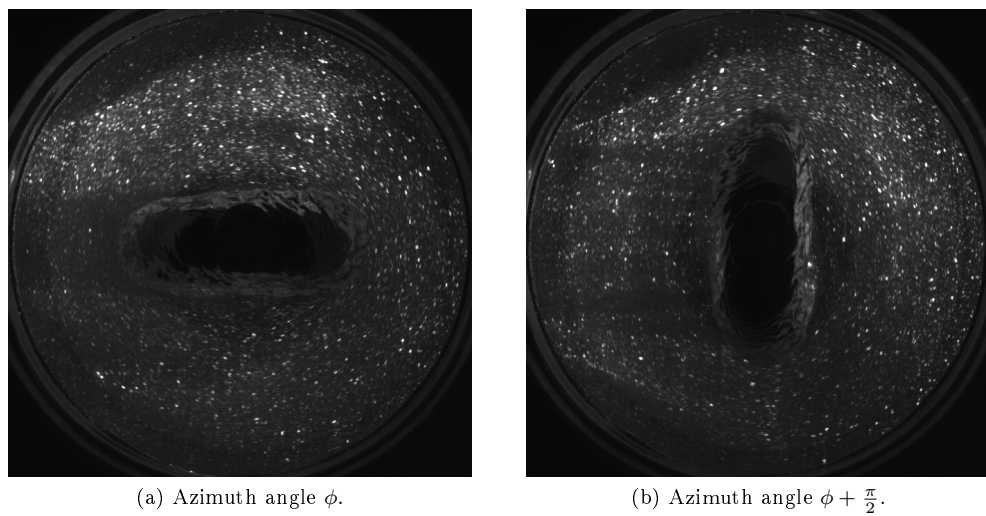(b) Azimuth angle $\phi + \frac{\pi}{2}$.

Figure 5.41: Azimuth plane PIV images for chamber configuration $CR = 5$ with head injectors.

As with the source PIV image seen in fig 5.33a for a chamber with $CR = 5$ and base injectors and the same chamber configuration with head injectors seen in fig 5.41, these both display significant vortex core deformation that is associated with a specific mode. If fig F.5 is referred to, then it is apparent that the vortex in fig 5.41 exhibits behaviour indicative of a columnar vortex being perturbed by mode $m = 2$. This also indicates that the vortices in chambers with base and head injectors are subject to different axial perturbations, which is likely attributed to the variation in chamber geometry, as the PIV data extracted shows that there is very little variation in the properties of the flow. Therefore the axial position of the injectors may play a vital role in affecting the local resonant wave structure that is established and may in turn significantly affect the mode shape of the mantle structure. The position of the injectors obviously has a great influence on the mantle structure, as represented by the 3D mantle structures seen for the inlet Reynolds number study in fig 5.14, but this was attributed to the localised increased kinetic energy perturbing the higher order modal structures. Either way, the various mode shapes that have been observed in the PIV data for chambers with both similar and dissimilar contraction ratios does indicate that chamber geometry greatly influences the structure of the vortex and incidentally the structure of the mantle.

## 5.6   Additional PIV analysis

A major problem with using 2D PIV to analyse confined vortices in the meridional plane of a hydrocyclone arises due to insufficient particle resolution. However, it is possible to circumvent the inabilities of planar PIV to describe the behaviour of the vortices if the full meridional cross section of the vortex is acquired and the flow is assumed to be axisymmetric as detailed in section D.3. As mentioned previously, this allows for any perspective distortion and vector contamination to be effectively removed and means that it is possible to properly resolve the mantle structure as errors in the axial velocity component are accounted for, although 3D stereoscopic PIV should always be employed if possible. Despite the PIV data that was acquired in the meridional plane being affected by these errors, it was found that the data obtained during the initial stages of the experiments may be suitable for analysis. Prior to acquisition of the bulk of PIV data presented thus far, several tests were conducted in order to calibrate the experimental rig and the PIV apparatus. The camera lens was configured using a lower f-stop and therefore larger aperture which allows an increased amount of incident light on the camera sensor. As a result of this, the images were deemed to be overexposed as there was significant light scatter from the seed particles, but this also meant that the contrast between the flow and the seed particles in the right half of the chamber was increased. Therefore it was possible to conduct cross correlation across the full cross section of the chamber, which meant that the velocity profiles in each part of the chamber could be combined, so that an average velocity profile could be obtained which also elucidates the structure of the mantle. Unfortunately the amount of chamber configurations for which corrected PIV data is available is limited, with the various axial velocity contour plots being presented in fig 5.42 in a similar format to previous results. Despite this, there is sufficient information available to assess the influence of contraction ratio in chamber configurations with head injectors over the full range of contraction ratios investigated, as seen in figs 5.43b-5.42h, while fig 5.43a depicts the axial velocity contour plot for a chamber configuration with base injectors and a contraction ratio of $CR = 5$. As with the results seen in the other parts of the investigation, the contraction ratio is the single parametric variable as the chamber aspect ratio remained constant at $\frac{L}{D} = 1.2$ and the inlet flow velocity was consistently $u_{in} = 1.88m/s$, which relates to a Reynolds number and Vortex number of $Re = 7.31 \times 10^4$ and $V = 4.83 \times 10^3$ respectively. It was possible to maintain a constant flow rate in these chamber configurations due to the addition of an Omega FL-1214 variable purge rotameter which was set at $Q = 3.15 \times 10^{-4}m^3/s$, although this was not required in later experiments. The mantles produced by CFD in the contraction ratio study have been elongated and presented along side the corrected PIV mantle structures, as the chamber aspect ratio study found that there is little variation in the mantle structure between chambers with aspect ratios in the range $\frac{L}{D} = 1.0 - 1.2$. Therefore this effectively allows for comparison of the experimental and numerical results to observe if there is any correlation in the form of their respective mantle structures.
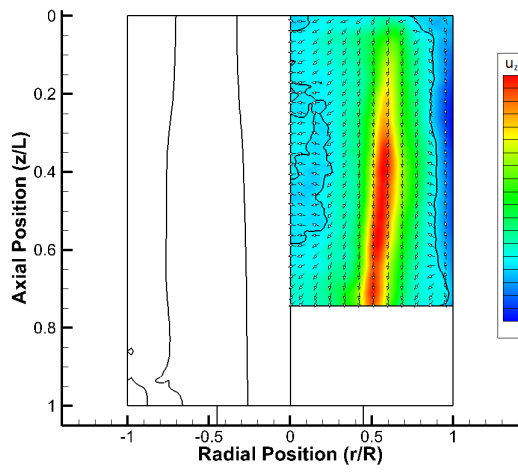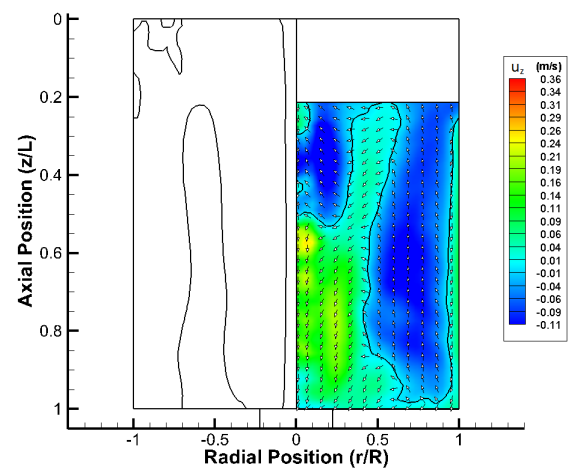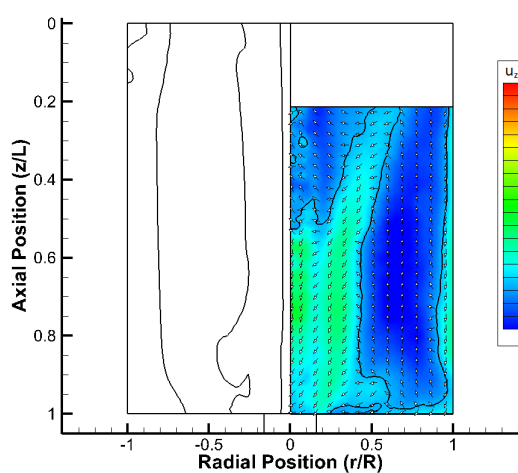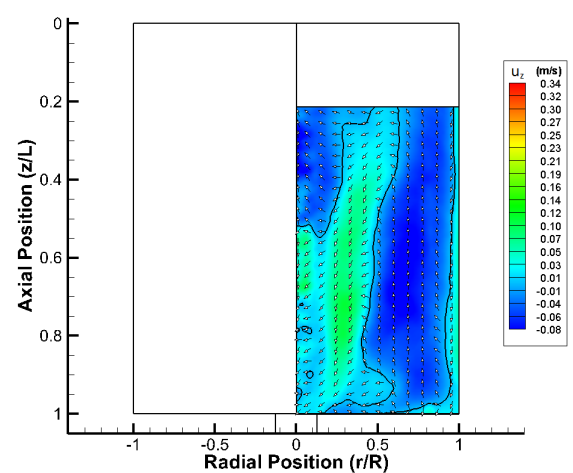
(a) Base $CR = 5$.
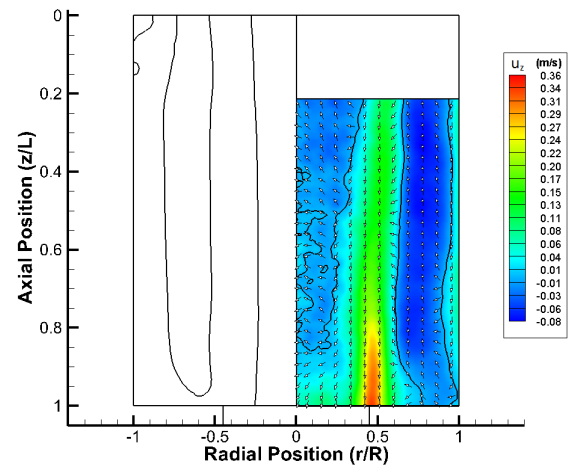
(b) Head $CR = 5$.
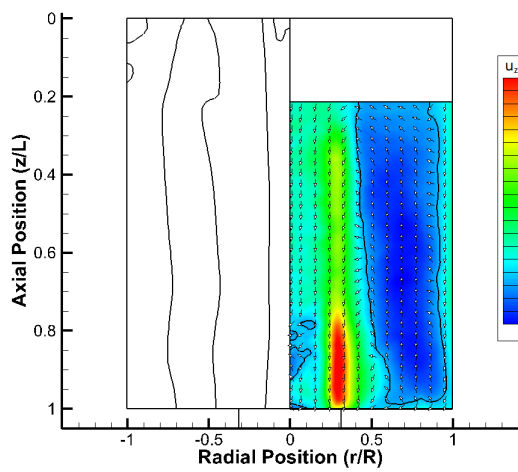
(c) Head $CR = 10$.

(d) Head $CR = 20$.

(e) Head $CR = 40$.

(f) Head $CR = 60$.
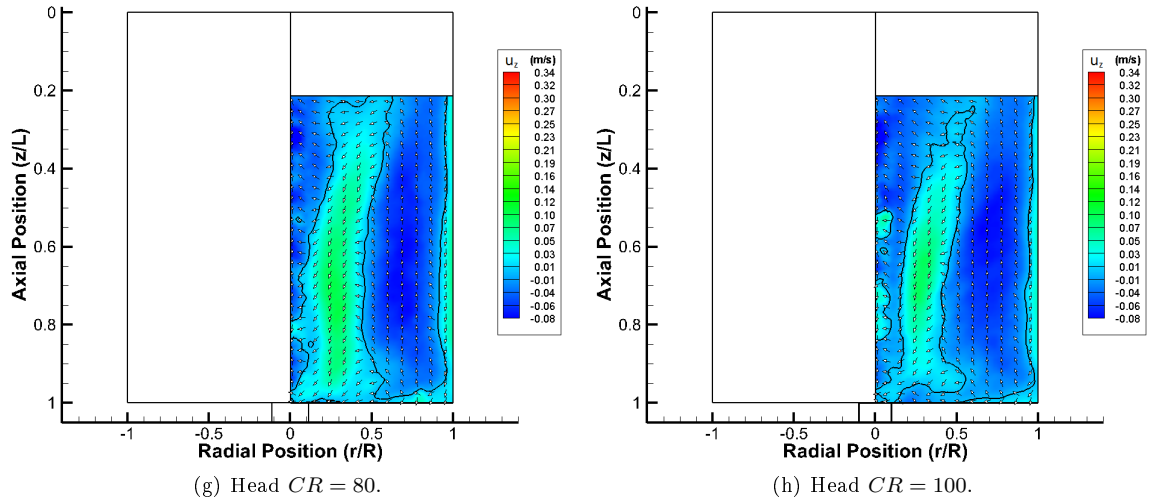
(g) Head $CR = 80$. (h) Head $CR = 100$.

Figure 5.42: Corrected PIV and CFD mantle structures.

It is immediately clear in fig 5.43a that the corrected PIV mantle is similar to that of the CFD results, in that it spans the length of the observable section of the chamber and occurs in the outer region of the chamber. However, the mantle extracted from the PIV data is positioned at an approximate radial position of $\frac{r}{R} = 0.88$, while the CFD mantle is located approximately at $\frac{r}{R} = 0.74$. The inlet flow conditions differ greatly between the data and could possibly affect the structure of the vortex and in turn the mantle structure. Despite evidence from the inlet Reynolds number study indicating that the inlet flow rate has little effect on the mantle structure, the inlet velocities for the corrected PIV data are considerably higher and it is unknown if a threshold exists above which there is a transition in the mantle structure as there is for geometrical parameters. This clearly warrants further investigation, but the vector map and corrected mantle structure in fig 5.43a does show that there is a single flow reversal as predicted by the CFD results. The experimental mantle structure seen in fig 5.43b is also shifted towards the periphery of the chamber relative to the numerical mantle, although the approximate radial positions of the inner and outer mantles are separated by a similar amount. Additionally the positive radial shift of the inner and outer mantles from the PIV data are shifted by approximately the same amount as seen for the similar chamber configuration with base injectors in fig 5.43b. This may be due to variations in the properties of the flow or possibly a systematic error, but again the experimental and numerical data are both in agreement that the double mantle structure results in a triple vortex. As the contraction ratio is increased to $CR = 10$, it can be seen in fig 5.43c that the separation between the individual mantles of the PIV data increases as the inner mantle tends towards the chamber axis. This is similar to the behaviour of the CFD mantle structures seen in the complementary internal dome study for chamber configurations with base injectors in section E.2, as the inner mantle aligned with the theoretical position revealed by the Beltramian solution. This widening of the mantle structure is indicative of a transitional state and when the contraction ratio of the chamber reaches $CR = 20$ it is apparent that there is further deformation of the mantle structure. Despite the central region of the flow where the PVC resides still being susceptible to error, the valid vectors that are calculated for the rest of the chamber cross section do indicate a transition in the mantle structure between chamber contraction ratios $CR = 10 - 20$ within the inner regions of the flow. The chamber configurations with contraction ratios in the range $CR = 20 - 100$, as displayed in figs 5.43d-5.42h respectively, all exhibit similar mantle structures and indicate an additional possible flow reversal adjacent the area of the results which are of dubious accuracy. This region can be approximately determined by the dimensions of the outlet, but the adjacent valid vectors are directed towards the head of the chamber and therefore must change direction as the flow approaches PVC boundary so that it can propagate along the vortex core and exit the chamber. If this is the case, then this means that there are 4 flow reversals occurring within these chamber configurations and indicates the presence of a quintuple

133

vortex. This demands further investigation to confirm whether a quintuple vortex is present, but irrespective of this, all the chamber configurations with head injectors in fig 5.42 clearly show the presence of a triple vortex structure. To the authors knowledge this is the first ever evidence confined coaxial bidirectional vortex triplets in a cyclonic devices and proves that it is possible to exceed the single mantle structure that is found in standard VIHRE configurations. The analytical solutions of the bidirectional vortex have always been formulated specifically to describe the flow in chamber configurations with base injectors and hypothesise on the possibility of multiple mantles. However, the results presented here not only establish that multiple flow reversals are possible, but that they can also be invoked in chamber configurations with head injectors.

Chapter 6

Evaluation

6.1 Introduction

The numerical and experimental methods employed in this investigation produced a vast amount of data that required extensive post-processing and analysis in order to extract relevant results. This wealth of data meant that it was possible to determine the effects of the various test parameters investigated, and make definitive conclusions regarding the influence of specific parameters on large scale coherent structures present in the flow. The results consistently exhibited what was initially thought to be anomalous behaviour and this was found to be caused by complex underlying mechanisms affecting the flow. Due to the lack of literature available regarding mantle structures and the physical mechanisms that cause their formation, it was necessary to investigate other areas of research associated with confined vortices in order resolve these anomalies. It was found that the dynamics of confined vortices are much more complex than initially anticipated and consideration of the spectral characteristics of the flow is required to provide explanations for the convoluted mantle structures that occur in cyclonic devices.

6.2 Conclusions

6.2.1 Methods

The hydrocyclone was found to be an acceptable analogue for investigating the complex vortices that occur in vortex rocket combustion chambers, as it operates in a similar manner to gas cyclones, which have been previously used to successfully investigate the non combusting flow in VIHRE configurations. CFD was found to be a suitable tool for simulating multiphase flow in a range of cyclonic devices and was able to accurately resolve a variety of features associated with confined vortices, such as the PVC and the air core that develops within it due to the radial pressure drop in chamber. It was also capable of calculating complex vortical flows containing convoluted mantles structures that provide evidence of multiple mantles and flow reversals, which has not previously been attempted. The RANS approach was found to be suitable for calculating complex vortical flows, but the RSM turbulence model represents the only viable RANS model that can be applied to such problems. Use of the RSM model was vital in resolving the individual Reynolds stresses, enabling reversed flow within the PVC so that the flow could be characterised correctly. In order to accurately resolve the flow and obtain a solution it is necessary to apply high order discretisation methods and relax the solution parameters to allow for an adequately converged solution to be achieved. A predominantly hexahedral mesh with increased mesh density near the axis of the chamber is also vital with regards to the accuracy and stability of the solution, so that the path of the flow is orthogonal to the orientation of the individual elements, despite the extra effort required during construction. Also the transient formulation of the CFD solver is required to resolve the PVC despite being a quasi steady state phenomenon, as the segregated steady state solver is unable account for the reversed flow along the chamber axis, which allows for the formation of the air

core. The VOF multiphase formulation was found to be the most suitable approach with regards to modelling hydrocyclonic flow due to the discrete distribution of the fluid phases, although the interface resolution was limited by the use of the modified HRIC discretisation scheme, which was the most accurate available method available in conjunction with other solver settings. Overall the optimum solver settings were applied considering the choice of the RSM turbulence model, where a compromise had to be made between solution accuracy and the complexity the numerical method, which would greatly impact the required amount of computational resources given the number of chamber configurations that needed to be investigated.

It is immediately apparent that 2D time resolved PIV is not suitable for observing the embedded mantle structure in cyclonic devices for a number of reasons, but the most pertinent is that is it unable to correctly resolve the axial velocity component, which is only accessible in the meridional plane of the chamber. The vortices produced within cyclonic devices are generally stable and because of this result in a quasi steady state flow, where the periodic behaviour of the flow is characterised by the rotation of the PVC. As the flow is essentially steady state, then the embedded mantle structure remains relatively constant over time and therefore a time resolved PIV method is not required, as a time averaged axial velocity field can sufficiently describe the structure of the mantle. 2D PIV methods are useful for characterising the structure of the flow in the azimuthal plane and have been shown to adequately resolve the forced and free regions of the vortex, and provide some evidence of modal structures in the tangential velocity component and the axial vorticity. This also allows for the relative strength of the vortex to be assessed in relation to variations in chamber geometry and is useful in determining the effects a single parameter has upon dimensional and scalar variables, such as the SBR transition or the air core radius. Discrepancies between the PIV and CFD data in the azimuthal plane are attributed to the axial position from which data was obtained, and the possible variation in local shear experienced by the flow caused by the proximity of a stationary boundary. This means that there is likely to be less discrepancy between the results if the interrogation plane is situated at the mid point of the chamber, where the increased shear associated with boundary proximity is not as prevalent.

Despite the limitations of planar PIV with regards to resolving the mantle structure in the meridional plane, a suitable method has been identified that can remove the detrimental influence of the significant out of plane tangential velocity component. However, this method is only applicable when images encapsulating the whole of the vortex chamber are acquired, in addition to sufficient particle resolution in the region of the chamber where illumination is affected by considerable light scatter from the PVC. This method is only applicable to the axial velocity component and requires the assumption of axisymmetry, as the mean velocity data is produced from the vector information calculated from both sides of the vortex chamber. It was possible to partially resolve the mantle structure for some chamber configurations, but unfortunately the majority of the PIV results in the meridional plane are meaningless. Overall, it is clear that in order to accurately resolve the individual velocity components of the flow and determine the mantle structure, it is vital that stereoscopic PIV measurements are obtained.

6.2.2   General observations

Despite the large variation observed in the structure of the mantle in response to the range of test parameters, the results suggest that the axial location of the injectors is also an important variable. This is because it is found to significantly affect the vortex structure and is instrumental in determining the characteristics of the flow. It was consistently found that for chamber configurations with base injectors, a single mantle that spans the length of the chamber will form, and is indicative of a standard coaxial bidirectional vortex. In chamber configurations with head injectors, there are effectively two mantles that form and span the length of the chamber, which indicates the presence of a triple vortex. The existence of this triple vortex in a cyclonic device has yet to be documented and the analytical solution omits the possibility of such a vortex, due to the assumption that multiple mantles can only occur in chamber configurations with base injectors. Therefore it provides crucial evidence that multiple flow reversals are possible and can be implemented in a range of applications where a cyclonic device is involved, whether it be vortex injection hybrid rockets or hydrocyclones.

The formation of the PVC is an integral part in the operation of cyclonic devices and therefore the influence it has upon the flow must be accounted for, which is especially relevant in the current investigation with regards to the definition of what a mantle is. The reversed flow within the PVC is separated from the rest of the core flow propagating towards the outlet of the chamber by a locus of zero axial velocity, which is by definition a mantle. It is not associated with flow reversal of the bulk flow, as it enters the chamber through the outlet and not through the tangential injectors, as well as being a different fluid in the case of a hydrocyclone. The radius of the air core is found to be dependent upon the contraction ratio of the chamber, as it is relatively invariant for all other test parameters investigated, but it does not affect the structure of the mantle and does not scale accordingly with variations in the radial transition of the SBR. When the chamber contraction ratio is constant, the radius of the air core calculated by the CFD will only vary by a discrete amount, in response to a significant variation in the structure of the mantle. Additionally the boundary of the air core is found to have negligible influence upon the radial positions of the mantle structure in the bulk fluid, which is especially noticeable in the contraction ratio study for chamber configurations with base injectors. Large variations in the radius of the air core are not reflected by the structure of the mantle, which remains relatively invariant, although there are large variations in both the radius of the air core and the mantle structure in chamber configurations with head injectors. In other parts of the study, the majority of variations in the mantle structure do not affect the radius of the air core, which suggests that both phenomenon are essentially independent of each other. More importantly, when the air core is considered to be a mantle, there are no correlations between the radial positions obtained by the numerical and analytical solutions, whereas they are in excellent agreement for multiple chamber configurations if the air core is omitted. Therefore, it can be assumed that the air core has negligible effect upon the structure of the mantle, although incorporation of the PVC into the analytical solution would aid in confirming whether this is true or not. Apart from the air core radius, it is additionally observed that there is no correlation between the dimensions of the SBR transition and the radial positions of the mantle structure. The radius of the forced vortex is also found to be heavily influenced by the contraction ratio of the chamber, but exhibits greater variation in radius, as it is also sensitive to variations in the magnitude of the velocity, which is primarily determined by the tangential velocity component.

Throughout the results, it is repeatedly found that the behaviour of the confined vortices and their associated embedded structures display evidence of complex characteristics that have not been widely observed experimentally in cyclonic devices, or predicted by the analytical Beltramian solutions. This primarily manifests itself as modal structures, which are detected in the distribution of velocity and vorticity components describing the behaviour of the flow. The concentric rings denoting the radial location of a mantle predicted by the analytical solutions are an example of modal structures, and are specific examples relating to cylindrical harmonics. The roots of the Bessel function of the first kind J_0 provides the radial positions of both the individual mantles and the nodes of a standing wave produced within a cylindrical geometry. However, the nodal structure of a standing wave is dependent upon the confining geometry and will deviate from a concentric ring form as the chamber geometry deviates from a purely cylindrical form. This is effect is directly observable in the 3D mantle structures produced by the CFD analysis, where the periodic structure of the mantle is caused by shear layer instability in the boundary layers attached to the axial boundaries of the chamber. These periodic structures indicate that the assumption of axisymmetry is invalid for real chamber geometries and that future analytical solutions must account for 3D effects in order to fully characterise the flow. It is important to note that while mode shapes are usually associated with structural mechanics, it is also possible for fluids to be affected by resonance if the correct conditions are applicable as they are for cyclonic devices.

Mode shapes are associated with specific resonant frequencies, and it is possible for a system to be subject to a range of frequencies which perturb several resonant modes, which then interact to form composite modal structures. The resulting geometry of the composite structure is an amalgam of the individual modal shapes, which is affected by the resonant amplitude of the individual constituent modes. This effect has been identified in close proximity to the axial boundaries of the vortex chamber, where the amplitude of additional non cylindrical modes is greater than at the mid point of the chamber. Therefore, there is significant evidence of periodicity in the mantle structure at these

axial boundaries, while the mantle is relatively unaffected at the mid point of the chamber where the chamber geometry is most representative of an infinite cylindrical geometry. This is supported by observations, that in chamber configurations with larger aspect ratios the mantle structure at the mid point of the chamber is less affected by non cylindrical mode shapes. In comparison to chamber configurations with low aspect ratios, where the reduced distance between the midpoint of the chamber and the axial boundaries causes the mantle structure to be affected by periodic mode shapes to a greater extent. This is also applicable to other velocity and vorticity components, which suggest that the chamber geometry has a significant effect upon the structure of the flow.

6.2.3 Inlet Reynolds number

The magnitude of the inlet velocity was found to have minimal impact upon the mantle structure over the range of inlet velocities investigated for both chamber configurations with base and head injectors. As the inlet velocity was increased this was reflected in the results obtained in the azimuthal plane of the chamber, as the tangential and radial velocity components increased accordingly as did the axial vorticity, signifying increased axial strain of the vortex and increased circulation as the strength of the vortex was effectively increased. Similarly the pressure drop in the chamber increased as the maximum static pressure within the chamber increased, although the pressure distribution was still found to correlate to the inverse square of the chamber radius. The CFD and PIV data differed with respect to the magnitude of the tangential and radial velocity components, as well as the radial location of the transition between the free and forced regions of the vortex, but this is attributed to the axial position of the interrogation plane and the differing amounts of local shear affecting the results.

The cross section of the mantle structure extracted from the CFD data in the azimuthal interrogation plane for chamber configurations with base injectors were in good agreement with the radial position predicted by the Beltrami based analytical solutions for the single mantle case. The well documented bidirectional vortex with a single mantle that spans the length of the chamber was observed, that results in a single flow reversal near the head of the chamber. However, the additional mantle structures that formed closed loop at the head of the chamber were not expected and no correlation between the numerical and analytical solutions was possible. Therefore the locus of zero axial velocity was only treated as a mantle for comparative purposes when it traverses the approximate full length of the chamber. When the azimuthal cross section mantle structures of the chamber configurations with head injectors were analysed, it was found that there is little correlation between the numerical and analytical results. This is likely due to the mantle structure being in a transitional state, which does not correspond with the simplified concentric cylindrical divisions predicted by the analytical solution. This is especially evident in other parts of the study, where the mantle structure morphs relative to the chamber geometry, and the radial positions of the numerical and analytical solutions converge when a specific form of the mantle structure is achieved. Despite this, the head injector chamber configurations resulted in a large mantle loop that can be considered to be two distinct mantles in the majority of the chamber and enabled a double flow reversal associated with a triple vortex flow. Additionally, significant evidence of periodicity in the structure of the mantle was observed in the chamber configurations with head injectors and was found to be most prominent at the axial boundaries of the chamber. This is most likely produced by the increased local shear produced between the stationary boundary and the intense rotating fluid, which possibly perturbs additional resonant frequencies of the chamber resulting in localised mode shapes.

6.2.4 Aspect ratio

As the chamber aspect ratio is reduced it is found that the relative strength of the vortex increases, as indicated by greater peak tangential velocities and axial vorticity, which is associated with general increases in all three velocity components. However, there is little variation in the radius of the SBR for both chamber configurations with base and head injectors, despite relatively large discrepancies in the magnitude of the tangential velocity component observed across the range of chambers investigated. This further corroborates the notion that the dimensions of the forced vortex are primarily affected by the contraction ratio of the chamber, as is the radius of the air core, which again only appears to exhibit a step variation in response to significant fluctuations in the mantle structure. The chamber aspect ratio is found to heavily influence the structure of the mantle and this is especially true for chamber configurations with head injectors, where there is no clear correlation between the form of these structures that occur for certain aspect ratios. For chamber configurations with base injectors, there is a definite evolution in the mantle structure as the aspect ratio is reduced from $\frac{L}{D} = 1.2$ to $\frac{L}{D} = 1.0$, where there is still a single mantle that spans the length of the chamber, but additionally there is a mantle loop that is attached to the head boundary of the chamber. This change in the mantle structure is accompanied by a sudden increase in the radius of the air core, although this is not reflected in the dimensions of the SBR. Similarly there is an increase in the radius of the air core for chamber configurations with head injectors as the aspect ratio is reduced from $\frac{L}{D} = 1.0$ to $\frac{L}{D} = 0.8$, which is also associated with a variation in the mantle structure but is considerably more evident.

The mantle loops that form in chamber configurations with base injectors with aspect ratios in the range of $\frac{L}{D} = 0.4 - 1.0$ occupy a similar axial proportion of the chamber and occur at a similar radial position. When these structures are compared directly there is a noticeable correlation as there is for the chamber configurations with aspect ratios in the range of $\frac{L}{D} = 1.2 - 1.4$, which effectively forms two distinct subsets of mantle structures. Despite this, the average radial position of the single mantle that spans the length of the chamber is in good agreement with the Beltramian solutions for all chamber configurations. This is not seen in the azimuthal interrogation plane due to the deformation of the mantle structure in the head region of the chamber. In the chamber configurations with head injectors, there are also two subsets of mantle structures for aspect ratios in the range of $\frac{L}{D} = 0.4 - 0.8$ and $\frac{L}{D} = 1.0 - 1.4$, which exhibit similar forms despite some variation in response to the chamber geometry. Again, it is found that each subset exhibits a different correlation to the radial positions predicted by the analytical solution, where below a threshold aspect ratio of $\frac{L}{D} = 1.0$ there is excellent agreement in the mantle structure, that relates to a triple vortex. Above this threshold value the correlation is poor, and suggests that as the mantle structure responds to variations in chamber geometry it will assume a relatively invariant form until another threshold value is exceeded, which causes transition to a new form. Overall, the aspect ratio of the vortex chamber is found to have a significant influence upon the mantle structure, which is likely due to the variation in chamber length altering the axial acoustics of the chamber and the associated resonant modes.

6.2.5 Contraction ratio

The contraction ratio was found to have the greatest impact on the characteristics of the vortex in relation to other test parameters investigated and also produced some similarly significant variations in the mantle structure, as seen in the chamber aspect ratio study. Through variation of the contraction ratio, it was possible to alter the dimensions of the air core and the forced vortex by considerable amounts, which was not possible for other test parameters as the dimensions of the inner regions of the vortex appear to be directly linked to the radius of the outlet. As the contraction was increased, it was observed that the relative strength of the vortex also increased, as further stretching of the vortex core results in greater tangential velocities. However, it was also observed that despite the increase in axial vorticity produced by reduction of the outlet radius, the magnitude of the tangential velocity component at the boundary of the SBR was greatest for chamber contraction ratios of $CR = 40$. Above this value the the peak tangential velocity was seen to decrease and may be due to a significant variation in the mantle structure, although it was not

possible to confirm this due to the lack of CFD data. The tangential velocity profiles acquired for chamber configurations with base and head injectors indicate that there is a transition in the general characteristics of the flow above contraction ratios of $CR = 20$, as the gradient of the free vortex deviates from that which is seen for chamber contraction ratios in the range of $CR = 5 - 20$. This is corroborated by the mantle structures obtained in the CFD analysis for chamber configurations with head injectors, where a significant change in the mantle structure occurs as the contraction ratio is increased from $CR = 20$ to $CR = 40$. The form of these mantles are similar to those of the subsets found in the aspect ratio study for chamber configurations with head injectors, when the chamber aspect ratio is decreased from $\frac{L}{D} = 1.0$ to $\frac{L}{D} = 0.8$. Both of these transitions are caused by variations in chamber geometry and are associated with an increase in the intensity of the vortex, and may indicate that a the kinetic energy must exceed a threshold amount in order to invoke a transition in the mantle structure. As the non dimensional radius of the air core is normalised by the chamber radius, there were no indications of a step variation in the air core radius in response to the large variation in the mantle structure. However, when the physical radius of the air core is normalised by the radius of the outlet, it is seen that there is a sudden variation in the radius for both chamber configurations with base and head injectors. Therefore this proves that large changes in the morphology of the mantle structure can be identified by distinct variations in the radius of the air core, as this was consistently observed in both the CFD and PIV analyses. Alternatively, another important observation is that the mantle structure is seemingly unaffected by large variations in the radius of the air core and suggests that the mantle can affect the air core but not vice versa as the phenomenon are not coupled.

The results obtained through CFD for the chamber configurations with base injectors and contraction ratios in the range $CR = 5 - 20$ all exhibit a single mantle that spans the length of the chamber, which occurs at approximately the same radial position, and are in good agreement with the analytical solution. As the contraction ratio is increased though, an inner mantle loop is established which increases in size relative to the increased intensity of the vortex as the flow is further confined. However, this behaviour is directly attributed to the influence of the chamber geometry rather than the intensity of the vortex, as the inlet Reynolds number study concluded that increased tangential velocity components have negligible effect upon the structure of the mantle. The results obtained for the chamber configurations with head injectors exhibit greater variations in the mantle structure with respect to the contraction ratio, and different forms exist for each contraction ratio. The most prominent transition occurs between chamber configurations with contraction ratios $CR = 20$ and $CR = 40$, but despite the differences in the mantle structures seen for contraction ratios in the range $CR = 5 - 20$ there are still obvious similarities which allow them to be considered as a subset.

The images acquired for the PIV analysis provide evidence of polygonal core structures which were identified by the boundary of the air core which correlate to specific azimuthal wave numbers. The most prominent polygonal structures occurred when the contraction ratio was $CR = 5$, where quadrilateral ($m = \pm 4$) and ellipse ($m = \pm 2$) vortex cores were observed in the chamber configurations with base and head injectors respectively. This indicates that the spectral characteristics of the confined vortices differ and must be produced by an axial perturbation of the vortex core as the flow has an axial component, which is necessary for mode structures to occur in columnar vortices. As the azimuth wave number of these vortices is different, then so must be the perturbation frequency of the core, which is influenced by chamber geometry and likely affected by the axial position of the injectors. The polygonal vortices observed in these chamber configurations were relatively stable and exhibit the same angular velocity, as they are subject to SBR like the forced vortex. However, evidence of polygonal air cores in other chamber configurations were observed that were unstable, with several mode shapes being temporarily visible and suggests that the structure of the vortex is in flux and unable to sustain a stable form. Alternatively it could be argued that it is instead subject to a triadic response, where the properties of the vortex are periodic with regards to geometry, but also in terms of time where a range of mode shapes will repeatedly occur over a set period.

6.2.6 Additional PIV

The corrected PIV results obtained in the meridional plane of the chamber provide the most important physical evidence of multiple mantle structures in the whole investigation and corroborate the findings of the numerical analysis. Despite the relatively small amount of data available, it was possible to identify different mantle structures that occur in chamber configurations with base and head injectors, as well as the axial direction of the flow in various regions of the chamber. It is well established that a single mantle will occur in cyclonic devices when the injectors are located at the base of the chamber, but it was previously unknown that it is possible to produce a triple vortex as defined by two individual mantles, when the injectors are instead located at the head of the chamber. Issues with the accuracy of the data in the central region of the flow is caused by the presence of an air core, but there is evidence of possible additional mantles, which may indicate the existence of quintuple vortices. Apart from this, it was also found that by increasing the contraction ratio of the chamber and reducing the radius of the outlet, it is possible to affect to structure of the mantle and the resultant characteristics of the flow. The mantle structures obtained from the PIV data were found to exhibit a significant variation in form between contraction ratios of $CR = 10 - 20$ as opposed to $CR = 20 - 40$, which was observed in the CFD analysis. However, this is attributed to the different aspect ratios of the chamber configurations that were used in the comparison and provides further evidence that chamber geometry has a significant effect upon the structure of the mantle.

6.2.7 Mantle structure maps

The various mantle structures observed throughout this investigation are complex and do not conform to discrete concentric ring structures which are defined by the analytical solutions. However, it is still possible to identify the specific forms of the mantle structure that occur in response to variation of geometrical parameters, which allows them to be classified and compared to each other. Fig 6.1 provides a visual means of assessing the effect various parameters such as inlet Reynolds number, chamber aspect ratio and contraction ratio have upon the structure of the mantle, as well as indicating the effects of the axial position of the injectors. For each parametric variable investigated the full range of the parameters are plotted against the number of mantles observed for each specific chamber configuration. Due to the complex form of the mantle structure it is difficult to assign a discrete number of mantles to many of the chamber configurations investigated, therefore the number of mantles in each chamber has been estimated to be a non integer value, based on observations in the meridional plane of the chamber. A single mantle is classified as the locus of zero axial velocity that spans the length of the chamber at any azimuth angle, and therefore may either span or not span the full length of the chamber at various azimuth angles. In doing this the complex conjoined mantle structures that are the result of periodicity are accounted for, while partial mantle structures will be defined by the non dimensional axial proportion of the chamber they occupy.

Overall, it is found that the inlet Reynolds number has a negligible effect upon the structure of the mantle, despite a single anomalous result suggesting otherwise, and both the results for the base and head injector configurations report a consistent number of mantles, relating to double and triple vortex flow respectively. The results for the aspect ratio study in fig 6.1b show that as the length of the chamber is reduced there is a gradual increase in the size of the inner partial mantle structure that occurs in chamber configurations with base injectors and indicates evolution in the mantle structure as it tends towards another form. Although this behaviour is not seen in the chamber configurations with head injectors, it must be noted that despite the consistent number of mantles observed that there is a very clear transition in the structure of the mantle between aspect ratios of $\frac{L}{D} = 0.8$ and $\frac{L}{D} = 1.0$. In fig 6.1c there is both CFD and PIV data available to discern the effects of the contraction ratio on the mantle structure, with the PIV data being provided by the corrected velocity contour maps of the meridional plane of the vortex chamber.

Despite the variation in the chamber aspect ratio between the CFD and PIV data it was felt that this would not significantly impact on the results, due to the similar mantle structures observed in the aspect ratio study for chamber configurations with aspect ratios of $\frac{L}{D} = 1.0$ and $\frac{L}{D} = 1.2$. The CFD data in fig 6.1c again shows that the mantle structure in the chamber configurations with

base injectors is affected by the parametric variable, while the chamber configuration with head injector are seemingly unaffected. This behaviour is similar to that seen in fig 6.1b, where the inner partial mantle structure for the base injector configurations is evolving in response to the increased contraction ratio. Where as the number of mantles in the head injector configurations remains constant, but again there is a very clear transition in the mantle structure between contraction ratios of $CR = 20$ and $CR = 40$. The PIV data however, suggests there is an additional partial inner mantle structure which occurs in chamber configurations with contraction ratios above $CR = 10$, which can be seen to grow as the contraction ratio is increased and the vortex is further confined. As mentioned previously, it is thought that the PIV data suggests evidence of a higher order flow reversal mode, although it is difficult to categorically say whether this is true or not due to the accuracy of the data in the core region of the flow. Despite this, the PIV data clearly shows that as the contraction ratio is increased there is a definite evolution in the mantle structure as it tends towards another form, which may possibly be a higher order flow reversal mode such as a quintuple vortex.
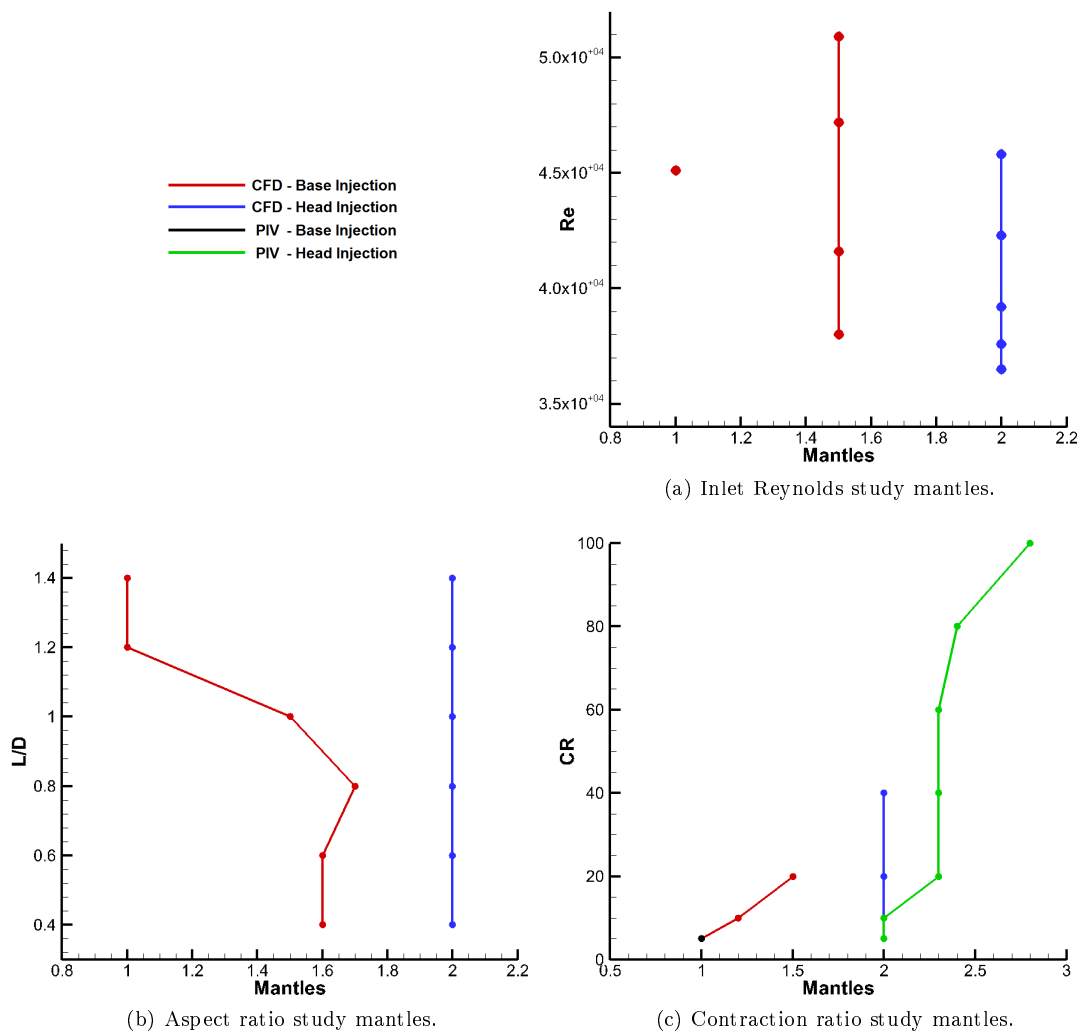

(a) Inlet Reynolds study mantles.

(b) Aspect ratio study mantles.

(c) Contraction ratio study mantles.

Figure 6.1: Mantle structure maps for parameters investigated.

6.2.8 Vortex core dynamics

The modal structures observed in the results are examples of cylindrical harmonics that are directly influenced by the chamber geometry, which defines the specific range of resonant modes that are possible and their associated frequencies. Resonance in fluids is caused by the propagation of internal waves, which are then reflected at solid boundaries, so that a standing wave is formed through superposition of the incident and reflected wave. The internal waves responsible for this are inertial waves, that can only occur in rotating fluids where the vortex is subject to SBR and axial perturbation. Inertial wave resonance will only occur if the axial perturbation frequency is less than twice the angular velocity of the flow $0 \leq \omega \leq 2\Omega$, as this relates to the limiting angle of the shear surfaces that are produced within the fluid as a result of wave propagation. A stable vortex is also necessary in order to sustain inertial waves, as radial oscillations are not possible otherwise as the Rayleigh stability criterion needs to be satisfied. The presence of a PVC indicates a stable vortical flow as it is a quasi steady state phenomenon with periodic properties with respect to time, which by definition is a vortex subject to axial perturbation.

The resonant modes of the vortex chamber geometry are identical to those of the fluid, as they are both defined by the same geometry and both exhibit nodes at radial positions described by the roots of the Bessel function of the first kind J_0. Therefore, the nodal structure predicted by modal analysis corresponds to the locus of zero axial velocity in a rotating fluid, and this mantle structure is produced by a specific arrangement of vortex cells. These vortex cells are subdivisions of the chamber geometry and define the tertiary behaviour of the flow, as well as determine flow reversal within the chamber. Manipulation of the vortex cell structure and the associated tertiary flow can be achieved through modulation of the axial perturbation frequency of the vortex core in order to invoke a different eigenmode or mantle structure.

It is possible to determine the spectral characteristics of a vortex core by acquiring the pressure time history at the centre of the chamber, then performing FFT in order to extract the resonant frequencies of the flow. The pressure oscillations which correspond to the axial perturbation frequency of the vortex core are caused by radial deformation in the structure of the vortex core at the head of the chamber. This variation in radius represents the amplitude of the transverse wave, which propagates axially along the vortex core and is responsible for the production of inertial waves which are emitted as conical waveforms, described by the ratio of the axial perturbation and angular frequencies of the fluid. These pressure oscillations can be used to determine the spectral content of the flow and means that it is also possible to produce forced pressure oscillations at the head of the chamber in order to perturb the local structure of the vortex core at specific frequencies. However, it is also possible to imbue the vortex core with specific spectral characteristics through pulsation of the inlet flow, where the inlet perturbation frequency will be reflected in the axial oscillation frequency of the vortex core. Therefore the PVC can be forced to oscillate at specific resonant frequencies that are associated with mantle structures that produce predetermined vortices with multiple flow reversals.

6.3 Summary

In this investigation it was intended to assess the effects of chamber geometry upon the embedded mantle structure and possibly determine whether it is possible to sustain confined vortices with multiple flow reversals. In pursuing this objective it was found that the fundamental fluid mechanics responsible for the mantle structure had to be investigated in order to reach any decisive conclusions. Many avenues of research were explored and produced results to varying degrees of success but the most important findings of this investigation are listed here:

- Vortices containing multiple mantles were observed and prove that confined vortices with multiple flow reversals are possible.

- The location of the tangential injectors has a significant influence on the mantle structure, with base and head injectors effectively producing an odd and even number of mantles respectively.

- Chamber configurations with head injectors repeatedly induced two flow reversals indicative of a triple vortex.

- Decreasing the chamber contraction ratio increases the intensity of the vortex and significantly affects the mantle structure.

- Reducing the chamber aspect ratio increases the intensity of the vortex and significantly affects the mantle structure.

- The inlet Reynolds number affects the intensity of the confined vortex, but has minimal effect upon the structure of the mantle.

- The mantle structure is inherently linked to the acoustic properties of the chamber and therefore directly influenced by chamber geometry.

- The mantle structure is an inertial mode caused by axial perturbation of the vortex core at the resonant frequencies of the chamber.

- The mantle exhibits evidence of both axisymmetry and periodicity, which is dependent on the position of the flow within the chamber.

- The structure of the mantle is complex and can not be simply defined by radial divisions of a cylindrical geometry.

- The mantle structure can experience substantial deformation in response to threshold geometrical parameters being exceeded.

- The angular frequency of the PVC scales linearly with respect to the inlet Reynolds number.

- 2D PIV is not suitable for investigating complex vortices in the meridional plane of the chamber and should not be used to resolve the mantle structure.

- 2D PIV is a suitable method for investigation of confined vortices in the azimuthal plane of the chamber, if the axial velocity component is relatively small.

- The hydrocyclone is an acceptable analog for investigation of complex vortices that are reported to occur in vortex rocket engines.

- The RANS based RSM turbulence model is suitable for performing CFD analysis of cyclonic flows and enabling initial characterisation of complex vortices.

6.4   Future work

It is hoped that this investigation has provided a scientific foundation for understanding the behaviour of embedded structures within confined vortical flows in response to geometrical parameters. Through identification of similar complex vortex behaviour in several other areas of research concerning vortex dynamics and through application of these findings to the current investigation, there is now scope for continued research into vortices exhibiting multiple flow reversals. This investigation provides a general overview of the effects of chamber geometry and identifies it as having a significant influence upon the mantle structure, although the observations made were passive, as they did not involve attempts to produce specific vortices. However, as the fundamental fluid mechanics describing the formation of the mantle structure is now known, future investigations concerning vortices with multiple flow reversals should be directed towards active control of the mantle structure, in order to produce vortices suitable for vortex injection hybrid rocket engine operations. Some of the possible future avenues of research are listed below and highlight several effective methods for observing and manipulating the properties of convoluted vortices:

- Modal analysis using FEM to extract the resonant frequencies of the vortex chamber to identify suitable PVC perturbation frequencies.

- Identify resonant frequencies that perturb both the independent and coupled axial and radial modes of the chamber to induce specific mantle structures.

- Use SEM to obtain high order DNS solutions of the flow to resolve the spectral characteristics of the vortex.

- Employ LES or DES fully transient FVM for increased solution accuracy and enhanced spectral resolution of the flow.

- Identify oscillating sources in numerical analyses that can induce resonance of inertial modes.

- Perform 3D stereoscopic PIV measurements in order to resolve the mantle structure in the meridional plane of the chamber.

- Attempt to eliminate the air core in hydrocyclonic flow and minimise the detrimental effects it has upon PIV measurements.

- Introduce controlled pressure pulses at the centre of the axial boundary at the head of the chamber to deform the vortex core.

- Pulse the inlet flow at predetermined frequencies to perturb the resonant modes of the vortex core.

- Observe conical shear layers and angular variation in response to perturbation frequency in cyclonic flow seeded with Kalliroscope flakes.

Bibliography

[1] M.J. Chiaverini and K.K. Kuo. *Fundamentals of hybrid rocket combustion and propulsion.* American Institute of Aeronautics and Astronautics, 2007.

[2] G.P. Sutton and O. Biblarz. *Rocket propulsion elements.* Wiley, 2011.

[3] A.K. Gupta. Swirl flows. 1984.

[4] T. Krepec, CK Kwok, and AI Georgantas. Vortex flow patterns in a cylindrical chamber. In *4th Fluid Mechanics, Plasma Dynamics and Lasers Conference*, volume 1, 1986.

[5] G.S. Haag. *Alternative geometry hybrid rockets for spacecraft orbit transfer.* PhD thesis, University of Surrey, 2001.

[6] G.S. Haag, M. Sweeting, and G. Richardson. Low cost propulsion development for small satellites at the surrey space centre. In *Proceeding of the 13th AIAA/USU Conference on Small Satellites, Logan, UT*, pages 1–10, 1999.

[7] WH Knuth, MJ Chiaverini, DJ Gramer, and JA Sauer. Experimental investigation of a vortex-driven high-regression rate hybrid rocket engine.

[8] E.M. Abu-Irshaid, J. Majdalani, and G. Casalis. Hydrodynamic instability of the bidirectional vortex. In *41 st AIAA/ASME/SAE/ASEE Joint Propulsion Conference & Exhibit*, pages 1–18, 2005.

[9] W.H. Knuth, M.J. Chiaverini, J. Sauer, and D.J. Gramer. Solid-fuel regression rate behavior of vortex hybrid rocket engines. *Journal of propulsion and power*, 18(3):600–609, 2002.

[10] W. Knuth, M. Chiaverini, JA Sauer, RH Whitesides, and R.A. Dill. Preliminary cfd analysis of the vortex hybrid rocket chamber and nozzle flow field. *AIAA Paper*, 1998.

[11] A.C. Hoffmann and L.E. Stein. *Gas cyclones and swirl tubes: principles, design and operation.* Springer Verlag, 2002.

[12] J.P. Vanyo. *Rotating fluids in engineering and science.* Dover Publications, 2001.

[13] Joshua W. Batterson, Joseph Majdalani, University of Tennessee Space Institute, Tullahoma, TN, and USA. On the viscous bidirectional vortex. part 2: Nonlinear beltramian motion. In *46th AIAA/ASME/SAE/ASEE Joint Propulsion Conference & Exhibit AIAA 2010-6764 25 - 28 July 2010, Nashville, TN*, 2010.

[14] A. Ogawa. *Vortex flow.* CRC, 1992.

[15] J.W. Batterson, B.A. Maicke, and J. Majdalani. Advancements in theoretical models of confined vortex flowfields. Technical report, DTIC Document, 2007.

[16] J.W. Batterson and J. Majdalani. Sidewall boundary layers of the bidirectional vortex. *Journal of Propulsion and Power*, 26(1):102, 2010.

[17] M.M. Ismailov. *Modeling of classical swirl injector dynamics.* PhD thesis, Purdue University, 2010.

[18] Joshua W. Batterson, Joseph Majdalani, University of Tennessee Space Institute, Tullahoma, TN, and USA. On the viscous bidirectional vortex. part 1: Linear beltramian motion. In *46th AIAA/ASME/SAE/ASEE Joint Propulsion Conference & Exhibit AIAA 2010-6763 25 - 28 July 2010, Nashville, TN*, 2010.

[19] Joshua W. Batterson, Joseph Majdalani, University of Tennessee Space Institute, Tullahoma, TN, and USA. On the viscous bidirectional vortex. part 3: Multiple mantles. In *46th AIAA/ASME/SAE/ASEE Joint Propulsion Conference & Exhibit AIAA 2010-6765 25 - 28 July 2010, Nashville, TN*, 2010.

[20] Wolfram. http://mathworld.wolfram.com/besselfunctionofthefirstkind.html.

[21] WS Lewellen, WJ Burns, and HJ Strickland. *Transonic swirling flow.* American Institute of Aeronautics and Astronautics, 1968.

[22] T. Saad and J. Majdalani. Energy based solutions of the bidirectional vortex with multiple mantles. 2009.

[23] A.B. Vyas, J. Majdalani, and M.J. Chiaverini. The bidirectional vortex. part 3: Multiple solutions. *AIAA Paper*, 5054:39, 2003.

[24] D. Fang, J. Majdalani, and M.J. Chiaverini. Simulation of the cold-wall swirl driven combustion chamber. *AIAA Paper*, 5055, 2003.

[25] M. Anderson, R. Valenzuela, C. Rom, R. Bonazza, and MJ Chiaverini. Vortex chamber flow field characterization for gelled propellant combustor applications. *AIAA Paper*, 4474, 2003.

[26] M. Slack. Application challenge: cyclone separator. *QNET, Sheffield, United Kingdom*, 2002.

[27] SV Alekseenko, PA Kuibin, and VL Okulov. *Theory of concentrated vortices.* Springer-Verlag Berlin Heidelberg, 2007.

[28] Ansys. *Fluent Users Manual 6.4*, 2005.

[29] MJ Jhung, WT Kim, and YH Ryu. Dynamic characteristics of cylindrical shells considering fluid–structure interaction. *Nucl. Eng. Technol*, 41(10):1333–1346, 2009.

[30] K.H. Baines, T.W. Momary, L.N. Fletcher, A.P. Showman, M. Roos-Serote, R.H. Brown, B.J. Buratti, R.N. Clark, and P.D. Nicholson. Saturn's north polar cyclone and hexagon at depth revealed by cassini/vims. *Planetary and Space Science*, 57(14):1671–1681, 2009.

[31] T.R.N. Jansson, M.P. Haspang, K.H. Jensen, P. Hersen, and T. Bohr. Polygons on a rotating fluid surface. *Physical review letters*, 96(17), 2006.

[32] P. George, S. Krishnan, PM Varkey, M. Ravindran, and L. Ramachandran. Fuel regression rate enhancement studies in htpb/gox hybrid rocket motors. *AIAA paper 98*, 3188, 1998.

[33] K.K. Kuo, G.A. Risha, B.J. Evans, and E. Boyer. Potential usage of energetic nano-sized powders for combustion and rocket propulsion. In *MRS Proceedings*, volume 800. Cambridge Univ Press, 2003.

[34] M.A. Karabeyoglu, B.J. Cantwell, and J. Stevens. Evaluation of homologous series of normal-alkanes as hybrid rocket fuels. In *41 st AIAA/ASME/SAE/ASEE Joint Propulsion Conference & Exhibit*, pages 1–42, 2005.

[35] H. Arisawa and TB Brill. Flash pyrolysis of hydroxyl-terminated polybutadiene (htpb) ii: Implications of the kinetics to combustion of organic polymers. *Combustion and flame*, 106(1):144–154, 1996.

[36] H. Arisawa and TB Brill. Flash pyrolysis of hydroxyl-terminated polybutadiene (htpb) i: Analysis and implications of the gaseous products. *Combustion and flame*, 106(1):131–143, 1996.

[37] R. J. Muzzy. Schlieren and shadowgraph studies of hybrid boundary layer combustion. *AIAA Journal*, vol.1 no.9 (2159-2160), 1963.

[38] B. Cantwell, A. Karabeyoglu, and D. Altman. Recent advances in hybrid propulsion. *International Journal of Energetic Materials and Chemical Propulsion*, 9(4), 2010.

[39] J.Z. Wu, H.Y. Ma, and M.D. Zhou. *Vorticity and vortex dynamics*. Springer, 2006.

[40] Pointwise. *Pointwise Manual*, 2011.

[41] M. Raffel, C.E. Willert, and J. Kompenhans. *Particle image velocimetry: a practical guide*. Springer Verlag, 1998.

[42] TSI. *Insight 4G Tutorial Guide*, 2011.

[43] TSI. *Insight 4G User's Guide*, 2011.

[44] Z. Liu, J. Jiao, and Y. Zheng. Study of axial velocity in gas cyclones by 2d-piv, 3d-piv, and simulation. *China Particuology*, 4(3):204–210, 2006.

[45] H.P. Greenspan. *The theory of rotating fluids*. H, P. Greenspan, 1990.

[46] J. Noir, D. Brito, K. Aldridge, P. Cardin, et al. Experimental evidence of inertial waves in a precessing spheroidal cavity. *Geophys. Res. Lett*, 28(19):3785–3788, 2001.

[47] R. Batchelor, HM Blackburn, and R. Manasseh. Simulations of axisymmetric inertial waves in a rotating container of fluid. 2010.

[48] J. D'Elía, N. Nigro, and M. Storti. Numerical simulations of axisymmetric inertial waves in a rotating sphere by finite elements. *International Journal of Computational Fluid Dynamics*, 20(10):673–685, 2006.

[49] Y. Duguet, J.F. Scott, and L. Le Penven. Oscillatory jets and instabilities in a rotating cylinder. *Physics of Fluids*, 18:104104, 2006.

[50] T. Dauxois, G. Bordes, F. Moisy, P.P. Cortet, et al. Experimental evidence of a triadic resonance of plane inertial waves in a rotating fluid. *Bulletin of the American Physical Society*, 57, 2012.

[51] F. Moisy, O. Doaré, T. Pasutto, O. Daube, and M. Rabaud. Experimental and numerical study of the shear layer instability between two counter-rotating disks. *Journal of Fluid Mechanics*, 507:175–202, 2004.

[52] D. Crowdy. Polygonal n-vortex arrays: A stuart model. *Physics of Fluids*, 15:3710, 2003.

[53] D.G. Crowdy. Exact solutions for rotating vortex arrays with finite-area cores. *Journal of Fluid Mechanics*, 469:209–235, 2002.

[54] E. Laudien, R. Pongratz, R. Pierro, and D. Preclik. Experimental procedures aiding the design of acoustic cavities. *Progress in Astronautics and Aeronautics*, 169:377–402, 1995.

[55] B. Ahn, M. Ismailov, and SD Heister. Experimental study swirl injector dynamic response using a hydromechanical pulsator. 2012.

[56] JL Smith Jr. An experimental study of the vortex in the cyclone separator. *Journal of Basic Engineering*, 84:602, 1962.

[57] W.H. Knuth, M. J. Chiaverini, D.J. Gramer, and J.A. Sauer. Development and testing of a vortex-driven, high-regression rate hybrid rocket engine (phase i). In *AIAA/ASME/SAE/ASEE Joint Propulsion Conference and Exhibit, 34th*, Cleveland, OH, 1998.

[58] EE Rice, DJ Gramer, C.P.S. Clair, and MJ Chiaverini. Mars isru co/o2 rocket engine development and testing. In *Seventh International Workshop on Microgravity Combustion and Chemically Reacting Systems*, page 101, 2003.

[59] M.J. Nusca and R.S. Michaels. Progress in the development of a computational model for the army's impinging stream vortex engine. In *The 40th AIAA/ASME/SAE/ASEE Joint Propulsion Conference*, 2004.

[60] A.B. Vyas and J. Majdalani. Characterization of the tangential boundary layers in the bidirectional vortex thrust chamber. *AIAA Paper*, 4888, 2006.

[61] A.B. Vyas, J. Majdalani, and M.J. Chiaverini. The bidirectional vortex. part 2: viscous core corrections. In *Proceedings of the 39th AIAA/ASME/SAE/ASEE Joint Propulsion Conference and Exhibit, USA*, page 5053, 2003.

[62] A.B. Vyas, J. Majdalani, and MJ Chiaveini. The bidirectional vortex. part 1: An exact inviscid solution. *AIAA paper*, 5052:39, 2003.

[63] N.J. Wall. Investigation of hybrid rocket technology. Master's thesis, Sheffield, 2006.

[64] W.H. Knuth. Personal communication, 2006.

[65] V.K. Dhir and F. Chang. Heat transfer enhancement using tangential injection. *ASHRAE Transactions*, vol 98, Part 2 (383-390), 1992.

[66] G. Marxman and M. Gilbert. Turbulent boundary layer combustion in the hybrid rocket. In *Symposium (International) on Combustion*, volume 9, pages 371–383. Elsevier, 1963.

[67] M. J. Chiaverini, G. C. Harting, Y. C. Lu, K. K. Kuo, A. Peretz, H. S. Jones, B. S. Wygle, and J. P. Arves. Pyrolysis behavior of hybrid-rocket solid fuels under rapid heating conditions. *Journal of Propulsion and Power*, 15(6):888–895, 1999.

[68] N. Syred. 40 years with swirl, vortex, cyclonic flows, and combustion. In *49th AIAA Aerospace Sciences Meeting including the New Horizons Forum and Aerospace Exposition 4 - 7 January 2011, Orlando, Florida*.

[69] A.B. Vyas and J. Majdalani. Exact solution of the bidirectional vortex. *AIAA journal*, 44(10):2208–2216, 2006.

[70] J. Majdalani and E. K. Halpenny. The bidirectional vortex with sidewall injection. In *44th AIAA/ASME/SAE/ASEE Joint Propulsion Conference and Exhibit*, 2008.

[71] BA Maicke and J. Majdalani. Heuristic representation of the swirl velocity in the core of the bidirectional vortex. *AIAA Paper*, 4122, 2007.

[72] Joshua W. Batterson, Joseph Majdalani, University of Tennessee Space Institute, Tullahoma, and TN. On the boundary layers of the bidirectional vortex. In *37th AIAA Fluid Dynamics Conference and Exhibit AIAA 2007-4123 25 - 28 June 2007, Miami, FL*, 2007.

[73] GH Vatistas, S. Lin, and CK Kwok. Theoretical and experimental studies on vortex chamber flows. *AIAA journal*, 24:635–642, 1986.

[74] AJ Hoekstra, JJ Derksen, and HEA Van Den Akker. An experimental and numerical study of turbulent swirling flow in gas cyclones. *Chemical Engineering Science*, 54(2055):2065, 1999.

[75] J. Majdalani, D. Fang, and S.W. Rienstra. On the bidirectional vortex and other similarity solutions in spherical geometry. *AIAA Paper*, 3675, 2004.

[76] J. Majdalani. Exact eulerian solutions of the cylindrical bidirectional vortex. *AIAA Paper*, 5307, 2009.

[77] M.J. Chiaverini, M.J. Malecki, J.A. Sauer, WH Knuth, and J. Majdalani. Vortex thrust chamber testing and analysis for o2-h2 propulsion applications. *AIAA Paper*, 4473, 2003.

[78] MIG Bloor and DB Ingham. Flow in industrial cyclones. *Journal of Fluid Mechanics*, 178(1):507–519, 1987.

[79] C.J. Rom, M.H. Anderson, and M.J. Chiaverini. Cold flow analysis of a vortex chamber engine for gelled propellant combustor applications. In *40 th AIAA/ASME/SAE/ASEE Joint Propulsion Conference and Exhibit*, 2004.

[80] Tony Saad, Joseph Majdalani, University of Tennessee Space Institute, Tullahoma, and TN. Energy based solutions of the bidirectional vortex. In *44th AIAA/ASME/SAE/ASEE Joint Propulsion Conference & Exhibit AIAA 2008-4832 21 - 23 July 2008, Hartford, CT*, 2008.

[81] Joshua Batterson and Joseph Majdalani. Biglobal instability of the bidirectional vortex. part 1: Formulation. In *Joint Propulsion Conferences*, pages –. American Institute of Aeronautics and Astronautics, July 2011.

[82] Tony Saad and Joseph Majdalani. Viscous flows revisited in simulated rockets with radially regressing walls. In *Joint Propulsion Conferences*, pages –. American Institute of Aeronautics and Astronautics, July 2011.

[83] RJ Woolhouse, JR Tippetts, and S.B.M. Beck. A comparison of the experimental and computational modelling of the fluidic turn-up vortex amplifier at full and zero swirl conditions. *Proceedings of the Institution of Mechanical Engineers, Part C: Journal of Mechanical Engineering Science*, 215(8):893–903, 2001.

[84] Joshua Batterson and Joseph Majdalani. Biglobal instability of the bidirectional vortex. part 2: Complex lamellar and beltramian motions. In *Joint Propulsion Conferences*, pages –. American Institute of Aeronautics and Astronautics, July 2011.

[85] R. Harwood and M. Slack. Cfd analysis of a cyclone. *QNET-CFD Network Newsletter*, 1(4):25–27, 2002.

[86] TG Chuah, J. Gimbun, and T.S.Y. Choong. A cfd study of the effect of cone dimensions on sampling aerocyclones performance and hydrodynamics. *Powder technology*, 162(2):126–132, 2006.

[87] J. Gimbun, TG Chuah, T.S.Y. Choong, and A. Fakhru'l-Razi. Prediction of the effects of cone tip diameter on the cyclone performance. *Journal of aerosol science*, 36(8):1056–1065, 2005.

[88] J. Gimbun, TG Chuah, A. Fakhru'l-Razi, and T.S.Y. Choong. The influence of temperature and inlet velocity on cyclone pressure drop: a cfd study. *Chemical Engineering and Processing: Process Intensification*, 44(1):7–12, 2005.

[89] I. Karagoz and F. Kaya. Cfd investigation of the flow and heat transfer characteristics in a tangential inlet cyclone. *International Communications in Heat and Mass Transfer*, 34(9):1119–1126, 2007.

[90] F. Kaya and I. Karagoz. Performance analysis of numerical schemes in highly swirling turbulent flows in cyclones. *Current science*, 94(10):1273–1278, 2008.

[91] K.U. Bhaskar, Y.R. Murthy, M.R. Raju, S. Tiwari, JK Srivastava, and N. Ramakrishnan. Cfd simulation and experimental validation studies on hydrocyclone. *Minerals Engineering*, 20(1):60–71, 2007.

[92] M. Brennan. Cfd simulations of hydrocyclones with an air core: comparison between large eddy simulations and a second moment closure. *Chemical Engineering Research and Design*, 84(6):495–505, 2006.

[93] M.S. Brennan, M. Narasimha, and P.N. Holtham. Multiphase modelling of hydrocyclones– prediction of cut-size. *Minerals engineering*, 20(4):395–406, 2007.

[94] J.A. Delgadillo and R.K. Rajamani. Exploration of hydrocyclone designs using computational fluid dynamics. *International Journal of Mineral Processing*, 84(1):252–261, 2007.

[95] J.A. Delgadillo and R.K. Rajamani. A comparative study of three turbulence-closure models for the hydrocyclone problem. *International journal of mineral processing*, 77(4):217–230, 2005.

[96] W.K. Evans, A. Suksangpanomrung, and A.F. Nowakowski. The simulation of the flow within a hydrocyclone operating with an air core and with an inserted metal rod. *Chemical Engineering Journal*, 143(1):51–61, 2008.

[97] R. Gupta, MD Kaulaskar, V. Kumar, R. Sripriya, BC Meikap, and S. Chakraborty. Studies on the understanding mechanism of air core and vortex formation in a hydrocyclone. *Chemical Engineering Journal*, 144(2):153–166, 2008.

[98] MJ Leeuwner and JJ Eksteen. Computational fluid dynamic modelling of two phase flow in a hydrocyclone. *Journal-South African Institute of Mining and Metallurgy*, 108(4):231, 2008.

[99] M. Narasimha, M. Brennan, and PN Holtham. Large eddy simulation of hydrocyclone predic- tion of air-core diameter and shape. *International Journal of Mineral Processing*, 80(1):1–14, 2006.

[100] A. Raoufi, M. Shams, M. Farzaneh, and R. Ebrahimi. Numerical simulation and optimiza- tion of fluid flow in cyclone vortex finder. *Chemical Engineering and Processing: Process Intensification*, 47(1):128–137, 2008.

[101] R. Sripriya, MD Kaulaskar, S. Chakraborty, and BC Meikap. Studies on the performance of a hydrocyclone and modeling for flow characterization in presence and absence of air core. *Chemical Engineering Science*, 62(22):6391–6402, 2007.

[102] B. Wang and AB Yu. Numerical study of particle–fluid flow in hydrocyclones with different body dimensions. *Minerals Engineering*, 19(10):1022–1033, 2006.

[103] C.G. Speziale, S. Sarkar, and T.B. Gatski. Modelling the pressure–strain correlation of turbu- lence: an invariant dynamical systems approach. *Journal of Fluid Mechanics*, 227(1):245–272, 1991.

[104] MM Gibson and BE Launder. Ground effects on pressure fluctuations in the atmospheric boundary layer. *Journal of Fluid Mechanics*, 86(03):491–511, 1978.

[105] G. Halász, B. Gyure, I.M. Jánosi, K.G. Szabó, and T. Tél. Vortex flow generated by a magnetic stirrer. *arXiv preprint physics/0702199*, 2007.

[106] Y. Chung, T. Khil, J. Yoon, Y. Yoon, and V. Bazarov. Experimental study on simplex swirl injector dynamics with varying geometry. *International Journal of Aeronautical and Space Sciences*, 12:57–62, 2011.

[107] Q. Fu and L. Yang. Theoretical investigation of the dynamics of a gas-liquid coaxial swirl injector. *Journal of Propulsion and Power*, 27(1):144, 2011.

[108] Q. Fu, L. Yang, Y. Qu, and B. Gu. Geometrical effects on the fluid dynamics of an open-end swirl injector. 2011.

[109] M. Ismailov, S.D. Heister, and E. Kim. Dynamic response of rocket swirl injectors, part i: Wave reflection and resonance. *Journal of Propulsion and Power*, 27(2):402–411, 2011.

[110] C.J Stairman. Pressure drop in cyclone separator. 1949.

[111] W Barth. Brennstoff-warme-kraft. 1956.

[112] L. D. Strand, M. D. Jones, and R. L. Ray. Characterization of hybrid rocket internal heat flux and htpb fuel pyrolysis. In *ASME, SAE, and ASEE, Joint Propulsion Conference and Exhibit, 30th*, volume AIAA-1994-2876, Indianapolis, IN, 1994.

[113] MA Karabeyoglu, D. Altman, and B.J. Cantwell. Combustion of liquefying hybrid propellants: Part 1, general theory. *Journal of propulsion and power*, 18(3):610–620, 2002.

[114] MA Karabeyoglu and B.J. Cantwell. Combustion of liquefying hybrid propellants: Part 2, stability of liquid films. *Journal of propulsion and power*, 18(3):621–630, 2002.

[115] P. Estey, D. Altman, J. McFarlane, et al. An evaluation of scaling effects for hybrid rocket motors. *AIAA Paper*, 2517, 1991.

[116] GA Marxman, CE Wooldridge, and RJ Muzzy. Fundamentals of hybrid boundary layer combustion. *Progress in Astronautics and Aeronautics*, 15:485–522, 1964.

[117] LD Smoot and CF Price. Regression rates of metalized hybrid fuel systems. *AIAA Journal*, 4(5):910–915, 1966.

[118] RJ Muzzy. Applied hybrid combustion theory. In *Proceedings of the 8th AIAAISAE Joint Propulsion Specialist Conference*, 1972.

[119] JH Faler and S. Leibovich. Disrupted states of vortex flow and vortex breakdown. *Physics of Fluids*, 20(9):1385, 1977.

[120] SV Alekseenko, PA Kuibin, VL Okulov, and SI Shtork. Helical vortices in swirl flow. *Journal of Fluid Mechanics*, 382(1):195–243, 1999.

[121] H. Jcr, AA Wray, and P. Moin. Eddies, stream, and convergence zones in turbulent flows. *Center for Turbulence Research Report CTR-S88*, pages 193–208, 1988.

[122] J. Jeong and F. Hussain. On the identification of a vortex. *Journal of Fluid Mechanics*, 285(69):69–94, 1995.

[123] Z. Liu, Y. Zheng, L. Jia, J. Jiao, and Q. Zhang. Stereoscopic piv studies on the swirling flow structure in a gas cyclone. *Chemical engineering science*, 61(13):4252–4261, 2006.

[124] L. Kelvin. Vibrations of a columnar vortex. *Phil. Mag*, 10(5):155–168, 1880.

[125] PG Saffman. Vortex dynamics. *Cambrige Monographs on Mechanics and Applied Mathematics. Cambridge University Press, reprint*, 1993.

[126] S. Chandrasekhar. Hydrodynamic and hydromagnetic stability. 1961. *Clarendon Press: Oxford). 0.0 0.5*, 1:1–5.

[127] D. Fultz. A note on overstability and the elastoid-inertia oscillations of kelvin, solberg, and bjerknes. *Journal of Meteorology*, 16(2):199–208, 1959.

[128] V. Bjerknes, J. Bjerknes, H.S. Solberg, and T. Bergeron. *Physikalische Hydrodynamik: mit Anwendung auf die dynamische Meteorologie*. J. Springer, 1933.

[129] H. Gortler. On forced oscillations in rotating fluids. In *Proc. 5th Midwestern Conf. on Fluid Mech*, pages 1–10, 1957.

[130] H. Oser. Erzwungene schwingungen in rotierenden flüssigkeiten. *Archive for Rational Mechanics and Analysis*, 1(1):81–96, 1957.

[131] H. Oser. Experimentelle untersuchung über harmonische schwingungen in rotierenden flüssigkeiten. *ZAMM-Journal of Applied Mathematics and Mechanics/Zeitschrift für Angewandte Mathematik und Mechanik*, 38(9-10):386–391, 2006.

[132] K.D. Aldridge. *An experimental study of axisymmetric inertial oscillations of a rotating liquid sphere*. PhD thesis, Massachusetts Institute of Technology, 1967.

[133] HM Blackburn and SJ Sherwin. Formulation of a galerkin spectral element–fourier method for three-dimensional incompressible flows in cylindrical geometries. *Journal of Computational Physics*, 197(2):759–778, 2004.

[134] L. Messio, C. Morize, M. Rabaud, and F. Moisy. Experimental observation using particle image velocimetry of inertial waves in a rotating fluid. *Experiments in Fluids*, 44(4):519–528, 2008.

[135] G. Gauthier, P. Gondret, F. Moisy, and M. Rabaud. Instabilities in the flow between co-and counter-rotating disks. *Journal of Fluid Mechanics*, 473:1–21, 2002.

[136] A.C. Barbosa Aguiar, P.L. Read, R.D. Wordsworth, T. Salter, and Y. Hiro Yamazaki. A laboratory model of saturn's north polar hexagon. *Icarus*, 206(2):755–763, 2010.

[137] R. Hide and CW Titman. Detached shear layers in a rotating fluid. *J. Fluid Mech*, 29(1):39–60, 1967.

[138] V. Yang. *Liquid rocket engine combustion instability*. Number 169. Aiaa, 1995.

[139] VG Bazarov. Liquid injector dynamics. *Mashinostroenie, Moscow*, 1979.

[140] VG Bazarov, V. Yang, P. Puneesh, V. Yang, M. Habiballah, J. Hulka, and M. Popp. Design and dynamics of jet and swirl injectors. *Liquid Rocket Thrust Chambers: Aspect of Modeling, Analysis, and Design, Progress in Astronautics and Aeronautics*, 200:19–104, 2004.

[141] M. Ismailov, S.D. Heister, and E. Kim. Dynamic response of rocket swirl injectors, part ii: Nonlinear dynamic response. *Journal of Propulsion and Power*, 27(2):412–421, 2011.

[142] H. Park. Flow characteristics of viscous high-speed jets in axial/swirl injectors. 2005.

[143] R. Richardson. *Linear and nonlinear dynamics of swirl injectors*. ProQuest, 2007.

Appendix A

Hybrid rocket combustion

A.1   Introduction

The combustion processes in a hybrid rocket engine differ from those that occur in liquid and solid rocket engines, as combustion occurs within the boundary layer adjacent to the fuel surface and is controlled by a diffusion flame rather than a premixed flame. Due to the use of both solid and liquid propellants, hybrid rockets introduce many of the difficulties associated with other rocket technologies, while providing additional issues associated with diffusion based combustion. The focus of research into hybrid rocket operation is predominantly directed towards characterising fuel regression rates and understanding the fundamental processes of combustion in classic engine configurations. As new methods for increasing engine performance are discovered, the findings of existing studies of combustion in classic engine configurations will need to be adapted for use in more complex engine designs.

A.2   Propellant selection

Due to the inherent safety associated with using inert solid fuels, hybrid rockets are granted significant design flexibility and in combination with the option to use solid oxidisers and liquid fuels. This provides great scope for suitable O/F combinations, which far exceed those that are currently available to solid and liquid rockets combined. In considering what factors are important in characterising the performance of a rocket, it is clear that the O/F combination must be able to provide large specific impulses and high characteristic velocities u^*. They have to operate at a suitable O/F ratio to provide efficient combustion, that enables these parameters to be as close as possible to the theoretically predicted values. Fig A.1 displays the specific impulses curves of various propellant combinations with respect to variation in O/F, which are important during the initial design stages of hybrid rocket design in characterising engine performance and determining propellant choice.

Due to solid fuels in hybrid rockets being inert there is great flexibility in fuel selection and fuel grain design allowing for many suitable compositions to be employed in hybrid combustion chambers. The majority of fuels tested are saturated hydrocarbons, typically being synthetic polymers or polymeric synthetic rubbers, as these substances are found to produce relatively high specific impulses and characteristic velocities in comparison to other fuels. The highest performance fuels are based on the polybutadiene monomer (C_4H_6), such as polybutadiene acrylonitrile ($PBAN$), polybutadiene acrylic acid ($PBAA$), hydroxyl-terminated polybutadiene ($HTPB$) and carbon terminated polybutadiene ($CTPB$). Polymeric synthetic rubbers result in increased performance, but other synthetic polymers such as polymethyl methyacrylate ($PMMA$) and high density polyethylene ($HDPE$) have been extensively tested. HTPB is the preferred polymeric solid fuel for various reasons, but the most important being that it provides the best performance and it is commonly used in combination with gaseous oxygen, although several studies have been conducted using nitrous oxide (N_2O) as an alternative. This is because of the reduced safety measures required during

handling, with only a small loss in optimum theoretical performance resultant, so $HTPB/N_2O$ is therefore the most suitable propellant choice when considering safety, as both substances are inert reducing the hazard risk considerably when compared to other O/F combinations.
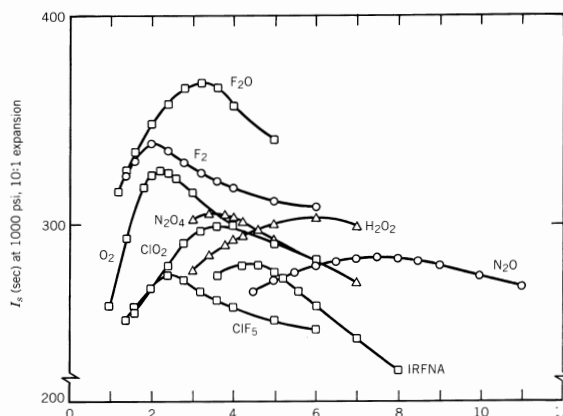

Figure A.1: Specific impulse produced by common oxidisers used with HTPB. [2]

A.3   Oxidiser composition

With regards to oxidiser selection there are several factors which can influence this decision, and the oxidiser which provides the best performance may not always be the most viable option. In table A.1 various typical oxidiser/fuel combinations are listed, along with their relative performance characteristics for a chamber pressure of $500psi$ with perfect nozzle flow expansion to atmospheric conditions of $14.7psi$. As expected, oxygen is found to produce the highest specific impulse and characteristic velocities in comparison to other oxidisers for identical solid fuels. The optimum O/F is also lower when injecting liquid oxygen (LOX), as the concentration of oxygen at low mass fluxes is equivalent to that of higher mass fluxes of other oxidisers. This is due to the molecular structure consisting purely of particles that are oxidising agents and not other particles which are involved in subsidiary reactions. Despite this, the use of oxygen introduces other issues which affect the decision for its application, such as the cryogenic state of liquid oxygen which requires reduces the total operational safety of the system, as special handling techniques are needed to handle the cryogenic pressure vessels. The oxygen flow may be gaseous upon entry into the combustion chamber, but it needs to be stored in a liquid phase to increase volumetric loading. From table A.1 it is obvious that $FLOX$ or fluorinated liquid oxygen results in increased performance in comparison to liquid oxygen, as the fluorine particles in the flow provide an energetic energy source. This is because fluorine is a highly reactive element and is a powerful oxidising agent that increases the rate of reactions it participates in because of a relatively low chemical timescale. The disadvantage of using fluorinated oxygen is that it increases the hazard risk of the oxidiser dramatically, as fluorine is a highly toxic element and extreme caution must be taken when handling such a material. Fluorine (F_2) alone has not reached operational status because it is very difficult to handle, being the strongest oxidising agent available and extremely corrosive, which counteracts the benefits of its use. It is this major impact on operational safety which limits the use of certain oxidisers and because of the toxic exhaust compounds they may produce during combustion. Other hazardous oxidisers displayed in table A.1 are dinitrogen tetroxide (N_2O_4) and red fuming nitric acid, which is a compound consisting mainly of nitric acid (HNO_3) and dinitrogen tetroxide. As with fluorine, both (N_2O_2) and $RFNA$ are highly toxic and corrosive by nature, which negates the inherent safety associated with hybrid rocket operations. Another oxidiser not listed in table A.1 that is becoming more frequently employed is hydrogen peroxide (H_2O_2) because it can be catalytically decomposed before injection into the chamber. The oxidiser flow is directed through a silver or platinum screen

Performance of hybrid propellants, $Pc = 500$ psia and $Pe = 14.7$ psia

Fuel	Oxidizer	Optimum O/F	Sea level I_{sp}, s	c^*, ft/s
HTPB	LOX	1.9	280	5972
PMM($C_5H_8O_2$)	LOX	1.5	259	5449
HTPB	N_2O	7.1	247	5264
HTPB	N_2O_4	3.5	258	5456
HTPB	RFNA	4.3	247	5219
HTPB	FLOX(OF_2)	3.3	314	6701
Li/LiH/HTPB	FLOX(OF_2)	2.8	326	6950
PE	LOX	2.5	279	5877
PE	N_2O	8.0	247	5248
Paraffin	LOX	2.5	281	5920
Paraffin	N_2O	8.0	248	5268
Paraffin	N_2O_4	4.0	259	5469
HTPB/Al(40%)	LOX	1.1	274	5766
HTPB/Al(40%)	N_2O	3.5	252	5370
HTPB/Al(40%)	N_2O_4	1.7	261	5509
HTPB/Al(60%)	FLOX(OF_2)	2.5	312	6582
Cellulose ($C_6H_{10}O_5$)	GOX	1.0	247	5159
Carbon	Air	11.3	184	4017
Carbon	LOX	1.9	249	5245
Carbon	N_2O	6.3	236	4992
Cryogenic hybrids				
Pentane(s)	LOX	2.7	279	5870
CH_4(s)	LOX	3.0	291	6140
CH_4(s)/Be(36%)	LOX	1.3	306	6292
NH_3(s)/Be(26%)	LOX	0.47	307	6452
Reverse hybrids				
JP-4	AN	17.0	216	4651
JP-4	AP	9.1	235	5007
JP-4	NP	3.6	259	5476

Table A.1: Performance characteristics of various propellants. [1]

catalyst bed, which decomposes it into water and oxygen by raising the flow temperature through exothermic energy release. This allows convective and radiative heat transfer from the flow to invoke solid fuel pyrolysis and initiate combustion, but high concentration hydrogen peroxide, commonly known as high test peroxide (HTP) is required for rocket applications and is corrosive and must be handled with care. HTP is less reactive than fluorine, having an oxidation potential of $1.8V$ in comparison to the $3.0V$ of fluorine, but can be decomposed into hydroxyl radicals ($.OH$) which have an oxidation potential of $2.8V$. It is because of the increased hazard risk associated with these substances that nitrous oxide (N_2O) is the preferred oxidiser for many hybrid rocket applications, as it is inert and stored in a liquid phase at non-cryogenic temperatures. It is also non-toxic and non-corrosive, which means that it is safe to handle without any specialist equipment or training, with the only possible hazard emanating from the high pressure storage tanks.

The amount of reverse hybrid propellant configurations are limited by the available oxidisers which can be stored in a solid phase. This is because of inadequate mechanical properties, with most solid oxidisers having crystalline microstructures to be able to withstand the volatile environment of a combustion chamber. There are also increased manufacturing costs associated with solid oxidisers, as they are difficult to cast for relatively large scale engines. Extra caution is required during fabrication for certain oxidisers such as nitronium perchlorate (NP), which is highly sensitive to temperature posing a possible explosion hazard. The majority of reverse hybrid configurations tested utilise $JP-4$, a 50% kerosene 50% petrol blend and is a defunct aviation fuel. This is a volatile liquid with a low flash point that is prone to static electricity build up and discharge that can result in fires. The combination of a volatile O/F mixture that produces relatively low performance is undesirable and because of this a limited amount of research has been conducted for reverse hybrid configurations.

A.4 Fuel composition

While polymeric synthetic rubbers result in increased performance, other synthetic polymers such as polymethyl methyacrylate ($PMMA$) and high density polyethylene ($HDPE$) have been extensively tested. These fuels produce lower regression rates, but the complexity associated with fabricating the fuel grains is reduced and these materials can easily be machined into required geometries directly from monolithic stock material. Unlike polymeric synthetic rubbers, which require the addition of curing agents to polymerise the short molecular chains such as diisocynates. The cast fuel grains also need to be contained within a vacuum chamber for several days to ensure complete polymerisation before usage. As a result, the composition of these fuels can vary because of the various polymer purities, applied curatives and processing methods, although the effect this has on overall engine performance is minimal. Apart from the bulk fuel material, other particulates can be incorporated into fuel grains that have various effects on combustion, depending on the additional material introduced. Most studies have focused on dispersing particulates within polymeric fuel matrices because of the optimum performance associated with these fuel types. A common fuel additive is aluminium Al particles which increase the total density of the fuel grain by increasing the volumetric loading. Aluminium also starts to combust at approximately $T = 873K$ and has been employed effectively in solid rockets to increase the temperature of the combustion gases, as the Al particles are denser than the bulk fuel and also result in increased mass flow rates compared to pure fuels for the same flow conditions. This also has the effect of reducing the optimum O/F ratio of the propellant mixture, which reduces ablation of the nozzle during operation, as lower concentrations of oxygen results in reduced gas corrosivity. This is an important factor, as increased ablation of the nozzle will result in larger nozzle throat areas, which directly affects the performance of the engine because the thrust profile will vary significantly during operation, as the mass flow rate through the nozzle will be transient. Investigations into $HTPB$ loaded with different mass fractions of Al have found that regression rates at relatively low oxidiser mass fluxes are significantly affected by the presence of Al particles in the flow. This is because of the reduced convective heat transfer that occurs at lower oxidiser mass fluxes, where the influence of radiative heat transfer on regression rates become more pronounced. The radiative heat transfer from the diffusion flame is further increased by the radiative heat flux from the Al particles in the flow, in turn causing increased pyrolysis of the fuel surface. Investigations have found that with the addition of 13% aluminium powder to $HTPB$ by volume have resulted in a 123% increase in regression rate in comparison to non-metallised fuels, and indicates the strong influence fuel grain composition and structure can have upon combustion. The effects of Al particle additives can be seen in the regression rate correlation in fig A.2 produced by George et al [32], which agrees with the findings of Strand et al [112] which are also plotted.
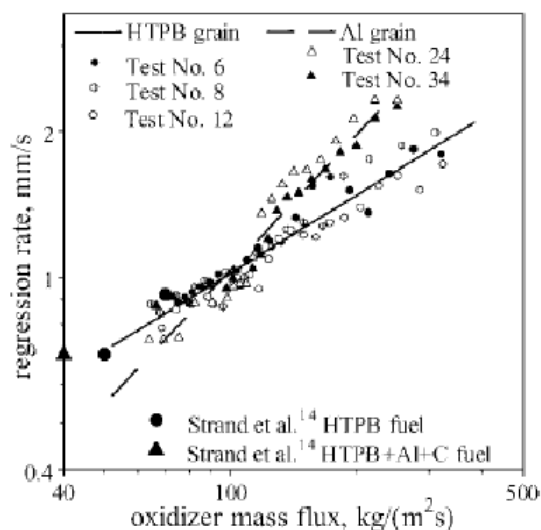

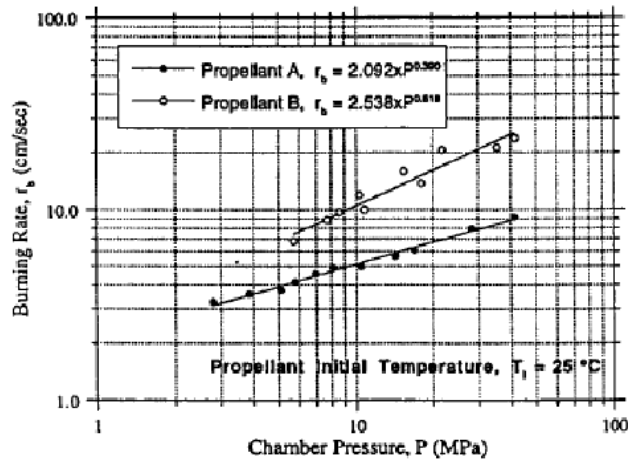Figure A.2: Effect of Al particle additives on fuel regression rate. [32]

Figure A.3: Effect of *Al* particle size on fuel regression rate. [33]

The size of the *Al* particles is an important factor and has found to have a significant effect on combustion. A comparison between two fuels containing different *Al* powders is presented in fig A.3, with propellant A containing conventional micro-particles and propellant B containing *Al* nano-particles known as $ALEX^{®}$. It is clear that smaller particles produce higher regression rates, which can be attributed to losses associated with the micro-sized particles. These two modes of energy loss are caused by incomplete combustion, due to agglomeration of aluminium particles at the fuel surface, preventing complete combustion resulting in decreased energy release, while kinetic energy losses stem from the increased drag induced by the larger particle sizes. The findings for improved combustion with $ALEX^{®}$ powder translates to other energetic fuel additives also, with typical advantages [33] of nano-sized energetic particles being:

- Shortened ignition delay.

- Shortened burn times, resulting in more complete combustion for volume limited propulsion systems.

- Enhanced heat transfer rates from higher specific surface area.

- Greater flexibility in designing new energetic fuel/propellants with desirable physical properties, such as increased mechanical strength.

- Nano-sized particles can also be dispersed into high temperature zones for direct oxidation reaction and rapid energy release.

- Enhanced propulsive performance with increased density impulse.

- Reduce sensitivity of engine to operating conditions, by damping combustion instabilities.

Other available materials that can be used for energetic fuel additives are shown in fig A.4a, which compares the volumetric and gravimetric heat of oxidation for various substances relative to $HTPB$, with table A.4b listing their respective densities. It is the values of volumetric heat of oxidation which are important, as these relate to the amount of energy release per unit volume of the material, indicating the relative energy density of the material.This factor needs to be maximized in all rocket engines so that increased energy release can be obtained for a dimensionally constrained combustion chamber, increasing the specific impulse of the rocket. An optimum combination between increasing the energy release during combustion and increasing the volumetric loading of the fuel grain is required to increase engine performance. It can be seen in fig A.4a that boron and beryllium have the highest volumetric heats of oxidation, but have lower densities than the transition metals such as iron, titanium, tungsten and zirconium, although these materials are all suitable fuel additives there

158
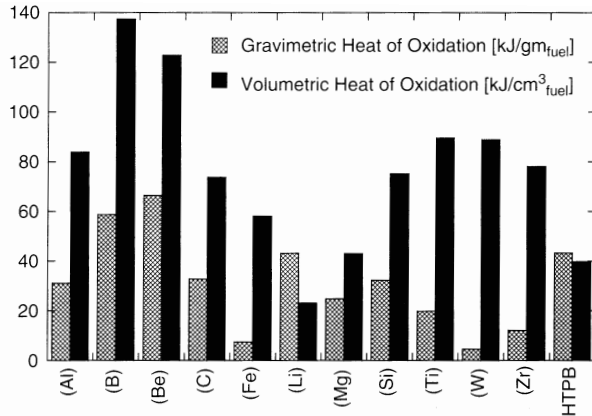
(a) Heats of oxidation.

Material	Density [g/cc]
Aluminum	2.700
Boron	2.340
Beryllium	1.850
Carbon	2.267
Iron	7.870
Lithium	0.534
Magnesium	1.740
Silicon	2.330
Titanium	4.510
Tungsten	19.300
Zirconium	6.520
HTPB	0.920

(b) Material densities.

Figure A.4: Various materials suitable as fuel additives. [33]

are drawbacks to their usage and affect their implementation. Transition metals such as titanium, tungsten and zirconium all have high densities in conjunction with high volumetric heats of oxidation which makes them suitable candidates. Despite this, research into the use of these materials has been deterred by limited or non availability of nano-sized powders, large material costs and especially in the case of tungsten very high melting ($T_{mlt} = 3695K$) and boiling temperatures ($T_{bo} = 5828K$). Boron has the highest volumetric heat of oxidation out of all the materials in fig A.4a and has a high ($T_{mlt} = 2348K$) and boiling temperature ($T_{bo} = 4273K$), but currently only micro-sized powders can be manufactured. These micro-particles are ineffective in improving performance, as there the timescales required for boron particles to melt upon heating are too high, which result in incomplete combustion and poor efficiencies. When nano-sized particles can be produced, boron will be an attractive energetic fuel additive, but until then other materials will have to be developed to increase engine performance.

Beryllium also has a very high volumetric heat of oxidation, with melting ($T_{mlt} = 1560K$) and boiling ($T_{bo} = 2742K$) temperatures lower than the highly energetic transition metals. The disadvantage to using beryllium is that beryllium oxide will be formed during combustion which is highly toxic. Due to the various disadvantages associated with the energetic materials in fig A.4a, the addition of nano-sized aluminium powder still remains the most effective method for increasing fuel regression rates. As it has the highest density and volumetric heat of oxidation in comparison to the other available materials, with existing engine test data indicating the benefits of its application. It is worth noting that many non-metallised fuel grains incorporate a small volume fraction of carbon black (soot) into fuel grains to prevent in depth penetration of radiative thermal fluxes. This also prevents subsurface physicochemical variations to the fuels molecular structure, but it contributes to increasing the bulk density of the fuel and energy density, with a volumetric heat of oxidation magnitude slightly lower than aluminium. Investigations into cryogenic solid fuels have found that regression rates several times that of $HTPB$ for similar operating conditions can be obtained, which also result in higher specific impulses and characteristic velocities than non-cryogenic solid fuels, as shown in table A.1. This is attributed to the formation of liquid layers on the fuel surface during combustion where mass entrainment causes increased fuel surface mass flux, which results in higher regression rates. Karabeyoglu et al [113, 114] developed the analytical theory to explain why this class of fuels out performs non-cryogenic fuels so that the mechanisms responsible for high regression rates could be characterized and incorporated into fuel grain design.

Despite the improved performance obtained by using cryogenic solid fuels there is an increased complexity associated with their manufacture in addition to the requirement for a large insulating volume surrounding the exterior of the combustion chamber that counteracts their superior performance. It is obvious that fuels which employ the liquid layer mass entrainment mechanism are a viable option for producing high regression rate fuels. Karabeyoglu et al [34] evaluated a homol-
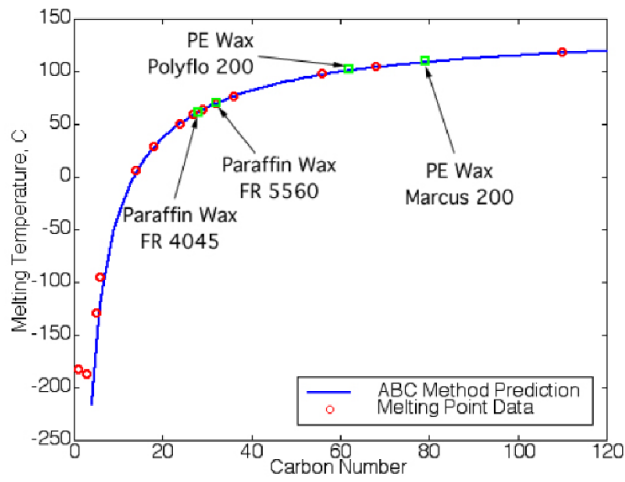
159

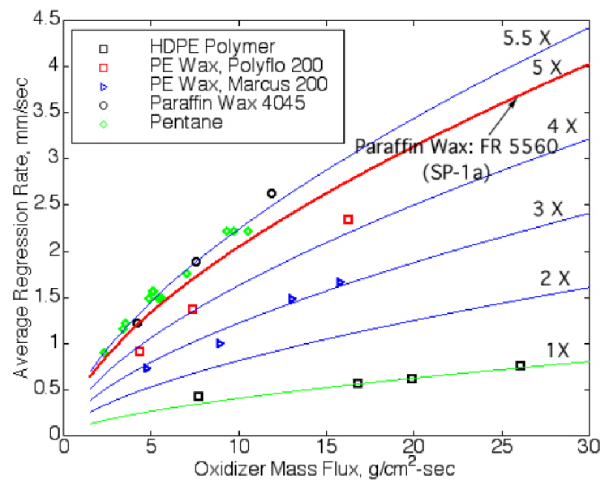Figure A.5: Effect of Carbon number on melting temperature. [34]

Figure A.6: Regression rates of short chain hydrocarbons that produce liquefying fuel layers. [34]

	Burn Rate Factor Relative to SP-1a	Burn Rate Factor Relative to HDPE
Pentane (C_5H_{12})	1.10	5.5
Paraffin Wax FR 4550	1.08	5.4
Paraffin Wax FR 5560 (SP-1a)	1.00	5.0
PE Wax Polyflo 200	0.80	4.0
PE Wax Marcus 200	0.60	3.0
HDPE Polymer	0.20	1.0

Table A.2: Regression rate enhancement relative to other liquefying fuels. [34]

ogous series of normal alkanes (C_nH_{n+2}) to establish a range of carbon numbers n at which fuels are able to produce a liquid melt layer, while remaining non-cryogenic. It was found that paraffin ($n = 28 - 32$) and polyethylene ($n = 60 - 80$) waxes were the most suitable candidates to perform hot fire engine tests with, where the melting temperatures of several fuel compositions relative to carbon number are shown in fig A.5. The paraffin waxes have melting temperatures of approximately ($T_{mlt} = 323 - 343K$) and the polyethylene waxes in the range of ($T_{mlt} = 373 - 388K$). Lower carbon number materials exhibited lower melting temperatures as expected because the enthalpies of fusion and vaporization are lower, because less energy is required to break the intra-molecular bonds of these materials.

This is reflected in fig A.6, which plots the regression rate data obtained for the various fuel compositions tested. Table A.2 displays the increase in regression rates of the fuels tested in comparison to $HDPE$ which has a high carbon number ($n > 100,000$) and does not produce a liquid melt layer. It can be seen that the paraffin waxes exhibit a fivefold increase in regression rate because of the effects of the mass entrainment mechanism. As stated in the analytical theory developed by Karabeyoglu et al [34], higher regression rates can be obtained with low carbon number materials as they produce low viscosity liquid surface layers. These fuels are more prone to Craik instabilities [114] and require reduced shear to produce surface roll waves that lead to droplet formation, which results in an overall increase in fuel surface mass flux, relating to increased regression rates. The regression rates of the paraffin waxes are not as high as pentane, but the benefits of having a material in a solid phase at ambient temperatures with adequate mechanical properties for use in a combustion chamber are preferable. As with other non-cryogenic solid fuels, both paraffin and polyethylene waxes allow for energetic fuel additives to be incorporated into the fuel matrix. The addition of small amounts of carbon black are necessary to increase the opacity of the fuel grain to minimize the effects of radiative heat fluxes penetrating the subsurface region of the fuel. Currently a transition from $HTPB$ to paraffin wax fuel compositions are being displayed by several research establishments, with the most significant being NASA, indicating the importance of paraffin waxes as hybrid rocket fuels.

A.5 Solid fuel decomposition and combustion processes

Understanding the physical decomposition of the solid fuel in hybrid rockets is of fundamental importance, as it is this which directly governs the regression rate of the fuel and in turn the overall performance of an engine. The diffusion flame controlled combustion that occurs consists of several complex physicochemical processes, where convective and radiative heat fluxes are closely coupled to the thermal decomposition of the fuel surface. There are many variables affecting these thermal fluxes, such as fuel composition, boundary layer height and corresponding diffusion flame zone, turbulence intensity, O/F ratio, surface blowing and associated blocking effects. The regression rate of a solid fuel can vary throughout the fuel grain as combustion is influenced by the localised energy hysteresis between the diffusion flame and the fuel surface. The mechanism controlling pyrolysis is dependent on the fuel surface temperature produced by convective and radiative heat flux from the diffusion flame. Bulk-phase kinetics occur at lower temperatures where polymer chain scission and reorganisation are dominant, but under rapid heating of the fuel there is a point where bulk-phase kinetics reach their maximum. This indicates the transition temperature between bulk-phase and desorption kinetics, where pyrolysis occurs through formation and desorption of species at the fuel surface [35]. The transition point between the two mechanisms is characterised by a sudden drop in activation energy E_{act}, as increased temperatures allow desorption of fragments with higher molecular weights. The reduced activation energy results in desorption kinetics controlled pyrolysis that produce higher regression rates, this mechanism operates in the majority of hybrid engines due to intense flame temperatures. This can be seen in figs A.7 and A.8 which highlight the transition point between mechanism kinetics. Detailed studies in this area have allowed temperature dependent regression rate Arhenius relationships to be formed for thermal decomposition of $HTPB$ fuel.
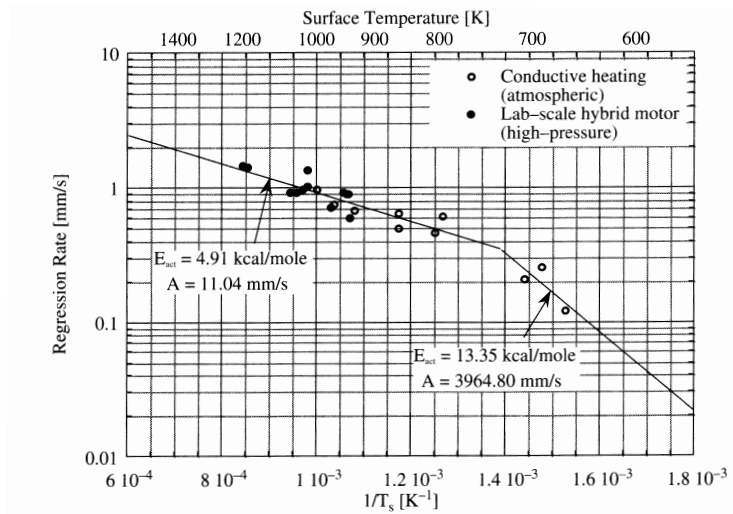
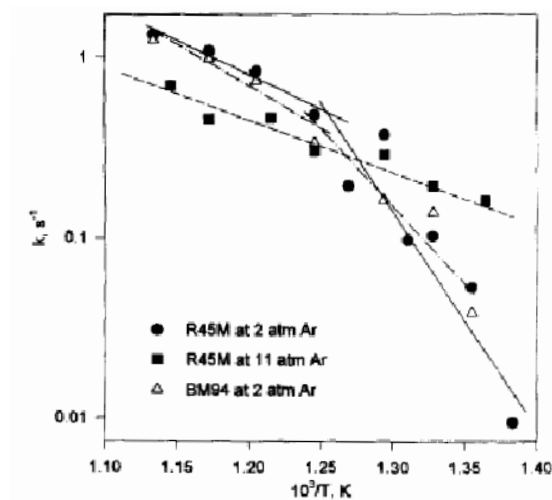Figure A.7: Arrhenius parameters derived from regression rate data. [35]

Figure A.8: Transition in chemical kinetics affecting combustion. [36]

The flame zone temperature is reliant upon local turbulence levels and allows mass diffusion of oxidiser into the boundary layer to mix with gaseous pyrolysed species, providing an adequate O/F ratio to sustain combustion. This strong interdependency of physicochemical processes, coupled with the various timescales required for them to occur, lead to a relatively large lag in system response. Sustainable combustion is achieved as the combustion process is self-regulatory, adapting to fluctuations in the boundary layer which alter the balance between convective and radiative thermal fluxes to the fuels surface. The boundary layer is established when oxidiser flow over the fuel surface is present and ignition has occurred, with the assumption that the boundary layer is turbulent as a result of the destabilising effect of oxidiser injection. The assumption of a turbulent boundary layer combined with shearing flow effects allows the Reynolds analogy to be applied. This is where the transport mechanisms of mass, momentum and energy within the momentum boundary layer over a flat plate are similar and provides a useful tool for analytical models as an initial estimate of heat transfer where shear stress is known. The diffusion flame zone is located at a distance normal the fuel surface approximate to 0.2δ and has a thickness of approximately 0.1δ, as can be seen in figs A.9 and A.10. The flame zone separates the fuel rich region near the surface and the oxidiser rich region at the edge of the boundary layer.

162
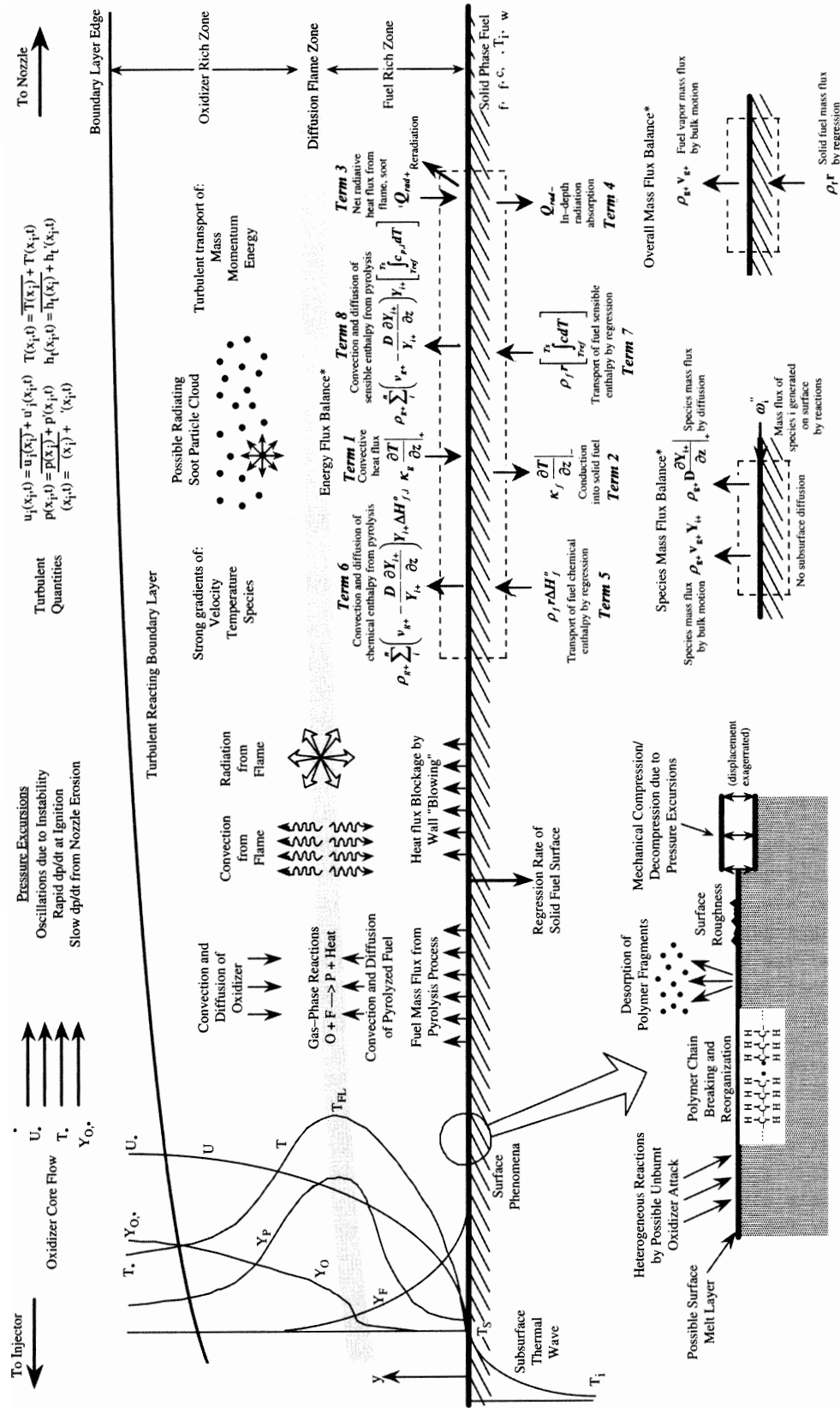
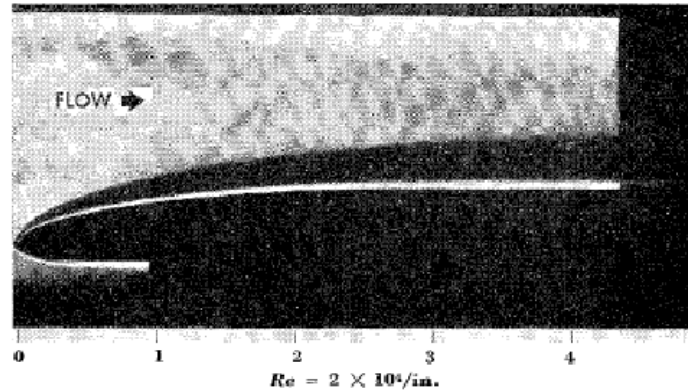Figure A.9: Boundary layer combustion processes. [1]

Figure A.10: Schlieren image of combusting boundary layer. [37]

The presence of the diffusion flame, in conjunction with a turbulent boundary layer means that strong gradients of velocity, temperature and species exist, with maximum velocity at the edge of the boundary layer and maximum temperature and species concentration within the flame zone. Convective heat flux from the flame zone is transported via the gaseous phase to the fuel surface where solid phase conduction into the fuel occurs, while simultaneous radiative heat fluxes from the flame, soot particles and metal particles in the boundary layer flow are incident on the fuel surface. The amount of radiation absorption into the fuel is mainly dependent on the optical properties of the fuel (opacity), which also determine the magnitude of reradiation into the boundary layer. If there is sufficient net energy flux incident at the surface, pyrolysis of the fuel occurs, releasing gaseous pyrolysed species into the boundary layer, which are then transported via convection and diffusion into the flame zone. The boundary conditions at the fuel surface represent the most complex region of the engine, where the energy balance between the gaseous and solid phase controls the process of fuel decomposition, that in turn regulates combustion. Pyrolysis is the dominant mechanism influencing surface mass flux, with pyrolysis products liberated once scission of chemical bonds and chain reorganisation has occurred to form new species. Other surface phenomenon include the effects of asperities, which can lead to desorption of fuel fragments as rough surfaces increase local turbulent shear, removing unpyrolysed material from the fuel surface. It is also possible for small amounts of uncombusted oxidiser to diffuse through the boundary layer, attacking the surface where heterogeneous reactions take place.

In surface regions where the incident energy flux is lower than the required enthalpy of gasification, a liquified melt layer may form that usually indicates low regression rates. The fuel grain surface also exhibits plastic deformation through application of various stresses, resultant of chamber pressure and flow conditions. Pressure oscillations cause continual compression and decompression of the surface, while flow induced shear forces can pattern the grain surface and create 'roll waves' in the melt layers. Advanced solid fuels employ low viscosity liquid layers which produce an oxidiser/fuel spray due to flow shear, significantly increasing regression rates through use of a mass entrainment mechanism and combustion is sustained, as the opposed flow of gaseous oxidiser and pyrolysis products diffuse into the flame zone. Release of vapour from the surface acts to inhibit pyrolysis by blocking incoming convective thermal flux, this is known as the mass blowing effect and is the result of fuel surface transpiration [66]. This is where the energy transfer to the surface is reduced and the regression rate of the fuel decreases due to the drop in localised surface mass flux and causes a weakening of the mass blowing effect, allowing increased convective heat flux to reach the fuel surface. Convection is the primary mechanism of heat transfer affecting regression rate, with the effects of radiation usually being less pronounced, but for metallised fuels containing embedded metal particles the proportion of incident radiation to convective flux is increased [115]. This is also true for engines operating at relatively low O/F ratios, where reduced levels of convective heat flux mean that radiative fluxes have a significant role in influencing regression rates [112]. The radiation is relatively unaffected by the blocking effect of mass blowing and methods of increasing radiative
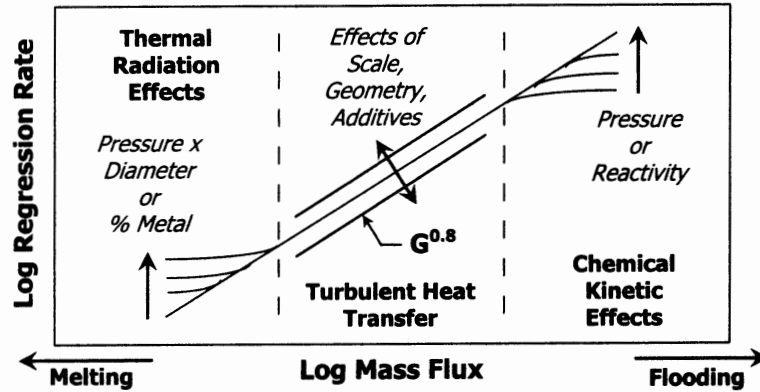
164

Figure A.11: Fuel regression regimes and factors that affect regression rate. [1]

heat flux are desirable since they can offset the reduction in the average regression rate from reduced convective flux. Permeation of radiative thermal fluxes below the fuel surface and local heat affected region is detrimental to operations, as homogeneous subsurface reactions occur and subsurface polymer chain scission and reorganisation of the fuels molecular structure affects the bulk properties of the material. This causes a reduction in combustion efficiency as other less energetic species are formed [116], but can be avoided by the addition of radiation absorbing particulates into the fuel grain, preventing in depth thermal penetration of the solid fuel by increasing the materials surface absorptivity s and opacity.

It has been established that hybrid engines can operate in one of three regression rate regimes which relate to extreme and typical modes of operation [117]. The normal regime is characterised by regression rates which adhere to the oxidiser mass flux power law where convective heat transfer is the dominant. Almost every engine tested to date is designed to operate within this regime because it provides stable combustion and semi-empirical models can accurately be applied. At increased levels of oxidiser mass flux the regression rate correlations become inaccurate as the dominant mechanism of heat transfer becomes dependent on gas-phase chemical reaction effects, this is known as 'flooding'. Hybrid combustion is usually relatively insensitive to chamber pressure, but this is only the case when operating within the convective heat transfer regime. In the gas-phase reaction regime regression rate increases with higher chamber pressures, and a pressure dependence similar to solid rockets is observed. As the oxidiser mass flux increases the conditions in the chamber tend towards the limits of operation, as an oxidiser rich environment can extinguish the flame sheet. As turbulence intensity increases with higher oxidiser mass fluxes it becomes harder to sustain combustion as turbulent time scales decrease, leading to Damkohler numbers below unity where chemical reactions are not possible due to the chemical timescales t_{chm} being larger than the turbulent time scales t_{tur}.

This provides an explanation for why many regression rate models fail to predict regression rates in this regime, as the regime is characterised by the effects of chemical kinetics and not species diffusion [118], putting an emphasis on the importance of Damkohler not Lewis numbers which most models incorporate. For highly reactive fuels the chemical timescale is shorter, allowing for higher possible oxidiser mass fluxes before reaching the 'flooding' limits of flame extinction. Deep thermal penetration of the solid fuel can occur when an engine is operating below of the limits of the convective heat transfer regime, which is known as 'cooking' and is indicated in fig A.11. When the oxidiser mass flux is reduced, so is the convective heat transfer to the fuel surface and in turn the regression rate, meaning that radiative heat transfer becomes the dominant mechanism of heat transfer. 'Cooking' refers to the subsurface depolymerisation and molecular reorganisation of the fuel as thermal loading is applied and can be accompanied by the formation of melt and char layers on the fuels surface which can reduce regression rates, as the carbonaceous surface inhibits the transport of radiation to the unpyrolysed fuel. There is an effective operational energy loss, as thermal energy transported from the flame zone is dissipated throughout the fuel during solid phase conduction and chemical energy released from subsurface depolymerisation is effectively lost, as energy that could

165

be used to provoke surface pyrolysis is conductively dissipated through the solid. The combined effects of 'cooking' and associated layer formation are detrimental to combustion efficiency as the thermal decomposition processes occurring are non-conducive for stable combustion. Operation of hybrid engines outside of the stable steady state combustion regime has to date received a relatively small amount of attention and a more detailed understanding of the transition zones required, as do hybrid boundary layer combustion processes in general, because error between regression rate models and empirical data still exists.

A.6   Regression rate theory

Current understanding of hybrid rocket boundary layer combustion processes are based upon regression rate models employing a combination of analytical, empirical and semi-empirical approaches. As of yet a universal regression rate model has not been developed, as all expressions to date are relative to the empirical data collected, with the majority of regression rate models fitted to a specific dataset. The most significant regression rate model seen in eqns A.1-A.2 were formulated by Marxman, Gilbert, Wooldridge and Muzzy [66, 116] for application to the classic hybrid configuration, where regression rate is limited by diffusion (transport). The analysis of Marxman et al [116] is significant as it was the first to effectively consider the energy flux balance between the flame zone and fuel surface as well as incorporating the concept of mass blowing. It was assumed that the boundary layer was turbulent and analogous to a flat plate so that existing boundary layer solutions could be applied. The effects of wall transpiration were included but they were assumed to have a negligible effect on the velocity profile, validating the use of skin friction coefficient to Reynolds number correlations for turbulent flow. The Reynolds analogy is useful in providing a simple relationship between heat transfer and skin friction coefficient, enabling a first approximation of heat transfer to be obtained with relative ease.

$$\rho_f \dot{r} h_{vap} = h \left(T_{flm} - T_s\right) = \dot{q}_s = k_g \left(\frac{\delta T}{\delta y}\right)_{y=0} \tag{A.1}$$

$$\dot{r} = aG^e \tag{A.2}$$

$$\dot{q}_w \approx \frac{\tau_w C_p \left(T_w - T_\infty\right)}{u_\infty} \tag{A.3}$$

$$Pr = \frac{\nu}{\alpha} = \frac{\mu C_p}{k_g} = \frac{viscous.diffusion.rate}{thermal.diffusion.rate} = 1 \tag{A.4}$$

$$Sc = \frac{\nu}{D} = \frac{viscous.diffusion.rate}{mass.diffusion.rate} = 1 \tag{A.5}$$

$$Le = \frac{\alpha}{D} = \frac{thermal.diffusion.rate}{mass.diffusion.rate} = 1 \tag{A.6}$$

Momentum, mass and energy transfer are assumed to be similar for turbulent flow because the Prandtl number varies little over a large temperature range and can be assumed to be unity, therefore meaning kinematic viscous diffusivity and thermal diffusivity are similar. When treating the Schmidt number as unity on the basis of simultaneous mass/momentum transfer through eddy transport, means that the Lewis number will also be unity. Conditions within the flame zone were ignored to apply these similarities, with the flame zone effectively treated as a singularity dividing the oxidiser and fuel rich regions of the boundary layer. The analysis by Marxman et al [116] provides a strong foundation for explaining fundamental processes that occur during diffusion limited boundary layer combustion, but is missing several other contributing factors such as radiative heat flux and chemical kinetics. Chiaverini et al [67], later focused on developing an Arrhenius relationship to determine regression rate based upon the surface temperature of the fuel. Through rapid conductive heating of $HTPB$ fuel slabs under atmospheric pressure the composition of pyrolysis product gases were

determined for a range of temperatures, placing significance on the influence on surface temperature. Several fuel compositions were tested and conductive heating results were found to agree well with empirical data obtained from lab-scale engine tests. This enabled the fuels to be characterised by finding the Arrhenius rate pre-exponential factors A and activation energies E_{act} for the various compositions tested, as shown in figs A.7 and A.8. In comparison to similar studies conducted by Arisawa and Brill [35, 36], the activation energies found by Chiaverini et al [67] are relatively low, indicating regression rates limited by the physical process of molecular desorption of pyrolysed fuel from the surface. Unlike higher activation energies which are characterised by bulk kinetics, where depolymerisation and chain reorganisation of the subsurface region limit regression. Apart from this, it was found that pressure had no effect on the regression rate and data from atmospheric and high pressure $(2.59 - 4.14MPa)$ tests correlating well, showing that it is the magnitude of surface temperature which dictates regression rate and pyrolysis product formation. The findings of Chiaverini et al [67] are important in proving that thermal decomposition of the fuel is the dominant mechanism controlling regression rate and showing variation in molar concentrations and species within the pyrolysed gases. As well as providing data that can be incorporated into numerical simulations to more accurately model combustion in hybrid rockets.

A.7   Liquefying fuel theory

The majority of solid fuels for use in hybrid rockets are polymeric substances which sublimate when exposed to thermal flux from the flame zone. The occurrence of a high viscosity melt layer is indicative of unstable combustion, due to insufficient pyrolysis gases been emitted from the fuel surface. This is associated with low regression rates for typical polymeric alkane fuels such as $HTPB$, $PMMA$ and $HDPE$, where the existence of a melt layer is undesirable because of its ability to reduce the incident thermal fluxes effectiveness in pyrolysing the fuel surface. Karabeyoglu et al [34] have characterised a range of non polymeric fuel suitable for hybrid rocket applications which display significantly higher regression rates compared to their polymeric counterparts, caused by the formation of a liquid melt layer on the fuel surface upon heating. Atomisation of the liquid layer occurs when roll waves caused by Kelvin-Helmholtz instability are formed and small liquid droplets are sheared from the tips of the waves, where they then become entrained in the turbulent flow. Eqn A.7 shows the relationship between entrained mass flow rate and how it is affected by operating conditions and more significantly the properties of the fuel. A fuel that produces a thick low viscosity liquid film is desirable, as lower surface tensions enable liquid film instabilities from which the boundary layer flow can shear liquid droplets. The increase in local dynamic pressure also produces increased levels of mass entrainment, which is achievable through increasing the oxidiser mass flux.

$$\dot{m}_{ent} = \dot{r}_{ent}\rho_f = K'\frac{C_f G^{2e} y_l^{\chi} \rho_l}{\sigma \mu_l} \tag{A.7}$$
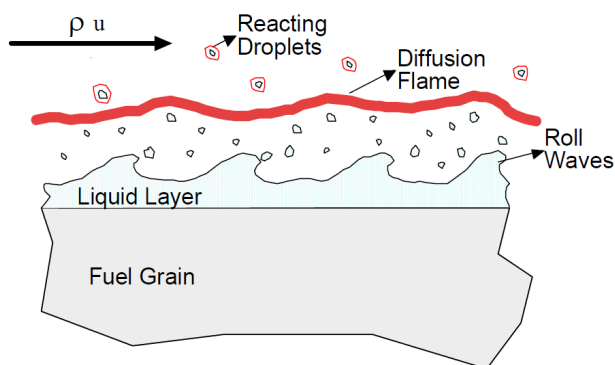

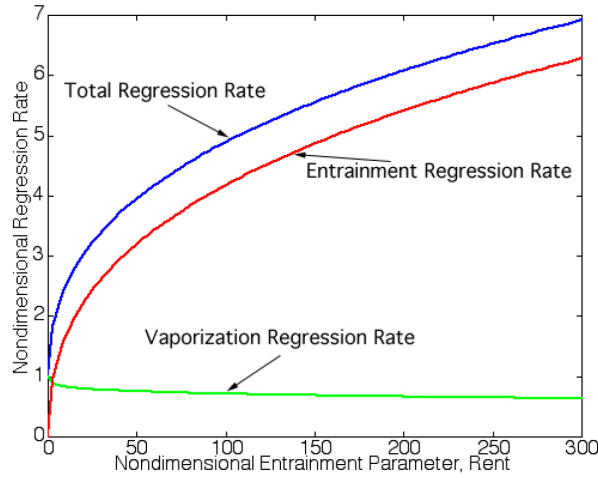Figure A.12: Development of liquid fuel spray above solid fuel surface. [38]

Figure A.13: Combined vaporisation and entrainment regression rates. [38]
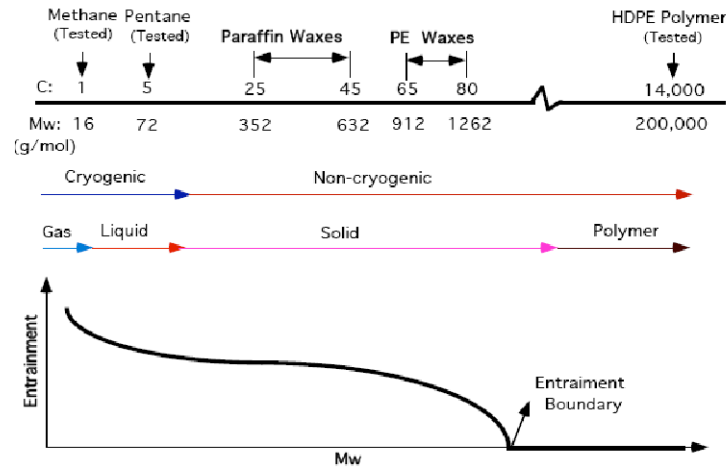

Figure A.14: Influence of Carbon number on fuel entrainment. [38]

The mass entrainment transfer mechanism shown in fig A.12 reduces the amount of energy required to vaporise fuel from the surface as the heat of gasification $\triangle h/h_g$ is less in comparison to standard fuels, where the energy equivalent to the latent heat of fusion also needs to be imparted to the solid fuel. This also implies that the sensible enthalpy of the liquid layer is higher, producing a net reduction in the enthalpy variation between the fuel surface and the flame zone. Though the decrease in the effective heat of gasification is more significant than the reduction of the enthalpy difference, and is therefore neglected in obtaining an initial approximation of regression rate. The mass, momentum and energy transfer characteristics of the entrained droplets are also neglected initially, so that only the effects of mass blowing due to gaseous products from the fuel surface affect incident convective fluxes. This makes the assumption that the flame zone approximation in Marxman and Gilberts [66] analysis is valid, and evaporation of liquid droplets in the fuel rich region below the flame does not occur. Instead they are transported directly into the flame sheet where they may react or pass through into the oxidiser rich region above the flame zone. The total regression rate is the sum of the regression caused by vaporisation and mass entrainment, where the modified diffusion limited model is used to correlate regression due to vaporisation. Eqns A.8-A.9 express the modified regression rate formulation, with fig A.13 showing the significant contribution that mass entrainment has on the overall regression rate.

$$\dot{r}_{tot} = \dot{r}_{vap} + \dot{r}_{ent} \tag{A.8}$$

$$\dot{r}_{ent} = C_{ent} \frac{G^{2e}}{\dot{r}^{\chi}} \tag{A.9}$$

Apart from the increase in regression rate due to the mass entrainment mechanism, the formation of roll waves in the liquid layer increases the surface roughness of the thin film, increasing the heat transfer to the fuel because of the increased free surface area. Through enhancement of the existing liquid layer theory a universal non-dimensionless regression rate theory was derived which accounts for the variation of physical phenomenon, including other fuel groups such as normal alcohols and normal acids. At a certain molecular weight, entrainment ceased as the thin film surface tension was higher than the shear of the flow, as depicted by fig A.14. The fuels with molecular weights below the entrainment boundary but above those of cryogenic fuels were then investigated further to assess their suitability for use in hybrid rocket operations.

Appendix B

Vortex characterisation

B.1   Precessing vortex core

The precessing vortex core is a large scale coherent structure observed in many confined vortical flows and is an important feature of the flow field seen within devices such as the VIHRE. The term PVC is generally considered to describe the inner region of a vortex with a finite radial dimension, where the vortex filament that describes the axis of the vortex precesses around a central location as seen in fig B.1a. It is also considered to be defined as the boundary of the region of reversed flow which occurs in the core of the vortex, which is denoted in fig B.1b. This is a phenomenon associated with highly swirling flows [3] $S > 0.6$ and can occur in either confined or free flows. It typically arises at sufficiently high Reynolds numbers where some mode of vortex breakdown has occurred and has allowed instabilities in the flow to develop. A example of this is when a stable columnar (rectilinear) vortex is perturbed axially, so that the vortex filament describing the axis of the vortex is no longer rectilinear, which induces axial and radial velocity components. Before this perturbation it can be assumed that the vortex filament is rectilinear and infinitely thin.

(a) Azimuthal plane view.   (b) Meridional plane view
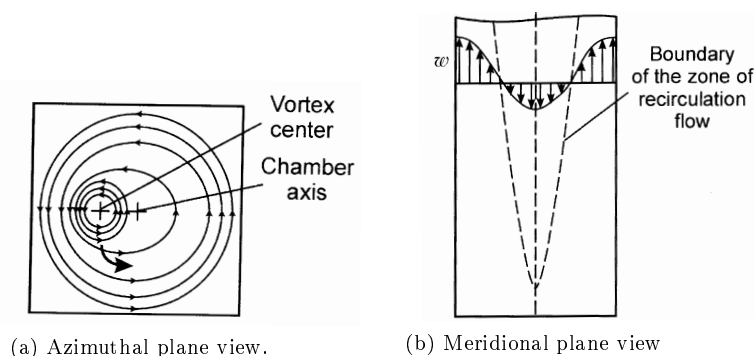
Figure B.1: Defining characteristics of the precessing vortex core. [39]

The Biot-Savart law can be used to describe the behaviour such a vortex if the fluid was considered to be ideal. This describes a purely toroidal flow with no axial or radial velocity component, as the velocity component induced by the vortex filament is orthogonal and occurs at a finite radius from the vortex filament. This means that the resultant velocity is purely tangential and it effectively describes a 2D point vortex. The flow also has zero vorticity and is potential (irrotational) with the velocity component described by eqn B.1, where the constant intensity or circulation Γ means that as $r \to 0$ then the velocity becomes unbounded at the axis as $u \to \infty$, which is not possible in a physical fluid due to viscosity. The simple formulation yielded for the tangential velocity component in eqn B.1 is useful however for describing a free vortex where viscous effects are included and is the basis for several analytical vortex models.

$$u = |\mathbf{u}| = \frac{\Gamma}{4\pi} \int\limits_{-\infty}^{\infty} \frac{\sin\theta}{r^2 + z^2} \partial z = \frac{\Gamma}{4\pi} \int\limits_{-\infty}^{\infty} \sin\theta.\partial\theta = \frac{\Gamma}{2\pi r} \qquad\qquad (B.1)$$

Vortex breakdown alone is a complex phenomenon and it can occur in several ways dependent on flow conditions and whether the flow is confined or not. When the vortex is confined it has been observed that 8 categories of vortex breakdown are possible, where these disruptional modes can possibly occur before the formation of the PVC. These categories of vortex breakdown for confined flows are detailed in table B.1, with fig B.3 representing a map of the flow conditions required to induce specific forms of vortex breakdown [39]. From this it can be inferred that it is the relative magnitudes of the axial and tangential velocities which affect what the of vortex breakdown that occurs. The dominant velocity component contributing to the Reynolds number on the vertical axis will be the tangential velocity component, whilst the ratio of this to the axial velocity component is what effectively defines the swirl number, indicated by the horizontal axis.
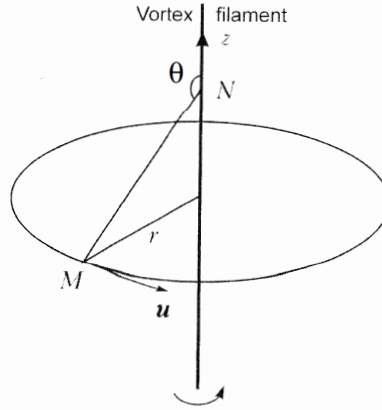
Figure B.2: Rectilinear vortex filament. [39]

Large variations in the flow properties occur during the transient period between flow initialization and pseudo steady state conditions, causing a progressive imbalance in the velocity components magnitude and allows a configuration of several vortex disruption modes to occur as vortex breakdown evolves. A common indicator of vortex breakdown is the existence of a recirculation region downstream of the chamber exit aligned with the axis, which indicates the inception of a PVC. This is where the adverse pressure gradient in the axial direction increases, so that the kinetic energy of the fluid is unable to overcome the static pressure. Also the radius of the vortex core increases as the axial velocity decreases in order to conserve angular momentum. Within confined cyclonic devices this recirculation region can take the form of a small axisymmetric bubble, which will increase in size at progressively higher swirl numbers, indicated by an increased tangential velocity component in comparison to the axial velocity, which aids the recirculation. As the recirculation intensifies, the disturbance moves upstream towards the chamber exit, where vortex breakdown will be more apparent due to the size of the recirculation bubble. This is dependent on an adequately high axial pressure gradient to allow for longitudinal recirculation zones and is characterized by common swirl flow parameters. Faler and Leibovich [119] found that the flow structure is not uniquely determined by Reynolds and swirl number, although vortex breakdown and the location at where it occurs are still highly dependent upon of both of these parameters. The flow structure is also found to have a strong dependence up on geometrical factors when the vortex is confined, something which has been reported in numerous investigations of vortices, in such devices as: cyclone separators, cyclone combustors, vortex tubes and Ranque-Hilsch tubes. Large contraction ratios are found to be beneficial as they are found to stabilize the PVC in preventing flow escaping directly through the exit, which increases coherency and relative strength of the vortex. In vortex chambers with a single
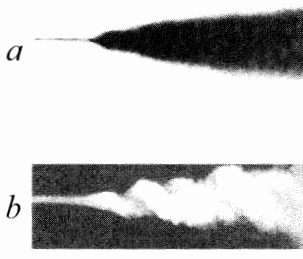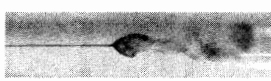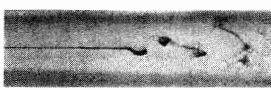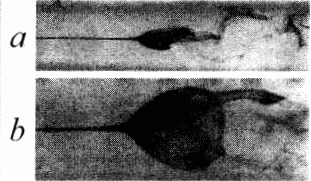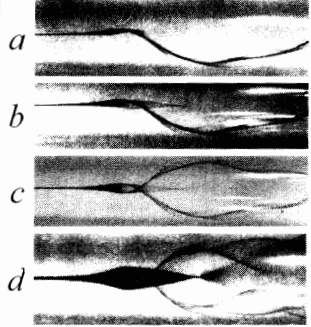
| Type	Designation	Image	Description
c	Conical	a b	Strongly turbulized wake with a conical envelope. In a short exposure time, two or three entangled helices screwed and rotating against the flow are observed. $a - \Delta\tau = 1/30$ s; Re = 105; $\Omega = 0.61$ $b - \Delta\tau = 6\cdot10^{-9}$ s; Re = $1.15\cdot10^{5}$; $\Omega = 0.31$
0	Axisymmetric closed (or bubble) vortex breakdown	Re = $2.56\cdot10^{3}$; $\Omega = 1.777$	One or two tails rotating together with the flow. Simultaneous emptying and filling of the bubble occur through the tail-part. A colored trickle is occasionally observed inside the bubble.
1	Axisymmetric open vortex breakdown		Fully opened tail-part.
2	Spiral breakdown		The helix is screwed along the flow and rotates with the flow.
3	Modification of spiral breakdown		
4	Flattened bubble breakdown	a b	No rotation a – side view b – top view
5	Double helix breakdown	a b c d	Appears from type 6. The structure formed is stable in shape and location. $a - t = 0$ $b - t = 5$ min $c - t = 10$ min $d - t = 15$ min
6	Filament disruption		The state is stable and fixed. The trickle is situated within the plane at slight deviations, and screwed along the flow at large deviations.

Table B.1: Classifications of vortex breakdown. [39]
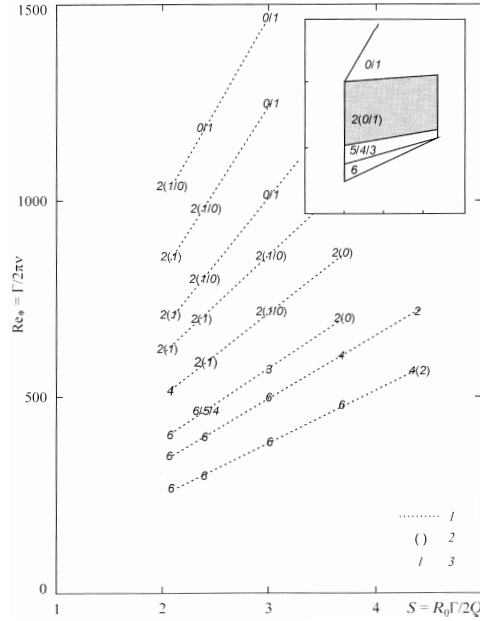
Figure B.3: Map of vortex breakdown regimes. [39]

tangential inlet the flow is found to become highly unstable if large chamber aspect ratios are used in combination with large outlet radii ($\frac{L}{D} > 1.5$ and $CR > 0.5$), as the vortex structure becomes non uniform due to excessive deformation of the vortex filament occurring, resulting in increased precession. Chambers with $\frac{L}{D} < 1$ are found to increase the stability of the flow as they can produce higher swirl numbers, which are indicative of coherent vortex structures. This can also be subjective due to the specific formulation of the swirl number used, as it can be greatly influenced by chamber geometry and actual flow measurement is preferable to determine the effects of chamber geometry upon the flow. Apart from this, small $\frac{A_t}{A_{in}}$ ratios have been found to be suitable, as these relate to small injector cross sectional areas that produce high tangential velocities in fluids, which increase the stability of the resultant vortex structure. This effectively implies that increased inlet Reynolds numbers are preferable as the inlet geometry results in larger tangential velocity components, which are associated with increasing the stability and relative strength of the vortex.

In an Euler fluid, a columnar vortex is defined as a single vortex filament perpendicular to the surface it is attached to, so that the tangential and radial velocity components are aligned with the plane of the surface with the vorticity vector aligned with the axis, as described by a point vortex. This causes the axial velocity component to be zero, as the fluid just rotates about the axis of the vortex filament. Newtonian fluids have viscosity, so the columnar vortex has a radius and exhibits solid body rotation due to fluid shear. Something which is not covered by the Biot-Savart law because of the assumption of an ideal fluid, resulting in the singularity at the axis. The columnar vortex is still effectively rectilinear and can be considered as a superposition of vortex filaments, which constitute the thickness of the vortex core. Flow reversal occurs as a result of vortex breakdown and there will be a negative axial velocity component along the length of the core, which perturbs the rectilinear vortex filaments. In doing this the vortex filaments will deform and it is this curvature and torsion of the vortex filaments that enables vortex precession to occur. These filaments do not explicitly change form, despite their rotational and translational motion which remains constant. As the curvature in the filament means that the vorticity vector is no longer aligned with the axis of the vortex core, although the filaments remain perpendicular at the boundaries at which the vortex filaments terminate. When the vorticity vector is not aligned with the axis the rotation of the fluid (filament torsion) it induces an axial velocity component opposite to the direction of the reversed flow. The combined effects of these deformed and possibly helical filaments is vortex precession, produced by the self induced velocity of the rotation of the vortex filament.

173

The PVC is a 3D time dependent structure with periodicity and therefore has a characteristic frequency. The frequency of rotation or the precessing frequency ($\omega = 2\pi f$) increases with higher volumetric flow rates and is dependent on the self induced velocity of the core. Alekseenko et al [120] found that the velocity at the channel axis and the velocity induced by the solid wall also affect the precession frequency, with higher velocities producing larger frequencies. The PVC is also able to precess about its axis as does the forced vortex region of the core due to flow instability making it asymmetric, although if a steady state assumption is made it is effectively axisymmetric. This can lead to excitation or coupling of acoustic modes when the flow is confined, making it possible for the PVC to drive instabilities [120] in the flow. This is an important consideration because when such structures are present in combustion chambers they can affect combustion instabilities, which are detrimental to the combustion efficiency. Pressure oscillations that arise from the acoustic modes of the chamber perturbed by the PVC and can become coupled with combustion processes, which may further increase the amplitude of oscillations and may damage the chamber is sufficiently large. Pre-mixed flames are found to increase PVC induced combustion instabilities, while diffusion flames are found to have the opposite effect and can damp oscillations by approximately an order of magnitude. Regarding VIHRE operations, this is obviously a benefit as the combustion efficiency of the engine is one of the primary factors that influences other performance metrics such as attainable specific impulse.

B.2 Vortex detection

A simple vortex detection method is to determine the locus of zero axial vorticity and provides a simple method for identifying coherent structures in the flow such as the forced vortex, although this is unable to distinguish between regions of vorticity and shear. This may require more advanced vortex detection schemes such as the Q criterion [121] to be employed, where the value $Q = 0$ would indicate the transition from rotational to irrotational flow. As this represents the point where the rotation rate and strain rate are in equilibrium, with positive values of Q indicating regions where vorticity is dominant relative to the rate of strain of the fluid, or rather the flow is subject to solid body rotation as opposed to deformation of the fluid. The Q criterion is defined as the second invariant of the velocity gradient tensor and is unaffected by local shear, and is expressed in Cartesian form by eqn B.3 for a 2D flow.

$$\omega = \frac{1}{2}\left(\frac{\partial u_y}{\partial x} - \frac{\partial u_x}{\partial y}\right) \tag{B.2}$$

$$Q = -\frac{1}{2}\left[\left(\frac{\partial u_x}{\partial x}\right)^2 + 2\left(\frac{\partial u_x}{\partial y}\right)\left(\frac{\partial u_y}{\partial x}\right) + \left(\frac{\partial u_y}{\partial y}\right)^2\right] \tag{B.3}$$

Another popular vortex detection method, which has been proposed by Jeong and Hussain [122] is the λ_2 criterion, which considers the symmetric and antisymmetric constituents of the velocity gradient tensor D, these being the strain rate tensor W and the vorticity tensor Ω respectively. The variable λ_2 represents the second eigenvalue of the symmetrical part of the velocity gradient tensor squared, expressed in eqn B.8, with isosurfaces of negative λ_2 values indicating coherent vortex structures. This is subjective as with any vortex detection technique, because it is a general purpose formulation that relies on knowledge of the specific behaviour of the flow and the ability to determine whether the vortex core obtained is a relevant solution. Regarding the bidirectional vortex, both the forced and free components can be considered quasi-periodic in that they exhibit spatio-temporal stability and the form of the vortex core is relatively invariant with respect to time. This means that vortex detection methods are suitable for describing the vortex core not only at an instant in time but also for steady-state conditions, allowing the vortex structure to be effectively deduced irrespective of time. Eqns B.4-B.8 highlight some of the stages in the derivation of the $\lambda_2$criterion, including the velocity gradient tensor matrix in its original, decomposed and decomposed square form, which reveals $\lambda_{2(S^2+\Omega^2)} = \lambda_{\Re i}^2 - \lambda_{\Im i}^2$, where ($\lambda_1 \le \lambda_2 \le \lambda_3$) and the swirling strength is defined by $\lambda_{\Im i}^2$, which is the square of imaginary part of the complex eigenvalue of the velocity gradient tensor. The

effects of the vortex Reynolds number upon the vorticity magnitude at the periphery of the chamber can also be seen in fig 3.4d, where similar increases in the magnitude of the variable are seen relative to larger vortex Reynolds numbers. The reduced radial distance causes an increase in vorticity and can be attributed to the thickness of the boundary layer, which decreases due to the increase in localised absolute velocity associated with larger vortex Reynolds numbers.

$$D = [d_{ij}] = \begin{bmatrix} d_{11} & d_{12} & d_{13} \\ d_{21} & d_{22} & d_{23} \\ d_{31} & d_{32} & d_{33} \end{bmatrix} = \begin{bmatrix} \frac{\partial u}{\partial x} & \frac{\partial u}{\partial y} & \frac{\partial u}{\partial z} \\ \frac{\partial v}{\partial x} & \frac{\partial v}{\partial y} & \frac{\partial v}{\partial z} \\ \frac{\partial w}{\partial x} & \frac{\partial w}{\partial y} & \frac{\partial w}{\partial z} \end{bmatrix} \tag{B.4}$$

$$D = W + \Omega \tag{B.5}$$

$$[d_{ij}] = [v_\Re v_{\Re i} v_{\Im i}] \begin{bmatrix} \lambda_\Re & 0 & 0 \\ 0 & \lambda_{\Re i} & \lambda_{\Im i} \\ 0 & -\lambda_{\Im i} & \lambda_{\Re i} \end{bmatrix} [v_\Re v_{\Re i} v_{\Im i}]^{-1} \tag{B.6}$$

$$Sym\left(D^2\right) = W^2 + \Omega^2 \tag{B.7}$$

$$[d_{ij}]^2 = [v_\Re v_{\Re i} v_{\Im i}] \begin{bmatrix} \lambda_\Re & 0 & 0 \\ 0 & \left(\lambda_{\Re i}^2 - \lambda_{\Im i}^2\right) & \left(2\lambda_{\Re i}\lambda_{\Im i}\right) \\ 0 & \left(-2\lambda_{\Re i}\lambda_{\Im i}\right) & \left(\lambda_{\Re i}^2 - \lambda_{\Im i}^2\right) \end{bmatrix} [v_\Re v_{\Re i} v_{\Im i}]^{-1} \tag{B.8}$$

Appendix C

# Numerical methods

C.1 Mesh quality

The quality of a mesh can be assessed in various ways, but the most common criteria are the equiangle skew, equivolume skew and maximum included angle, which all describe the quality of individual elements. The equiangle skew is represented as the maximum ratio of the cell's included angle to the angle of an equilateral element [40], and can be calculated using eqn C.1. The equivolume skewness function is represented as the ratio of the cell's volume to the optimum cell volume [40], and is expressed by eqn C.2, although this is only applicable to tetrahedral elements. The maximum included angle is a measure of skewness, represented by the maximum internal angle at any vertex of an element in degrees. Both the equiangle and equivolume skew criteria result in a value between $0 \rightarrow 1$ for any given element, where a lower value is indicative of a high quality element. For example, the hexahedral element displayed in fig C.1a will have an equiangle skew of $Q_{eas} = 0$, while the tetrahedral element seen in fig C.1b will have an equiangle skew of approximately $Q_{eas} \approx 0.6$, and is therefore of lower quality. Highly skewed elements are unavoidable in a lot of geometries, but efforts must be made to minimise the total number of skewed elements in a mesh, as they are detrimental to the stability of the CFD calculations and can lead to solution divergence. Standard CFD practice is to create a mesh where the streamlines of the flow are parallel or orthogonal to the facets of the element, as this results in reduced false numerical diffusion that is detrimental to the accuracy of the final solution.
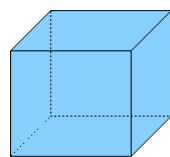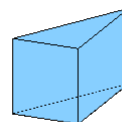

(a) Hexahedral.
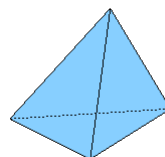
(b) Tetrahedral.
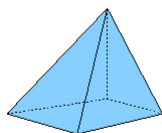
(c) Pyramid.

(d) Wedge.

Figure C.1: Element types available for meshing. [40]

Numerical diffusion is inherent in CFD calculations, due to the discretisation of the Navier-Stokes equations and resultant from the deviation of the virtual systems behaviour to that of the original physical system. However, by properly aligning the grid with the flow, a lower order discretisation scheme can be employed which will produce reduced false numerical diffusion in comparison to a grid not aligned with the flow. Effectively, this means that in order to obtain an accurate solution using an unstructured mesh that is comparable to a structured mesh then higher order discretisation schemes must be employed, which greatly increases the demand on computational resources. The size of the mesh is also an important parameter with regards to false numerical diffusion, as an unstructured mesh generally requires smaller elements to provide sufficient spatial resolution to resolve the gradients in the flow, which also necessitates increased computational resources. In algebraic multi grid solvers, the error in the solution at the coarsest grid level is disseminated down through the intermediate grids to the original mesh, which is exacerbated by insufficient discretisation, that predominantly stems from inadequate grid resolution. Therefore, if possible it is always preferable to build an unstructured mesh to avoid these effects and obtain an accurate solution with the least possible amount of computational resources, as this also reduces the overall computation time. However, as is the case for the vortex chamber seen in fig 4.5 this is not possible, so a hybrid mesh is constructed which contains both hexahedral and tetrahedral elements, although the facets of these elements are quadrilateral and triangular respectively. This requires interstitial elements known as pyramids, as depicted by fig C.1c to form a connection between the the structured and unstructured regions of the mesh. Another example of an interstitial element is the wedge element seen in fig C.1d, which is useful in applications where curved geometry requires a triangular surface mesh to effectively map the geometry, but the elements adjacent to the surface must exhibit little skew. This is particularly relevant in aerodynamic design, where the viscous sublayer of the boundary layer needs to be resolved to accurately predict lift and drag coefficients, requiring a high quality mesh with significant spatial resolution. The wedge element is ideal in any situation where a triangular surface mesh is necessary and the mesh can be extruded orthogonally from the surface.

$$Q_{eas} = max \left[\frac{(Q_{max} - Q_{eq})}{(180° - Q_{eq})}, \frac{(Q_{eq} - Q_{min})}{Q_{eq}} \right] \tag{C.1}$$

$$Q_{evs} = \frac{(Optimal.cell.size - Actual.cell.size)}{Optimal.cell.size} \tag{C.2}$$

It was decided that the method adopted by Anderson et al [25] provides the most suitable means of creating a mesh suitable for simulating confined vortical flows, as it minimises the tetrahedral element content of the mesh and reduces the computational load of the CFD calculations. Also through decomposition of the geometry a modular CAD model can be built, where various regions of the mesh can be activated or deactivated to provide multiple chamber configurations from a single model. It is common practice in the design of gas cyclones and hydrocyclones to use inlets with rectangular cross sections that allow for completely unstructured meshes, but cylindrical inlets will be used in the CFD study to exactly replicate the geometry of the experimental rig. The only difference between the numerical and experimental chamber configurations will be in the rotational direction of the flow with respect to chambers with head injectors. As stated previously, it is assumed that the rotational direction of the flow has a negligible effect on the overall structure of the vortex, so should exhibit little or no impact upon the results. Also mentioned previously, was that the tangential injectors of the experimental rig are offset by a small axial distance from either the base or head boundaries, which is to provide adequate clearance so that highly skewed elements are avoided in the localised unstructured mesh. This clearance also means that the geometry around the injector interface can be decomposed, to further reduce the total number of tetrahedral elements and increase the local content of hexahedral elements. This is important, as the large tangential component of the inlet flow and proximity to the axial boundary is likely to result in large radial gradients in the flow, where a high quality mesh is crucial. A close up of the injector interface can be seen in fig 4.8a, where it is clear that the tetrahedral content of the mesh has been heavily restricted through proper decomposition of the geometry.

C.2 Discretisation schemes

Due to the convoluted helical pathlines produced by the bidirectional vortex, it is necessary to perform 3D calculations of the flow and also ensure an accurate solution is obtained to adequately resolve the salient features of the flow, such as the mantle structure. Based on previous studies and available resources, the commercial finite volume Navier-Stokes solver Fluent 6.4 provided by Ansys was chosen to calculate the numerical solutions. A 64 bit parallel double precision version of the solver is used, as this allows the code to access the maximum amount of memory for storage of floating point data, minimising the effects of truncation errors, which would then be further scaled through dissemination of the solution through the algebraic multi grid solver. The average cell count of the meshes used in the CFD study are not significantly large in comparison to those used in external aerodynamics problems, where the solver still benefits from enhanced performance when the problem is multi threaded and run on several CPU cores simultaneously, necessitating the use of the parallel solver. A study of the effects of time to solution versus number of threads was conducted, so that the optimum configuration for producing numerical data could be realised, to process the numerous chamber configurations as efficiently as possible. This resulted in 6 CPU cores being used for every test case, where the solutions were run on the University of Sheffield's HPC cluster Iceberg, where the AMD based part of the cluster was used, which employs Opteron cores each allocated 2GB of memory and the nodes are connected via gigabit ethernet.

As the flow is assumed to be incompressible, the segregated or pressure based solver was chosen, as it is less computationally intensive in comparison to the coupled or density based solver that is generally required to solve compressible problems. Also the choice of solver is limited by compatibility issues with the physical models required to effectively simulate the flow, where the multiphase formulation prevents the use of the coupled solver. It is possible to model compressibility of the gas phase through use of the couple pressure-velocity coupling scheme, but this was deemed unnecessary as it introduces further demand on computational resources and is not necessary unless the velocity of the gas phase exceed $Ma > 0.3$. The SIMPLE pressure-velocity coupling scheme was chosen because it is a reliable and robust numerical method that is applicable to a wide range of flows and does not exhibit compatibility issues with any of the discretisation schemes required by other relevant physical models. It also results in similar convergence rates relative to more complex pressure-velocity schemes such as the SIMPLEC and PISO algorithms, which require additional resources to calculate skewness correction. The bidirectional vortex contains a PVC that can be described as being quasi-steady state due to its periodicity, and the mantle structure is thought to be independent of time so the transient solver was used, as the physical vortex is fundamentally spatio-temporal structure, so should be treated as such numerically. This also affords insight into the possible transient form of the mantle and the vortex breakdown that occurs prior to the formation of the PVC, so it can be determined how the embedded structures in the flow react to this. A second order implicit transient formulation is employed to maintain high temporal accuracy while remaining numerically stable relative to the size of the time step, and this is also suggested to be best practice by Ansys when simulating the flow in cyclonic separators [26].

An example of the VOF interface resolution is shown in fig C.2, where fig C.2a represents the actual physical interface, while fig C.2b and fig C.2c depict the piece-wise linear and donor-acceptor geometric reconstruction discretisation schemes available with the explicit method. Fig C.2d represents the basic interface resolution obtainable with spatial discretisation schemes available for the implicit method, which effectively require prior knowledge of where the interface will occur so that the local grid density can be increased. However, the modified high resolution interface capturing (HRIC) scheme is available with the implicit VOF method and provides the most accurate interface resolution, this resolves the boundary in a similar manner to the donor-acceptor discretisation method detailed in fig C.2c. The modified HRIC is one of the most resource intensive spatial discretisation schemes available with the implicit VOF formulation, but is less computationally expensive than the piecewise-linear geo-reconstruct scheme, whilst providing adequately accurate interface resolution. In spite of this, the increased mesh resolution in the core region of the chamber necessitated by the large gradients induced by the vortex, is also beneficial to more accurately predicting the dimensions of the PVC which may affect the mantle structure. In addition to the spatial and tem-

poral discretisation schemes applied to the VOF formulation, the implicit body force treatment is also activated, as it is stated that the extra corrective terms it introduces increase the robustness of the VOF model and allows the flow to achieve a realistic pressure field very early in the iterative process [28]. By using the VOF formulation the pressure staggering option (PRESTO!) pressure interpolation scheme is automatically invoked, which is the recommended method for calculation of intense swirling flows, where the fluid domain is curved and the flow inherently exhibits large streamline curvature. A pressure interpolation scheme is required as the solver stores information regarding the pressure and velocity and the centroid of the control volumes, but the values of pressure also need to be determined at the interfaces between these elements, so that the pressure field can be obtained by solving the governing momentum equation.

(a) Real boundary.   (b) Piecewise-linear.

(c) Donor-acceptor.   (d) Basic resolution.
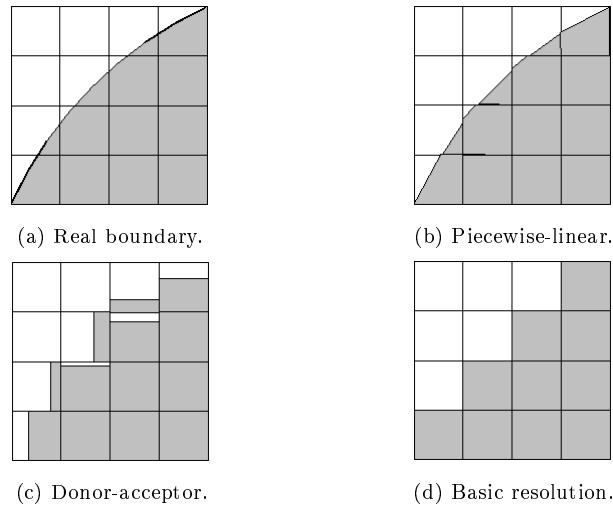
Figure C.2: Methods for resolution of the liquid free surface in VOF calculations. [28]

The PRESTO! scheme is suitable when discontinuous explicit body forces, such as the Coriolis, gravity and swirl need to be accounted for, as well as discontinuous pressure gradients where sudden variations in density can occur, such as VOF calculations. Therefore making it highly suitable for calculation of the pressure field within a hydrocyclone, where the flow is dominated by swirl and contains discrete liquid and gaseous phases. Apart from this, other convective fluxes such as momentum, turbulent kinetic energy, turbulent dissipation rate and the Reynolds stresses are spatially discretised using the quadratic upstream interpolation for convective kinematics (QUICK) scheme. The QUICK scheme is specifically well suited to structured grids where the elements are aligned with the direction of the flow, and can be considered to be an intermediate spatial discretisation method between the 2nd order and 3rd order monotone upstream-centered schemes for conservation laws (MUSCL). The QUICK scheme is only applicable to hexahedral elements, but it is still suitable for hybrid meshes, where the 2nd order discretisation scheme will be used instead to describe the convective fluxes at the faces of the elements that form the unstructured regions of the mesh. In addition to the solver settings already documented, the QUICK scheme is found to be suitably accurate for numerical calculations of hydrocyclones and can be considered best practice for this specific type of problem. As shown in fig 4.12, the RSM turbulence model is able to predict the axial velocity distribution in a gas cyclone to a satisfactory standard when employing the 2nd order spatial discretisation scheme for momentum, turbulent kinetic energy, turbulent energy dissipation and Reynolds stresses. Therefore, the more complex QUICK discretisation scheme provides a suitable high order method for resolving the PVC and flow reversals that occur within the bidirectional vortex and is specifically suited to the mesh that discretises the fluid domain. Other solver settings include the cycle types used by the AMG solver to determine how the solution propagates through the grid hierarchy, as seen in fig C.3. The flexible cycle, which is a hybrid of the V and W cycles, is applied to all the flow variables described by the governing equations, apart from pressure which

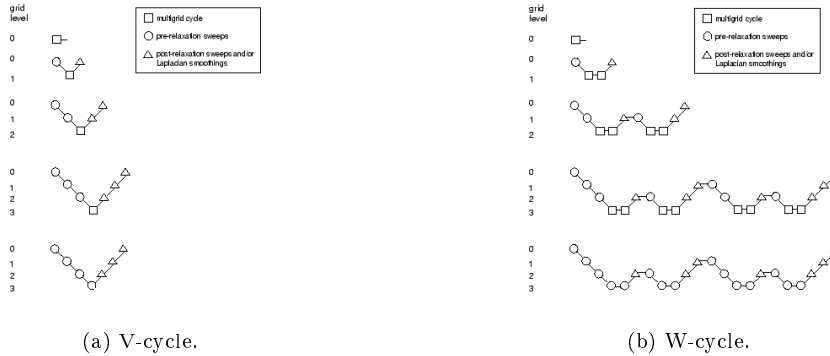(a) V-cycle.   (b) W-cycle.

Figure C.3: Hierarchical cycling methods of AMG solver. [28]

utilises the V cycle. The Green-Gauss cell based method was chosen for evaluation of gradients and derivatives, as the variables calculated at each of the faces of an element are averaged to produce a gradient for any given variable that is representative of the control volume. The Green-Gauss node based method provides similar accuracy to the cell based method for structured grids, but is more computationally expensive so it was deemed unnecessary, as the unstructured regions of mesh where it would provide increased accuracy are not significantly large enough to warrant its use.

Obtaining a fully converged numerical solution of a hydrocyclone is a relatively complex task and each calculation needs to be split into several stages, where the complexity of the model can be successively increased upon adequate convergence at each sub step, till the final solution is obtained. This is predominantly the result of using the RSM turbulence model, which is notoriously prone to stability and convergence issues relative to the other available RANS models [28]. As a result of this, a solution strategy consisting of three parts has been devised so that the solution remains consistently stable and also to allow target convergence criteria to be met. Initially only the primary liquid phase will be calculated, where the VOF equation will be deactivated and the RSM turbulence model will be used to establish the single phase flow field for steady state conditions. Upon reading the mesh into the solver, the quality of the grid is reassessed before the the domain is reordered using the reverse Cuthill-McKee method, which reorders the positions of the grid nodes assigned to the matrix which describes the system. In doing this the bandwidth of the matrix is reduced, which effectively reduces the maximum distance between the cells that are described by the matrix, and is beneficial to improving the calculation speed of the solution.

As the inlet boundary conditions of the CFD study are based on values obtained from the experimental study, they represent the most physically correct boundary conditions available, so therefore will be used to initialise the flow field. For steady state calculations involving the RSM model, large oscillations in the residual error of the solution is indicative of periodic time dependent behaviour that the solver is unable to resolve, which requires a transient solution to be calculated. However, an initial steady state solution provides a method of establishing the bidirectional vortex, where the turbulence model exhibits acceptable convergent behaviour when 1st order spatial discretisation schemes are applied, within a relatively short period of time. The steady state solution is not representative of the physical solution as it is unable to predict the PVC, which means that the transient solver must be invoked, so that vortex breakdown can occur to enable the CRZ to form in the vortex core. In the second part of the solution, higher order spatial discretisation schemes are applied, as they are instrumental in accurately resolving the core flow of the vortex and allow the PVC to be calculated, while solution stability is maintained because of the baseline solution provided in the first step. The higher order discretisation schemes adversely affect the stability of the solution, as the stiffness of the governing equations increases, which means that other parameters need to be altered to counteract this in order to avoid divergent behaviour. The two main methods of doing this are to reduce the size of the time step, so that the variation in the solution is decreased at each calculated interval and to also reduce the explicit relaxation, which is commonly defined through under relaxation factors (URF). Under relaxation factors exist for each of the properties of the flow

	Stage 1	Stage 2	Stage 3
Pressure	PRESTO!	PRESTO!	PRESTO!
Momentum	1st Order	QUICK	QUICK
Volume Fraction	N/A	N/A	Modified HRIC
Turbulent Kinetic Energy	1st Order	QUICK	QUICK
Turbulent dissipation rate	1st Order	QUICK	QUICK
Reynolds Stresses	1st Order	QUICK	QUICK

(a) Discretisation methods for each stage of solution.

	Stage 1	Stage 2	Stage 3
Pressure	0.1	0.2	0.3
Density	1.0	1.0	1.0
Body Forces	1.0	1.0	1.0
Momentum	0.5	0.5	0.7
Volume Fraction	N/A	N/A	0.2
Turbulent Kinetic Energy	0.6	0.6	0.8
Turbulent dissipation rate	0.6	0.6	0.8
Turbulent Viscosity	0.8	0.8	1.0
Reynolds Stresses	0.3	0.3	0.5

(b) Under relaxation factors for each stage of solution.

Figure C.4: Solution strategy variables.

solved by the governing group of non linear equations and work in a similar manner to the time step, in minimising the discontinuities calculated by the governing non linear equations, by effectively dampening the localised discontinuities. As with the size of the time step, reduction of the URF will be beneficial with regards to stabilising the solution, but at the expense of increased wall time required by the calculation. In the second part of the solution a time step of $\partial t = 1.0 \times 10^{-4}s$ was utilised, as it was sufficiently small enough to prevent divergence and minimise the oscillations in the residual errors, while time marching the solution at an acceptable rate. This was also applied during the third step of the solution, but was later increased to $\partial t = 5.0 \times 10^{-4}s$ once the solution was stable, in order to accelerate convergence. A fixed time step was chosen as it was found to provide optimal progress of the solution and prevented the solver from enforcing time step intervals that would preclude obtaining the final solution in a viable time frame. At each time step the maximum amount of iterations was set to 20, as this allows for adequate convergence in the early stages of the solution, while is not excessive to impede the overall progress of the solution. As with the spatial discretisation schemes listed in table C.4a, the under relaxation factors were also adjusted accordingly throughout the solution as seen in table C.4b, so that a compromise could be made between solution stability and convergence speeds.

Example residual error plots can be seen in fig C.5, where fig C.5a indicates a converged solution, as the residual errors for each of the flow equations are all below 10^{-4} and exhibit a relatively small amount of oscillation around the baseline values. This is not the case in fig C.5b, which represents an unconverged solution, as there is significant oscillation in the individual residual errors, and the baseline value of the continuity error does not fall below 10^{-4}. The continuity residual error is the primary indicator of a converged solution as well as the general behaviour of the solution, and is it is vital that the correct solution strategy is employed so that convergence is achieved, so that the results produced are suitably accurate. Oscillations in the residual errors are indicative of solution instability and indicate that the time step is not small enough to adequately resolve the time scale of the flow, although this can dramatically increase the time of the calculation and is not always acceptable solution. However, if oscillations occur about a baseline value, and if the amplitude of the oscillations does not interfere with convergence criteria, then this is acceptable, as this indicates that the flow has periodic characteristics which can be sufficiently resolved with the time step employed.

Residuals

Continuity
X - Velocity
Y - Velocity
Z - Velocity
k
Epsilon
UU - Stress
VV - Stress
WW - Stress
UV - Stress
VW - Stress
UW - Stress
Vf - Phase 2
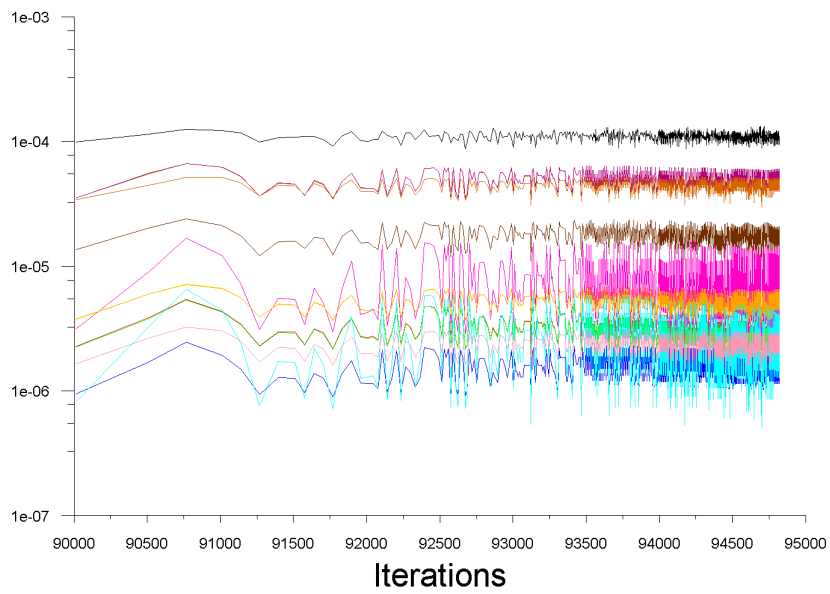
(a) Converged solution.
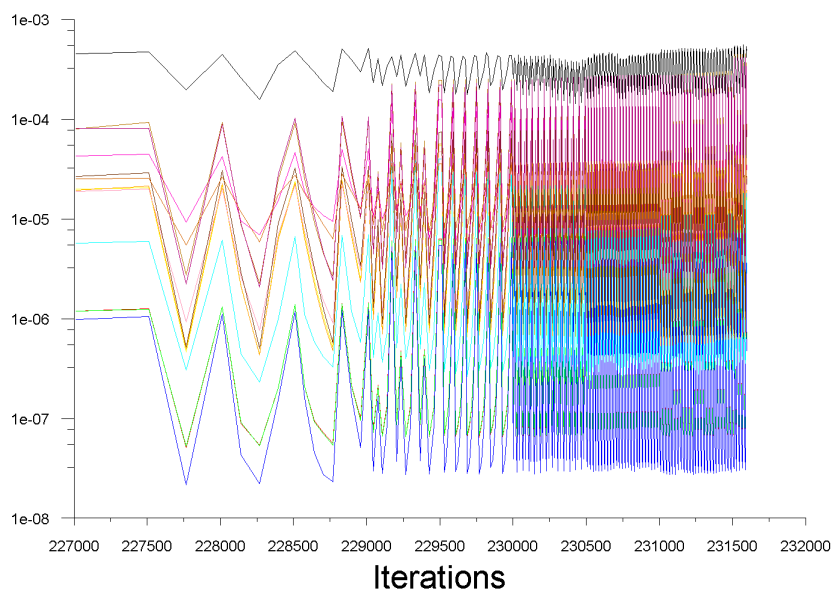
(b) Unconverged solution.

Figure C.5: CFD residual error plots .

Appendix D

Experimental methods

D.1 Fundamentals of PIV

Particle image velocimetry (PIV) is a non intrusive method used for investigating fluid dynamics, but unlike other laser based non intrusive methods such as LDA, it is a whole field technique. This makes it possible to obtain data over large sections of the flow simultaneously, rather than at a single point. It indirectly measures the velocity of the flow by measuring the displacement of tracer or seed particles in the flow, which are assumed to faithfully emulate the behaviour of the flow, so that a velocity field can be inferred. There are several methods available for conducting a PIV investigation, planar PIV or 2D2C PIV is currently the most widespread technique employed and has become the *de facto* standard for non intrusive flow measurement. Despite planar PIV being relatively simple in relation to more advanced techniques such as tomographic or holographic PIV, these methods are still in their infancy, while planar PIV is a tried and tested method and is applicable to a wide variety of flows. However, planar PIV is still an advanced method for measuring the properties of a flow and requires several components, which include a high speed camera, a high power laser and light sheet forming optics, as well as specialist image processing software that can convert the raw image data into useful results. All of these components combined can become prohibitively expensive, with more advanced PIV techniques requiring additional components that further increase the cost of the system, which means that PIV is generally only available to the research community.
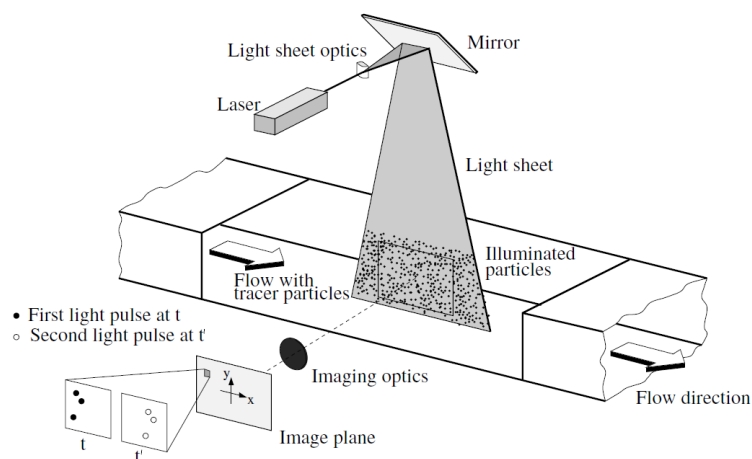

Figure D.1: Experimental setup used for 2D PIV measurements. [41]

PIV involves seeding the flow under investigation with tracer particles, which are small enough so that their trajectories can be considered to accurately represent the behaviour of the flow. These tracer particles are then illuminated by a laser light sheet as shown in fig D.1, where the plane of the light sheet is coincident with the observation plane that describes the region of fluid under investigation. A camera is then positioned orthogonally to the light sheet so that the plane of the camera sensor is parallel to that of the light sheet, in order to minimise perspective distortion which adversely affects the vector field that is calculated. Image pairs are acquired which represent the flow at two points in time, where the interval between the exposures is dependent upon the velocity of the flow, as it is the displacement of the seed particles which are used to describe the flow. The camera and the laser head are both triggered by a synchroniser, which is used to precisely control the timing of the camera exposure and the laser pulses, this ensures that the particle images are not streaks and can describe the instantaneous flow. Multiple image pairs are obtained, which allows for an ensemble vector field to be obtained that represents the mean characteristics of the flow, where the erratic behaviour of the instantaneous flow is removed by calculation of a time-averaged result. This is a similar concept to the LES data sampling technique used in CFD, where information regarding the flow is collected over time, so that coherent structures or periodic behaviour can be observed that are not easily discerned from the instantaneous flow field. To do this, image processing software is required, which compares the displacement of the particles in the image pairs and spatially discretises the flow, so that vectors can be calculated that characterise the localised properties of the flow through cross correlation of the images.
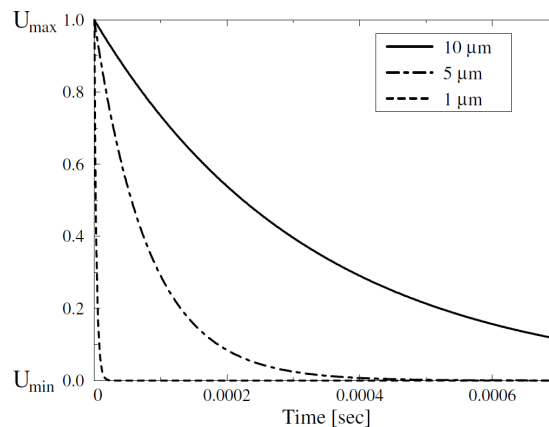

Figure D.2: Time response of seed particles relative to diameter. [41]

A major issue when conducting PIV is to ensure the flow is properly seeded, as this determines whether or not the particle image displacements are representative of the flow and whether the images are suitable for producing an accurate vector field. This means that many variables need to be considered, such as the: size, shape, density, refractive index and composition of the seeding particles, in addition to what techniques are available to introduce the particles into the flow, or how the seeding density can be controlled. The primary concern is to minimise the effects of velocity lag or reduce the drag of the particles, so that their time response is reduced, meaning that the seed particles faithfully describe the behaviour of the flow. The time response or characteristic time of a particle t_p can be approximated by calculating the Stokes drag, where the particles abilities to accurately track the flow can be improved by reducing the particle size, decreasing the particles density or increasing the viscosity of the fluid under investigation. However, it is preferable to seed the flow with neutrally buoyant particles, as attenuation of the fluids viscosity through temperature is limited, which means that velocity lag is commonly controlled through the dimensions of the seed particles. An example of the effect particle size has upon the relative time response can be seen in fig D.2 [41] which details the time response of oil droplets in air. It is clear that smaller particles are preferable as they produce less drag across a range of velocities and therefore their

motion is representative of the flow. The size of the particles are highly dependent on the velocity and properties of the fluid, which means that the Stokes particle number is commonly used to characterise not only the characteristic time of the particles t_p but also the characteristic time of the flow t_{fl}. The velocity lag of the particles is deemed appropriate when the Stokes number described by eqn D.1 is $S_k < 0.1$, which indicates that the motion of the seed particles is representative of the flow. This however, is based on the assumption that the particles are spherical, which means that hollow glass spheres as seen in fig D.3 [41] or air bubbles are commonly used to seed liquid flow, while atomised oil droplets are used to seed gaseous flow so that both the size and shape of the particles can be controlled.

$$S_k = \frac{t_p}{t_{fl}} \tag{D.1}$$

Although it is preferable to seed the flow with small particles to reduce the velocity lag, it is also necessary to ensure that the particles are large enough to scatter an adequate amount of light, so that high contrast images are obtained. Larger particles are able to scatter increased amounts of light, where the intensity of the scattered light at a specific distance from the particle is greater for a larger particle in comparison to a smaller particle. An example of this is depicted in fig D.4, which describe the radiation patterns that occur when spherical particles with various diameters that are subject to a single incident ray of light. It is clear that as the diameter of the particle is increased, the distance over which the intensity of scattered light is non trivial and also increases, in addition to variation in the radiative patterns. The intensity of the scattered light is subject to the inverse square law with regards to increased radial distance from the particle $I \propto \frac{1}{r}$, which therefore means that in order to scatter the incident light further from the particle, the intensity of the light in close proximity to the larger particle must be significantly greater than that scattered by the smaller particle. As a result of this, it is necessary to achieve a compromise between the time response of the seed particles and their light scattering characteristics, although this is less of an issue for liquid flows where the size of the seed particles are generally larger. If however, an increase in the diameter of the seed particles is detrimental to the accuracy of the PIV measurements, such is the case for gaseous flow, then the intensity of the scattered light can be increased by use of a high powered laser to ensure adequate image contrast is achieved.
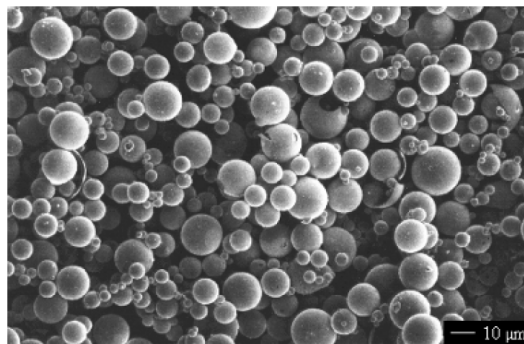

Figure D.3: Hollow glass spheres commonly used for seeding liquid flows. [41]

Apart from the size distribution of the seed particles, another major concern is the distribution of the particles within the flow and the particle image density in the images that are acquired. The velocity of the flow is inferred by the displacement of particles within sub domains of the FOV, which defines the area of the flow under investigation. In order to obtain a vector that accurately describes the motion of the fluid in each sub domain or interrogation zone, the acquired image of the flow needs to contain a sufficient amount of information so that an effective comparison can be made between the image pairs. This is determined by the amount of particles in each interrogation zone and needs to be carefully monitored so that a desirable particle image density is maintained,

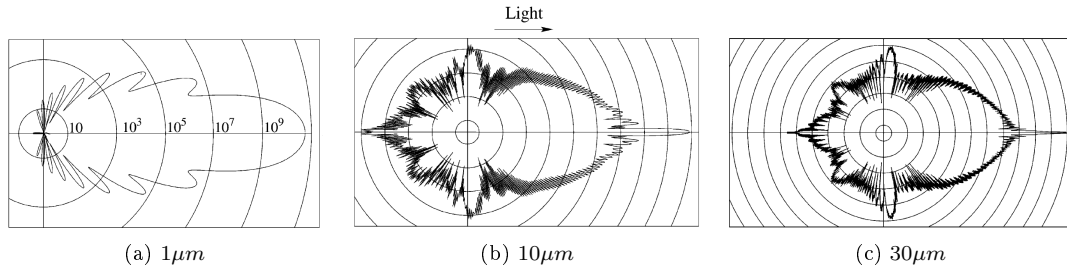185

(a) $1\mu m$ (b) $10\mu m$ (c) $30\mu m$

Figure D.4: Effect of particle diameter on light scattering properties. [41]

such as that seen in fig D.5b, which is an example of medium seeding density, while the low and high particle image densities seen in figs D.5a and D.5c respectively are not suitable for PIV analysis. The low particle density provides an insufficient number of intensity peaks in the image, which are used during image processing and means that the calculated vector may not be representative of the localised flow. The high particle density provides an excess of image intensity peaks, in addition to a greater amount of noise, that adversely affected the SNR during image processing and increases the possible error in the calculated vector. The medium seeding density represents an ideal balance between a sufficient number of particles to describe the flow, but results in an acceptable SNR that enables the particle displacements in the image pair to be correctly resolved.

(a) Under seeded.   (b) Adequately seeded.   (c) Over seeded.
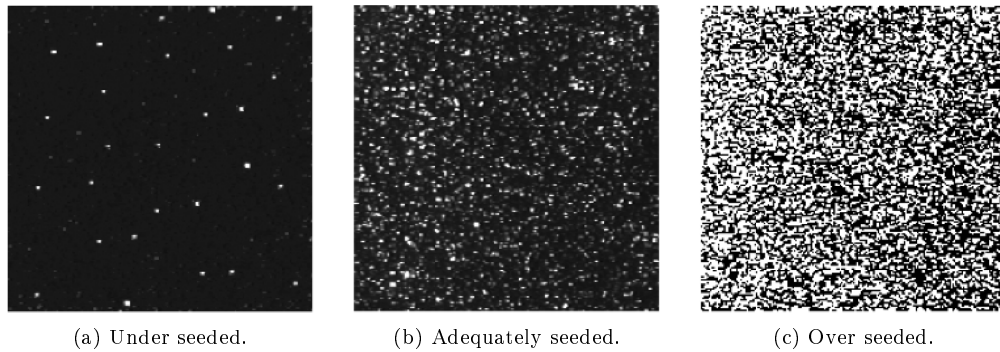
Figure D.5: PIV images produced by various flow seeding densities. [41]

The planar sheet is an integral part of any PIV investigation as it defines the region of the fluid under investigation and provides the illumination required to obtain high contrast particle images that characterise the flow. It is important that the light sheet is sufficiently thin so that the motion of illuminated particles can be considered to occur entirely within a single plane, and therefore the velocity vector can be assumed to be the resultant of the two in plane velocity components. Lasers are required for particle illumination as they produce a monochromatic highly collimated coherent beam of light which exhibits a small amount of divergence, unlike standard light sources, and is therefore suitable for producing relatively large light sheets which are sufficiently thin and of uniform thickness. These lasers operate in transverse emission mode TEM_{00}, which focuses to a point and results in high irradiance, but the beam can be easily manipulated through use of a cylindrical lens to form a light sheet, then focused with tertiary lenses that results in relatively high irradiance and produces intense light scatter from seed particles. It is not possible to resolve the out of plane velocity component when conducting planar PIV, so the interrogation volume defined by the laser sheet must be adequately thin and uniform so that projection of the interrogation volume in the camera sensor plane can be assumed to 2D, as shown in fig D.6. Control of the laser pulse timing is also an important aspect of any PIV investigation as it is responsible for the temporal resolution of the particle images acquired. The type of laser and pulse timing method is dependent upon the type of camera sensor technology and whether the images pairs are either
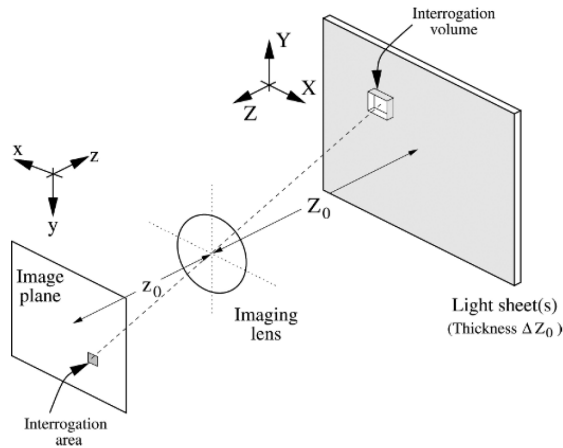
186

Figure D.6: Image projection of interrogation region. [41]

acquired continuously or staggered. High speed CCD based cameras acquire staggered image pairs through double exposures, while high speed CMOS based cameras can acquire images continuously and allow for the instantaneous time resolved flow to be analysed. Due to this variation in exposure sequencing, a diode pumped solid state (DPSS) twin head Nd:YAG laser is commonly used in combination with double exposure cameras, while a copper vapour gas laser (CVL) can be used with either technology, due to their high repetition rates. The main priority with either laser, is to provide sufficiently intense illumination of the seed particles over a small period of time that occurs within the exposure period of the camera and effectively freezes the particle motion in time. As a result of these different acquisition techniques, the pulse timing of the laser needs to be adjusted accordingly, and while a single laser pulse per exposure is suitable for the continuous recording of CMOS cameras where it is possible to adjust the image acquisition frame rate, this is not applicable to double exposure CCD cameras. These require timing of the laser pulses in a frame straddling configuration, where the first pulse occurs near the end of the first exposure and the second pulse occurs near the start of the second exposure. In arranging the laser pulses in such a way, it is possible to obtain image pairs that are separated by the inter frame transfer period of the camera, and represents the shortest possible separation period between the two exposures, which is necessary for image acquisition of high speed flow.
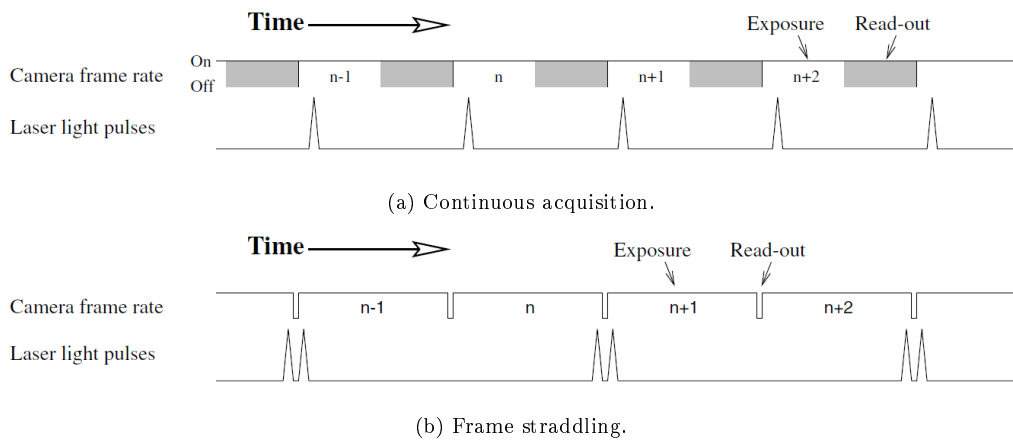

(a) Continuous acquisition.

(b) Frame straddling.

Figure D.7: Timing configurations for modern PIV experiments. [41]

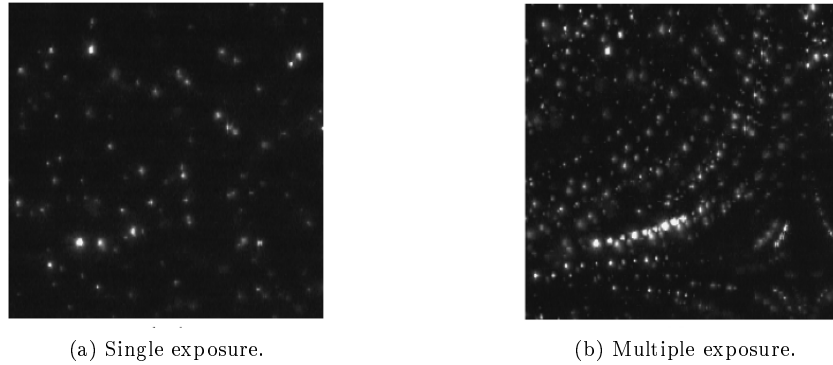(a) Single exposure.   (b) Multiple exposure.

Figure D.8: PIV images acquired using different exposure techniques. [41]

Examples of the timing configurations employed for continuous CMOS and CCD frame straddling camera are shown in figs D.7a and D.7b respectively, which also highlight the short pulse width of the laser relative the exposure of the camera. The timing configuration is predominantly dependent on specific camera sensor technology and the frame transfer procedure, but it is also dependent on the type of image processing algorithm that is employed to resolve the velocity field of the flow. Figs D.8a and D.8b are examples of single frame particle images that are also single and multiple exposures respectively, which are produced by varying the number of laser pulses that occur during the period that the cameras electronic shutter is open. The single exposure in fig D.8a provides insufficient information to infer the motion of the fluid, although it is possible to resolve the behaviour of the flow from the multiple exposure in fig D.8b through autocorrelation. It is possible to conduct PIV analysis using images with multiple exposures, but the autocorrelation method results in directional ambiguity of the velocity field, as it is unable to determine whether the sign of the vector from the intensity peaks in the image. It is for this reason that modern PIV systems are based around high speed cameras and the acquisition of image pairs, which allows for analysis through cross correlation and eliminates the directional ambiguity associated with autocorrelation techniques.
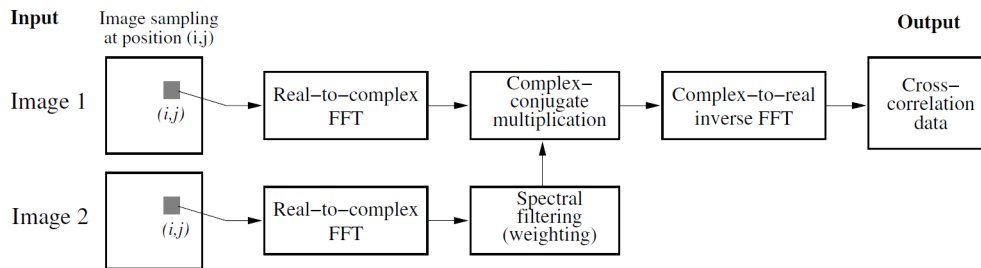

Figure D.9: Flow chart of cross correlation operations. [41]

Cross correlation is a signal processing technique that compares the similarity of two waveforms as a function of the time interval which separates the waveforms. These two waveforms can be described by two independent variables, where the relative displacement of the waveforms with respect to time can be discerned statistically. In relation to PIV, the waveforms are provided by the image pairs, where the time interval is the period between the laser pulses, and the independent variables are represented by the x and y coordinates that define the observation plane. Therefore it is possible to resolve the 2D velocity components of the flow from the displacement per unit of time of the waveforms. A block diagram of the cross correlation process is included in fig D.9, which indicates how the pixel intensity map that represents the particle images are converted into the complex domain by fast Fourier transform (FFT), so that waveforms based on pixel intensity can be produced to enable cross correlation to be performed. Cross correlation calculates a single displacement or

(a) 1st pass.

(b) 2nd pass.

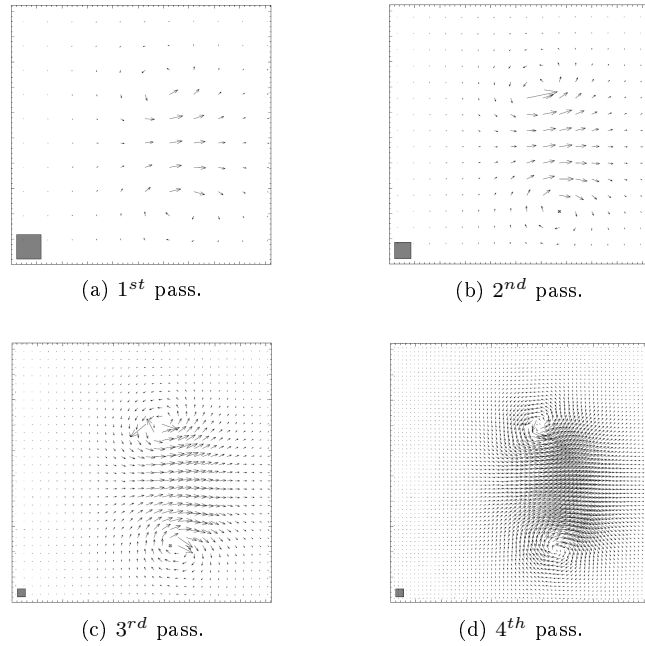(c) 3rd pass.

(d) 4th pass.

Figure D.10: Increased flow resolution obtained with multiple pass multi-grid approach. [41]

vector, which means that it is necessary to spatially discretise the fluid domain into smaller regions or interrogation zones, so that it is possible to obtain vectors that characterise localised properties of the flow. Therefore overall producing a vector field that describes the behaviour of the flow across the entire FOV, where decreasing the dimensions of the interrogation zones results in increased spatial resolution of the flow as shown in fig D.10. Once the particle images have been transformed through FFT, the pixel intensity fields of the image pair I and $I^{'}$ in the complex plane are multiplied together to produce a convolution function $R_{II'}$, whose magnitude is defined by the correlation coefficient. The correlation coefficient is a measure of the correlation between the pixel intensities of the image pair, where the large correlation peak seen in fig D.11a is indicative of an image pair where the large pixel intensities caused by the presence of seed particles compare well. Effectively, this means that there is a sufficient seed particle density within the interrogation zone and there is also a good contrast between the seed particles and the flow, which is indicated by the desirable SNR of the correlation coefficient peak, such as fig D.5b. In physical terms though, this indicates that all the seed particles within the interrogation zone exhibit a similar displacement, which is reflected by the large correlation coefficient peak and therefore the resultant vector can be considered to accurately represent the local behaviour of the flow. However, in fig D.11b there is a considerable amount of noise in the correlation plane, and the correlation coefficient peak is not clearly defined like in fig D.11a, exhibiting a poor SNR that is the likely result of a high seeding density as seen earlier in fig D.5c.
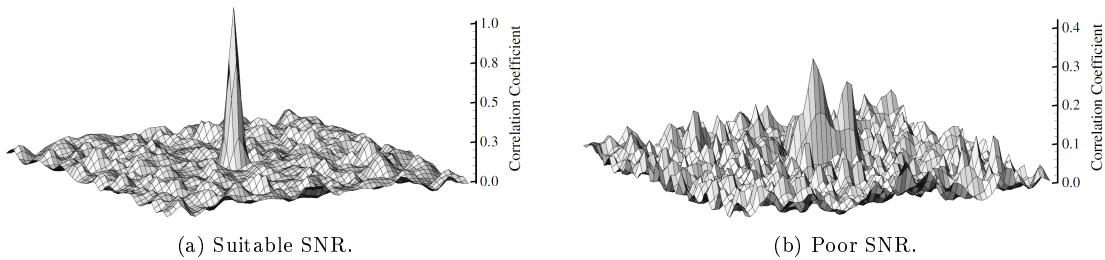

(a) Suitable SNR.

(b) Poor SNR.

Figure D.11: Effect of SNR on peak locking. [41]

(a) Initial intensity field. (b) Second intensity field. (c) Representation of processed fields.
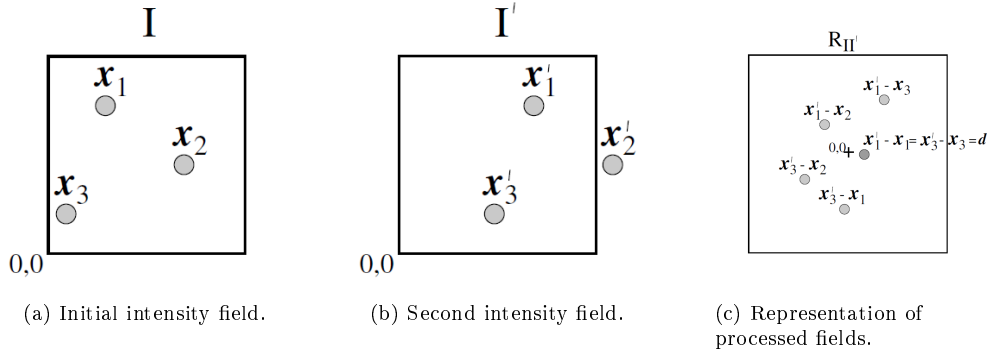
Figure D.12: Cross correlation of pixel intensity fields. [41]

Examples of the base I and cross I' intensity fields that describe the image pair are shown in figs D.12a and D.12b respectively, while a schematic representation of the cross correlation of the intensity fields is depicted in fig D.12c. This shows that the displacement of the particles x_1, x_2 and x_3 can be effectively represented by a single displacement of magnitude d relative to the origin of the interrogation window. This effective displacement is retrieved by inverse FFT of the convolution function $R_{II'}$, where position of the correlation coefficient peak in the complex domain relates to the point where the displacement terminates. This allows for a velocity vector based on the particle image displacement in the real plane to be obtained, which characterises the behaviour of local the flow within the interrogation window.
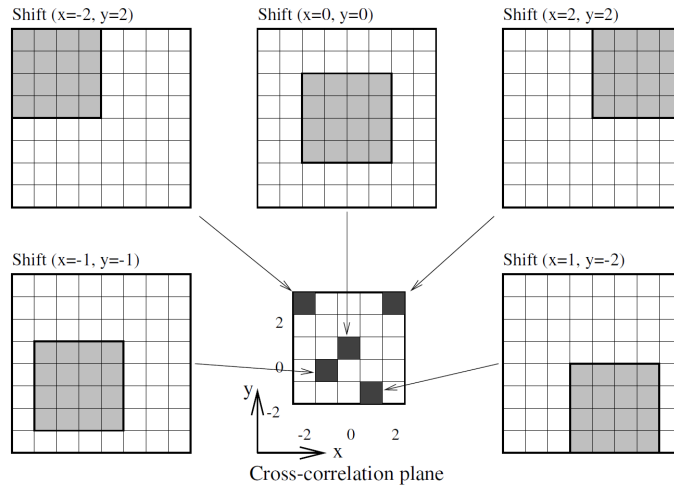

Figure D.13: Interrogation window search pattern with 50% overlap. [41]

During processing of a single interrogation window it is unlikely that there will be a similar particle distribution in both the base and cross images, as particles enter and leave the sub domain. As a result of this, it is necessary for the interrogation window to be shifted locally so that the particles that have left the sub domain can be found and allow for peak detection of the greatest correlation coefficient, which reveals the displacement vector. Standard window shifting techniques do not alter the geometry of the interrogation window and designate a search area in the correlation plane, where the window shift in any Cartesian direction is a fraction of the dimensions of the interrogation window. The cross correlation function is estimated by multiplication of the complex conjugates of the Fourier coefficients produced by the Fourier transforms of the base and cross images,

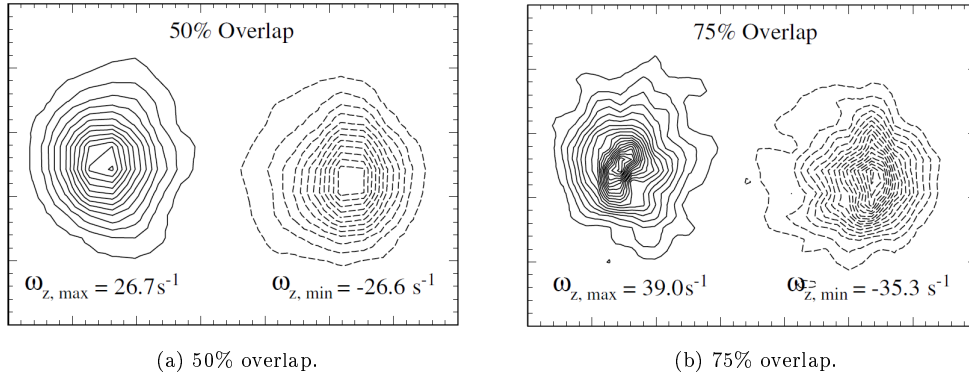(a) 50% overlap.   (b) 75% overlap.

Figure D.14: Effect of window overlap on detection of vortex pair. [41]

in order to improve calculation speeds. This means that the correlation is based in the frequency domain and the sample size $n \times n$ of the FFT, which is equivalent to the spatial sample size $x \times y$ and is subject to fixed sample sizes which have base-2 dimensions such as 64×64, 32×32 and 16×16, due to the FFT implementation. It is also affected by other sampling criteria, as the dimensions of the interrogation window are $n \times n$, and the maximum recoverable range of displacements are limited to $\pm n/2$ in order to prevent aliasing of the correlation peak, because the sampling resolution needs to be at least twice that of the signal, which is denoted by the particle image displacement. This is in order to satisfy the Nyquist condition, and it is common practice to limit maximum particle displacement range in each interrogation window to a conservative value of $n/4$, or a $4\times$ sampling resolution to prevent aliasing of the signal. This also means that to prevent aliasing when searching for particles that have left the sub domain, the shifted interrogation window should not be displaced more than $\pm n/2$, where the maximum search area is defined as $2n \times 2n$, or otherwise known as a Nyquist grid as shown in fig D.13. If the interrogation window overlap is greater than 50% and the maximum search area exceeds $2n \times 2n$, then the signal will be adversely affected not only by aliasing but also through the introduction of excessive noise. An example of this is seen in fig D.14, which depicts the vorticity fields obtained from PIV measurements of a pair of laminar vortices, where the vorticity contours of the actual vortices are known to be curved and smooth . The vorticity contours in fig D.14a where the window overlap is defined as 50%, do exhibit a similar form to the physical vortices but this is not true of the results in fig D.14b, where the window overlap is defined as 75%, and the shape of the contours are irregular due to the effects of increased noise. Planar PIV resolves the velocity field of the flow in 2D, but this provides adequate information to allow several other variables to be calculated based on velocity gradients in the flow, such as vorticity, shear strain and normal strain as seen in fig D.15 to aid characterisation of the flow.
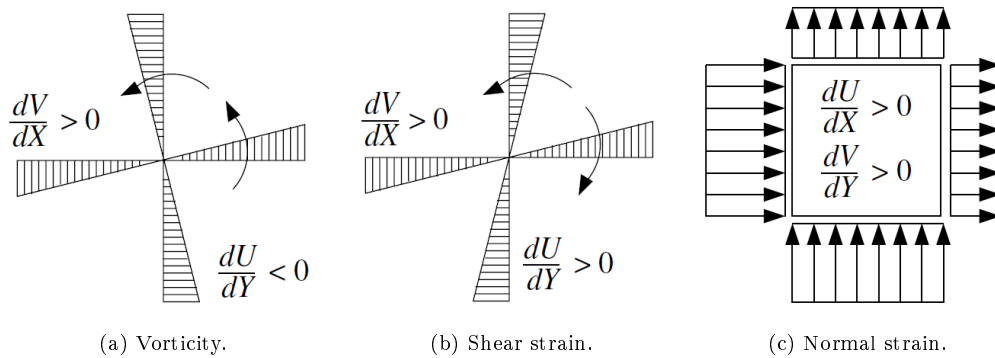

(a) Vorticity.   (b) Shear strain.   (c) Normal strain.

Figure D.15: Velocity derivatives applicable to 2D PIV. [41]

191

D.2 PIV processing

The PIV images acquired were processed using VidPIV 4.6 from Intelligent Laser Application GmbH, where the sequential images were imported according to the following sequence: 1-2, 2-3, 3-4, etc. This is done so that cross correlation can be performed, which requires two images for each vector map that is calculated, being a base image and a cross image, but this method also means that the time interval between the vector maps remains as the reciprocal of the image capture frame rate. The images acquired in the meridional plane are separated by $T = 500\mu s$, while the images acquired from the azimuthal plane are separated by $T = 250\mu s$, and the image resolution results in a spatial resolution of $88\mu m^2$ and $115\mu m^2$ respectively, which is the size of a single pixel. A linear spatial mapping is applied to the images in the azimuthal plane, while a perspective mapping is applied to the images in the meridional plane to account for the lensing effect caused by the cylindrical Borosilicate viewing window. This is in addition to the perspective distortion in the vertical axis caused by the fiducial points of the test chamber and the camera sensor not being coincident, which would require a specialist tilt-shift lens to satisfy the Scheimpflug condition which is applicable in stereoscopic PIV measurements. Based on the PIV rules of thumb, a standard 32x32 pixel interrogation zone was chosen for the meridional plane data, as a 16x16 pixel interrogation zone did not have a sufficient particle density, based on a square interrogation window. Initially cross correlation of the data was performed using a Nyquist 50% interrogation window overlap, with a Gaussian spectral filter being applied to produce a convolution function in the correlation plane to aid peak detection. After this a local mean velocity filter is applied, based on a 3x3 interrogation zone kernel that removes any spurious vectors, before they are replaced by interpolation of outlying valid vectors which are sourced from a similar 3x3 kernel, before all the velocity vector are smoothed, again based on a 3x3 kernel. This set of cross correlation results forms the foundation of the PIV analysis and is calculated so that adaptive cross correlation can be performed, which is an advanced analysis technique that incorporates additional methods that increase the accuracy of the vector field obtained.
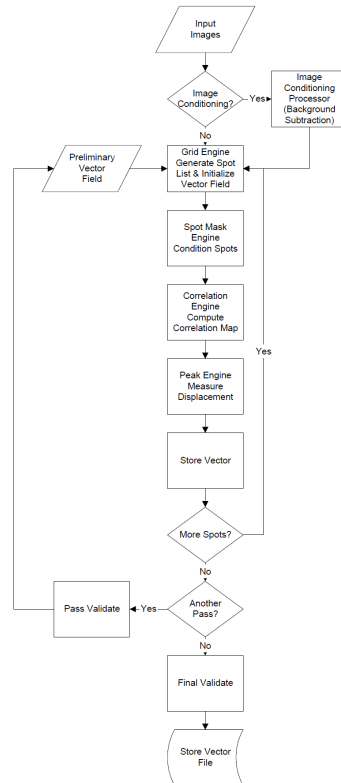

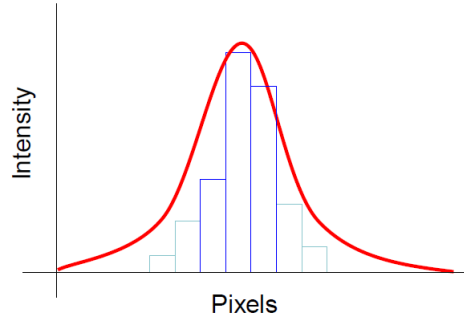Figure D.16: Iterative PIV image processing flow chart. [42]

Figure D.17: Gaussian peak fitting function. [43]

Adaptive cross correlation is an iterative multi pass method which relies on interrogation window deformation and sub pixel fitting methods, that can also minimise the effects of oversampling if the image overlap is too large, as the interrogation window is processed several times to obtain the most accurate vector. A similar method as described for the images obtained from the meridional plane of the chamber is applied to the images obtained in the azimuthal plane of the chamber, although an extra step is included as a further adaptive cross correlation analysis is conducted. It was found that there is sufficient seeding density in the azimuthal plane images to allow for a 16x16 pixel interrogation window to be used, which results in more vectors being calculated to describe the flow in increased detail, and is important in accurately reproducing the tangential velocity profile. The size of the interrogation windows were decided predominantly by consulting the PIV rules of thumb, but the accuracy of the vectors obtained from these sub domains also need to be considered, as criteria need to be established that can determine whether a vector is valid or not. This is why a velocity filter is applied to the vector field, in addition to interpolation of outliers, to calculate approximately valid vectors in place of those which are rejected by the velocity filter. The images taken from the meridional plane of the chamber were cropped before being imported into VidPIV, so that only the left hand part of the chamber where there is adequate light scatter from the particles is processed, also this reduces calculation times. Despite this, it was found that the increased light scatter in close proximity to the PVC prevented valid vectors from being obtained, resulting in approximately 87% of the vectors being valid, which is insufficiently accurate even with interpolation to replace invalid vectors. A blanking mask was then applied to the region affected by the intense light scatter from the PVC so that no vectors were calculated for in region. The result of this was an increase in the amount of valid vectors to approximately 95%, which was deemed an acceptable amount of error and the global vector map could be considered to be representative of the physical flow. A similar problem was encountered when processing the images in the azimuthal plane of the chamber, so a similar approach was adopted to process only the left hand side of the chamber and introduce a blanking mask over the PVC. The full cross section of the chamber produced approximately 91% valid vectors, while the reduced global interrogation region produced approximately 98% valid vectors. This in combination with the increased vector density, results in a high degree of confidence in the tangential profile obtained and effectively characterises the bidirectional vortex observed. The procedure for processing images during a PIV analysis is detailed by the flowchart in fig D.16 and highlights the multi pass iterative method involved in adaptive cross correlation of the vector field.

Sub pixel shifting is able to detect a correlation peak even when the the peak is narrow, as a result of small particle images which are $D_p = 2 - 3$ pixels in diameter. It is possible to obtain sub pixel accuracies up to a maximum 5% of a single pixel, when a 32x32 pixel interrogation window is applied to an 8 bit monochrome image such as those acquired in this PIV study, highlighting the importance of the method for accurate resolution of the flow field. If focused properly, particle images can be described by an Airy intensity function, which are approximated very well by a Gaussian intensity distribution [41]. The Gaussian peak fitting function as shown in fig D.17 can be estimated
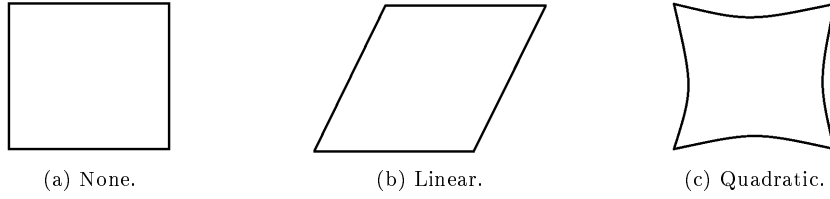
(a) None.　　　　　　　(b) Linear.　　　　　　　(c) Quadratic.

Figure D.18: Types of interrogation window deformation.

from three points, so that the sub pixel position of the correlation peak can be resolved. This is important, as it allows correlation peak detection from particles that would otherwise be omitted during the calculation and this effectively increases the SNR of an interrogation zone, as there is increased differentiation between seeding particles and background noise. However, if the diameter of the particle is below $D_p < 1.5$, then the fitting function will not be able to correctly resolve the correlation peak as it will be adversely affected by local noise, as the SNR will be reduced due to the smaller peak created from the decreased distance between the three point estimator. Ideally the particle size should be approximately $D_p = 3 - 5$ pixels in accordance with the PIV rules of thumb, although defocusing of the camera lens is also commonly employed to increase the effective size of the particles for improved correlation peak fitting. The image processing software VidPIV does not include a Gaussian peak fitting function, so a 5th order B-spline fitting function is used instead, which is suitable as the limit of a B-spline converges to a Gaussian function, and a 5th order B-spline sufficiently emulates the behaviour of a Gaussian function and therefore an Airy intensity function as well. Apart from sub pixel shifting, adaptive cross correlation also incorporates deformation of the interrogation window, where the initial vector associated with a square interrogation zone is then used to determine the shape of the interrogation window next iterative sweep. The windows deformation is based on several criteria such as the desired particle image displacement, the signal strength and the SNR, where the gradient, curvature and acceleration effects [41] also need to be taken into account. Multiple passes occur, and the interrogation window is further deformed until an optimum solution is arrived at, where the shape of the interrogation window reflects the local properties of the flow and the composition of the image that is being interrogated. VidPIV was set up to allow both linear and quadratic deformation of the interrogation windows, with examples of possible window shapes included in fig D.18. Fig D.19 provides an example of interrogation window deformation and highlights how the curvature and gradients in the flow can be accounted for locally. Adaptive cross correlation does improve the accuracy of the final vector map, but the additional features and multi pass iterative processing do increase the demand on computational resources and calculations, and require approximately 30 times more wall time. Upon completion of the image analysis in VidPIV, an ensemble image is produced from the 1000 images acquired, which is then exported to Tecplot 360 so that it can be merged with the CFD data and allow an in depth analysis to be performed.
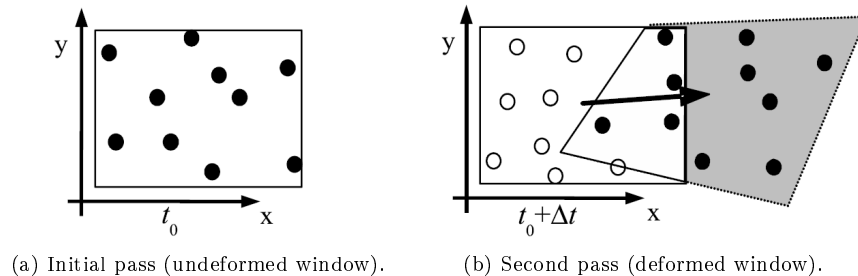

(a) Initial pass (undeformed window).　　　(b) Second pass (deformed window).

Figure D.19: Effect of multiple pass algorithms and window deformation. [41]

194

D.3   Limitations of planar PIV

An inherent problem with planar PIV with regards to cyclonic flows, is that it is only capable of capturing information about the flow in the incident plane of the light sheet, which means that any velocity component normal to the plane will not be resolved and can lead to an incomplete characterisation of the flow. A relevant example of this problem is depicted in fig D.20, where the observation plane is parallel to the chamber of the axis, where the orthogonal streamlines can be seen to repeatedly intersect the observation plane rather than traverse it. This is not a problem when taking measurements in the azimuthal plane of a vortex chamber, as the axial velocity component is relatively small in comparison to the tangential velocity component which dominates the flow. However, problems arise when acquiring data in the meridional plane of the chamber, as the out of plane tangential velocity component is significantly large enough prevent image pairs of particles being acquired, as the particles are likely to move out of the light sheet between camera exposures.
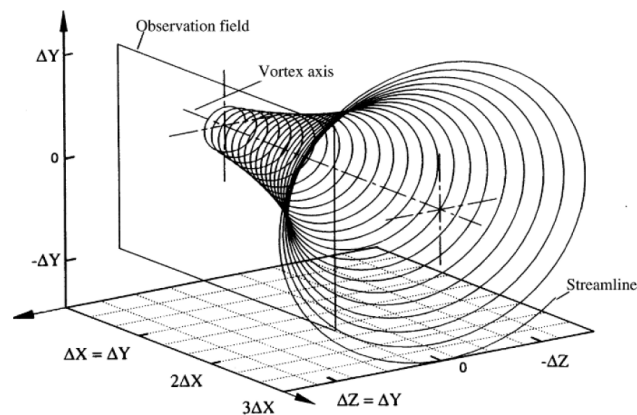

Figure D.20: 3D pathlines of a point vortex relative to axially aligned observation field. [42]

This can be limited by reducing the period between exposures to reduce the effective particle displacement between images and also by increasing the seeding density, to ensure there are sufficient pairs of particles in the images to allow for calculation of a valid vector. Despite this, it leads to an alias vector map being produced where the axial and radial velocity components calculated by the image processing software in the meridional plane inadvertently include contributions from the tangential velocity component due to perspective distortion. It is assumed that the out plane velocity component is negligible in planar PIV experiments, which allows the in plane velocity components to be correctly resolved. If the out of plane velocity component is significant then the in plane velocity components will be influenced according to the magnitude and orthogonal direction of the tangential component, as well as the position of the flow relative to the fiduciary reticule of the images. The magnitude of perspective distortion caused by the tangential velocity component is more pronounced as the distance from the image reticule is increased as shown in fig D.21, where the effect of a uniform out of plane velocity component can be seen on the measured displacement field.

A comparison of the possible particle trajectories that can be resolved by both planar and stereoscopic PIV methods are shown in fig D.22, where it can be seen that perspective distortion can be eliminated when two cameras are available to provide separate points of view. Stereoscopic PIV does however greatly increase the complexity of the experimental setup, as specialist tilt-shift lenses are required, so that the observation plane is aligned with the camera sensor plane and this also effectively reduces the depth of field (DOF). This method also requires several calibration images to be acquired which traverse the thickness of the light sheet, in addition to advanced image processing software to combine the two fields of view, so that a 2D three component vector field can be calculated. Despite planar PIV generally being an inappropriate method for investigating
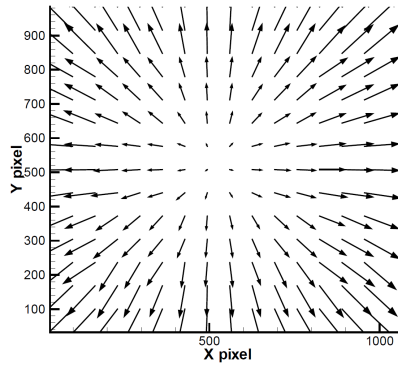
Figure D.21: Measured displacement field of uniform out of plane motion. [42]

the meridional plane of vortices, there are post processing methods available which allow for several characteristics of a vortical flow to be discerned, even in the absence of a full 3D vector field. Due to the relatively small pitch of the helical flow path in the bidirectional vortex, the contribution of the distortion from tangential velocity component upon the radial velocity component is considerably higher than the contribution towards the axial velocity component. The distortion of the axial velocity component is predominantly affected by the displacement error associated with increased distance from the reticule. This can be effectively removed, providing there is sufficient data to span the diameter of the chamber and if both the position of the image reticule and axial velocity profile is known to be symmetric about the chamber axis. The tangential velocity component is antisymmetric about the chamber axis due to the rotation of the vortex, where the flow is being directed either in or out of the observation plane and indicates the tangential velocity component is either positive or negative. This bipolar effect relative to the chamber axis also affects the axial and radial velocity components, which are antisymmetrical and axisymmetrical respectively. Therefore, this means that the contamination of the axial velocity component by the tangential velocity component can be eliminated by calculating the mean axial velocity profile through combining the data from the left and right hand regions of the chamber. This effectively cancels out the distortive effects of the tangential velocity component and a corrected axial velocity profile is produced, which is valid as long as the flow is axisymmetric.
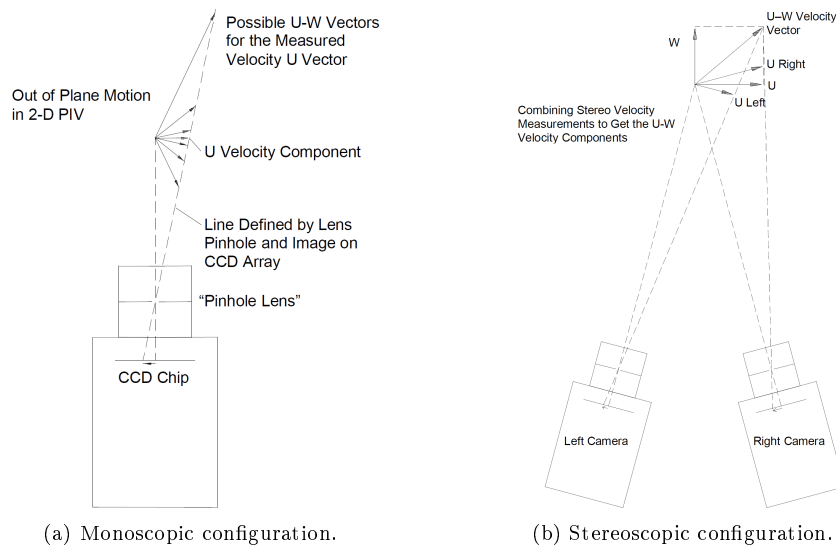

(a) Monoscopic configuration.

(b) Stereoscopic configuration.

Figure D.22: Measured image displacement of out of plane particle motion. [42]

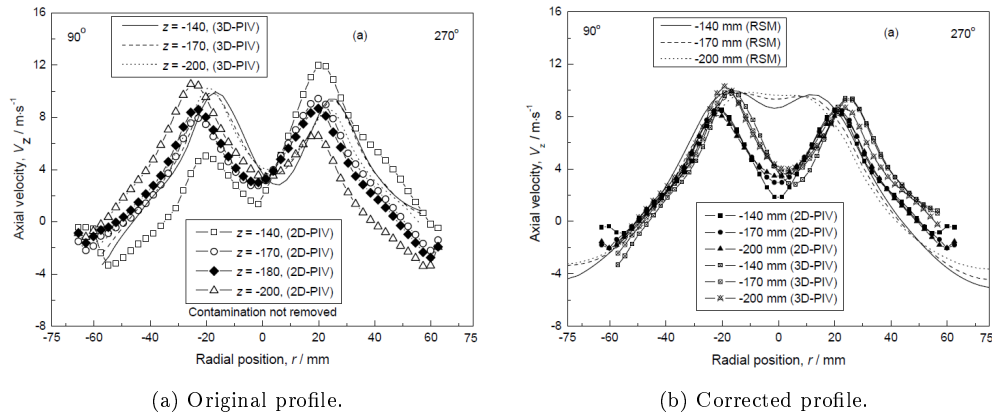(a) Original profile.   (b) Corrected profile.

Figure D.23: Axial velocity profiles obtained by 2D PIV of gas cyclone. [44]

An example of this is shown in fig D.23 [44], which compares the original and corrected axial velocity profiles in a gas cyclone that were obtained by planar PIV. Comparisons were also made between the corrected planar PIV results and data obtained via stereoscopic PIV, where the axial velocity profiles were found to compare favourably [44, 123]. Axial velocity contour maps of the original planar PIV data and the stereoscopic PIV data are displayed in fig D.24 and highlight the inadequacy of the planar PIV method in correctly resolving the axial flow in a confined bidirectional vortex. It is clear from the planar PIV, that the regions of maximum positive and negative axial velocity only span approximately half the length of the observation window, unlike the stereoscopic PIV which displays a relatively uniform axial distribution of axial velocity. For clarity, the position of the mantles have also been included, which are denoted by the black lines on the contour map and clearly show how the antisymmetry of the axial velocity components skews the structure of the mantle. It was found that the radial position of the mantles retrieved from the corrected planar PIV and the stereoscopic PIV data compare reasonably well, and both exhibit an insensitivity to the magnitude of the inlet flow velocity. Unfortunately, this method could not be implemented in the current study because of the increased light scatter caused by the PVC, which prevented adequate illumination of the entire observation plane and meant that only partial images of the meridional plane were processed. Another factor which could affect the validity of this method is the possibility of asymmetric flow, as the CFD data produced for this study indicates the presence of periodic structures embedded within the bidirectional vortex. However, if this method could be applied, it would prove invaluable in extracting the approximate structure of the mantle and most importantly be able to discern whether or not multiple mantles are present. This would be an important step in providing solid evidence that proves the existence of bidirectional vortices that contain multiple mantles, and therefore exhibit multiple flow reversals.
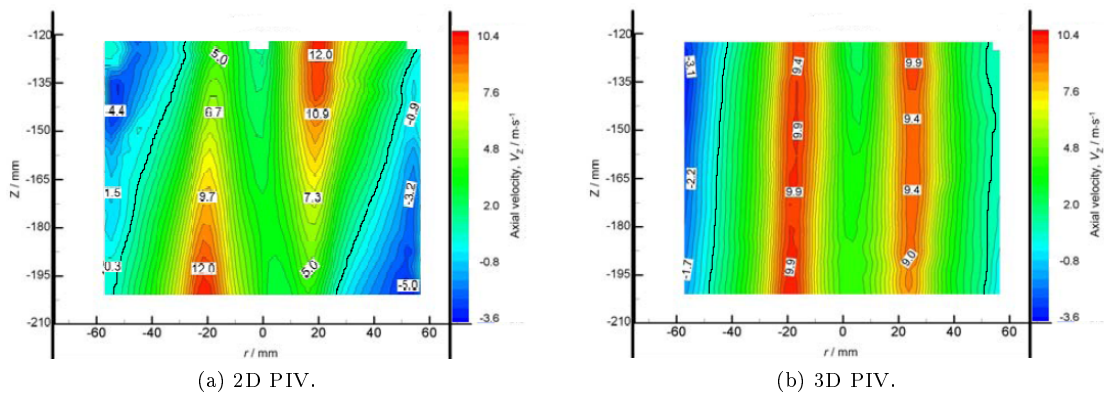

(a) 2D PIV.   (b) 3D PIV.

Figure D.24: Axial velocity contour maps of cyclonic gas flow. [44]

197

Appendix E

Additional results

E.1 Introduction

Apart from the main parameters investigated relating to the inlet flow and chamber geometry, for which both CFD and PIV data were obtained, it was decided to briefly investigate other parameters which may affect the structure of the mantle. The parametric variables chosen for the main study are based primarily on the Beltramian and energy based solutions of the bidirectional vortex, which indicate what conditions may lead to the formation of complex mantle structures with multiple flow reversals. They were also chosen because the SED analysis conducted by Knuth et al [9] of various VIHRE configurations, found that engine performance was enhanced when the inlet flow rate or other geometrical constraints were adjusted. This allowed for the individual contributive effects of each parameter to be characterised which is visually depicted in fig 2.12. The most influential variables in order of effectiveness were found to be: oxidiser flow rate, chamber diameter, chamber length, injector cross sectional area, throat cross sectional area, number of injectors and the tilt angle of the injectors respectively. The majority of these variables are accounted for in the parametric variables of the main investigation, but no consideration has yet been given to effects related to the configuration of the injectors, apart from them being located at either the base or head of the chamber. Decreasing the number of tangential injectors and their angle relative to the azimuthal plane of the chamber was found to be beneficial with regards to engine performance, but these effects were minimal. In spite of this, it was decided to investigate these two parameters independently, to assess whether or not they do influence the bidirectional vortex, in order to determine whether the mantle structure can be manipulated by variables other than the chamber geometry parameters which have been seen in the results presented so far. In lieu of additional injector plates for use with the experimental rig, it was not possible to obtain PIV data for these studies and the results generated are provided purely by CFD, although this should prove sufficient for identifying any behavioural trends in the mantle structure, as seen in other parts of this investigation. The results of these studies are provided within the appendices as it is felt that a brief overview of the observed behaviour is necessary rather than the in depth analysis, which has been applied to the results in the main part of the investigation.

In addition to the three main parameters investigated, consideration was given to the possibility of vortex chambers with variable axial dimensions, as preliminary CFD indicates the presence of two mantles in a novel gas cyclone chamber with head injectors. This can be seen earlier in fig 4.1 where the direction of the vortex tubes are indicated by arrows and it was deemed appropriate to further investigate this experimentally, which resulted in the idea of placing partial spherical surfaces at the axial boundaries that intersect the chamber radius. This results in a fully curved surface at both the head and base of the chamber, with an outlet section bored into the base surface with a contraction ratio of $CR = 20$ to allow the flow to escape. As the radius of the sphere defining the surface is decreased, the curvature of the surface increases, which causes the peak of the dome located at the chamber axis to ingress further into the chamber. These domes are defined by their maximum height relative to the planar axial boundaries of the chamber and increase in $5mm$ intervals to ensure there

is significant variation in the axial dimensions of the fluid domain. By employing a large range of parameters, it is possible to create internal chamber geometries which contrast significantly and may provide suitable conditions for inducing multiple mantles. The chamber parameters for this part of the investigation are presented in table 4.1, where it is worth reiterating that the aspect ratio and contraction ratio remains constant for all configurations, in accordance with the parametric approach. Also it must be mentioned that due to issues with optical access, only chamber configurations with head injectors have internal domed surfaces at both ends of the chamber, while configurations with base injectors only have a dome at the base of the chamber. Diagrams representing the range of parameters relating to the dome height study are included in fig E.1 to aid in visualising the various chamber geometries investigated.

(a) $H = 5mm$ (b) $H = 10mm$ (c) $H = 15mm$

(d) $H = 20mm$ (e) $H = 25mm$ (f) $H = 30mm$

(g) $H = 35mm$
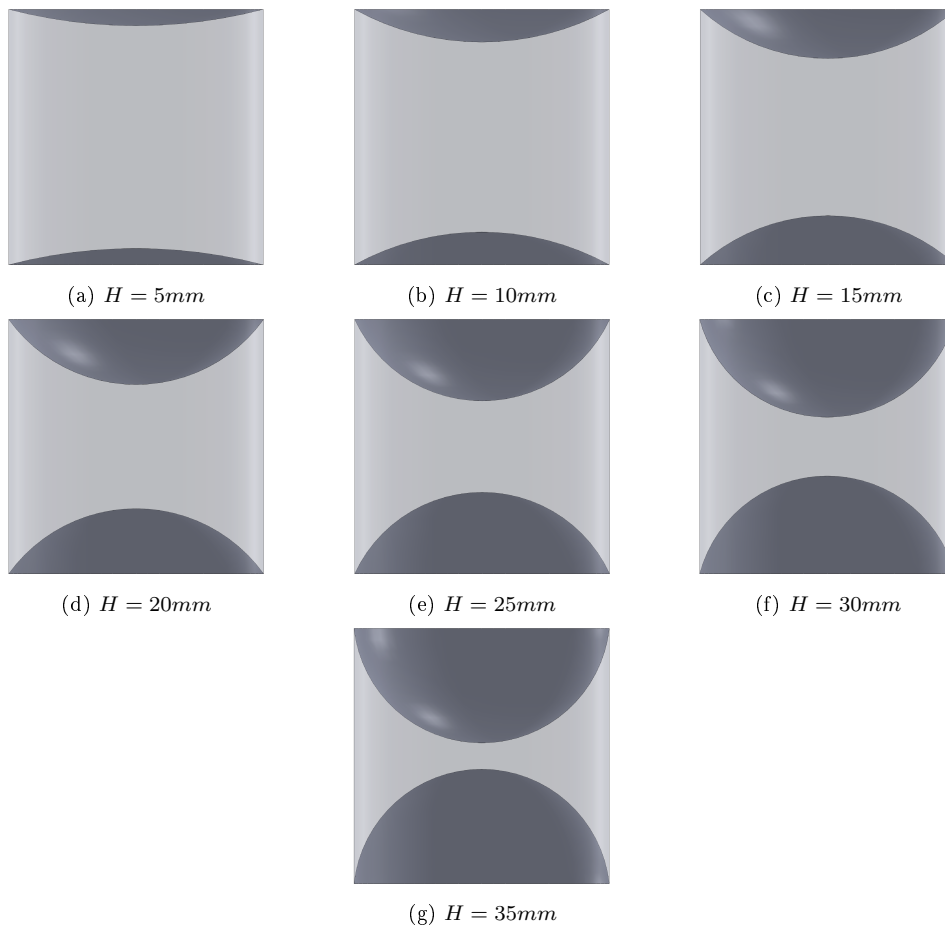
Figure E.1: Chamber configurations for the internal dome height study.

E.2 Effect of internal dome height

E.2.1 Base injection

To enable PIV measurements to be obtained for the various chamber configurations with internal domes with base injectors, only a single dome is present and is located at the base of the chamber. The most salient information extracted from the CFD and PIV data for these chamber configurations is presented in table E.1, although it was only possible to obtain numerical data for domes which have a maximum height of $H = 5 - 25mm$ due to convergence issues. As with other parts of the investigation into the effects of chamber geometry, this is attributed to the large gradients that occur within the core region of the flow which affect solution stability. It is found that as the height of the dome is increased, the magnitude of the inlet velocity tends to increase, but over a small range relative to other parts of the study. This appears to be contradicted by the static pressure at the inlets which also increases with greater dome heights, where the opposite would be expected, but the range of pressures is relatively small as with the inlet velocities. Both the CFD and PIV data concur in that the normalised radius of the PVC does decrease as the dome height is increased and are generally of similar magnitude, although the PIV data exhibits a sudden increase above $H = 25mm$. It is unknown whether this is anomalous or due to the lack of CFD data for domes with heights in the range $H = 30 - 35mm$. There is some variation in the radius of the PVC but the same effect is not seen in the radii of the forced vortex, which displays no discernible trend for the PIV data and the radius of the forced vortex shows little variation with respect to dome height. It is clear that the CFD results appear to under predict the radius of the SBR region, which has been seen repeatedly throughout the whole investigation and may indicate that the model constants of the RSM turbulence model need to be adjusted. However, the CFD results do indicate a consistent reduction in both the radius of the PVC and SBR region, which is reflected by the increased peak tangential velocities that occur in the chambers with larger domes. When these values are normalised by the inlet velocities, the variation across this range of values is diminished, although this is not the case for the normalised peak tangential velocities extracted from the PIV data. The peak tangential velocities for the PIV data as seen in table E.1b display the opposite behaviour and the magnitude decreases with respect to increased dome height, which is also evident in the values normalised by the inlet velocities. Apart from this, the addition of an internal dome appears to have little impact on the properties of the flow and the reduced peak tangential velocities that occur in spite of the minimal variation in the structure of the vortex core, may be caused by the reduced length of the core. The uniform contraction ratio of the chamber induces a relatively dimensionally invariant PVC, but the vortices in the chambers with larger domes are less intense than those with smaller domes. This contradicts what is found in the chamber aspect ratio study, where shorter chambers are seen to produce more intense vortices and there is a definite correlation between peak tangential velocities and the aspect ratio of the chamber. Regarding the data presented in table E.1, it can be concluded that for the range of conditions tested that the effect of internal dome height has little influence on the properties of the flow and there are no appreciable transitions in the figures which would indicate an evolution of the embedded mantle structure.

The plots displayed in fig E.1 are taken from the azimuthal plane of the chamber, where the combined CFD and PIV data is presented separately due to the lack of CFD data across the full range of dome heights investigated. As explained previously, the combined tangential velocity plot seen in fig E.2a shows how the forced vortex calculated by the CFD is again lower than that of the PIV, and also exhibits higher peak tangential velocities, which is to be expected as the reduced core radius is indicative of increased vortex stretching. The small variations in the peak values across the range of dome heights $H = 5 - 25mm$ is also reflected by the minimal variation in the form of the tangential velocity profile for both the CFD and PIV data sets. It can be difficult to discern this behaviour visually from a graph, but the angular velocity of the forced vortex and the inverse gradient of the free vortex presented in table E.1b corroborates this. There is some variation in the angular velocity, caused by the range of peak tangential velocities, in combination with consistent SBR radii and this especially highlights the similarities in the gradient of the irrotational flow. The tangential velocity profiles obtained from the PIV data as seen in fig E.2b, incorporate the full range of dome heights

(a)

Dome Height H (mm)	Inlet Velocity u_{in} (m/s)	Inlet Pressure (CFD) p_{in} (Kpa)	Inlet Reynolds Number Re	Vortex Reynolds Number V	Strouhal Number (CFD) Sh	Strouhal Number (PIV) Sh	Normalised Air Core Radius (CFD) r_{core}	Normalised Air Core Radius (PIV) r_{core}	Normalised Forced Vortex Radius (CFD) r_{SBR}	Normalised Forced Vortex Radius (PIV) r_{SBR}	Liquid Dimension of Forced Vortex (CFD) $r_{SBR}\cdot r_{core}$	Liquid Dimension of Forced Vortex (PIV) $r_{SBR}\cdot r_{core}$	Precessing Vortex Core Frequency (CFD) f_{PVC} (Hz)
5	1.17	13.23	4.55E+04	3.01E+03	7.57	3.12	0.081	0.081	0.144	0.252	0.063	0.171	113.77
10	1.19	14.10	4.61E+04	3.05E+03	7.98	3.14	0.081	0.080	0.140	0.249	0.059	0.169	121.57
15	1.13	12.94	4.40E+04	2.91E+03	7.93	3.21	0.081	0.084	0.141	0.255	0.060	0.171	115.24
20	1.21	15.06	4.68E+04	3.10E+03	8.22	2.92	0.076	0.067	0.139	0.249	0.063	0.182	127.15
25	1.22	14.88	4.74E+04	3.13E+03	8.18	2.80	0.074	0.066	0.137	0.242	0.063	0.176	128.00
30	1.22	×	4.72E+04	3.12E+03	×	2.59	×	0.076	×	0.252	×	0.176	×
35	1.21	×	4.70E+04	3.11E+03	×	2.75	×	0.076	×	0.253	×	0.177	×

(b)

| Dome Height H (mm)	Peak Tangential Velocity (CFD) u_ϕ (m/s)	Peak Tangential Velocity Ratio (CFD) u_ϕ/u_{in}	Peak Tangential Velocity (PIV) u_ϕ (m/s)	Peak Tangential Velocity Ratio (PIV) u_ϕ/u_{in}	CFD Forced Vortex Angular Velocity $(\partial u_\phi/\partial r)$ ω (rad/s)	PIV Forced Vortex Angular Velocity $(\partial u_\phi/\partial r)$ ω (rad/s)	CFD Free Vortex Inverse Gradient $(\partial r/\partial u_\phi)$ $\partial r/\partial u_\phi$	PIV Free Vortex Inverse Gradient $(\partial r/\partial u_\phi)$ $\partial r/\partial u_\phi$	CFD Normalised Boundary layer height at chamber wall δ_w	PIV Normalised Boundary layer height at chamber wall δ_w	Maximum Axial Velocity (CFD) u_z (m/s)	Minimum Axial Velocity (CFD) u_z (m/s)	Maximum Axial Velocity (PIV) u_z (m/s)
5	4.02	3.43	2.90	2.47	714.86	294.65	86.25	96.70	0.02	0.03	2.88	-2.36	0.27
10	4.16	3.50	2.92	2.46	763.87	300.56	86.50	92.14	0.02	0.04	2.96	-5.06	0.28
15	3.97	3.50	2.91	2.57	724.07	292.92	82.92	97.73	0.02	0.03	2.78	-5.22	0.28
20	4.32	3.58	2.76	2.28	798.93	284.09	87.62	92.29	0.02	0.03	2.96	-5.51	0.24
25	4.30	3.52	2.61	2.13	804.27	275.87	85.49	83.93	0.02	0.03	2.93	-5.53	0.16
30	×	×	2.50	2.05	×	253.51	×	80.61	0.02	0.03	×	×	0.13
35	×	×	2.64	2.18	×	268.22	×	83.81	0.02	0.04	×	×	0.10

Table E.1: Flow variables for chambers with base injection.

investigated and like the profiles seen in fig E.2a for the limited range, display no specific relationship between peak tangential velocity and dome height. The similarities in the gradients of the free and forced vortices extend across the full range of the test parameter, although these similarities in the profiles do tend to diverge in close proximity to the periphery of the chamber, although there is still minimal variation in the normalised height of the boundary layer, as reported in table E.1b. The plot of the radial velocity distributions extracted from the CFD data displayed in fig E.2c are similar to those seen for all base injector chamber configurations, which suggests that despite the obvious differences that are seen in the mantle structure due to geometrical influences, this is not the case with the radial velocity component. This does not agree with the Beltramian theory, which finds that the zeroes of radial velocity can be predicted by the zeroes of the Bessel function of the first kind J_1. However, the Beltramian theory does not currently account for the boundary layers at the end walls of the chamber and the similarities in the radial velocity profile seen for all base injector chamber configurations is the likely result of the position of the azimuthal observation plane. The radial velocity component is significantly smaller than the tangential component and even the axial velocity component, where the increased radial velocities that have been observed can be attributed to the increased cross flow that occurs at the head of the chamber. Therefore, the radial velocity profiles are most probably influenced by the local geometry forcing the flow towards the chamber axis, where the effects due to mantle structure would be minimal in comparison. In fig E.2d, it can be seen that for chamber configurations with dome heights of $H = 5$, 20 and $25mm$ that the peak radial velocity magnitude is positive, while for chambers with dome heights of $H = 10$, 15, 30 and $35mm$ the peak value is negative, as the flow is directed towards the chamber axis. As with the tangential velocity profiles, there is no distinct relationship between the radial velocity component and the test parameter. The variation of this small range of values may be the result of inconsistencies in the CFD calculations, which could be due to various issues associated with the solver and the final state of the converged solution.

The axial vorticity plot seen in fig E.2e confirms the presence of vortices of greater intensity in the CFD data, as indicated by the tangential velocity profiles in fig E.2a, and again highlights the similarities in the results across the range of dome heights investigated. These similarities are also reflected in the axial vorticity distributions taken from the PIV data shown in fig E.2f, where little variation in the profiles can be seen across the full range of dome heights and all exhibit similar peak values. It has been noted that the results obtained in this part of the study exhibit many similarities to the majority of the results for other chamber configurations, but this is especially true of the chambers in the inlet Reynolds number study with base injectors. This, in combination with the small influence the internal dome geometry has been found to have upon the flow, also suggests that a similar mantle structure would be expected which also displays little variation with respect to dome height. The radial static pressure distribution taken from the CFD data is displayed in fig E.1g and like other values of interest, shows no correlation to variation in the height of the internal dome. This is made even clearer by the normalised pressure distributions seen in fig E.1h, where the plots are almost identical and provide no evidence to suggest chamber geometry has any influence in this case.
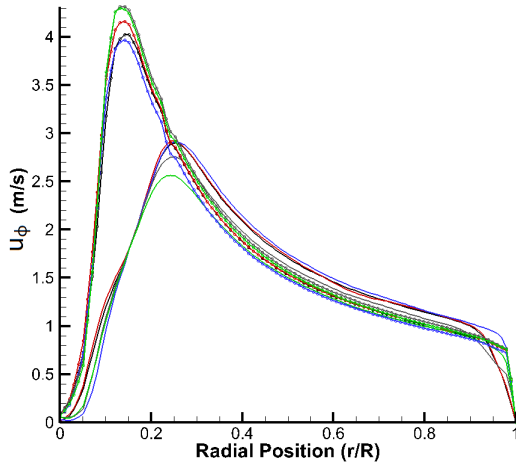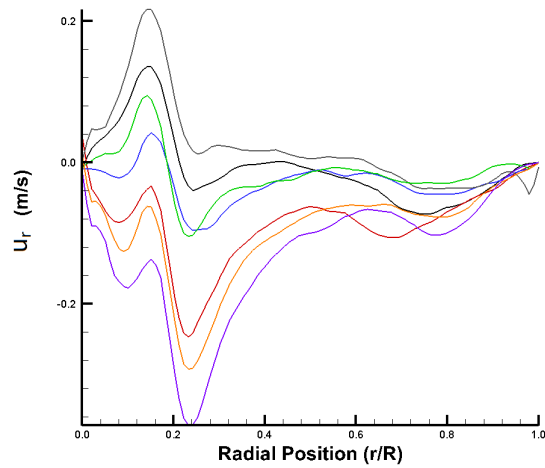
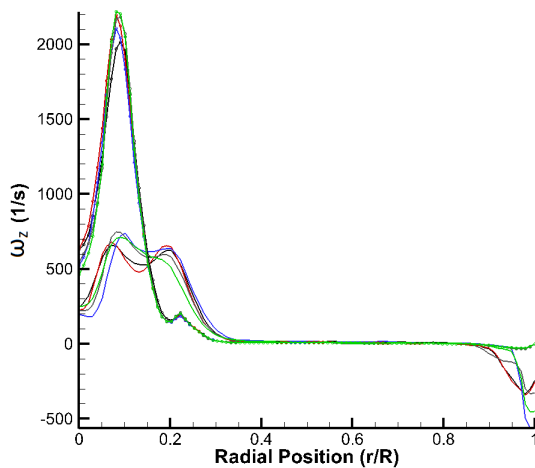(a) Tangential velocity profile (CFD & PIV).
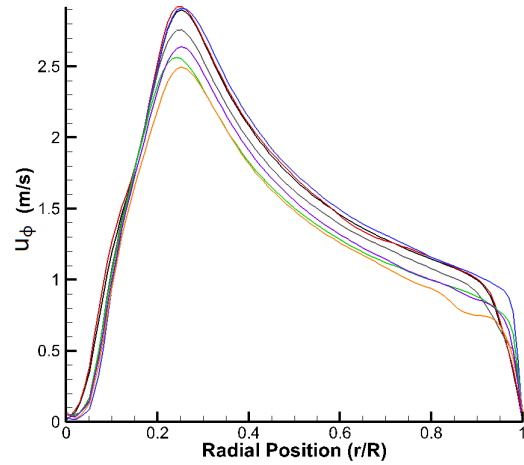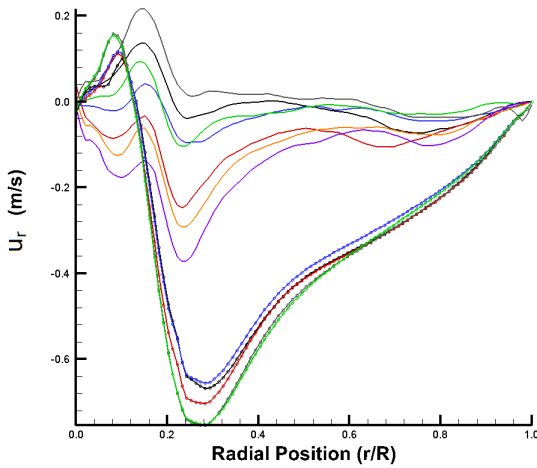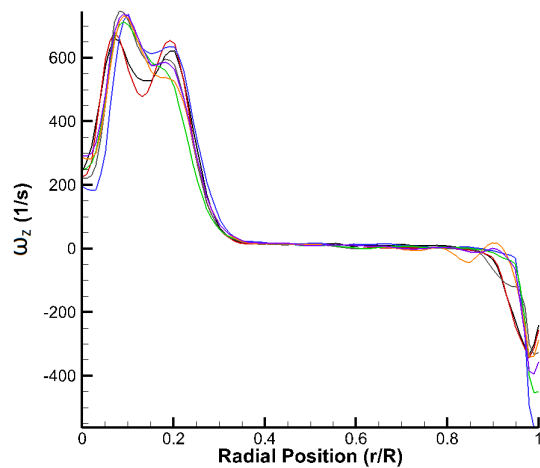
(b) Tangential velocity profile (PIV).

(c) Radial velocity profile (CFD & PIV).

(d) Radial velocity profile (PIV).

(e) Axial vorticity profile (CFD & PIV).
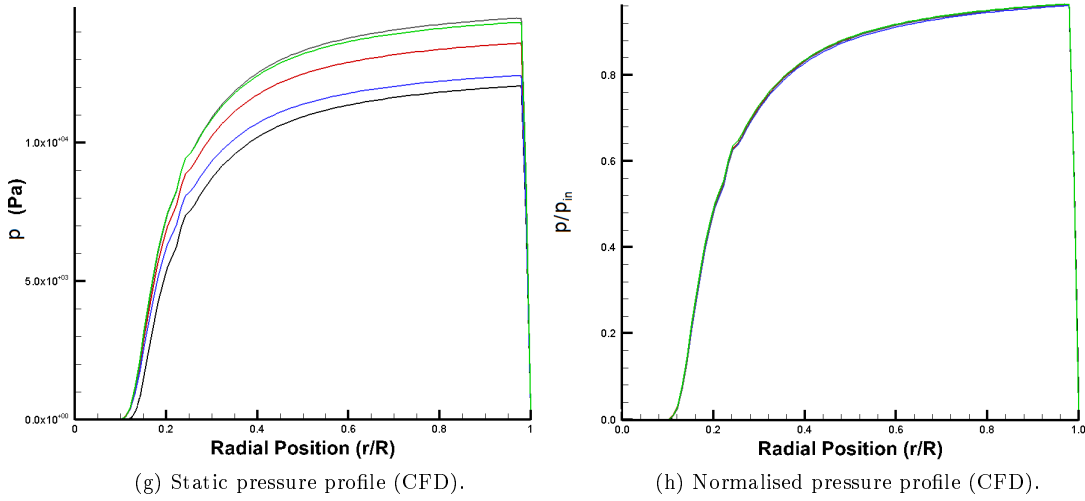
(f) Axial vorticity profile (PIV).

203

(g) Static pressure profile (CFD).

(h) Normalised pressure profile (CFD).

Figure E.1: Tangential profiles for vortex chambers with base injection.

The axial velocity contour plots and associated mantle structures for the chamber configurations with internal domes and injector located at the base of the chamber are displayed in fig E.2. As explained previously, the data suggests that due to the minimal variation in the flow properties it is expected that this would also apply to the structure of the mantle, where fig E.3b shows that this is partially true. The mantle structures are similar, in that they exhibit a single mantle that spans the length of the chamber and they also consist of a loop structure that is seen in the other studies involving base injectors. In figs E.3a-E.3e where CFD data is available, it can be seen that as the height of the dome increases the inner mantle loop separates into two sections when the dome height is $H = 15mm$, which is similar to that seen repeatedly in the inlet Reynolds number study. As the dome height is increased to $H = 20$ and $25mm$, the small loop at the head of the chamber merges with the outer mantle, as seen in the aspect ratio study when $\frac{L}{D} < 0.8$. The mantle structure seen in figs E.3a and E.3b is similar to that seen in the aspect ratio study when $\frac{L}{D} = 0.8$. Therefore the mantle structure does appear to evolve with respect to increasing the height of the internal dome, but not in a similar way that has been observed to occur in the aspect ratio study when the length of the chamber is reduced. Reducing the length of the chamber in this part of the study is found to have different effects to those seen in the aspect ratio study, but it must be noted that there are similarities in the mantle structures resultant from chamber geometry. The inclusion of a study of the effects of internal dome geometry is based on conjecture through analysis of the Beltramian theory, and does not provide obvious arguments for how it may affect mantle structure, as it does for other test parameters. However, it has been shown, that although the addition of internal domes suggests that the properties of the flow are relatively unaffected, the variation in chamber geometry is responsible for producing a variety of mantle structures and further highlights the importance of chamber geometry upon the structure of the bidirectional vortex. A diagram detailing the geometry of the various domes investigated is shown in fig E.3a, with the combined CFD/PIV and PIV mantles obtained being displayed in figs E.3b and E.3c respectively. The combined mantle plot in fig E.3b clearly shows the invariance in both the position of the outer mantle and the boundary of the PVC as the internal dome height is increased. The only feature of the mantle structure which differs to those seen in other parts of the investigation is seen in the close proximity to the curved surface of the dome, which exists over the entire base wall boundary of the chamber. This appears to be the result of an increased local radial velocity component forcing the flow inwards towards the chamber exit rather than towards the head of the chamber, and is also being opposed by the positive axial velocity component of the bulk flow. As with all the other PIV data obtained in the meridional plane of the chamber, it is difficult to discern any useful information, although the minimal variation in mantle structure at least reflects what is observed in the CFD data.
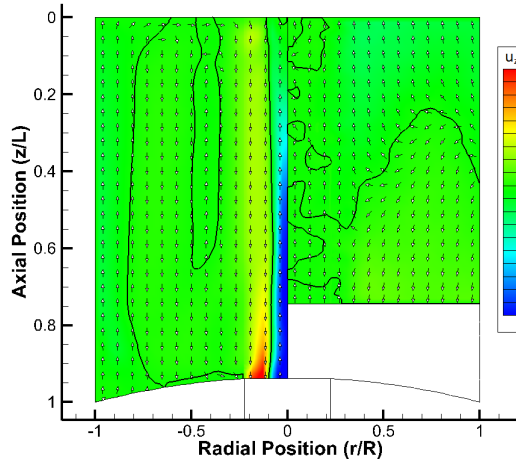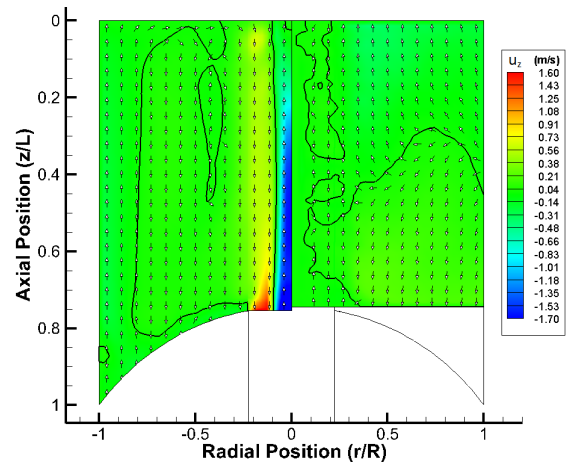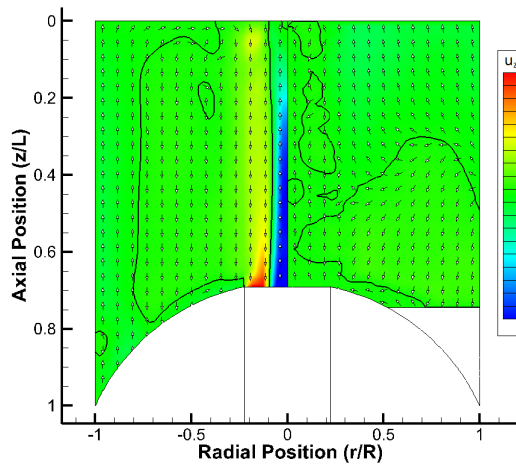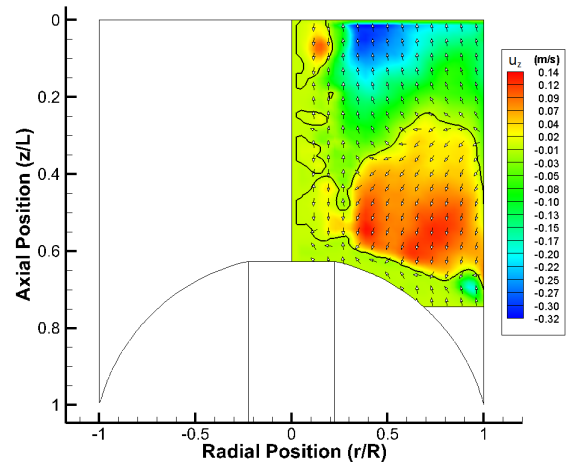
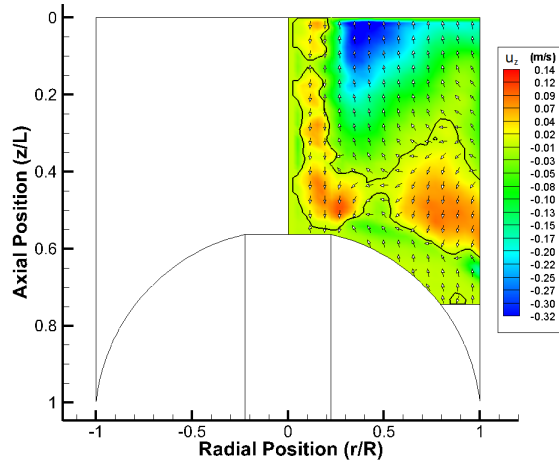(a) $H = 5mm$.
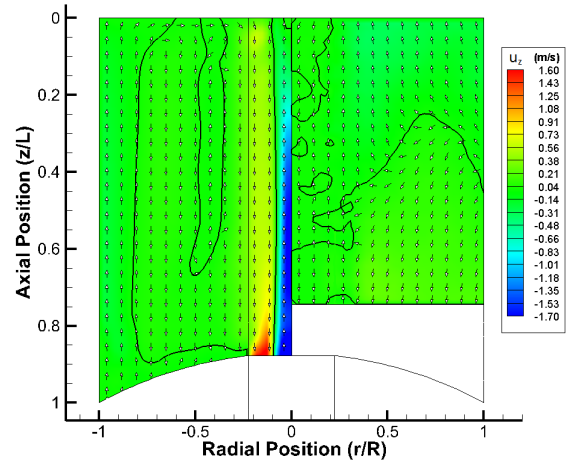
(b) $H = 10mm$.
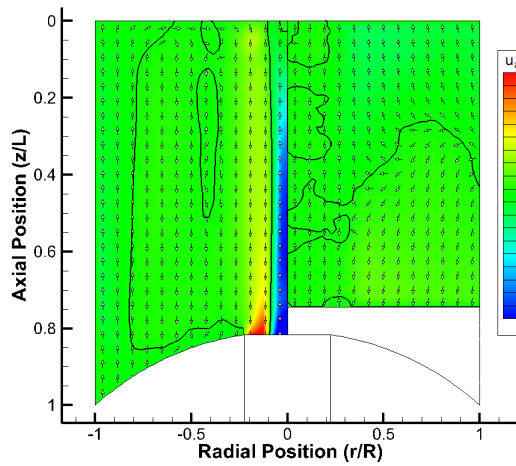
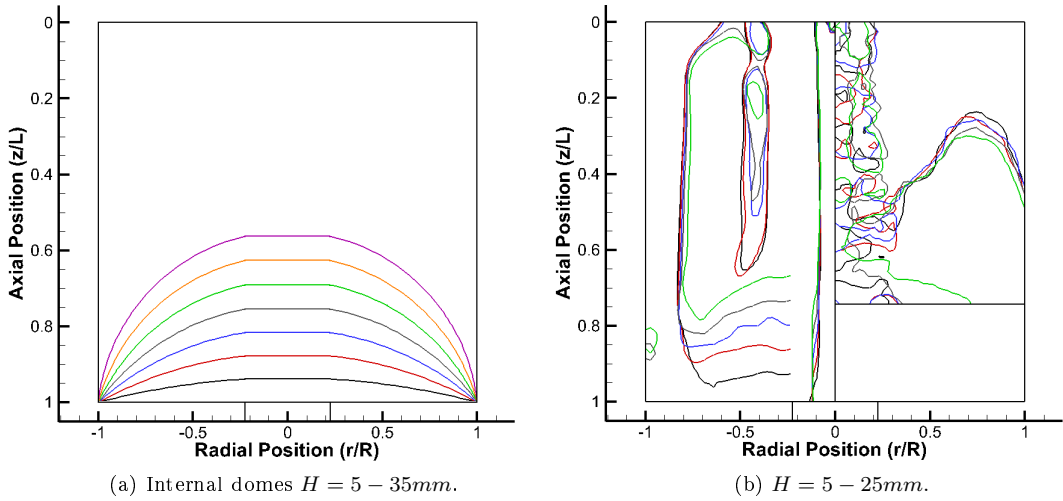(c) $H = 15mm$.

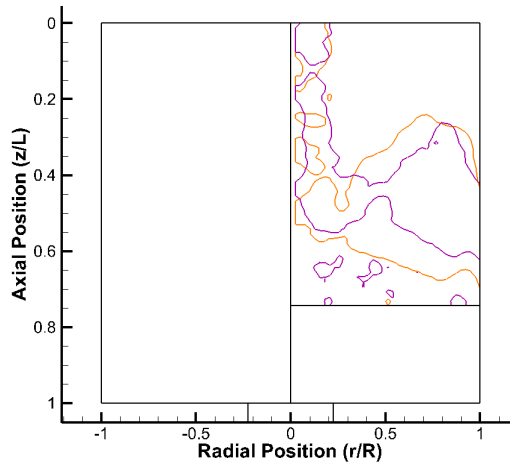(d) $H = 20mm$.

(e) $H = 25mm$.

(f) $H = 30mm$.

(g) $H = 35mm$.

Figure E.2: Axial velocity contour plots for vortex chambers with base injection.

(a) Internal domes $H = 5 - 35mm$.

(b) $H = 5 - 25mm$.

(c) $H = 30 - 35mm$.

Figure E.3: Axial plots of mantles for chambers with base injection.

(a) $H = 5mm$.

(b) $H = 10mm$.

(c) $H = 15mm$.

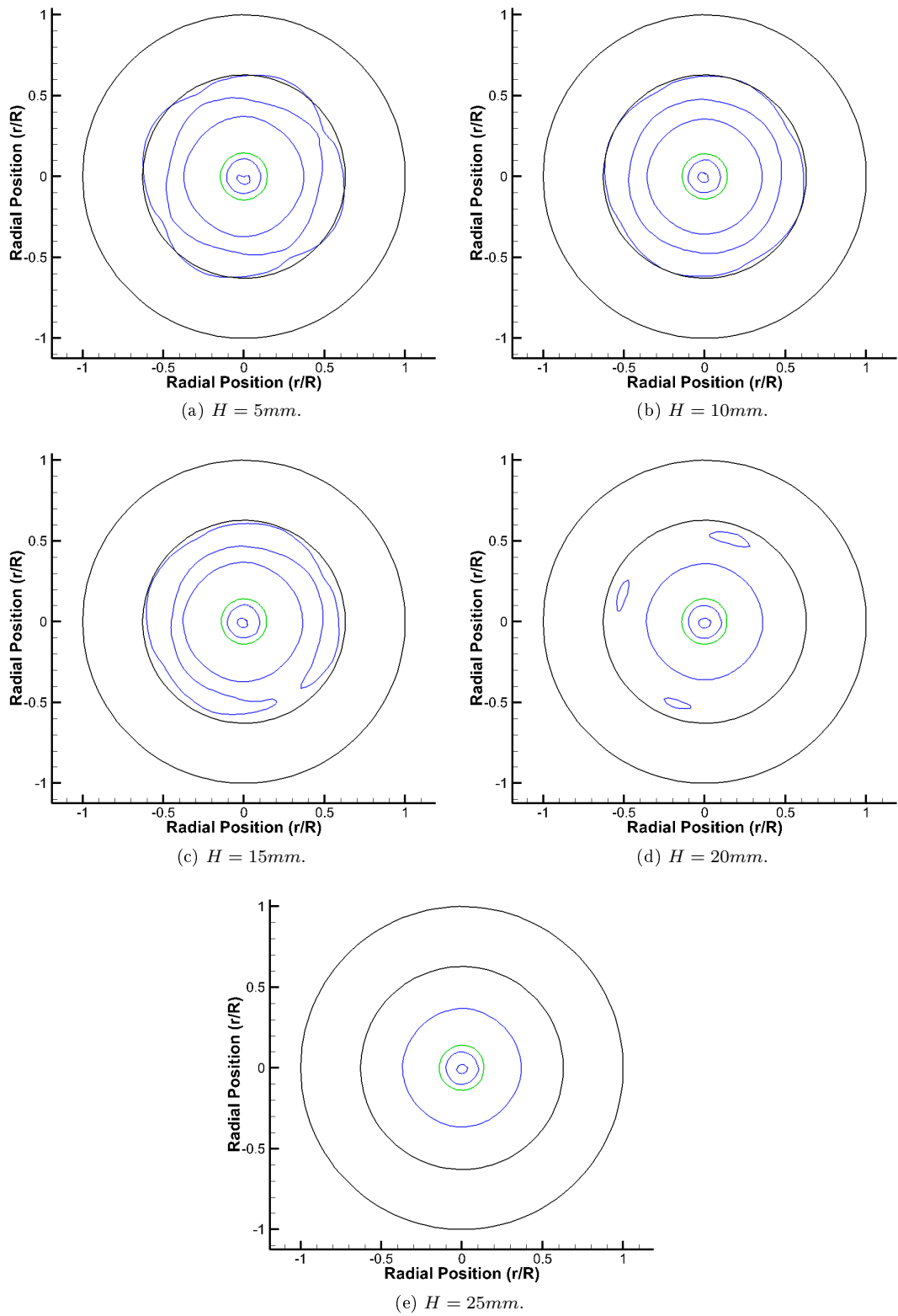(d) $H = 20mm$.

(e) $H = 25mm$.

Figure E.4: Azimuthal plots of mantles and SBR for chambers with base injection.

The azimuthal plane plots in fig E.4 describe the mantle structures and SBR boundaries obtained from the CFD data for chambers with dome heights in the range $H = 5 - 25mm$. As with the mantle plots from the meridional plane of the chamber seen in fig E.3, those in the azimuthal plane of the chamber do display some variation in the mantle structure. It has been noted previously, that the structure of the mantle is reminiscent of those seen in the inlet Reynolds number study for base injectors, and this is also true for the majority of chamber configurations in fig E.4. Figs E.4a and E.4b exhibit a similar single outer mantle that coincides with the theoretical position predicted by the Beltramian solution, in addition to displaying obvious signs of periodicity. There is also evidence of the same loop structure at the head of the chamber, which is represented by the two concentric rings situated between the outer mantle and the SBR boundary, which are also subject to periodic effects to varying degrees. In fig E.4a this inner periodic structure is most prominent and possesses the same phase lag between the inner and outer mantle structures, which means that it is an example of an identical mode number to those seen in the inlet Reynolds number study. As the height of the internal dome is increased beyond $H = 10mm$, the concentric ring form of the mantle begins to break down as the mantle structure appears to be undergoing a transition into a new form, which is evident in figs E.4c and E.4d. In fig E.4e the mantle consists of a single ring that does not appear to be significantly affected by the periodic effects seen in other chamber configurations such as fig E.4d, which shows clear signs of periodicity. The single mantle seen in fig E.4e does not agree well with the radial position predicted by the Beltramian theory, but this is due to the merging of the outer and inner mantle structures seen in fig E.4e, and is representative of the inner most mantle seen in fig E.4a and E.4b. The mantle structures extracted from the azimuthal plane of the chamber express a similar evolution in the mantle structure to those seen in fig E.4, where a transition begins to occur when the dome height is $H = 15mm$, then continues to change as the dome height is increased.

E.2.2 Head injection

In this part of the study two internal domes were employed to see how they affect the flow, but as a result of this it is not possible to obtain PIV data from the azimuthal plane of the chamber because of the design of the experimental rig. Therefore, the information presented in table E.2 only relates to the values that could be extracted from the CFD data, but this still allows comparisons to be made between the chamber configurations with both base and head injectors. The inlet velocities which occur over the full range of dome heights $H = 5 - 25mm$ are shown to exist over a small range, like for the chambers with base injectors and are also erratic in a similar manner. There is no appreciable difference in the majority of the values presented in table E.2a, and again indicates the properties of the flow are relatively unaffected by the variation in height of the internal domes. This lack of variation is most obvious in the normalised radii of the PVC and the forced vortex, which show no or little deviation respectively, despite the considerably different internal geometries of the chambers at the upper and lower boundaries of the parametric test range. Both the PVC and SBR radii are found to be smaller than those for the base injector configurations, where the radii for both the base and head injector configurations mirror those found in the inlet Reynolds number study. The difference between the base and head injector configurations is therefore also likely to be resultant from the local flow conditions which occur in close proximity to the head wall boundary of the chamber, which is thought to affect the flow in the inlet Reynolds number study. The peak tangential velocities in table E.2b also vary over a small range and display a weak relationship to the dome height, as the magnitude of the tangential velocity component tends to decrease as the height of the internal domes increase. However, when these are normalised by the inlet velocity, the variation across the range of chamber configurations is minimised further, although there is still evidence of less intense vortices in the chambers with larger domes, being the opposite to what is seen in the base injector configuration results. Then again, there is no definite correlation between the magnitude of the tangential velocity component and the dome height for chambers with either base or head injectors. This is also reflected in the axial velocity data for both the CFD and PIV results, while the normalised boundary layer height is constant throughout and identical to the results found for the other parametric studies.

Table (a):

Dome Height H (mm)	Inlet Velocity u_{in} (m/s)	Inlet Pressure (CFD) p_{in} (Kpa)	Inlet Reynolds Number Re	Vortex Reynolds Number V	Strouhal Number (CFD) Sh	Normalised Air Core Radius (CFD) r_{core}	Normalised Forced Vortex Radius (CFD) r_{SBR}	Liquid Dimension of Forced Vortex (CFD) $r_{SBR}-r_{core}$	Precessing Vortex Core Frequency (CFD) f_{PVC} (Hz)
5	1.16	12.82	4.48E+04	2.96E+03	8.10	0.061	0.134	0.073	119.91
10	0.97	8.81	3.76E+04	2.49E+03	8.00	0.061	0.135	0.074	99.49
15	1.07	11.04	4.15E+04	2.74E+03	8.12	0.061	0.135	0.074	111.28
20	1.03	9.85	4.01E+04	2.65E+03	7.94	0.061	0.134	0.073	105.07
25	1.04	9.81	4.04E+04	2.67E+03	8.02	0.061	0.132	0.071	107.08
30	0.97	×	3.76E+04	2.49E+03	×	×	×	×	×
35	1.00	×	3.87E+04	2.56E+03	×	×	×	×	×

Table (b):

Dome Height H (mm)	Peak Tangential Velocity (CFD) u_{ϕ} (m/s)	Peak Tangential Velocity Ratio (CFD) u_{ϕ}/u_{in}	CFD Forced Vortex Angular Velocity $(\partial u_{\phi}/\partial r)$ ω (rad/s)	CFD Free Vortex Inverse Gradient $(\partial r/\partial u_{\phi})$ $\partial r/\partial u_{\phi}$	CFD Normalised Boundary layer height at chamber wall δ_w	Maximum Axial Velocity (CFD) u_z (m/s)	Minimum Axial Velocity (CFD) u_z (m/s)	Maximum Axial Velocity (PIV) u_z (m/s)	Minimum Axial Velocity (PIV) u_z (m/s)
5	3.94	3.41	753.42	90.82	0.02	2.68	-3.29	0.26	-0.20
10	3.29	3.39	625.09	75.31	0.02	2.37	-3.18	0.27	-0.21
15	3.68	3.44	699.16	86.18	0.02	2.56	-3.54	0.27	-0.18
20	3.45	3.34	660.15	84.98	0.02	2.36	-3.50	0.23	-0.18
25	3.46	3.33	672.81	85.75	0.02	2.34	-3.41	0.28	-0.13
30	×	×	×	×	0.02	×	×	0.18	-0.35
35	×	×	×	×	0.02	×	×	0.22	-0.22

(a)   (b)

Table E.2: Flow variables for chambers with head injection.

The plots in fig E.5 relate to the tangential velocity, radial velocity, axial vorticity, static pressure and normalised pressure distribution respectively for the chambers with internal domes and head injectors. The tangential velocity plot seen in fig E.5a highlights the similarities between the properties of the flow for the various chamber configurations, as all the profiles are fairly congruous in form and exhibit similar gradients in the irrotational region of the flow, as confirmed by table E.2b. The only noticeable difference is the variation in the peak tangential velocities which occur, and the inherent increase in the angular velocity of the forced vortex as a result, although the radius of the forced to free vortex transition is unaffected. The radial velocity distribution in fig E.5b shows that there is some agreement between the profiles produced by the various chamber configurations, in that the maximum outwardly velocity occurs within the core flow and the maxima and minima within the free vortex are fairly consistent. As expected, there is also little variation in the axial vorticity distribution seen in fig E.5c, which again indicates that the chambers in which the largest peak tangential velocities occur, result in greater axial vorticity and therefore more intense vortices. The maximum axial vorticity occurs at the same radius for all chamber configurations and is located in close proximity to the multiphase boundary where the volume fraction is entirely liquid $v_f = 1$, as it has been seen to occur in the majority of the results presented thus far. The static pressure distribution displayed in fig E.5d exhibits the same progressive increase in magnitude associated with each chamber configuration, as seen in the tangential velocity and axial vorticity plots. There is no discernible connection between the properties of the flow and the internal dome height, it is clear that the most intense vortices occur in the chambers with the greatest static pressure at the inlets. This replicates the behaviour seen for all the other chamber configurations throughout this investigation and reinforces the notion that an increased pressure drop is the result of an intense vortex being present. In a similar manner to the normalised peak tangential velocities, the normalised static pressure distributions seen in fig E.5e highlight that when variation in the inlet flow is accounted for the variation in the actual properties of the flow is minimal.

The axial velocity contour plots and the associated mantle structures for the available CFD and PIV data are presented in fig E.6, where CFD data exists for chamber configurations with internal dome heights in the range $H = 5 - 25mm$. Many similarities have been observed between the results of the inlet Reynolds number study and the effects of internal dome geometry, but the mantle structures seen in fig E.6 are significantly different to those seen in fig 5.11, unlike for the base injectors where there is a clear resemblance. The mantle structures seen in this part of the study are unlike those seen previously for chamber configurations with head injectors, and despite the lack of any definite variation in the properties of the flow, there is a pronounced variation in the mantle structure due to the effects of chamber geometry. As with the structures that occur in the chambers with base injectors, the mantle is attached to the curved surface at the base of the chamber, which intersects with the outlet and forms a loop that is initially attached to the bottom circumferential corner of the chamber. The mantle seen in fig E.7a does exhibit some similarities to that of the chamber configuration with a contraction ratio of $CR = 10$, where there is evidence of multiple flow reversal, which results in a triple vortex. This triple vortex structure is consistent throughout the CFD results and provides more defined regions of bidirectional flow in comparison to the mantle structures produced in the inlet Reynolds number study with head injectors, even when there is little variation of the internal geometry such as seen in fig E.7a. It is interesting to note, that despite the similarities in the general characteristics of the flow, a small change in the chamber geometry can invoke appreciable changes within the behaviour of the tertiary flow and in turn the embedded coherent structures. There are no sudden transitions in the properties of the flow, but there are neither any in the mantle structure, where there is a clear evolution in the form as the height of the internal domes is progressively increased, unlike the study of the effects of the aspect and contraction ratio of the chamber. As with the mantle structures seen in other chamber configurations with head injectors, there are no defined individual mantles that span the length of the chamber. Rather two mantles that are connected near to the head of the chamber and occupy an range of radial positions dependent on their respective axial location, which makes it difficult to make direct comparisons to the radial positions predicted by the Beltramian theory as a result. As the dome height is increased, it can be seen that the wider separation between the two parts of the mantle which occurs in the upper region of the chamber begins to propagate towards the base of

(a) Tangential velocity profile (CFD).

(b) Radial velocity profile (CFD).

(c) Axial vorticity profile (CFD).

(d) Static pressure profile (CFD).

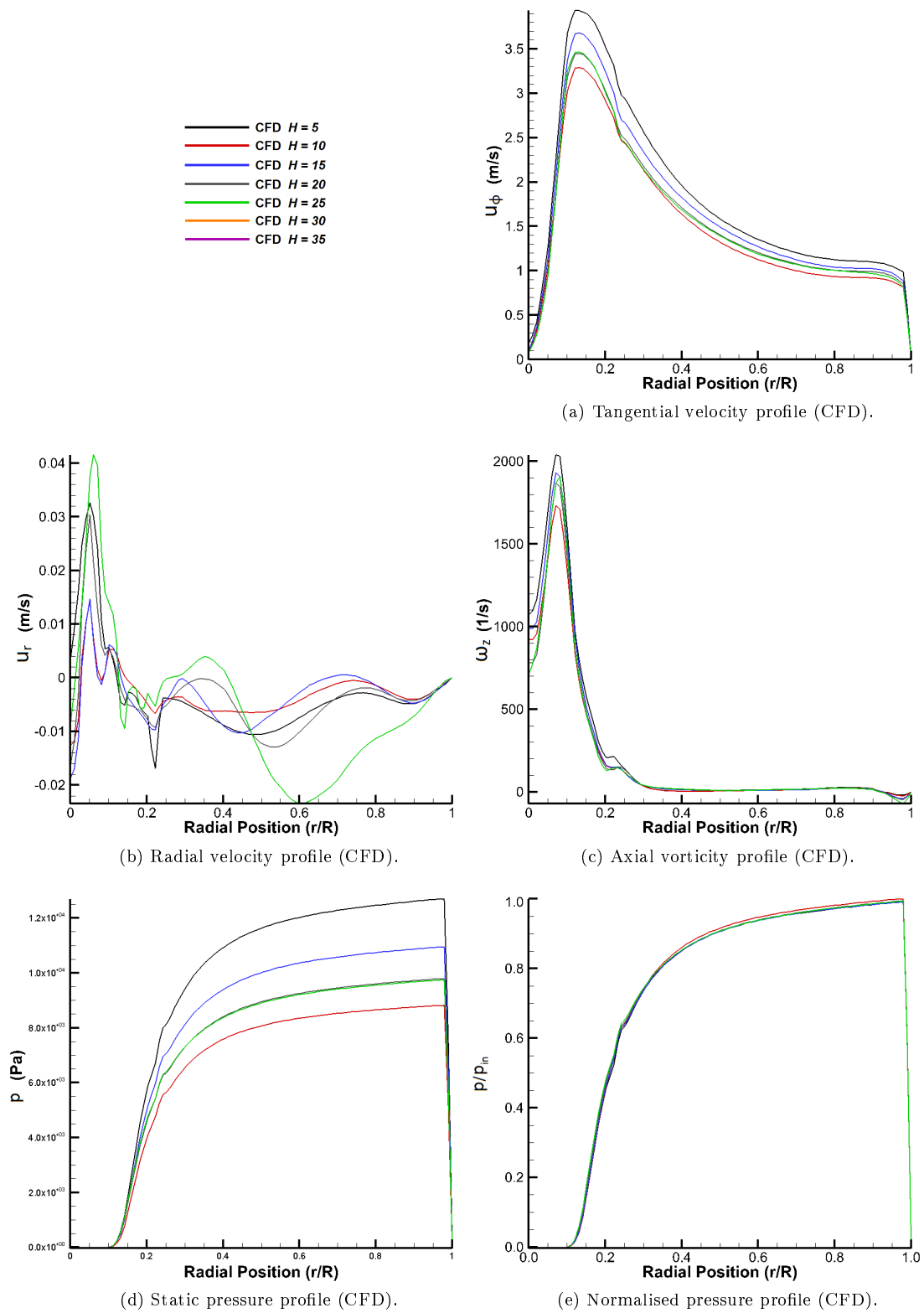(e) Normalised pressure profile (CFD).

Figure E.5: Tangential profiles for vortex chambers with head injection.

the chamber. This is most evident in fig E.7d where there is an internal loop in the mantle, as the widening process of the whole structure approaches the base of the chamber, before it is apparently completed as the height of the dome is further increased, as denoted by fig E.7e. If it is possible to influence the structure of the mantle alone by the internal geometry of the chamber, then it opens up the possibility of using various surfaces of revolution to assess what shapes have the greatest influence on the mantle and whether they may result in increased performance when employed in VIHRE configurations. Due to the cross section of the meridional plane of these chambers with two internal domes, this configuration has been dubbed the *'vortex axe'*, and it is hoped further studies will be conducted to confirm the presence of the triple vortex predicted by the CFD results, as it has the potential to greatly enhance the already significant benefits of the double vortex structure found in VIHRE configurations. The internal chamber geometry and mantles seen in the various chamber configurations are displayed in fig E.7, where it can be seen that the CFD results in fig E.7b show that there is little variation in the outer mantle. The inner mantle that results from the widening process also exhibits little variation in radial position, despite undergoing appreciable deformation as the height of the internal domes is increased.

The mantle positions and SBR boundary extracted from the CFD results are plotted in fig E.8, but here the azimuthal observation plane is located at the mid point of the chamber due to the effects of the curved surface at the head of the chamber. It can be seen in figs E.8a and E.8b that the outer mantle is in good agreement with the predicted theoretical mantle position at $\frac{r}{R} = 0.787$, while the inner mantle in either case does not show any correlation with the theoretical mantle position at $\frac{r}{R} = 0.343$. However, when the internal dome height is increased to $H = 15mm$ both of the mantle positions extracted from the CFD data occur at approximately the same radial positions as those derived from the Beltramian theory for a case with two mantles. This is also true in figs E.8d and E.8e, which relate to the chamber configurations with dome heights of $H = 20 - 25mm$ respectively, with the outer mantle in fig E.8e coinciding precisely with that proposed by the analytical solution. As seen in the mantle plots of the meridional plane of the chamber in fig E.6, the radial distance between the individual mantles appears to increase across the full length of the chamber as the dome height is increased, and the resultant position of the inner mantle corresponds well to the predicted theoretical position. It can be assumed that the structure of the mantle evolves as a reaction to the chamber geometry, as it is tending from one form to another through a gradual transition, where defined individual mantles that span the majority of the chamber length begin to align with the zeroes of the Bessel function of the first kind J_0. This is also seen in the accompanying study with base injectors, where the well defined single mantle corresponds well to the theoretical mantle position at $\frac{r}{R} = 0.628$. Despite the lack of appropriate PIV data to determine the position of the individual mantles, it is remarkable how those obtained from the CFD and Beltramian solution complement each other and is seen throughout this investigation, giving credence to both the theoretical formulation and the use of CFD as a tool to analyse multiple flow reversals.
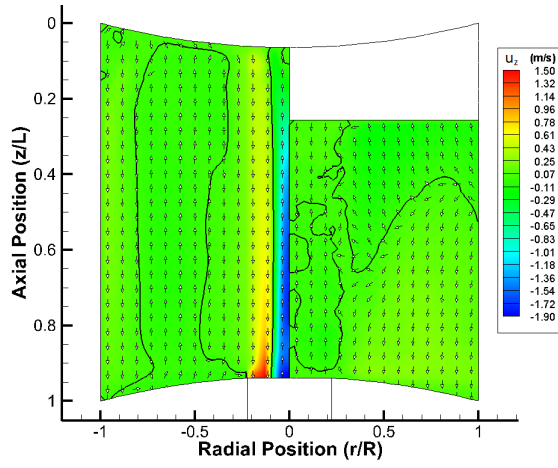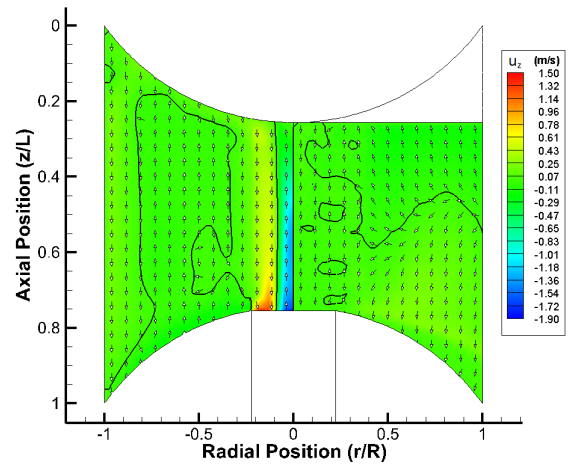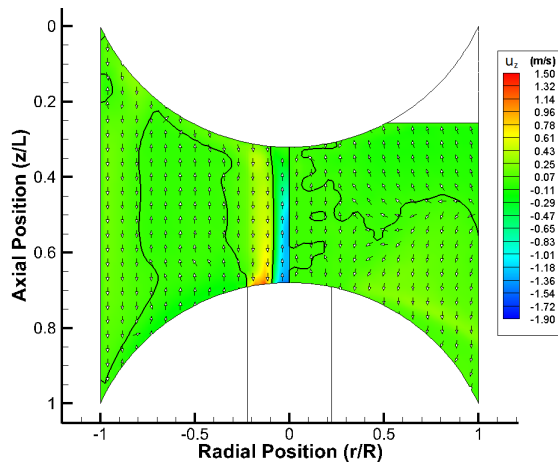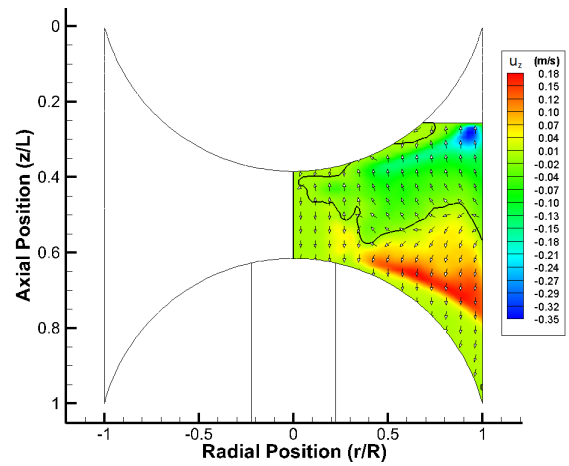
(a) $H = 5mm$.
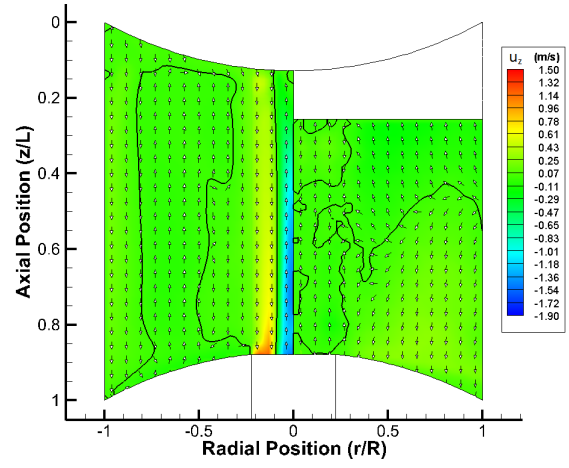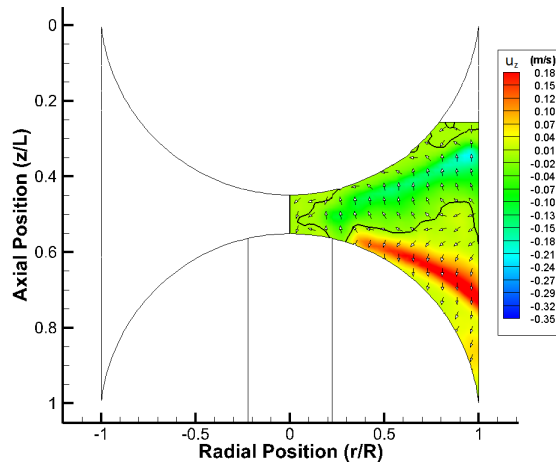
(b) $H = 10mm$.
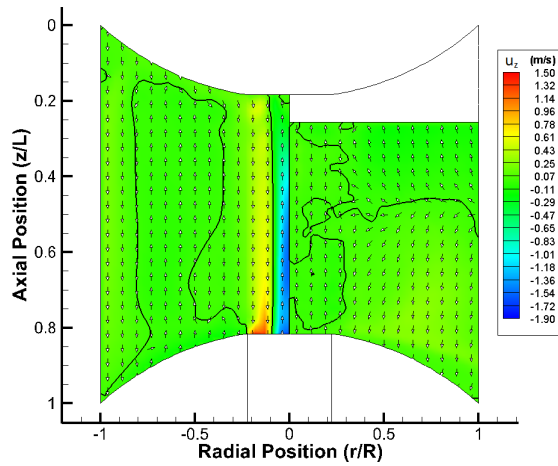
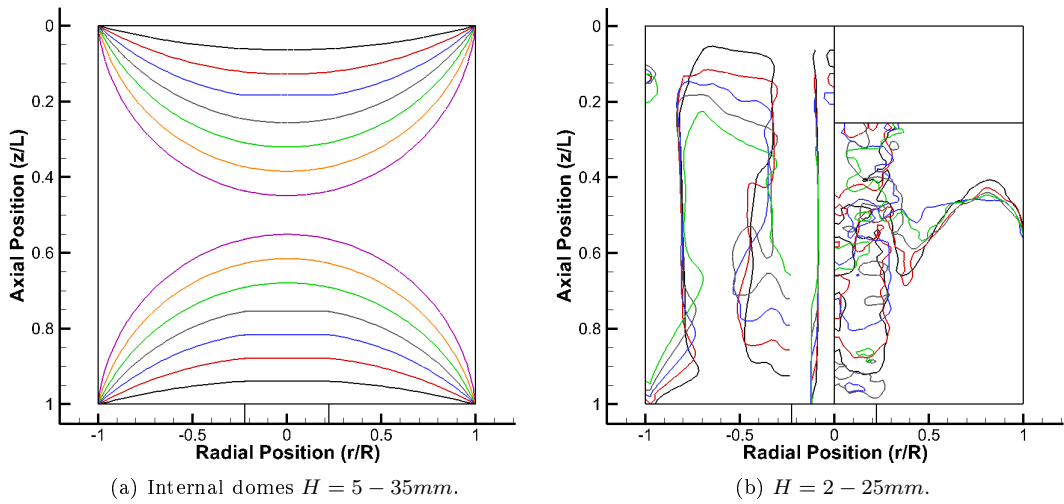(c) $H = 15mm$.

(d) $H = 20mm$.
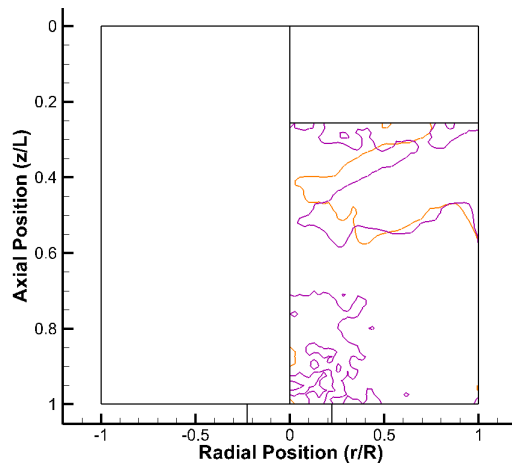
(e) $H = 25mm$.

(f) $H = 30mm$.

(g) $H = 35mm$.

Figure E.6: Axial velocity contour plots for vortex chambers with head injection.

(a) Internal domes $H = 5 - 35mm$.

(b) $H = 2 - 25mm$.

(c) $H = 30 - 35mm$.

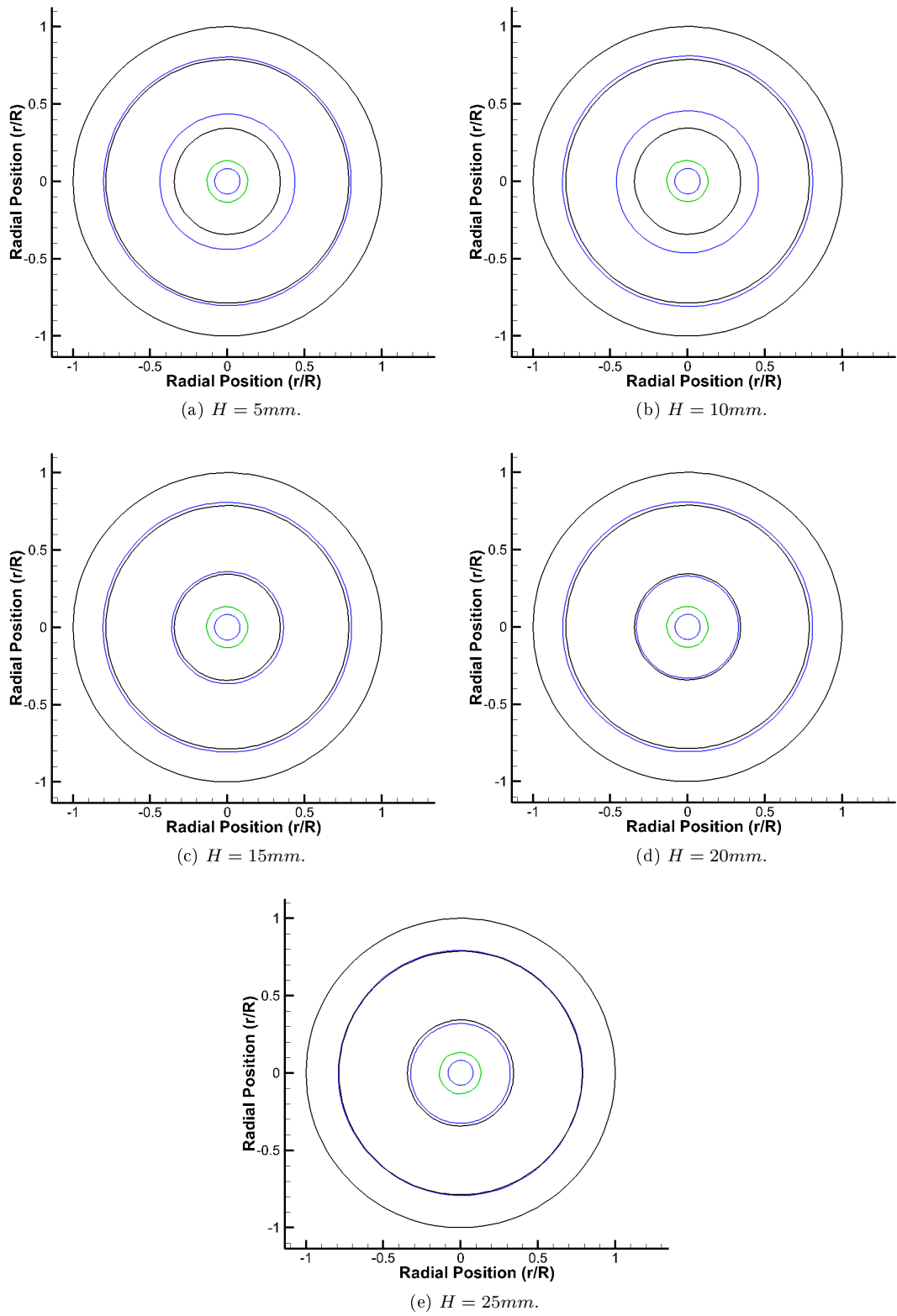Figure E.7: Axial plots of mantles for chambers with head injection.

(a) $H = 5mm$.

(b) $H = 10mm$.

(c) $H = 15mm$.

(d) $H = 20mm$.

(e) $H = 25mm$.

Figure E.8: Azimuthal plots of mantles and SBR for chambers with head injection.

E.2.3 Internal dome conclusions

As the height of the internal domes were increased, the velocity and vorticity components were found to increase, indicating vortices of increasing intensity would occur as the volume of the chamber was reduced. Due to the shape of the internal domes, the effective length of the chamber varies with respect to radius and the greatest reduction in length occurs along the axis of the chamber. The increase in vortex intensity caused by larger internal dome geometries was found to have a similar effect upon the flow as reducing the length of the entire chamber, which occurred in the chamber aspect ratio study. The chamber configurations with both base and head injectors were found to affect the structure of the mantle, but the greatest deformations in response to dome height occurred in the chambers configurations with head injectors. This is attributed to the significant variation in internal geometry produced by incorporating two internal domes into the chamber geometry, as opposed to the single dome located at the base for chamber configurations with base injectors.

The results produced for chamber configurations with base injectors for dome heights in the range $H = 5 - 10mm$ exhibit a similar mantle structure to that seen in chambers with an aspect ratio of $\frac{L}{D} = 0.8$, where there is no internal dome. Chamber configurations with dome heights of $H = 15, 20$ and 25 are reminiscent of those observed for chamber aspect ratios of $\frac{L}{D} = 1.0, 0.6$ and 0.4, which suggests that increasing the dome height has a similar effect upon the mantle structure as reducing the uniform length of the chamber. When the reduction in effective chamber length is considered in terms of aspect ratio with regards to the axis of the chamber, then the dome heights of $H = 5, 10,$ 15, 20 and 25 correspond to aspect ratios of $\frac{L}{D} = 0.936, 0.907, 0.808, 0.744$ and 0.680 respectively. This indicates that the axial dimensions of the core region of the chamber may be responsible for causing alterations in the structure of the mantle, as well as the intensity of the vortex. Additionally, it was found that negative axial flow occurs at the base of the chamber in close proximity to the surface of the internal dome and affects the local mantle structure, in that it replicates the curvature of the dome, before terminating at the outlet where flow reversal occurs and the fluid exits the chamber. This effect was also seen in chamber configurations with head injectors, and occurs at both axial boundaries where the presence of the dome directs the flow towards the mid section of the chamber. Despite the continual variation in the structure of the mantle with respect to dome height, a clear correlation in their respective forms can be seen and there is no sudden variation that occurs when the axial dimensions of the chamber are altered, unlike in the aspect ratio study. This is reflected by the mantle cross sections extracted from the mid point of the chamber, which exhibit little variation with respect to dome height and is also accompanied by a negligible variation in the radius of the air core, which has been shown to be indicative of large variations in the mantle structure. Due to the axial position of these mantle structures, there is no evidence of periodicity and there is also an excellent agreement between the radial positions predicted by the analytical solution and the numerical results. This provides evidence that the mantle structure is most susceptible to non cylindrical modes at the axial boundaries of the chamber, which is seen for all other chamber configurations where the interrogation plane is situated at the head of the chamber. Overall, the addition of internal domes was found to affect the mantle structure and similarities exist between the forms observed in the aspect ratio study, although no significant variations occurred, allowing the structures to be considered as a subset. Additionally, it was found that chamber configurations with head injectors repeatedly induce mantle structures which span the length of the chamber and result in triple vortices, suitable for increasing the effective length of the chamber.

E.3 Effect of number of injectors

E.3.1 Results overview

In the number of injectors study, the reference chamber geometry with an aspect ratio of $\frac{L}{D} = 1$ and a contraction ratio $CR = 20$ is used, where the inlet velocity is set by the value for the 50% pump throttle case from the inlet Reynolds number study for both chamber configurations with base and head injectors. An additional 4 geometries were constructed in addition to the reference case, so that the number of injectors ranged from $N = 2 - 5$, although convergence issues meant that results are only available for the range $N = 2 - 4$. In each chamber configuration the injectors are placed at regular intervals about the periphery of the chamber to ensure periodic symmetry of the geometry, with examples provided in fig E.9. The content of the results is similar to that seen in the other parametric studies, so that sufficient information is available to effectively compare any variation in the properties of the flow over the range of test parameters. Both the chamber configurations with base and head injectors similarly show that as the number of injector is increased the static pressure at the inlet increases, as do the tangential, radial and axial velocity components. As seen in the inlet Reynolds number study and the internal dome study, the radial position of the boundary of the PVC remains constant throughout with the radius being identical for both the chambers with base and head injectors. The normalised radius of the forced vortex is seen to decrease with respect to an increased number of injectors for chambers with base injectors, but increase in chambers with head injectors. Despite this, the results consistently show that the angular velocity and precession frequency of the vortex core increase as additional inlets are introduced, which is also seen in the inverse gradient of the free vortex, where there is greater decay in the magnitude of the tangential velocity component with respect to radius. It must be noted that it was decided to enforce a uniform inlet velocity so that the inlet Reynolds number remained constant across all chamber configurations, but as a result of this the mass flow rate through the chambers varies significantly and is thought to be the major factor which causes variation in the results. The reduced mass flow in the chambers with $N = 2 - 3$ injectors also suffered from convergence issues, and while the solutions were deemed to meet the convergence criteria, there was a significant amount of oscillation in the residual error of the solution. This is generally indicative of periodic behaviour that is not being adequately resolved by the solver and is detrimental to the overall accuracy of the solution, but it was necessary to accept the solution in this state of flux as the problem did not subside with additional iterations. It soon becomes clear by looking at the 3D mantles extracted from the chamber configurations with $N = 2$ head injectors, that the reduced mass flow rate through the chamber was detrimental to the stability of the PVC, which is deformed in close proximity to the exit of the fluid domain. The PVC still exhibits periodic behaviour and precesses about the chamber axis, the rotation of this asymmetric form affects the local characteristics of the flow and prevents a quasi steady state solution from being achieved and in turn affects the accuracy of the results.

When looking at the mantle structures in the meridional plane of the chamber configurations with base injectors there is very little variation as they all exhibit a single mantle that spans the length of the camber at approximately the same radial position. This is also true of the boundary of the PVC which has been found to possess a similar radius to the vortices that occur in other chambers with a contraction ratio of $CR = 20$, which again suggests that this is one of the primary variables for controlling the characteristics of the vortex core. There is some evidence of inner mantle loops for the chamber with $N = 3$ injectors, it is thought that this is an anomalous result due to the issues associated with oscillations in the residual error of the solution, and would likely disappear with a sufficiently large amount of additional iterations. The 3D mantles for the chamber configurations with base injectors clearly show the influence the number of injectors has upon the periodic structure of the mantle, where it appears that by increasing the number of inlets the mantle is forced into a cylindrical axisymmetric form. What is interesting to see, is that each mantle exhibits the same period and phase irrespective of the number of inlets, which must mean that the specific periodic form of the mantle is entirely the result of the chamber geometry, where the flow is responsible for the extent of each mode shape being observed in the mantle structure. Of course, these same mode shapes which have occurred repeatedly through out all the results may be due

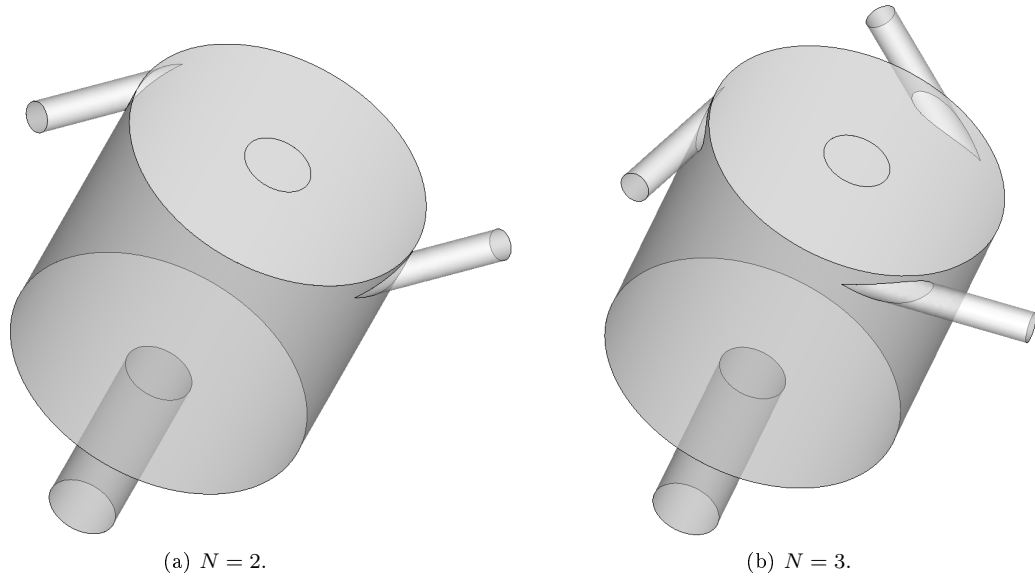(a) $N = 2$.   (b) $N = 3$.

Figure E.9: Chamber configurations with multiple injectors.

to the limited range of flow conditions tested. None the less, they do indicate that the complex interaction between chamber geometry and the energy content of the flow are responsible for the form of these structures, and therefore that of the mantle as well. Unlike the mantles seen in the meridional plane of the chamber configurations with base injectors, those with head injectors do exhibit some variation in their respective forms as the number of inlets is varied. However, this may again be due to the influence of the deformed PVC at the exit of the fluid domain, as the 3D mantle structures appear irregular and not completely formed in the head of the chamber. In spite of this, the mantle structures in the chamber configurations with $N = 2 - 3$ injectors possess two individual mantles that span the length of the chamber, and the velocity vectors in the meridional plane indicate multiple flow reversals and the presence of a triple vortex. The associated 3D mantles clearly show periodic behaviour at the base of the chamber which is significant in the chamber with $N = 3$ injectors, but still exhibits the same period as seen in other chamber configurations, as well as the same phase angle. Some of the results in this part of the study are marred by accuracy issues, but it is still possible to determine that by increasing the number of tangential inlets, the mantle structure can be affected and the amount of injectors appears to have no bearing upon the period of the mode shapes observed. However, this may also possibly be the result of the various mass flow rates through each chamber configuration, and warrants further investigation to confirm whether this is responsible for the variation in the mantle structure.

E.3.2 Base injection

(a)

Number of Injectors N	Inlet Velocity u_{in} (m/s)	Inlet Pressure (CFD) p_{in} (Kpa)	Inlet Reynolds Number Re	Vortex Reynolds Number V	Strouhal Number (CFD) Sh	Normalised Air Core Radius (CFD) r_{core}	Normalised Forced Vortex Radius (CFD) r_{SBR}	Liquid Dimension of Forced Vortex (CFD) $r_{SBR}\text{-}r_{core}$	Precessing Vortex Core Frequency (CFD) f_{PVC} (Hz)
2	1.16	3.98	4.51E+04	1.49E+03	3.08	0.081	0.178	0.097	45.85
3	1.16	5.52	4.51E+04	2.24E+03	5.59	0.081	0.147	0.066	83.28
4	1.16	13.12	4.51E+04	2.98E+03	7.61	0.081	0.144	0.063	113.36

(b)

Number of Injectors N	Peak Tangential Velocity (CFD) u_{ϕ} (m/s)	Peak Tangential Velocity Ratio (CFD) u_{ϕ}/u_{in}	CFD Forced Vortex Angular Velocity ($\partial u_{\phi}/\partial r$) ω (rad/s)	CFD Free Vortex Inverse Gradient ($\partial r/\partial u_{\phi}$)	CFD Normalised Boundary layer height at chamber wall δ_w	Maximum Axial Velocity (CFD) u_z (m/s)	Minimum Axial Velocity (CFD) u_z (m/s)
2	1.80	1.55	288.10	53.98	0.02	1.10	-1.44
3	1.90	1.64	523.29	71.75	0.02	1.52	-1.98
4	3.92	3.38	712.25	82.86	0.02	1.62	-2.28

Table E.3: Flow variables for chambers with base injection.

(a) Tangential velocity profile (CFD).

(b) Radial velocity profile (CFD).

(c) Axial vorticity profile (CFD).

(d) Normalised pressure profile (CFD).
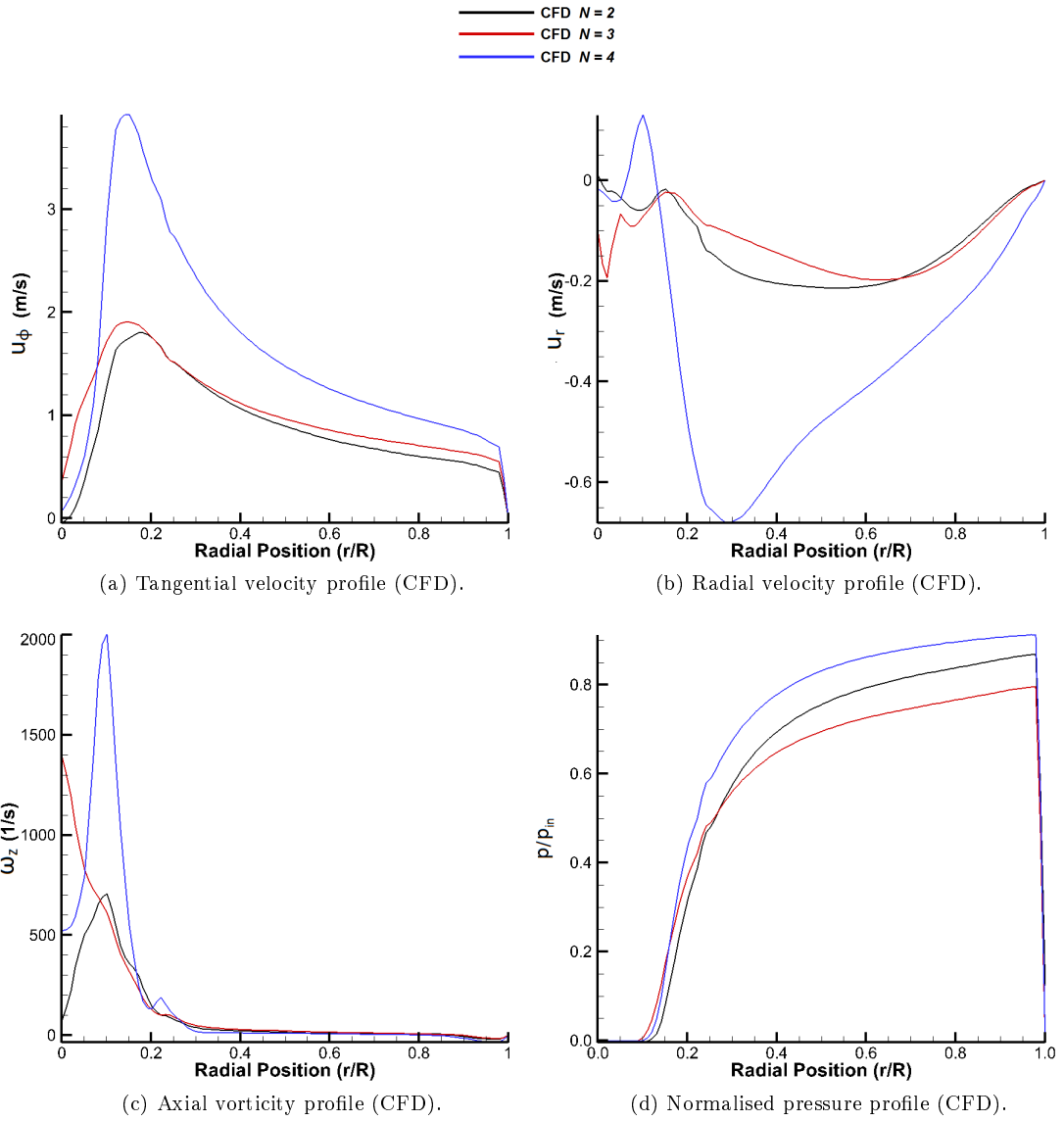
Figure E.10: Tangential profiles for vortex chambers with base injection.

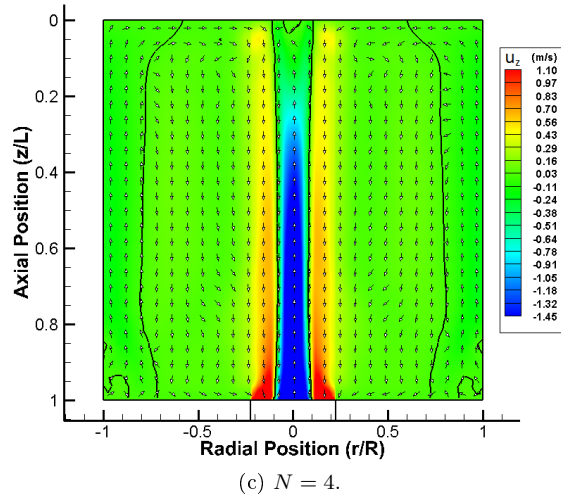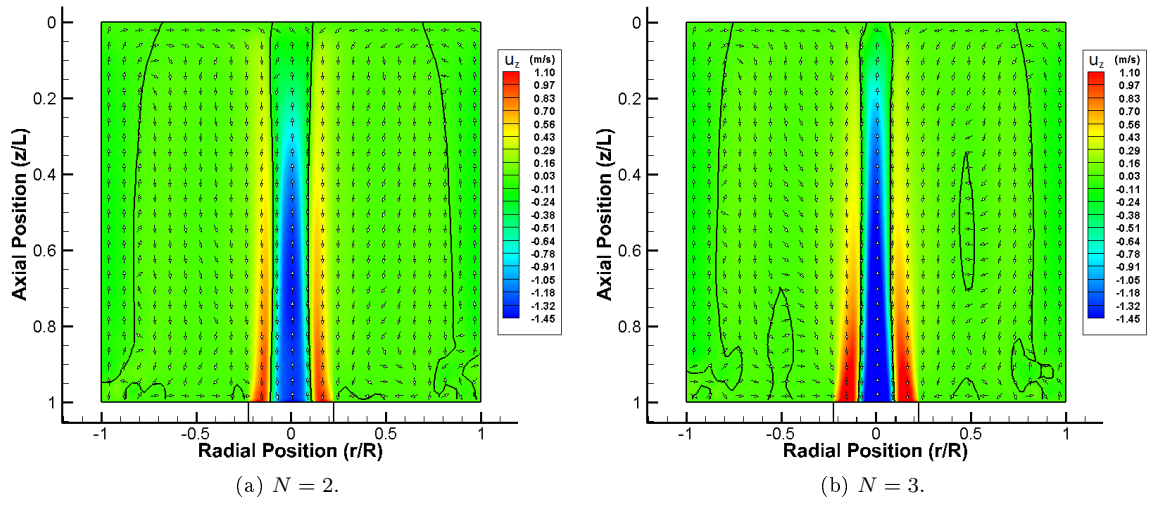(a) $N = 2$.

(b) $N = 3$.

(c) $N = 4$.

Figure E.11: Axial velocity contour plots for vortex chambers with base injection.
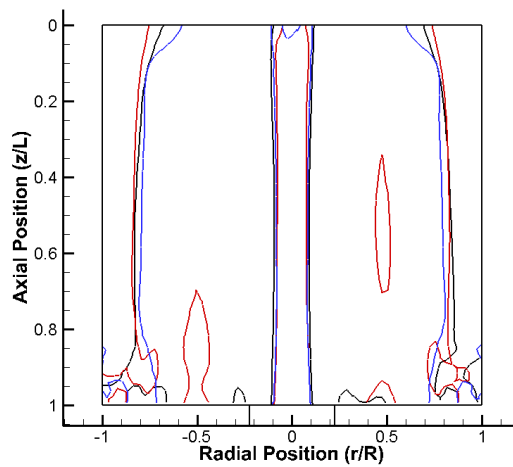
Figure E.12: Axial plot of combined mantles for chambers with base injection.
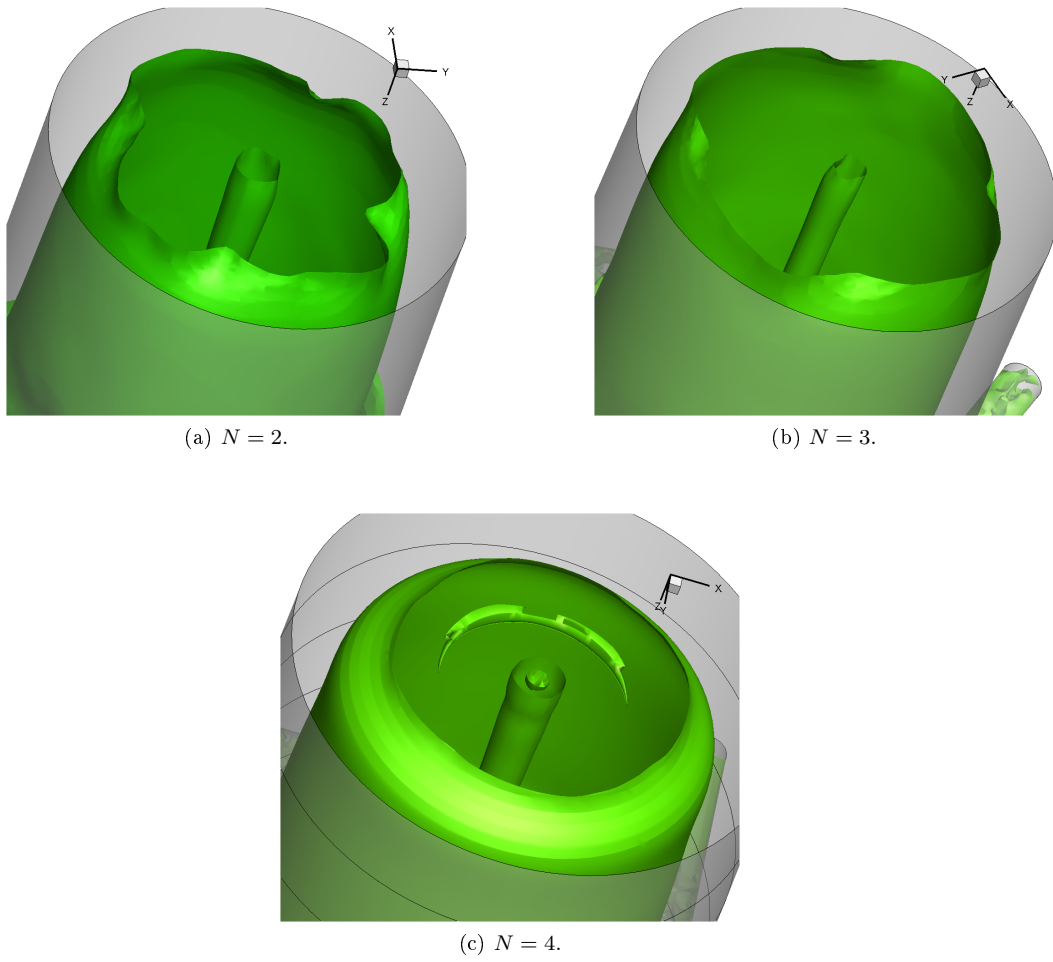
(a) $N = 2$.

(b) $N = 3$.

(c) $N = 4$.

Figure E.13: 3D mantle structures at head of chamber for base injection configurations.

E.3.3 Head injection

(a)

		N = 2	N = 3	N = 4
Number of Injectors	N	2	3	4
Inlet Velocity	u_{in} (m/s)	1.01	1.01	1.01
Inlet Pressure (CFD)	p_{in} (Kpa)	2.97	3.80	6.70
Inlet Reynolds Number	Re	3.92E+04	3.92E+04	3.92E+04
Vortex Reynolds Number	V	1.30E+03	1.94E+03	2.59E+03
Strouhal Number (CFD)	Sh	5.08	5.63	7.93
Normalised Air Core Radius (CFD)	r_{core}	0.081	0.081	0.081
Normalised Forced Vortex Radius (CFD)	r_{SBR}	0.124	0.168	0.159
Liquid Dimension of Forced Vortex (CFD)	$r_{SBR}\text{-}r_{core}$	0.043	0.087	0.078
Precessing Vortex Core Frequency (CFD)	f_{PVC} (Hz)	65.82	72.87	102.66

(b)

		N = 2	N = 3	N = 4
Number of Injectors	N	2	3	4
Peak Tangential Velocity (CFD)	u_{ϕ} (m/s)	1.68	2.26	2.32
Peak Tangential Velocity Ratio (CFD)	u_{ϕ}/u_{in}	1.66	2.24	2.29
CFD Forced Vortex Angular Velocity $(\partial u_{\phi}/\partial r)$	ω (rad/s)	413.56	457.88	645.06
CFD Free Vortex Inverse Gradient $(\partial r/\partial u_{\phi})$	$\partial r/\partial u_{\phi}$	60.19	57.82	83.26
CFD Normalised Boundary layer height at chamber wall	δ_w	0.02	0.02	0.02
Maximum Axial Velocity (CFD)	u_z (m/s)	0.65	1.07	1.51
Minimum Axial Velocity (CFD)	u_z (m/s)	-0.42	-1.50	-2.28

Table E.4: Flow variables for chambers with head injection.

(a) Tangential velocity profile (CFD).

(b) Radial velocity profile (CFD).

(c) Axial vorticity profile (CFD).

(d) Normalised pressure profile (CFD).
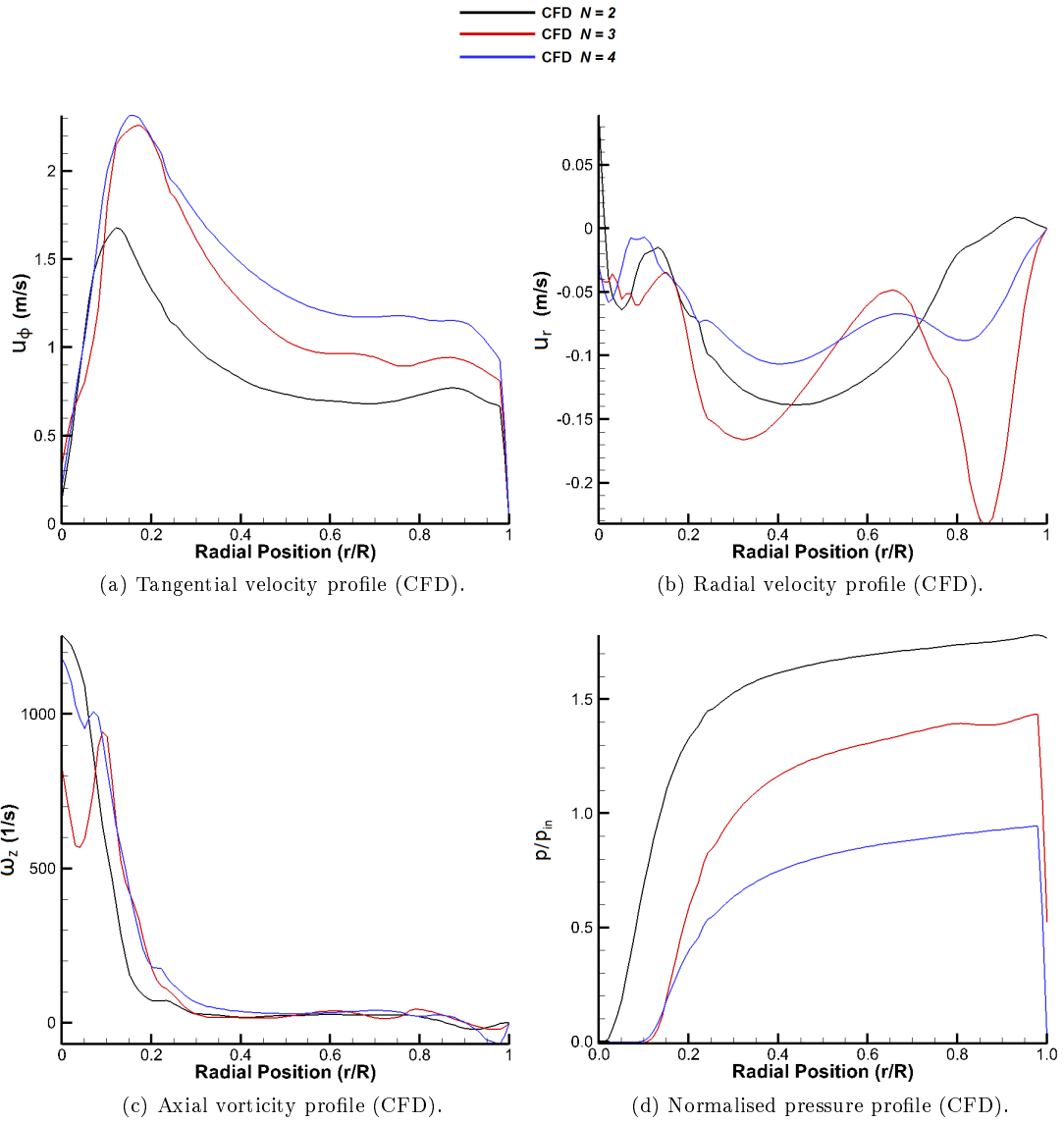
Figure E.14: Tangential profiles for vortex chambers with head injection.

(a) $N = 2$.
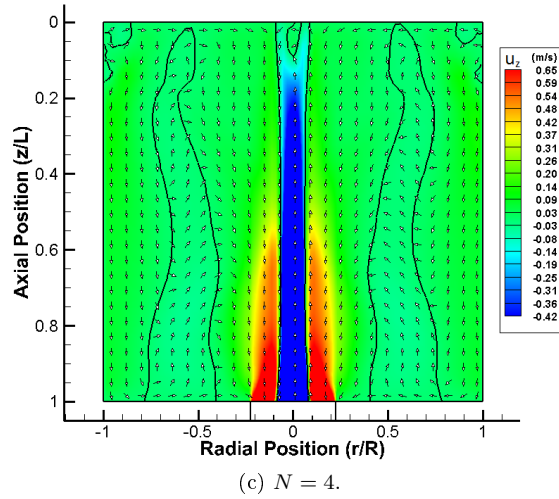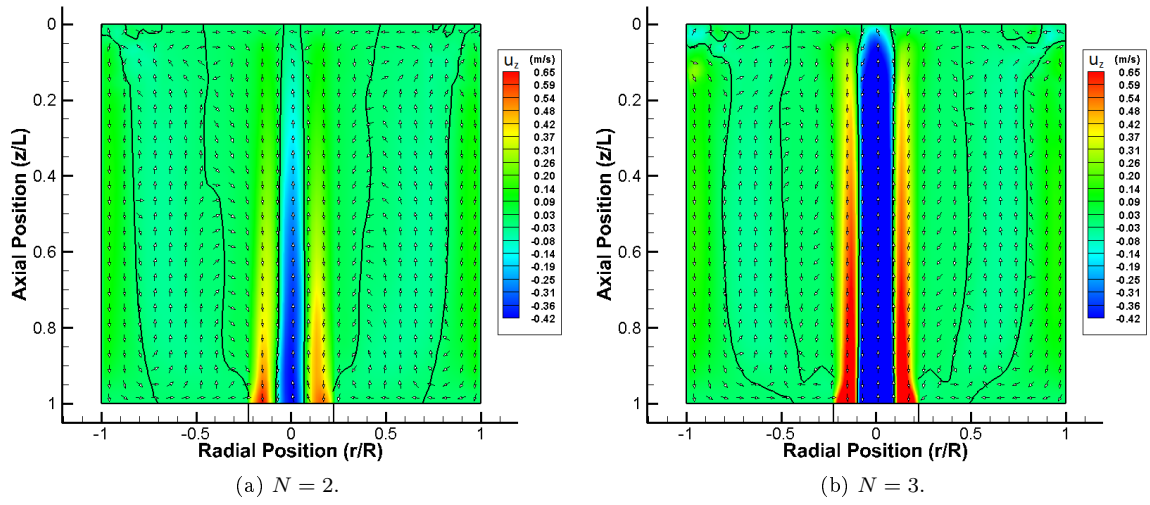
(b) $N = 3$.

(c) $N = 4$.

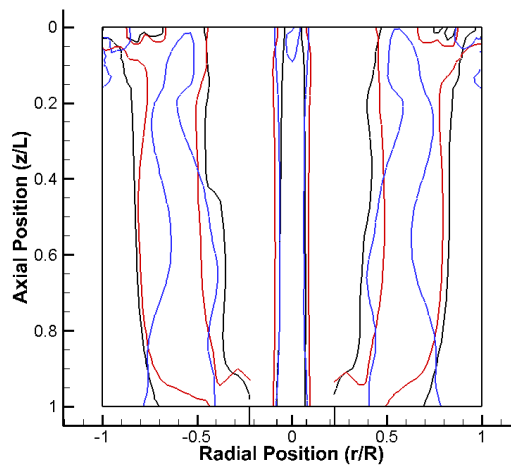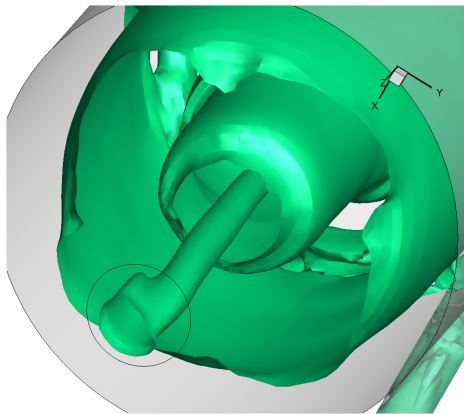Figure E.15: Axial velocity contour plots for vortex chambers with head injection.
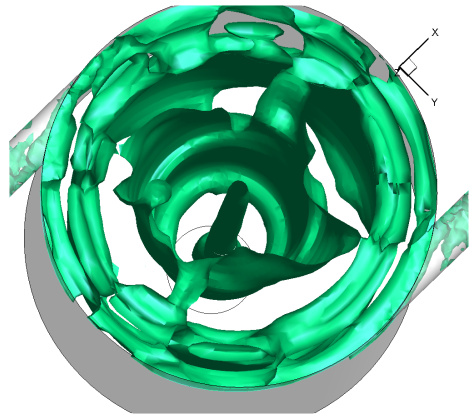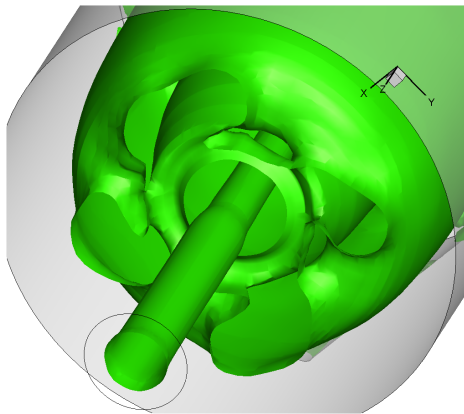

Figure E.16: Axial plot of combined mantles for chambers with head injection.
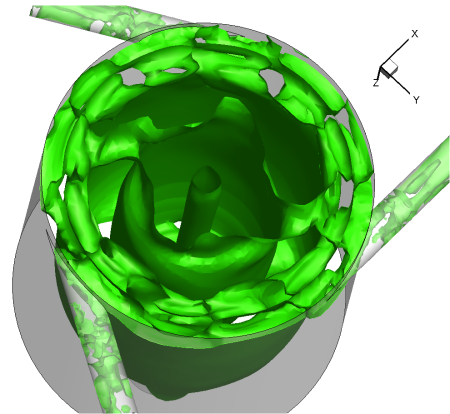
(a) Base of chamber $N = 2$.

(b) Head of chamber $N = 2$.

(c) Base of chamber $N = 3$.

(d) Head of chamber $N = 3$.

Figure E.17: 3D mantle structures for head injection configurations.

E.4 Effect of injector tilt angle

E.4.1 Results overview

The tilt angle of the injectors is defined as the angle of the injector axis relative to azimuthal plane of the chamber which intersects the injectors, where the injector tilt angle seen in all previous chamber configurations is $\vartheta = 0°$. The injector tilt angle is also dependent on the axial position of the injector, as a positive tilt angle for a base injector introduces a negative axial component to the flow, while head injectors introduce a positive axial component, as the inlet flow is directed to the opposing end wall boundaries of the chamber. Examples of chamber configurations with base and head injectors subject to a $\vartheta = 20°$ tilt angle are included in figs E.18a and E.18b respectively for clarity. Several injector tilt angles were chosen for investigation, but the upper boundary of the range was limited in magnitude by constraints placed on the geometry to ensure a high quality mesh was obtained. The range of injector tilt angles investigated are $\vartheta = 5°$, $10°$ and $20°$, which were deemed to provide a suitably sufficient range of test parameters to discern whether the injector tilt angle has any influence upon the mantle structure. When the results displayed below are consulted, it is clear that there is little appreciable variation in the properties of the flow for both base and head injector chamber configurations, as the tangential velocity, radial velocity, axial velocity and normalised static pressure distributions are very similar, irrespective of injector tilt angle. The peak tangential velocity is found to vary over a small range but does not exhibit any relationship between the injector tilt angle, this is also seen in the angular velocity of the forced vortex and the gradient of the free vortex. The only significant variation in the results occurs for the chamber configuration with head injectors that have a $\vartheta = 5°$ tilt angle, although it is thought that this is anomalous data where the accuracy of the numerical solution appears to be affected by oscillations in the residual error. This manifests itself predominantly in the tangential and radial velocity profiles, where the magnitude of these respective components is significantly lower than in the other chamber configurations with irregular profiles and suggests this is due to errors in the solution, rather than been representative of the flow. Despite this, all the results in this part of the study concur with regards to the radius of the PVC and the forced vortex, as both the base and head injector chamber configurations exhibit minimal variation in these dimensions and correlate well to those seen in the inlet Reynolds number study. Increasing the injector tilt angle increases the axial component of the inlet flow, but this does not seem to affect the maximum and minimum axial velocities within the chamber which occur with the core flow of the vortex, and suggest that the characteristics of the vortex are also unaffected. Therefore, it appears that the properties of the vortex are determined by the chamber geometry and the mass flow rate through the chamber, as seen multiple times previously in other parts of the investigation.

The lack of variation in the properties of the flow is also reflected by the 3D and cross sections of the mantle structure in the meridional plane of the chamber, for the chamber configurations with base injectors. There is a single mantle that spans the length of the chamber and is positioned at a virtually identical radius across the majority of the chamber for all configurations, which is also seen in the boundary of the PVC and again highlights the minimal variation in the structure of the vortex core. When the 3D mantles are compared, it is clear that the similarities seen in the meridional plane of the chamber also apply to the full structure of the mantle, as they all exhibit very similar periodic forms and all possess the same phase angle, but do indicate that the tilt angle of the injectors does affect the structure. The chamber configurations with base injectors in this part of the study are similar to those in the inlet Reynolds number study, although there is a considerable difference in the tertiary mantle structures which form in the central region of the chamber. The outer mantle structures are fairly indistinguishable and occur at similar radial positions, but there are no loop structures which form near the head of the chamber, as seen in the inlet Reynolds number study. Instead, there are four distinct small bubble structures that form at the base of the chamber, which in combination with the outer mantle that is in close proximity to the head wall boundary, highlight the significant periodicity which exists in the mantle structure. This is unlike the cross section of the mantle structure in the azimuthal observation plane for chambers configurations with base injectors, where in the inlet Reynolds numbers study the periodic form of the mantle is very
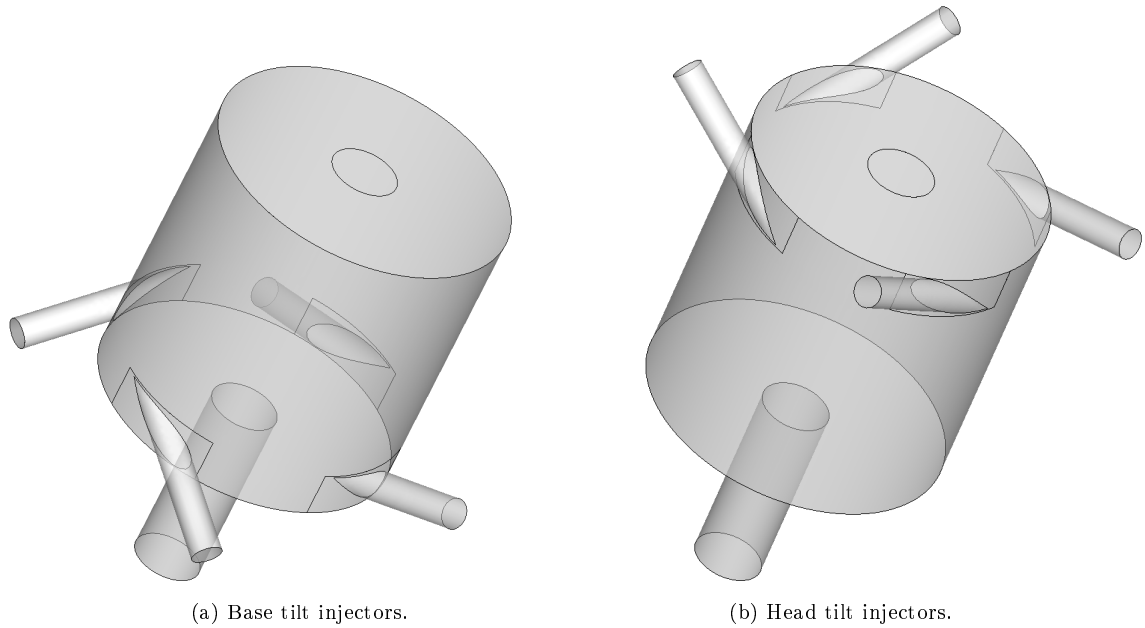
(a) Base tilt injectors.　　　　　　　　　(b) Head tilt injectors.

Figure E.18: Chamber configurations with injector tilt angle $\vartheta = 20°$.

pronounced. This suggests that by altering the axial component of the flow at the periphery of the chamber, the non cylindrical modes that cause the shape of the mantle are being perturbed to a greater degree than the cylindrical modes. In turn, this may indicate that the modal structure is dependent on the axial characteristics of the flow in addition to the chamber geometry, although the mantle structure displays minimal variation over the range of injector tilt angles $\vartheta = 5° - 20°$. When the mantle structures in the meridional plane of the chamber configurations with head injectors are analysed, there are also clear similarities between these forms which occur when the injector tilt angle is $\vartheta = 10°$ or $\vartheta = 20°$. These mantle structures are virtually identical, but while the outer part of the mantle correlates well with the radial position predicted by the Beltramian theory, the inner part does not and may be an example of the interstitial form of the mantle prior to it evolving further, as seen in the internal dome study. As with the base injector chamber configurations, the cross section of the mantle structure for the chamber configurations with head injectors display little resemblance to those seen in the inlet Reynolds number study. More surprisingly, these are reminiscent of the mantle structure seen in the contraction ratio study for the chamber configuration with head injectors and a contraction ratio of $CR = 5$, where the mantle loop is attached to the head wall boundary of the chamber. What is immediately evident when looking at the 3D mantle structures of the chamber configurations with head injectors, is that there is a considerable amount of periodicity which occurs at both the base and head of the chamber. The results for the chamber with head injectors that have a tilt angle of $\vartheta = 5°$ are thought to be anomalous, but the solution still displays evidence of periodic symmetry, where the mantle structure at the base of the chamber appears to take the form of a highly perturbed $(4, 2)$ mode shape. The 3D mantle structures for the chamber configurations with head injector tilt angles of $\vartheta = 10°$ and $20°$ are both similar in form and phase angle, and are good examples of how complex the mantle structure is in comparison to the cylindrical tubes proposed by the analytical solution. It also highlights how the mantle is prone to extensive deformation at the base and head boundaries of the chamber, where flow turning occurs, and how it is vital that future analytical solutions of the confined bidirectional vortex must properly account for these effects in order to better characterise the flow. Overall, the study of the effects of injector tilt angle upon the bidirectional vortex reveals that although there is negligible variation in the properties of the flow, the embedded mantle structure is significantly affected. It is still unknown whether this is due to the additional axial component of the inlet flow, or the variation in geometry that occurs at the interface of the injectors and the periphery of the chamber.

E.4.2 Base injection

Table (a):

Injector Tilt Angle θ	Inlet Velocity u_{in} (m/s)	Inlet Pressure (CFD) p_{in} (Kpa)	Inlet Reynolds Number Re	Vortex Reynolds Number V	Strouhal Number (CFD) Sh	Normalised Air Core Radius (CFD) r_{core}	Normalised Forced Vortex Radius (CFD) r_{SBR}	Liquid Dimension of Forced Vortex (CFD) $r_{SBR}-r_{core}$	Precessing Vortex Core Frequency (CFD) f_{PVC} (Hz)
5	1.16	12.73	4.51E+04	2.98E+03	6.58	0.081	0.144	0.063	98.05
10	1.16	12.69	4.51E+04	2.98E+03	6.57	0.081	0.146	0.065	97.92
20	1.16	12.20	4.51E+04	2.98E+03	6.46	0.081	0.145	0.064	96.25

Table (b):

Injector Tilt Angle θ	Peak Tangential Velocity (CFD) u_{ϕ} (m/s)	Peak Tangential Velocity Ratio (CFD) u_{ϕ}/u_{in}	CFD Forced Vortex Angular Velocity ω (rad/s) $(\partial u_{\phi}/\partial r)$	CFD Free Vortex Inverse Gradient $\partial r/\partial u_{\phi}$	CFD Normalised Boundary layer height at chamber wall δ_{w}	Maximum Axial Velocity (CFD) u_z (m/s)	Minimum Axial Velocity (CFD) u_z (m/s)
5	3.46	2.98	616.06	76.88	0.02	2.08	-2.86
10	3.50	3.01	615.23	78.87	0.02	2.07	-2.84
20	3.42	2.94	604.78	78.88	0.02	2.03	-2.77

(a) (b)

Table E.5: Flow variables for chambers with base injection.

(a) Tangential velocity profile (CFD).

(b) Radial velocity profile (CFD).

(c) Axial vorticity profile (CFD).

(d) Normalised pressure profile (CFD).
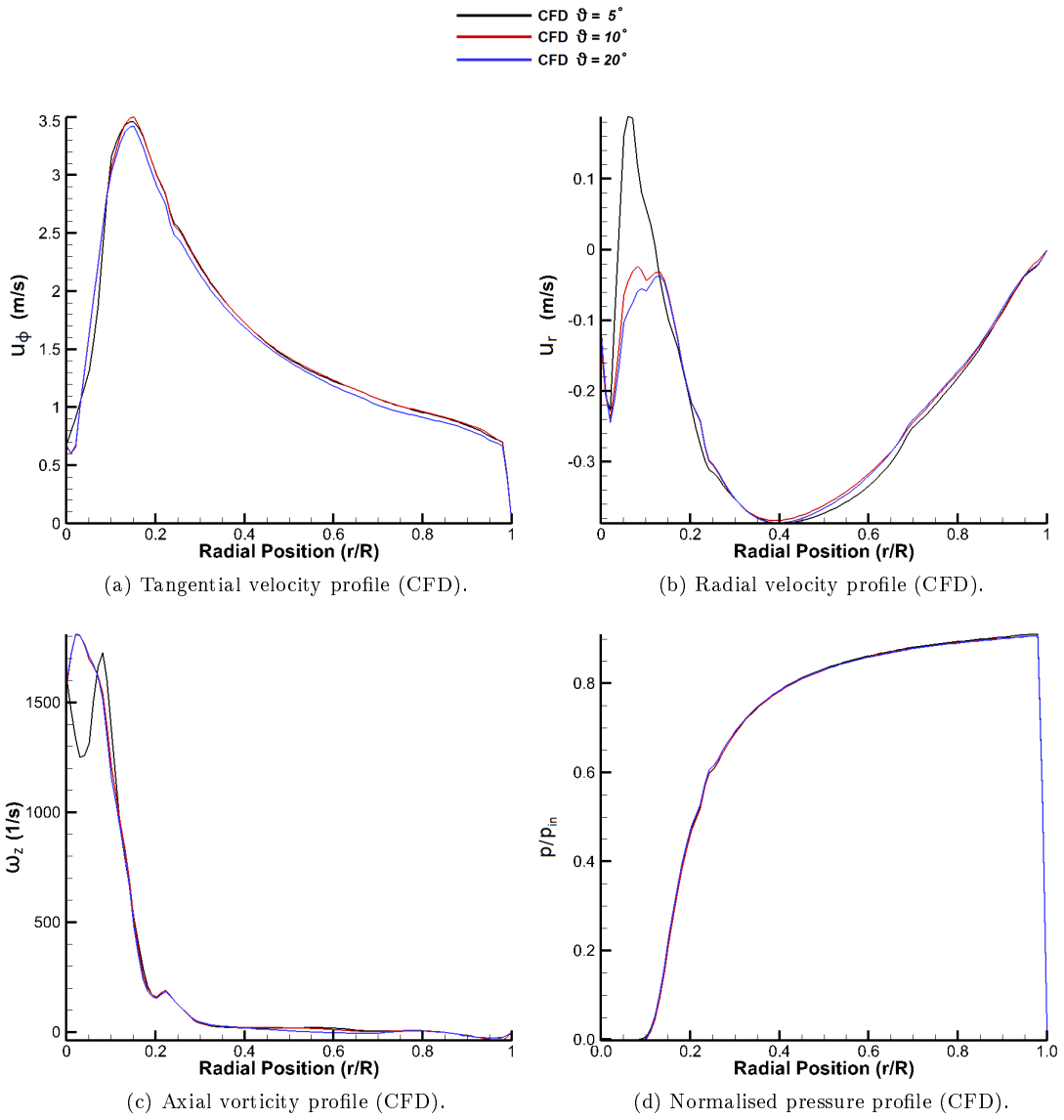
Figure E.19: Tangential profiles for vortex chambers with base injection.

(a) $\vartheta = 5°$
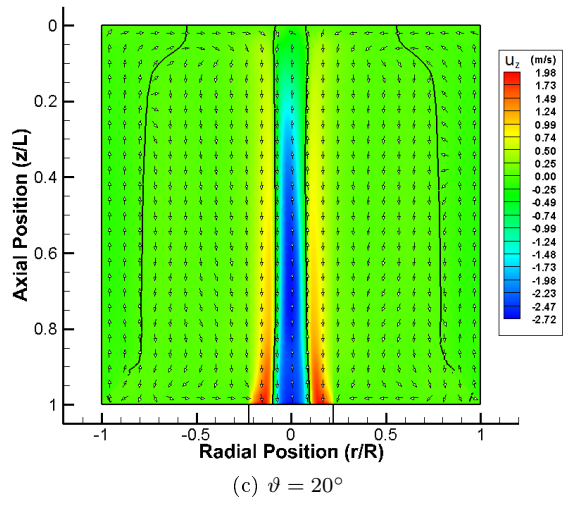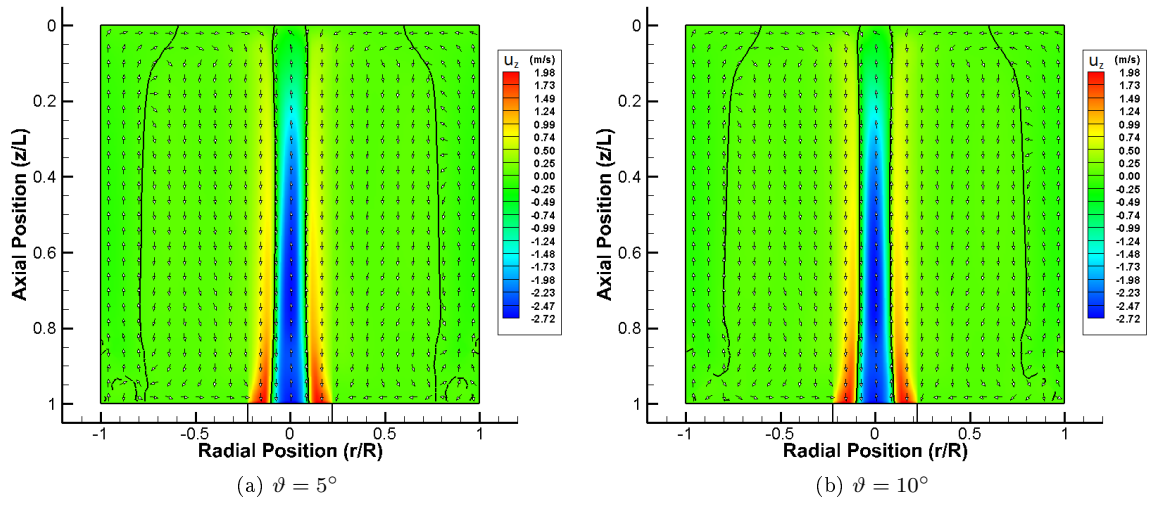
(b) $\vartheta = 10°$

(c) $\vartheta = 20°$

Figure E.20: Axial velocity contour plots for vortex chambers with base injection.
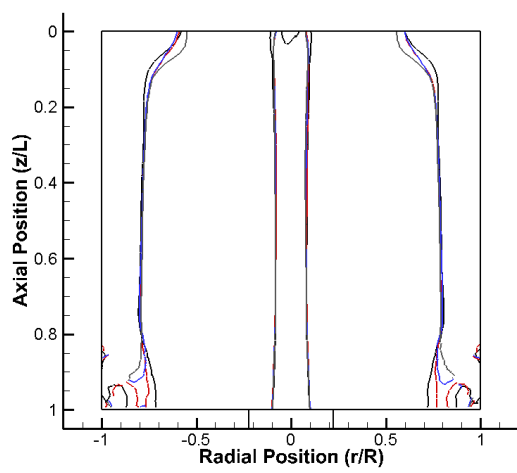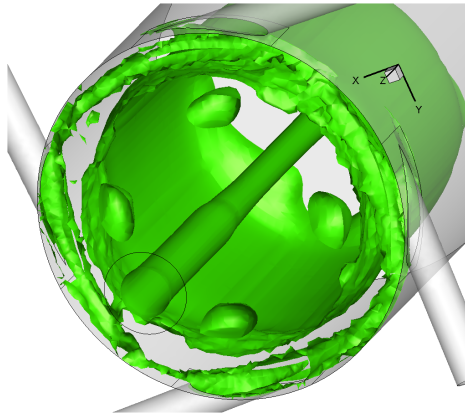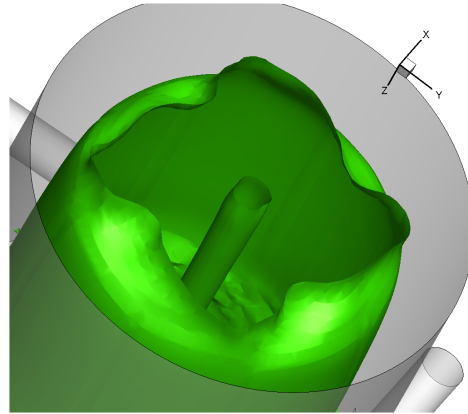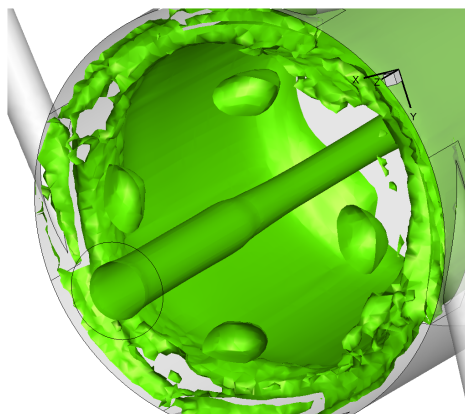

Figure E.21: Axial plot of combined mantles for chambers with base injection.
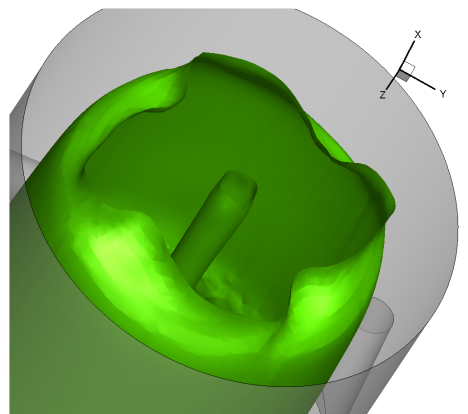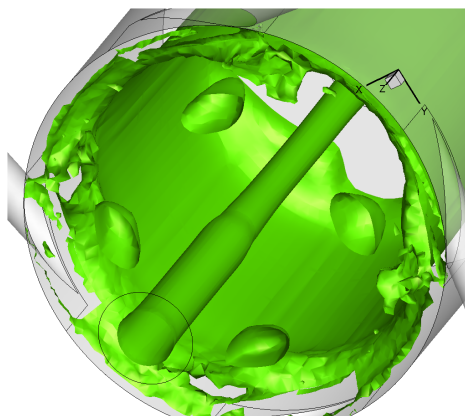
(a) Base of chamber $\vartheta = 5°$

(b) Head of chamber $\vartheta = 5°$

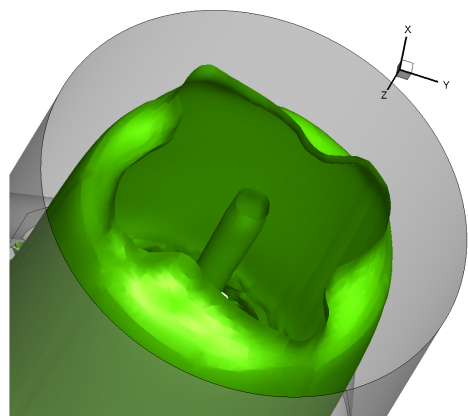(c) Base of chamber $\vartheta = 10°$

(d) Head of chamber $\vartheta = 10°$

(e) Base of chamber $\vartheta = 20°$

(f) Head of chamber $\vartheta = 20°$

Figure E.22: 3D mantle structures for base injection configurations.

E.4.3 Head injection

(a)

Variable	Symbol			
Precessing Vortex Core Frequency (CFD)	f_{PVC} (Hz)	47.50	88.39	82.30
Liquid Dimension of Forced Vortex (CFD)	$r_{SBR}-r_{core}$	0.073	0.082	0.085
Normalised Forced Vortex Radius (CFD)	r_{SBR}	0.134	0.143	0.146
Normalised Air Core Radius (CFD)	r_{core}	0.061	0.061	0.061
Strouhal Number (CFD)	Sh	3.67	6.83	6.36
Vortex Reynolds Number	V	2.59E+03	2.59E+03	2.59E+03
Inlet Reynolds Number	Re	3.92E+04	3.92E+04	3.92E+04
Inlet Pressure (CFD)	p_{in} (Kpa)	4.00	8.85	8.39
Inlet Velocity	u_{in} (m/s)	1.01	1.01	1.01
Injector Tilt Angle	θ	5	10	20

(b)

Variable	Symbol			
Minimum Axial Velocity (CFD)	u_z (m/s)	-2.47	-2.37	-2.36
Maximum Axial Velocity (CFD)	u_z (m/s)	1.48	1.44	1.44
CFD Normalised Boundary layer height at chamber wall	δ_w	0.02	0.02	0.02
CFD Free Vortex Inverse Gradient ($\partial r/\partial u_\phi$)	$\partial r/\partial u_\phi$	75.93	77.07	73.21
CFD Forced Vortex Angular Velocity ($\partial u_\phi/\partial r$)	ω (rad/s)	298.45	555.37	517.10
Peak Tangential Velocity Ratio (CFD)	u_ϕ/u_{in}	1.54	3.07	2.92
Peak Tangential Velocity (CFD)	u_ϕ (m/s)	1.56	3.10	2.94
Injector Tilt Angle	θ	5	10	20

Table E.6: Flow variables for chambers with head injection.

(a) Tangential velocity profile (CFD).

(b) Radial velocity profile (CFD).

(c) Axial vorticity profile (CFD).

(d) Normalised profile (CFD).
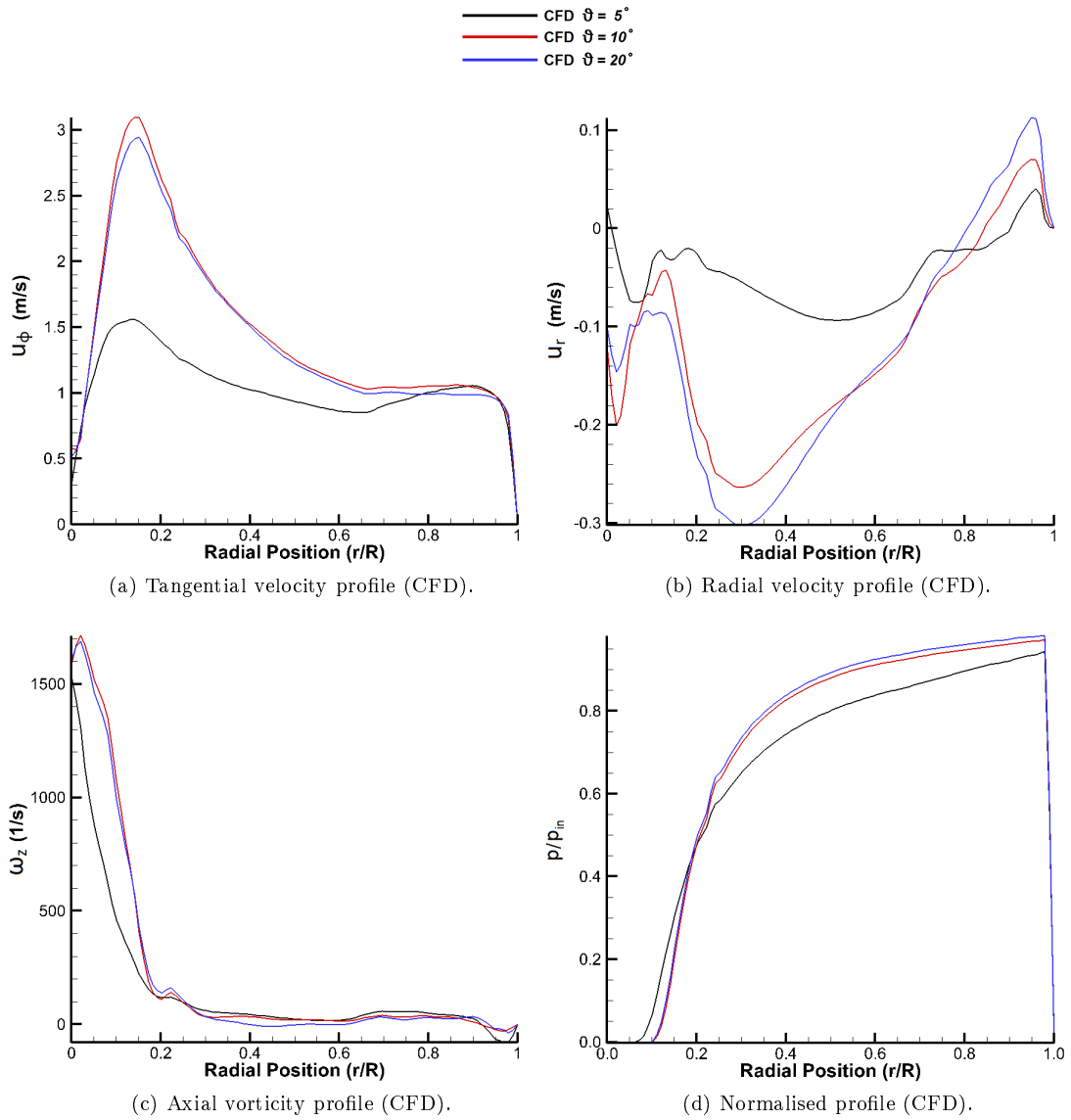
Figure E.23: Tangential profiles for vortex chambers with head injection.

(a) $\vartheta = 5°$

(b) $\vartheta = 10°$

(c) $\vartheta = 20°$
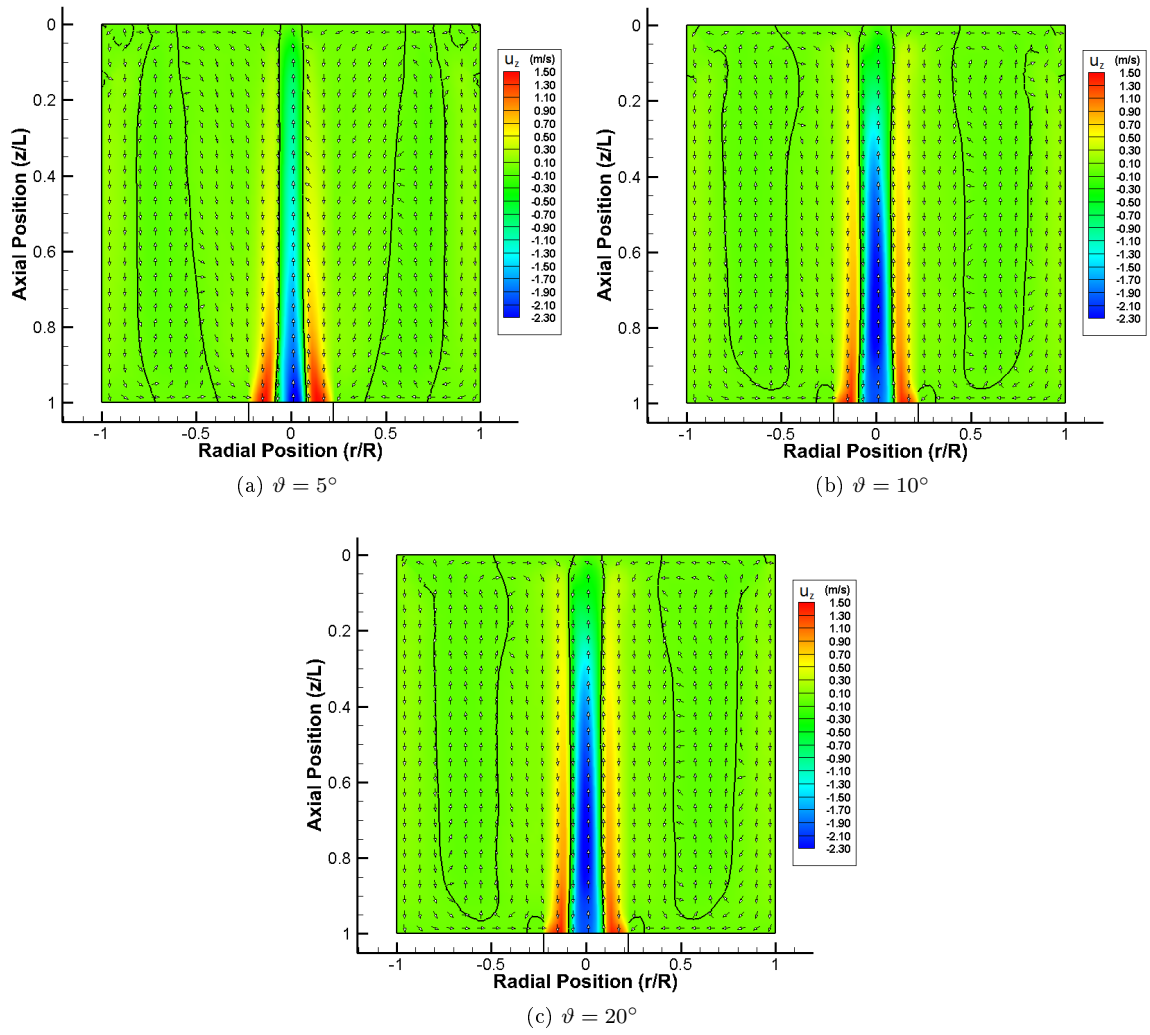
Figure E.24: Axial velocity contour plots for vortex chambers with head injection.
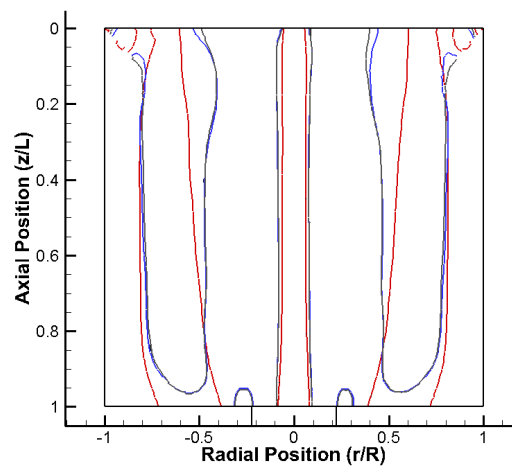
Figure E.25: Axial plot of combined mantles for chambers with head injection.
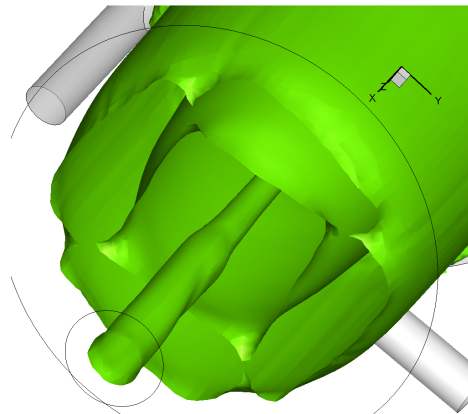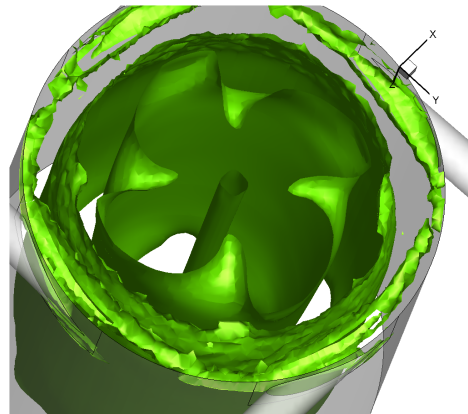
235

(a) Base of chamber $\vartheta = 5°$
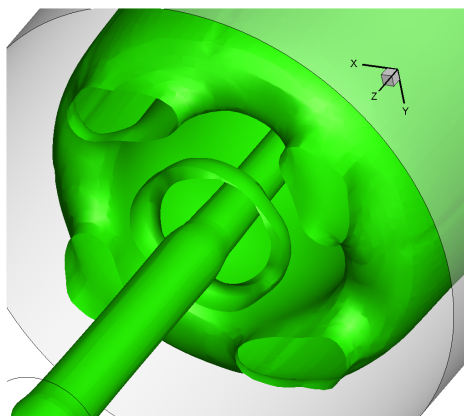
(b) Head of chamber $\vartheta = 5°$
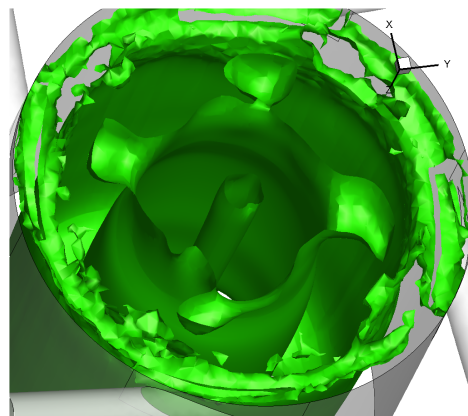
(c) Base of chamber $\vartheta = 10°$
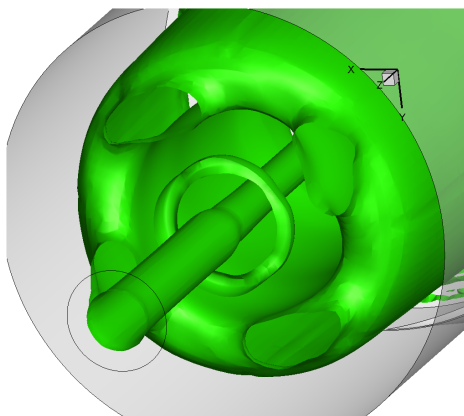
(d) Head of chamber $\vartheta = 10°$
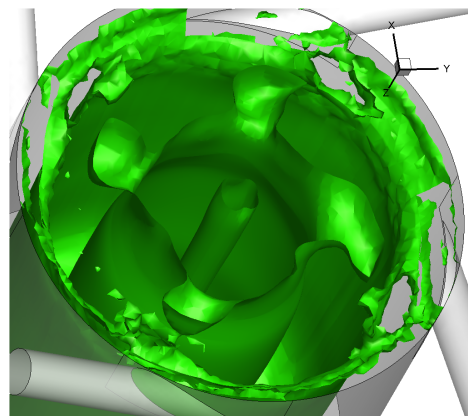
(e) Base of chamber $\vartheta = 20°$

(f) Head of chamber $\vartheta = 20°$

Figure E.26: 3D mantle structures for head injection configurations.

E.5   Additional CFD conclusions

The CFD studies investigating the effects the number of injectors and the tilt angle were performed in order to assess the influence of injector configurations on the behaviour of the flow, rather than the chamber geometry. It was found that by increasing the number of injectors, the associated increase in the mass flow rate produced intense vortices, although the mantle structure was relatively unaffected and corroborates the findings of the inlet Reynolds number study. The various angular positions of the injectors required for uniform azimuthal distribution did not affect the periodicity of the mantle structure, which still exhibited a tendency towards a quadrilateral form. The phase of the mantle structure was similarly unaffected, and despite issues with solution accuracy, this suggests that it is the chamber geometry which is predominantly responsible for the modal structure of the mantle for the range of test conditions investigated. However, it was observed that increased periodicity occurs when the mass flow rate through the chamber is decreased and may indicate that the flow is more susceptible to non cylindrical resonant modes when the relative strength and stability of the vortex is reduced. Overall, the number of injectors was found to have negligible influence on the mantle structure, which was also the finding of the injector tilt angle study, where no noticeable variations in the mantle structure were observed. The only definite conclusion drawn from these additional CFD investigations are that the periodicity and general form of the mantle structure are unaffected by the injector geometry and therefore must be caused instead by the chamber geometry.

Appendix F

Internal waves in rotating fluids

F.1   Introduction

Throughout this investigation, evidence of complex forms have been seen repeatedly in the results, but most importantly in the form of the structure of the mantle. The cross section of the mantle at various axial locations in the azimuthal plane of the chamber resembles mode shapes, that occur due to wave interference and superposition, which result in standing wave arrangements that are found to occur in cylindrical geometries. The mode shapes that have been identified in the results are associated specifically with cylindrical geometries and are examples of cylindrical harmonics, where a discrete perturbation frequency causes a specific modal structure to occur. These mode shapes denote the nodal positions of the standing wave structure and can also be described as eigenmodes, as they are associated with a discrete set of solutions or eigenfrequencies with respect to cylindrical harmonics. These eigenmodes can occur in any system that is in resonance, where the natural, resonant or fundamental frequency relates to the fundamental mode of the system. Examples of these eigenmodes can be found throughout physics and occur predominantly in areas such as: quantum mechanics, electromagnetism, optics, structural mechanics and molecular dynamics, but can be found in any field where wave interaction occurs. Regarding fluid dynamics, there are two types of waves that can affect a fluid and are commonly referred to as either surface or internal waves, where the former occurs at the boundary of the fluid phase, while the latter occurs within the bulk fluid. It is relatively simple to induce surface waves through perturbation of the fluid, internal or inertial waves can only occur if the fluid medium is rotating. This is because the restoring force that resists the initial perturbation is the Coriolis force, therefore inertial waves can only exist in a non-inertial or rotating frame of reference where the Coriolis force is present. In the non-inertial frame of reference, the fictitious non-inertial frame centrifugal force that acts in the positive radial direction is counteracted by the Coriolis force that acts in the negative radial direction, these opposing forces overshoot and result in inertial oscillations. These forces occur as the rotating frame of reference is constantly accelerating in the inertial frame of reference, as the fluid has an angular velocity. According to Newtons second law of motion $F = ma = m\omega r^2$, this centripetal force means that the acceleration of the fluid is relative to the square of the radial position. As these forces act orthogonally to the direction of motion, the inertial oscillations they produce are transverse waves and are similar to Rossby waves, which are found in atmospheric dynamics and oceanography despite their explicit definitions.

F.2 Columnar vortex stability

Circular Couette flow can be produced within a fluid filled annulus where the angular velocity of the inner boundary is less than that of the outer boundary $\Omega_1 < \Omega_2$, this occurs at radii R_1 and R_2 respectively, as seen in fig F.1. This results in a columnar vortex with a linear distribution of azimuthal velocity u_ϕ and exhibits solid body rotation as found in a forced vortex, and is stable if subjected to small perturbations as it satisfies the Rayleigh stability criterion. The Rayleigh stability criterion considers a small fluid element that is inviscid, incompressible and rotating at a radius r about a fixed axis, and compares the magnitudes of the centrifugal force to the radial pressure gradient along a circular pathline. Specifically it assesses whether the negative radial force produced by the radial pressure gradient $-\frac{\partial p}{\partial r}$ is sufficiently large to provide the centripetal acceleration $\frac{-u_\phi^2}{r}$ required to maintain the trajectory of the fluid element along a defined circular path. If the fluid element is perturbed, its radial position will either increase or decrease, moving from r_1 to r_2, but it is assumed that it will still have the same amount of angular momentum per unit mass $B = ru_\phi$, as depicted in fig F.2. As the original magnitude of the angular momentum is retained in order to conserve angular momentum, the new velocity of the fluid element u_{crt} at the displaced radial position r_2 can be described by $r_2 u_{crt} = r_1 u_1$, or eqn F.1. The new velocity of the perturbed fluid element can be greater or lesser than that of the ambient fluid at the new radius, depending upon the radial velocity gradient $\frac{\partial u}{\partial r}$ of the flow [12] .If the centripetal acceleration of the perturbed fluid element and the radial pressure gradient of the ambient flow are compared then this results in eqn F.2, which can be combined with eqn F.1 to yield the radial pressure gradient of the ambient fluid that affects the perturbed fluid element, described by eqn F.3.

The Rayleigh stability criterion states that the flow is stable to small perturbations if the ambient pressure gradient is greater than the centripetal acceleration of the perturbed fluid element, as expressed by eqn F.4. The flow is similarly stable if the square of the final angular momentum is greater than the square of the initial angular momentum, as expressed by eqn F.5. Effectively, this means that if a fluid element is radially displaced, it will return to its initial position if the flow is stable, but unless this motion is sufficiently dampened then the fluid element will overshoot the equilibrium position and begin to oscillate. This oscillatory wave motion is an inertial wave, and is the only type of wave that can occur in a rotational flow that satisfies the Rayleigh stability criterion and is undergoing solid body rotation, as stability requires $\frac{\partial B}{\partial r} > 0$ in a viscous fluid where $B = ru_\phi$. Regarding circular Couette flow, the azimuthal velocity can be described as $u_\phi = \omega r$, but because the flow exhibits solid body rotation the angular velocity is constant, which allows the Rayleigh stability criterion to take the form seen in eqn F.6.
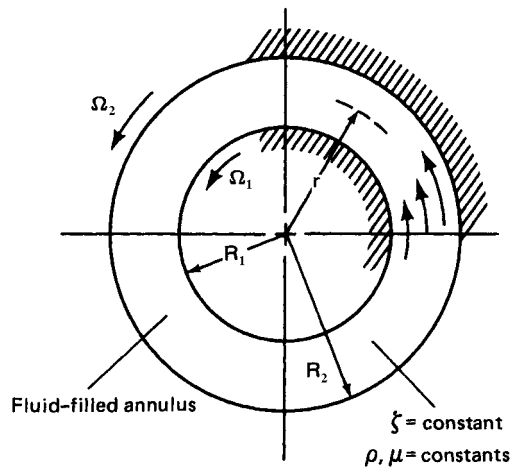

Figure F.1: Circular Couette flow. [12]
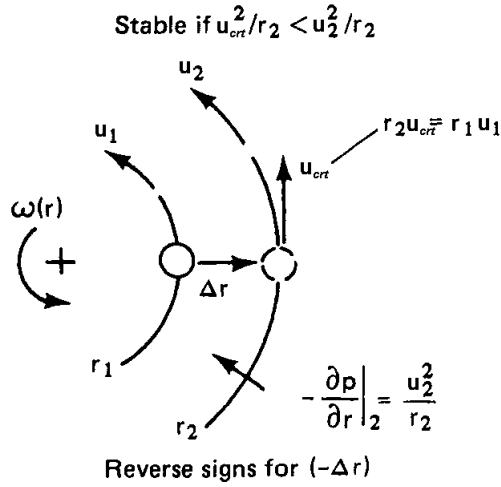
Figure F.2: Rayleigh stability in terms of a fluid element. [12]

Stability of circular Couette flow is dependent on several variables such as: μ, ρ, Ω_1, Ω_2, R_1 and R_2, as well as the ratios between these values, where stability is commonly determined by the ratio of the angular velocities of the inner and outer boundaries of the annulus. If circular Coutte flow is subject to instability it will result in Taylor vortices, these are counter rotating vortex rings stacked upon on each other and is an example of a stable sustainable flow field, as seen in fig F.3. In an incompressible fluid, the formation of a wave, or a convective motion that results from instability, necessitates the displacement of the surrounding fluid, so that conservation of mass is preserved. When Taylor vortices occur, the convective motion caused by Rayleigh instability occurs in both the positive and negative radial direction, where conservation of mass leads to axial flow that forms counter rotating vortex rings. As the toroidal vortices rotate about an enclosed vortex filament, they also rotate about the axis of the column, which transports the radial and axial components of the convective flow in the azimuthal direction of the column. The vorticity of the singular toroidal vortex that defines circular Couette flow increases as instability develops, as the displaced fluid caused by convective motion results in vortex stretching. The vortex filaments aligned with the axis of the annulus are deformed accordingly, and rearrange themselves in the azimuthal plane of the chamber as equally spaced vortex rings that span the void of the annulus.

$$u_{crt} = \frac{r_1 u_1}{r_2} \tag{F.1}$$

$$-\frac{u_{crt}^2}{r_2} = -\frac{(r_1 u_1)^2}{r_2^3} \tag{F.2}$$

$$\frac{1}{\rho}\frac{\partial p}{\partial r}\Big|_2 = -\frac{u_1^2}{r_2} \tag{F.3}$$

$$\frac{u_2^2}{r_2} > \frac{(r_1 u_1)^2}{r_2^3} \tag{F.4}$$

$$(r_2 u_2)^2 > (r_1 u_1)^2 \tag{F.5}$$

$$\left(\omega r_2^2\right)^2 > \left(\omega r_1^2\right)^2 \tag{F.6}$$

Figure F.3: Taylor vortices within a rotating fluid annulus. [12]

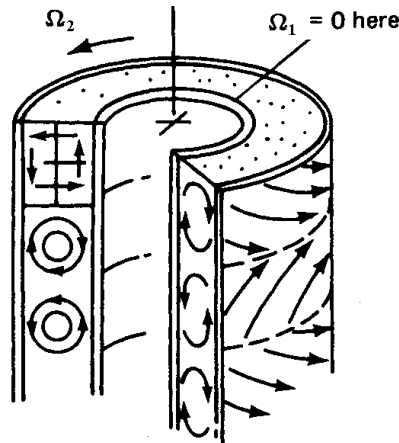Taylor vortices are also dependent on viscosity as they are sustained through the shear flow that exists between the cylindrical boundaries of the annulus, and will occur above a threshold value where the shear rate is sufficient to maintain the vortex rings. The rotation of these vortex rings about circular vortex filaments is a tertiary flow and allows momentum transport between the inner and outer boundaries of the annulus, which allows for both mass and momentum to be conserved. The transition from circular Couette flow to Taylor vortices is an example of vortex breakdown which is caused by instability, and results in secondary vortical motions. Instability may also cause linear or non linear waves to propagate throughout the flow, which can lead to vortex breakdown or establish standing wave arrangements in the fluid, based on the harmonics of the chamber geometry. As the columnar vortex subdivides into individual vortex rings, the dimensions of the region of fluid they occupy is replicated along the axis of the column, forming vortex cells that encapsulate the vorticity distribution of the individual vortex rings. The array of individual cells that form the Taylor column can be thought of as a cell structure that is stable over a specific range of conditions, similar to the stable single toroidal cell structure of circular Couette flow, where the same variables which affect stability apply. The number of these axial cells, as is the case with stability, dependent on the properties of the flow, where each configuration of axial cells is an example of an eigenmode, as the cell structure is a mode shape that is associated with a specific resonant frequency. For a columnar vortex with a linear distribution of azimuthal velocity, such as circular Couette and Taylor flow, the flow is stable and can withstand small perturbations, even though Taylor vortices stem from Rayleigh instability. As a result of this, inertial waves can propagate in both types of flow, where the vortex cell structure is caused by resonance of the inertial waves, and result in inertial modes that are the resonant modes of the chamber geometry. Therefore, the inertial waves are responsible for perturbing the chamber geometry, which characterises the specific modal structures that can occur within the fluid, and in turn controls the tertiary vortex flow.

F.3 Perturbation of a columnar vortex

Vortex flow within a fluid filled annulus was initially investigated by Kelvin [124], who found that while a fluid undergoing solid body rotation is stable if perturbed by a small disturbance, and the same is also true of the Rankine vortex. The Rankine vortex is unsuitable for describing physical vortical flows, but it still provides a valid approximation for columnar vortices and vortex filaments. Kelvin found that the Rankine vortex in the absence of axial flow, is stable to both axisymmetric and spiral mode instabilities that result in corresponding forms of vortex breakdown, as seen in fig B.1. If a uniform rectangular axial velocity profile is applied to the stable forced vortex, in addition to a dissimilar uniform rectangular axial velocity profile applied to the potential flow surrounding the core, instability is possible. At the boundary of the vortex core there is a flow discontinuity, where there is a jump in the magnitude of the axial velocity component that enables the rotational and irrotational regions of the vortex to possess different axial velocities, while maintaining a uniform rectangular velocity profile. This allows for several flow configurations to be assessed with regards to stability, including a jet with co-current flow, a jet with counter flow, a wake with counter flow and a wake with co-current flow, as depicted by figs F.4a-F.4d respectively. Fig F.4b is an example of bidirectional flow as seen in VIHRE configurations, and indicates it is possible to conduct stability analysis for such types of flow and determine what parameters affect stability, or possibly cause instability to invoke flow transition to a different stable state, as with a Taylor column.

Stability is considered for three separate regions of the Rankine vortex, which are the vortex core $r < r_{SBR}$, the outer vortex $r > r_{SBR}$ and the boundary of the vortex core $r = r_{SBR}$. The boundary of the vortex core is assumed to be a cylindrical vortex sheet and therefore allows stability analysis to be conducted, based on the stability criteria established for a planar vortex sheet with the addition of non-inertial frame forces. Perturbations of the core of the Rankine vortex are sometimes referred to as Kelvin waves, for which exact solutions exist describing the effects of small harmonic perturbations of the vortex core, which are an explicit description of inertial waves. This formulation was concerned with the results for the axisymmetric and bending modes of the vortex core in response to waves with large wavelengths $\lambda \gg r_{SBR}$, while later studies by Saffman [125] provided results the effects of short waves $\lambda \approx r_{SBR}$ and $\lambda < r_{SBR}$. To put the magnitude of these wavelengths into context, an example of a $\lambda \gg r_{SBR}$ wave would be Crow instability that develops in the wake vortices of aircraft, while $\lambda < r_{SBR}$ waves are observed in the source images obtained during the PIV experiments, denoted by the deformation of the PVC in the meridional plane of the chamber. If no axial velocity profile is applied to the Rankine vortex, then the solutions of the wave dispersion equations are found to be propagating neutral waves, where the exponent of the solution is described by eqn F.7. The variables k and m are the axial and azimuthal wave numbers respectively, while ϕ is the azimuthal angle and ω is the frequency. This form that describes propagating these neutral waves is the same as for inertial waves, which are commonly referred to as neutral waves, as they are not the result of instability and exist in a neutrally stable flow. Regarding neutral stability, Chandrasekhar [126] found that free irrotational vortices with $u \propto \frac{1}{r^n}$ can be stable according to the Rayleigh stability criterion, based on the exponent integer of the radial position n, which determines

(a) Jet with co-current flow.

(b) Jet with counter flow.

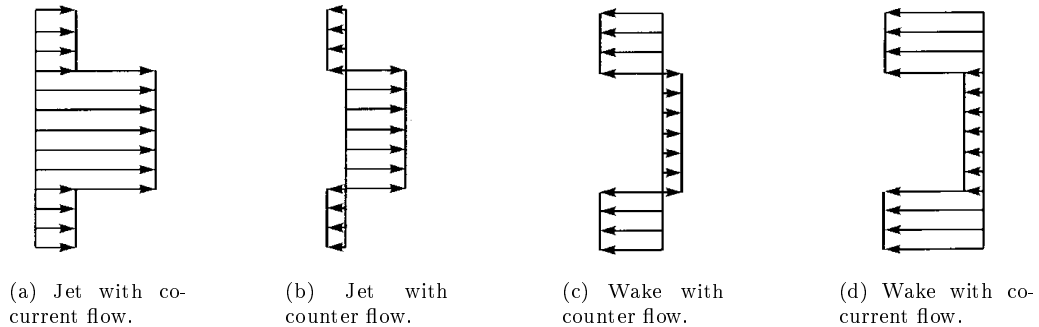(c) Wake with counter flow.

(d) Wake with co-current flow.

Figure F.4: Possible axial velocity profiles of the Rankine vortex. [39]

the velocity gradient of the vortex. This is expressed by eqn F.8, and states that for $n < 1$ the flow is stable, while for eqn F.9 and $n > 1$, the flow is unstable, but it can also remain neutrally stable if $n = 1$ as seen in eqn F.10 where the relationship reduces to unity. This corroborates Kelvins assessment of the Rankine vortex as it shows that both forced and free vortices can satisfy the Rayleigh stability criterion and therefore act as a medium through which inertial waves can propagate.

$$e^{i(kz+m\phi+\omega t)} \tag{F.7}$$

$$\left(r_2^{1-n}\right)^2 > \left(r_1^{1-n}\right)^2 \tag{F.8}$$

$$\left(r_2^{1-n}\right)^2 < \left(r_1^{1-n}\right)^2 \tag{F.9}$$

$$\left(r_2^0\right)^2 = \left(r_1^0\right)^2 \tag{F.10}$$

When the dispersion equations are applied to the axisymmetric mode $m = 0$ of the core of the Rankine vortex, then it is possible to obtain an exact solution when the core is perturbed by waves with long wavelengths. These long waves are commonly defined by $kr_{SBR} \ll 1$ and the wavelength can be deduced from eqn F.13, where small axial wave numbers are applicable. The solution of the dispersion equations for this case reduces to the Bessel function of the first kind J_0, where the roots of the function yield the radial wave numbers n that are indicative of the radial modes where resonance occurs. The solution of the dispersion equations for short waves $kr_{SBR} \gtrsim 1$ has to be obtained numerically, but the roots of the solution are still determined by the roots of the Bessel function of the first kind J_0. Considering that inertial waves at resonance produce inertial modes that are equivalent to the natural resonant modes of the confining geometry, then in an axisymmetric cylindrical geometry the radial divisions between the individual radial cells will occur at the roots of J_0. This solution and the associated roots, are identical to those that occur in cylindrical harmonics for any cylindrical geometry that is in resonance, whether it be a perturbed solid structure or a confined quantum particle. Specifically, this shows that in a confined rotating fluid where the boundary is cylindrical, the radial modes can be discerned from the roots of J_0, which is also what is found by the Beltramian solution of the bidirectional vortex when axisymmetric boundary conditions are imposed. This is also seen repeatedly in the numerical results, where the effects of asymmetry are minimal and the mantle structures correlate well with the theoretical positions obtained from the roots of J_0. Where the radial mode describes the amount of flow reversal occurring within the vortex chamber, and if the parameters that perturb these modes can be defined, then it may be possible to invoke specific vortical flows.

In assessing the stability of the core of a columnar vortex, perturbations are classified as either axisymmetric $m = 0$ or asymmetric $m \neq 0$, and are concerned with the azimuthal plane of the vortex. Examples of perturbations of the vortex core can be seen in fig F.5, where pointer numbered 1 indicates the boundary of the forced vortex, and the radius of an undisturbed core is defined as $r = R$. In linear stability analysis the velocity profile of the vortex has a discontinuity or velocity derivative at the boundary of the vortex core, where there is commonly a transition to a free vortex in confined vortical flows. If this boundary is perturbed by a single frequency or a linear monochromatic disturbance, then the radius of the vortex core can be described by eqn F.11. The amplitude of the wave a is significantly smaller than the radius of the undisturbed vortex core so that $a \ll r_{SBR}$, and the azimuthal wave number m is an integer, while the term ωt refers to the transient form of the vortex core. The deformed vortex core boundaries displayed in fig F.5 can be described by eqn F.12, where the axial wavenumber is real and the perturbed core shape is irrespective of time $t = 0$. The wave propagates in the direction of the vortex axis, while oscillation occurs orthogonally in the azimuthal plane, denoting a transverse wave that characterises the motion of inertial waves, while the exponent of eqn F.11 is also in the form of a neutral wave, as expressed previously in eqn F.7. The circumferential and helical lines denoted by pointer 2 in fig F.5 are the lines of fixed
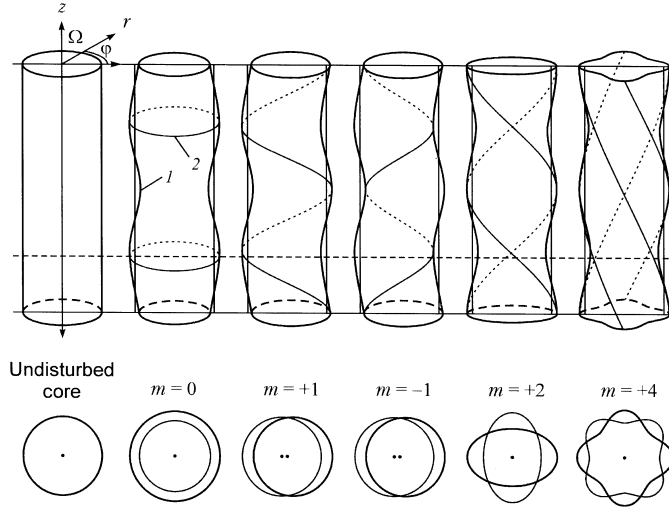
Figure F.5: Types of core perturbation of a columnar vortex. [39]

phase, which occur when $kz + m\phi = constant$, and the wavelengths of axisymmetric and asymmetric modes can be calculated by eqn F.13 and eqn F.14 respectively . The axisymmetric mode $m = 0$, or breathing mode of the vortex tube exhibits no phase shift and the radius varies by $r = r_{SBR} \pm a$, as all parts of the vortex rotate about the axis. When the azimuthal mode number is $m = \pm 1$, the deformation of the vortex core is asymmetric and are referred to as bending modes, as the vortex filament that describes the axis of rotation is helical and results in vortex core precession, with the $m = 1$ and $m = -1$ referring to left and right handed helical paths respectively. If the asymmetric mode is $m \geqslant 2$, then the axis of rotation returns to its original undisturbed linear state due to the periodic symmetry of the deformed vortex core, while the pitch of the helical lines of fixed phase and constant velocity, increases accordingly with higher azimuthal wave numbers. The periodic symmetry exhibited by the asymmetric modes where $m \geqslant 2$, has been observed in the deformed PVC boundaries obtained in the PIV investigation, with modes in the range $2 \leqslant m \leqslant 5$ being identified, as well as evidence of vortex precession that also indicates the influence of the $m = \pm 1$ bending modes. This physical evidence proves that inertial waves were present in the experiments, and that the periodic geometry of the PVC means that these waves are in resonance which results in inertial modes, and therefore the chamber geometry must be in resonance, which is defined by cylindrical harmonics. The radial divisions between individual bidirectional vortex tubes are obtained from the roots of the Bessel function of the first kind J_0, and denote the position and structure of the mantle. The mantle structure could not be resolved from the experimental data, but the numerical results also repeatedly show that the axisymmetric mantle structures correlate well with the roots of J_0, while those which exhibit periodic symmetry are indicative of mode shapes associated with cylindrical harmonics, and therefore the flow must be in resonance.

$$r = r_{SBR} + a\Re e^{i(kz + m\phi - \omega t)} \tag{F.11}$$

$$r = r_{SBR} + a\cos\left(kz + m\phi\right) \tag{F.12}$$

$$\lambda = \frac{2\pi}{k} \tag{F.13}$$

$$\lambda = \frac{2\pi}{k|m|} \tag{F.14}$$

244

F.4   Inertial modes

Inertial modes arise from the resonance of inertial waves that can occur in a rotating fluid and are produced by oscillations of the non-inertial frame forces, this ensures equilibrium as well as the inherent stability of the rotating system. The fundamental inertial mode describes the least complex configuration of the flow while it also requires the least energy to sustain, an example of this is Couette flow, which is the fundamental inertial mode that occurs in a cylindrical geometry. As further energy is introduced into the flow it becomes possible to perturb higher order inertial modes, as the flow becomes unstable and undergoes transition into a another stable but more complex flow configuration. As the order of the inertial mode increases, the fluid domain subdivides into progressively smaller regions which encapsulate the increasing number of large scale coherent vortices, as the fluid motion must conserve both mass and momentum. The equations of motion that describe the flow have discrete solutions or eigenfunctions, which pertain to the geometry of the inertial modes and can yield eigenvalues which represent the discrete frequencies required to invoke specific modal structures. These eigenfunctions generally take the form of Legendre polynomials and Bessel functions that are influenced by the geometrical boundaries of the domain, which means that the inertial modes possible in a confined rotating fluid will be determined by the container geometry.
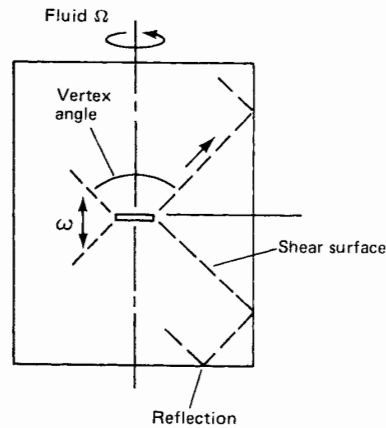

Figure F.6: Shear surfaces produced along flow path of progressive inertial waves. [12]

In a columnar vortex, axial perturbations of the vortex core can result in inertial waves, therefore if inertial modes are dependent on the spectral characteristics of the perturbation, it is possible to observe a range of inertial modes by adjusting the frequency and amplitude of a monochromatic disturbance for a defined chamber geometry. Fultz [127] conducted experiments investigating inertial modes in a cylindrical volume of fluid undergoing solid body rotation and subject to axial perturbations, induced by a vertically oscillating disc aligned with the chamber axis as depicted in fig F.6. The fluid rotates at a frequency of Ω, while the disc oscillates at a frequency of ω, where the Prandtl number is below a critical value so that the upper and lower boundaries of the fluid can be assumed to be free liquid surfaces, and not subject to viscous shear [127]. As the disc oscillates it displaces the adjacent fluid, which produces radial perturbations that are counteracted by the Coriolis force induced by rotation, and results in inertial oscillations in accordance with the Rayleigh stability criterion. These oscillations propagate within the meridional plane of the fluid as progressive inertial waves, which have both an axial and radial component, as seen in fig F.7a. The inertial waves produce conical shear surfaces within the fluid, which are then reflected by the chamber geometry and establish a standing wave structure. These inertial modes will occur if the fluid is subject to specific rotational Ω or perturbation frequencies ω, resulting in vortex cells as seen in fig F.7b. In order to characterise these parameters, the non dimensional frequency ratio $\frac{\omega}{\Omega}$ is employed, as it is a ratio of the local temporal acceleration of the fluid $\frac{\partial \mathbf{u}}{\partial t}$ with respect to the Coriolis acceleration ($2\Omega \times \mathbf{u}$) [12].

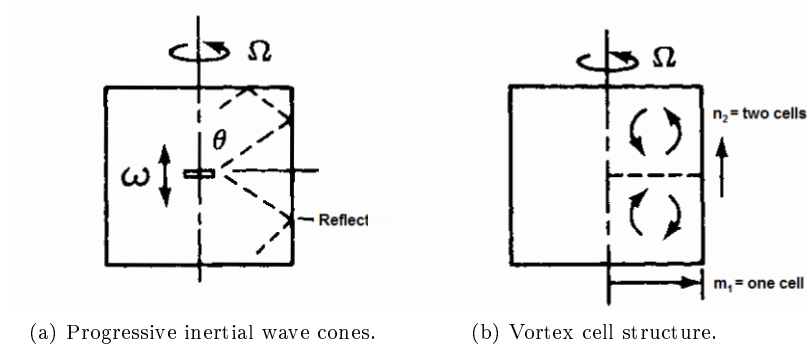(a) Progressive inertial wave cones.   (b) Vortex cell structure.

Figure F.7: Experimental setup of vortex chamber used by Fultz. [12]

Greenspan later derived the eigensolution of the inviscid problem, which is expressed in eqn F.15 for $k = 0$ and n, $k = \pm 1$, ± 2, ..., where k and n are the azimuthal and axial wave modes respectively [45]. A positive azimuthal wave mode k results in a positive eigenvalue λ, while the opposite is true for negative values of k, which means that λ does not correspond to $\pm k$ and that the modal solutions represent propagating waves where the entire spectrum can be determined by positive eigenvalues. The effects of viscosity are accounted for in eqn F.16, where the eigenvalue of each mode is separated into an inviscid component and a boundary layer perturbation, although this fails when the wavelength of the oscillation is comparable to the thickness of the boundary layer, as described in eqn F.17. When there are an increasing number of axial divisions in the flow the axial wave mode k increases accordingly, which results in smaller axial divisions and eventually will be of a similar scale to that of the Ekman layer, which is the thin layer of fluid at the axial boundaries of the chamber. This is unlikely to be a problem with regards to physical flows, as experiments to date have only observed low order axial wave modes whose dimensions are significantly greater than that of the associated Ekman layers [45, 127].

$$\lambda_{nmk} = 2 \left(1 + \frac{\varphi_{nmk}^2}{n^2 \pi^2 \left(\frac{R}{L} \right)^2} \right)^{-\frac{1}{2}} \tag{F.15}$$

$$\lambda_{nmk} = 2 \left(1 + \frac{\varphi_{nmk}^2}{n^2 \pi^2 \left(\frac{R}{L} \right)^2} \right)^{-\frac{1}{2}} + iEk \left(n^2 \pi^2 + \frac{\varphi^2}{\left(\frac{R}{L} \right)^2} \right) \tag{F.16}$$

$$k = \left(n^2 \pi^2 + \frac{\varphi^2}{\left(\frac{R}{L} \right)^2} \right)^{\frac{1}{2}} = Ek^{-\frac{1}{2}} \tag{F.17}$$

$$Ek = \frac{\nu}{\Omega l^2} \tag{F.18}$$

$$Ro = \frac{u}{\Omega l} \tag{F.19}$$

During Fultz's investigation, the inertial modes were initially identified through injection of coloured dye in close proximity to the oscillating disc, and path of the dye within the flow was then observed as it became dispersed within the fluid. This established toroidal regions of recirculation which are indicative of the mantle, or more specifically define the boundaries of the individual vortex cells associated with the modal structure. Example images acquired during these experiments are presented in fig F.8, and are representative of axisymmetric inertial modes $k = 0$ with two radial cells $m = 1$, which relates to a single mantle that spans the length of the chamber, but incorporate a different numbers of axial cells of $n = 2$ and 3 respectively. This method is rather subjective, but Fultz was able to determine several inertial modes that occurred in a range of cylindrical geometries

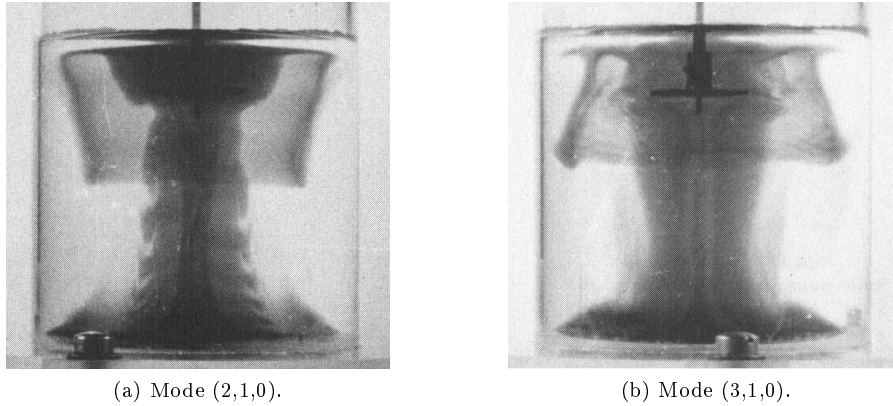(a) Mode (2,1,0).   (b) Mode (3,1,0).

Figure F.8: Inertial modes identified by dye experiments. [45]

over a range of frequency ratios. Based on the earlier work of Kelvin [124], Bjerknes and Solberg [128], the Eulerian expressions for the velocity components of a fluid within a rotating cylindrical volume were used to derive the stream function in the meridional plane of the chamber. The velocity components and the stream function are all based around the Bessel functions of the first kind J_0 and J_1 and are comparable to those derived in the Beltramian solutions. From this, Fultz was able to determine the radial amplitude dependencies of the axial, radial and azimuthal velocity components. This results in the frequency equation for the inertial modes as expressed by eqn F.20, from the linearised equations where φ_i is the placeholder or $i'th$ root of the function J_1. Eqn F.20 resolves the theoretical eigenperiod τ_{th} normalised by the rotation period τ_{rot} for an inviscid fluid, as does the eigensolution arrived at in eqn F.15 by Greenspan, but despite this, the theoretical and experimental results are remarkably similar. A comparison of these values is presented in table F.1, where it can be seen that several modes with a single axial cell $n = 1$ were identified but had a varying amount of radial cells in the range $m = 1 - 4$, this is indicative of confined vortex flow with multiple flow reversals. The visual method for determining the inertial modes may not compare well to modern fluid measurements techniques, but it is undeniable that the correlation between the results shows that specific modal structures will occur at discrete forcing frequencies. Therefore, if an appropriate method can be found to perturb the flow within a vortex chamber such as a VIHRE configuration, then it may be possible to induce specific flow reversal patterns to enhance engine performance.

$$\tau_{th} = \frac{1}{2}\left[\left(\frac{\varphi_i}{n\pi}\right)^2 \left(\frac{R}{L}\right)^2 + 1\right]^{\frac{1}{2}} \tag{F.20}$$

In experiments performed by Görtler [129] and Oser [130,131] the coloured dye was replaced with small Aluminium flakes distributed homogeneously throughout the fluid, which only align themselves with the conical shear surfaces that indicate the path of the inertial waves. Additionally, the disc located along the chamber axis perturbed the adjacent fluid with infinitesimal oscillations, rather than the large oscillations required in Fultz's experiments to induce circulation of the coloured dye, although the disc is still located at the approximate axial division between vortex cells. When illuminated by a light sheet, the embedded shear surfaces can be identified visually from the scattered light from the seed particles, this can be used to infer the vortex cell structure and determine the inertial mode of the vortex. These shear surfaces can be considered to be internal boundary layers and are actually viscosity modified characteristic surfaces, typically found in hyperbolic or wave problems [45].

Mode (n, m, k)	$\dfrac{\text{radius}}{\text{height}}$	Eigenvalue	
		Theory	Experiment
(1, 1, 0)	2·0	1·708	1·754
	0·667	0·959	0·966
	0·4	0·623	0·617
(1, 2, 0)	2·0	1·487	1·351
	0·667	0·572	0·581
	0·286	0·254	0·253
(1, 3, 0)	2·0	1·051	1·052
	1·0	0·590	0·595
	0·4	0·245	0·243
(1, 4, 0)	0·5	0·234	0·234
(2, 1, 0)	2·0	1·913	1·923
	0·4	1·096	1·099
(2, 2, 0)	0·667	1·025	1·020
	0·4	0·674	0·676
(3, 1, 0)	1·0	1·852	1·887
	0·4	1·402	1·408

Table F.1: Theoretical and experimental eigenmodes for a cylindrical volume. [45]

(a) Half apex angle $\theta = 59°$ (theoretical $\theta = 56°$).

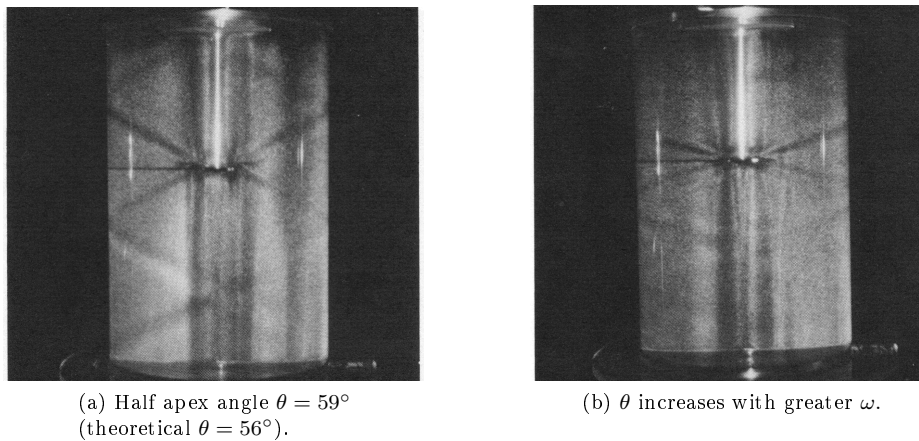(b) θ increases with greater ω.

Figure F.9: Shear surfaces indicated by alignment of Kalliroscope flakes $\left(\frac{\omega}{\Omega} = 1.75 \right)$. [45]

Example images acquired using this method are seen in fig F.9, where the shear surfaces are easily identified and additionally allow the half apex angle θ of the characteristic wave cones to measured, which can be used to calculate the eigenperiod τ of the oscillations using eqn F.21, where $\tau_{th} = \frac{\tau}{\tau_{rot}}$ and $\tau_{rot} = \frac{2\pi}{\Omega}$. In the linear, inviscid, time-dependent theory formulated by Greenspan [45] for a rotating cylindrical volume of fluid, the characteristic surfaces of the progressive wave cones are found to be described by eqn F.22 for real eigenvalues $|2| < \lambda$. The governing equation for this solution is hyperbolic and indicates that the shear surfaces described by eqn F.22 can only exist over a specific range of half apex angles, and therefore limits the range frequencies that will produce inertial waves. This has been confirmed experimentally by both Görtler [129] and Oser [130,131], who found that the half apex angle is dependent on the oscillation frequency of the disc and that inertial waves can only occur when $0 \leq \omega \leq 2\Omega$. This is due to the lower geometrical limit that results when $L \ll R$, so that $\tau_{th} = \frac{1}{2}$, and means $\frac{\tau}{\tau_{rot}} \geq \frac{1}{2}$, which is equivalent to $\frac{\omega}{\Omega} \leq 2$, requiring the disturbance frequency to be less than or equal to twice the precessional frequency of the fluid. When $\frac{\omega}{\Omega} > 2$ the equations that define the solution become elliptical and therefore the eigensolution in eqn F.22 is invalid, as $|2| > \lambda$ and the oscillation of the disc only results in agitation of the adjacent fluid. When $\omega = 0$ the shear surfaces are aligned with the axis of rotation $\theta = 0°$ and the flow is identical to that of Couette flow, but at the limiting case of $\omega = 2\Omega$ the shear surfaces are horizontal therefore inertial waves are not possible.

$$cos\theta = \frac{1}{2\tau_{th}} = \frac{\omega}{2\Omega} \tag{F.21}$$

$$\left(x^2 + y^2\right)^{\frac{1}{2}} \pm \lambda \left(4 - \lambda^2\right)^{-\frac{1}{2}} z = constant \tag{F.22}$$

In addition to cylindrical geometries, there is also some interest in the rotation of fluids within a cylindrical shell, as this can be considered to be an analogue of the Earth and provide an insight into planetary core dynamics. Aldridge et al [132] investigated inertial oscillations within such a cylindrical shell which rotates about a vertical axis, and by employing a similar method to that of Görtler [129] and Oser [130, 131] were able to observe a range of inertial modes when the fluid was perturbed by oscillations of consistent magnitude. Seeding the flow with metallic flakes can indicate the structure of the embedded shear surfaces, but consideration must be given to the time response characteristics of the flow and seed particles. Experiments performed by Noir et al [46] were successful in applying this technique to rotating fluid filled spherical shells as depicted in fig F.10, but also commented that when the characteristic response time of the seed particles was greater than the period of the inertial oscillation, then no shear surfaces were observed. This is because the particles do not have sufficient time to align themselves with the shear surfaces, so care must be taken to ensure that the inverse shear rate used to estimate the time response is less than that of the predicted eigenperiods of the oscillations provided by analytical solutions.
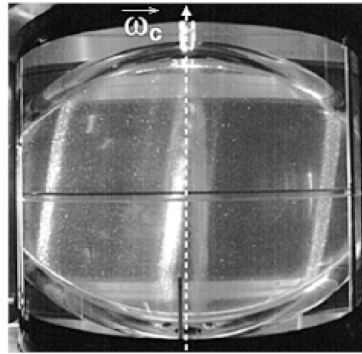

Figure F.10: Shear surfaces in spherical volume at resonance. [46]

In fig F.11 several of the circulation patterns of the low order modes are included to indicate how an entirely different geometry still tends to progressively subdivide into an array of vortex cells, where the individual vortices are counter rotating. The cylindrical geometry described previously Greenspan [45] also provides an analysis of rotating spherical geometries and obtains an eigensolution to the problem, which yields a range of eigenvalues that correlate to a range of inertial modes. These eigenmodes are presented in table F.2 along side their respective theoretical and experimental eigenvalues and it is clear that there is an excellent correlation between these values, as seen in the data for the cylindrical configurations in table F.1. In addition to this, Alridge et al [132] also measured the static pressure at the centre of the sphere, which results in fig F.12, this indicates that the inertial modes are associated with distinct peaks in the pressure amplitude. This shows that as resonance is achieved, oscillations in the local static pressure increase significantly in amplitude for the symmetrical inertial modes $k = 0$, and fig F.12 resembles a power spectral density (PSD) plot of a signal with several resonant peaks. What is interesting about fig F.12 is that as the magnitude of the inverse eigenvalue is increased, which in this case is the oscillation frequency, it is possible to perturb higher order modes as is seen in cylindrical geometries. The inertial modes only seem to occur at the peaks of the pressure amplitude and may provide a mechanism for invoking inertial modes in lieu of a physical perturbation device. If so, it may be possible to perturb the vortex core within a confined vortex with pressure pulses tuned to the resonant frequencies associated with specific inertial modes, and therefore invoke prescribed flow reversal modes.
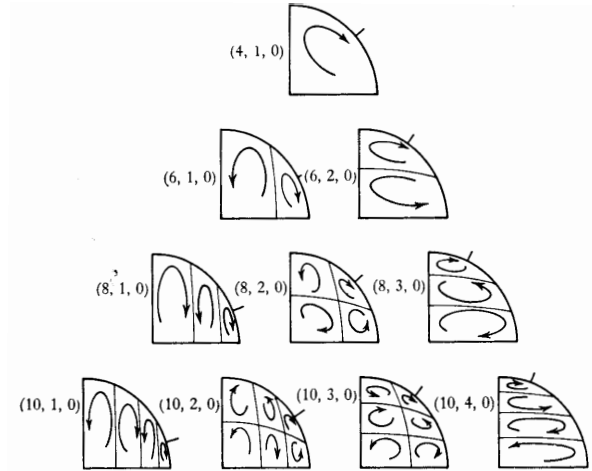
Figure F.11: Inertial modes possible in a spherical volume. [46]

Mode identification (n, m, k)	Eigenvalue λ_{nmk}	Decay Factor $\delta_{nmk,1}$	Experimental values	
			λ_{nmk}	$\mathscr{R}e\, \delta_{nmk,1}$
(2, 1, 1)	1·0	$-2\cdot62+0\cdot259i$	1·0	$-2\cdot82$
(4, 1, 0)	1·309	$-3\cdot38+0\cdot434i$	1·302	$-3\cdot88$
(4, 1, 1)	0·820	$-3\cdot87+0\cdot315i$	—	—
(4, 2, 1)	1·708	$-2\cdot64+0\cdot504i$	—	—
(4, 3, 1)	0·612	$-3\cdot95+0\cdot180i$	—	—
(6, 1, 0)	0·938	$-4\cdot64+0\cdot329i$	0·935	$-5\cdot17$
(6, 2, 0)	1·660	$-3\cdot50+0\cdot568i$	—	—
(8, 1, 0)	0·726	$-5\cdot62+0\cdot266i$	0·724	$-6\cdot32$
(8, 2, 0)	1·354	$-4\cdot87+0\cdot487i$	—	—
(8, 3, 0)	1·800	$-3\cdot53+0\cdot632i$	—	—

Table F.2: Theoretical and experimental eigenmodes for a spherical volume. [45]

Figure F.12: Core pressure amplitude plotted against inverse eigenvalue. [45]

250

Advances in computational methods with regards to fluid dynamics, have now made it possible to investigate the phenomenon of in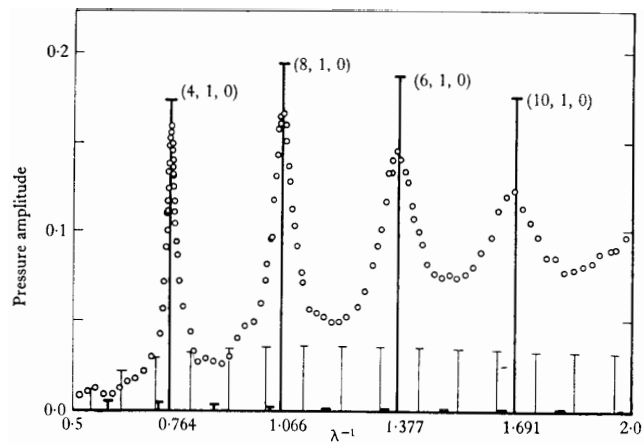ertial waves numerically, and characterise the necessary parameters to invoke specific modal structures for a range of chamber geometries. Studies by Batchelor et al [47] have focused on replicating the experiments conducted by Fultz through application of the spectral element method (SEM) to solve the incompressible Navier-Stokes equations for axisymmetric geometries. Specifically, a quadrilateral Galerkin spectral element direct numerical simulation (DNS) research code named Semtex [133] was employed, which enables high spatial resolution through high order nodal element shape functions and fast convergence rates, making DNS solutions possible. Two chamber geometries with aspect ratios of $\frac{L}{D} = 0.25$ and $\frac{L}{D} = 1.25$ were investigated whose radial velocity contour plots and associated streamline lines are included in fig F.13 and fig F.14 respectively. All of the velocity fields calculated are axisymmetric, in accordance with the formulation of the solver so that $k = 0$, while it was possible to resolve a range of low order radial and axial cells, which are depicted in the meridional plane.

In fig F.13 each chamber configuration contains a single axial cell $n = 1$, while the number of radial cells range between $m = 1 - 4$, which indicates the presence of several mantles that span the length of the chamber, in addition to multiple flow reversals where the individual vortices are counter rotational with respect to the meridional plane. In fig F.14 it can be seen that it is possible to induce vortex cell structures with a single axial cell, but multiple radial cells in chamber geometries with greater aspect ratios, which are more comparable to those of current VIHRE configurations. Fig F.14b is representative of the single mantle structure found in current vortex devices, while fig F.14c exhibits two mantles and is representative of the triple vortex flow shown previously in the corrected PIV results that is associated with chamber configurations with head injectors. Regarding the modal structures with a single axial cell, it was found that the number of radial cells increased as the eigenperiod of the oscillation was increased, as depicted by the plot in fig F.15, which defines the conditions for which the inertial modes shown in fig F.13 and fig F.14 will occur. To assess resonance, the kinetic energy of the flow was integrated over the entire numerical domain for both instantaneous and time average values and compared for a range of eigenperiods. It was assumed that maximums in the kinetic energy profile would occur when the fluid was in resonance, as the reinforcement of the inertial wave structure would produce a noticeable increase in the oscillation of the fluid. The effects of viscosity dampened the oscillations and prevented distinct peaks occurring, unlike what would be observed for an ideal fluid, as described by the analytical solutions of Fultz [127] and Greenspan [45]. Despite this, it was still possible to gain an agreeable correlation between the maximums of kinetic energy and the respective eigenperiods associated with the inertial modes.
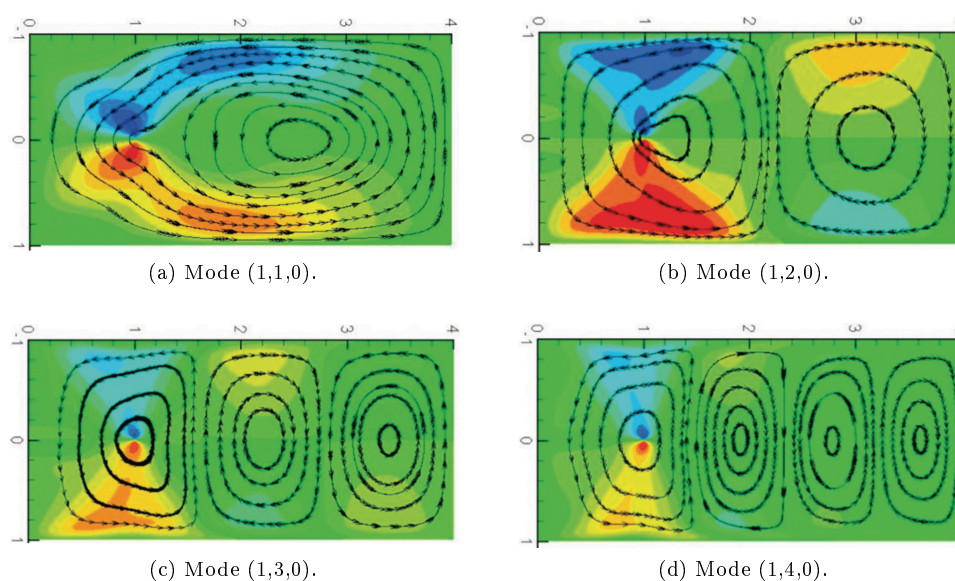

(a) Mode (1,1,0).

(b) Mode (1,2,0).

(c) Mode (1,3,0).

(d) Mode (1,4,0).

Figure F.13: Inertial modes calculated using SEMTEX for a cylinder with $\frac{L}{D} = 0.25$. [47]

(a) Mode (1,1,0).   (b) Mode (1,2,0).   (c) Mode (1,3,0).   (d) Mode (3,1,0).
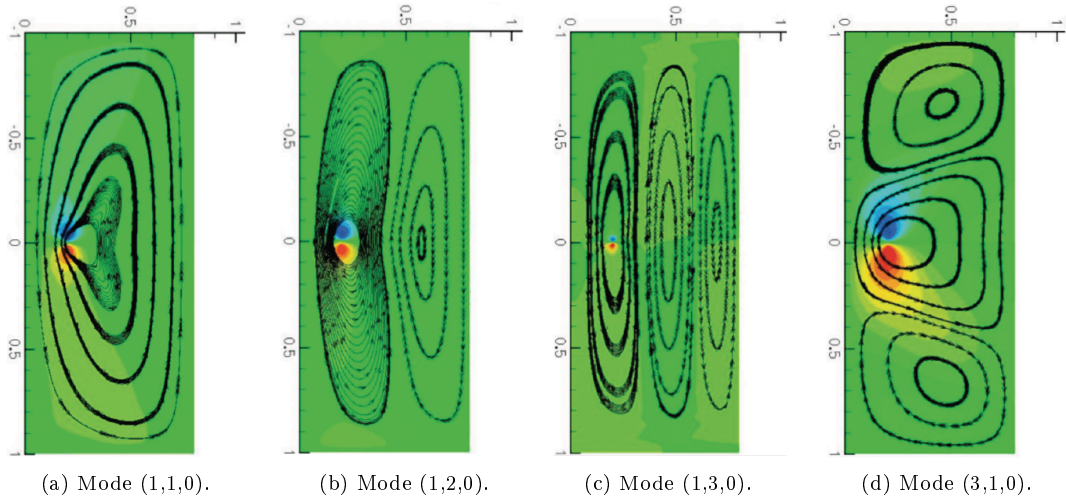
Figure F.14: Inertial modes calculated using SEMTEX for a cylinder with $\frac{L}{D} = 1.25$. [47]
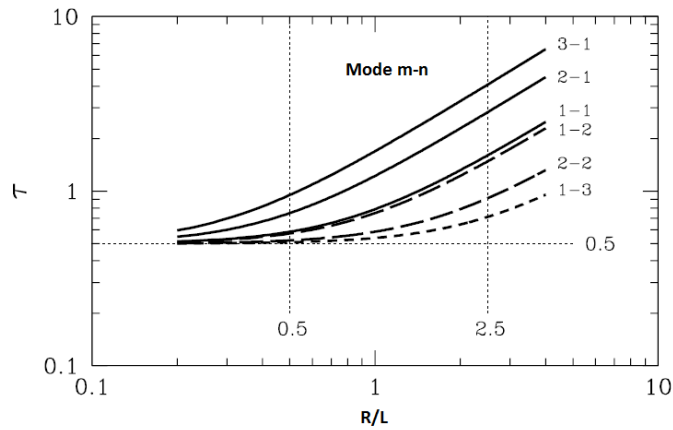

Figure F.15: Geometrical chamber parameters plotted against eigenperiod. [47]

In a study by D'Elia et al [48], a streamline upwind Petrov Galerkin and pressure stabilised Petrov Galerkin (SUPG-PSPG) based finite element method (FEM) was utilised, in order to replicate the experiments performed by Aldridge [132] investigating inertial modes in rotating spherical shells containing fluid. The numerical domain was axisymmetric, while the fluid was viscous and incompressible, with the flow being laminar, this resulted in several inertial modes being identified, as seen in fig F.16. The magnitude of the pressure coefficient was used to assess resonance with regards to the frequency ratio $\frac{\omega}{\Omega}$, akin to the pressure amplitude versus the reciprocal of the eigenvalue seen in fig F.12. The pressure coefficient is systematically overestimated in the numerical study, but it is clear in fig F.16 that there is an excellent correlation between the pressure coefficient peaks that occur when resonance is achieved, and highlights to effectiveness of this approach in identifying inertial modes both experimentally and numerically.

The spectral element has also been implemented by Duguet et al [49], who investigated instabilities in rotating cylindrical volumes of fluid, where the spectral element code was able to resolve the shear layers embedded within the flow. Example plots of the velocity vectors in the meridional plane where the azimuthal velocity component has been omitted are presented in fig F.17a, in addition to the inertial wave cone structure in fig F.17b, where the thick black lines that define the vortex cell structure correspond with the loci of zero axial velocity in fig F.17a. The dashed lines in fig F.17b represent wave reflections whose paths are either parallel or orthogonal to the initial wave cones, as
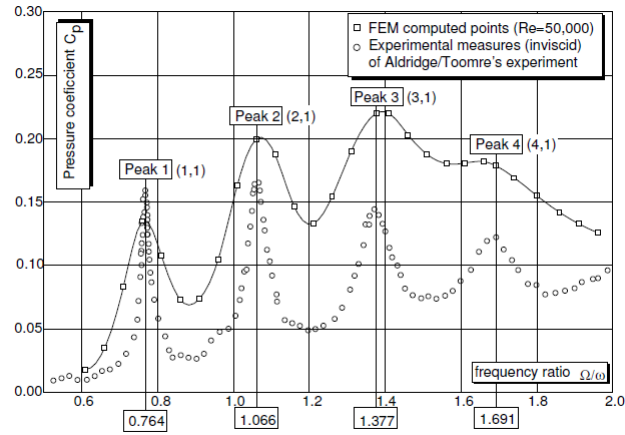
Figure F.16: Pressure coefficient C_p at centre of sphere as a function of frequency ratio $\frac{\Omega}{\omega}$. [48]

the boundaries of the cylindrical geometry are horizontal and vertical, which cause the angles of in-
cidence and reflection to be identical. It was also found, that if the amplitude of the disturbance was
small, then the inertial wave structures mentioned previously will occur and the system is stable, but
if the amplitude of the disturbance is large, then this will lead to instability. When the perturbation
frequency produces resonance in conjunction with that of a lower order inertial mode, then this can
lead to subharmonic instability and result in mode-triad resonance, which deviates from the linear
behaviour exhibited by the flow for small amplitude disturbances. This is when several modes can
occur simultaneously, as the increased amplitude of the disturbance allows harmonics of the initial
inertial mode to be excited, which then interact with each other, causing instability and resulting in
non-linear behaviour. These parametric instabilities provide mechanisms to allow for quasiperiodic
behaviour in the flow, where the individual vortices within the vortex cells will alter their rotational
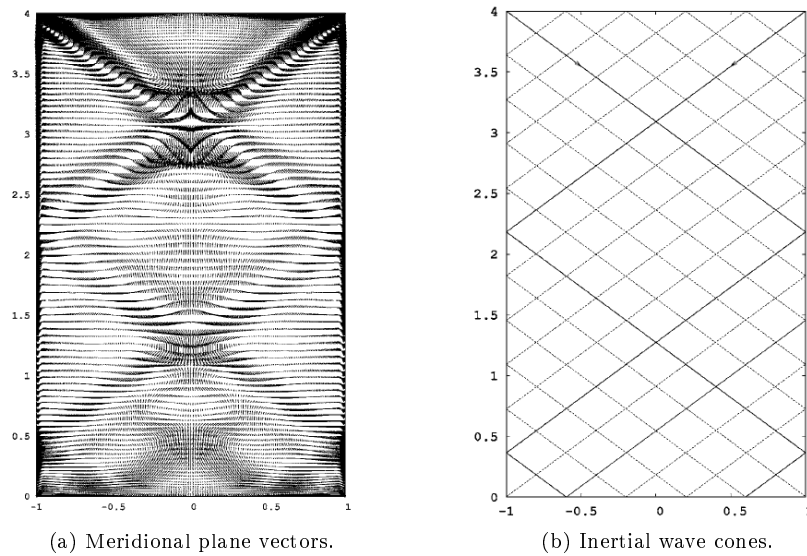direction over a period of time.

(a) Meridional plane vectors.

(b) Inertial wave cones.

Figure F.17: Oscillating jets calculated by spectral Galerkin method. [49]
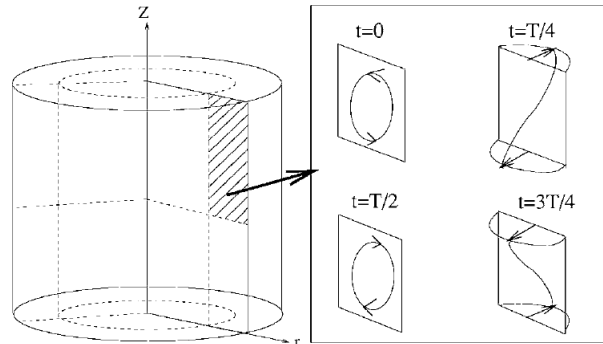
253

Figure F.18: Triadic response of a single vortex cell. [50]

An example of quasiperiodic behaviour is shown in fig F.18, where mode-triad resonance can be seen when the perturbation resonant frequencies become coupled with those for other inertial modes, so that the flow is continuously but periodically evolving, as at it cycles through various configurations associated with each individual inertial mode. There is again an excellent agreement between analytical theory and the numerical solutions with regards to linear inertial wave behaviour, despite the addition of viscosity and the non-linear behaviour described by Duguet et al, that may not be able to be explained analytically. This shows that the spectral element method provides a valuable tool in predicting non-linear behaviour and determining the response of a rotating fluid system subject to various disturbances, that may be difficult to discern both analytically and experimentally. It also highlights the necessity of time resolved techniques when investigating such phenomenon experimentally, in order to determine whether the flow exhibits steady state or periodic behaviour.

Spectral element methods are suitable for investigating inertial wave problems as they provide very high spatial resolution, that enables DNS solutions to be obtained which capture all of the spectral characteristics of the flow, unlike standard transient finite volume methods which are limited. This is due to the time step, which represents the reciprocal of the maximum characteristic frequency that can be resolved, so high frequency phenomenon such as turbulence can not normally be directly resolved because of the prohibitively low time step required. This combined with the requirement for very high grid resolution, means that DNS solutions obtained using the finite volume method are generally only solved for relatively simple 2D problems, which still require a considerable amount of computational resources and wall time to obtain. It is possible to obtain solutions for inertial wave problems using an inherently transient method such as detached eddy simulation (DES), large eddy simulation (LES) or DNS, but these methods progressively require increased amounts of computational resources. These are not always viable options when the influence of a large amount of design criteria need to be assessed, as is the case with this investigation, especially when complex sub-grid turbulence and multiphase physical models are required. This issue is solved through use of RANS models, even with a transient formulation the spectral characteristics of the flow are not resolved directly, as the turbulence models predict the average conditions that characterise the flow, rather than the fluctuating properties of the flow. Spectral element solvers are specifically designed for fluid dynamics problems, but they are still in their infancy and are currently unable to account for the physics which occur in the majority of fluid dynamics problems, although they have been shown to provide valuable insight into the behaviour of inertial waves in rotating fluids. However, finite volume methods in combination with RANS turbulence modelling should not be completely disregarded, as it avoids the large computational resource overheads associated with more accurate methods, but is still capable of adequately describing the characteristics of the flow. Problems involving inertial waves are inherently transient and can require higher order methods to characterise the spectral characteristics of the flow, although the main focus of this investigation is to resolve the embedded mantle structure. This is invariant with time and could be effectively resolved using a steady state formulation if convergence issues were not an issue, and as the definition of the inertial

(a) Small perturbation frequency $\left(\frac{\omega}{2\Omega} = 0.24\right)$. (b) Large perturbation frequency $\left(\frac{\omega}{2\Omega} = 0.74\right)$.
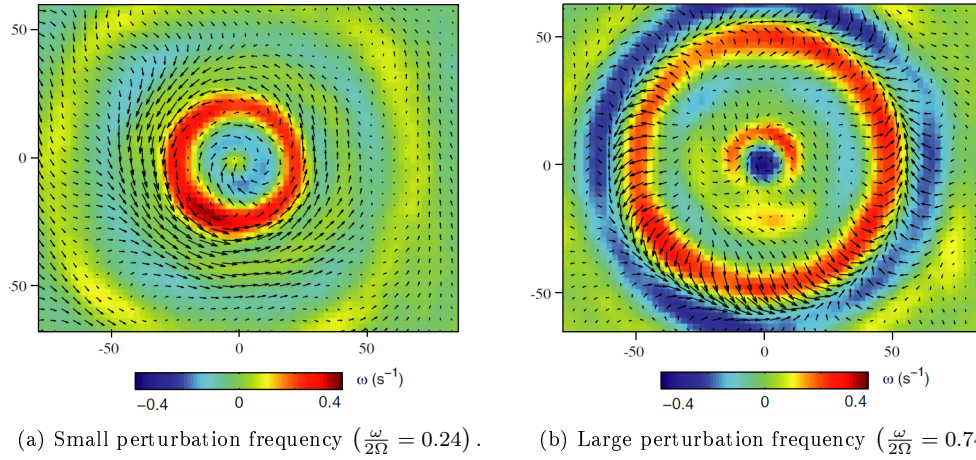
Figure F.19: PIV axial vorticity contours and velocity vectors of perturbed cylindrical volume. [51]

modes is directly linked to the mantle structure, then they must be able to be resolved by RANS methods as seen in the results show. Despite the irrelevance of the time resolved PIV technique employed during this investigation, it has allowed the temporal behaviour of the mantle to be observed and categorically confirms that the mantle does not vary with respect to time, as indicated during calculation of the CFD results. There is insufficient grid resolution to adequately resolve the individual shear layers in the flow, and in turn determine the exact form of the vortex cells and resolve the specific inertial modes, but the mantle structure does provide more useful information relative to VIHRE design. By understanding how the chamber geometry and flow conditions affects the structure of the vortex, this can be used to manipulate the mantle structure and ensure specific flow reversal configurations that are beneficial to VIHRE applications.

Although there are a relatively small amount of experimental studies focused on investigation of inertial waves due to the inherent difficulties associated with their identification, certain PIV techniques have proved useful in characterising such types of flow. As inertial waves arise in fluids that exhibit solid body rotation, it is necessary to observe the flow in the rotating non-inertial frame of reference, which means that experimentally any imaging equipment needs to be setup so that it is co-rotating. In doing this the PIV measurements obtained are phase locked, as the imaging equipment and the fluid rotate at the same angular velocity, which allows for the time resolved and average behaviour to be observed, irrespective of fluid rotation. Such an example, is the work of Messio et al [134] who replicated the experimental setup of Fultz, but with the aid of modern flow analysis techniques were able to resolve the velocity components in the azimuthal plane of the chamber, in addition to the axial vorticity. Examples of instantaneous axial vorticity contour maps and their associated velocity vectors are presented in figs F.19a and F.19b, which relate to comparatively small and large perturbation frequencies respectively. It can be seen that regions of intense vorticity are concentrated into annuli of opposing signs, where the locus of zero axial vorticity between these regions denotes the intersection of the conical wave packet with the observation plane. As expected, the radius of this intersection increases as the perturbation frequency is increased, as the cone half angle decreases when the conical wave packets tend towards the azimuthal plane. In fig F.19a, the lighter rings that appear near the periphery of the chamber are due to wave reflections at the boundary, and like the more pronounced annuli, correlate well with the predicted radii based on chamber geometry and the perturbation frequency ratio. Moisy et al [51] investigated inertial waves within a rotating rectangular volume of fluid, and applied PIV techniques to observe the dispersion relationships that result from the vertical oscillations of a submerged cylindrical bar that produces planar rather than conical waves. As with the study of Messio et al [134], there was good agreement between the resultant wave structures and the theoretical structures predicted by linear viscous theory, but it also highlighted the problems associated with obtaining useful results due to the small amplitudes of the disturbances within the flow. In order to resolve these inertial waves, a

highly stable experimental rig was required that was isolated from other possible frequency sources, and a high SNR was also vital as the small magnitude of the inertial waves can easily be obscured by background noise in the images obtained. Signal noise can be effectively attenuated through phase averaging over a large number of oscillations, but it still remains a difficult task to capture the behaviour of inertial waves via PIV techniques, even when they are the primary characteristic of interest within a simple flow configuration. Given that these studies were concerned with fluids undergoing solid body rotation, it is unlikely that these experimental methods would be applicable to confined vortex devices, where both forced and free vortices are present with significantly increased amount of azimuthal shear in addition to boundary layer effects. Not only would it be difficult to setup a corotating experimental rig, but the turbulent flow within such a vortex chamber would make it incredibly difficult to obtain PIV images with a sufficient SNR to deduce anything useful about the structure of the flow. Therefore, as a result of this it is advisable to characterise the mantle structure in VIHRE configurations purely through resolution of the axial velocity component and effectively ignore the underlying wave mechanics, in order to obtain results that are specifically relevant to increasing engine performance. It is necessary to understand the fundamental mechanisms which result in mantle structures, but the relationship between chamber geometry and flow properties with regards to the internal wave arrangements can instead be more effectively investigated using spectral numerical methods.

F.5 Shear layer instability

Moisy et al [51] also conducted studies into the flow between two rotating discs and the resulting characteristics that arise from shear layer instabilities, revealing embedded polygonal structures reminiscent of mode shapes. Gauthier et al [135] found that as the relative angular velocity between the discs is increased the initially homogenous flow undergoes bifurcation and a propagating circular wavelike structure appears, which can be seen in the central region of the flow in fig F.20, this a similar visualisation method to that of Görtler [129] and Oser [130, 131] . As the relative angular velocity is increased further spiral arms begin to develop, which can be seen in the outer regions of the fluid in fig F.20, where the spiral arms are referred to as positive due to the positive angle of the arms with respect to the azimuthal velocity of the fluid. This is due to the increased local shear between the surface of the disc and the fluid, where the observed patterns manifest as a result of boundary layer instabilities, or more specifically a type of instability akin to that of Kelvin-Helmoltz. Several chambers with various aspect ratios were investigated and it was found that the circular wavelike vortices that propagate towards the axis of the chamber occur above a threshold angular velocity and can occur both naturally or by small modulations, where the forcing amplitude is the angular velocity. As with the studies of inertial waves in cylindrical geometries, it is possible to invoke mode shapes through modulation of the amplitude of the forcing mechanism, which produces these embedded structures.
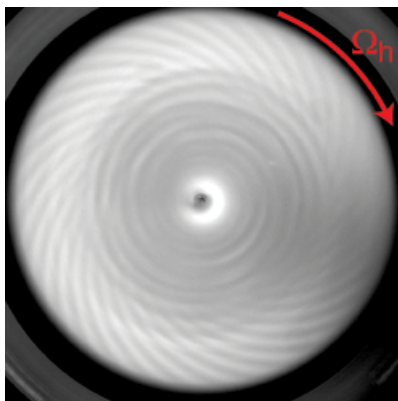

Figure F.20: Positive spiral and circular wave boundary layer instabilities. [51]

(a) Polygonal vortices $N = 3$.

(b) Polygonal vortices $N = 4$.

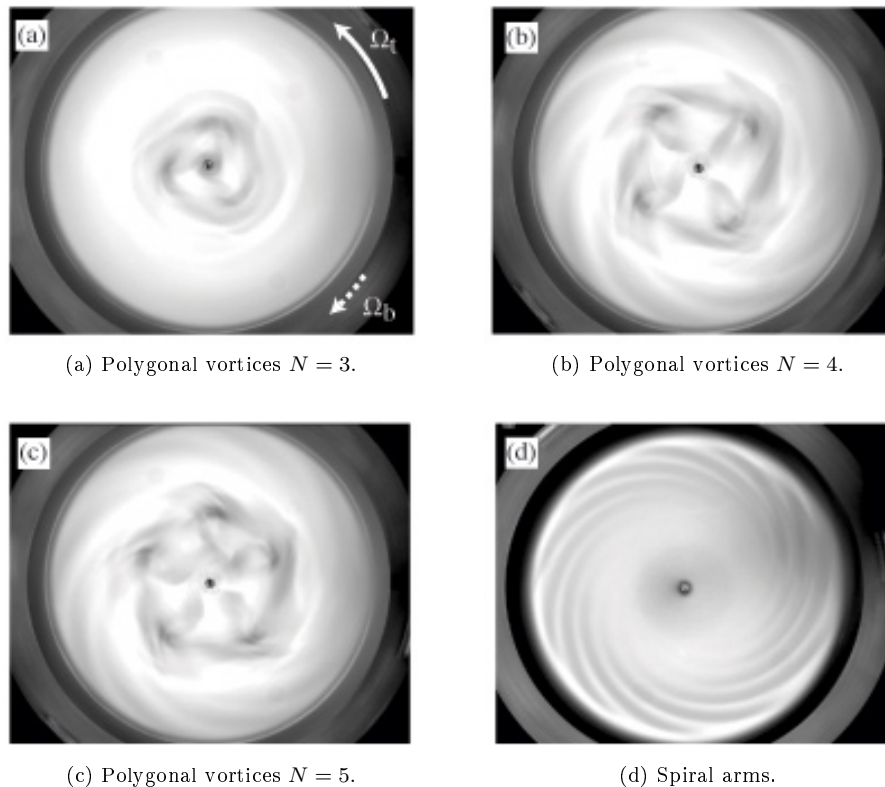(c) Polygonal vortices $N = 5$.

(d) Spiral arms.

Figure F.21: Kalliroscope visualisations of shear layer instabilities. [51]

Moisy et al [51] similarly investigated the effects of the chamber aspect ratio upon the flow, where the relative variation in the angular velocity was produced by both co-rotating and counter rotating discs. In fig F.21 the effects of increasing the relative angular velocity between the rotating discs can be seen, where in fig F.21a there is evidence of polygonal vortices alone. Through further increasing the angular velocity negative spiral arms begin to develop in the outer regions of the chamber and become more prominent until just the negative spiral arms exist, as seen in fig F.21d. It is immediately clear that as the relative angular velocity is increased additional vortices are formed within the vortex core as the number of polygonal nodes increases, and therefore these embedded structures must be directly influenced by the magnitude of shear stress in the boundary layers. A simple visualisation technique is adding coloured dye to a fluid rotating at a different angular velocity to the chamber, as seen in fig F.22, which was obtained by Barbosa et al [136]. Similarly work by Hunt et al [137] clearly shows the existence of vortices, similar to mode shapes observed throughout the results of this investigation. This quadrilateral structure rotates with the fluid and it is possible to replicate the hexagonal structure observed at the south pole of Saturn, as seen previously in fig 5.35, through increasing the relative angular velocity between the chamber and the fluid.

Hide et al [137] found that the vertical shear layers aligned with the chamber axis and those attached to the end walls of the chamber were susceptible to instabilities when the angular frequency of the rotating disc exceeds that of the fluid, but this also occurs when the angular frequency is less than that of the fluid. As with the findings of Gauthier et al [135], a critical angular velocity or equivalent Rossby number needs to be exceeded so that instability will develop, this value is also found to be dependent upon the aspect ratio of the chamber. For chamber aspect ratios $\frac{L}{D} < 0.036$, it was found that only spiral arms existed, while for chambers with aspect ratios in the range $0.083 < \frac{L}{D} < 0.25$ only polygonal vortices were observed, although it is likely that polygonal vortices can also be observed for larger chamber aspect ratios that were not investigated experimentally. The polygonal vortices are purported to arise from instabilities in the vertical shear layer, while the spiral arms are caused by the interaction of the shear layer and the Ekman layers that exist at the axial

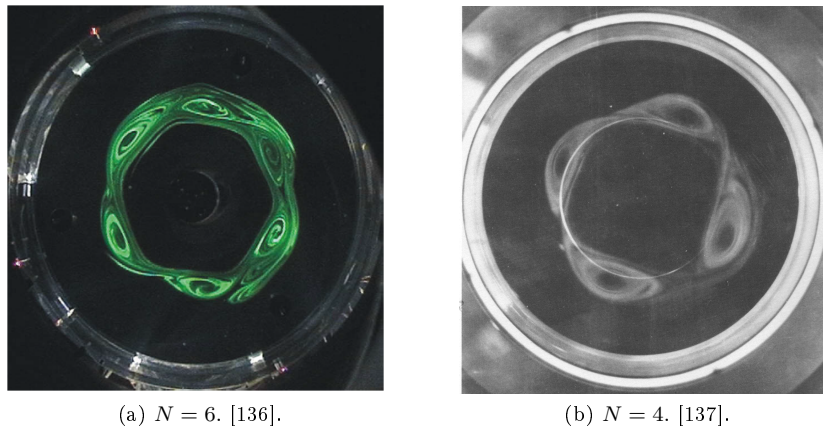(a) $N = 6$. [136].   (b) $N = 4$. [137].

Figure F.22: Polygonal vortices produced by shear instability when $\Omega_d > \Omega_{fl}$.

boundaries of the chamber. Ekman layers are responsible for fluid transport in rotating fluids as they rotate with the fluid and during spin up, with regards to confined vortices, where the angular velocity of the fluid in non-homogenous. The Ekman layers transport fluid from non rotational regions of fluid into rotational regions until the bulk fluid is subject to solid body rotation and introduce additional shear into the flow, in combination with the boundary layers. Ekman transport can also be referred to as Ekman pumping, where the fluid is transported in a radial direction at the axial boundaries of a chamber, and can result in internal convective currents within the fluid as radial pumping provides a mechanism for creating tertiary flow patterns in rotating fluids. A possible explanation for the polygonal and spiral arm structures observed is that a variable pumping effect produced by Ekman transport is providing a forcing frequency, which invokes specific characteristics in the flow as occurs for inertial waves. The modulation effects of the relative angular velocity may actually be the result of variation in the pumping characteristics of the Ekman layers.

In a subsequent study Moisy et al [51] obtained PIV measurements of the flow in the azimuthal plane of the chamber to gain further insight into the effects of shear layer instabilities caused by rotating discs. Presented in fig F.23 are PIV measurements taken from the midplane of the chamber, where the contour map depicts the axial vorticity and velocity vectors for various rotation rates. As the relative angular velocity between the discs is decreased the regions of intense annular shear deviate from a circular to polygonal form, where further decrease in the rotation rate results in a reduction in the sides of the polygon. These annular shear layers are subject to Kelvin-Helmholtz type instabilities, as was also discovered by Hide et al [137], where the instability causes the axisymmetry of the flow to break resulting in equilateral polygonal structures. As explained previously, it is possible to perturb a columnar vortex so that the shape of the vortex core deforms and becomes polygonal in form, as is seen in fig F.23, where the shear layer instability perturbs the confined vortex and results in vortices with azimuthal wavenumbers $m = 0, 5, 4$ and 3 respectively. Numerical results provided by Moisy et al also corroborate the possibility of polygonal structures, but also indicate that while a vortex will retain the same azimuthal wave number through out the structure of the vortex in low aspect ratio chambers, it does exhibit some variation in the structure with respect to axial location. In fig F.24 are examples of cross section through a vortex, with $m = 5$ depicting the magnitude of axial vorticity and axial velocity respectively, this also highlights that the local and maxima and minima correlate well and indicate that the polygonal structures are in phase, although there is evidence of phase shift with regards to axial position. Regarding the polygonal structures observed throughout the results presented in this investigation, both the numerical and experimental results agree that several flow parameters including the azimuthal velocity, radial velocity and axial vorticity all exhibit periodicity, but more specifically they repeatedly indicate the presence of mode shapes with $m = 4$. It is reassuring to find evidence of the relationship between shear layer instability and polygonal structures in the regions of rotating fluid that are in close proximity to an axial boundary as seen in the results obtained in this study.
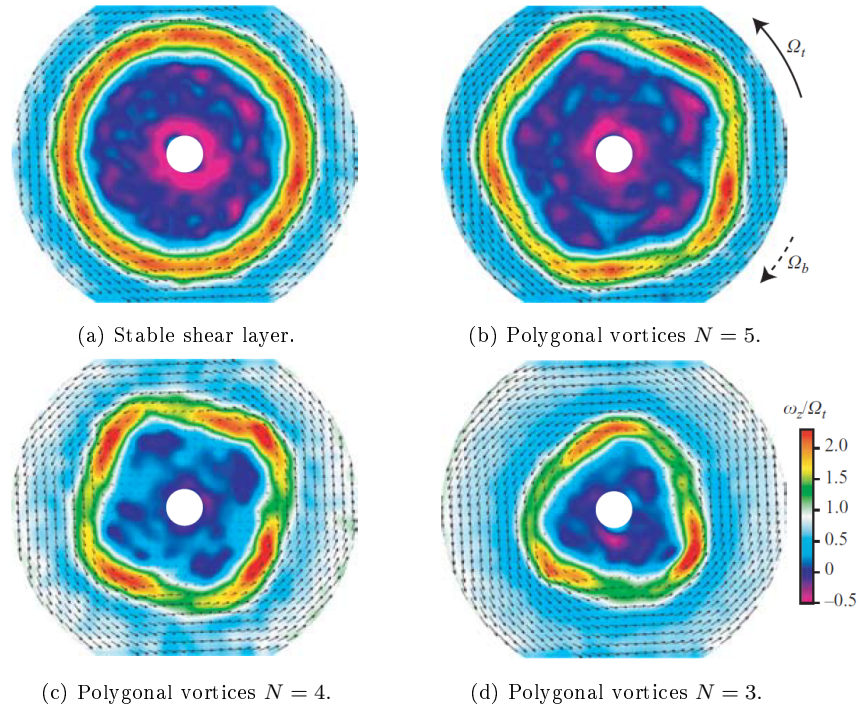
(a) Stable shear layer.

(b) Polygonal vortices $N = 5$.

(c) Polygonal vortices $N = 4$.

(d) Polygonal vortices $N = 3$.

Figure F.23: PIV axial vorticity contours indicating shear layer instability as Ω_d increases. [51]

Fig F.24b shows that the axial velocity distribution in such regions rotating of fluid are susceptible to symmetry breaking and can result in polygonal structures, which inherently will be reflected in the structure of the mantle as well. It therefore provides a mechanism in addition to the presence of inertial waves that influences the structure of the mantle, and more specifically explains why evidence of periodicity in the flow is most pronounced at the axial boundaries of the chamber. Experimental evidence is only available for the region of fluid in close proximity to the head wall of the vortex chamber, which indicates the influence of shear layer instability, but the numerical data is available throughout the whole chamber and allows the periodic structure to be analysed with respect to axial position. As noted previously, the 3D mantle structures all exhibit periodicity to a varying extent, but this is most prominent in the fluid regions adjacent to the head and base boundaries of the chamber. The midplane mantle structure essentially remains axisymmetric and the mantle locations correlate well with those predicted by cylindrical harmonics for a flow with an azimuth wavenumber of $m = 0$. The magnitude of the absolute velocity is considerably less at the periphery of the chamber than at the boundary of the vortex core within the central region of the flow, and as a result the shear stress at the radial boundaries of the chamber is insufficient to cause symmetry breaking. However, the intense region of core flow is in contact with physical boundaries at the head and base of the chamber, which results in considerable shear in addition to the presence of Ekman layers, which combined promote shear layer instability and result in the observed embedded polygonal structures. The chamber geometry influences the structure of the mantle with regards to inertial waves and explains why periodicity is not observed in the central regions of the vortex chamber, as the local structure is only affected by resonance and will take the form of either the fundamental mode or a higher order harmonic of this, so therefore retains a cylindrical form. The mantle structure in close proximity to the axial boundaries of the chamber will be affected by both inertial waves and shear layer instabilities, and produce much more complex forms which are dependent on both chamber geometry and the local properties of the flow. The effect of the increased local shear at the head of the chamber was directly observed through the shape of the PVC boundary, which was seen to exhibit a range of azimuthal wavenumbers with respect to the chamber contraction ratio. An indirect effect of the contraction ratio was that reduction in the outlet radius produced a more intense vortex with increased greater azimuthal velocities, which in turn resulted in

259
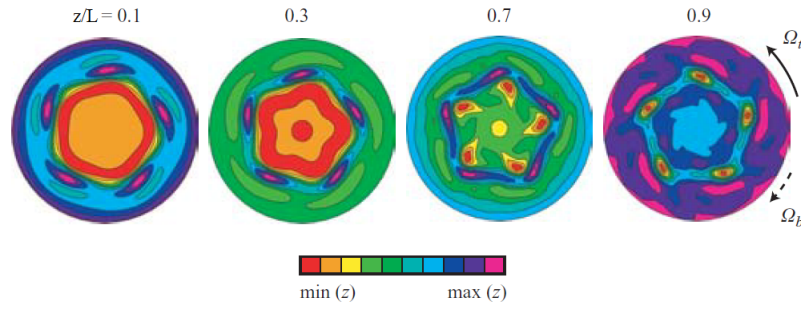
(a) Axial vorticity contours at various axial positions $\frac{z}{L}$.
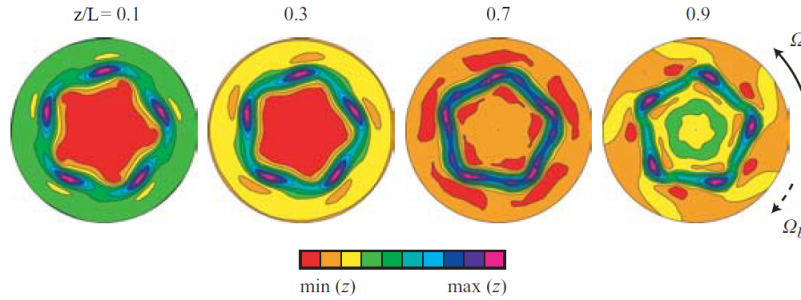
(b) Axial velocity contours at various axial positions $\frac{z}{L}$.

Figure F.24: Contour maps of the polygonal vortex structure at various axial positions. [51]

greater localised flow gradients as indicated by the increased axial vorticity, which also indicates an increased amount of local shear. The other investigations into the effects of chamber geometry did exhibit signs of periodicity in the structure of the PVC boundary, but they were not as prominent as those seen in the contraction ratio study, where the variation in chamber geometry produced the greatest range of azimuthal velocities across the whole parametric range. The polygonal structures observed in close proximity to the axial boundaries of the chamber are the caused by shear layer instability, but it can be argued that chamber geometry is also responsible for these structure as it is for inertial waves, because in this study it was found to be the most important parameter with regards to manipulating the properties of the confined vortex.

An analytical treatment provided by Crowdy [52] of planar vortices based upon the Euler equations focused on the conditions which affect N-vortex arrays, otherwise known as multipolar vortices, and result in similar polygonal structures being observed. These structures were found to be primarily influenced by the out of plane or axial vorticity, where the number of vortices N increases accordingly with an increase in the magnitude of the axial vorticity. In fig F.25 streamlines and isovorticity contours for several vortex arrays are seen which represent vortices with $N = 4$, 5 and 10 poles respectively, where the vorticity of the decapole configuration is approximately ten times greater than that of the quadrupole configuration. The decapole configuration seen in fig F.25c differs from the quadrupole and pentapole configurations as it does not contain a singular central vortex located at the origin. Initially only a single vortex is present, but as the axial vorticity is increased, further satellite vortices occur and establish a periodic symmetrical structure about the central vortex. The limit of the solution is when vorticity tends towards infinity, at which point the increasing number of satellite vortices effectively form a single vortex and the problem reduces to a point vortex. What is immediately clear, is that the pentapole vortex array is remarkably similar to both the mantle structures seen in the numerical results and the simulations of a vibrating circular membrane, because all are examples of cylindrical harmonics. Considering the correlation between the axial vorticity and axial velocity highlighted in fig F.24, it can be assumed that the polygonal vortex arrays produced by Crowdy [52,53] are also applicable to the structure of the mantle. There-
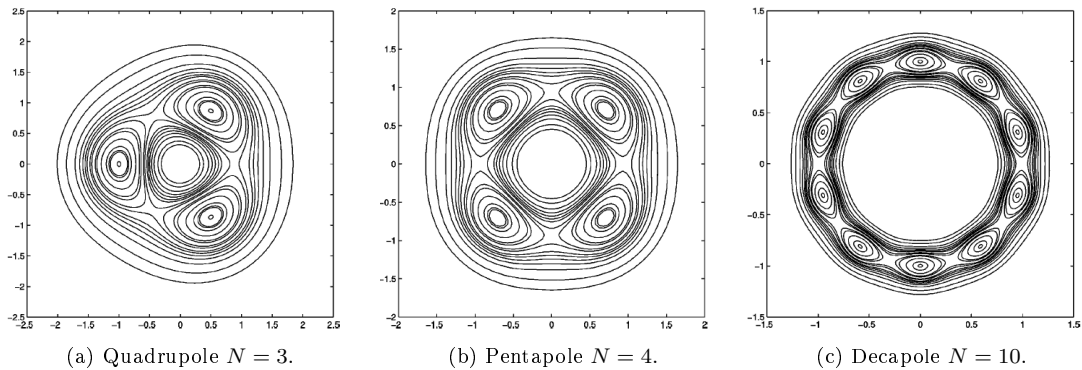
(a) Quadrupole $N = 3$.

(b) Pentapole $N = 4$.

(c) Decapole $N = 10$.

Figure F.25: Streamlines and isovorticity contours of polygonal $N-$vortex arrays. [52]

fore, the increased vorticity responsible for producing large vortex arrays would also similarly affect the mantle and provides a method for predicting the structure of the mantle in close proximity to the axial boundaries of the chamber. The pentapole vortex array also represents the superposition of inertial waves for two separate inertial modes, each associated with a distinct perturbation frequency, which means therefore that other vortex arrays can similarly be produced by superposition of various inertial modes. It must be noted that the vortex arrays presented in fig F.25 are produced by enforcing parametric conditions with regards to axial vorticity, although manipulation of other parameters can result in more complex vortex arrays, such as those seen in fig F.26. In these configurations there is no point vortex around which satellite vortices form and the central region is defined by a boundary referred to as a limiting patch or $V-$state, where the geometry of this boundary is reflected by the number of vortices in the array.

When analysing the high speed images obtained for the current study, it was found that similar shapes were found to define the boundary of the PVC and are inherently linked with the spectral characteristics of the flow, as they indicate both the azimuth wave number and provide evidence of polygonal structures similar to those observed in the PIV results. It is important to clarify that all the studies referred to that elucidate these polygonal structures found that these structures were rotating, where the poles of the satellite vortices exhibit the same angular velocity as the bulk of the fluid subject to solid body rotation. This is considered to be the primary motion of the flow in the inertial frame of reference, while the vortical motion about the satellite vortex poles are considered to be a tertiary motion, although they constitute the primary motion in the non-inertial rotating frame of reference. However, the numerical results obtained in the current study found that the polygonal structures observed for all the velocity components and axial vorticity are static and do not exhibit the rotational behaviour observed in other studies. This is likely due to several factors, such as the different boundary conditions imposed in these experiments, where a rotating chamber was employed to impart energy to the flow and produce rotation, rather than rotating flow in a stationary chamber.
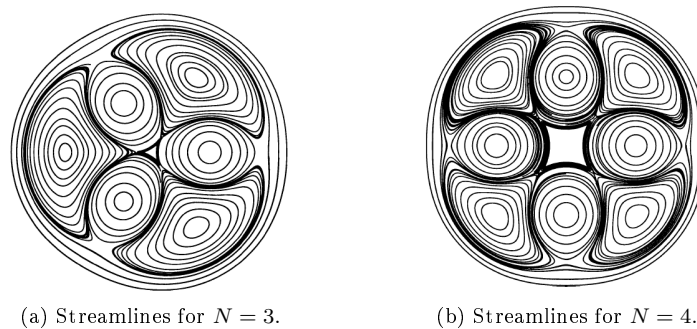

(a) Streamlines for $N = 3$.

(b) Streamlines for $N = 4$.

Figure F.26: $V-$state boundaries formed by polygonal satellite vortices. [53]

261

The fluid motion in the vortex chambers investigated are produced by the momentum of the flow at the tangential inlets of the chamber and the geometry is static, these combined may prevent rotation but provide sufficient shear stress to invoke polygonal structures. This does not account for the polygonal structures observed in the PVC boundary, which must be associated with a rotating configuration of satellite vortices within the vortex core. This obviously warrants further investigation, but considering the complex behaviour of confined bidirectional vortices and the numerous amount of mechanisms affecting the behaviour of the flow, prevents each individual mechanism being assessed and focus has to remain primarily on characterising the structure of the mantle.

In order to resolve the motion of these vortices using PIV it is necessary to either have the imaging equipment setup in a corotational configuration or otherwise ensure the exposures are phase locked, where the inter frame delay and exposure times are sufficiently small enough to properly characterise the flow. It is possible to resolve tertiary vortex motion from images acquired in the inertial frame of reference, but this requires a sufficiently large amount of images so that POD analysis can be performed. This allows for POD modes to be extracted, which identify tertiary motions associated with lower energy content from the primary vortex motion, which the majority of energy in the flow is responsible for producing. However, the motion of the flow extracted through POD analysis that occurs for higher order POD modes contains considerably less energy content than the initial POD mode that represents the mean behaviour of the entire flow. As a result of this, considerable effort is required to ensure that the PIV images acquired are accurate and exhibit a high SNR, as excessive noise adversely affect the tertiary motions resolved by POD analysis, which is sensitive to these errors that are inadvertently introduced. Unfortunately, the application of POD analysis was not considered with regards to the current investigation, and it was not possible to obtain any further insight into possible tertiary motions produced by a multipolar vortex array due to the influence of noise in the images acquired.

F.6 Swirl injector dynamics

A swirl injector is generally a small scale vortex chamber into which a liquid flow is injected tangentially at the head of the chamber and produces a vortex that propagates towards the outlet of the device. The geometry of a swirl injector can either be open ended or closed, where the chamber geometry can consist of a cylindrical tube with constant radius, or additionally incorporate a convergent section near the chamber outlet. These vortex devices are also known as pressure swirl atomisers or simplex atomisers, as the induced swirl results in the liquid annulus contained in the chamber geometry forming into a thin sheet as it exits the chamber, this then breaks up to form droplets due to shearing and Kelvin-Helmholtz instability. Swirl injectors provide a simple but effective solution to atomise liquids into spray form and are commonly employed within the injector plates of liquid rocket engines. Coaxial swirl injectors allow for effective mixing of both the liquid oxidiser and fuel within the spray sheet, in addition to increasing the surface of the propellant mixture upon entering the combustion chamber to increase combustion efficiency. The induced swirl causes a liquid annulus to be established, where the flow inside a swirl injector is multiphase and consists of both liquid and gaseous volume fractions that are separated by the free surface of the liquid, otherwise known as the boundary of the PVC. As with all vortex devices, there are many similarities in chamber design and they all operate in a similar manner, and are capable of producing a range of flow fields, but closed swirl injectors are specific examples of the liquid vortex chambers with head injectors investigated throughout this current study. Swirl injectors are prominent in the development of liquid rocket engines and there is considerable interest in fully characterising the dynamics of swirl injectors with regards to their influence on chamber acoustics and combustion instability [138]. As a result of this, studies regarding the dynamic response of swirl injectors hold particular relevance to the current study, as the solutions produced to explain the spectral characteristics of the vortices within swirl injectors are similarly applicable to many of the chamber configurations with head injectors investigated in this study.

During operation of rocket engines, instabilities can develop within the chamber and arise due the influence of various parameters, each of which are associated with a specific range of frequencies. These instabilities are generally categorised into three types. These include chugging, which is a low frequency oscillation associated with the coupling of the combustion chamber and the feed system, and occurs over a frequency range of $f = 10 - 400Hz$, but can usually be mitigated by increasing the pressure drop across the injectors to prevent upstream travelling waves. The second type of instability is known as buzzing, and occurs over a frequency range of $f = 400 - 1000Hz$ and is associated with the acoustic properties of the chamber, which are directly influenced by the dimensions and geometry of the chamber, in addition to the sonic velocity of the combustion gas. The third and most problematic type of instability is referred to as screaming, due to the sound produced by the engine during firing and occurs at frequencies above $f = 1000Hz$, where increased energy levels are associated with high frequency disturbances that can result in almost instantaneous destruction of the engine if not damped sufficiently. This is produced by combustion processes and the associated production of high frequency pressure waves, these can become coupled with the acoustic resonance properties of the chamber and can disrupt the thermal boundary layer at the chamber walls and melt holes in the chamber itself. Rocket engine combustion chambers and swirl injectors have similar geometry in that they are both cylindrical chambers that are closed at one end and consist of a convergent conical section at the other, which with regards to acoustic analysis can be effectively treated as a fully closed cylinder. The convergent section of the chamber dampens waves propagating longitudinally and reduces wave reflection, which is why the number of radial and tangential transverse modes in a combustion chamber is usually greater than the amount of axial modes [2]. The eigenfrequency solution for a cylindrical chamber with closed ends is expressed by eqn F.23, where the eigenvalue λ_{km} is associated with the transverse chamber modes, these are the azimuth and radial modes respectively [138]. Despite the solution describing a simple cylindrical geometry, it is clear that the resonant frequencies of the geometry are affected by the axial and radial dimensions of the chamber, as well as the sonic velocity.

$$f_{kmn} = \frac{c}{2\pi} \left(\frac{\lambda_{km}^2}{R^2} + \frac{z^2 \pi^2}{L^2} \right)^{\frac{1}{2}} \tag{F.23}$$

Acoustic characterisation of a combustion chamber is initially conducted under non reacting flow conditions as it provides a reliable method for determining the acoustic response of the chamber during operation, as the eigenfrequencies are multiplied by a scale factor related to the respective sonic velocities. The acoustic pressure amplitudes of the transverse modes occur at different positions in the chamber, with tangential modes characterised by a node at the centre of the chamber and an antinode at the periphery of the chamber, while this is the reverse for radial modes. Liquid rocket engines are particularly susceptible to tangential modes, as the antinode at the periphery of the chamber coincides with the approximate position of the thermal boundary layer, which can become disturbed by excessive pressure oscillations and result in damage to the chamber. Destructive instabilities such as these need to be minimised to ensure safe operation of the engine, and necessitates the addition of acoustic resonators at the periphery of the injector plate where pressure oscillations can be significant, while acoustic resonators located at the centre of the faceplate are employed to dampen radial modes. There are several techniques available for damping transverse modes, but it is common practice now to incorporate additional acoustic cavities in either the form of quater-wave or Helmholtz resonators that are tuned to the resonant frequencies of the chamber and absorb the energy of the pressure oscillations. Controlling combustion instability is a widespread problem and an important issue with regards to rocket engine design, which means that numerous studies have investigated methods for minimising the undesirable effects it can have. Many different types of injector designs exist, which all produce various acoustic responses, and there is currently no defined guidelines for matching specific injector designs with combustion chambers in order to prevent instabilities due to the complex mechanisms involved [54]. However, it is possible to produce reliably accurate analytical models of instability suppression devices such as acoustic resonators, as their behaviour is relatively easier to characterise and involves less unknown variables. Examples of a Helmholtz resonator and quarter-wave resonator can be seen in fig F.27a and F.27b respec-

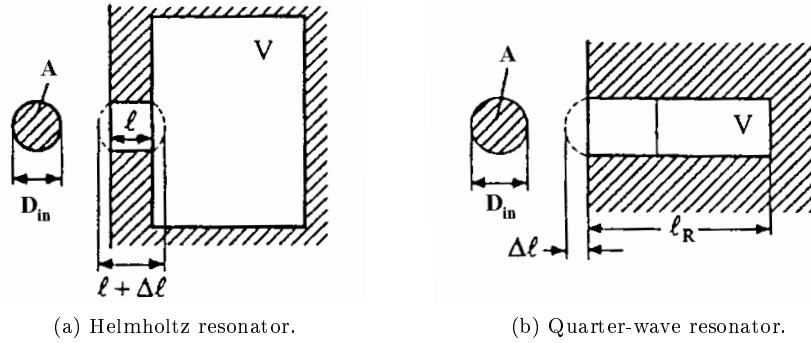(a) Helmholtz resonator.   (b) Quarter-wave resonator.

Figure F.27: Resonant cavities used for acoustic damping in liquid rocket engines. [54]

tively, while expressions describing their fundamental eigenfrequencies are given by eqns F.24 and F.27 respectively. It can be seen that while the geometry of the quarter-wave resonator is a simple cylindrical cavity closed at one end, the Helmholtz resonator is a cylindrical cavity with a smaller cylindrical inlet, replicating the effective geometry of swirl injectors and vortex chambers alike. As the acoustic properties of a chamber are determined primarily by the chamber geometry, it means that an analysis of a Helmholtz resonator will be equally applicable to other devices with similar geometries.

$$f_0 = \frac{c}{2\pi} \left(\frac{A}{v \left(l + \triangle l \right)} \right)^{\frac{1}{2}} \tag{F.24}$$

$$f_0 = \frac{c}{4 \left(l_R + \triangle l \right)} \tag{F.25}$$

While swirl injectors do have similar geometry to Helmholtz resonators, any analysis of swirl injectors need to additionally consider the effects of the confined liquid vortex and how that may affect the dynamic characteristics of the device. The problem of swirl injector dynamics was initially investigated by Bazarov [139], who established an analytical framework that incorporates both the swirling motion of the flow and the free surface created by the rotation of the liquid phase. An analytical linear wave theory was applied by Bazarov, that states that the free surface of the PVC is subject to small disturbances that propagate in the axial direction. The flow is assumed to be 2D, axisymmetric, incompressible, inviscid and omits surface tension effects to simplify the problem, and also means that the small disturbance assumption is valid, as wave energy is not dissipated by fluid viscosity. Both the geometry of the chamber and the gaseous core are simplified, where the convergent section of the chamber is omitted in place of a single cylindrical section, while the expansion of the PVC radius in the entrance of the nozzle section is modelled as a step, as seen in fig F.28. The radius of the core within the vortex chamber is constant, and does not account for the reduced radius that occurs at the head of the chamber where the axial component of the flow is negligible. Therefore this results in a larger tangential component and means that in order the conserve angular momentum the radius of the core must decrease. The free surface boundaries of the simplified core geometry are parallel to the chamber axis, and therefore waves propagating along the core are limited to travel in either positive or negative axial directions. This means that while wave reflection is observed, there is no accounting for wave refraction that physically occurs at the transition points of the core, where the radius varies due to the influence of local axial acceleration of the bulk flow.

The solution provided by Bazarov is based on the wave analysis performed by Kelvin [124] of a hollow vortex column, where the radius of the vortex core represents the boundary between two fluids and is equivalent to the free surface that occurs in swirl injectors. The liquid region of the flow is described by an irrotational free vortex, while the inner region of the flow is assumed to be quiescent and effectively has no influence on the structure of the vortex core. The long wave approximation
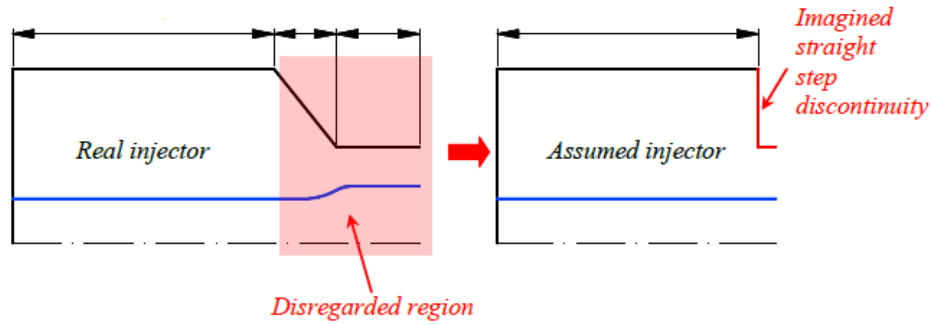
Figure F.28: Idealised swirl injector geometry. [17]

$\lambda \gg r_{SBR}$ that Kelvin employed in other similar analyses of vortex columns as discussed previously is applied, which means that the analysis is valid for low frequency disturbances. The long wave approximation also assumes that the magnitude of the radial velocity is negligible in comparison to the axial velocity and that the wave speed is not dependent upon the disturbance frequency, which means that the wave solution is non-dispersive. By assuming that the free surface is perturbed by small disturbances, it enables linearisation of the governing flow equations, so that the amplitude of the free surface wave can be precisely characterised in terms of the fluctuating and steady state values of the mass flow rate and the pressure drop. Bazarov determined separate response functions for the inlet, vortex chamber and nozzle, so that they could be combined to produce an overall expression for the response of the swirl injector, where the specific wave types are detailed in fig F.29. Plane waves are produced by the initial disturbance originating in the inlets, these perturb the the free surface and cause it to oscillate, which results in both surface and vorticity waves within the chamber. The surface waves are caused by the periodic deflection of the free surface at the head end of the core and can propagate in either axial direction along the core. Vorticity waves are the result of periodic fluctuations in the radial velocity and can propagate in either radial direction within the liquid fluid region, bounded by the free surface of the core and the periphery of the chamber. The plane waves that occur within the inlets were produced empirically by Bazarov [139, 140] through use of a pulsed water supply, this replicates the inlet mass flow rate fluctuations described by the analytical theory that induce oscillations of the free surface. Also electrodes were placed within the outlet section of the chamber so that the thickness of the liquid annulus could be measured through electrical conductivity with respect to time, revealing the frequency and amplitude of the surface waves. It was found that there was a reasonable correlation between the analytical and experimental results which predicted the maximum amplitude of the surface waves, although this was only noticeable below perturbation frequencies of $f = 1000Hz$. This is possibly due to the long wave approximation employed by the analytical theory, which is no longer valid at higher frequencies where the wavelength of the disturbance is comparable to the chamber geometry.

Despite several issues regarding the solution produced by Bazarov, it provides a vital foundation for following more comprehensive treatments of the dynamic response of swirl injectors. A study by Ismailov [17, 109, 141] focused on further developing the work of Bazarov, by considering additional effects such as both wave reflection and refraction, where the original step profile of the core is replaced with the smooth contour that is observed during operation, as depicted in fig F.30. Wave reflection was considered by Bazarov, but it was only applicable to disturbances propagating downstream because the local flow velocity in the nozzle region exceeds the wave speed, therefore preventing it from propagating upstream. Ismailov investigated wave reflection further and incorporated wave reflection in both streamwise directions into the analysis, so that at each discontinuity in the free surface of the core, part of the wave energy would be transmitted while the rest in reflected. As with the analysis of Bazarov, a node exists at the head wall of the chamber and an antinode at the entrance to the nozzle, as seen in fig F.30, which in combination with wave reflection causes standing waves to be produced by oblique reflections. Wave dynamics in a swirl injector is akin to that of wave propagation in a harbour, where a significant fractional variation in depth within a
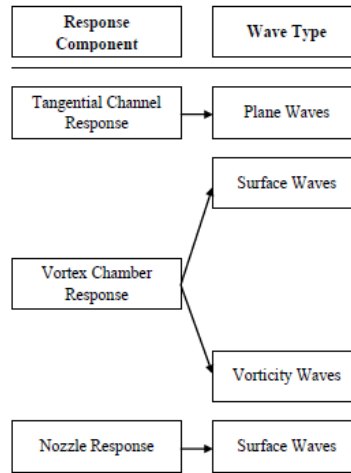
265

Figure F.29: Response characteristics of individual injector components. [17]

single wavelength such as the intersection between the chamber and nozzle, will scatter an incident wave and results in an appreciable amount of wave reflection. The formation of a wave at any plane boundary of a fluid medium will generate a pattern of standing waves in the fluid [17]. The amplitude of a standing wave is therefore dependent upon the reflection and transmission coefficients of the chamber, which dictate the properties of the wave. These coefficients are dependent on the frequency of the disturbance, where the maximum amplitude will occur when the frequency matches the resonant frequency of the chamber. Therefore, when the chamber geometry in close proximity to discontinuities in the free surface core, it is responsible for the reflection and transmission coefficients of the wave and will effectively determine the maximum possible amplitude of a standing wave. In fig F.30 the convergent section associated with swirl injector design is incorporated, and the effects of the convergent section angle were assessed to determine the influence the chamber geometry had upon the characteristics of both the transmitted and reflected parts of the incident surface wave. It was found that as the convergent section angle of the chamber tended towards $\theta = 90°$ this resulted in greater reflection coefficients suitable for producing standing waves with large amplitudes. Reducing the convergent section angle towards $\theta = 0°$ resulted in less wave reflection, but greater transmission coefficients as expected, because the geometry tended towards an open end swirl tube where no appreciable flow discontinuities occur that can cause wave reflection. The increased wave amplitude that can be seen to occur in the unsteady free surface of the core in the nozzle section of fig F.30 is due to the local reduction in wavelength, that results in a larger amplitude to conserve wave energy.
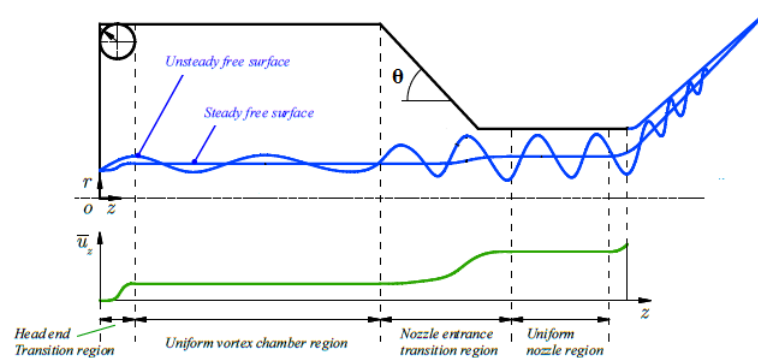

Figure F.30: Axial profile of liquid free surface and oscillation amplitude. [17]

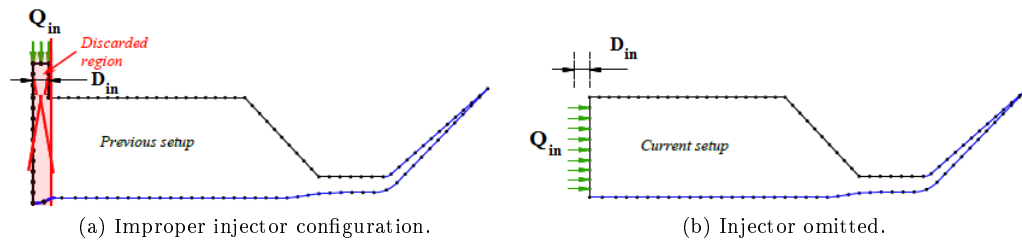(a) Improper injector configuration.   (b) Injector omitted.

Figure F.31: BEM numerical domains of a swirl injector. [17]

Ismailov also developed a 2D, axisymmetric, incompressible and irrotational boundary element method (BEM) code to investigate the nonlinear dynamic response of swirl injectors [141] based on previous studies by Park [142] and Richardson [143]. A diagram of the BEM domain is included in fig F.31b and indicates how the inlet section is omitted, unlike the previous studies seen in fig F.31a, as it better replicates the boundary conditions of the analytical solutions. Various parameters relating to chamber length and inlet flow conditions were investigated, with the calculated results then compared to those predicted by the abrupt convergence resonance model (ACRM) and the conical convergence resonance model (CCRM). These analytical models relate to chamber geometries similar to those investigated by Bazarov and chambers incorporating a conical convergent section respectively, where the resonant frequencies of the chambers were used to identify any correlation between each method and existing experimental data. Bazarov conducted experiments to assess the validity of the initial solution but details regarding the design of these swirl injectors are unavailable, meaning additional studies are required to fully assess the effectiveness of the solutions provided by Ismailov. Despite this, it was found that swirl injector resonance is comparable to that of a quarter-wave oscillator and similarly exhibits a node and an antinode at the head and base ends of the chamber respectively. When in resonance, large dimensionless pulsations in the outlet mass flow rate were found to occur, these are significantly greater than the dimensionless pressure drop perturbations applied in lieu of inlet geometry. This further reinforces the notion that the spectral characteristics of the core are affected by pulsations occurring in the inlets, as the oscillating mass flow rate at the outlet can only be produced by a similar oscillating mass flow rate at the inlet, to ensure conservation of mass. Regarding chamber geometry, the analytical and numerical solutions found that the chamber radius had the greatest effect on injector resonance, where a decrease in radius resulted in reduced response at lower frequencies, although the resonant peaks became more defined. By increasing the length of the chamber it was found that the injector response increased at lower frequencies, but when relatively short chambers were investigated there was a fundamental difference in the character of the response, where broad resonant peaks were observed instead. The dimensions of the chamber were found to have a strong effect on the injector response, but this was not the case for the convergent section of the nozzle where the influence of length was negligible, although larger convergence angles did improve injector response and produce better defined resonant peaks. The fundamental resonant peaks predicted by the ACRM model compare favourably with the BEM results, although the CCRM model consistently under predicted these frequencies, and the discrepancy is purported to be caused by the additional physics considered by the solution. The ACRM model was in consistent agreement with the numerical results and experimental data, where applicable it provides a valuable design tool for initial determination of a swirl injectors dynamic response when the convergence angle is sufficiently large. The ACRM model predicts the same resonant frequencies as found by the expression in eqn F.26, which result from simple wave analysis and provide a readily available method for determining resonance in terms of chamber geometry. Overall, Ismailov shows that unsteady injector flow is responsible for both refraction and reflection of disturbance waves, and that injector response is determined by the resonant properties of the vortex chamber. Therefore, hydrodynamic instability is inherently linked with spatial instability as it provides the forcing mechanism affecting injector response, and the frequency of the free surface disturbance is defined by the frequency of the initial disturbance originating at the inlets.

267

$$f_0 = n\frac{\pi}{2L}\left((u_\phi r)^2 \frac{R^2 - r_c^2}{2r_c^4}\right)^{\frac{1}{2}} \quad n = 1, 3, 5, ... \tag{F.26}$$

A recent study by Ahn et al [55] aims to corroborate the findings of Ismailov by providing experimental data for two vortex chamber designs that are fed by an oscillating liquid supply, in order to assess how perturbation of the inlet mass flow rate affects of the the dynamics of the injector up to frequencies of $f = 500Hz$. High speed images were acquired in the meridional plane of the chamber so that any variation in the structure of the air core could be discerned with respect to the perturbation frequency with a steady state mass flow rate at the inlet, resulting in deformation of the PVC or variation in the cone spray angle at the outlet. At certain frequencies the free surface was observed to deflect significantly, this can be seen by the marker in fig F.32a and F.32b which relate to the peak and trough of the surface wave respectively. Initially, correlation between the resonant frequencies of the air core and those predicted by the ACRM model of Ismailov [109] were poor, but this was attributed to a water hammer effect that was induced by the pulsating feed system. After a correction was applied to the analytical solution to account for the variation in manifold pressure caused by the water hammer effect, it was found that the resonant frequency of the fundamental mode displays an excellent correlation to those obtained empirically. This corroborates the effectiveness of the ACRM model for determining the fundamental mode, but more importantly confirms that the perturbation frequency is identical to that of the air core oscillation frequency. Additionally, surface waves were observed to propagate downstream even when the wave was not in resonance, which confirms the behaviour of the vortex core predicted by Bazarov [139].

Another recent study by Chung et al [106] investigating the effects of inlet flow pulsation in swirl injectors recreates the experimental setup first employed by Bazarov, in order to assess the effects of the inlet perturbation frequency upon the mass flow rate at the outlet. A general observation irrespective of perturbation frequency, was that as the diameter of the chamber was decreased and the length of the chamber increased, the steady state mass flow rate through the chamber increases. The total pressure at the inlet remained constant for all chamber configuration, and therefore means that as the chamber aspect ratio decreases the static pressure within the chamber must increase, so the mass flow rate at the inlets is reduced, as observed in the current investigation. Apart from this, it was found that as the inlet perturbation frequency is increased, this is reflected by the frequency of the mass flow rate oscillations observed at the outlet, corroborating the findings of Ahn et al [55]. As the chamber aspect ratio is increased, the amplitude of the oscillation in the mass flow rate reduced and infers that a high aspect ratio promotes stability in the PVC, which is desirable with regards to instabilities in combustion chambers. However, conversely this suggests that a low chamber aspect ratio is more susceptible to mass flow oscillations of larger amplitudes, which may provide sufficient energy to perturb transverse chamber modes, especially if coupled with the an axial chamber mode.

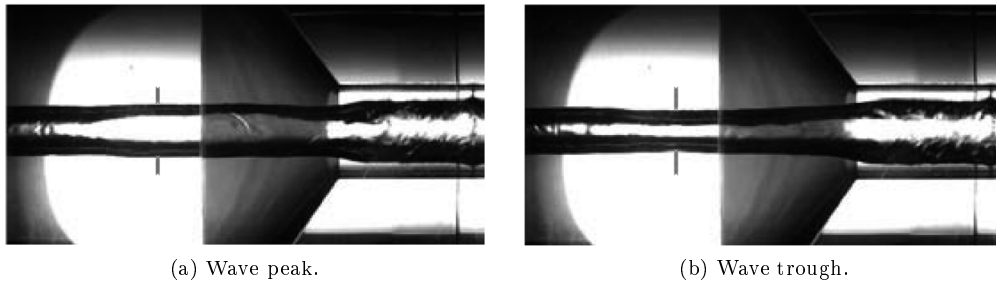(a) Wave peak.   (b) Wave trough.

Figure F.32: Axial wave propagation along liquid free surface. [55]

Experimental and numerical evidence of vorticity waves observed in confined rotating fluids previously referred to, finds that vorticity waves are actually the result of inertial waves, and that the radial nodal structure of the vorticity waves coincides with that of the inertial wave structure. Therefore, if surface waves are responsible for vorticity waves, then the propagation of axial disturbances along the vortex core is representative of the axial perturbations produced by the oscillating disc employed in the experiments by Fultz, as the axial oscillation frequency of the disc was found to be the determining factor in producing inertial modes. This implies that the oscillation frequency of the surface waves travelling along the core is responsible for the wave structure of the vorticity waves. However more importantly, the frequency of the surface waves determines the characteristics of the embedded inertial waves, and if the core oscillates at the same frequency as the resonant modes of the chamber then specific inertial modes will occur, which produce defined vortex cells associated with mantle structures. Regarding confined vortices, Gupta et al [3] stated that at points where the natural resonant frequency of the enclosure and the frequency of the PVC coincide, high intensity oscillations are expected. This means that it is possible for the resonant modes of the chamber geometry to be perturbed by the spectral characteristics of the PVC, where the resonant frequencies of the chamber are identical to those of the inertial modes. Therefore, this allows for specific mantle structures to be invoked, that produce predetermined vortices, if the axial oscillation frequency of the PVC can be manipulated so that they coincide with the resonant characteristics of the chamber. This has proven to be possible through pulsation of the inlet flow in swirl injectors and provides a possible mechanism for controlling the mantle structure within vortex rocket engines.